

EARTHQUAKE-RESISTANT T-SHAPED CONCRETE WALLS WITH HIGH-STRENGTH REINFORCEMENT

by

Erick Antonio Burgos Ganuza

M.S., State University of New York at Buffalo, 2006

B.S., Universidad Centroamericana “José Simeón Cañas”, 2002

Submitted to the graduate degree program in the Department of Civil, Environmental and Architectural Engineering and the Graduate Faculty of The University of Kansas in partial fulfillment of the requirements for the degree of Doctor of Philosophy.

Chair: Andrés Lepage

Rémy D. Lequesne

Matt O'Reilly

Masoud Darabi

Juan Bravo-Suárez

Date Defended: August 28, 2018

The Dissertation Committee for Erick Antonio Burgos Ganuza certifies
that this is the approved version of the following dissertation:

**EARTHQUAKE-RESISTANT T-SHAPED CONCRETE WALLS
WITH HIGH-STRENGTH REINFORCEMENT**

Chair: Andrés Lepage

Date Approved: September 4, 2018

ABSTRACT

This study examined the effects of the mechanical properties of high-strength reinforcement on the seismic behavior of concrete walls. The primary variables were the yield strength f_y and the tensile-to-yield strength ratio f_t/f_y . Two large-scale T-shaped structural walls were subjected to reversed cyclic loading to assess their strength and deformation capacity. Test results were compared with data from walls recently tested by Huq et al. (2017) at The University of Kansas to evaluate the influence of the uniform elongation ε_{su} and the fracture elongation ε_{sf} , in addition to f_y and f_t/f_y of high-strength reinforcement, on the deformation capacity of concrete walls subjected to reversed cyclic displacements.

Two walls were tested, one with Grade 120 (830) reinforcement (Wall T5), the other with Grade 100 (690) reinforcement (Wall T6). Confined boundary elements were provided at the three tips of the T section to concentrate the main flexural reinforcement (No. 6 or 19 mm bars) enclosed by No. 3 (10 mm) hoops. Outside the boundary elements, No. 4 (13 mm) bars were used as longitudinal and transverse reinforcement. The nominal concrete compressive strength of 8 ksi (55 MPa) and wall dimensions were kept constant in both specimens with a wall thickness of 10 in. (25 mm) and height-to-length ratio of 3. Wall stem and flanges were 100-in. (2540-mm) long. The axial load was limited to the self-weight and the weight of the testing apparatus. The T-shaped cross section allowed a shallow neutral axis depth (within the flange) at flexural nominal capacity and induced large tensile strain demands in the main flexural reinforcement (within the stem). The specimens were designed such that flexural behavior controlled their response inducing a maximum shear stress of approximately $4\sqrt{f'_c}$, psi ($0.33\sqrt{f'_c}$, MPa). The design of the specimens complied with ACI Building Code (ACI 318-14) and incorporated the additional detailing recommendations in ATC 115 for Grade 100 reinforcement.

Wall T6 with Grade 100 (690) reinforcement had similar strength and deformation capacity to the four walls tested by Huq et al. (2017) at The University of Kansas with Grade 60 (420) reinforcement in T1 and Grade 100 (690) reinforcement in T2, T3, and T4. These walls had a drift ratio capacity not less than 3% if the tensile-to-yield strength ratio (f_t/f_y) of the flexural reinforcement was greater than 1.18, the uniform elongation (ϵ_{su}) was greater than 6%, and the fracture elongation (ϵ_{sf}) was greater than 10%. Wall T5 had a drift ratio capacity of 2.3% with Grade 120 (830) reinforcement having $f_t/f_y = 1.32$, $\epsilon_{su} = 5.3\%$, and $\epsilon_{sf} = 8.6\%$.

Moment-curvature analyses were conducted to support the development of closed-form solutions for estimating the deformation capacity of the walls and strain demands on reinforcing bars and concrete. Formulations were derived to include deformations due to shear and strain penetration (or bond slip) to provide conservative (safe) estimates of deformation capacity and strain demands.

ACKNOWLEDGMENTS

Primary financial support for the experimental program was provided by Commercial Metals Company and MMFX Technologies Corporation. Additional support was provided by the Ministry of Education of the Government of El Salvador through a FANTEL “Talento Salvadoreño” scholarship and by the Universidad Centroamericana “José Simeón Cañas”.

I would like to express my eternal gratitude to the hands that got dirty to make possible this project. A special thanks goes to the Laboratory Coordinator David Woody and the Laboratory Technologist Kent Dye for their support throughout the construction and demolition of the specimens. I am also very grateful to undergraduate students involved in the project: Samantha Sosa, Peter Madrigal, Jesus Leos, Lilly Scott, Jhonatan Batrez, Bruno Soria, Eslam Elattar, and Logan Yanisch.

Thanks are due to my peer graduate students for their help and advice during the experimental work, specially Ashwin Poudel and Eduardo Guillen. Particular thanks to Samir Yasso for his bright and practical solutions to technical issues found during the construction of the specimens. Special appreciation is also expressed to Mohammad Sajedul Huq who shared his technical expertise and to Alexander Weber-Kamin for his friendship, companionship, goodness, and sense of humor. This endeavor could not have been possible without the friendship of Abdalkader Al-Sabawy, Muna Hano, Chaohui Li, Ryan Landreneau, Amin Najvani, Shahedreen Ameen, Ali Ajaam, Danqing Yu, and Luay Nazzal.

I express my sincere gratitude to my advisors, Dr. Andrés Lepage and Dr. Rémy Lequesne for their guidance, comments, and patience throughout this research endeavor and for letting me be part of their research group as an apprentice. The long discussions we had together helped shape my understanding of the behavior of reinforced concrete structures. Their willingness to

share their knowledge and expertise is fully appreciated. I also would like to thank the other committee members: Dr. Matt O'Reilly, Dr. Masoud Darabi, and Dr. Juan Bravo-Suárez for their time and comments that helped improved the manuscript.

Finally, my joy shows no bounds to express my gratitude to my lovely wife Esmeralda and daughter Amelia for their encouragement and unconditional support throughout my studies. Their love, smiles, company, patience, and time, gave me strength to accomplish this life goal.

TABLE OF CONTENTS

ABSTRACT	iii
ACKNOWLEDGMENTS	v
LIST OF TABLES.....	x
LIST OF FIGURES.....	xii
1 INTRODUCTION	1
1.1 Problem Statement	1
1.2 Objectives and Scope.....	2
1.3 Organization.....	3
2 PREVIOUS STUDIES.....	5
2.1 Overview.....	5
2.2 High-Strength Steel.....	6
2.3 Concrete Members with High-Strength Reinforcement.....	7
2.4 High-Strength Reinforcement in Building Codes	9
3 EXPERIMENTAL PROGRAM	12
3.1 Design of Specimens.....	13
3.2 Material Properties.....	14
3.3 Construction of Specimens.....	15
3.4 Test Setup.....	16
3.4.1 Description.....	16
3.4.2 Instrumentation.....	17
3.4.3 Loading Protocol.....	19
4 EXPERIMENTAL RESULTS	20
4.1 Measured Shear versus Drift Ratio.....	20

4.2	Damage Progression.....	22
4.3	Reinforcement Strains.....	24
4.3.1	Stem Longitudinal Reinforcement.....	25
4.3.2	Flange Longitudinal Reinforcement	27
4.3.3	Transverse Reinforcement.....	28
4.3.4	Reinforcement Strain Comparisons.....	29
4.4	Concrete Strains	30
4.4.1	Stem Longitudinal Strains	31
4.4.2	Flange Longitudinal Strains.....	34
4.4.3	Concrete Strain Comparisons	35
4.5	Drift Components	37
4.5.1	Shear Component.....	37
4.5.2	Base Shearing Component	40
4.5.3	Flexural Component.....	41
4.5.4	Base Opening Component	43
4.5.5	Drift Component Comparisons.....	44
4.6	Crack Widths.....	46
4.7	Wall Elongation	47
4.8	Wall Stiffness	49
4.8.1	Effective Initial Stiffness.....	49
4.8.2	Unloading Stiffness	51
4.9	Hysteretic Behavior	52
4.9.1	Takeda Model.....	52
4.9.2	Energy Dissipation.....	53
4.9.3	Modeling Parameters	54
5	WALL RESPONSE COMPARISONS.....	56
5.1	Wall Properties.....	56

5.2	Shear versus Drift Ratio	58
5.3	Reinforcement Strain Envelopes	59
5.4	Concrete Strain Envelopes.....	60
5.5	Deformation Components.....	61
5.6	Effective initial stiffness and Unloading Stiffness	61
5.7	Hysteretic Behavior	63
6	ESTIMATES OF DEFORMATION CAPACITY AND STRAIN DEMANDS	64
6.1	Material Models.....	64
6.1.1	Concrete Stress-Strain Relationships.....	64
6.1.2	Steel Stress-Strain Relationships	65
6.2	Moment-Curvature Analysis.....	65
6.2.1	Computed Results	66
6.3	Displacement Capacity	68
6.3.1	Analytical Models.....	68
6.3.2	Computed Results	72
6.4	Strain Estimates	73
6.4.1	Analytical models.....	73
6.4.2	Computed Results	75
7	CONCLUDING REMARKS.....	76
8	REFERENCES.....	79
	TABLES	89
	FIGURES.....	117
	APPENDIX A: NOTATION.....	318
	APPENDIX B: POST-YIELD STRAIN PENETRATION	325

LIST OF TABLES

Table 1 – Summary of required mechanical properties for deformed reinforcing bars in ASTM standards.....	90
Table 2 – Historical development of high-strength steel as concrete reinforcement.....	90
Table 3 – Summary of test program.....	92
Table 4 – Loading protocol	93
Table 5 – Computed nominal flexural strength	94
Table 6 – Dates for specimen casting and testing.....	95
Table 7 – Proportions for concrete mixture.....	96
Table 8 – Concrete strength measured at test day	97
Table 9 – Reinforcing steel properties.....	98
Table 10 – Maximum measured shear force and drift ratio.....	99
Table 11 – Drift cycle and bar location where bar buckling or bar fracture first occurred.....	100
Table 12 – Secant stiffness from measured shear-drift envelope	101
Table 13 – Wall data for cracked stiffness calculation	102
Table 14 – Unloading stiffness derived from measured shear versus drift ratio	103
Table 15 – Modeling parameters for nonlinear analysis.....	104
Table 16 – Measured concrete strength at test day for walls tested at The University of Kansas.....	105
Table 17 – Reinforcing steel properties for walls tested at The University of Kansas.....	106
Table 18 – Computed nominal flexural strength for walls tested at The University of Kansas	107
Table 19 – Stress-strain parameters for concrete	108
Table 20 – Stress-strain parameters for reinforcing steel.....	109

Table 21 – Maximum measured shear force and drift ratio for walls tested at The University of Kansas	110
Table 22 – Moment-curvature data.....	111
Table 23 – Plastic hinge length for Model B	112
Table 24 – Deformation capacity determined using Model A1 based only on flexural deformations (concrete compressive strain limited to 0.015)	113
Table 25 – Deformation capacity using Model B1 based only on flexural deformations (concrete compressive strain limited to 0.015).....	114
Table 26 – Deformation capacity using Model A2 based on flexure, shear, and strain penetration (concrete compressive strain limited to 0.015)	115
Table 27 – Deformation capacity using Model B2 based on flexure, shear, and strain penetration (concrete compressive strain limited to 0.015)	116
Table B.1 – Strain penetration amplification factor α_{sp} based on Eq. B.12.....	331
Table B.2 – Strain penetration amplification factor α_{sp} based on Eq. B.12.....	332

LIST OF FIGURES

Figure 1 – Percentage of cost per building type	118
Figure 2 – Failures in reinforced concrete structural walls after the Maule (Chile) 2010 earthquake	118
Figure 3 – Failures in reinforced concrete structural walls after the Christchurch (New Zealand) 2011 earthquake	118
Figure 4 – Reinforcement layout for wall T5 and T6.....	119
Figure 5 – Confined boundary element in stem of T5 and T6	120
Figure 7 – Reinforcement data and wall section properties	121
Figure 8 – Typical wall elevation.....	122
Figure 9 – Illustration of loading protocol described in Table 9.....	123
Figure 10 – Measured stress versus strain for No. 6 (19) bars.....	124
Figure 11 – Measured stress versus strain for No. 4 (13) bars.....	125
Figure 12 – Construction stages	127
Figure 13 – Test setup.....	128
Figure 14 – Steel spreader beams below laboratory strong floor for base block hold-downs.....	129
Figure 15 – Wall instrumentation (elevation view of wall stem).....	130
Figure 16 – Wall instrumentation (elevation view of wall flange)	131
Figure 17 – Locations of optical markers on wall stem.....	132
Figure 18 – Locations of optical markers on wall flange.....	132
Figure 19 – Plan view of base block indicating locations of optical markers, B1 through B9 and S1 through S6	133
Figure 20 – Strain gauge locations in T5.....	134

Figure 21 – Strain gauge locations in T6.....	135
Figure 22 – Shear versus drift ratio for T5	136
Figure 23 – Shear versus drift ratio for T6	136
Figure 24 – Shear versus drift ratio for T5 indicating fracture of longitudinal bars.....	137
Figure 25 – Shear versus drift ratio for T6 indicating fracture of longitudinal bars.....	137
Figure 26 – Map of buckled bars	138
Figure 27 – Map of fractured bars	138
Figure 28 – Wall T5 at 1% drift ratio (second cycle)	139
Figure 29 – Wall T6 at 1% drift ratio (second cycle)	139
Figure 30 – Wall T5 at 2% drift ratio (second cycle)	140
Figure 31 – Wall T6 at 2% drift ratio (second cycle)	140
Figure 32 – Wall T5 at 3% drift ratio (first cycle)	141
Figure 33 – Wall T6 at 3% drift ratio (second cycle)	141
Figure 34 – Wall T5 at 4% drift ratio (first cycle)	142
Figure 35 – Wall T6 at 4% drift ratio (first cycle)	142
Figure 36 – Wall T5 without buckled bars in confined and unconfined stem during second cycle to 2% drift ratio (stem in compression)	143
Figure 37 – Wall T5 with fractured bars in confined and unconfined stem during first cycle to 3% drift ratio (stem in tension)	143
Figure 38 – Wall T6 with buckled bars in confined stem during second cycle to 3% drift ratio (stem in compression)	144
Figure 39 – Wall T6 with fractured bars in confined stem during second cycle to 3% drift ratio (stem in tension).....	144

Figure 40 – Wall T6 with buckled bars in unconfined flange during second cycle to 3% drift ratio (stem in tension).....	145
Figure 41 – Wall T6 with fractured bars in unconfined stem during first cycle to 4% drift ratio (stem in tension).....	145
Figure 42 – Condition of confined stem in compression leading to bar fracture in T5	146
Figure 43 – Condition of confined stem in compression leading to bar buckling before bar fracture in T6	146
Figure 44 – Condition of stem in T5 at peak of second cycle to 2% drift ratio.....	147
Figure 45 – Condition of stem in T6 at peak of second cycle to 2% drift ratio.....	148
Figure 46 – Condition of flange in T5 at peak of second cycle to 2% drift ratio	149
Figure 47 – Condition of flange in T6 at peak of second cycle to 2% drift ratio	150
Figure 48 – Measured strain in longitudinal bar at confined stem 18 in. (457 mm) below base of T5.....	151
Figure 49 – Measured strain in longitudinal bar at confined stem 18 in. (457 mm) below base of T6.....	151
Figure 50 – Measured strain in longitudinal bar at confined stem 18 in. (457 mm) below base of T5.....	152
Figure 51 – Measured strain in longitudinal bar at confined stem 18 in. (457 mm) below base of T6.....	152
Figure 52 – Measured strain in longitudinal bar at confined stem 9 in. (229 mm) below base of T5	153
Figure 53 – Measured strain in longitudinal bar at confined stem 9 in. (229 mm) below base of T6	153
Figure 54 – Measured strain in longitudinal bar at confined stem 9 in. (229 mm) below base of T5	154
Figure 55 – Measured strain in longitudinal bar at confined stem 9 in. (229 mm) below base of T6	154
Figure 56 – Measured strain in longitudinal bar at confined stem 0.5 in. (13 mm) above base of T5.....	155
Figure 57 – Measured strain in longitudinal bar at confined stem 0.5 in. (13 mm) above base of T6.....	155
Figure 58 – Measured strain in longitudinal bar at confined stem 0.5 in. (13 mm) above base of T5.....	156
Figure 59 – Measured strain in longitudinal bar at confined stem 0.5 in. (13 mm) above base of T6.....	156
Figure 60 – Measured strain in longitudinal bar at confined stem 0.5 in. (13 mm) above base of T5.....	157

Figure 61 – Measured strain in longitudinal bar at confined stem 0.5 in. (13 mm) above base of T6.....	157
Figure 62 – Measured strain in longitudinal bar at confined stem 25 in. (635 mm) above base of T5.....	158
Figure 63 – Measured strain in longitudinal bar at confined stem 25 in. (635 mm) above base of T6.....	158
Figure 64 – Measured strain in longitudinal bar at confined stem 25 in. (635 mm) above base of T5.....	159
Figure 65 – Measured strain in longitudinal bar at confined stem 25 in. (635 mm) above base of T6.....	159
Figure 66 – Measured strain in longitudinal bar at confined stem 50 in. (1270 mm) above base of T5	160
Figure 67 – Measured strain in longitudinal bar at confined stem 50 in. (1270 mm) above base of T6	160
Figure 68 – Measured strain in longitudinal bar at confined stem 50 in. (1270 mm) above base of T5	161
Figure 69 – Measured strain in longitudinal bar at confined stem 50 in. (1270 mm) above base of T6	161
Figure 70 – Measured strain in longitudinal bar at confined stem 100 in. (2540 mm) above base of T5	162
Figure 71 – Measured strain in longitudinal bar at confined stem 100 in. (2540 mm) above base of T6	162
Figure 72 – Measured strain in longitudinal bar at confined stem 100 in. (2540 mm) above base of T5	163
Figure 73 – Measured strain in longitudinal bar at confined stem 100 in. (2540 mm) above base of T6	163
Figure 74 – Measured strain in longitudinal bar at confined stem 144 in. (3660 mm) above base of T5	164
Figure 75 – Measured strain in longitudinal bar at confined stem 144 in. (3660 mm) above base of T6	164
Figure 76 – Measured strain in longitudinal bar at unconfined stem 2 in. (51 mm) above base of T5.....	165
Figure 77 – Measured strain in longitudinal bar at unconfined stem 2 in. (51 mm) above base of T6.....	165
Figure 78 – Measured strain in longitudinal bar at unconfined stem 25 in. (635 mm) above base of T5.....	166
Figure 79 – Measured strain in longitudinal bar at unconfined stem 25 in. (635 mm) above base of T6.....	166
Figure 80 – Measured strain in longitudinal bar at unconfined stem 50 in. (1270 mm) above base of T5.....	167
Figure 81 – Measured strain in longitudinal bar at unconfined stem 50 in. (1270 mm) above base of T6.....	167
Figure 82 – Measured strain in longitudinal bar at unconfined stem 100 in. (2540 mm) above base of T5	168
Figure 83 – Measured strain in longitudinal bar at unconfined stem 100 in. (2540 mm) above base of T6	168

Figure 84 – Measured strain in longitudinal bar at confined flange 2 in. (51 mm) above base of T5.....	169
Figure 85 – Measured strain in longitudinal bar at confined flange 2 in. (51 mm) above base of T6.....	169
Figure 86 – Measured strain in longitudinal bar at confined flange 2 in. (51 mm) above base of T5.....	170
Figure 87 – Measured strain in longitudinal bar at confined flange 2 in. (51 mm) above base of T6.....	170
Figure 88 – Measured strain in longitudinal bar at confined flange 50 in. (1270 mm) above base of T5.....	171
Figure 89 – Measured strain in longitudinal bar at confined flange 50 in. (1270 mm) above base of T6.....	171
Figure 90 – Measured strain in longitudinal bar at confined flange 50 in. (1270 mm) above base of T5.....	172
Figure 91 – Measured strain in longitudinal bar at confined flange 50 in. (1270 mm) above base of T6.....	172
Figure 92 – Measured strain in longitudinal bar at confined flange 100 in. (2540 mm) above base of T5.....	173
Figure 93 – Measured strain in longitudinal bar at confined flange 100 in. (2540 mm) above base of T6.....	173
Figure 94 – Measured strain in longitudinal bar at confined flange 100 in. (2540 mm) above base of T5.....	174
Figure 95 – Measured strain in longitudinal bar at confined flange 100 in. (2540 mm) above base of T6.....	174
Figure 96 – Measured strain in longitudinal bar at unconfined flange 2 in. (51 mm) above base of T5.....	175
Figure 97 – Measured strain in longitudinal bar at unconfined flange 2 in. (51 mm) above base of T6.....	175
Figure 98 – Measured strain in longitudinal bar at unconfined flange 25 in. (635 mm) above base of T5.....	176
Figure 99 – Measured strain in longitudinal bar at unconfined flange 25 in. (635 mm) above base of T6.....	176
Figure 100 – Measured strain in longitudinal bar at unconfined flange 25 in. (635 mm) above base of T5.....	177
Figure 101 – Measured strain in longitudinal bar at unconfined flange 25 in. (635 mm) above base of T6.....	177
Figure 102 – Measured strain in longitudinal bar at unconfined flange 50 in. (1270 mm) above base of T5.....	178
Figure 103 – Measured strain in longitudinal bar at unconfined flange 50 in. (1270 mm) above base of T6.....	178
Figure 104 – Measured strain in longitudinal bar at unconfined flange 100 in. (2540 mm) above base of T5.....	179

Figure 105 – Measured strain in longitudinal bar at unconfined flange 100 in. (2540 mm) above base of T6	179
Figure 106 – Measured strain in hoop at confined stem 1.5 in. (38 mm) above base of T5.....	180
Figure 107 – Measured strain in hoop at confined stem 1.5 in. (38 mm) above base of T6.....	180
Figure 108 – Measured strain in hoop at confined stem 1.5 in. (38 mm) above base of T5.....	181
Figure 109 – Measured strain in hoop at confined stem 1.5 in. (38 mm) above base of T6.....	181
Figure 110 – Measured strain in hoop at confined stem 1.5 in. (38 mm) above base of T5.....	182
Figure 111 – Measured strain in hoop at confined stem 1.5 in. (38 mm) above base of T6.....	182
Figure 112 – Measured strain in hoop at confined stem 4.5 in. (114 mm) above base of T5	183
Figure 113 – Measured strain in hoop at confined stem 4.5 in. (114 mm) above base of T6	183
Figure 114 – Measured strain in hoop at confined stem 4.5 in. (114 mm) above base of T5	184
Figure 115 – Measured strain in hoop at confined stem 4.5 in. (114 mm) above base of T6	184
Figure 116 – Measured strain in hoop at confined stem 4.5 in. (114 mm) above base of T5	185
Figure 117 – Measured strain in hoop at confined stem 4.5 in. (114 mm) above base of T6	185
Figure 118 – Measured strain in horizontal bar at unconfined stem 22.5 in. (572 mm) above base of T5.....	186
Figure 119 – Measured strain in horizontal bar at unconfined stem 22.5 in. (572 mm) above base of T6.....	186
Figure 120 – Measured strain in horizontal bar at unconfined stem 52.5 in. (1330 mm) above base of T5	187
Figure 121 – Measured strain in horizontal bar at unconfined stem 52.5 in. (1330 mm) above base of T6	187
Figure 122 – Envelopes of measured strain in longitudinal bars at confined stem for 1.5% drift ratio.....	188
Figure 123 – Envelopes of measured strain in longitudinal bars at confined stem for 2% drift ratio	189
Figure 124 – Envelopes of measured strain in longitudinal bars at confined flange for 1.5% drift ratio	190
Figure 125 – Envelopes of measured strain in longitudinal bars at confined flange for 2% drift ratio.....	191
Figure 126 – Envelopes of measured strain in longitudinal bars at unconfined flange for 1.5% drift ratio.....	192

Figure 127 – Envelopes of measured strain in longitudinal bars at unconfined flange for 2% drift ratio	193
Figure 128 – Calculated average concrete strain along Column 1 for stem of T5.....	194
Figure 129 – Calculated average concrete strain along Column 2 for stem of T5.....	195
Figure 130 – Calculated average concrete strain along Column 3 for stem of T5.....	196
Figure 131 – Calculated average concrete strain along Column 4 for stem of T5.....	197
Figure 132 – Calculated average concrete strain along Column 5 for stem of T5.....	198
Figure 133 – Calculated average concrete strain along Column 6 for stem of T5.....	199
Figure 134 – Calculated average concrete strain along Column 7 for stem of T5.....	200
Figure 135 – Calculated average concrete strain along Column 8 for stem of T5.....	201
Figure 136 – Calculated average concrete strain along Column 1 for stem of T6.....	202
Figure 137 – Calculated average concrete strain along Column 2 for stem of T6.....	203
Figure 138 – Calculated average concrete strain along Column 3 for stem of T6.....	204
Figure 139 – Calculated average concrete strain along Column 4 for stem of T6.....	205
Figure 140 – Calculated average concrete strain along Column 5 for stem of T6.....	206
Figure 141 – Calculated average concrete strain along Column 6 for stem of T6.....	207
Figure 142 – Calculated average concrete strain along Column 7 for stem of T6.....	208
Figure 143 – Calculated average concrete strain along Column 8 for stem of T6.....	209
Figure 144 – Calculated average concrete strain in Layer 1 for flange of T5.....	210
Figure 145 – Calculated average concrete strain in Layer 2 for flange of T5.....	211
Figure 146 – Calculated average concrete strain in Layer 3 for flange of T5.....	212
Figure 147 – Calculated average concrete strain in Layer 4 for flange of T5.....	213
Figure 148 – Calculated average concrete strain in Layer 5 for flange of T5.....	214
Figure 149 – Calculated average concrete strain in Layer 6 for flange of T5.....	215

Figure 150 – Calculated average concrete strain in Layer 1 for flange of T6.....	216
Figure 151 – Calculated average concrete strain in Layer 2 for flange of T6.....	217
Figure 152 – Calculated average concrete strain in Layer 3 for flange of T6.....	218
Figure 153 – Calculated average concrete strain in Layer 4 for flange of T6.....	219
Figure 154 – Calculated average concrete strain in Layer 5 for flange of T6.....	220
Figure 155 – Calculated average concrete strain in Layer 6 for flange of T6.....	221
Figure 156 – Envelopes of concrete strain for confined stem at 1.5% drift ratio (data from optical markers along Columns 1 and 2).....	222
Figure 157 – Envelopes of concrete strain for confined stem at 2% drift ratio (data from optical markers along Columns 1 and 2).....	223
Figure 158 – Envelopes of concrete strain for confined flange at 1.5% drift ratio (data from optical markers along Column 11).....	224
Figure 159 – Envelopes of concrete strain for confined flange at 2% drift ratio (data from optical markers along Column 11).....	225
Figure 160 – Envelopes of concrete strain for unconfined flange at 1.5% drift ratio (data from optical markers along Columns 8, 9, and 10).....	226
Figure 161 – Envelopes of concrete strain for unconfined flange at 2% drift ratio (data from optical markers along Columns 8, 9, and 10).....	227
Figure 162 – Shear component of displacement from Layer 2.....	228
Figure 163 – General deformed shape for a station.....	228
Figure 164 – Components of angular change for a station.....	228
Figure 165 – Calculated shear distortion for T5, data from optical markers, Columns 1 through 8.....	229
Figure 166 – Calculated shear distortion for T6, data from optical markers, Columns 1 through 8.....	230
Figure 167 – Base shearing displacement of T5 based on data from optical markers.....	231

Figure 168 – Base shearing displacement of T6 based on data from optical markers	231
Figure 169 – Calculated flexural rotation for T5, data from optical markers, Columns 1 through 8	232
Figure 170 – Calculated flexural rotation for T6, data from optical markers, Columns 1 through 8	233
Figure 171 – Wall T5 at a drift ratio of 3%	234
Figure 172 – Rotation due to base opening versus drift ratio for T5 (data from optical markers)	235
Figure 173 – Rotation due to base opening versus drift ratio for T6 (data from optical markers)	235
Figure 174 – Contribution of deformation components from bottom 87 in. (2210 mm) for T5.....	236
Figure 175 – Contribution of deformation components from bottom 87 in. (2210 mm) for T6.....	237
Figure 176 – Cumulative contribution of deformation components from bottom 87 in. (2210 mm) for T5 ...	238
Figure 177 – Cumulative contribution of deformation components from bottom 87 in. (2210 mm) for T6 ...	239
Figure 178 – Measured crack width at peak drift versus drift ratio, stem in compression (1 in. = 25.4 mm).	240
Figure 179 – Measured crack width at zero shear versus maximum drift ratio attained, stem in compression	241
Figure 180 – Measured crack width at peak drift versus drift ratio, stem in tension	242
Figure 181 – Measured crack width at zero shear versus maximum drift ratio attained, stem in tension	243
Figure 182 – Crack width ratio versus drift ratio for positive loading direction, stem in compression.....	244
Figure 183 – Crack width ratio versus drift ratio for negative loading direction, stem in tension	245
Figure 184 – Calculated elongation at zero shear for T5, data from optical markers, Columns 1 through 8 ...	246
Figure 185 – Calculated elongation at zero shear for T6, data from optical markers, Columns 1 through 8 ...	246
Figure 186 – Idealized force-displacement curve and hysteresis model.....	247
Figure 187 – Envelope of shear versus drift ratio for T5	248
Figure 188 – Envelope of shear versus drift ratio for T6	248
Figure 189 – Envelopes of shear versus drift ratio	249

Figure 190 – Effective initial stiffness K_e normalized by flexural stiffness based on gross section	250
Figure 191 – Cracked moment of inertia normalized by gross moment of inertia.....	250
Figure 192 – Unloading stiffness versus drift ratio.....	251
Figure 193 – Normalized unloading stiffness versus drift ratio	251
Figure 194 – Stiffness reducing exponent versus normalized displacement.....	252
Figure 195 – Comparison of measured response with Takeda hysteresis model for T5.....	253
Figure 196 – Comparison of measured response with Takeda hysteresis model for T6.....	253
Figure 197 – Shear versus drift ratio during first cycle to 1% drift ratio	254
Figure 198 – Shear versus drift ratio during first cycle to 1.5% drift ratio	254
Figure 199 – Shear versus drift ratio during first cycle to 2% drift ratio	255
Figure 200 – Shear versus drift ratio during first cycle to 3% drift ratio	255
Figure 201 – Hysteretic energy dissipation index.....	256
Figure 202 – Hysteretic energy dissipation index versus drift ratio.....	257
Figure 203 – Measured shear versus drift ratio compared with modeling parameters from Table 15.....	258
Figure 204 – Geometry and reinforcement layout for T1	259
Figure 205 – Geometry and reinforcement layout for T2 and T3	260
Figure 206 – Geometry and reinforcement layout for T4.....	261
Figure 207 – Geometry and reinforcement layout for T5 and T6	262
Figure 208 – Drift ratio versus uniform elongation of longitudinal reinforcing bars	263
Figure 209 – Drift ratio versus fracture elongation of longitudinal reinforcing bars.....	263
Figure 210 – Shear versus drift ratio.....	264
Figure 211 – Envelopes of measured strain in longitudinal bars at confined stem for 1.5% drift ratio.....	265
Figure 212 – Envelopes of measured strain in longitudinal bars at confined stem for 2% drift ratio	266

Figure 213 – Envelopes of measured strain in longitudinal bars at confined flange for 1.5% drift ratio	267
Figure 214 – Envelopes of measured strain in longitudinal bars at confined flange for 2% drift ratio	268
Figure 215 – Envelopes of measured strain in longitudinal bars at unconfined flange for 1.5% drift ratio.....	269
Figure 216 – Envelopes of measured strain in longitudinal bars at unconfined flange for 2% drift ratio	270
Figure 217 – Envelopes of concrete strain for confined stem at 1.5% drift ratio (data from optical markers along Columns 1 and 2).....	271
Figure 218 – Envelopes of concrete strain for confined stem at 2% drift ratio (data from optical markers along Columns 1 and 2).....	272
Figure 219 – Envelopes of concrete strain for confined flange at 1.5% drift ratio (data from optical markers along Column 11).....	273
Figure 220 – Envelopes of concrete strain for confined flange at 2% drift ratio (data from optical markers along Column 11).....	274
Figure 221 – Envelopes of concrete strain for unconfined flange at 1.5% drift ratio (data from optical markers along Columns 8, 9, and 10)	275
Figure 222 – Envelopes of concrete strain for unconfined flange at 2% drift ratio (data from optical markers along Columns 8, 9, and 10)	276
Figure 223 – Contribution of deformation components from bottom 87 in. (2210 mm), stem in compression	277
Figure 224 – Contribution of deformation components from bottom 87 in. (2210 mm), stem in tension	278
Figure 225 – Cumulative contribution of deformation components from bottom 87 in. (2210 mm), stem in compression	279
Figure 226 – Cumulative contribution of deformation components from bottom 87 in. (2210 mm), stem in tension.....	279
Figure 227 – Envelopes of shear versus drift ratio	280

Figure 228 – Envelope comparisons of shear versus drift ratio	281
Figure 229 – Normalized effective initial stiffness K_e	282
Figure 230 – Normalized cracked moment of inertia.....	282
Figure 231 – Unloading stiffness versus drift ratio.....	283
Figure 232 – Normalized unloading stiffness versus drift ratio	283
Figure 233 – Stiffness reducing exponent versus normalized displacement.....	284
Figure 234 – Hysteretic energy dissipation index versus drift ratio.....	285
Figure 235 – Idealized stress-strain relationships.....	286
Figure 236 – Stress-strain relationship for confined and unconfined concrete in compression using parameter values from Table 19 compared with model proposed by Mander et al.....	287
Figure 237 – Comparison between measured and calibrated stress-strain relationships for No. 6 (19) bars	288
Figure 238 – Moment-curvature relationships for T1.....	289
Figure 239 – Moment-curvature relationships for T2.....	290
Figure 240 – Moment-curvature relationships for T3.....	291
Figure 241 – Moment-curvature relationships for T4.....	292
Figure 242 – Moment-curvature relationships for T5.....	293
Figure 243 – Moment-curvature relationships for T6.....	294
Figure 244 – Moment-curvature relationships for all walls	295
Figure 245 – Normalized maximum measured moment to nominal flexural strength	296
Figure 246 – Normalized maximum measured moment to calculated moment	296
Figure 247 – Computed curvature for relevant events.....	297
Figure 248 – Idealized Moment-Curvature relationship.....	298
Figure 249 – Idealized moment and curvature distributions for Model A.....	299

Figure 250 – Events used to defined the idealized moment-curvature relationship for T1	300
Figure 251 – Events used to defined the idealized moment-curvature relationship for T2	301
Figure 252 – Events used to defined the idealized moment-curvature relationship for T3	302
Figure 253 – Events used to defined the idealized moment-curvature relationship for T4	303
Figure 254 – Events used to defined the idealized moment-curvature relationship for T5	304
Figure 255 – Events used to defined the idealized moment-curvature relationship for T6	305
Figure 256 – Inverse of ϕ_K versus drift ratio for bottom 50 in. (1270 mm)	306
Figure 257 – Inverse of ϕ_K versus drift ratio for bottom 50 in. (1270 mm) of wall (data from Figure 256) ...	307
Figure 258 – Idealized moment and curvature distributions for Model B.....	308
Figure 259 – Comparison of measured and calculated deformation capacity.....	309
Figure 260 – Measured and calculated maximum tensile strain of the reinforcement using Model A.....	310
Figure 261 – Measured and calculated maximum tensile strain of concrete surface on a gauge length of 14 in. (356 mm) using Model A	310
Figure 262 – Measured and calculated maximum compressive strain of concrete surface on a gauge length of 14 in. (356 mm) using Model A.....	311
Figure 263 – Measured and calculated maximum tensile strain of the reinforcement using Model B.....	312
Figure 264 – Measured and calculated maximum tensile strain of concrete surface on a gauge length of 14 in. (356 mm) using Model B	312
Figure 265 – Measured and calculated maximum compressive strain of concrete surface on a gauge length of 14 in. (356 mm) using Model B.....	313
Figure 266 – Average of measured-to-calculated maximum tensile strain of reinforcement using Model A ..	314
Figure 267 – Average of measured-to-calculated maximum tensile strain of concrete surface using Model A.....	314

Figure 268 – Average of measured-to-calculated maximum compressive strain of concrete surface using Model A.....	315
Figure 269 – Average of measured-to-calculated maximum tensile strain of reinforcement using Model B ..	316
Figure 270 – Average of measured-to-calculated maximum tensile strain of concrete surface using Model B.....	316
Figure 271 – Average of measured-to-calculated maximum compressive strain of concrete surface using Model B.....	317
Figure B.1 – Post-yield strain penetration assumptions	333
Figure B.2 – Influence of β_u and β_y on β_ℓ	334
Figure B.3 – Strain penetration amplification factor α_{sp} versus drift ratio, based on Table B.1	334
Figure B.4 – Strain penetration factor α_{sp} versus drift ratio, based on Table B.2.....	335

1 INTRODUCTION

1.1 Problem Statement

Reinforced concrete structural walls have been used for many years as part of the lateral-force-resisting system of multi-story buildings located in regions of moderate to high seismic risk. If adequately designed and detailed, walls provide efficient resistance to in-plane forces induced by strong ground motions and offer high stiffness for the control of lateral drift. Drift control helps protect against damage of non-structural components and building contents, both of which account for 80% or more of the total cost of office, hotel, and hospital buildings^[15], see Figure 1.

During severe ground shaking, structural members are subjected to large inelastic deformations. To tolerate deformation demands, walls need to be properly detailed for ductile behavior. For instance, if the response is controlled by flexure, yielding of the main flexural reinforcement would be expected and concentration of inelastic deformations are likely to occur at the critical section, typically located at the base of the wall (i.e., the plastic hinge region). Brittle modes of failure are precluded with proper reinforcing details and by limiting stresses induced by the expected flexural overstrength.

Damage in buildings that use structural walls as the main lateral-force-resisting system has been observed after recent earthquakes: Maule, Chile 2010; Christchurch, New Zealand 2011; and Tohoku, Japan 2011. During these events, concrete crushing at wall boundary elements, global buckling of wall segments, and buckling and fracture of reinforcing bars^[29,76,98] were observed (see Figure 2 and Figure 3). The damage experienced by reinforced concrete structural walls drove changes to buildings codes, especially on design provisions related to wall boundary elements and wall slenderness.

To achieve satisfactory performance, ACI 318 limits the acceptable range of values for selected mechanical properties of reinforcing bars, such as yield strength, tensile-to-yield strength ratio, and fracture elongation. These mechanical properties are typically specified via ASTM specifications, see Table 1. Further restrictions in ACI 318 are imposed on the maximum yield strength permitted for design purposes based on the application. These limitations were imposed to prevent brittle failures of members and to attain sufficient deformation capacity.

The use of high-strength reinforcement with yield strength in excess of 80 ksi (550 MPa) has been debated among structural engineers and the construction community for several years. Many advantages of using high-strength reinforcement have been recognized by the construction industry including reduced congestion of reinforcing bars, improved quality of construction, reduced constructions time, smaller member sizes, and more usable space.^[18,87] Furthermore, structural engineers seek more efficient and safer structures. High-strength steel has not been fully adopted because of insufficient test data on the performance of structural members (including walls) with this type of steel.

Concerns arise with the use of high-strength reinforcement, including but not limited to^[16,59]: the strain values to define tension- and compression-controlled sections, the strain limit to prevent brittle failures, the impact of the absence of a yield plateau on member deformation capacity, the influence of longitudinal reinforcement strains on shear strength, and the parameters required to control serviceability (minimum reinforcement ratio, member thickness, and effective stiffness).

1.2 Objectives and Scope

The primary objective of this research is to evaluate through physical testing the impact of mechanical properties of high-strength reinforcement on the behavior of non-symmetric reinforced concrete structural walls (T-shaped) subjected to reversed cyclic transverse displacements. The

study aims to complement the experimental data obtained from previous similar tests conducted at The University of Kansas.

The main variables in this study are the mechanical properties of high-strength steel bars, primarily the yield strength (f_y), the tensile-to-yield strength ratio (f_t/f_y), and the uniform elongation (ε_{su}) of the longitudinal reinforcement in confined boundary elements. The controlled reinforcement parameters in the experimental program are the yield strength, amount and layout of the transverse and confining reinforcement, and the amount and layout of the longitudinal reinforcement. The focus of the study is on slender structural walls with a nominal shear span-to-depth ratio of 3.

Axial load is limited to the self-weight of the specimen and testing apparatus. Test specimens are built using concrete with the same nominal compressive strength.

A secondary objective of this research is to develop a simplified numerical model to estimate strain demands and deformation capacity of the specimens, including the effects of cracking, yielding, and ultimate strains combined with deformations due to shear and strain penetration.

1.3 Organization

This study is organized in seven chapters and two appendices. Chapter 2 provides an overview of the behavior of reinforced concrete structural walls subjected to lateral loads as well as a summary of previous work on walls with non-symmetric cross sections reinforced with conventional and high-strength steel bars. The chapter also summarizes the evolution of the design provisions in building codes for the use of high-strength reinforcement.

Chapter 3 contains a detailed description of the experimental program, including the design and construction of specimens, test setup, loading protocol, and instrumentation.

Chapter 4 provides a detailed description of the collected experimental data. Numerous tables and figures are included to help understand the behavior of the specimens. The shear versus drift ratio, damage progression, displacement components, and wall elongation describe the overall behavior of the walls. The vertical distribution of the measured reinforcement and concrete strains are included for understanding the local behavior. The processed data also includes determining initial stiffness, unloading stiffness, and hysteretic energy dissipation.

Chapter 5 documents response comparisons of six slender T-shaped walls tested at The University of Kansas with similar research objectives and scope.

Chapter 6 describes two simplified models for estimating strain demands and deformation capacity. The models use data from moment-curvature analyses combined with the effects of deformations due to shear and strain penetration.

Chapter 7 documents the main observations and conclusion from the preceding chapters. The manuscript closes with two appendices: Appendix A contains the notation and terminology used throughout the dissertation, and Appendix B describes a model to determine deformations due to strain penetration (or bond slip) in reinforced concrete members responding in the inelastic range.

2 PREVIOUS STUDIES

2.1 Overview

Traditionally, structural walls subjected to lateral loads (due to earthquake, wind, or blast) are classified depending on their height-to-length ratio (or aspect ratio) as slender walls for $h_w/\ell_w \geq 2$ or squat walls for $h_w/\ell_w < 1.5$, refer to Appendix A for notation. The primary mode of failure in slender walls is generally controlled by yielding of the longitudinal reinforcement due to flexure, whereas in squat walls failure is generally controlled by shear. The behavior of intermediate walls are dominated by both flexural and shear resisting mechanisms.

In an effort to fully understand these differences, many researchers have performed experimental tests on walls with different aspect ratios (slender and squat)^[23,39,48,78,91], cross sections (planar and non-planar)^[19,21,23,39,60-64,69]; loading conditions (monotonic and cyclic), loading directions (unidirectional and multidirectional)^[20,21,25,38,43]; axial load magnitudes^[25,50], concrete compressive strengths (normal- and high-strength)^[36]; reinforcement mechanical properties (low and high tensile-to-yield strength)^[37], and amount of reinforcement at confined and unconfined regions^[82,88]. Past studies have shown a direct relation between wall deformation capacity and the amount of transverse reinforcement at wall boundary elements^[88,89,93-97]. Results from these studies have contributed to the development of design provisions for reinforced concrete seismic-force-resisting systems.

Most of the research on structural walls have considered material properties within the limits defined in ACI 318, including a maximum yield strength of 60 ksi in special structural walls for use in high-seismic regions. A total of 150 tests of slender walls (with rectangular or barbell cross section) were found in the ACI 445 database^[83]. Most of the test specimens used Grade 60 or Grade 40 reinforcement and approximately 10% had reinforcement with yield strengths near 80 ksi. In the case of slender walls with unsymmetrical cross section, only five research studies^[36,37,47,53,67] (totaling

13 tests) have evaluated the effects of high-strength reinforcing bars. Despite the ample experimental test data available for understanding the behavior of structural concrete walls, very limited data have addressed the response of walls with high-strength reinforcement subjected to cyclic loading. More test data are needed to explore new limits for the yield strength of the reinforcement in earthquake-resistant construction. The intention of this chapter is to describe the behavior of structural walls subjected to reversed cyclic loading, summarize relevant previous research on structural walls with unsymmetrical cross sections, and identify research needed to support the use of high-strength reinforcement bars in future editions of the ACI 318 Code.

2.2 High-Strength Steel

The use of high-strength steel bars has been debated among structural engineers and the construction community for several years. High-strength steel (HSS) is defined as a class of steels with yield strengths greater than 80 ksi (550 MPa). ACI 318 Committee has upgraded the code provisions related to reinforcing bars once new findings from research projects and new ASTM standards are published. The historical development of HSS is illustrated in Table 1. Changes in ACI 318 and ASTM standards are included in chronological order and shown in different columns to better visualize how ACI 318 has incorporated the changes in ASTM standards.

Many advantages of using HSS has been recognized by the construction industry: reducing congestion, improving the quality of cast-in-place concrete, and reducing the speed of construction time. From the structural point of view, the use of reinforcement with higher yield strength will lead to a more efficient use of steel bars. However, many issues need to be addressed before fully adopting HSS as concrete reinforcement. Concerns about the ability of this type of steel in providing adequate ductility in earthquake-resistant structures prevent its full adoption in ACI 318.

In 2013 two independent documents studied the feasibility of using high-strength steel in reinforced concrete. The first one, titled *Use of High-Strength Reinforcement in Earthquake-Resistant*

Concrete Structures^[59] confirmed the viability of using HSS in seismic applications. The second one titled *Roadmap for the Use of High-Strength Reinforcement in Reinforced Concrete Design*^[16] identified the changes and research needed to update ACI 318 for allowing higher grades of reinforcement.

The roadmap in ATC 115^[16] suggested that before making changes in the code, it is necessary to understand the effects of the mechanical properties of high-strength steel on the response of structural members subjected to reversed cyclic loading. Among other requirements, this included the determination of the member strength under flexure or combined flexure and axial loads. Other items of concerns were to define the net tensile strain for compression-control sections (ϵ_{ty}) and tension-control sections, as well as determine whether the strength reduction factors of Section 21.2 of ACI 318-14^[1] are adequate when using high-strength reinforcing bars.

2.3 Concrete Members with High-Strength Reinforcement

Among the early studies of concrete members reinforced with high strength steel was the investigation made by Richart and Brown (1934)^[75], who studied the behavior of columns reinforced with bars having a yield strength between 80 and 96 ksi (550 and 660 MPa). However, it was in the late 1950's that the research community paid more close attention to this type of reinforcement when, in 1959, ASTM A431 introduced the first standard that included a steel with a yield strength of 75 ksi or 520 MPa. This standard was later renamed ASTM A615 in 1968, and allowed reinforcing bars Grade 40 (280), 60 (420) and 75 (520).

In 1955, the Portland Cement Association started a research program aimed to understand the behavior of concrete members with different types of reinforcement, including high-strength steel. The scope of these projects included the evaluation of member strength, deformation capacity, crack control, and durability. The findings were published in a series of reports in the 1960's ^[31,33,34,40-42,70,71]. They found cracks width were proportional to the stress of the steel and that the concrete cover of the main reinforcement was a key parameter for crack control. Additionally, members

reinforced with HSS were able to achieve acceptable levels of deformation without losing load carrying capacity^[66,74,90].

Significant research has been done since the early 1970's aimed to understand the seismic behavior of members with conventional and high-strength transverse reinforcement. The objectives included evaluating the effects of confining reinforcement on the ultimate compression deformation capacity, control of bar buckling, and member ductility. The work done by Wight and Sozen^[99], Muguruma et al.^[57], Sato et al.^[79], Bing et al.^[22], Azizinamini and Saatcioglu^[17], Lin and Lee^[51], Budek et al.^[24], and Restrepo et al.^[74] found that transverse reinforcement enhanced axial strength of confined concrete, improved flexural ductility, and delayed bar buckling.

Research projects in Japan^[4,45,46] tested concrete walls with reinforcement of yield strength between 100 and 210 ksi (690 and 1450 MPa). However, the specimen geometry and detailing are not typically used in the United States. Test results showed that walls failed due to flexural compression and bar buckling at a drift ratio of 2.0% for specimens subjected to axial loads of $0.1f_c'A_g$. Dazio et al.^[27] evaluated the effects that different amount and grade of flexural reinforcement has on the performance of structural walls. The report concluded that reduced ductility was obtained if low amount of flexural reinforcement or steel with low uniform elongation is used. Early bar buckling was observed in specimens with transverse reinforcement in the boundary elements spaced between $6.25d_b$ and $7.5d_b$, not complying with the requirement of ACI 318.

The main focus of the research done by Lowes et al.^[52] was to test four planar rectangular walls under reversed cyclic loading and to develop tools to enable performance-based earthquake engineering of structural walls. Two of the walls had reinforcement with a yield strength of approximately 80 ksi (550 MPa). Test results showed that the main flexural reinforcement buckled prior to fracture, without exceeding a drift ratio of 1.5%.

In the last 15 years, a series of research programs have tested beams, columns and walls reinforced with HSS subjected to reversed cyclic loading. The work done by Rautenberg et al.^[73] Tavallali et al.^[86], Pfund^[72], and Tretiakova^[92] studied the cyclic response of concrete beams and columns reinforced with steel bars having yield strengths as high as 120 ksi (830 MPa). Huq et al.^[37] tested four T-shaped slender walls using a similar loading protocol (three of them used HSS). They concluded that RC members with HSS had similar deformation capacity to members with conventional reinforcement (Grade 60 or 420 MPa), and were able to attain nearly the same target flexural strength. The evidence suggested that HSS is feasible as reinforcement for concrete members located in regions with high seismic hazard.

Two of the L-shaped walls tested by Hosaka et al.^[36] used high-strength steel as flexural reinforcement at the boundary element located at the corner of the L-shaped wall with $f_y = 106$ ksi (731 MPa) and Grade 60 (420) was used elsewhere. The L-shaped specimens tested by Kono et al.^[47] used steel with $f_y = 102$ ksi (703 MPa) as vertical reinforcement. Other studies^[44,58] used high-strength wires as concrete reinforcement. The study by Huq et al.^[37] was the only reference found for unsymmetrical structural walls with high-strength steel deformed bars as flexural, shear, and confining reinforcement.

2.4 High-Strength Reinforcement in Building Codes

Section 20.1.2.3 of ACI 318-14^[1] allows the use of high-strength steel ASTM A1035^[11] as concrete confining reinforcement. The maximum yield strength allowed for design calculations is 100 ksi, even though ASTM A1035 has two grades, Grade 100 (690) and 120 (830). ACI 318 allows high-strength confinement based on experimental data ^[24,56,84] from tests of columns confined with high-strength steel wires and strands with yield strengths ranging from 120 to 200 ksi (830 to 1380 MPa).

The other key requirement for reinforcing bars is in Table 20.2.2.4a for flexural, axial, and shrinkage and temperature reinforcement required to have a maximum yield strength of 60 ksi (420

MPa) for special seismic structures or 80 ksi (550 MPa) otherwise. This requirement applies for special moment resisting frames and special structural walls including coupling beams and wall piers. Due to insufficient of experimental evidence in the performance of special seismic structures when the code was written, Grade 80 (830) was excluded from the provisions. However, recent tests in beams and columns have shown reinforcement bars Grade 80 are appropriate for seismic applications^[59].

When A615 Grade 60 steel is used, ACI 318-14^[1] requirements (i) through (iii) shall be met and (i) and (ii) need to be satisfied for Grade 40:

- (i) The actual yield strength does not exceed the specified yield strength by more than 18 ksi.
- (ii) The tensile-to-yield strength ratio is at least 1.25
- (iii) The minimum elongation in 8 in. (205 mm) gauge length shall be 14% for bar sizes No. 3 (10) through No. 6 (19), 12% for No. 7 (22) through No. 11 (36), and 10% for No. 14 (43) and No. 18 (57).

Table 2 compares the mechanical properties of different types of ASTM steel available in the United States. The comparison is made in terms of the minimum and maximum yield strength, tensile strength, and fracture elongation for different bar diameters. When a particular ASTM standard does not specify a requirement, a hyphen (-) is used. Note that only ASTM A706 steel specifies a maximum yield strength. ASTM A615 and A706 Gr. 60 are included for comparison purposes since both are allowed in ACI 318-14^[1] for seismic applications.

The main reason ACI 318-14^[1] limit the yield strength is because by the time the critical section of a member reaches the yield point, higher shear and bond stresses will be developed if the flexural reinforcement has a yield strength higher than the one assumed in design. These higher stresses cause a sudden reduction in the load carrying capacity of the member (a brittle failure),

condition that shall be avoided if the structure is located in earthquake-prone areas^[1]. Additionally, there is insufficient experimental data on the cyclic response of members with a yield strength greater than 80 ksi (550). The tensile-to-yield strength ratio requirement was imposed to promote spread of plasticity in regions where yielding is expected (plastic hinge regions). The shear reinforcement cannot exceed Grade 60 (420) in special seismic systems. In all of these cases, steel ASTM A615^[7] and ASTM A706^[8] are permitted.

Other types of steel, namely ASTM A995^[9] and ASTM A996^[10], are permitted as deformed bars per ACI 318-14^[1] Table 20.2.2.4a and low-carbon chromium steel^[11] in plain spirals per ACI 318-14^[1] Table 20.2.2.4b with similar maximum stress limits for design depending on the application. These types of steels and wires are not covered in this study.

As shown in Table 1, the ACI 318 code has incorporated new material strengths over the years enabling safer and more efficient designs. NIST^[59] and ATC^[16] documents identified areas of needed research to advance the state of the art in concrete members with high-strength reinforcement. In particular, experimental data are needed to evaluate the seismic response of reinforced concrete structural systems using high-strength steel bars. This study focuses on the response of slender cantilever T-shaped concrete walls reinforced with high-strength steel bars under quasi-static reversed cyclic loading.

3 EXPERIMENTAL PROGRAM

A summary of the experimental program is presented in this chapter including a description of material properties, construction of specimens, test setup, instrumentation, and loading protocol. Two T-shaped concrete walls reinforced with high-strength steel were built and tested under reversed cyclic loading. A summary of the test program in Table 3 indicates where the nominal yield strength (f_y), the target tensile-to-yield strength ratio (f_t/f_y), and the nominal concrete compressive strength (f'_c) of the walls. Specimen T5 had Grade 120 (830) flexural and shear reinforcement with $f_t/f_y = 1.30$, whereas T6 had Grade 100 (690) reinforcement with $f_t/f_y = 1.15$. The same nominal compressive strength of 8 ksi (55) and the same Grade 120 (830) confining reinforcement were used in both walls.

The T-shaped specimens were 300-in. (7620-mm) tall with a thickness of 10 in. (254 mm), and a 100-in. (2540-mm) long stem with a 100-in. (2540-mm) long flange. The No. 6 (19) longitudinal reinforcement was concentrated at three different boundary elements, one located at the tip of the stem and one at each tip of the flange. These regions were confined using No. 3 (10) hoops and crossties spaced at 3 in. (76.2 mm) in the bottom half of the walls and at 6 in. (152 mm) in the top half. Non-confined regions were used elsewhere, including the flange-stem intersection. The geometry and the reinforcement layout of the walls, as well as details of the confined regions, are shown in Figure 4 through Figure 6. The reinforcement data and cross section properties are shown in Figure 7. A typical wall elevation with the reinforcement layout is presented in Figure 8.

To evaluate the performance of the walls under transverse lateral loads, a reversed cyclic loading was applied parallel to the stem at the top of the wall. The loading protocol followed the recommendations in FEMA 461^[30], as shown in Figure 9 and Table 4. The load was applied at a nominal height of 300 in. (7620 mm) above the base of the wall to have a shear span-to-depth ratio of 3.0.

3.1 Design of Specimens

Similar to the approach followed by Huq et al.^[37], the specimens were designed to be controlled by flexure. The flexural strength (M_n) was determined based on the shear strength (V_n) calculated using the minimum transverse reinforcement ratio allowed by ACI 318-14^[1] for $\rho_t = 0.0025$ and satisfying $0.9M_n \approx 0.6V_n h_w$, where $h_w = 300$ in. (7620 mm) corresponds to the shear span. The shear strength was calculated as the contribution of the concrete and steel per the following expression:

$$V_n = V_c + V_s = 2\sqrt{f'_c, \text{psi}} \ell_w t_w + \rho_t f_y \ell_w t_w \quad \text{Eq. 1}$$

where $\ell_w = 100$ in. (2540 mm) is the wall length, $t_w = 10$ in. (254 mm) is the wall thickness, f'_c is the specified concrete compressive strength, and f_y is the transverse reinforcement yield strength. The data needed to calculate the nominal flexural strength of each wall are shown in Table 5, where the strength in the positive direction (stem in compression) is approximately 15% greater than the strength in the negative direction. The calculated nominal flexural strength (negative direction) was 6470 ft-kips (8780 m-kN) and 5650 ft-kips (7660 m-kN) for T5 and T6, respectively. A shallow neutral axis depth (within the flange) at nominal flexural strength was desired to attain maximum tensile strain demands (at the stem boundary element). Assuming a T-shaped cross section and a fully-effective flange, a neutral axis depth of approximately 3% of the wall length was attained as indicated in Table 5.

The walls were detailed to comply with the requirements prescribed for special structural walls by ACI 318-14^[1], which is limited to Grade 60 (420) reinforcement. For Grades 100 (690) and 120 (830) the spacing of the confining reinforcement at the wall boundary elements was based on the recommendations of ATC 115^[16] and NIST^[59]. Both of these documents recommend that the ratio

of buckling-to-yield stress (Eq. 2) for Grade 100 (690) reinforcement be similar to the ratio for Grade 60. Considering that the hoop spacing for Grade 60 (420) longitudinal reinforcement prescribed in ACI 318-14^[1] is $s = 6d_b$, Eq. 2 was used to determine the spacing of the transverse reinforcement for T5 and T6. The resulting spacing was $4.2d_b$ for Grade 120 (830) steel and $4.6d_b$ for Grade 100 (690) steel. A minimum spacing of $4d_b$ was selected for both T5 and T6 to account for the effect of construction tolerances.

$$\frac{f_{cr}}{f_y} = \frac{\pi^2 E_s}{f_y \left(\frac{s}{d_b/4} \right)} \quad \text{Eq. 2}$$

The confined boundary element in the stem used three legs in the direction of the applied load even though two legs were sufficient to satisfy the requirements for confining reinforcement. The additional leg was provided to laterally restrain all of the longitudinal bars located at the extreme layer of the stem.

3.2 Material Properties

The specimens were cast in four segments: the base block, Lift 1, Lift 2, and the top block, with three construction joints as shown in Figure 8. The key dates for specimen casting and testing are listed in Table 6. A target concrete compressive strength of 8 ksi (55 MPa) was provided by a local ready-mix plant. Actual batched mixture proportions are shown in Table 7. The mechanical properties of the concrete were obtained following ASTM C39^[12] for compressive strength and ASTM C496^[13] for tensile strength. The measured strengths at test day are indicated in Table 8.

Two types of reinforcing bars were used as flexural and shear reinforcement in this project: Grade 120 (830) for specimen T5 and Grade 100 (690) for T6. The confining reinforcement of the boundary elements of both walls consisted of No. 3 (10) Grade 120 (830) reinforcement from the

same heat. The mechanical properties of the reinforcement were measured in accordance with the standard testing method specified in ASTM A370^[6]. Reinforcement mill certifications indicated that No. 4 (13) and No. 6 (19) steel bars in wall T5 complied with ASTM A1035^[11] Grade 120 (830) specification whereas bars in T6 complied with ASTM A615^[7] Grade 100 (690). Figure 10 and Figure 11 illustrate representative stress-strain curves obtained for the No. 6 (19) and No. 4 (13) reinforcing bars. The peak stress associated with the uniform elongation (following ASTM E8^[14]) is also indicated in these figures. None of the stress-strain curves showed a yield plateau; therefore, the yield strength was determined following the 0.2% method in accordance with ASTM A370^[6] as permitted in section 20.2.1.2 of ACI 318-14^[1].

A summary of the tensile test results is presented in Table 9 including the yield strength, tensile strength, tensile-to-yield strength ratio, and uniform and fracture elongation. The reported values are the average of two tests. The uniform elongation (ϵ_{su}) was calculated using the second method specified in ASTM E8^[14], where ϵ_{su} was taken as the average of the two strains obtained from the intersection of the stress-strain curve with a horizontal line at 99.5% of the peak stress. Reinforcement in T5 showed a higher tensile-to-yield strength ratio ($f_t/f_y = 1.33$) and lower uniform elongation ($\epsilon_{su} = 5.4\%$) than the reinforcement in T6 ($f_t/f_y = 1.18$ and $\epsilon_{su} = 7.1\%$). Fracture elongation for the No. 4(13) and No. 6 (19) bars, were between 8.6 and 10.1%, with the lower value for the No. 4 (13) Grade 100 (690) and the higher value for the No. 6 (19) Grade 120 (830).

3.3 Construction of Specimens

Conventional construction methods were used to build the specimens, i.e., wood formwork assembly, installation of the reinforcement cage, casting with ready-mix concrete, curing with wet burlap and plastic, and formwork removal. The formwork was removed three to four days after casting. The concrete surface at the construction joints was intentionally roughened to enhance the

shear transfer mechanism. Concrete cylinders were made to track the compressive strength of the concrete cast on each of the four segments (base block, Lift 1, Lift 2, and top block). The cylinders were kept inside the laboratory at the same environmental conditions of the walls until test day.

Conventional Grade 60 (420) reinforcing bars were used in the base and top blocks. The vertical wall reinforcement was spliced at the top of Lift 1, see Figure 8, with the splice length determined based on ACI 408^[2,49]. The specimens were painted using an oil-based white paint to facilitate the marking and visibility of the cracks. Figure 12 shows the state of the specimens at different stages of construction.

3.4 Test Setup.

3.4.1 Description

The specimens were anchored to the strong floor using 14 No. 14 (43) Grade 100 (690) threaded rods passing through the 27-in. (686-mm) deep base block, see Figure 13. To reduce the stress on the strong floor, the tension force on the threaded rods reacted on spreader beams under the floor (Figure 14). The external horizontal force was applied by two MTS 201.70 Hydraulic Actuators with a force capacity of 220 kips (980 kN) and a stroke of 40 in. (1020 mm). Each actuator was installed at 297 in. (7544 mm) above the top of the base block for a shear span-to-depth ratio of 3.0. To control twisting of the specimens, the distance from the centerline of the wall stem to the center of the actuators was 27 in. (686 mm). The actuators were attached on one end to the strong wall and on the other to the top block by means of HP18x204 steel sections.

To prevent out-of-plane buckling, the walls were braced near midheight as shown in Figure 13. Two steel bracing systems were provided: (1) internal bracing to prevent relative horizontal movement between the stem and flange, and (2) external bracing to prevent global twisting. Friction between the external brace and the wall was minimized by using nylon pads reacting on a mirror-finished steel plates attached to the walls.

3.4.2 Instrumentation

External and internal instrumentation were installed to collect relevant data for understanding the behavior of the specimens. Linear variable differential transformers (LVDT), string potentiometers (string pots), infrared non-contact position measurement system, and electrical resistance strain gauges bonded to the reinforcement bars. The instrumentation arrangement was designed to determine the contributions of deformations due to flexure, shear, and strain penetration to the total lateral deformation.

Figure 15 and Figure 16 show the instrumentation layout on both the stem and flange. To measure the total lateral deformation and twisting of the specimen, two 40-in. (1020-mm) string potentiometers were installed 10 in. (254 mm) below the horizontal plane of action of the actuators at the top of the wall and spaced 72 in. (1830 mm) apart. An additional 20-in. (508-mm) string potentiometer was installed at the centerline of the wall for redundancy. Two LVDTs were installed at a height of 19 in. (483 mm) above the strong floor and spaced 78 in. (1980 mm) apart to measure horizontal sliding and twisting of the base block relative to the floor.

To calculate the elongation and flexural rotation, four vertical LVDTs were mounted at opposite ends of the wall. Two of them were installed at different elevations at the edge of the stem whereas the other two were placed at the center of the flange also at different elevations. The deformations of the bottom 90 in. (2290 mm) of the wall were measured using two string potentiometers with a stroke of 20 in. (508 mm). Deformations at the top 210 in. (5330 mm) were measured using two 4-in. (102-mm) stroke potentiometers attached at a height of 90 in. (2290 mm) above the base block and near the top of the wall. Finally, to measure the shear distortion of the top two-thirds of the wall, two 4-in. (102-mm) LVDTs were attached along two diagonals between 90 and 270 in. (2290 and 6860 mm) above the base.

A motion capture system served to measure the three-dimensional displacement field of the bottom 90-in. (2290-mm) region of the wall. A square grid, nominally 14-in. (356-mm) wide, of optical markers were glued on the surface of the stem (east surface) and on one-half of the flange (northeast surface) as indicated in Figure 17 and Figure 18. The other half of the flange (northwest surface) was used to mark cracks. Six additional markers were installed on a secondary grid between Columns 1 and 2 and Rows 1 and 7 to collect a more detailed deformation profile for the confined stem. Due to limited visibility of the cameras to track the optical markers, the first row was installed 3 in. (76 mm) above the base of the wall. The data collected with the motion capture system is presented by column, row, layer, or station, where a layer is the region of the wall between two consecutive rows (for a total of 6 layers) and a station is the region bounded by four adjacent markers (two consecutive columns and rows) on the primary grid (for a total of 54 stations), see Figure 17 and Figure 18.

Nine markers were mounted at the top of the base block to measure the rigid body motion of the base block (markers B1 through B9 in Figure 19) and six additional markers were installed at the strong floor (S1 to S6 in Figure 19) as redundant points of reference.

To measure the deformation of the longitudinal and transverse reinforcement, thirty four electrical resistance strain gauges were glued at different locations of selected reinforcing bars. Five longitudinal reinforcing bars located at the confined boundary element (three at the stem and two at the flange) as well as four vertical and two horizontal bars at unconfined regions of the walls were instrumented as indicated in Figure 20 for T5 and Figure 21 for T6. The strain gauges located above the base block were used to measure the strain demands as a function of drift ratio and in relation to wall elevation. The strain gauges placed inside the base block were intended to measure the effects of strain penetration. The hoops at the base of the stem were also instrumented, see Figure 20 and Figure 21.

3.4.3 Loading Protocol

The loading protocol recommended by FEMA 461^[30], listed in Table 4 and illustrated in Figure 9, was applied at the top of the wall. This type of loading is used to evaluate the performance characteristics of structural and nonstructural components under seismic conditions. Based on this protocol, continuously increasing target lateral displacements varying from 0.6 to 12 in. (15 to 305 mm) were applied by the actuators. The displacement history corresponds to a target drift ratio varying from 0.2% to 4%, where the drift ratio is defined as the lateral displacement at the top of the wall with respect to the base block divided by the distance from the top of the base block to the point of load application. The applied protocol had 9 steps, each consisting of two cycles.

To overcome imprecisions of displacement measurements at low drift ratios (up to 0.5%), displacements during the initial loading steps were imposed by targeting a force level. Later in the test, at drift ratios of 0.75% and greater, the actuator imposed the target displacements. Loading rates were set as 0.01 in./sec (0.25 mm/sec) for drift ratios not exceeding 0.75%, 0.02 in./sec (0.51 mm/sec) for 1% drift ratio, and 0.03 in./sec (0.76 mm/sec) for drift ratios in excess of 1%.

During the tests, displacements measured at the top of the wall neglected the base block rotation (due to uplift); therefore, actual drift ratios imposed on the wall resulted generally lower than the target drift ratios.

4 EXPERIMENTAL RESULTS

4.1 Measured Shear versus Drift Ratio

Measured shear versus drift ratio is plotted in Figure 22 for T5 and Figure 23 for T6. The drift ratio (DR), expressed in percent, is plotted on the horizontal axis and the vertical axis represents the applied shear (V), in kips, at the top of the wall. The drift ratio, is defined as the relative displacement between the top and the base of the wall divided by the height of the wall measured from the top of the base block to the level where the top displacement was measured. The following expression was used to calculate DR :

$$DR = \frac{\delta_{top} - \delta_{base}}{h_y} - \theta_{base} \quad \text{Eq. 3}$$

where δ_{top} is the displacement measured at the level of the three potentiometers installed 11 in. (279 mm) below the plane of action of the actuators; δ_{base} is the average displacement from two potentiometers located 8 in. (203 mm) below the top of the base block (Figure 15 and Figure 16) measuring the horizontal translation (in the direction of loading) of the base block; h_y is the height from the top of the base block to the three potentiometers installed at 286 in. (7260 mm) for both walls; and θ_{base} is the rotation of the base block about an axis normal to the plane of the wall stem calculated using markers B1 and B6 (Figure 19). The effect of θ_{base} on δ_{base} was small and therefore neglected.

For each of the walls, the measured V versus DR is shown in Figure 22 and Figure 23. The same figures are annotated in Figure 24 and Figure 25 to identify instances of bar buckling and bar fracture. All of the reinforcing bars that buckled and fractured are mapped in Figure 26 and Figure 27.

The hysteretic curve of T5 (Figure 22) did not exhibit a well-defined yield point. Instead, a smooth transition between the elastic and the inelastic range was observed, similar to the transition shown in the stress-strain curve of the reinforcing bars of T5 in Figure 10 and Figure 11.

The first considerable change in lateral stiffness (measured by the slope of V versus DR curve) in T5 occurred when loading in the positive direction (stem in compression) near $V = 100$ kips (445 kN) and near $V = 60$ kips (267 kN) in the negative direction (stem in tension). The stiffness change corresponds to flexural cracking for a modulus of rupture of 5.5 and $8.2\sqrt{f'_c, \text{psi}}$ (0.46 and $0.68\sqrt{f'_c, \text{MPa}}$) in the positive and negative loading directions, respectively. Wall T5 completed two cycles to 2% drift ratio and failed during the first excursion to -3% drift ratio (stem in tension). A total of 15 bars fractured simultaneously, including all No. 6 (19) bars in the confined stem and one No. 4 (13) bar in the unconfined stem. After these bars fractured, the wall lost its lateral load-carrying capacity in the negative loading direction, as shown in Figure 22 by the sudden drop of the applied shear en route to -3% drift ratio. Bar buckling was not observed prior to bar fracture.

Flexural cracking in T6 occurred at approximately 110 kips and 60 kips, for the positive and negative loading directions, respectively. These correspond to a modulus of rupture of 5.8 and $7.8\sqrt{f'_c, \text{psi}}$ (0.48 and $0.65\sqrt{f'_c, \text{MPa}}$) for positive and negative loading, respectively. Wall T6 completed one cycle to 3% drift ratio and failed during the second excursion to -3% drift ratio. During the second excursion to -3%, one No. 6 (19) bar fractured near -1% drift ratio, and two more fractured near -1.7%. Prior to these fractures, the bars buckled at +3% drift ratio in the preceding half cycle (stem in compression). The wall completed the second cycle to -3% with a strength loss of approximately 25% and when loaded to +4%, it retained 85% of the strength. When loaded to -4% drift ratio, additional No. 6 (19) bars in the confined stem started fracturing at -2.2% drift ratio (without reaching -4%). A total of 14 No. 6 (19) bars of the confined stem and two No. 4 (13) bars of

the unconfined stem had fractured after attempting completion of the first cycle to 4% drift ratio, as shown in Figure 27. Out of the 16 bars that fractured, only 7 were observed to have buckled.

The maximum measured shear force (V_{max}) and drift ratio (DR_{max}) during the wall tests are shown in Table 10. The peak forces were 395 and 290 kips (1760 and 1290 kN) in the positive direction and 303 and 240 kips (1350 and 1070 kN) in the negative direction for T5 and T6, respectively. As indicated in Table 10, these values correspond to $4.6\sqrt{f_{cm}}$ and $3.2\sqrt{f_{cm}}$ in one direction and $3.5\sqrt{f_{cm}}$ and $2.7\sqrt{f_{cm}}$ in the other, where f_{cm} is the measured compressive strength reported in Table 8 (average of Lift 1 and 2). In the positive direction of loading, the recorded lateral strength for T5 was 30% greater than in the negative direction, whereas for T6 the lateral strength in the positive direction exceeded the negative direction by 20%. The strength in the positive direction was greater than in the negative direction because when the flange is in tension, more reinforcement is near the extreme tension fiber. The larger overstrength of T5 is explained by the greater tensile-to-yield strength ratio of the Grade 120 (830) bars.

The maximum drift ratio (DR_{max}) achieved by both walls are shown in Table 10 and correspond to the maximum drift ratio attained without losing more than 20% of the maximum applied shear (each direction considered separately). Values of DR_{max} were 2.8% and 3.9% for T5 and T6, respectively, when the stem was in compression, and 2.3% for T5 and 3.1% for T6 when the stem was in tension. The lower value of DR_{max} in T5 is correlated with the lower uniform elongation of 5.4% for No. 6 (19) bars and 5.3% for No. 4 (13) bars when compared with those of T6, 7.1 and 7.3% for No. 6 (19) and No.4 (13) bars, respectively.

4.2 Damage Progression

The damage progression of both walls is shown in Figure 28 through Figure 47. Photographs in Figure 28 through Figure 35 show the condition of the walls at peak displacements to target drift ratios of 1, 2, 3 and 4%. The photos correspond to the maximum deformation during second cycles

except for Figure 32 and Figure 35, which were taken at peak drift during first cycles. Horizontal cracks due to flexure were observed in the confined stem during the cycle to -0.2%. The spacing of the flexural cracks near the tip of the stem nearly coincided with the 3-in. (76-mm) spacing of the confining hoops. The length of these cracks was approximately equal to the length of the confined boundary element (30 in. or 760 mm) and generally diminished with wall elevation. At a drift ratio of +0.3%, two types of cracks occurred in the flange: (1) horizontal cracks spaced at approximately 6 in. (150 mm) were observed at the confined flange, and (2) V-shaped diagonal cracks spaced at approximately 13 in. (330 mm) were observed with the vertex located at the center of the flange. The first shear cracks (along the stem) occurred when loading in the negative direction (stem in tension) at a drift ratio of -0.2%. When loading in the positive direction, shear cracks were first observed at a drift ratio of +0.3%.

As the target drift ratio increased from 0.5%, the damage progression was similar for both specimens. From drift ratio between 0.75% and 1.5%, few additional diagonal cracks formed at the unconfined stem when loading in both directions. When loading in the positive direction, the cracks formed a “fan” shape (i.e., diagonal cracks had shallower slope near the bottom of the wall with a vertex near the bottom corner of the stem boundary element). At values of drift ratio greater than 2%, new diagonal cracks were not observed but the existing cracks continued to widen. The major difference between the crack patterns for both walls was in the penetration (or extent) of the diagonal cracks into the confined stem, when the stem was in compression. For T5, the diagonal cracks extended into the tip of the stem from the base to an elevation of 46 in. (1170 mm), whereas for T6 the diagonal cracks extended into the confined stem for up to 20 in. (506 mm) above the base. These elevations coincided with the height of the spalled concrete.

Concrete spalling in T5 was noticeable at the stem boundary element near a drift ratio of +1.0% during the first cycle to +1.5%. The measured concrete strain (average surface strain) using

the bottom two markers of Column 1 (Figure 17) at a drift ratio of 1% was 0.0027 over a length of 7 in. (178 mm). Concrete spalling in T6 was observed at the edge of the stem boundary element during the cycle to +1% drift and was limited to the bottom 3 in. (76 mm) of the wall.

Bar fracture of the No. 6 (19) bars in the confined stem of T6 was preceded by bar buckling. The first three No. 6 (19) bars of the confined stem fractured during the second cycle to -3%. Table 11 identifies the drift cycle and bar location where bar buckling or bar fracture first occurred for both walls. Most of these events are also identified in Figure 36 through Figure 47. In T5, a total of 15 bars fractured simultaneously, 14 of which were No. 6 (19) bars located at the confined stem and one No. 4 (13) bar at the unconfined stem. None of these bars buckled prior to their fracture and therefore most of the bars showed evidence of necking. In contrast, the outermost bars in the confined stem of T6 fractured without necking because the bars had buckled.

The vertical No. 4 (13) bars of the unconfined stem of both walls were located inside the horizontal reinforcement, with a nominal cover of 2.375 in. (60 mm). Buckling of these bars was not apparent during the test. It is plausible that the extra cover played a role in precluding bar buckling.

4.3 Reinforcement Strains

Reinforcing bars were instrumented with electrical resistance strain gauges to measure the changes in strain during the test. The locations of the gauges are shown in Figure 20 and Figure 21. A total of 34 strain gauges were installed in T5, whereas 36 were used in T6 (additional gauges were placed on hoops). The strains measured in vertical bars are shown in Figure 48 through Figure 105. The strains in the hoops are shown in Figure 106 through Figure 117, and the strains in horizontal bars are shown in Figure 118 through Figure 121. In these figures, the horizontal axis represents the drift ratio and the vertical axis represents the elongation of the bars, with negative elongation indicating shortening of the bar. All strain gauge readings were zeroed prior to starting the test.

4.3.1 Stem Longitudinal Reinforcement

The strains measured in the longitudinal reinforcement inside the base block and within the confined stem are shown in Figure 48 through Figure 55. The data indicate that the reinforcing bars for both walls yielded at a depth of 18 in. (457 mm) from the top of the base block but the yield point was not apparent. At a depth of 9 in. (229 mm) inside the base block, the bars yielded at a drift ratio near -0.9% for T5 and -0.6% for T6. At a drift of -2% the recorded strain was approximately 0.8% for both walls.

The recorded strains of the longitudinal reinforcement of the confined stem at different heights above the top of the base block are shown in Figure 56 through Figure 75. The strains were recorded at four different elevations between 0.5 in. (13 mm) and 100 in. (2540 mm) above the base block. Additionally, two No. 6 (19) bars at the confined stem and flange regions were instrumented at 144 in. (3660 mm). Based on the data in Figure 56 through Figure 61, the reinforcement at the base of the wall (0.5 in. or 13 mm above the base block) yielded during the cycle to 0.75% for T6 but for T5 the yield point was not apparent. The maximum strain recorded at this elevation was 3.4% (Figure 56) and 5.2% (Figure 61) for T5 and T6, respectively. The longitudinal reinforcement of the confined stem yielded at elevations of 25 in. (635 mm), 50 in. (1270 mm), and 100 in. (2540 mm) above the base block in both walls (Figure 62 through Figure 73). At an elevation of 144 in. (3660 mm) a strain gauges recorded values slightly greater than the yield strain in both walls.

For T6, when loading to the second cycle to -3%, the recorded strains remained nearly constant at an elevation of 50 in. or 1270 mm (Figure 67 and Figure 69) and at 100 in. (2540 mm) above the base block (Figure 71 and Figure 73). This behavior was observed after buckling of the three outermost No. 6 (19) bars in the confined stem. It is possible that when loading in the negative direction (stem in tension), the bars above 50 in. (1270 mm) did not elongate because the deformation concentrated at the level of the buckled bars to straighten them. This deformation

pattern was not observed at 25 in. (635 mm) because the strain gauges stopped working at a drift ratio of -2% when loading to the first cycle to -3%.

The recorded strain data for the vertical reinforcement in the confined stem of T5 did not clearly show the yield point. Instead, a smooth transition between the elastic and inelastic range was observed. In contrast, most of the strain data for T6 clearly showed the point where yielding occurred. Typically, yielding occurred at drift ratios below 1% for an elevation of 25 in. (635 mm) and above 1% for an elevation of 50 in. (1270 mm) or greater.

Figure 74 and Figure 75 show the data recorded at an elevation of 144 in. (3660 mm) above the base block for T5 and T6, respectively. These figures suggest the instrumented No. 6 (19) vertical bar of the confined stem in both walls exceeded the yield strain corresponding to the yield stress reported in Table 9.

The measured strain of the vertical reinforcement located at the unconfined stem are shown in Figure 76 through Figure 83. The data indicate that for both T5 and T6 the No. 4 (13) vertical bars in the stem were subjected to positive tensile strains throughout the test. At the base of the wall (2 in. or 51 mm above the base block) these bars yielded during the cycles to 1.5% drift ratio for T5 (Figure 76) and 1% for T6 (Figure 77). At this elevation, a maximum strain demand of 2.9% was recorded for T5 at a drift ratio of +2.4%. T6 experienced a maximum strain demand of 1% at a drift ratio of +1.4% before the strain gauge stopped working. The recorded strain data indicate that at an elevation of 25 in. (635 mm) above the base block, yielding occurred at a drift ratio above 1% for T5 and below 1% for T6 (Figure 78 and Figure 79). At an elevation of 50 in. (1270 mm) above the base block, the instrumented No. 4 (13) vertical bars experienced yielding near 1% drift ratio for both walls (Figure 80 and Figure 81), whereas at an elevation of 100 in. (2540 mm) the bars of T5 yielded near 1.6% drift ratio, as shown in Figure 82. Once the bars in the confined stem of T6 buckled, the strain data of the No. 4 (13) vertical bars at an elevation of 50 in. (1270 mm) suggest the bar did not

sustain an increase in tensile elongation. Instead, the elongation diminished as shown in Figure 81. Data for T6 were not available to support this observation at an elevation of 25 in. (635 mm) since the strain gauge stopped working before buckling of the bars in the confined stem (Figure 79).

4.3.2 Flange Longitudinal Reinforcement

Figure 84 through Figure 105 show data recorded by strain gauges installed at different elevations in the vertical reinforcement at both the confined and unconfined flanges of the walls. Data from elevations of 2 in. (51 mm), 50 in. (1270 mm), and 100 in. (2450 mm) are reported. The instrumented bars show that at 2 in. (51 mm) yielding occurred approaching 1% drift ratio for T5 and near 0.7% for T6 (Figure 84 through Figure 87). The maximum strain demand recorded at this elevation was 3% and 5.6% for T5 and T6, respectively. The drift ratio at which this elongation was attained was 2.8% for T5 and 3.5% for T6. After the flange reinforcement yielded in tension, plastic elongations remained positive throughout the test. For T5 and T6, yielding of the confined flange reinforcement at 50 in. (1270 mm) and 100 in. (2450 mm) was observed at a drift ratio in excess of 1%.

The elongation of the longitudinal reinforcement recorded at different elevations at the unconfined flange are shown in Figure 96 through Figure 105. A few of these figures indicate “Data not available” for cases where the strain gauge malfunctioned. For T5, the data indicate the reinforcement yielded near a drift ratio of 1% at an elevation of 2 in. (51 mm), as shown in Figure 96. The maximum strain observed at this location was 7% at a drift ratio of +2.28%. This value was 30% greater than the uniform elongation for this type of reinforcement ($\epsilon_{su} = 5.4\%$) and 30% smaller than the fracture elongation ($\epsilon_{sf} = 9.9\%$). Refer to No. 4 (13) Grade 120 bars in Table 9 and Figure 11. Figure 96 shows a strain jump of 4.5% was associated with the drift ratio changing from approximately 2 to 3% in the positive loading direction (stem in compression). At peak lateral displacement, near 3% drift ratio, no considerable damage was observed at the base of the wall

(other than the main crack at the wall-base block interface) to justify such large strain values, see Figure 32(a).

At an elevation of 25 in. (635 mm) above the base block, Figure 98 through Figure 101 indicate the reinforcement yielded during the cycle to 1.5% drift ratio for T5 with insufficient data for T6 to clearly identify yielding. At an elevation of 50 in. (1270 mm) above the base of T6, Figure 103 shows that non-zero strains at zero drift ratio started to grow at drift ratios near 1.5%, an indication of yielding taking place at this elevation. The strain gauge malfunctioned for T5 at this elevation. Strains greater than the strain associated with the yield stress were also recorded at an elevation of 100 in. (2450 mm) above the base block.

4.3.3 Transverse Reinforcement

The strain data recorded at the bottom two hoops of the confined stem are shown in Figure 106 through Figure 117. During the tests, none of the instrumented hoops of both walls reached the strain associated with the yield stress. At an elevation of 1.5 in. (38 mm) above the base block, the maximum measured hoop strain was 0.4% for T5 and 0.3% for T6. At an elevation of 4.5 in. (115 mm), the maximum hoop strain was 0.4% for both walls. These strain maxima were below the strain associated with the yield stress of 140 ksi (965 MPa) for the No. 3 (10) bars, see Table 9.

The strain data for the horizontal bars along the unconfined stem are shown in Figure 118 through Figure 121. For T5, the recorded data indicate that the bars located at 22.5 in. (572 mm) above the base block did not reach the strain corresponding to the yield stress of the No. 3 (10) bars. In the positive loading direction (stem in compression), the recorded maximum strain was 0.3% at a drift ratio near 3%. For T6, the maximum recorded strain did not exceed 0.25% because the gauge stopped working at a drift ratio near 2%. At an elevation of 52.5 in. (1330 mm), the horizontal No. 4 (13) bars Grade 120 (830) in T5 exceeded the strain associated with the yield stress during the cycle

to 3% drift ratio. For T6, the horizontal bar located at this elevation did not yield and recorded a maximum strain of 0.3% during the cycles to 3% drift ratio.

4.3.4 Reinforcement Strain Comparisons

Figure 121 through Figure 126 show the envelope of the longitudinal reinforcement strains in the confined stem, confined flange, and unconfined flange at the end of the loading cycles to target drift ratios of 1.5 and 2%. Figure 122(a) and Figure 123(b) indicates that the reinforcement of the confined stem of T5 experienced greater compressive strains than in T6. In contrast, T6 experienced greater tensile strain than in T5. Given that both walls have the same reinforcement ratio, maximum tensile strains occurred in T6 because the No. 6 (19) bars in the confined stem have a lower yield strain than in T5. The distribution of maximum tensile strains over the height of the wall shows greater strains in T6 than in T5 up to an elevation of 50 in. (1270 mm) above the base block. At elevations greater than 50 in. (1270 mm) the envelope tensile strains in both T5 and T6 were similar at target drift ratios of 1.5 and 2%. The maximum measured strains inside the base block were similar in both T5 and T6 with minima near zero when loading in the positive direction (stem in compression) and maxima of approximately 0.007 when loading in the negative direction (stem in tension).

The maximum strains recorded in the No. 6 (19) bars of the confined flange are shown in Figure 124 and Figure 125 for target drift ratios of 1.5 and 2%. The figures show decreasing maximum strains with an increase in elevation when the stem is in compression (positive loading direction). When the stem is in tension, the strain envelopes in the confined flange are small and nearly constant with values close to zero at an elevation of 100 in. (2540 mm) above the base block. Maximum tensile strains in the confined flange were greater in T6 than in T5 up to an elevation of 50 in. (1270 mm) with similar strain maxima at an elevation of 100 in. (2540 mm).

Figure 126 and Figure 127 show the strain envelopes for the vertical No. 4 (13) bars of the unconfined flange for target drift ratios of 1.5 and 2%. The data indicate that maximum tensile strains were greater in T5 than in T6. These envelopes differ from the pattern showed in Figure 124 and Figure 125 where the maximum tensile strains of the confined flange were greater in T6 than in T5. This discrepancy may be due to having primary flexural cracks at the unconfined flange of T5 closer to strain gauges than in T6.

4.4 Concrete Strains

Longitudinal (vertical) strain profiles were calculated at the concrete surface using data from the grid of optical markers installed on the stem (Figure 17) and the flange (Figure 18). The concrete strain (surface strain) between two adjacent markers was determined as the ratio of the change in vertical distance between two adjacent markers to the initial vertical distance between markers. Considering that the markers were installed at a nominal distance of 14 in. (356 mm), the calculated strains represent an average strain along that distance (calculated strains are based on actual, not nominal, initial distance between markers). Additional markers were used at the first two columns of the confined stem (Figure 16) to allow calculation of average strains along a nominal distance of 7 in. (178 mm). Reinforcing bar strains (Section 4.3) are generally much greater at a crack location than the reported average concrete surface strains.

The strain profiles reported in this section were calculated at the peak drift of the second cycle to target drift ratios of 1, 1.5, 2, and 3% for each loading direction. However, T5 failed during the first cycle toward a target drift of -3%, whereas T6 failed during the second cycle toward a target drift of -3%. Therefore, the strain profile reported for a target drift ratio of 3% when the wall stem was in tension represents the concrete strains during the cycle at which the wall failed (first cycle for T5 and second cycle for T6).

The calculated strain profiles associated with the eight columns of markers installed on the stem are shown in Figure 128 through Figure 143. The vertical distribution of the average concrete strain from 3 to 87 in. (76 to 2210 mm) above the base block is plotted for both directions of loading. Thirteen rows of markers were installed on Columns 1 and 2 and seven on Columns 3 to 8, enabling a more dense strain profile near the tip of the stem, see Figure 17.

Figure 144 through Figure 155 show the vertical distribution of the calculated concrete strain in the flange of the walls. A grid of four columns and seven rows was used to define the position of the markers on the flange (Figure 18). The concrete strains at the flange were calculated in the same way as in the stem. However, to visualize the strain distribution along the width of the flange, the strain is plotted versus the horizontal distance from the stem centerline. A comparison of the maximum and minimum strain profiles (envelope data) calculated for the confined stem, confined flange, and unconfined flange for both walls are shown in Figure 156 through Figure 161. The envelope are reported as elevation versus strain for both walls at target drift ratios of 1.5 and 2%.

4.4.1 Stem Longitudinal Strains

The vertical distributions of the measured concrete strain at the stem of wall T5 are shown in Figure 128 through Figure 135 for Column 1 through Column 8. When loading in the positive direction (stem in compression), an approximately uniform compressive strain distribution was observed at Column 1 throughout the height of the wall. A similar pattern is observed at Column 2 for elevations above 30 in. (760 mm) from the base, although the magnitude of the negative (compressive) strains were smaller than in Column 1. Below this point, the magnitude of concrete strains were generally maximum at the base and reduced with elevation. As the distance from the edge of the wall increased (away from the tip of the stem), Columns 3 through 8, tensile strains were recorded within 87 in. (2210 mm) from the base of the wall (case of stem in compression). At Column 3, the strain profile was nearly uniform with maximum tensile strain at the bottom of the wall (Layer

1) and minimum at the top (Layer 6). This pattern was observed throughout the range of values of drift ratios reported in these figures. Furthermore, the magnitude of the tensile strain (in Columns 3 through 8) for a given drift ratio increased in proportion to the distance from the tip of the stem, with the maximum at Column 8 (located at the flange). The unconfined stem was subjected to positive (tensile) strains throughout the test, consistent with strain gauge data from the longitudinal reinforcement of the unconfined stem (see Section 4.3.1).

When loading in the negative direction (stem in tension), a nearly linear strain distribution with maxima at the base of the wall was observed between Columns 2 and 7. The maximum strains at the perimeter of the confined stem measured at Column 2 were approximately 0.006, 0.011, 0.017, and 0.031 at target drift ratios of -1, -1.5, -2, and -3%. The tensile strain magnitudes generally decreased with distance from the tip of the stem, as shown in Figure 129 through Figure 134 for Columns 2 through Column 7 (data for Column 1 were not available for bottom rows). Furthermore, the strains generally increased with deformation demand. A compressive strain distribution was recorded at Column 8 up to a target drift ratio of -1.5%. At a target drift ratios of -2% and -3%, tensile strains were recorded in Layer 2 and above. Maximum tensile strains in the stem of T5 were approximately 0.03 in Columns 2 and 8 for the negative and positive direction of loading, respectively, measured during the cycle to 3% drift ratio. The marker of Column 1 would have measured larger strains than in Column 2 but the markers in Column 1 at the base of the confined stem detached from the concrete surface before completion of the 1.5% drift cycles.

The measured maximum strains at Columns 4 and 5 were similar in shape and magnitude for both directions of loading. The maximum strains at the unconfined stem (Columns 3 through 7) were +0.01 for Column 3 and +0.028 for Column 7 when the stem was in compression and between +0.022 for Column 3 and +0.013 for Column 7 when the stem was in tension.

Concrete strains in the stem of T6 are plotted in Figure 136 through Figure 143. When loading in the positive direction (stem in compression), a nearly uniform compressive strain distribution was observed at Column 1 up to a target drift ratio of 1.5%. At higher deformation demands (2 and 3% drift ratios), compressive strains occurred above 45 in. (1140 mm), whereas residual tensile strains occurred below this point. This observation is consistent with strain gauge data from the longitudinal reinforcement of the confined stem located at 0.5 in. or 13 mm (Figure 61), and 25 in. or 635 mm (Figure 63 and Figure 65), above the base block.

The maximum strains within the unconfined stem (Columns 3 through 7) at the base of T6 (case of stem in compression for 3% drift ratio) were all tensile strains with values of +0.023 for Column 3 and +0.036 for Column 7. The overall maximum strain was +0.045 occurring at Column 6 within Layer 2. The larger strain was due to three wide cracks that developed in Layer 2, concentrating the deformation away from other layers.

In the negative loading direction (stem in tension), for target drift ratios between 1 and 3%, tensile strains were recorded from Column 1 (Figure 136) through Column 7 (Figure 142), except for Layer 6 in Column 7. At a target drift ratio of -1.5%, the strain recorded at Columns 1 and 2 showed a strain concentration at an elevation near 27 in. (686 mm) above the base of the wall. The maximum tensile strains generally reduced with distance from the tip of the stem. The maximum tensile strains in the stem, during negative loading, varied between 0.05 and 0.06 in Columns 1 through 3 at the bottom three layers. Compressive strains occurred at Layer 1 of Column 8 (Figure 143) up to a drift of -1.5%. As the magnitude of the imposed deformation increased, the maximum tensile strain was 0.008 at Layer 3 of Column 8, whereas a small tensile strain was observed in Layer 1 (0.001) and Layer 5 (0.002). This indicates that the flexural cracks in the wall at the flange-stem intersection (Column 8) were more widely open in Layers 2 through 4 during the cycles to 2 and 3% drift ratios.

4.4.2 Flange Longitudinal Strains

The strain profile derived from markers along half-width of the flange (Figure 18) is shown in Figure 144 through Figure 149 for T5 and in Figure 150 through Figure 155 for T6. The horizontal distribution of strains at different heights (defined by six layers) above the base of the wall are presented for both loading directions. When the stem of T5 was in compression, average surface concrete strains were approximately uniform throughout the width of the flange at different levels of deformation demands, with the exception of Layer 1 (Figure 144) at target drift ratios of 2 and 3%, where the strain at the stem centerline was nearly twice the strain at the confined flange. This exception is consistent with the crack pattern observed during the test where the number of cracks at the tip of the flange exceeded those developing in the vicinity of the flange-stem intersection. It is also consistent with data from longitudinal bars in the flange (confined and unconfined) with strain gauges at 2 in. (51 mm) above the base (Figure 84 and Figure 96). Considerably larger reinforcement strains were recorded at the unconfined flange throughout the test. The longitudinal and transverse reinforcement ratio may have played a role on the tensile strain distribution given that in T5, the No. 6 (19) bars used at the flange boundary elements had very similar mechanical properties (yield strength, tensile-to-yield strength ratio, and uniform elongation) to those of the No. 4 (13) bars used at the unconfined flange (see Table 9). The lower reinforcement ratio at the flange-stem intersection compared with the confined flange may have caused fewer but wider cracks with larger reinforcement strains in the vicinity of the cracks.

When T5 was loaded in the negative direction (stem in tension), the concrete surface strains in the flange were negative (compressive) for the first three layers (below 45 in. or 1140 mm) up to a drift ratio of -2% with tensile strains occurring for a target drift ratio of -3%, see Figure 144 through Figure 146. At the top three layers (Layers 4 through 6) from 45 in. (1140 mm) to 87 in. (2210 mm), compressive strains occurred at lower drift ratios (1 and 1.5%), whereas tensile strains occurred at higher drift ratios (2 and 3%), see Figure 147 through Figure 149. The maximum tensile strain

demands in the flange of T5 occurred in the bottom three layers (Figure 144 through Figure 146). For the unconfined flange, maximum values were 0.012, 0.018, and 0.03 for drift ratios of 1.5, 2, and 3%, respectively. The maximum tensile strain demands at the confined flange were 0.0087, 0.010, and 0.018 for drift ratios of -1.5, -2, and -3%.

Concrete strain profiles for T6 are shown in Figure 150 through Figure 155. The distribution of strains were generally uniform along the half-width of the flange throughout the bottom 87 in. (2210 mm) of the wall except for tensile strains in Layer 1 at drift ratios of 2 and 3% and in Layer 2 at a drift ratio of 3%. The tensile strains decreased with height in a way similar to what was observed in T5. At Layer 1 (Figure 150), greater tensile strains occurred near the flange-stem intersection with tensile strains generally decreasing toward the confined flange, similar to what was observed in T5. The No. 6 (19) bars used at the confined flange had yield strength and uniform elongation, $f_y = 112$ ksi (772 MPa) and $\epsilon_{su} = 7.1\%$, similar to the No. 4 (13) bars used at the unconfined flange, $f_y = 109$ ksi (752 MPa) and $\epsilon_{su} = 7.3\%$. However, the tensile-to-yield strength ratio was different, $f_t/f_y = 1.18$ for the No. 6 (19) bars and $f_t/f_y = 1.24$ for the No. 4 (13) bars. The lower f_t/f_y for the bars at the confined flange may have played a role for having maximum tensile strains in Layer 1 at the unconfined flange within 20% of the maximum strains at the confined flange. For the negative loading direction (stem in tension), the flange strain profile in T6 were very similar to those of T5.

The maximum tensile strain (on concrete surface) in the unconfined flange of T6 were 0.014, 0.025, and 0.038 for target drift ratios of 1.5, 2, and 3%, respectively. The maximum tensile strain in the confined flange were 0.012, 0.021, and 0.032 for target drift ratios of 1.5, 2, and 3%.

4.4.3 Concrete Strain Comparisons

A comparison of the maximum and minimum concrete strain distributions at the confined stem, confined flange, and unconfined flange are shown in Figure 156 through Figure 161. The reported values correspond to the strain measured during the second cycle at target drift ratios of

1.5 and 2%. At a drift ratio of 1.5%, the maximum tensile strains at the confined stem were 0.014 and 0.023 for T5 and T6, respectively. The maximum tensile strains at the confined flange were 0.009 for T5 and 0.012 for T6 at the same target drift ratio. Greater concrete tensile strains were obtained at the unconfined flange with 0.012 for T5 and 0.015 for T6.

At a drift ratio of 2%, the maximum concrete tensile strains at the confined stem were 0.018 and 0.032 for T5 and T6, respectively. At the confined flange, the maximum tensile strains were 0.011 and 0.022 for T5 and T6, and at the unconfined flange maximum tensile strains were 0.018 and 0.025 for T5 and T6.

The ratio between the maximum concrete tensile strain in the confined stem to the maximum in the flange was approximately 1.2 for T5 and 1.5 for T6 at a drift ratio of 1.5%. These ratios reduced to approximately 1.0 for T5 and 1.3 for T6 at a drift ratio of 2%. The ratio was greater in T6 very likely due to the presence of a yield plateau in the stress-strain curves of the reinforcement used in T5 causing a strain jump at first yield.

The concrete strain envelopes reported in Figure 156 through Figure 161 resemble the reinforcement strain envelopes reported in Figure 122 through Figure 127 at the confined stem and confined flange. For T5, the bottom three markers of Column 1 were lost at a drift ratio of 1.5% as did the bottommost marker of Column 1 for T6. Therefore, the bottom three points of the profile for T5 and the one located at the bottom for T6 correspond to the strains calculated with the data recorded at Column 2.

The maximum tensile strain at the concrete surface for the confined stem at 1.5% drift ratio when the stem was in tension was approximately two-thirds of the maximum strain recorded by the strain gauges (Figure 56 through Figure 75) for both T5 and T6. At a target drift ratio of 2%, the ratio between the measured maximum tensile strain on the concrete surface to that of the longitudinal reinforcement was approximately 0.6 for T5 and 0.8 for T6. Compressive strains (negative values in

Figure 156 and Figure 157) measured on the concrete surface between markers at 3 and 10 in. (76.2 and 254 mm) above the base block were greater in T5 than in T6 but this was not the case between markers at 10 and 17 in. (254 and 432 mm) above the base block. Concrete spalling at the tip of the stem was likely the cause for having greater compressive strains in T6 than in T5.

It is important to note that when the stem was in tension, the minimum concrete strains in the flange (confined and unconfined) were always positive (tensile strain) throughout the bottom 87 in. (2210 mm) above the base block, see Figure 158 through Figure 161. This is an indication that compressive stresses in the flange reinforcement did not reset the residual tensile strains possibly due to having greater amount of reinforcement in the flange than in the confined stem.

4.5 Drift Components

The total measured lateral drift can be considered as the sum of four different deformation components: flexural, shear, base shearing, and base opening. The data collected by the grid of markers installed at the bottom 87 in. (2210 mm) of the wall (Figure 17 and Figure 18) were used to calculate the aforementioned deformation components. It was assumed that all the inelastic deformation was concentrated in the bottom region of the wall (nearly one-third of the wall height) and that the top region responded in the elastic range.

4.5.1 Shear Component

The shear component of drift was determined for the bottom region of the wall using data from the grid of optical markers (Figure 162). Each grid layer was divided into seven stations. The coordinates of the corners of each station were measured throughout the tests using the grid of markers installed at the stem of the wall (Figure 17). The shear distortion in each of the stations was calculated and then averaged for each horizontal layer. Thus, the distortion of one layer was defined

as the average of the distortion of seven stations. Each of the four angles on each station were measured at the beginning of the test ($A_0, B_0, C_0,$ and D_0) and at an arbitrary instant in time k . The angles $A, B, C,$ and D (Figure 163) were determined using Eq. 4 through Eq. 7 based on the law of cosines with the calculated distances between the corners of that station:

$$A_k = \cos^{-1} \left\{ \frac{h_t^2 + v_l^2 - d_2^2}{2h_tv_l} \right\} \quad \text{Eq. 4}$$

$$B_k = \cos^{-1} \left\{ \frac{h_t^2 + v_r^2 - d_1^2}{2h_tv_r} \right\} \quad \text{Eq. 5}$$

$$C_k = \cos^{-1} \left\{ \frac{h_b^2 + v_r^2 - d_2^2}{2h_bv_r} \right\} \quad \text{Eq. 6}$$

$$D_k = \cos^{-1} \left\{ \frac{h_b^2 + v_l^2 - d_1^2}{2h_bv_l} \right\} \quad \text{Eq. 7}$$

It was assumed that the change in angles of a distorted station has three components: flexural rotation, θ ; shear distortion, γ' ; and core expansion, ψ , as shown in Figure 164. These components were defined as the difference between the angles at instant k and the initial angles (at the start of the test: $A_0, B_0, C_0,$ and D_0) using Eq. 8 through Eq. 11.

$$A_k - A_0 = -\frac{\theta}{2} + \gamma' - \psi \quad \text{Eq. 8}$$

$$B_k - B_0 = +\frac{\theta}{2} - \gamma' - \psi \quad \text{Eq. 9}$$

$$C_k - C_0 = +\frac{\theta}{2} + \gamma' + \psi \quad \text{Eq. 10}$$

$$D_k - D_0 = -\frac{\theta}{2} - \gamma' + \psi \quad \text{Eq. 11}$$

Since the vertical and horizontal distance of a station was small 14 in. (356 mm), approximately equal to $1/20h_w$ and $1/7l_w$, a constant curvature along its height and length was

assumed. Under this condition, the combination of the previous equations led to the following expression to calculate the shear distortion:

$$\gamma' = \frac{1}{4}[(A_k - A_0) - (B_k - B_0) + (C_k - C_0) - (D_k - D_0)] \quad \text{Eq. 12}$$

Finally, the average shear distortion of Layer i during time step k ($\gamma_{i,k}$) was calculated as the average shear distortion contributed by each Station j (Eq. 13). In this expression, n_s represents the number of stations per layer, ℓ is the length of the station, and the negative sign was used to have positive shear distortion coincide with positive drift ratio (stem in compression).

$$\gamma_{i,k} = -\frac{\sum_{j=1}^{n_s} \gamma'_{i,j,k} \ell_j}{\sum_{j=1}^{n_s} \ell_j} \quad \text{Eq. 13}$$

The calculated shear distortions for each loading direction are shown in Figure 165 and Figure 166 for walls T5 and T6, respectively. In these figures, the calculated distortion of each layer is plotted with the vertical distance from the base to the centroid of the layer. These figures consider four different target drift ratios (1, 1.5, 2, and 3%) to evaluate the shear distortion profile. The plotted shear distortion value corresponds to the peak drift during second cycles to drift ratios of 1, 1.5, and 2%. For a target drift ratio of 3%, the first cycle was used for both walls because T5 was not subjected to a second cycle due to bar fracture occurring during the first cycle.

The shear distortion of T5 is shown in Figure 165. When the stem was in compression, an approximate uniform distribution along the bottom 87 in. (2210 mm) was observed up to a drift ratio of 2%. However, a minimum value was observed near the base of the wall (at Layer 1) throughout the test. The maximum shear distortion generally occurred at Layer 4. The maximum shear distortions were 0.003, 0.005, 0.008, and 0.014 rad for 1, 1.5, 2, and 3%. At a drift ratio of 3%, the

shear distortion of Layer 1 was 0.0075 rad when the stem was in tension, shear distortions were generally greater in Layers 3 and 6, with the lower values generally occurring in Layers 1 and 5. Maximum shear distortions of 0.005, 0.007, and 0.009 rad at -1, -1.5, and -2%, respectively, occurred at Layer 6. At higher drift ratios, the maximum distortion of 0.013 rad occurred at Layer 3 (52 in. or 1320 mm above the base block). It is important to note that based on Figure 120, the largest strain recorded for the transverse shear reinforcement was nearly 0.5% at an elevation of 52.5 in. (1330 mm) above the base (i.e., within Layer 3).

Figure 166 shows the vertical profile of the shear distortion for specimen T6. At a drift ratio of 1%, the profile of shear distortion was nearly uniform for Layers 1 through 6 in both loading directions. As the imposed drift increased, greater shear distortions generally occurred in Layers 1 through 3 with Layers 4 through 6 exhibiting a nearly uniform profile. In the positive loading direction, maximum shear distortions of 0.003, 0.009, 0.014, and 0.019 generally occurred in Layer 1 at 1, 1.5, 2, and 3% drift ratios, respectively. In the negative loading direction, maximum shear distortions generally occurred in Layer 2 with values of 0.004, 0.007, 0.014, and 0.024 at drift ratios of -1, -1.5, -2, and -3%, drift ratio.

4.5.2 Base Shearing Component

The second component of deformation considered, base shearing, was defined as the horizontal displacement (in the direction of loading) between the first row of markers ($\Delta_{X_{R1}}$) and the markers installed on the top of the base block ($\Delta_{X_{Base}}$). Sliding along the joint between the wall and the base block plus the shear distortion of the bottom 3 in. (76 mm) of the wall are considered in this component. The measured horizontal displacements are not corrected for flexural rotation, which is assumed negligible in a 3-in. (76-mm) layer.

The shear displacement caused by base shearing for T5 and T6 are shown in Figure 167 and Figure 168, respectively. In these figures, the displacement is plotted against the drift ratio. It can be seen that the maximum base shearing distortion attained for both walls during the first cycle to a target drift ratio of 2% did not exceed 0.1 in. (2.5 mm). During the cycles to 3% drift ratio, the contributions of base shearing approached 0.20 in. (5 mm) in the negative leading direction for both T5 and T6, and to 0.25 in. (6.4 mm) in the positive loading direction for T6. The larger increase in base shearing deformations of T6 during the second cycle to 3% drift ratio was likely due to the severe damage in the stem due to spalling of the concrete and buckling of the bars in the confined stem. Wall T5 did not complete the first cycle to a drift ratio of 3%, which limited the compression damage of the stem.

4.5.3 Flexural Component

The flexural component of a layer was defined as the relative rotation between the two horizontal rows that bound the layer (Figure 162). The rotation was calculated using Eq. 14, where the first term is the rotation of the top row, and the second term is the rotation of the bottom row. The rotation of each row was calculated as the relative vertical displacement of the two extreme markers (located at Columns 1 and 8) divided by the initial horizontal distance between the two columns.

$$\theta_i = \frac{(y_{R_{i+1},C_8} - y_{R_{i+1},C_1})}{\ell_{C_8C_1}} - \frac{(y_{R_i,C_8} - y_{R_i,C_1})}{\ell_{C_8C_1}} \quad \text{Eq. 14}$$

In Eq. 14, θ_i is the flexural rotation of Layer i and $y_{R,C}$ refers to the vertical displacement of the markers at Row R and Column C relative to their initial position. The denominator in both terms, $\ell_{C_8C_1}$ is the initial horizontal distance between markers in Row $i + 1$ at Columns 1 and 8.

The calculated flexural rotations for T5 and T6 are shown in Figure 169 and Figure 170, where the rotations for the six layers representing the bottom 87 in. (2210 mm) of the wall are plotted for different values of drift ratios. For positive drift ratios (stem in compression), Figure 169 shows two plots of the flexural rotation of T5 based on the use of Columns 1 and 8 or Columns 2 and 7. After a drift ratio of 2% on the way to the first cycle of 3%, the presence of a wide crack between Rows 4 and 5 (indicated with arrows in Figure 171) caused a reduction of the angle of rotation for Row 4. The wide crack affected the calculated flexural rotation of Layers 3 and 4 (represented in the top left plot of Figure 169 by the third and fourth point above the base). When using Columns 2 and 7, the flexural rotation showed a different profile. In general, the flexural rotation increased with an increase in drift ratio and reduced with an increase in elevation from the base of the wall. When the stem was in compression, the maximum flexural rotations (based on data from Columns 2 and 7) were 0.0014, 0.0018, 0.0026, and 0.0044 rad at target drift ratios of 1, 1.5, 2, and 3%, respectively. When loading in the negative direction (stem in tension), an approximate linear distribution is observed with maximum flexural rotations at the base of the wall of 0.0010, 0.0018, 0.0028, and 0.0043 rad at drift ratios of -1, -1.5, -2, and -3%, respectively. At a drift of -3%, the flexural rotation diminished considerably in Layers 3 through 6. Considering that the data in the figure were calculated at the peak force during this half cycle (just before the bars fractured), the concentration of flexural deformation at the base of the wall is likely associated with longitudinal bars at the onset of fracture in the confined stem.

The flexural rotation for T6 is shown in Figure 170. A nearly linear distribution was observed when the stem was in compression with a maximum rotation at the base of the wall. The maximum flexural rotations generally occurred at the base of the wall with values of 0.0012, 0.0024, 0.0041, and 0.0063 rad for drift ratios of 1, 1.5, 2, and 3%, respectively. The flexural rotations in the negative loading direction were also generally greater at the base of the wall. When loading in the negative direction (stem in tension) maximum flexural deformations of 0.0014, 0.0026, 0.0036, and 0.0067

rad are reported for drift ratios of -1, -1.5, -2, and -3%. At a drift ratio of -3%, the flexural rotation increased considerably in Layer 1 and diminished in the top two layers (Layers 5 and 6) to magnitudes corresponding to lower drift ratios. The large rotations in Layer 1 are indicative of concentrated damage due to spalling of concrete and bar buckling at the perimeter of the confined stem.

4.5.4 Base Opening Component

The component of drift due to base opening was defined to include flexural rotations occurring within the bottommost 3 in. (76 mm) of the wall and rotation due to elongation of the bars within the base block. Base opening (θ_{bo}) was calculated using

$$\theta_{bo} = \frac{(y_{R_1,C_8} - y_{R_1,C_1})}{\ell_{C_8C_1}} - \theta_{base} \quad \text{Eq. 15}$$

where y_{R_1,C_8} and y_{R_1,C_1} are the change in position (along the vertical y axis) of markers in Row 1 at Columns 8 and 1, and $\ell_{C_8C_1}$ is the distance between markers in Columns 1 and 8 (at Row 1). The rotation of the base (θ_{base}) about an axis normal to the plane of the wall stem was calculated using the positions of markers B1 and B6 (Figure 19). This deformation component accounts for the additional rotation caused by strain penetration (or bond slip) of the longitudinal reinforcement developed into the base block.

The base opening rotation versus drift ratio is shown in Figure 172 for T5 and Figure 173 for T6. Base opening increased in proportion to drift ratio in both loading directions up to $DR = 2\%$ for T5 and $DR = 1.5\%$ for T6. At $DR = 1\%$, both walls exhibited a base opening of approximately 0.0015 rad. Base opening in T5 at $DR > 2\%$ shows a positive shift for base opening rotation possibly due to

concrete spalling at the tip of the stem. The nearly linear relationship between base opening and drift ratio for T5, even after yielding of the flange reinforcement, was possibly affected by the lack of yield plateau and high tensile-to-yield strength ratio for the reinforcement in T5.

Base opening of T6 increased at a lower rate for the positive loading direction (stem in compression) up to the first cycle to $DR = 3\%$ and remained nearly proportional to drift ratio in the negative loading direction. This implies that upon tension yielding of the flange and given the low tensile-to-yield strength ratio of the reinforcement in T6, strain penetration and curvature at the base of the wall increased at a lower rate with increased drift ratio. Deviations in base opening rotation of T6 during the second cycle to $DR = 3\%$ (with respect to the first cycle) were affected by spalling of concrete and bar buckling at the base of the confined stem. The flattening of the curve was not as apparent in the negative loading direction possibly due to the more gradual yielding of the reinforcement layers in the stem.

4.5.5 Drift Component Comparisons

The contribution of the four components of drift (shear, base shearing, flexure, and base opening) to the total lateral deformation is determined in this section based on the second cycle of each step of the loading protocol (Figure 9) for target drift ratios between 0.5 and 2%. The following expressions were used to calculate the deformations due to shear (Δ_v), base shearing (Δ_{bs}), flexure (Δ_f), and base opening (Δ_{bo}):

$$\text{Shear:} \quad \Delta_v = \sum_{i=1}^{n_l} \gamma_i h_i \quad \text{Eq. 16}$$

$$\text{Base shearing:} \quad \Delta_{bs} = -(\Delta_{X_{R1}} - \Delta_{X_{Base}}) \quad \text{Eq. 17}$$

$$\text{Flexure:} \quad \Delta_f = \sum_{i=1}^{n_l} \theta_i h_{y,i} \quad \text{Eq. 18}$$

Base opening:

$$\Delta_{bo} = \theta_{bo} h_y \quad \text{Eq. 19}$$

where all terms are defined in Appendix A.

To derive the percent contributions shown in Figure 174 through Figure 177, the drift components were divided by the total displacement at the top of the wall (elevation 286 in. or 7260 mm above the base block) during second cycles. The use of Eq. 16 through Eq. 19 was all dependent on data measured by the motion capture system tracking the position of the optical markers on the bottom 87 in. (2210 mm) of the wall (see Figure 15 through Figure 19).

The shear distortion of the first 3 in. (76 mm) above the base block was determined using Eq. 17, where the negative sign is introduced to make the positive base shearing coincide with positive drift (stem in compression). Eq. 18 assumes curvature due to flexure is uniformly distributed along the height and length of each layer; and Eq. 19 includes flexural deformation of the bottom 3 in. (76 mm) of the wall due to effects of strain penetration (into the base block) and curvature (below markers in Row 1, see Figure 17).

Figure 174 and Figure 175 show that both walls exhibited a behavior dominated by flexure (including base opening), which accounted for more than 50% of the total deformation for drift ratios between 1 to 3%. A nearly constant contribution of shear distortion between 10 and 15% was found throughout the test, whereas the deformation due to base shearing contributed with approximately 2%. Clearly, base shearing played a minor role throughout the test. The contribution of the rotation due to base opening varied between specimens. For T5, this component provided approximately 15% of the total lateral drift when the stem was in compression, and 10% when the stem was in tension. For T6, the contribution of base opening to total deformation was nearly constant at approximately

18% when the stem was in tension, and varied between 18 and 8% when the stem was in compression, with lower values for higher drift ratios.

The cumulative contribution of each component to the total lateral drift is shown in Figure 176 for T5 and Figure 177 for T6. In these figures, the contribution is expressed in percentage and is plotted against drift ratio. Considering that only data from the bottom 87 in. (2210 mm) of the wall were included, the reported cumulative percentage is less than 100%. According to these figures, for values of drift ratios between 1 and 3%, the bottom 87 in. (2210 mm) of the wall contributed with 80 to 95% of the total imposed deformation, with the exception of T5 in the negative loading direction (stem in tension), where 70% of the deformation was concentrated at the bottom region of the wall.

The greater contribution of flexural deformation in the positive direction of loading (stem in compression) is likely related to having the primary flexural reinforcement within 10 in. (254 mm) from the edge of the wall, which causes a nearly simultaneous yield of the flange reinforcement. The smaller contribution of flexural deformations in T5 (for negative loading) were very likely influenced by the stress-strain curves of the Grade 120 (830) reinforcement (Figure 10 and Figure 11) without a yield plateau and with greater tensile-to-yield strength ratio, delaying the development and concentration of plastic curvatures at the base of the wall.

4.6 Crack Widths

In earthquake-resistant design of reinforced concrete members, crack control is typically of secondary concern given that members are detailed to withstand flexural yielding. However, crack widths can be used as an approximate external measure of damage.

Crack widths were recorded to evaluate the influence of the grade of reinforcement on crack control in members subjected to inelastic displacement reversals. Four locations were selected to take measurements: the confined and unconfined flange, and the confined and unconfined stem,

where the concrete surface was free of any type of instrumentation. A crack comparator was used to sequentially measure the cracks during the second cycle of each loading step up to $DR = 2\%$: at peak positive drift ratio (stem in compression), zero shear force (after unloading), peak negative drift ratio (stem in tension), and zero shear force (at end of loading step).

Figure 178 illustrates the crack width history versus drift ratio for the confined and unconfined flange when the stem was in compression (positive direction) followed by the measurements at zero applied shear force in Figure 179. When loading in the negative direction (stem in tension), the crack widths at peak drift are shown in Figure 180, whereas Figure 181 plots crack widths measured at the end of the loading step. It can be seen that both walls exhibited a similar behavior up to $DR = 2\%$.

To evaluate the effect of inelastic displacement reversals on crack widths, the ratio of crack width at zero lateral force (w_{zero}) to crack width at the preceding peak displacement (w_{peak}) was calculated and reported in Figure 182 for the confined and unconfined flange when loaded in the positive direction (stem in compression) and Figure 183 for the confined and unconfined stem when loaded in the negative direction (stem in tension). For both walls, at the end of the second cycle to a drift ratio of 2%, the cracks at zero force were approximately 60% of the cracks at peak displacement for the confined and unconfined stem and for the confined and unconfined flange. For loading cycles with drift ratios lower than 2%, the crack width ratios varied between 20 to 80%.

4.7 Wall Elongation

The elongation of the wall was calculated using the markers installed at the bottom region of each wall (87 in. or 2210 mm above the top of the base block), including the bottommost 3 in. or 76 mm (Figure 162). Elongation was defined as the change in the vertical distance between two adjacent markers on the same column of markers (see Figure 17) determined at the end of a loading step (Figure 9). Elongations for the loading steps associated with the target drift ratios of 0.75, 1, 1.5, 2,

and 3% were calculated. For a drift ratio of 3%, elongation data for T5 were not available given that T5 failed before completing the first cycle to 3% drift, whereas for T6 the first cycle to 3% drift were used given that T6 failed during the second cycle. Vertical distributions of the calculated elongations are presented in Figure 184 and Figure 185 for T5 and T6, respectively. The bottom points in these figures correspond to the elongation calculated for a 3-in. (76-mm) thick layer, whereas 14-in. (356-mm) thick layer was used for other points.

As shown in the figures, a nearly uniform elongation was recorded for drift ratios less than 1%, with maximum elongations of approximately 0.02 in. (0.5 mm) for T5 and 0.03 in. (0.8 mm) for T6. These values are an indication of very limited damage. As the imposed drift ratio increased, the elongation over the height of the wall increased. Starting at a drift ratio of 1.5%, the distribution of the elongation changed considerably between the specimens. The elongation profile for T5 was approximately uniform over the height with a maximum of 0.07 in. (2 mm) for Layer 2 at elevations between 17 and 31 in. (432 and 787 mm) above the base, while the elongation profile for T6 showed a more pronounced increase for Layers 1 and 2, with a maximum of 0.13 in. (3.3 mm). This deformation was nearly twice the elongation of T5.

At a drift ratio of 2%, both walls exhibited maximum elongations in Layers 1 and 2 at elevations between 3 and 31 in. (76 and 787 mm). The maximum elongation for T5 was of 0.12 in. (3 mm), whereas 0.25 in. (6.4 mm) was reported for T6. Even though the elongation profiles of both walls were similar at this level of drift ratio, the elongation of T6 was approximately two times that of T5. These differences may be due to the tensile-to-yield strength ratios of the No. 6 (19) primary flexural reinforcement with $f_t/f_y = 1.33$ for T5 and $f_t/f_y = 1.18$ for T6. In addition, the No. 6 (19) bars in T5 did not exhibit a yield plateau, which helped reduce plastic deformations. The ratio of maximum-to-minimum residual deformation at a drift ratio of 2% was approximately 2 for T5 and 4 for T6.

4.8 Wall Stiffness

Two types of stiffness were calculated for each wall, the effective initial stiffness (K_e) and the unloading stiffness (K_u). Stiffness K_e is defined as the secant stiffness to the notional yield point (Δ_y, F_y) of an idealized force-deformation relationship (Figure 186). Stiffness K_u is defined as the secant stiffness from the maximum displacement of a loading cycle to the point of zero force (Figure 186). Both K_e and K_u are key parameters for representing nonlinear response of reinforced concrete members subjected to strong ground motions.^[65,85]

4.8.1 Effective Initial Stiffness

The envelopes of the measured shear-drift response are shown in Figure 187 and Figure 188 for T5 and T6, respectively. The breakpoints correspond to the maximum shear attained during each loading step (Figure 9) and its corresponding drift ratio. The coordinates of each breakpoint are listed in Table 12. For direct comparison, the envelopes of both walls are plotted in Figure 189. The figure also shows the shear strengths associated with the nominal flexural strengths ($V_{M_n}^+$ and $V_{M_n}^-$) calculated using specified material properties (see Table 5). The figure shows that the walls exceeded the calculated strength for each loading direction. Greater deformation capacity was achieved by T6 in both loading directions. However, the strength of T5 was 25% greater than the strength of T6 in the positive direction and 35% in the negative direction. These differences are mainly due to T5 having a higher grade of reinforcement and a higher tensile-to-yield strength ratio.

The key parameters used to determine the effective initial stiffness are shown in Figure 189, where the maximum shear (V_{max}) and the notional yield force ($0.8V_{max}$) are shown for both walls. The secant stiffness (K) associated with each breakpoint in Figure 188 is included in Table 12, where the effective initial stiffness corresponding to the point where $V = 0.8V_{max}$ was derived using linear interpolation as indicated at the bottom of Table 12. The average measured values of K_e for T5 were 93 kips/in. (16.3 kN/mm) and 130 kips/in. (22.8 kN/mm). These measured values include the effects

of flexure, shear, and strain penetration. For both walls, the measured effective initial stiffness (K_e) normalized by the flexural stiffness calculated based on gross section properties ($K_{f,I_g} = 3E_c I_g / h_w^3$) is shown in Figure 190 and the cracked moment of inertia (I_{cr}) normalized by the gross moment of inertia (I_g) is shown in Figure 191. The calculated stiffness ratios in Figure 190 were approximately 0.09 for T5 and 0.13 for T6. Given that both walls had identical reinforcement ratio, the cracked-to-uncracked stiffness ratio was nearly the same, with I_{cr} based on values from Table 13.

The stiffness associated with flexural and shear deformations was calculated using formulas based on beam theory, as described in the footnotes of Table 13. The stiffness associated with strain penetration (or bond slip), also described in Table 13, was based on the development length of the No. 6 (19) bars. The measured-to-calculated stiffness ratio in Table 13 indicate that the calculated stiffness for T5 was greater than the measured stiffness. For T6, the calculated stiffness was less than the measured stiffness. The calculated stiffness assumes cracked sections properties throughout the height of the wall. The table considered values for the stiffness reduction factor (ϕ_k) proposed by Moehle^[55].

The calculated stiffness of wall T5 resulted approximately 20% greater than the measured stiffness. The overestimation is in part due to the reduced modulus of elasticity of Grade 120 (830) reinforcing bars starting at a stress of approximately 100 ksi (690 MPa), near 80% of the nominal yield stress (see Figure 10 and Figure 11). The transformed cracked section moment of inertia (I_{cr}) used in the calculated flexural stiffness was based on a constant modulus of 29,000 ksi (200,000 MPa) for the reinforcement. The calculated stiffness of wall T6 resulted approximately 10% lower than the measured stiffness, an indication that flexural and shear cracking did not extend throughout the wall height as assumed in the calculations.

The displacement due to strain penetration is assumed to cause a rigid body rotation at the base of the wall. This contribution was calculated assuming the primary flexural reinforcement

develops f_y for an embedment length of $2\lambda d_b$ into the foundation with a uniform bond stress. An average strain of $\varepsilon_y/2$ was assumed along the embedment length. The design equation for development length in ACI 408^[2] was used to determine λ . Values of $\lambda = 20$ for T5 and 16 for T6 were derived for $\phi = 1$, confined concrete, f_{cm} , and actual f_y .

4.8.2 Unloading Stiffness

The unloading stiffness was defined as the secant stiffness calculated from the point of maximum drift (Δ_{max}, V_{max}) of a loading cycle to the point of zero shear force ($\Delta_o, 0$) after unloading from the point of maximum drift. The unloading stiffness shown in Table 14 and illustrated in Figure 192 corresponds to data measured during the second cycle for each step of the loading protocol (Table 4), starting from step 2 with a target drift ratio of 0.3%. In this figure, K_u was plotted against drift ratio showing a reduction of approximately 35% from $DR = 1\%$ to $DR = 2\%$ for both walls. T6 exhibited a reduction in the value of K_u of nearly 50% from $DR = 1\%$ to $DR = 3\%$. The unloading stiffness normalized with respect to the flexural stiffness based on gross moment of inertia ($K_u/K_{f,Ig}$) is shown in Figure 193, where the unloading stiffness at high levels of deformation can be as low as 5% of the uncracked stiffness.

For each loading direction, the unloading stiffness (K_u) is generally defined as a function of the effective initial stiffness (K_e)^[65] based on Eq. 20:

$$K_u = K_e \left(\frac{\Delta_y}{\Delta_{max}} \right)^\alpha \quad \text{Eq. 20}$$

where Δ_{max} is the previously attained maximum displacement and Δ_y is the notional yield displacement (refer to Section 4.8.1), both defined for each direction of loading. Parameter α is the stiffness reducing exponent. For reinforced concrete, α normally ranges between 0 and 0.5^[65], and controls stiffness retention during computed inelastic cyclic response. Using the data from Table 14

for K_u and Δ_{max} , the values of α were determined for different drift ratios based on Eq. 20, where the notional yield displacement (Δ_y) was taken as the deformation associated with $V_y = 0.8V_{max}$ (per loading direction) divided by K_e (taken as the average of K_e^- and K_e^+ , reported in Table 12). The calculated values of α are shown in Figure 194 for both walls as a function of the normalized yield displacement (Δ_y/Δ_{max}). For T6 the values of α varied between 0.3 and 0.5 for normalized displacements between 2 and 4. The limited data derived for T5 resulted in values of α similar to those obtained for T6.

4.9 Hysteretic Behavior

4.9.1 Takeda Model

A simplified force-deformation relationship based on the Takeda hysteresis model^[65,85] was developed to compare the measured response of both walls. The parameters needed to describe the model are illustrated in Figure 186. In this figure, the initial stiffness (K_e) in both directions was taken as the average of the measured stiffness in the positive and negative loading directions, reported at the bottom of Table 12. The post-yield stiffness (K_{py}) was taken as $0.15K_e$ for T5 and $0.05K_e$ for T6; the yield force (F_y) was the value associated with $V = 0.8V_{max}$, and the stiffness reduction exponent α was taken as 0.35 for both walls based on Figure 194.

The comparison between the calculated force-deformation relationship (based on Takeda model) and the measured response is shown in Figure 195 and Figure 196. The initial line segments of the Takeda model connect the origin to the yield points of coordinates $(F_y/K_e, F_y)$ followed by post-yield line segments of slope K_{py} connecting the points corresponding to peak drift in Table 14. At each peak drift, the model unloads based on the value of α and reloads in the opposite direction toward the previously attained maximum displacement in the direction of loading. A reasonable agreement is observed between both curves, indicating the selected parameter values are satisfactory.

4.9.2 Energy Dissipation

Comparisons of the measured shear versus drift ratio for T5 and T6 during the second cycle to 1, 1.5, 2, and 3% drift ratios are illustrated in Figure 197 through Figure 200. During the cycle corresponding to a target drift ratio of 1%, both walls showed similar stiffness and area enclosed by the hysteretic loop. However, starting from the cycle to a target drift ratio of 1.5% through the end of the test, the area under the curve for T6 increased with respect to that of T5. The shear at drift ratios greater than 1% were greater in T5 than in T6, an indication that T5 yielded at a greater drift ratio than T6 (given that both walls had the same reinforcement ratio).

The area under the curve of the hysteretic cycles shown in these figures was used to calculate the hysteretic energy dissipation index (E_h) defined by Eq. 21:

$$E_h = \frac{W}{\pi \Delta_m V_m} \quad \text{Eq. 21}$$

A separate index was calculated for each loading direction for target drift ratios of 1, 1.5, 2, and 3%. In Eq. 21, W is the hysteretic energy dissipated per half cycle for each loading direction, Δ_m is the maximum displacement of the half cycle considered, and V_m is the shear associated with Δ_m (Figure 201). The index E_h follows the definition by Otani^[65] to represent the equivalent viscous damping factor of a linear-elastic system capable of dissipating W in one cycle under steady-state oscillation.

The calculated values of E_h are plotted against drift ratio in Figure 202. Consistent with the observations made in Figure 197 through Figure 200, values of E_h were greater for T6 in both loading directions, indicating more energy was dissipated in T6 (with Grade 100 reinforcement) than in T5 (with Grade 120 reinforcement). At low drift ratios ($DR = 1\%$), similar values of E_h were obtained. The difference increased as more deformation was applied to the walls. At $DR = 2\%$, the difference

was approximately 40% when the stem was in compression and 65% when the stem was in tension. The greater values of E_h for T6 are due to the lower grade of reinforcement, which yielded at a lower drift ratio and led to increased ductility demands. Data is not shown for T5 at $DR = -3\%$ because the wall failed before completing the first cycle to 3% drift ratio.

4.9.3 Modeling Parameters

ASCE 41 (2017)^[5] gives recommendations for developing the generalized force-deformation relationship of structural walls to perform nonlinear seismic analysis. The recommended envelope and modeling parameters are shown in Figure 10-1(a) and Table 10-19 of ASCE 41-17 with the definitions of points *A* through *E* (see Table 15). In ASCE 41 (2017), the initial line segment *AB* is defined by the effective initial stiffness based on I_{eff} and $A_{cv,eff}$, in combination with the strength at *B* based on M_n (see Table 15). The capping or peak force defines point *C* based on M_{pr} , and the residual strength defines points *D* and *E*. The values in Table 15 for ASCE 41 correspond to walls controlled by flexure and subjected to low axial stress. For T5, the normalized shear stress of $V/A_{cv}\sqrt{f_{cm}} \text{ (psi)} = 4.6$ (0.38 for MPa) requires linear interpolation between the tabulated values of 4 and 6. In addition to ASCE 41 recommendations, Table 15 includes proposed values specific for walls with Grade 100 (690) reinforcement based on Huq et al.^[37] and for Grade 120 (830) the values are based on data from T5.

A comparison between the measured hysteretic response and the envelopes defined in Table 15 is shown in Figure 203 for both walls. The plotted data show that the proposed values for I_{eff}/I_g and $A_{cv,eff}/A_{cv}$ are more realistic than those obtained following ASCE 41. It is important to note that both models (Proposed and ASCE 41) consider the combined effects of the effective flexural and shear stiffness on the initial stiffness.

The data in Figure 203 show that the measured response for both walls intersects the proposed post-yield line between points *B* and *C*, whereas the proposed post-yield line based on ASCE

41 (2017) only intersects the measured response of T5 in the positive loading direction. The proposed value of $1.1M_n$ instead of M_{pr} (see footnote *h* in Table 15) provides a reasonable estimate of the expected strength. Regarding the deformation capacity and residual strength defined by segment *DE*, the curves for T5 and T6 exceed segment *DE* in both loading directions, an indication that the proposed envelope represents reasonable limits.

The above observations suggest that the modeling parameters in ASCE 41 (2017) for structural walls subjected to low axial stress need to be modified; in particular, the values associated with initial effective stiffness (to define point *B* or yield point) and peak force (to define point *C* or capping point).

5 WALL RESPONSE COMPARISONS

The responses of walls T5 and T6 are compared with the results obtained by Huq et al.^[37], who tested four walls (T1 through T4) with nearly identical geometry, test setup, and loading protocol. One of these walls (T1) was the control specimen with conventional reinforcement (Grade 60 or 420 MPa), the other three (T2, T3, and T4) were reinforced with Grade 100 (690 MPa) steel bars. The comparisons presented in this chapter refer to shear versus drift ratio, reinforcing bar strain, concrete surface strain, components of drifts, effective initial stiffness and unloading stiffness, and hysteretic energy dissipation index.

5.1 Wall Properties

The nominal dimensions of the walls tested by Huq et al.^[37] were identical to those of the walls tested in this project. The walls differed in the mechanical properties of the reinforcement and the number of longitudinal bars in the confined boundary elements. The mechanical properties of the concrete and steel for all six walls are listed in Table 16 and Table 17. Wall cross section and reinforcement are shown in Figure 204 through Figure 207. Walls T1 through T4 had nearly identical ρf_y in the stem boundary element. Wall T1 had 27 No. 6 (19) bars Grade 60 (420) at the confined stem, whereas T2, T3, and T4 had 16 No. 6 (19) bars Grade 100 (690). The confined stem of T5 was reinforced with 14 No. 6 (19) bars Grade 120 (830) and T6 was also reinforced with 14 No. 6 (19) bars but Grade 100 (690). The amount of longitudinal reinforcement in the confined flanges was 12 No. 6 (19) bars in T1 and 6 No. 6 (19) bars in all other walls. The amount of longitudinal and transverse reinforcement in the unconfined stem and flange was identical in T1 through T6. The amount of confining reinforcement in T2 through T6 was identical.

As indicated in Table 17, the tensile-to-yield strength ratios (f_t/f_y) of the longitudinal reinforcement varied from 1.34 to 1.39 for Grade 60 in T1, 1.10 to 1.36 for Grade 100 (690) in T2, T3,

T4, and T6, and 1.32 to 1.33 for Grade 120 (830) in T5. The uniform elongation (ϵ_{su}) in all of reinforcing bars was greater than 6% except for the No. 4 bars in T2 and all bars in T5.

Figure 208 shows the wall drift ratio capacity (DR_{cap} from Table 21) versus the uniform elongation (ϵ_{su} from Table 17) of the longitudinal reinforcing bars for each wall. The data in Figure 208 show that walls having longitudinal reinforcement with $\epsilon_{su} \geq 6\%$ and $f_t/f_y \geq 1.2$, had a drift ratio capacity of 3% or greater. Figure 209 shows the wall drift ratio capacity versus the fracture elongation (ϵ_{sf} from Table 17) of the longitudinal reinforcing bars for each wall. The figure shows that walls with longitudinal reinforcement having $\epsilon_{sf} \geq 10\%$ and $f_t/f_y \geq 1.2$, had a drift capacity not less than 3%.

The lines defining the quadrants in Figure 208 and Figure 209 were chosen based on the data corresponding to T4, which reached a drift ratio capacity of 3.9% with reinforcing bars having f_t/f_y , ϵ_{su} , and ϵ_{sf} as low as 1.20, 6.5%, and 10.9%, respectively. The boundaries of the quadrants were set after rounding down values of DR , f_t/f_y , ϵ_{su} , and ϵ_{sf} to 3%, 1.2, 6%, and 10%, respectively.

The importance of the uniform elongation in the response of the walls is revealed when comparing T2 with T6. Both walls had reinforcing bars with tensile-to-yield strength ratios less than 1.20 (1.10 for T2 and 1.18 for T6) and fracture elongations not less than 10% (10% for T2 and 10.1% for T6). However, the uniform elongation of the bars that controlled the response in T6 was 7.1%, whereas in T2 the uniform elongation was 5.7%. This 25% difference in uniform elongation, combined with the lower values of f_t/f_y and ϵ_{st} for T2, had effect on the deformation capacity of T2 ($DR_{cap} = 1.8\%$) compared with T6 ($DR_{cap} = 3.1\%$). In addition, when comparing two walls with reinforcing bars having similar uniform elongation (5.7% for T2 and 5.4% for T5), and similar fracture elongation (10% for T2 and 9.9% for T5), but different tensile-to-yield strength ratios (1.10 for T2 and 1.33 for T5), the deformation capacities of both T2 and T5 were below 3% (1.8% for T2

and 2.3% for T5). The data suggest that the combined effect of tensile-to-yield strength ratio and uniform elongation played a major role in the deformation capacity of the walls.

5.2 Shear versus Drift Ratio

The shear versus drift ratio of all six walls tested at The University of Kansas are plotted in Figure 210. The dashed lines represent the shear (V_{M_n}) associated with the nominal flexural strength (M_n) calculated based on ACI 318-14^[1]. The plotted data show that the calculated flexural strength was exceeded in all cases except in the negative loading direction (stem in tension) for T2. This result was mainly attributed to the premature failure of the No. 4 (13) bars at the unconfined flange, which had a low uniform elongation (5.7%), and tensile-to-yield strength ratio (1.10), refer to Huq et al.^[37] for more details.

The difference between the calculated nominal flexural strength and the measured strength varied approximately between 5 and 25% in the positive loading direction and between 5 and 20% in the negative loading direction. The difference was nearly proportional to the tensile-to-yield strength ratio (see Table 18) and to the ratio of measured-to-nominal yield strength of the flexural reinforcement.

Three walls (T1, T3, and T4) were able to complete two cycles at 3% drift ratio without a 20% loss of lateral strength. In these walls, fracture of flexural reinforcement occurred during the first cycle to a drift ratio of 4%. The bars that fractured had buckled during the previous half cycle. Wall T6 completed one cycle to 3% drift ratio and failed due to bar fracture during the second cycle to 3% after bar buckling was observed. However, the bars that fractured in T2 and T5 did not buckle in previous cycles, suggesting that the uniform or fracture elongation of the bars in T2 and T5 was insufficient to mobilize bar buckling followed by bar fracture. It is important to note that bar buckling occurred without a 20% loss of lateral strength.

5.3 Reinforcement Strain Envelopes

The envelopes of the measured strain in the longitudinal bars at the confined stem, confined flange, and unconfined flange are shown in Figure 211 through Figure 216. The profiles in these figures represent the maximum and minimum strains corresponding to peak drifts during the second cycles to 1.5 and 2% drift ratios. The overall maximum tensile strains in the No. 6 (19) bars of the confined stem occurred in T2 at 0.5 in. (13 mm) above the base of the wall, followed by T6. For a drift ratio of 1.5% (Figure 211), the longitudinal reinforcement of the confined stem of T6 shows a peak tensile strain at the base of the wall similar to that of T2. For a drift ratio of 2% (Figure 212), the maximum tensile strain at the base of T2 was nearly 8% (or approximately twice the maximum strain measured at a drift ratio of 1.5%), whereas for T6 the maximum tensile strain remained nearly proportional to the increase in drift ratio. Note that the No. 6 (19) bars in the confined stem of T2 and T6 had similar tensile-to-yield strength ratio ($f_t/f_y = 1.15$ for T2 and $f_t/f_y = 1.18$ for T6) and bars in T6 did not exhibit a yield plateau. The envelope of minimum strains (compressive strains) recorded for the reinforcement in the confined stem were similar in all six walls except for T1 and T2 at the base of the wall showing strains of -0.005 at drift ratios of 1.5%. These large compressive strains are typically associated with concrete spalling at the tip of the stem.

The maximum and minimum strain profiles of the No 6. (19) bars of the confined flange are shown in Figure 213 and Figure 214 for drift ratios of 1.5 and 2%. Except for T2, the profiles for all walls are similar. The maximum and minimum strains for T2 were always positive (tensile strains) with values two to three times greater than those in other walls. As the target drift ratio increased from 1.5% to 2% (Figure 214), the maximum strains increased in proportion to the imposed drift ratio. Tensile strains did not concentrate at the base of the walls, except for T2, which experienced fracture of the No. 4 (13) bars located at the unconfined flange, see Huq et al.^[37] for more details.

Strain envelopes for the unconfined flange are shown in Figure 215 and Figure 216 for drift ratios of 1.5 and 2%. The maximum recorded reinforcement strain when the stem was in compression were similar at the base of the walls (2 in. or 51 mm above the base block) with the exception of T2, which had No. 4 (13) bars with the lowest tensile-to-yield strength ratio ($f_t/f_y = 1.10$). For the stem in compression the profiles of the strain envelopes for T5 and T6 were similar to the strain profiles of other walls.

5.4 Concrete Strain Envelopes

The envelopes of the concrete strain measured on the surface of the confined stem, confined flange, and unconfined flange are shown in Figure 217 through Figure 222. These concrete strain profiles show the maximum and minimum strains corresponding to peak drifts during second cycles to target drift ratios of 1.5 and 2%. In the negative loading direction (stem in tension), the strain distribution of T5 at 1.5% drift ratio for the confined stem in Figure 217 shows a uniform distribution over the height because at Column 1 the bottom three markers detached before reaching 1.5% (data for T5 in Figure 217 correspond to Column 2).

At a target drift ratio of 2%, Figure 218 show that the maximum tensile strains in the confined stem, when the stem was in tension, occurred in T2 and T6 in the bottom two layers. These strains were greater in T2 possibly due to the lower f_t/f_y of their No.6 (19) bars in the confined stem ($f_t/f_y = 1.15$ for T2 and 1.18 for T6). Figure 220 also shows T2 and T6 at a drift ratio of 2% with maximum tensile strains at the base of the confined flange, which is also reinforced with No. 6 (19) longitudinal (vertical) bars. In the positive loading direction (stem in compression), compressive strains occurred in Columns 1 and 2 throughout the bottom 87 in. (2210 mm) of the walls for target drift ratios of 1.5 and 2%.

The maximum tensile strains in the flange and stem, at a drift ratio of 2% indicate that the unconfined flange at the lower layers had strains between 0.015 and 0.03, whereas for the confined

flange maximum values were between 0.01 and 0.02, and maxima in the confined stem were similar to maxima in the unconfined flange.

5.5 Deformation Components

Based on the four deformation components (shear, base shearing, flexure, and base opening) described in Section 4.5, the relative contributions of each to the total wall drift were calculated for the second cycle of loading to each target drift ratio from 0.5 to 3% (plots for T2 were limited to a drift ratio of 2% because of wall failure). The loading protocol is described in Section 3.4.3.

The calculated relative contributions to drift are shown in Figure 223 through Figure 226 for each deformation component within the bottom 87 in. (2210 mm) of the wall instrumented with optical markers (see Figure 17 and Figure 18). The calculated data are plotted as a percentage of total drift versus drift ratio. The sum of the relative contributions do not add to 100% because contributions from the top 70% of the wall height are not considered.

Walls T5 and T6 show relative contributions to drifts similar to other walls reinforced with high-strength steel bars. In all six walls, flexural rotations (including the effects of base opening) were the largest deformation component, accounting for 50 to 80% of total drift for drift ratios between 1 and 3%.

Shear distortion in T5 and T6 accounted for 10 to 15% of overall drift, depending on the level of drift demand, with higher contributions typically corresponding to higher drift ratios. Less than 2% was contributed by the base shearing component. For a more detailed comparison between walls T1, T2, T3, T4, refer to Huq et al.^[37]

5.6 Effective initial stiffness and Unloading Stiffness

Figure 227 shows the envelope of the shear versus drift ratio for each of the six walls in individual plots. These plots are combined in Figure 228. The plotted data show in the positive

loading direction that all the walls with high-strength reinforcement exhibited similar behavior, as did T1 with conventional Grade 60 (420) reinforcement. Some differences are apparent in the strength, though. The main exception was T2, which showed a sudden drop in shear after the No. 4 (13) bars fractured prematurely at 1.8% drift ratio, and T5 which reached the highest shear. In the negative loading direction, the level of shear attained did not vary as much as it did per the positive loading direction, with T5 reaching the highest shear. This can be attributed to the higher measured-to-specified yield strength ratio and one of the highest tensile-to-yield strength ratios. However, its deformation capacity was small, as explained before.

The shear-drift envelopes were used to calculate the effective initial stiffness, as explained in section 4.8. The normalized effective initial stiffness is shown in Figure 229 and the normalized moment of inertia in Figure 230 for all six walls. The wall with conventional Grade 60 (420) reinforcement showed the highest normalized stiffness and normalized moment of inertia. Walls with Grade 100 (690) reinforcement showed similar values except for T5 and T6.

Values for normalized moment of inertia for T5 and T6 when the stem was in compression were similar to the values of T2 through T4 because the same amount of reinforcement was used on the flange, and the variation of the measured compressive strength of the concrete was within 10%. When the stem was in tension, the ratios of T5 and T6 were smaller with respect to the other high-strength steel walls because these two walls had fewer No. 6 (19) bars at the stem boundary element, resulting in smaller cracked moment of inertia.

The unloading stiffness calculated for all six walls was plotted against the drift ratio in Figure 231 and Figure 232 shows the unloading stiffness normalized by the flexural stiffness based on gross moment of inertia. Similar values of the unloading stiffness were obtained for T5 and T6 when the stem was in compression (positive drift ratio in the figures).

Figure 233 shows the stiffness reducing exponent (α) versus the normalized displacement (Δ_{max}/Δ_y) for all six walls. When the stem was in tension, a good agreement between T5 and T6 was obtained when compared with the other high-strength steel walls. The values of α varied between 0.25 and 0.5 for T5 and T6. When the stem was in compression, the values of T6 were greater than the ones obtained for T2 through T4. The coefficient varied between 0.35 and 0.5 for T5 and T6, whereas values from 0.2 to 0.45 were obtained for the rest of the high-strength steel walls.

5.7 Hysteretic Behavior

A comparison of values for the hysteretic energy dissipation index is presented in Figure 234 for both directions of loading. When the stem was in compression, the calculated index values for T6 at different drift ratios were similar to those of T4 at 1.5, 2, and 3% drift ratios. For T5, energy dissipation index values were smaller regardless of the level of deformation experienced by the wall, consistent with the closed hysteretic loops presented in Figure 197 to Figure 200. At 1% drift, the indexes of all walls were similar in both directions. In the negative loading direction (stem in tension), the index values for T6 and T5 showed similar results to those obtained for the positive loading direction.

6 ESTIMATES OF DEFORMATION CAPACITY AND STRAIN DEMANDS

6.1 Material Models

6.1.1 Concrete Stress-Strain Relationships

A typical one-dimensional constitutive relationship is used to model the nonlinear response of the unconfined and confined concrete in compression based on the approach used by Huq et al.^[37], where the constitutive relationship proposed by Park et al.^[68] was modified to include a plateau such that the peak stress is associated with a larger strain. The stress-strain relationship followed the models proposed by other researchers^[55,81]. A representative stress-strain curve for concrete is shown in Figure 235(a), and the parameters needed to develop both the confined and unconfined models are listed in Table 19. For simplicity, the behavior in tension is assumed to be linear up to a tensile strength of $7.5\sqrt{f_c''}$ (psi) ($0.62\sqrt{f_c''}$ (MPa)) with zero post-cracking strength.

The ascending branch of the unconfined concrete model followed the parabolic curve recommended by Hognestad^[32], where the maximum stress f_c'' is taken equal to f_{cm} from the average reported in Table 16 (average of Lift 1 and Lift 2). The strain at peak stress ϵ_0 was calculated after the idealized curves shown in Darwin et al.^[26] The softening parameter Z_{uc} was derived considering the experimental data and the formulation proposed by Mander et al.^[54]

To develop the stress-strain relationship for the confined concrete, the factor K_{cc} is included to account for the increment in the compressive stress due to confinement, based on the modified Kent and Park^[68] stress-strain model. The peak stress f_{cc}'' of the confined concrete was calculated using Eqs. 22 through 23.

$$f_{cc}'' = K_{cc}f_c'' \quad \text{Eq. 22}$$

$$K_{cc} = 1 + \frac{\rho_s f_y h}{f_c''} \quad \text{Eq. 23}$$

where ρ_s is the volumetric transverse reinforcement ratio measured to the outside of the peripheral confining reinforcement, and f_{yh} is the yield strength of the hoops. The softening parameter Z_{cc} for the descending branch of the confined concrete was derived based on experimental data and formulation presented by Mander et al.^[54]

A comparison between the stress-strain relationship developed using the parameter values from Table 19 with the model proposed by Mander et al.^[54] is shown in Figure 236. Close agreement was obtained in all cases regarding initial slope, peak stress, and descending branch up to strains of 0.0075 for unconfined concrete and 0.025 for confined concrete.

6.1.2 Steel Stress-Strain Relationships

Two models were considered for the uniaxial stress-strain relationships of steel bars: a perfectly elastoplastic model and a nonlinear strain-hardening model. The elastoplastic model was used to determine the nominal flexural strength M_n of the walls. The strain-hardening model was adopted to derive the moment-curvature relationships. The elastoplastic model was defined using the yield strength and the modulus of elasticity of steel, while the strain-hardening model was defined using the parameters shown in Figure 235 and listed in Table 20. Figure 237 shows close agreement between the measured and calculated stress-strain curves (based on the strain-hardening model) for the No. 6 (19) steel bars used in T1 through T6.

6.2 Moment-Curvature Analysis

Moment-curvature relationships were calculated using the material models described in the previous section with the following assumptions: concrete clear cover was 0.75 in. (19 mm); location of steel bars was based on Figure 204 through Figure 207; confined concrete was assigned to the stem and flange boundary elements (excluding the concrete cover), and unconfined concrete was

assigned elsewhere (including the concrete cover to confined boundary elements); all bars were assigned an identical steel model; cross section was subjected to an axial load of 60.9 kips (271 kN) representing the self-weight of the specimen and testing apparatus; two directions of analysis were considered (M^+ for stem in compression and M^- for stem in tension); strains were varied linearly through the depth of the cross section; and bar buckling was not accounted for. All moment-curvature relationships were calculated using computer program QBIAX^[28].

The flexural capacity M_n for each direction of analysis (M_n^+ and M_n^-) was defined as the moment associated with a compressive strain of $\epsilon_c = 0.003$ at the extreme concrete fiber and a steel stress limited to its yield strength, in accordance with ACI 318-14^[1].

6.2.1 Computed Results

The moment-curvature relationships for all specimens are shown in Figure 238 to Figure 243 for both loading directions. Figure 238 shows the results for T1 reinforced with conventional Grade 60 (420) reinforcement, the other figures correspond to walls T2 through T6 with high-strength reinforcement. All of these figures identify key events: first yielding of the steel tension fiber (M_{y1}); nominal flexural strength (M_n); the point where the extreme tension fiber reached the uniform elongation (ϵ_{su}); and the points at which the extreme fiber of the confined concrete reached a compressive strain ($\epsilon_{c,core}$) of 0.010 and 0.015. Key values from the moment-curvature analyses are shown in Table 22.

Computed moment-curvature relationships show significant differences for each direction of analysis but the sequence of relevant events (for each direction) was similar for all walls. When the stem was in tension, the response was controlled by the uniform elongation of the steel regardless of the type of steel used (conventional or high-strength). The specimen reinforced with Grade 60 (420) steel achieved its nominal flexural strength (M_n) before the reinforcement reached its peak stress associated with ϵ_{su} . In contrast, all section with high-strength steel achieved M_n at steel strains

exceeding ε_{su} . These results are particular to the use of the perfectly elastoplastic model for steel. Computed maximum moments associated with the strain-hardening model always exceeded M_n .

Results of moment-curvature analyses for the stem in compression show that the nominal flexural strength and the maximum moment for all six walls were achieved before the strain in the steel reached its uniform elongation ε_{su} . The moment associated with a maximum compressive strain of 0.01 for the confined concrete was within 5% of the maximum moment. Increasing the limiting strain from 0.01 to 0.015 reduced the moment by approximately 5% and increased the curvature by approximately 25%. The maximum moment was attained when the extreme fiber within the confined boundary element of the stem reached compressive strains of 0.0081, 0.0069, 0.0079, 0.0076, 0.0074, and 0.0070 for T1 through T6, respectively, with the smaller strain values corresponding to T2 and T6 (walls with lowest f_t/f_y). In all cases, uniform elongation of the reinforcement was reached at a curvature greater than the curvatures associated with concrete compressive strains of $\varepsilon_{c,core} = 0.015$.

The moment curvature relationships for all six walls are shown in Figure 244 for both directions of analysis. The curvature (x -axis) scale was modified to facilitate comparison of results. For the case of stem in compression, T1 shows curvature capacity comparable to other walls if the limiting curvature is based on $\varepsilon_{c,core}$, see also Figure 247. For the case of stem in tension, T1 shows more curvature capacity than the other walls based on $\varepsilon_s = \varepsilon_{su}$, see also Figure 247.

The maximum moment ($V_{max}h_w$) measured during the test normalized by the calculated nominal flexural strength (M_n) is shown in Figure 245 and normalized to the maximum calculated moment (\bar{M} based on moment-curvature analysis) in Figure 246. The data in Figure 245 show that the nominal strength is smaller than the measured moment in all cases, except for the negative direction of T2. During the test, T2 did not mobilize its flexural strength because bars fractured before completing the 2% drift cycle. The maximum moment from the moment-curvature analysis was

generally greater than the measured moment resulting in ratios less than one in Figure 246, which identifies a limitation of monotonic moment-curvature analysis to estimate strength of unsymmetrical wall sections subjected to reversed cyclic loading.

6.3 Displacement Capacity

6.3.1 Analytical Models

Two simplified analytical models, referred to as Model A and Model B, are used to estimate the deformation capacity of T-shaped cantilever walls. The load-displacement response of slender structural walls can be represented with reasonable accuracy if the total lateral displacement considers the contribution of three different components of drift: flexural (Δ_f), shear (Δ_v), and strain penetration (Δ_{sp}). The base shearing (or sliding component) is typically neglected in slender walls ($h_w/\ell_w \geq 2$).

Model A

Model A is based on the use of an idealized moment-curvature relationship represented by a trilinear curve defined by moment-curvature data of three points: cracking, yielding, and ultimate, as shown in Figure 248. For this model, the assumed moment and curvature distributions along the height of the cantilever wall are shown in Figure 249, where the points for cracking, yielding, and ultimate are indicated in Figure 249(b) and Figure 249(c). The contribution of curvature to displacement is calculated by integrating curvature along the height times the distance to the top of the cantilever. This model was used by Saiidi and Sozen^[77] and Hopper^[35] to derive moment-rotation relationships.

$$\theta_f = \Delta_f/h_w = \frac{h_w}{6} \left[2\lambda_1^2 \phi_{cr} + \left(1 + \lambda_2 - \frac{2\lambda_1^3}{\lambda_2} \right) \phi_y + (2 - \lambda_2(1 + \lambda_2)) \phi_u \right] \quad \text{Eq. 24}$$

where ϕ_{cr} , ϕ_y , and ϕ_u are the cracking, yielding, and ultimate curvature, respectively, and λ_1 and λ_2 are coefficients to define the shape of the curvature diagram indicated in Figure 249(c). These coefficients depend on the relative values of the moments at cracking (M_{cr}), yielding (M_y), and ultimate (M_u) depending on the flexural rotation being calculated using Eq. 24: at cracking, $\lambda_1 = 1$ and $\lambda_2 = 1$ to determine θ_{cr} ; at yielding, $\lambda_1 = M_{cr}/M_y$ and $\lambda_2 = 1$ to determine θ_y ; and at ultimate, $\lambda_1 = M_{cr}/M_u$ and $\lambda_2 = M_y/M_u$ to determine θ_u . The displacement associated with each of these rotations is obtained by multiplying the rotation times the height h_w of the cantilever wall.

The cracking moment is calculated based on the modulus of rupture recommended in ACI 318-14^[1]. Different definitions of the yield point were evaluated based on: (a) yield strain at the extreme tensile reinforcement, M_{y1} , (b) yield strain at the centroid of the boundary element in tension, and (c) yield strain at distance $0.8l_w$ from the extreme compression fiber, M_{yd} . These definitions are shown with different symbols in Figure 250 through Figure 255 for each of the six walls. Of the three definitions, M_{yd} best represented the point where a significant slope change occurred in both direction of analysis.

Two different definitions were used to determine the ultimate point depending on the loading direction. For the case of stem in compression, the strain at the extreme compressive fiber of the confined boundary element ($\epsilon_{c,core}$) is limited to either 0.010 or 0.015. These points are shown as open and solid squares in Figure 250 through Figure 255. For the case of stem in tension, the strain of the No. 6 (19) bars is limited to the uniform elongation (ϵ_{su}). This condition is illustrated with an open triangle in the same set of figures.

To determine the displacement associated with shear deformations (Δ_v), the walls were assumed to have a bottom and a top region with different properties. It was assumed that the shear deformations of the bottom region (bottom one-third of the wall) was greater than the shear

deformation of the top region (top two-thirds of the wall). Thus, Δ_v was calculated using the following expressions:

$$\Delta_v = \Delta_{v,bot} + \Delta_{v,top} \quad \text{Eq. 25}$$

$$\Delta_{v,bot} = \frac{V_u(1 - \lambda_2)h_w}{\phi_{K,bot}A_{cv}G_c} \quad \text{Eq. 26}$$

$$\Delta_{v,top} = \frac{V_u\lambda_2h_w}{\phi_{K,top}A_{cv}G_c} \quad \text{Eq. 27}$$

where $\Delta_{v,bot}$ is the displacement due to shear deformations in the plastic hinge region defined by $(1 - \lambda_2)h_w$ with $\lambda_2 = M_y/M_u$; $\Delta_{v,top}$ is the displacement due to shear deformations in the top two-thirds of the wall; V_u is the shear force associated with M_u based on ϕ_u ; $A_{cv} = t_w l_w$ is the effective area of the concrete resisting shear; and ϕ_K is the ratio of effective shear stiffness to uncracked shear stiffness for the top and bottom regions of the wall, determined as explained below.

The shear stiffness of the top region of the wall was assumed to be 1/10 the uncracked stiffness of the wall, as recommended by Huq et al.^[37] Therefore, $\phi_{K,top} = 1/10$ was used throughout the analysis. The values of $\phi_{K,bot}$ for the plastic hinge region were derived based on the average shear distortion in the bottom 50 in. (127 mm) of each wall (Figure 256). The data show that $\phi_{K,bot}$ is nearly linear proportional to drift ratio. Based on the data in Figure 257, Eq. 28 is proposed for $\phi_{K,bot}$ for all walls regardless of the loading direction.

$$1/\phi_{K,bot} = 10 + 50(DR - 1) \quad \text{Eq. 28}$$

Figure 257 shows that at a drift ratio of 1%, the effective shear stiffness is approximately 1/10 of the uncracked stiffness, as assumed for the top 2/3 of the wall, and as obtained from Eq. 28.

For drift ratios of 1.5, 2, and 3%, values of $\phi_{K,bot}$ from Eq. 28 result in 1/35, 1/60, and 1/110, respectively.

The displacement due to strain penetration Δ_{sp} , was calculated using Eq. 29, which is derived in APPENDIX B:

$$\Delta_{sp} = \alpha_{sp} \lambda d_b \phi_y h_w \quad \text{Eq. 29}$$

where ϕ_y is the yield curvature, d_b is the diameter of the primary longitudinal reinforcement, and λ is the number of bar diameters that define the length over which the reinforcement strain is assumed constant to develop f_y . The value of λ for T1, T2, T3, and T4 are taken from Table 12 in reference 38, and for T5 and T6 from Table 13 in this manuscript.

Model B

Model B is based on the plastic hinge model illustrated in Figure 258, where the curvature is assumed to vary linearly from zero at the tip of the cantilever wall to the point where the yield moment occurs. A constant plastic curvature ($\phi_u - \phi_y$) is assumed over the plastic hinge length l_p . The flexural displacement component was calculated considering contributions from the elastic and plastic curvatures. The displacement at the top of the wall due to the curvature diagram in Figure 258(c) is given by

$$\Delta_f = \Delta_{f,y} + \Delta_{f,p} = \frac{1}{3} \phi_y h_w^2 + (\phi_u - \phi_y) l_p \left(h_w - \frac{l_p}{2} \right) \quad \text{Eq. 30}$$

where $\Delta_{f,y}$ is the displacement corresponding to the yield curvature ϕ_y , $\Delta_{f,p}$ is the displacement associated with the plastic curvature ($\phi_u - \phi_y$), l_p is the length of the plastic hinge, and h_w is the

height of the wall (from base to point of load application). The plastic hinge length is typically taken as $0.5h_w$ when considering flexural deformations and neglecting other sources of deformations (shear and strain penetration). A more general expression for the plastic hinge length ℓ_p directly accounts for the extent of the plastic curvature:

$$\ell_p = \frac{1}{2}h_w \left(1 - \frac{M_y}{\bar{M}}\right) \quad \text{Eq. 31}$$

where M_y is the yield moment and \bar{M} is the maximum moment from the moment-curvature relationship. The coefficient of $1/2$ adjusts the assumed constant plastic curvature $(\phi_u - \phi_y)$ to the average value $(\phi_u - \phi_y)/2$ extending over the length ℓ_p . A summary of the parameters used to determine ℓ_p are shown in Table 23. It is clear that the differences in the calculated values depend on the loading direction. The values in Table 23 give an average plastic hinge length of 35 and 50 in. (889 and 1270 mm) for the positive and negative loading directions, respectively. Assuming $M_y = 0.8\bar{M}$, Eq. 31 simplifies to $\ell_p = 0.1h_w$, or $\ell_p = 0.3\ell_w$ for $h_w/\ell_w = 3$.

6.3.2 Computed Results

Based on the moment-curvature analyses, the deformation capacity was controlled by the stem in compression. The curvatures corresponding to $\varepsilon_{c,core} = 0.015$ were in all cases smaller than the curvature corresponding to ε_{su} (for stem in tension). Considering that moment-curvature analyses do not account for reversed cyclic loading, it was assumed that a compressive concrete strain of 0.015 at the extreme fiber of the boundary element represent the onset of bar buckling, a key event in the failure mechanism of most of the T-shaped walls considered.

The effects of shear deformations and strain penetration on the total deformation were examined for two scenarios: one based only on flexural deformations, the other based on the combined effects of deformations due to flexure, shear, and strain penetration. Therefore, a total of

four model variations were considered: A1, A2, B1, and B2, where Models A1 and B1, account only for flexural deformations; and models A2 and B2, account for flexure plus shear and strain penetration.

A comparison between the experimental and calculated deformation capacities is shown in Figure 259, based on the parameters shown in Table 24 and Table 25 for Models A1 and B1 and Table 26 and Table 27 for Models A2 and B2. Results for Model A1 are not shown separately in Figure 259 as they can be inferred directly from the data shown for Model A2.

The plotted data in Figure 259 based on the stem in compression show that estimates of deformation capacity for all models were generally conservative (safe), except for T2, which was the wall that failed prematurely mostly due to the combined effects of low f_t/f_y and ϵ_{su} . Excluding T2, Model B1 was generally closer to the measured deformation capacity than the other models.

Estimates of deformation capacity based on the stem in tension were not generally conservative, a clear indication that the T-shaped walls herein considered were controlled by the stem in compression. Deformation capacities based on elongation of the reinforcement should be based on a fraction of the uniform elongation (ϵ_{su}) to indirectly account for the effects of buckling on reducing the tensile elongation capacity of a buckled bar.

6.4 Strain Estimates

6.4.1 Analytical models

The maximum tensile strains developed in the steel bars and on the surface of the concrete, as well as the maximum compressive strains on the concrete were calculated for all six walls using Models A and B described in the previous section. The calculated strains were compared with the experimental data measured during the tests. Measured and calculated tensile strains for the longitudinal reinforcement and concrete surface are reported for target drift ratios of 1.5 and 2%.

Calculated compressive strains are compared with concrete surface strains (based on data from optical markers) for a target drift ratio of 2%. Strains are calculated based on the curvature ϕ' required to attain the target drift ratio Δ_{target} . The value of ϕ' is determined from Eq. 32 through Eq. 35 depending on the model used.

For Model A1:

$$\Delta_{target} = \frac{h_w^2}{6} \left[2\lambda_1^2 \phi_{cr} + \left(1 + \lambda_2 - \frac{2\lambda_1^3}{\lambda_2} \right) \phi_y + (2 - \lambda_2(1 + \lambda_2)) \phi' \right] + \frac{V h_w}{A_{cv} G_c} \left(\frac{1 - \lambda_2}{\phi_{K,bot}} + \frac{\lambda_2}{\phi_{K,top}} \right) + \alpha_{sp} \lambda d_b \phi_y h_w \quad \text{Eq. 32}$$

For Model A2:

$$\Delta_{target} = \frac{h_w^2}{6} \left[2\lambda_1^2 \phi_{cr} + \left(1 + \lambda_2 - \frac{2\lambda_1^3}{\lambda_2} \right) \phi_y + (2 - \lambda_2(1 + \lambda_2)) \phi' \right] \quad \text{Eq. 33}$$

For Model B1:

$$\Delta_{target} = \frac{\phi_y h_w^2}{3} + (\phi' - \phi_y) \ell_p \left(h_w - \frac{\ell_p}{2} \right) + \frac{V}{A_{cv} G_c} \left(\frac{\ell_p}{\phi_{K,bot}} + \frac{h_w - \ell_p}{\phi_{K,top}} \right) + \alpha_{sp} \lambda d_b \phi_y h_w \quad \text{Eq. 34}$$

For Model B2:

$$\Delta_{target} = \frac{\phi_y h_w^2}{3} + (\phi' - \phi_y) \ell_p \left(h_w - \frac{\ell_p}{2} \right) \quad \text{Eq. 35}$$

6.4.2 Computed Results

A comparison between the measured and calculated maximum strains in the steel bars and concrete are shown in Figure 260 through Figure 265. In these figures, the white symbols represent calculated strains considering only flexural deformations, the gray symbols account for deformation due to flexure, shear, and strain penetration and the black symbols represent the measured strains.

The measured and calculated strain data are shown for target drift ratios of 1 and 2% for Models A and B. Figure 260 through Figure 262 correspond to the calculated strain data for Model A and Figure 263 through Figure 265 to those for Model B. The calculated strains based on Model A were greater than those calculated based on Model B and both models generally provided strain estimates that were greater than the measured strains.

Model A1 (based on flexure) resulted in strains that were greater than Model A2 (based on combined flexure, shear, and strain penetration), because to attain the target drift ratio the effects of flexure (and therefore curvature and strains) were reduced after considering deformations due to shear and strain penetration.

Model B1 (based on flexure with $\ell_p = 0.5\ell_w$) resulted in strains that were similar to the strains calculated with Model B2 (based on combined flexure, shear, and strain penetration, with $\ell_p = 0.3\ell_w$). The results from models B1 and B2 were comparable because the greater value of ℓ_p in Model B1 compensated for the neglected deformations (shear and strain penetration).

Figure 266 through Figure 268 show the average measured-to-calculated strain ratios for each of the six walls based on Model A and Figure 269 through Figure 271 based on Model B. Ratios were generally lower than one, which indicate that the models are generally conservative (safe) for estimating strains.

7 CONCLUDING REMARKS

Results were reported from tests of two large-scale T-shaped reinforced concrete structural walls (T5 and T6) subjected to reversed cyclic loading to assess their deformation capacity. The primary variables were the yield strength (f_y) and the tensile-to-yield strength ratio (f_t/f_y). The results were compared with experimental data from four walls (T1, T2, T3, and T4) tested by Huq et al. (2017) at The University of Kansas to evaluate the influence of the uniform elongation (ϵ_{su}) and fracture elongation (ϵ_{sf}), in addition to f_y and f_t/f_y of high-strength reinforcement on the behavior of concrete walls subjected to reversed cyclic loading.

The design of the walls complied with ACI Building Code (ACI 318-14) and the detailing recommendation in ATC 115 for Grade 100 reinforcement. Wall T5 used Grade 120 (830) reinforcement with f_t/f_y of 1.33 and T6 used Grade 100 (690) reinforcement with f_t/f_y of 1.18. Confined boundary elements were considered at the three tips of the T section to concentrate the main flexural reinforcement (No. 6 or 19 mm bars) enclosed by No. 3 (10 mm) hoops. No. 4 (13 mm) bars were used outside the boundary elements as longitudinal and horizontal reinforcement. The nominal concrete compressive strength of 8 Ksi (55 MPa) and wall dimensions were kept constant in both specimens with a wall thickness of 10 in. (25 mm) and height-to-length ratio of 3. Wall stem and flanges were 100-in. (2540-mm). The axial load was limited to the self-weight of the walls and the weight of the testing apparatus. The specimens were design such that flexural behavior controlled their response inducing a shear stress of approximately $4\sqrt{f'_c}$, psi ($0.33\sqrt{f'_c}$, MPa).

The following conclusions and observations were found:

- 1) Test results confirmed the recommendations made by Huq et al.^[37] for high-strength reinforcement in earthquake-resistant walls: to satisfy $f_t/f_y \geq 1.2$, $\varepsilon_{su} \geq 6\%$, and $\varepsilon_{sf} \geq 10\%$ in order to achieve deformation capacities similar to those of walls reinforced with conventional Grade 60 (420) reinforcement.
- 2) Regardless of the value of f_t/f_y (in the range between 1.1 and 1.33), high-strength reinforcement with $\varepsilon_{su} < 6\%$ exhibited a reduced deformation capacity compared with that of walls reinforced with conventional Grade 60 (420) reinforcement, as demonstrated by T5 with flexural reinforcement having $f_t/f_y = 1.33$ and $\varepsilon_{su} = 5.5\%$ and T2 with $f_t/f_y = 1.10$ and $\varepsilon_{su} = 5.7\%$. Both T5 and T2 failed due to bar fracture (without prior bar buckling) at drift ratios below 3% (2.3% for T5 and 1.8% for T2). In contrast, T6 with high-strength reinforcement having $f_t/f_y = 1.18$ and $\varepsilon_{su} = 7.1\%$ failed at a drift ratio of 3.1% due to bar fracture (with prior bar buckling).
- 3) Similar to the behavior of T1, reinforced with conventional Grade 60 (420) steel bars, bar buckling was observed in the flexural reinforcement of T6 at the confined boundary element of the stem. Bar buckling occurred despite having the confining reinforcement spaced at four times the longitudinal bar diameter. Although bar buckling did not have a noticeable effect on lateral strength, it led to bar fracture of the buckled bars in subsequent cycles. In T1 and T6, bar buckling of the primary flexural reinforcement was first observed during the second cycle to 3% and both T1 and T6 failed (due to bar fracture) during the first cycle to 4% drift ratio, reaching a drift ratio capacity in excess of 3% (3.7% for T1 and 3.1% for T6).
- 4) The envelopes of tensile strains recorded by strain gauges in reinforcing bars had similar distribution over the height of the wall to those derived from optical markers on the surface of the concrete. Generally, measured steel strains were greater than those reported for the concrete surface because concrete strains were averaged over 14 in. (356 mm) gauge length.

- 5) The strength of walls T5 and T6, in both loading directions, exceeded the shear strength associated with the nominal flexural strength (M_n) calculated based on ACI 318-14 using measured material properties.
- 6) Walls T5 and T6 showed relative contributions to drifts similar to other walls with high-strength and conventional reinforcement. Flexural deformations (including the effects of base opening) were the largest deformation component, accounting for 50 to 80% of total drift for drift ratios between 1 and 3%.
- 7) The ratio between the effective initial stiffness to flexural stiffness based on gross section properties was approximately 0.12 for T6 with Grade 100 (690) reinforcement. An average ratio of 0.11 was obtained for the walls with high-strength steel bars (T2, T3, and T4) tested by Huq et al.^[37] The ratio reduced to 0.09 in T5 with Grade 120 (830) reinforcement. The ratio between the cracked moment of inertia to the gross moment of inertia was 0.14 for both T5 and T6, a slightly smaller value than 0.15 obtained for T2, T3, and T4. The reduced ratio was nearly proportional to the reduced amount of reinforcement in T5 and T6 in relation to the other walls.
- 8) The deformation capacity estimated for all models considered (Models A and B) were generally conservative (safe), in all six walls except for T2, which failed prematurely mostly due to the combined effects of low f_t/f_y and ϵ_{su} . Excluding T2, Model B1 was generally closer to the measured deformation capacity than the other models.
- 9) The strains calculated based on both models considered (Models A and B) generally provided strain estimates that were greater than the measured strains (safe). In general, Model A estimated greater strains than those calculated based on Model B.

8 REFERENCES

1. ACI 318 (2014). Building Code Requirements for Structural Concrete (ACI 318-14) and Commentary (318R-14). American Concrete Institute, Farmington Hills, Michigan.
2. ACI 408 (2003). Bond and Development of Straight Reinforcing Bars in Tension (ACI 408R-03). American Concrete Institute, Farmington Hills, Michigan.
3. Air Worldwide (2010). Chile Earthquake. <<http://alert.air-worldwide.com/EventSummary.aspx?e=502&tp=79&c=1>>. (January, 2018).
4. Aoyama H., Ed. (2001). Design of Modern Highrise Reinforced Concrete Structures. Imperial College Press, London, United Kingdom.
5. ASCE 41 (2017). Seismic Evaluation and Retrofit of Existing Buildings (ASCE/SEI 41-17). American Society of Civil Engineers, Reston, Virginia.
6. ASTM A370 (2017). Standard Test Methods and Definitions for Mechanical Testing of Steel Products (ASTM A370-17). ASTM International, West Conshohocken, Pennsylvania.
7. ASTM A615 (2016). Standard Specification for Deformed and Plain Carbon-Steel Bars for Concrete Reinforcement (ASTM A615/A615M-16). ASTM International, West Conshohocken, Pennsylvania.
8. ASTM A706 (2016). Standard Specification for Deformed and Plain Low-Alloy Steel Bars for Concrete Reinforcement (ASTM A706/A706M-16). ASTM International, West Conshohocken, Pennsylvania.
9. ASTM A955 (2017). Standard Specification for Deformed and Plain Stainless-Steel Bars for Concrete Reinforcement (ASTM A955/A955M-17). ASTM International, West Conshohocken, Pennsylvania.
10. ASTM A996 (2016). Standard Specification for Rail-Steel and Axle-Steel Deformed Bars for Concrete Reinforcement (ASTM A996/A996M-16). ASTM International, West Conshohocken, Pennsylvania.

11. ASTM A1035 (2016). Standard Specification for Deformed and Plain, Low-Carbon, Chromium, Steel Bars for Concrete Reinforcement (ASTM A1035/A1035M-16b). ASTM International, West Conshohocken, Pennsylvania.
12. ASTM C39 (2017). Standard Test Method for Compressive Strength of Cylindrical Concrete Specimens (ASTM C39/C39M-17a). ASTM International, West Conshohocken, Pennsylvania.
13. ASTM C496 (2011). Standard Test Method for Splitting Tensile Strength of Cylindrical Concrete Specimens (ASTM C496/C496M-11). ASTM International, West Conshohocken, Pennsylvania.
14. ASTM E8 (2016). Standard Test Methods for Tension Testing of Metallic Materials (ASTM E8/E8M-16a). ASTM International, West Conshohocken, Pennsylvania.
15. Astrella M. and Whittaker A. (2005). The Performance-Based Design Paradigm. Multidisciplinary Center for Earthquake Engineering Research, Technical Report MCEER-05-0011, Buffalo, New York.
16. ATC 115 (2014). Roadmap for the Use of High-Strength Reinforcement in Reinforced Concrete Design. Applied Technology Council, Redwood City, California.
17. Azizinamini A. and Saatcioglu M. (1998). Performance of High-Strength Concrete (HSC) Columns Confined with Rectilinear Reinforcement. ACI Special Publication 176, High Strength Concrete in Seismic Regions, Farmington Hills, Michigan, 213-236.
18. Barbachyn S. M., Devine R. D., Thrall A. P., and Kurama Y. C. (2017). Economic Evaluation of High-Strength Materials in Stocky Reinforced Concrete Shear Walls. ASCE Journal of Construction Engineering and Management, 143(10).
19. Barda F., Hanson J. M., and Corley W. G. (1977). Shear Strength of Low-Rise Walls with Boundary Elements. ACI Special Publication 53, Reinforced Concrete Structures in Seismic Zones, Detroit, Michigan, 149-202.
20. Behrouzi A., Welt T., Lehman D., Lowes L., LaFave J., and Kuchma D. (2017). Experimental and Numerical Investigation of Flexural Concrete Wall Design Details. Proceedings, ASCE/SEI Structures Congress, Denver, Colorado.

21. Beyer K., Dazio A., and Priestley M. J. N. (2008). Quasi-Static Cyclic Tests of Two U-shaped Reinforced Concrete Walls. *Journal of Earthquake Engineering*, 12(7), 1023-1053.
22. Bing L., Park R., and Tanaka H. (1994). Strength and Ductility of Reinforced Concrete Members and Frames Constructed Using High Strength Concrete. University of Canterbury, Research Report No. 94-5, Christchurch, New Zealand.
23. Brueggen B. L., French C. E., and Sritharan S. (2017). T-Shaped RC Structural Walls Subjected to Multidirectional Loading: Test Results and Design Recommendations. *ASCE Journal of Structural Engineering*, 143(7).
24. Budek A. M., Priestley M. J. N., and Lee C. O. (2002). Seismic Design of Columns with High-Strength Wire and Strand as Spiral Reinforcement. *ACI Structural Journal*, 99(5), 660-670.
25. Constantin R. and Beyer K. (2016). Behaviour of U-Shaped RC Walls Under Quasi-Static Cyclic Diagonal Loading. *Engineering Structures*, 106, 36-52.
26. Darwin D., Dolan C. W., and Nilson A. H. (2016). *Design of Concrete Structures*. 15th Edition, McGraw-Hill Education, New York, New York.
27. Dazio A., Beyer K., and Bachmann H. (2009). Quasi-Static Cyclic Tests and Plastic Hinge Analysis of RC Structural Walls. *Engineering Structures*, 31(7), 1556-1571.
28. Dragovich J. J. (1996). An Experimental Study of Torsional Response of Reinforced Concrete Structures to Earthquake Excitation. PhD Dissertation, University of Illinois, Urbana, Illinois.
29. Elwood K. J. (2013). Performance of Concrete Buildings in the 22 February 2011 Christchurch Earthquake and Implications for Canadian Codes. *Canadian Journal of Civil Engineering*, 40(3), 759-776.
30. FEMA 461 (2007). Interim Testing Protocols for Determining the Seismic Performance Characteristics of Structural and Nonstructural Components. Applied Technology Council, Redwood City, California.
31. Gaston J. R. and Hognestad E. (1962). High-Strength Bars as Concrete Reinforcement, Part 3: Tests of Full-Scale Roof Girder. *Journal of the PCA Research and Development Laboratories*, 4(2), 10-23.

32. Hognestad E. (1951). A Study of Combined Bending and Axial Load in Reinforced Concrete Members. University of Illinois, Engineering Experiment Station, Bulletin Series No. 399, Urbana, Illinois.
33. Hognestad E. (1961). High-Strength Bars as Concrete Reinforcement, Part 1: Introduction to a Series of Experimental Reports. *Journal of the PCA Research and Development Laboratories*, 3(3), 23-29.
34. Hognestad E. (1962). High-Strength Bars as Concrete Reinforcement, Part 2: Control of Flexural Cracking. *Journal of the PCA Research and Development Laboratories*, 4(1), 46-63.
35. Hopper M. W. (2009). Analytical Models for the Nonlinear Seismic Response of Reinforced Concrete Frames. MS Thesis, The Pennsylvania State University, University Park, Pennsylvania.
36. Hosaka G., Funaki H., Hosoya H., and Imai H. (2008). Experimental Study on Structural Performance of RC Shear Wall with L-Shaped Section. *Proceedings, 14th World Conference on Earthquake Engineering*, Beijing, China.
37. Huq M. S., Weber-Kamin A., Ameen S., Lequesne R., and Lepage A. (2018). High-Strength Steel Bars in Earthquake-Resistant T-Shaped Concrete Walls. SM Report No. 128, The University of Kansas, Center for Research Inc., Lawrence, Kansas.
38. Ile N. and Reynouard J. M. (2005). Behavior of U-Shaped Walls Subjected to Uniaxial and Biaxial Cyclic Lateral Loading. *Journal of Earthquake Engineering*, 9(1), 67-94.
39. Inada K., Chosa K., Sato H., Kono S., and Watanabe F. (2008). Seismic Performance of RC L-Shaped Core Structural Walls. *Proceedings, 14th World Conference on Earthquake Engineering*, Beijing, China.
40. Kaar P. H. and Mattock A. H. (1963). High Strength Bars as Concrete Reinforcement, Part 4: Control of Cracking. *Journal of the PCA Research and Development Laboratories*, 5(1), 15-38.
41. Kaar P. H. and Hognestad E. (1965). High Strength Bars as Concrete Reinforcement, Part 7: Control of Cracking in T-Beam Flanges. *Journal of the PCA Research and Development Laboratories*, 7(1), 42-53.

42. Kaar P. H. (1966). High Strength Bars as Concrete Reinforcement, Part 8: Similitude in Flexural Cracking of T-Beam Flanges. *Journal of the PCA Research and Development Laboratories*, 8(2), 2-12.
43. Kabeyasawa T., Shiohara H., Otani S., and Aoyama H. (1983). Analysis of the Full-Scale Seven-Story Reinforced Concrete Test Structure. *Journal of the Faculty of Engineering, The University of Tokyo*, 37(2), 431-478.
44. Kabeyasawa T., Ohkubo T., and Nakamura Y. (1996). Tests and Analysis of Hybrid Wall Systems. *Proceedings, 11th World Conference on Earthquake Engineering, Acapulco, Mexico*.
45. Kabeyasawa T. and Hiraishi H. (1998). Tests and Analyses of High-Strength Reinforced Concrete Shear Walls in Japan. *ACI Special Publication 176, High Strength Concrete in Seismic Regions, Farmington Hills, Michigan*, 281-310.
46. Kimura H. and Ishikawa Y. (2008). Seismic Performance of High-Strength Reinforced Concrete Slender Walls Subjected to High Axial Loading. *Proceedings, 8th International Symposium on Utilization of High-Strength and High-Performance Concrete, Tokyo, Japan*, 945-950.
47. Kono S., Sakamoto K., and Sakashita M. (2011). Simulation of Seismic Load Resistance of Core-Walls for Tall Buildings. *Applied Mechanics and Materials*, 82, 386-391.
48. Lefas I. D., Kotsovos M. D., and Ambraseys N. N. (1990). Behavior of Reinforced Concrete Structural Walls: Strength, Deformation Characteristics, and Failure Mechanism. *ACI Structural Journal*, 87(1), 23-31.
49. Lepage A., Yasso S., and Darwin D. (2018). Recommended Provisions and Commentary on Development Length for High-Strength Reinforcement in Tension. *FIB Bulletin: Advances on Bond in Concrete, International Federation for Structural Concrete, (In Press)*.
50. Li W. and Li Q. (2012). Seismic Performance of L-Shaped RC Shear Wall Subjected to Cyclic Loading. *The Structural Design of Tall and Special Buildings*, 21(12), 855-866.
51. Lin C. H. and Lee F. S. (2001). Ductility of High-Performance Concrete Beams with High-Strength Lateral Reinforcement. *ACI Structural Journal*, 98(4), 600-608.

52. Lowes L. N., Lehman D. E., Birely A. C., Kuchma D. A., Marley K. P., and Hart C. R. (2012). Earthquake Response of Slender Planar Concrete Walls with Modern Detailing. *Engineering Structures*, 43, 31-47.
53. Ma J. and Li B. (2017). Seismic Behavior of L-Shaped RC Squat Walls under Various Lateral Loading Directions. *Journal of Earthquake Engineering*, 1-22.
54. Mander J. B., Priestley M. J. N., and Park R. (1988). Theoretical Stress-Strain Model for Confined Concrete. *ASCE Journal of Structural Engineering*, 114(8), 1804-1826.
55. Moehle J. (2014). *Seismic Design of Reinforced Concrete Buildings*. McGraw Hill Education, New York, New York.
56. Muguruma H. and Watanabe F. (1990). Ductility Improvement of High-Strength Concrete Columns with Lateral Confinement. *ACI Special Publication 121, High-Strength Concrete*, Detroit, Michigan, 47-60.
57. Muguruma H., Nishiyama M., Watanabe F., and Tanaka H. (1991). Ductile Behaviour of High Strength Concrete Columns Confined by High Strength Transverse Reinforcement. *ACI Special Publication 128, Evaluation and Rehabilitation of Concrete Structures and Innovations in Design*, Detroit, Michigan, 877-892.
58. Nakachi T., Toda T., and Tabata K. (1996). Experimental Study on Deformation Capacity of Reinforced Concrete Core Walls after Flexural Yielding. *Proceedings, 11th World Conference on Earthquake Engineering*, Acapulco, Mexico.
59. NIST GCR 14-917-30 (2014). *Use of High-Strength Reinforcement in Earthquake-Resistant Concrete Structures*. National Institute of Standards and Technology, Gaithersburg, Maryland.
60. Oesterle R. G., Fiorato A. E., Johal L. S., Carpenter J. E., Russell H. G., and Corley W. G. (1976). *Earthquake Resistant Structural Walls - Tests of Isolated Walls - Phase I*. Report to National Science Foundation, Portland Cement Association, Skokie, Illinois.
61. Oesterle R. G., Aristizabal-Ochoa J. D., Fiorato A. E., Russell H. G., and Corley W. G. (1979). *Earthquake Resistant Structural Walls - Tests of Isolated Walls - Phase II*. Report to National Science Foundation, Portland Cement Association, Skokie, Illinois.

62. Oesterle R. G., Fiorato A. E., Aristizabal-Ochoa J. D., and Corley W. G. (1980). Hysteretic Response of Reinforced Concrete Structural Walls. ACI Special Publication 63, Reinforced Concrete Structures Subjected to Wind and Earthquake Forces, Detroit, Michigan, 243-273.
63. Oesterle R. G. (1986). Inelastic Analysis for In-Plane Strength of Reinforced Concrete Shear Walls. PhD Dissertation, Northwestern University, Evanston, Illinois.
64. Oh Y. H., Han S. W., and Choi Y. S. (2006). Evaluation and Improvement of Deformation Capacities of Shear Walls Using Displacement-Based Seismic Design. International Journal of Concrete Structures and Materials, 18(1E), 55-61.
65. Otani S. (1981). Hysteresis Models of Reinforced Concrete for Earthquake Response Analysis. Journal of the Faculty of Engineering, The University of Tokyo, 36(2), 407-441.
66. Otani S., Nagai S., and Aoyama H. (1996). Load-Deformation Relationship of High Strength Reinforced Concrete Beams. ACI Special Publication 162, Mete A Sozen Symposium, Farmington Hills, Michigan, 35-52.
67. Palermo D. and Vecchio F. J. (2002). Behavior of Three-Dimensional Reinforced Concrete Shear Walls. ACI Structural Journal, 99(1), 1/1/2002, 81-89.
68. Park R., Priestley M. J. N., and Gill W. D. (1982). Ductility of Square-Confined Concrete Columns. ASCE Journal of the Structural Division, 108(4), 929-950.
69. Paulay T. and Goodsir W. J. (1985). The Ductility of Structural Walls. Bulletin of the New Zealand National Society for Earthquake Engineering, 18(3), 250-269.
70. Pfister J. F. and Mattock A. H. (1963). High Strength Bars as Concrete Reinforcement, Part 5: Lapped Splices in Concentrically Loaded Columns. Journal of the PCA Research and Development Laboratories, 5(2), 27-40.
71. Pfister J. F. and Hognestad E. (1964). High Strength Bars as Concrete Reinforcement, Part 6: Fatigue Tests. Journal of the PCA Research and Development Laboratories, 6(1), 65-84.
72. Pfund S. J. (2012). Cyclic Response of Concrete Beams Reinforced with ASTM A1035 Grade-120 Steel Bars. MS Thesis, The Pennsylvania State University, University Park, Pennsylvania.

73. Rautenberg J. M., Pujol S., Tavallali H., and Lepage A. (2014). Drift Capacity of Concrete Columns Reinforced with High-Strength Steel. *ACI Structural Journal*, 110(2), 307-317.
74. Restrepo J. I., Seible F., Stephan B., and Schoettler M. J. (2006). Seismic Testing of Bridge Columns Incorporating High-Performance Materials. *ACI Structural Journal*, 103(4), 496-504.
75. Richart F. E. and Brown R. L. (1934). An Investigation of Reinforced Concrete Columns. Engineering Experiment Station, Bulletin No. 267, University of Illinois, Urbana, Illinois.
76. Saatcioglu M., Palermo D., Ghobarah A., Mitchell D., Simpson R., Adebar P., Tremblay R., Ventura C., and Hong H. (2013). Performance of Reinforced Concrete Buildings During the 27 February 2010 Maule (Chile) Earthquake. *Canadian Journal of Civil Engineering*, 40(8), 693-710.
77. Saiidi M. and Sozen M. A. (1979). Simple and Complex Models for Nonlinear Seismic Response of Reinforced Concrete Structures. *Civil Engineering Studies, Structural Research Series No. 465*, University of Illinois, Urbana, Illinois.
78. Salonikios T. N., Kappos A. J., Tegos I. A., and Penelis G. G. (2000). Cyclic Load Behavior of Low-Slenderness Reinforced Concrete Walls: Failure Modes, Strength and Deformation Analysis, and Design Implications. *ACI Structural Journal*, 97(1), 132-141.
79. Sato Y., Tanaka H., and Park R. (1993). Reinforced Concrete Columns with Mixed-Grade Longitudinal Reinforcement. University of Canterbury, Research Report No. 93-7, Christchurch, New Zealand.
80. Sezen H. and Moehle J. P. (2003). Bond-Slip Behavior of Reinforced Concrete Members. Proceedings, FIB Symposium on Concrete Structures in Seismic Regions, Athens, Greece.
81. Sheikh S. A. and Uzumeri S. M. (1982). Analytical Model for Concrete Confinement in Tied Columns. *ASCE Journal of the Structural Division*, 108(12), 2703-2722.
82. Sittipunt C. and Wood S. L. (1993). Finite Element Analysis of Reinforced Concrete Shear Walls. *Civil Engineering Studies, Structural Research Series No. 584*, University of Illinois, Urbana, Illinois.
83. Song C., Wang Y., Puranam A., Pujol S., ACI 445B, and Usta M. (2015). ACI 445B Shear Wall Database. <<https://datacenterhub.org/resources/142>>. (January, 2018).

84. Sugano S., Nagashima T., Kimura H., Tamura A., and Ichikawa A. (1990). Experimental Studies on Seismic Behavior of Reinforced Concrete Members of High-Strength Concrete. ACI Special Publication 121, High-Strength Concrete, Detroit, Michigan, 61-88.
85. Takeda T., Sozen M. A., and Nielsen M. N. (1970). Reinforced Concrete Response to Simulated Earthquakes. ASCE Journal of the Structural Division, 96(ST12), 2557-2573.
86. Tavallali H., Lepage A., Rautenberg J. M., and Pujol S. (2014). Concrete Beams Reinforced with High-Strength Steel Subjected to Displacement Reversals. ACI Structural Journal, 111(5), 1037-1047.
87. Thomas A., Davis B., Dadi G. B., and Goodrum P. M. (2013). Case Study on the Effect of 690 MPa (100 ksi) Steel Reinforcement on Concrete Productivity in Buildings. ASCE Journal of Construction Engineering and Management, 139(11).
88. Thomsen IV J. H. and Wallace J. W. (1995). Displacement-Based Design of Reinforced Concrete Structural Walls: Experimental Studies of Walls with Rectangular and T-Shaped Cross Sections. Clarkson University, Report No. CU/CEE-95/06, Postdam, New York.
89. Thomsen IV J. H. and Wallace J. W. (2004). Displacement-Based Design of Slender Reinforced Concrete Structural Walls – Experimental Verification. ASCE Journal of Structural Engineering, 130(4), 618-630.
90. Todeschini C. E., Bianchini A. C., and Kesler C. E. (1964). Behavior of Concrete Columns Reinforced with High Strength Steels. Journal of the American Concrete Institute, 61(6), 701-715.
91. Tran T. A. and Wallace J. W. (2015). Cyclic Testing of Moderate-Aspect-Ratio Reinforced Concrete Structural Walls. ACI Structural Journal, 112(6), 653-665.
92. Tretiakova K. (2013). Cyclic Response of Concrete Columns Reinforced with SAS 670 Grade-97 Steel Bars. MS Thesis, The Pennsylvania State University, University Park, Pennsylvania.
93. Wallace J. W. and Moehle J. P. (1992). Ductility and Detailing Requirements of Bearing Wall Buildings. ASCE Journal of Structural Engineering, 118(6), 1625-1644.
94. Wallace J. W. (1994). New Methodology for Seismic Design of RC Shear Walls. ASCE Journal of Structural Engineering, 120(3), 863-884.

95. Wallace J. W. (1995). Seismic Design of RC Structural Walls. Part I: New Code Format. ASCE Journal of Structural Engineering, 121(1), 75-87.
96. Wallace J. W. and Thomsen IV J. H. (1995). Seismic Design of RC Structural Walls. Part II: Applications. ASCE Journal of Structural Engineering, 121(1), 88-101.
97. Wallace J. W. and Orakcal K. (2002). ACI 318-99 Provisions for Seismic Design of Structural Walls. ACI Structural Journal, 99(4), 499-508.
98. Wallace J. W. (2012). Behavior, Design, and Modeling of Structural Walls and Coupling Beams – Lessons from Recent Laboratory Tests and Earthquakes. International Journal of Concrete Structures and Materials, 6(1), 3-18.
99. Wight J. K. and Sozen M. A. (1973). Shear Strength Decay in Reinforced Concrete Columns Subjected to Large Deflection Reversals. Civil Engineering Studies, Structural Research Series No. 403, University of Illinois, Urbana, Illinois.

TABLES

Table 1 – Historical development of high-strength steel as concrete reinforcement

Year	ACI 318	Year	ASTM
1963	Grades 60 (420) and 75 (520) steel are allowed.	1959	ASTM A432 Grade 60 (420) and A431 Grade 75 (520) are introduced.
1971	Specified yield strength of 80 ksi is allowed for non-seismic applications. A limit of 60 ksi is used for seismic applications and remains in place through ACI 318-14 (except for confining reinforcement, where 100 ksi is allowed in 2008).	1968	ASTM A432 and A431 are replaced by ASTM A615 Grades 40 (280), 60 (420) and 75 (520).
1977	ASTM A706 Grade 60 (420) is allowed.	1972	Grade 75 (520) is removed from ASTM A615.
1983	ASTM A706 Grade 60 (420) is allowed for seismic applications. ASTM A615 is allowed as a substitute for ASTM A706 with limitations on yield and tensile strength.	1974	ASTM A706 Grade 60 (420) is first published with limited range of values for tensile properties and chemical components for weldability.
2005	Yield strength of 100 ksi is allowed for non-seismic applications as confining reinforcement.	1987	Grade 75 (520) is reintroduced in ASTM A615.
2008	ASTM A1035 Grade 100 (690) is allowed for seismic applications as confining reinforcement.	2001	ASTM A955 Grade 75 (520) is introduced.
2011	ASTM A706 Grade 80 (550) is not permitted for seismic applications.	2004	First appearance of ASTM A1035 Grade 100 (690).
2014	ASTM A615 Grade 60 (420) is allowed as a substitute for ASTM A706 with limitations on fracture elongation, maximum yield strength, and tensile-to-yield strength ratio. ASTM A615 and A1035 Grade 100 (690) are allowed as confining reinforcement (seismic and non-seismic applications).	2007	ASTM A1035 Grade 120 (830) is introduced.
		2009	ASTM A615 and A706 Grade 80 (550) are introduced.
		2015	ASTM A615 Grade 100 (690) is introduced. Three different alloy types are introduced in ASTM A1035: A1035 CL, A1035 CM, and A1035 CS.

Table 2 – Summary of required mechanical properties for deformed reinforcing bars in ASTM standards (1 ksi = 6.89 MPa)

Property	Units	ASTM A615 ^{a,d}				ASTM A706 ^{b,d}		ASTM A1035 ^{c,e,f}	
		Grade 60 ^g	Grade 75	Grade 80	Grade 100	Grade 60	Grade 80	Grade 100	Grade 120
Tensile strength, min	ksi	90	100	105	115	80 ^h	100 ^h	150	150
Yield strength, min	ksi	60	75	80	100	60	80	100	120
Yield strength, max	ksi	-	-	-	-	78	98	-	-
Elongation in 8 in.									
Bar size									
3, 4, 5, 6	%	9	7	7	7	14	12	7	7
7, 8	%	8	7	7	7	12	12	7	7
9, 10, 11	%	7	6	6	6	12	12	7	7
14, 18	%	7	6	6	6	10	10	6	6
20	%	7	6	6	6	-	-	6	6

^a Per ASTM A615/A615M-16^[7].

^b Per ASTM A706/A706M-16^[8].

^c Per ASTM A1035/A1035M-16b^[11]. Three types of steel are available (ASTM A1035 CL, A1035 CM, and A1035 CS) with different chromium content.

^d Two methods are allowed to determine the yield strength: (1) the 0.2% offset method and (2) the half-of-force method.

^e The 0.2% offset method shall be used to determine the yield strength.

^f The stress corresponding to an extension under load of 0.35% is required as follows: 80 ksi for Grade 100 and 90 ksi for Grade 120.

^g Further restrictions are required per ACI 318-14^[1] in f_t/f_y ratio and bar elongation for use in special seismic systems.

^h The tensile strength shall not be less than 1.25 the actual yield strength.

Table 3 – Summary of test program (1 ksi = 6.89 MPa)

Wall	Yield Strength f_y ^a ksi	Tensile-to-Yield Strength Ratio f_t/f_y ^b	Concrete Compressive Strength f'_c ^b ksi
T5 ^c	120	1.30	8
T6 ^d	100	1.15	8

^aNominal yield strength for flexural and shear reinforcement. Confining reinforcement for both walls was Grade 120 (830).

^bTarget values, see Table 8 (concrete) and Table 9 (reinforcing steel) for measured properties.

^cTested in spring 2017.

^dTested in summer 2017.

Table 4 – Loading protocol

Step ^a	Drift Ratio
	DR^b %
1 ^c	0.2
2 ^c	0.3
3 ^d	0.5
4 ^d	0.75
5 ^d	1
6 ^d	1.5
7 ^d	2
8 ^d	3
9 ^d	4

^a Each step has two cycles of loading following FEMA 461^[30], see Figure 9.

^b Drift (lateral displacement) divided by height (from base of wall to point of drift measurement). See notation in Appendix A.

^c Displacement-controlled to a target force.

^d Displacement-controlled to a target displacement.

Table 5 – Computed nominal flexural strength (1 in. = 25 mm, 1 ft = 305 mm, 1 kip = 4.45 kN)

Wall	f'_c ksi	f_y^a ksi	P^b kips	M_n^{+c} ft-kips	c^{+d} in.	V_{Mn}^{+e} kips	M_n^{-c} ft-kips	c^{-d} in.	V_{Mn}^{-e} kips
T5	8	120	61	7520	21.9	303	6470	3.1	261
T6	8	100	61	6770	19.3	273	5650	2.6	226

^a Reinforcement nominal yield strength.

^b Total axial load at base of wall: self-weight of wall (44.9 kips), top block (9.0 kips), internal bracing (0.2 kips), and tributary weight of loading apparatus (6.8 kips).

^c Nominal flexural strength: M_n^+ for stem in compression and M_n^- for stem in tension. Calculated based on ACI 318 using a concrete strain limited to 0.003 and a concrete stress defined by the equivalent rectangular stress block. Reinforcing steel stress was limited to the nominal yield strength f_y . For reinforcement area and location, see Figure 7.

^d Neutral axis depth measured from extreme compression fiber, c^+ corresponds to M_n^+ and c^- to M_n^- , see footnote c.

^e Shear associated with M_n^+ or M_n^- based on a nominal shear span of 300 in.

Table 6 – Dates for specimen casting and testing

Location	Specimen					
	T5			T6		
	Cast day	Test day	Age days	Cast day	Test day	Age days
Base Block	10/5/2016		286	2/3/2017		185
Wall Lift 1	10/28/2016	7/18/2017	263	2/20/2017	8/7/2017	168
Wall Lift 2	11/21/2016		239	3/6/2017		154
Top Block	12/14/2016		216	3/20/2017		140

Table 7 – Proportions for concrete mixture (1 gal = 3.79 liters, 1 oz = 0.278 N, 1 lb = 4.45 N, 1 in. = 25.4 mm)

Proportions (per cubic yard)	Unit	Specimen			
		T5		T6	
		Wall Lift 1	Wall Lift 2	Wall Lift 1	Wall Lift 2
Water	gal	34	33	34	34
Cementitious Material (<i>CM</i>):					
Cement	lb	646	659	651	646
Fly Ash	lb	149	155	165	157
Fine Aggregate	lb	1689	1683	1683	1690
Coarse Aggregate ^a	lb	1206	1190	1200	1207
Admixtures:					
Retarder	oz	32	32	32	32
Rheology Modifier	oz	48	48	48	48
Water Reducer ^b	oz	56	56	56	56
Water/ <i>CM</i>		0.36	0.35	0.35	0.35
Initial Slump ^c	in.	9.0	9.0	9.5	4.5

^a Maximum aggregate size of 1/2 in.

^b Concrete arrived at construction site with tabulated amounts of admixtures. Supplemental water-reducing admixture was added to achieve a minimum 20 in. spread before casting.

^c Slump measured at time of arrival to construction site prior to adding supplemental water-reducing admixture.

Table 8 – Concrete strength measured at test day (1 in. = 25.4 mm, 1 ksi = 6.89 MPa)

Location	Specimen			
	T5		T6	
	f_{cm}^a ksi	f_{ct}^b ksi	f_{cm}^a ksi	f_{ct}^b ksi
Base Block	6.6 ^c	0.61 ^d	7.3 ^d	0.51 ^d
Wall Lift 1	7.5 ^d	0.61 ^d	7.3 ^d	0.66 ^d
Wall Lift 2	7.6 ^d	0.62 ^d	9.2 ^d	0.70 ^d
Lift Average	7.5	0.61	8.2	0.68
Top Block	7.8 ^d	0.61 ^d	7.5 ^d	0.59 ^d

^a Compressive strength of concrete following ASTM C39^[12] measured within one week of test day (Table 6).

^b Splitting tensile strength of concrete following ASTM C496^[13] measured within one week of test day (Table 6).

^c Reported value based on the average of three 4 x 8 in. cylinders.

^d Reported value based on the average of two 6 x 12 in. cylinders.

Table 9 – Reinforcing steel properties (1 in. = 25.4 mm, 1 ksi = 6.89 MPa)

Wall	Bar Designation No.	Nominal Bar Diameter in.	Yield Strength f_y ^a ksi	Tensile Strength f_t ^b ksi	f_t/f_y	Uniform Elongation ϵ_{su} ^c	Fracture Elongation ϵ_{sf} ^d
T5	6 (19) ^e	0.750	129	171	1.33	5.4%	9.9%
	4 (13) ^e	0.500	127	167	1.32	5.3%	8.6%
	3 (10) ^f	0.375	140	174	1.24	4.7%	7.3%
T6	6 (19) ^e	0.750	112	132	1.18	7.1%	10.1%
	4 (13) ^e	0.500	109	134	1.24	7.3%	9.7%
	3 (10) ^f	0.375	140	174	1.24	4.7%	7.3%

^a Measured from laboratory tests following ASTM A370^[6] using the 0.2% offset method. Reported values correspond to average of two tests.

^b Measured from laboratory tests following ASTM A370^[6]. Reported values correspond to average of two tests.

^c Corresponds to strain at peak stress (tensile strength) following ASTM E8^[14].

^d Based on 8-in. gauge length following ASTM A370^[6].

^e Mechanical properties of No. 6 (19) and No. 4 (13) bars comply with ASTM A1035 Grade 120 (830) for T5 and ASTM A615 Grade 100 (690) for T6.

^f Mechanical properties of No. 3 (10) bars comply with ASTM A1035 Grade 120 (830) for both T5 and T6.

Table 10 – Maximum measured shear force and drift ratio (1 kip = 4.45 kN, 1 psi = 0.00689 MPa)

Wall	V_{max}^a		v_{max}^b		DR_{max}^c		DR_{cap}^d
	kips		$\sqrt{f_{cm}}$ (psi)		%		%
	–	+	–	+	–	+	
T5	303	395	3.5	4.6	2.3	2.8	2.3
T6	240	290	2.7	3.2	3.1	3.9	3.1

^aMaximum measured shear force for each loading direction during the loading protocol (Table 4).

^bShear stress calculated using $V_{max}/(\ell_w t_w)$ expressed as a fraction of $\sqrt{f_{cm}}$ (psi), where $t_w = 10$ in., $\ell_w = 100$ in., and f_{cm} is the lift average compressive strength taken from Table 8.

^cMaximum drift ratio attained for each loading direction during the loading protocol (Table 4) while maintaining a shear force not less than 80% of V_{max} .

^dDrift ratio capacity obtained from the minimum DR_{max} .

Table 11 – Drift cycle and bar location where bar buckling or bar fracture first occurred

Wall	Bar Location ^a		Drift Cycle ^b											
			2%				3%				4%			
			i+	i-	ii+	ii-	i+	i-	ii+	ii-	i+	i-	ii+	ii-
T5	Flange	Unconfined												
		Confined												
	Stem	Unconfined					F							
		Confined					F							
T6	Flange	Unconfined												
		Confined												
	Stem	Unconfined											F	
		Confined							B	F				

^a Confined regions refer to boundary elements with closely spaced transverse reinforcement. Unconfined flange includes the intersection of flange and stem (See Figure 4).

^b Notation:

i+ : first cycle, stem in compression; i- : first cycle, stem in tension;

ii+ : second cycle, stem in compression; ii- : second cycle, stem in tension;

B: buckling of longitudinal reinforcement; F: fracture of longitudinal reinforcement.

Table 12 – Secant stiffness from measured shear-drift envelope
(1 in. = 25.4 mm, 1 kip = 4.45 kN)

T5				T6			
Drift Ratio	Shear		Secant Stiffness	Drift Ratio	Shear		Secant Stiffness
DR^a	V	V/V_{max}^b	K^c	DR^a	V	V/V_{max}^b	K^c
%	kips		kips/in.	%	kips		kips/in.
-2.26	-303	1.00	47	-2.16	-112	0.47	18
-1.78	-297	0.98	58	-3.09	-240	1.00	27
-1.38	-280	0.92	71	-2.05	-236	0.99	40
-0.93	-241	0.79	90	-1.58	-236	0.99	52
-0.69	-208	0.69	106	-1.06	-230	0.96	76
-0.39	-170	0.56	152	-0.85	-225	0.94	92
-0.24	-117	0.39	174	-0.38	-175	0.73	159
0	0	0	-	-0.29	-130	0.54	157
0.24	130	0.33	187	0	0	0	-
0.39	175	0.44	159	0.23	131	0.45	203
0.50	225	0.57	157	0.39	175	0.61	155
0.75	268	0.68	124	0.55	225	0.78	142
1.26	325	0.82	90	0.78	261	0.90	117
1.76	362	0.92	72	1.31	290	1.00	77
2.77	395	1.00	50	1.81	288	0.99	56
				2.83	290	1.00	36
				3.92	247	0.85	22
$V_{0.8}^- =$	-242	$K_e^- =$	89	$V_{0.8}^- =$	-192	$K_e^- =$	124
$V_{0.8}^+ =$	316	$K_e^+ =$	96	$V_{0.8}^+ =$	232	$K_e^+ =$	136

^a Identifies drift ratio DR associated with peak force for each step (two cycles per step) of the loading protocol starting from step 2 (Table 4). DR is the measured drift divided by height h_y , where $h_y = 286$ in.

^b V_{max} is the maximum measured shear force per loading direction.

^c K is calculated using $V/(DR h_y)$ see footnote a. The value of K_e at the base of this table corresponds to the secant stiffness at $V = V_{0.8} = 0.8V_{max}$, based on linear interpolation.

Table 13 – Wall data for cracked stiffness calculation (1 in. = 25.4 mm, 1 kip = 4.45 kN)

Term ^a	Unit	T5		T6	
		V ⁻	V ⁺	V ⁻	V ⁺
h_w	in.	297	297	297	297
h_y	in.	286	286	286	286
ℓ_w	in.	100	100	100	100
t_w	in.	10	10	10	10
f_{cm} ^b	ksi	7.5	7.5	8.2	8.2
f_y ^c	ksi	129	129	112	112
E_c ^d	ksi	4,940	4,940	5,160	5,160
G_c ^e	ksi	2,060	2,060	2,150	2,150
E_s	ksi	29,000	29,000	29,000	29,000
$X_{cg,cr}$	in.	7.7	23.9	7.5	23.5
I_{cr}	in. ⁴	244,000	266,000	234,000	256,000
ϕ_K		1/10	1/10	1/10	1/10
d_b	in.	0.75	0.75	0.75	0.75
λ ^f		20	20	16	16
K_f ^g = $\frac{6E_c I_{cr}}{h_y^2(3h_w - h_y)}$	kips/in.	146	159	146	160
K_v ^h = $\frac{G_c \ell_w t_w \phi_K}{h_y}$	kips/in.	720	720	752	752
K_{sp} ⁱ = $\frac{E_c I_{cr}}{h_w h_y (\lambda d_b)}$	kips/in.	950	1030	1180	1300
$K_{wall,calc}$ ^j	kips/in.	108	116	111	120
$K_{wall,meas}$ ^k	kips/in.	89	96	124	136
$\frac{K_{wall,meas}}{K_{wall,calc}}$		0.82	0.83	1.12	1.13

^a For notation and definitions see APPENDIX A: NOTATION.

^b Measured average compressive strength of concrete (average of Lift 1 and 2, from Table 8).

^c Measured yield strength of the main flexural reinforcement (No. 6 (19) bar, from Table 9).

^d Modulus of Elasticity of concrete, $57\sqrt{1000f_{cm}}$, ksi.

^e Shear modulus of concrete: $E_c/2.4$ ksi.

^f From $2\lambda = \ell_d/d_b$ where ℓ_d is based on Eq. (4-11a) in ACI 408^[2] using $\phi = 1$, $\omega = 1$, and $(c\omega + K_{tr})/d_b = 4$:

$$\ell_d/d_b = \left(\frac{1000f_y}{f_c'^{\frac{1}{4}}} - 2400 \right) / 305, \text{ where } f_c' = 1000f_{cm} \text{ for base block in Table 8 } (f_{cm} = 6.6 \text{ ksi for T5 and } 7.3 \text{ ksi for T6}).$$

^g From flexural deflection Δ_f an at elevation h_y of a cantilever beam with flexural rigidity $E_c I_{cr}$ and subjected to point load V at h_w :

$$\Delta_f = Vh_y^2(3h_w - h_y)/(6E_c I_{cr}).$$

^h From shear deflection Δ_v an at elevation h_y of a cantilever beam with shear rigidity $G_c \ell_w t_w \phi_K$ and subjected to point load V at h_w (see Moehle^[55] for typical values of ϕ_K):

$$\Delta_v = Vh_y/(G_c \ell_w t_w \phi_K).$$

ⁱ From deflection due to strain penetration Δ_{sp} an at elevation h_y assuming an additional curvature of $Vh_w/(E_c I_{cr})$ over a distance λd_b lumped at the base of the wall:

$$\Delta_{sp} = Vh_w h_y \lambda d_b / (E_c I_{cr}).$$

^j Calculated stiffness of wall: $K_{wall,calc} = 1/(1/K_f + 1/K_v + 1/K_{sp})$.

^k Based on K_e , secant stiffness from measured shear-drift envelope, see Table 12, footnote c.

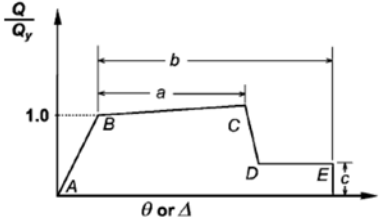
Table 14 – Unloading stiffness derived from measured shear versus drift ratio
(1 in. = 25.4 mm, 1 kip = 4.45 kN)

Target Drift Ratio DR^a %		T5			T6		
		Actual Drift	Shear	Unloading Stiffness	Actual Drift	Shear	Unloading Stiffness
		Δ^a in.	V_m^a kips	K_u^b kips/in.	Δ^a in.	V_m^a Kips	K_u^b kips/in.
-3	Δ_m				-8.77	-174	53
	Δ_0				-5.51	0	
-2	Δ_m	-5.32	-284	74	-5.86	-220	69
	Δ_0	-1.46	0		-2.66	0	
-1.5	Δ_m	-4.04	-266	91	-4.57	-221	79
	Δ_0	-1.11	0		-1.77	0	
-1	Δ_m	-2.71	-229	117	-2.93	-216	102
	Δ_0	-0.75	0		-0.82	0	
-0.75	Δ_m	-1.99	-195	138	-2.52	-216	127
	Δ_0	-0.58	0		-0.82	0	
0.75	Δ_m	1.54	218	160	1.58	216	134
	Δ_0	0.18	0		-0.03	0	
1	Δ_m	2.32	259	117	2.27	244	119
	Δ_0	0.11	0		0.21	0	
1.5	Δ_m	3.63	302	89	3.70	256	81
	Δ_0	0.23	0		0.53	0	
2	Δ_m	5.07	337	79	5.27	260	79
	Δ_0	0.81	0		1.98	0	
3	Δ_m				8.13	248	65
	Δ_0				4.31	0	

^a For a given target drift ratio DR , shear V_m corresponds to peak drift Δ_m during second cycle to DR . Drift Δ_0 corresponds to zero shear (unloading from Δ_m) and is measured during second cycle to DR .

^b K_u is calculated using $V_m/(\Delta_m - \Delta_0)$

Table 15 – Modeling parameters for nonlinear analysis (1 psi = 0.00689 MPa)

Parameters ^a	ASCE 41 (2017) ^a		Proposed	Envelope
	$\frac{V}{A_{cv}\sqrt{f_{cm}} \text{ (psi)}} \leq 4$	$\frac{V}{A_{cv}\sqrt{f_{cm}} \text{ (psi)}} \geq 6$		
a	0.015	0.009	Same as ASCE 41	 <p>From ASCE 41 (2017) Figure 10-1 (a)</p>
b	0.020	0.15	Same as ASCE 41	
c	0.75	0.40	Same as ASCE 41	
I_{eff}/I_g ^b	0.35	0.35	1/7 (Grade 100) ^{c,d} 1/9 (Grade 120) ^c	
$A_{cv,eff}/A_{cv}$ ^b	1.0	1.0	1/10 ^d	
Q_B ^e	M_n ^f	M_n ^f	$0.9M_n$ ^{f,d}	
Q_C ^g	M_{pr} ^h	M_{pr} ^h	$1.1M_n$ ^{f,d}	

^aSee Figure 10-1(a) in this table. These parameters correspond to the case when the normalized axial $P \leq 0.10f_{cm}A_g$.

^bNormalized effective section properties to the gross section properties.

^cGrade of flexural reinforcement.

^dFrom Huq et al.^[37]

^eForce at point B of the envelope.

^f M_n based on expected (or measured) properties.

^gForce at point C of the envelope.

^hAccording to ASCE 41^[5], M_{pr} is based on $1.25f_y$ and f_y is based on expected (or measured) value.

Table 16 – Measured concrete strength at test day for walls tested at The University of Kansas (1 ksi=6.89 MPa)

Location	Specimen											
	T1 ^a		T2 ^a		T3 ^a		T4 ^a		T5		T6	
	f_{cm}^b ksi	f_{ct}^c ksi	f_{cm}^b ksi	f_{ct}^c ksi	f_{cm}^b ksi	f_{ct}^c ksi	f_{cm}^b ksi	f_{ct}^c ksi	f_{cm}^a ksi	f_{ct}^b ksi	f_{cm}^a ksi	f_{ct}^b ksi
Bottom Block	8.0 ^d	-	6.9 ^d	0.42 ^d	7.6 ^d	-	7.4 ^d	0.52 ^e	6.6 ^d	0.61 ^e	7.3 ^e	0.51 ^e
Wall Lift 1	7.2 ^e	0.55 ^e	7.9 ^d	0.48 ^d	7.3 ^e	0.52 ^e	8.6 ^d	0.52 ^e	7.5 ^e	0.61 ^e	7.3 ^e	0.66 ^e
Wall Lift 2	7.4 ^e	0.46 ^e	7.7 ^d	0.48 ^d	7.2 ^d	0.54 ^e	7.2 ^d	0.54 ^e	7.6 ^e	0.62 ^e	9.2 ^e	0.70 ^e
Lift Average	7.3	0.51	7.8	0.48	7.3	0.53	7.9	0.53	7.5	0.61	8.2	0.68
Top Block	6.8 ^e	0.50 ^e	6.4 ^d	0.46 ^d	5.4 ^d	0.39 ^e	6.6 ^d	0.44 ^e	7.8 ^e	0.61 ^e	7.5 ^e	0.59 ^e

^aFrom Huq et al.[37]

^bCompressive strength of concrete following ASTM C39[12].

^cSplitting tensile strength of concrete following ASTM C496[13].

^dReported value based on the average of three 4 x 8 in. (100 x 200 mm) cylinders.

^eReported value based on the average of two 6 x 12 in. (150 x 300 mm) cylinders.

Table 17 – Reinforcing steel properties for walls tested at The University of Kansas
(1 in. = 25.4 mm, 1 ksi = 6.89 MPa)

Wall	Bar Designation No.	Nominal Bar Diameter in.	Yield Strength f_y^a ksi	Tensile Strength f_t^b ksi	f_t/f_y	Uniform Elongation ϵ_{su}^c	Fracture Elongation ϵ_{sf}^d
T1 ^e	6 (19)	0.750	70	94	1.34	12.2%	15.0% ^f
	4 (13)	0.500	76	106	1.39	11.0%	14.0% ^f
	3 (10)	0.375	60 ^f	91 ^f	1.52	-	16.5% ^f
T2 ^e	6 (19)	0.750	108	124	1.15	8.9%	13.0% ^f
	4 (13)	0.500	108	119	1.10	5.7%	10.0% ^f
	3 (10)	0.375	109 ^f	134 ^f	1.23	-	11.3% ^f
T3 ^e	6 (19)	0.750	99	122	1.23	9.4%	12.5% ^f
	4 (13)	0.500	101	122	1.21	6.6%	12.5% ^f
	3 (10)	0.375	109 ^f	134 ^f	1.23	-	11.3% ^f
T4 ^e	6 (19)	0.750	96	131	1.36	8.6%	12.5% ^f
	4 (13)	0.500	107	128	1.20	6.5%	10.9% ^f
	3 (10)	0.375	109 ^f	134 ^f	1.23	-	11.3% ^f
T5	6 (19)	0.750	129	171	1.33	5.4%	9.9%
	4 (13)	0.500	127	167	1.32	5.3%	8.6%
	3 (10)	0.375	140	174	1.24	4.7%	7.3%
T6	6 (19)	0.750	112	132	1.18	7.1%	10.1%
	4 (13)	0.500	109	134	1.24	7.3%	9.7%
	3 (10)	0.375	140	174	1.24	4.7%	7.3%

^a Measured from laboratory tests following ASTM A370^[6] using the 0.2% offset method. Reported values correspond to average of two tests.

^b Measured from laboratory tests following ASTM A370^[6]. Reported values correspond to average of two tests.

^c Corresponds to strain at peak stress following ASTM E8^[14].

^d Based on 8 in. gauge length following ASTM A370^[6]. Reported values correspond to average of two tests.

^e From Huq et al.^[37]

^f Reported on manufacturer mill certification.

Table 18 – Computed nominal flexural strength for walls tested at The University of Kansas
(1 in. = 25 mm, 1 ft = 305 mm, 1 kip = 4.45 kN)

Wall	f'_c ksi	f_y^a ksi	P^b kips	$M_n^+ c$ ft-kips	$c^+ d$ in.	$V_{Mn}^+ e$ kips	$M_n^- c$ ft-kips	$c^- d$ in.	$V_{Mn}^- e$ kips
T1 ^f	8	60	61	6340	17.5	254	5610	2.5	224
T2 T3, T4 ^f	8	100	61	6160	17.9	246	5690	2.6	228
T5	8	120	61	7520	21.9	303	6470	3.1	261
T6	8	100	61	6770	19.3	273	5650	2.6	226

^a Reinforcement nominal yield strength.

^b Total axial load at base of wall: self-weight of wall (44.9 kips), top block (9.0 kips), internal bracing (0.2 kips), and tributary weight of loading apparatus (6.8 kips).

^c Nominal flexural strength: M_n^+ for stem in compression and M_n^- for stem in tension. Calculated based on ACI 318 using a concrete strain limited to 0.003 and a concrete stress defined by the equivalent rectangular stress block. Reinforcing steel stress was limited to the nominal yield strength f_y . For reinforcement area and location, see Figure 204 through Figure 207.

^d Neutral axis depth measured from extreme compression fiber, c^+ corresponds to M_n^+ and c^- to M_n^- , see footnote c.

^e Shear associated with M_n^+ or M_n^- based on a nominal shear span of 300 in.

^f Data from Huq et al.^[37]

Table 19 – Stress-strain parameters for concrete (1 ksi = 6.89 MPa)

Parameter	Unit	Wall					
		T1 ^a	T2 ^a	T3 ^a	T4 ^a	T5	T6
Unconfined concrete							
f_c'' ^b	ksi	7.3	7.8	7.3	7.9	7.5	8.2
ϵ_o ^c		0.0025	0.0025	0.0025	0.0025	0.0025	0.0025
Z_{uc} ^d		117	120	110	120	120	121
f_r ^e	ksi	0.64	0.66	0.64	0.67	0.65	0.68
E_c ^f	ksi	4870	5030	4870	5070	4940	5160
Confined concrete							
K_{cc} ^g		1.20	1.29	1.31	1.29	1.39	1.35
$K_{cc}\epsilon_o$		0.0030	0.0032	0.0033	0.0032	0.0035	0.0035
f_{cc}'' ^h	ksi	8.8	10.1	9.6	10.2	10.4	11.1
ϵ_{cc} ⁱ		0.0050	0.0061	0.0064	0.0061	0.0073	0.0071
Z_{cc} ^j		21	14	13	14	11	12
f_r ^e	ksi	0.64	0.66	0.64	0.67	0.65	0.68
E_c ^f	ksi	4870	5030	4870	5070	4940	5160

^a Data from Huq et al.^[37]

^b Peak stress of unconfined concrete based on f_{cm} (Table 16).

^c Strain corresponding to maximum stress for unconfined concrete.

^d Strain softening parameter for the unconfined concrete.

^e Modulus of rupture of concrete, $f_r = 7.5\sqrt{1000f_c''}/1000$, ksi.

^f Modulus of elasticity of concrete, $E_c = 57\sqrt{1000f_c''}$, ksi.

^g Ratio of the confined to unconfined concrete compressive strength.

^h Peak stress for confined concrete, $f_{cc}'' = K_{cc}f_c''$.

ⁱ Strain corresponding to maximum stress for confined concrete.

^j Strain softening parameter for the confined concrete.

Table 20 – Stress-strain parameters for reinforcing steel (1 ksi = 6.89 MPa)

Parameter ^a	Unit	Wall					
		T1 ^b	T2 ^b	T3 ^b	T4 ^b	T5	T6
f_{yp} ^c	ksi	70	108	99	92	135	112
E_s	ksi	29000	29000	29000	29000	29000	29000
ε_{sh} ^d		1.1%	1.7%	1.2%	0.3%	0.0%	0.0%
E_{sh} ^d	ksi	630	670	790	1380	2550	865
f_t ^e	ksi	94	124	122	131	171	132
ε_{su} ^e		12.2%	8.9%	9.4%	8.6%	5.4%	7.1%
f_{st} ^e	ksi	93	123	122	130	127	112
ε_{st} ^f		15.3%	13.4%	12.9%	12.9%	10.3%	10.5%

^a For notation and definitions, see APPENDIX A: NOTATION.

^b Data from Huq et al.^[37]

^c Stress defining the proportional limit, $f_{yp} = f_y$ only for reinforcement with a yield plateau intersected by the line defined by the 0.2% offset method.

^d Variable to define the strain-hardening model, see Figure 235 and Figure 237. Values were derived from the measured stress-strain relationship.

^e Refer to data for No. 6 (19) bars in Table 17.

^f Based on $\varepsilon_{st} = \varepsilon_{sf} + f_{st}/29000$, where ε_{sf} corresponds to No. 6 (19) bar in Table 17.

Table 21 – Maximum measured shear force and drift ratio for walls tested at The University of Kansas (1 kip = 4.45 kN, 1 psi = 0.00689 MPa)

Wall	V_{max}^a kips		v_{max}^b $\sqrt{f_{cm}}$ (psi)		DR_{max}^c %		DR_{cap}^d %
	–	+	–	+	–	+	
T1 ^e	282	303	3.3	3.5	6.00 ^f	3.73	3.7
T2 ^e	237	282	2.7	3.2	1.80	2.05	1.8
T3 ^e	242	275	2.8	3.2	2.95	3.95	3.0
T4 ^e	253	293	2.8	3.3	3.87	4.05	3.9
T5	303	395	3.4	4.6	2.30	2.80	2.3
T6	240	290	2.6	3.2	3.10	3.90	3.1

^a Maximum measured shear force for each loading direction during the loading protocol (Table 4).

^b Shear stress calculated using $V_{max}/(\ell_w t_w)$ expressed as a fraction of $\sqrt{f_{cm}}$ (psi), where $t_w = 10$ in., $\ell_w = 100$ in., and f_{cm} is the lift average compressive strength taken from Table 16.

^c Maximum drift ratio attained for each loading direction during the loading protocol (Table 4) while maintaining a shear force not less than 80% of V_{max} .

^d Drift ratio capacity obtained from the minimum DR_{max} .

^e Data from Huq et al.^[37]

^f After reaching the target drift ratio of 4% in each loading direction, T1 was subjected to a final push up to the limitations of the testing apparatus, which was a displacement of nearly 20 in. (508 mm) at the horizontal plane of action of the actuators.

Table 22 – Moment-curvature data (1 in. = 25.4 mm, 1 ft = 305 mm, 1 kip = 4.45 kN)

Wall Direction	Event ^a									
	M_{cr}	M_{y1}	M_{yd}	M_n	\bar{M}	$\epsilon_{c,Core} = 0.010$	$\epsilon_{c,Core} = 0.015$	$\epsilon_{t,No.4} = \epsilon_{su}$	$\epsilon_{t,No.6} = \epsilon_{su}$	
T1	M, ft-kips	3351	6261	6647	7239	8012	7967	7716	7722	7755
	ϕ , 10 ⁻⁴ /in.	0.036	0.354	0.456	1.72	4.34	4.92	6.23	20.6	23.0
T2	M, ft-kips	1348	5151	5846	6563	8574	-	-	-	8537
	ϕ , 10 ⁻⁴ /in.	0.018	0.276	0.348	11.5	15.1	-	-	-	12.8
T3	M, ft-kips	3464	5779	6158	6637	7088	6976	6626	6498	6272
	ϕ , 10 ⁻⁴ /in.	0.036	0.504	0.648	1.84	4.32	5.40	6.64	7.75	13.0
T4	M, ft-kips	1393	4846	5479	6136	6943	-	-	-	6933
	ϕ , 10 ⁻⁴ /in.	0.018	0.414	0.516	13.4	10.3	-	-	-	9.29
T5	M, ft-kips	3351	5324	5659	6132	6792	6731	6423	6206	6130
	ϕ , 10 ⁻⁴ /in.	0.036	0.468	0.600	1.75	4.71	5.41	6.67	9.27	13.8
T6	M, ft-kips	1348	4473	5025	5638	6810	-	-	-	6790
	ϕ , 10 ⁻⁴ /in.	0.018	0.384	0.474	13.7	10.9	-	-	-	9.81
T7	M, ft-kips	3486	5078	5380	6052	7210	6423	6804	6586	6551
	ϕ , 10 ⁻⁴ /in.	0.036	0.444	0.570	1.97	4.54	6.67	6.46	9.30	12.7
T8	M, ft-kips	1402	4268	4781	5481	7276	-	-	-	7260
	ϕ , 10 ⁻⁴ /in.	0.018	0.366	0.462	15.1	10.1	-	-	-	8.98
T9	M, ft-kips	3397	6791	7372	7639	9238	6206	8684	8333	8324
	ϕ , 10 ⁻⁴ /in.	0.036	0.606	0.786	1.58	3.62	9.27	5.51	8.17	8.34
T10	M, ft-kips	1366	5095	5779	6455	8303	-	-	-	8263
	ϕ , 10 ⁻⁴ /in.	0.018	0.492	0.618	11.8	6.6	-	-	-	5.68
T11	M, ft-kips	3552	5984	6414	6853	7647	6130	7055	6572	6586
	ϕ , 10 ⁻⁴ /in.	0.036	0.522	0.672	1.81	4.04	13.8	6.43	10.8	10.5
T12	M, ft-kips	1428	4448	5037	5676	6568	-	-	-	6545
	ϕ , 10 ⁻⁴ /in.	0.018	0.426	0.534	14.3	7.7	-	-	-	7.42

^aFor notation and definitions see APPENDIX A: NOTATION.

Table 23 – Plastic hinge length for Model B (1 in. = 25.4 mm, 1 ksi = 6.89 MPa)

Parameter	Unit	Wall											
		T1	T2	T3	T4	T5	T6	T1	T2	T3	T4	T5	T6
M_{y1}^a	ksi	6261	5151	5779	4846	5324	4473	5078	4268	6791	5095	5993	5052
\bar{M}^b	ksi	8012	8537	7088	6933	6808	6796	7168	7260	9238	8263	7710	7354
$\left(1 - \frac{M_y}{\bar{M}}\right)$		0.22	0.40	0.18	0.30	0.22	0.34	0.39	0.41	0.26	0.38	0.22	0.31
l_p^c	in.	33	60	28	45	33	51	44	62	40	58	33	47

^a Moment associated with the first yield of the longitudinal reinforcement.

^b Maximum moment calculated from the moment-curvature relationship.

^c Length of the plastic hinge based on Eq. 31.

Table 24 – Deformation capacity determined using Model A1 based only on flexural deformations (concrete compressive strain limited to 0.015) (1 in. = 25.4 mm, 1 ft = 305 mm, 1 kip = 4.45kN)

Term ^a	Unit	Wall					
		T1	T2	T3	T4	T5	T6
h_w	in.	300	300	300	300	300	300
ϕ_{cr} ^b	10 ⁻³ /in.	0.004	0.004	0.004	0.004	0.004	0.004
ϕ_y ^c	10 ⁻³ /in.	0.046	0.065	0.060	0.057	0.079	0.067
ϕ_u ^d	10 ⁻³ /in.	0.623	0.664	0.667	0.646	0.551	0.643
M_{cr}	ft-kips	3351	3464	3351	3486	3397	3552
M_y	ft-kips	6647	6158	5659	5380	7372	6414
M_u	ft-kips	8012	7088	6792	7210	9238	7647
λ_1		0.42	0.49	0.49	0.49	0.37	0.46
λ_2		0.83	0.87	0.83	0.75	0.80	0.83
Δ_f ^e	%	5.66	5.33	6.15	7.91	6.66	6.05
$DR_{f,calc}$ ^f	%	1.9	1.8	2.0	2.6	2.2	2.0

^a For notation and definitions, see APPENDIX A: NOTATION.

^b Cracking curvature.

^c Yield curvature corresponding to a yield tensile strain at a distance $0.8\ell_w$ from the extreme compression fiber.

^d Ultimate curvature associated to a maximum compressive strain of 0.015 in the confined concrete.

^e Calculated based on Eq. 25 and $\Delta_f = \theta_f h_w$.

^f Calculated drift capacity based only on flexural deformation, $DR_{f,calc} = \Delta_f/h_w$.

Table 25 – Deformation capacity using Model B1 based only on flexural deformations (concrete compressive strain limited to 0.015) (1 in. = 25.4 mm)

Term ^a	Unit	Wall					
		T1	T2	T3	T4	T5	T6
h_w	in.	300	300	300	300	300	300
ℓ_w	in.	100	100	100	100	100	100
t_w	in.	10	10	10	10	10	10
ℓ_p ^b	in.	50	50	50	50	50	50
ϕ_y ^c	10 ⁻³ /in.	0.046	0.065	0.060	0.057	0.079	0.067
ϕ_u ^d	10 ⁻³ /in.	0.623	0.664	0.667	0.646	0.551	0.643
$\Delta_{f,y}$ ^e	in.	1.37	1.94	1.80	1.71	2.36	2.02
$\Delta_{f,p}$ ^e	in.	7.94	8.24	8.35	8.10	6.49	7.91
Δ_f ^e	%	9.31	10.18	10.15	9.81	8.85	9.93
$DR_{f,calc}$ ^f	%	3.1	3.4	3.4	3.3	3.0	3.3

^a For notation and definitions, see APPENDIX A: NOTATION.

^b Length of plastic hinge estimated to be equal to $0.5\ell_w$.

^c Yield curvature corresponding to a yield tensile strain at a distance $0.8\ell_w$ from the extreme compression fiber.

^d Ultimate curvature associated to a maximum compressive strain of 0.015 in the confined concrete.

^e Calculated based on Eq. 32.

^f Calculated drift capacity based only on flexural deformation, $DR_{f,calc} = \Delta_f/h_w$.

Table 26 – Deformation capacity using Model A2 based on flexure, shear, and strain penetration (concrete compressive strain limited to 0.015) (1 in. = 25.4 mm, 1 ft = 305 mm, 1 kip = 4.45kN)

Term ^a	Unit	Wall					
		T1	T2	T3	T4	T5	T6
h_w	in.	300	300	300	300	300	300
ℓ_w	in.	100	100	100	100	100	100
t_w	in.	10	10	10	10	10	10
M_{cr}	ft-kips	3351	3464	3351	3486	3397	3552
M_y	ft-kips	6647	6158	5659	5380	7372	6414
M_u	ft-kips	8012	7088	6792	7210	9238	7647
ϕ_{cr}^b	$10^{-3}/\text{in.}$	0.004	0.004	0.004	0.004	0.004	0.004
ϕ_y^c	$10^{-3}/\text{in.}$	0.046	0.065	0.060	0.057	0.079	0.067
ϕ_u^d	$10^{-3}/\text{in.}$	0.623	0.664	0.667	0.646	0.551	0.643
λ_1		0.42	0.49	0.49	0.49	0.37	0.46
λ_2		0.83	0.87	0.83	0.75	0.80	0.84
c^e	in.	24.6	23.1	23.0	23.7	27.7	23.9
V_u^f	kips	320	284	272	288	370	306
G_c	ksi	2030	2100	2030	2110	2060	2150
$\phi_{K,bottom}^g$		100	100	100	100	100	100
$\phi_{K,top}^h$		10	10	10	10	10	10
α_{sp}^i		6.1	4.7	5.0	5.0	3.5	4.4
λ		8	15	13	13	20	16
d_b	in.	0.75	0.75	0.75	0.75	0.75	0.75
Δ_f^j	%	5.66	5.33	6.15	7.91	6.66	6.05
Δ_v^k	%	1.20	0.88	1.00	1.32	1.52	1.05
Δ_{sp}^l	%	0.50	1.03	0.95	0.83	1.17	1.01
$DR_{t,calc}^m$	%	2.5	2.4	2.7	3.4	3.1	2.7

^a For notation and definitions, see APPENDIX A: NOTATION.

^b Cracking curvature.

^c Yield curvature corresponding to a yield tensile strain at a distance $0.8\ell_w$ from the extreme compression fiber.

^d Ultimate curvature associated to a maximum compressive strain of 0.015 in the confined concrete.

^e Neutral axis depth associated with ϕ_u measured from the extreme compression fiber.

^f Calculated based on $V_u = \bar{M}^+/h_w$.

^g Ratio of cracked shear stiffness to uncracked stiffness throughout a distance $(1 - \lambda_2)h_w$.

^h Ratio of cracked shear stiffness to uncracked stiffness throughout a distance $\lambda_2 h_w$.

ⁱ Based on $\alpha_{sp} = \left[1 + \beta_\ell \left(1 + \frac{\varepsilon_s}{\varepsilon_y}\right)\right]$ using $\beta_\ell = 1/3$, $\varepsilon_y = f_y/E_s$ (from Table 17), $\varepsilon_s = \phi_u(d_t - c)$ with ϕ_u and c following footnotes d and e, and $d_t = 80$ in.

^j Calculated based on Eq. 25 and $\Delta_f = \theta_f h_w$.

^k Calculated based on Eq. 26 through Eq. 28.

^l Based on Table 13 in this manuscript and Table 12 in reference 38.

^m Calculated drift capacity considering flexure, shear and strain penetration, $DR_{t,calc} = (\Delta_f + \Delta_v + \Delta_{sp})/h_w$.

Table 27 – Deformation capacity using Model B2 based on flexure, shear, and strain penetration (concrete compressive strain limited to 0.015) (1 in. = 25.4 mm, 1 kip = 4.45 kN)

Term ^a	Unit	Wall					
		T1	T2	T3	T4	T5	T6
h_w	in.	300	300	300	300	300	300
ℓ_w	in.	100	100	100	100	100	100
t_w	in.	10	10	10	10	10	10
ℓ_p^b	in.	30	30	30	30	30	30
ϕ_y^c	10 ⁻³ /in.	0.046	0.065	0.060	0.057	0.079	0.067
ϕ_u^d	10 ⁻³ /in.	0.623	0.664	0.667	0.646	0.551	0.643
c^e	in.	24.6	23.1	23.0	23.7	27.7	23.9
$\Delta_{f,y}^f$	in.	1.37	1.94	1.80	1.71	2.36	2.02
$\Delta_{f,p}^f$	in.	4.94	5.12	5.19	5.04	4.04	4.92
V_u^g	kips	320	284	272	287	370	306
A_{cv}	in. ²	1000	1000	1000	1000	1000	1000
G_c	ksi	2030	2100	2030	2110	2060	2150
$\phi_{K,bottom}^h$		100	100	100	100	100	100
$\phi_{K,top}^i$		10	10	10	10	10	10
α_{sp}^j		6.1	4.7	5.0	5.0	3.5	4.4
λ		8	15	14	13	19	15
d_b	in.	0.75	0.75	0.75	0.75	0.75	0.75
Δ_f^f	%	6.30	7.07	6.99	6.75	6.40	6.94
Δ_v^k	%	0.90	0.77	0.76	0.77	1.02	0.81
Δ_{sp}^l	%	0.50	1.03	0.95	0.83	1.17	1.01
$DR_{t,cap}^m$	%	2.6	3.0	2.9	2.8	2.9	2.9

^a For notation and definitions, see APPENDIX A: NOTATION.

^b Length of plastic hinge estimated to be equal to $0.3\ell_w$.

^c Yield curvature corresponding to a yield tensile strain at a distance $0.8\ell_w$ from the extreme compression fiber.

^d Ultimate curvature associated to a maximum compressive strain of 0.015 in the confined concrete.

^e Neutral axis depth associated with ϕ_u measured from the extreme compression fiber.

^f Calculated based on Eq. 30.

^g Calculated based on $V_u = \bar{M}^+/h_w$.

^h Ratio of cracked shear stiffness to uncracked stiffness throughout the assumed plastic hinge length, ℓ_p .

ⁱ Ratio of cracked shear stiffness to uncracked stiffness outside the plastic hinge length, $h_w - \ell_p$.

^j Based on $\alpha_{sp} = \left[1 + \beta_\ell \left(1 + \frac{\varepsilon_s}{\varepsilon_y} \right) \right]$ using $\beta_\ell = 1/3$, $\varepsilon_y = f_y/E_s$ (from Table 17), $\varepsilon_s = \phi_u(d_t - c)$ with ϕ_u and c following footnotes d and e, and $d_t = 80$ in.

^k Calculated based on Eq. 25 through Eq. 27.

^l Calculated based on Eq. 29.

^m Calculated drift capacity considering flexure, shear and strain penetration, $DR_{t,calc} = (\Delta_f + \Delta_v + \Delta_{sp})/h_w$.

FIGURES

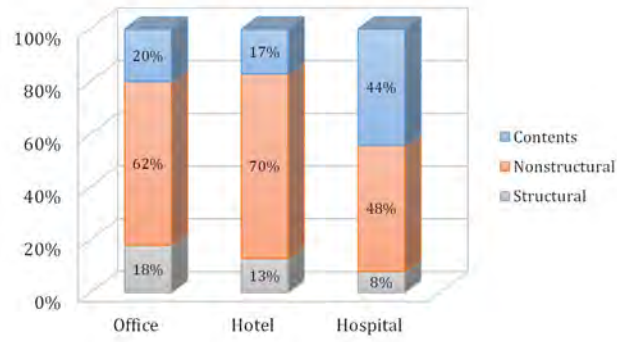


Figure 1 – Percentage of cost per building type^[15]

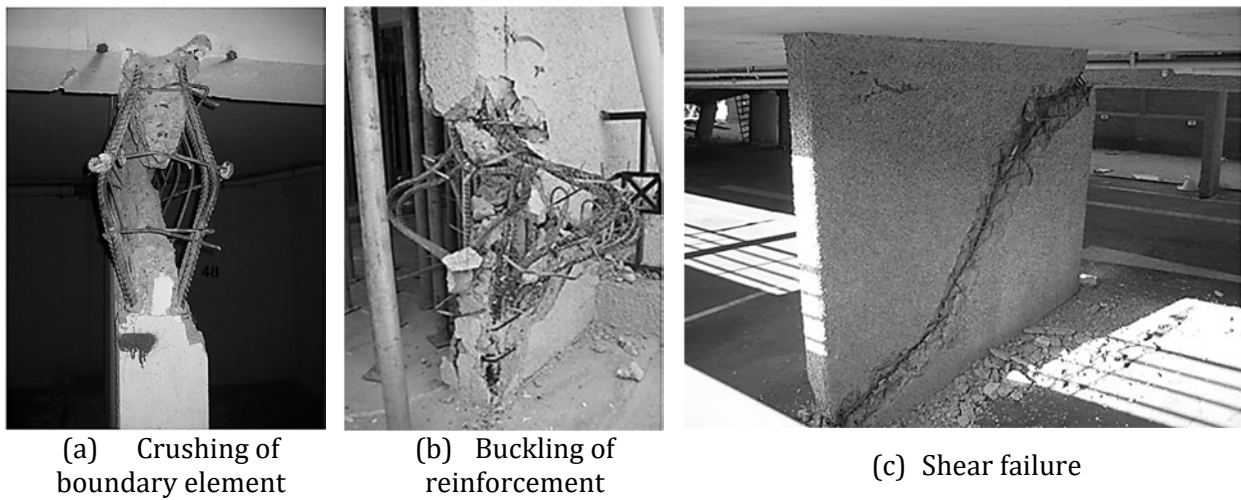


Figure 2 – Failures in reinforced concrete structural walls after the Maule (Chile) 2010 earthquake^[3]

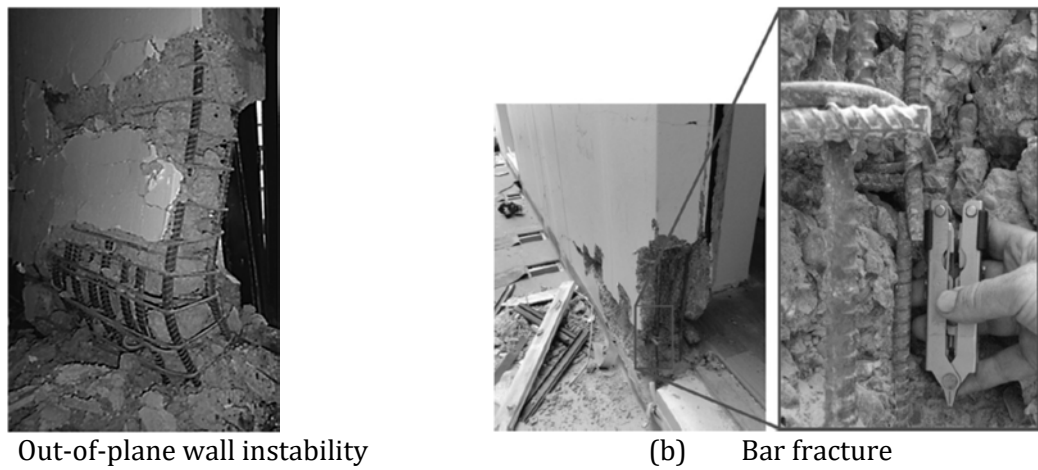


Figure 3 – Failures in reinforced concrete structural walls after the Christchurch (New Zealand) 2011 earthquake^[29]

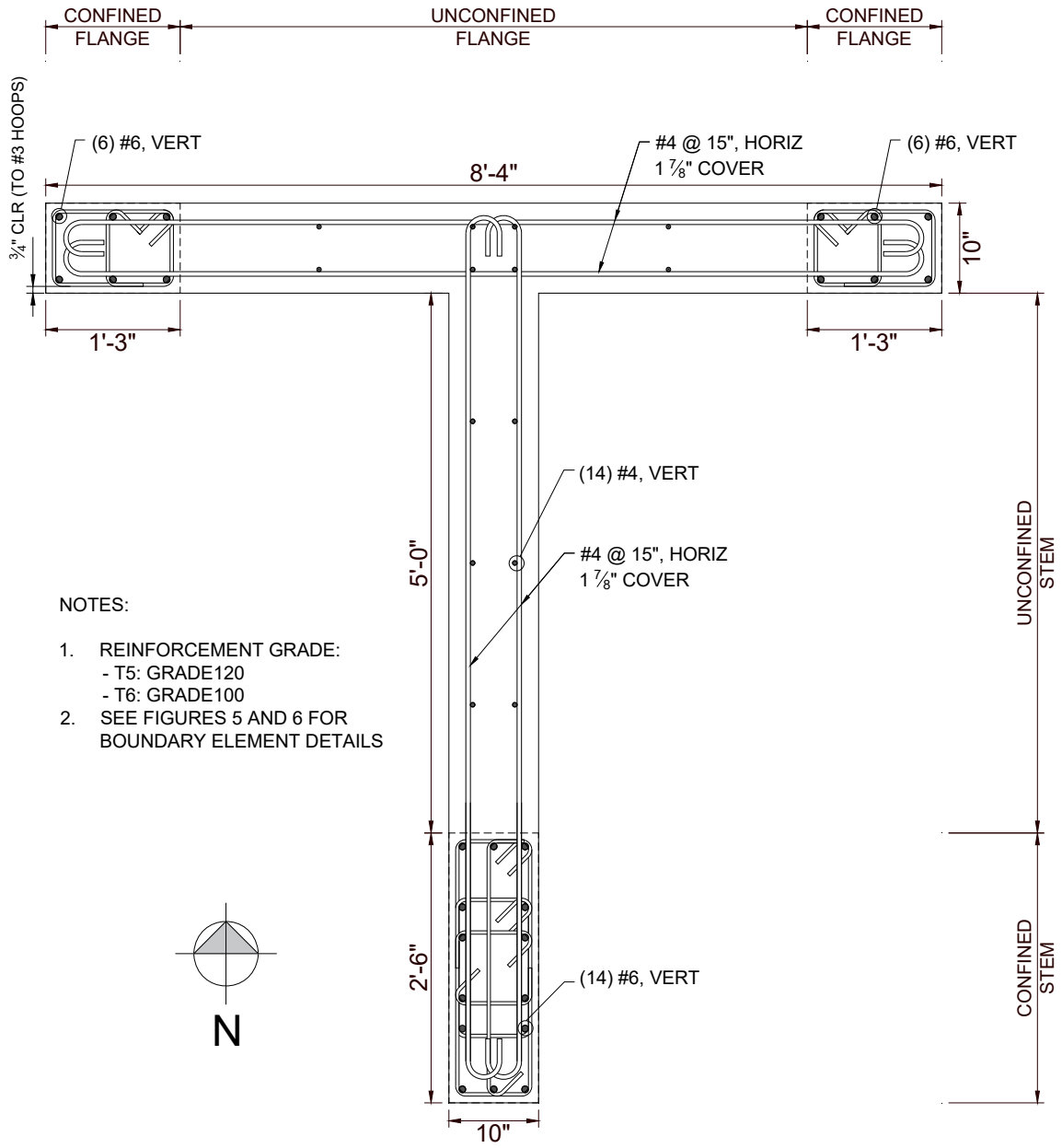


Figure 4 – Reinforcement layout for wall T5 and T6 (1 in. = 25.4 mm)

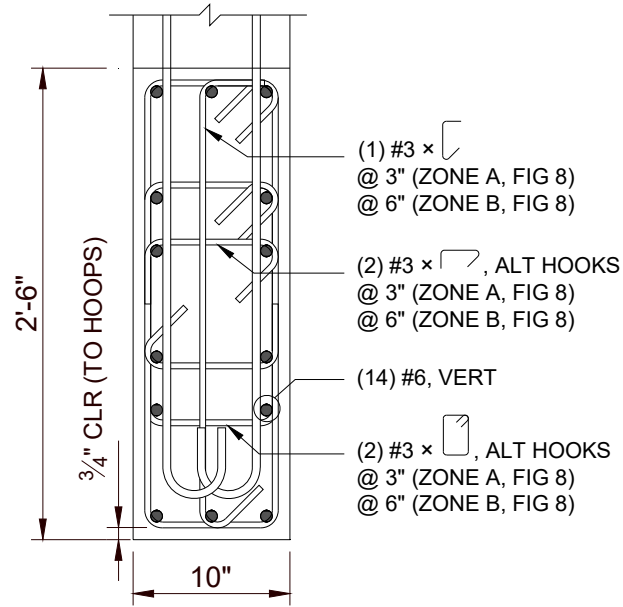


Figure 5 – Confined boundary element in stem of T5 and T6 (1 in. = 25.4 mm)

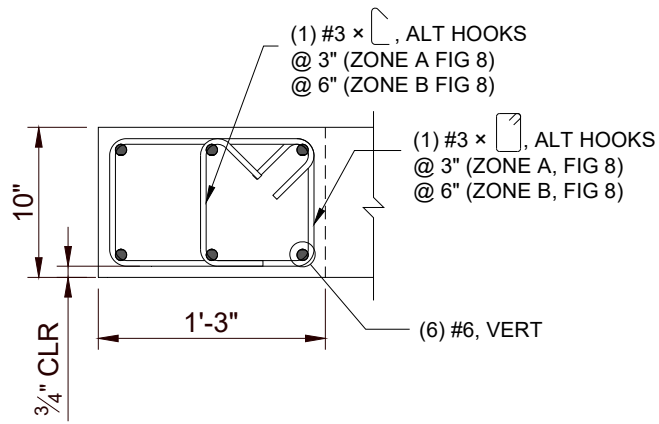


Figure 6 – Confined boundary element in flange of T5 and T6 (1 in. = 25.4 mm)

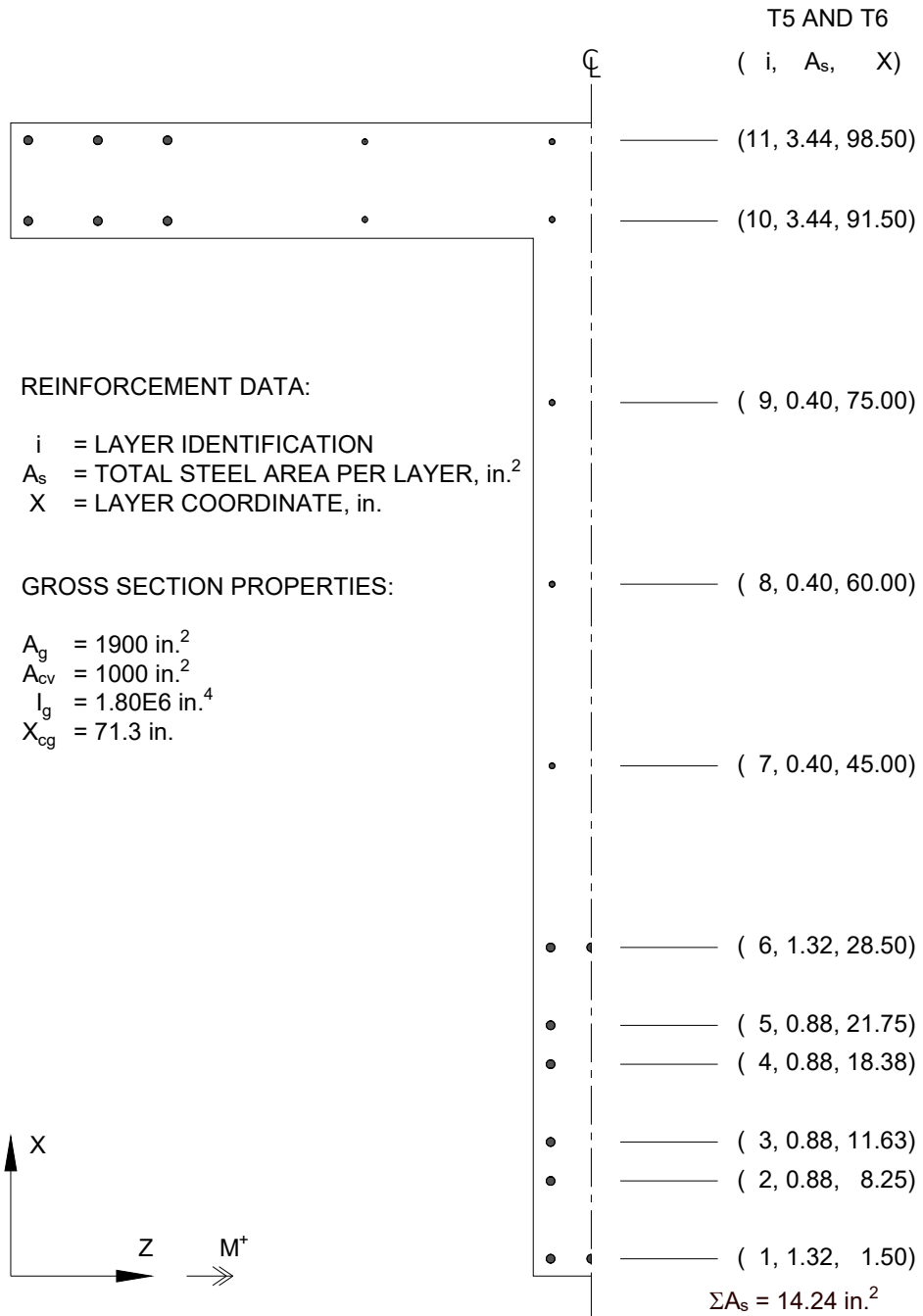


Figure 7 – Reinforcement data and wall section properties (1 in. = 25.4 mm)

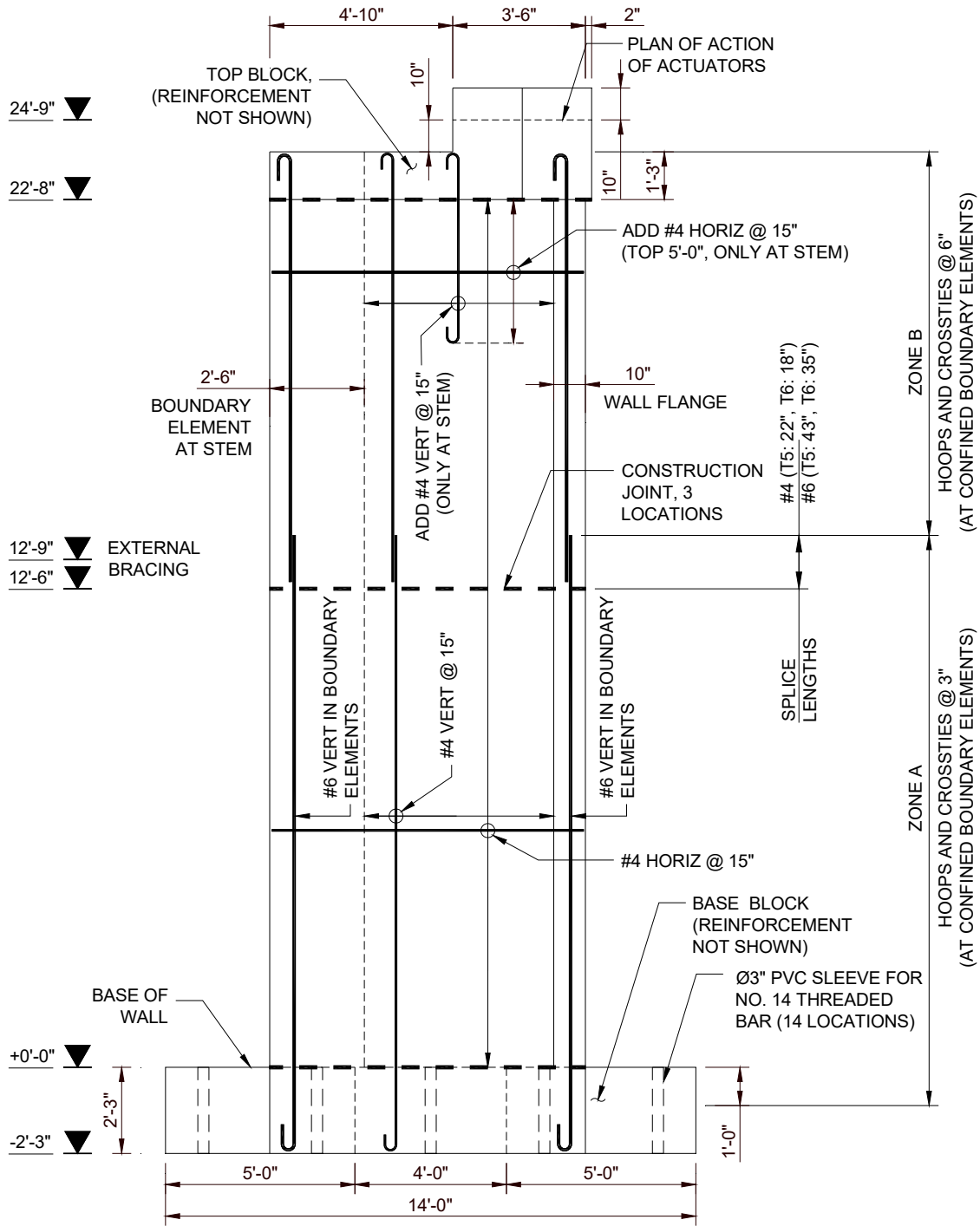


Figure 8 - Typical wall elevation (1 in. = 25.4 mm)

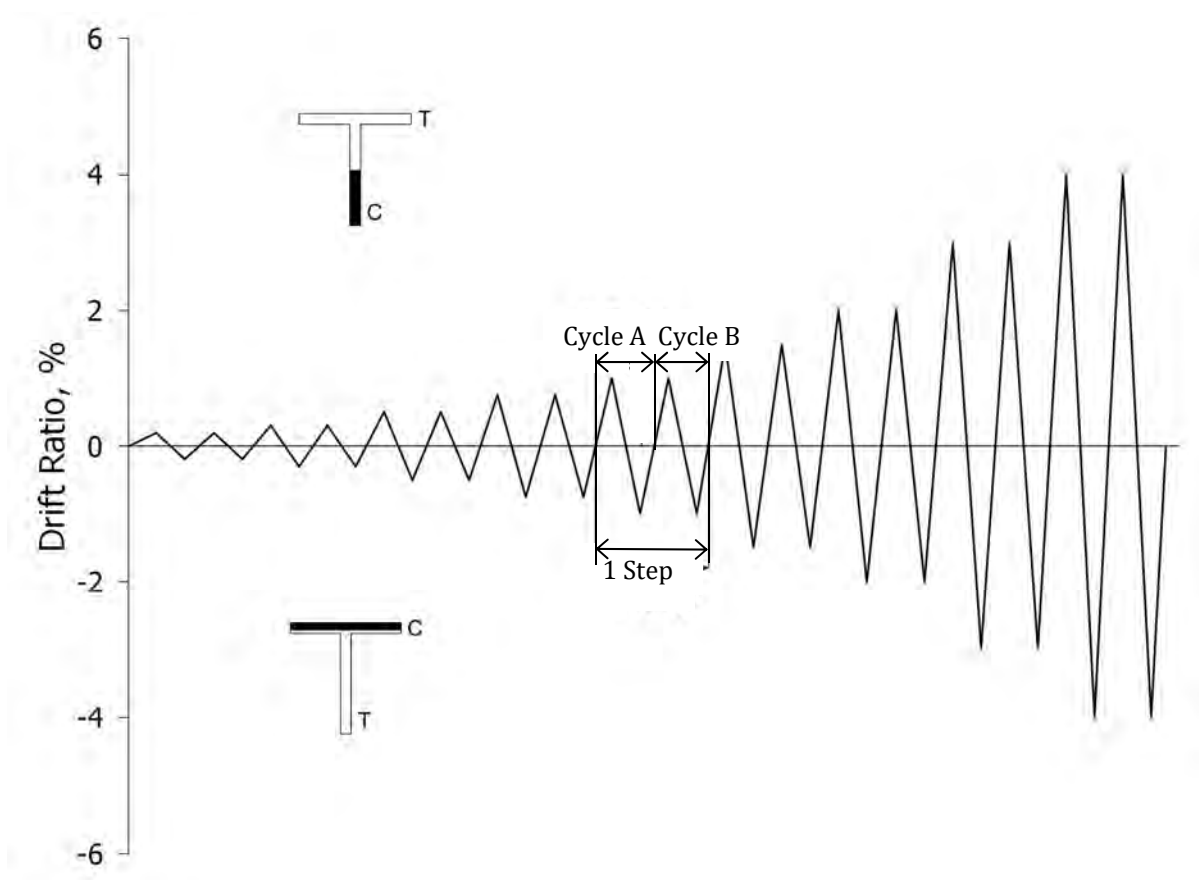


Figure 9 - Illustration of loading protocol described in Table 9

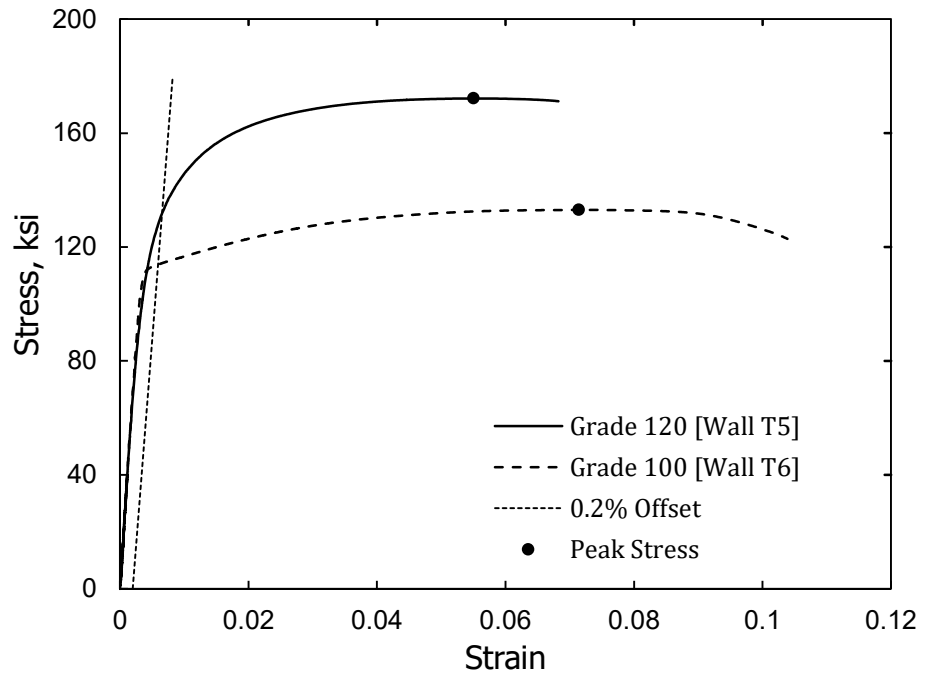


Figure 10 – Measured stress versus strain for No. 6 (19) bars (1 ksi = 6.89 MPa)

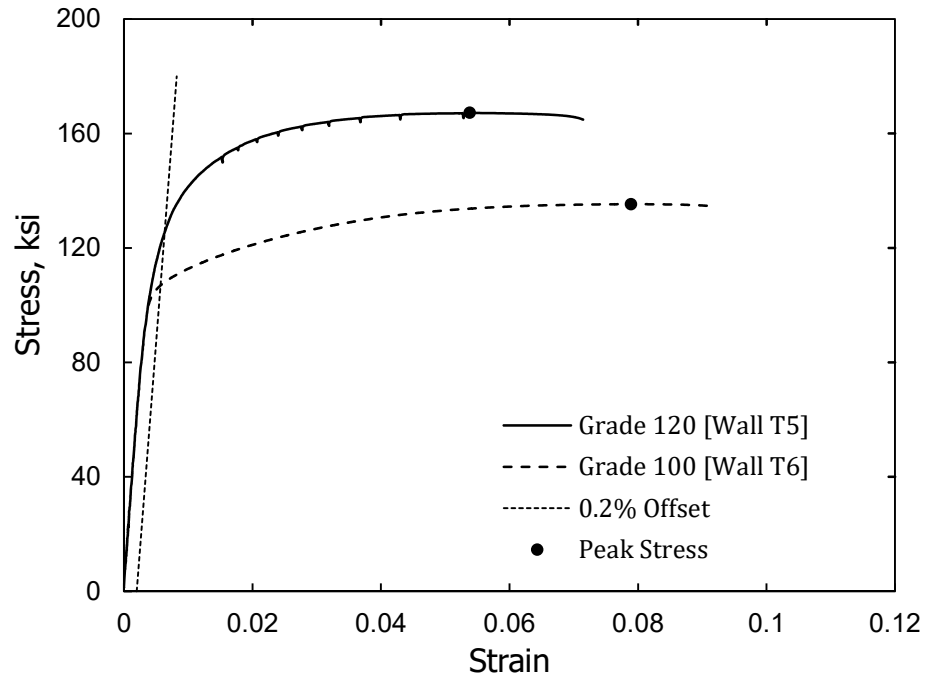


Figure 11 – Measured stress versus strain for No. 4 (13) bars (1 ksi = 6.89 MPa)



(a) Base block steel cage



(b) Lift 1 steel cage

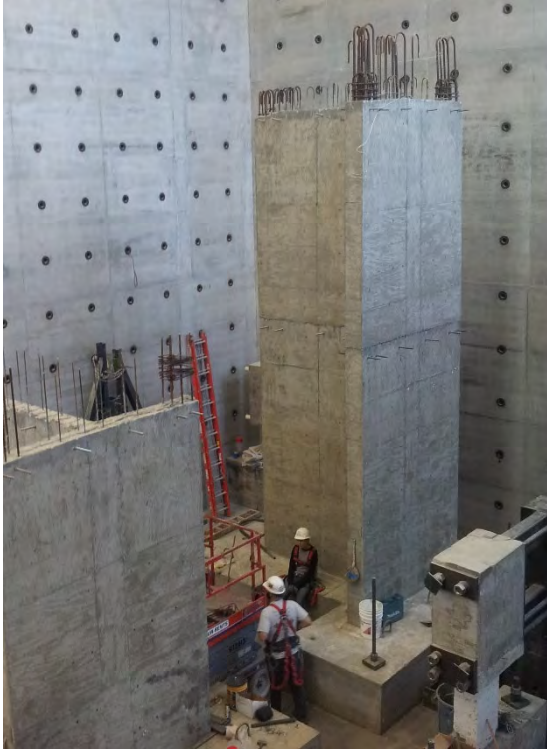


(c) Lift 1

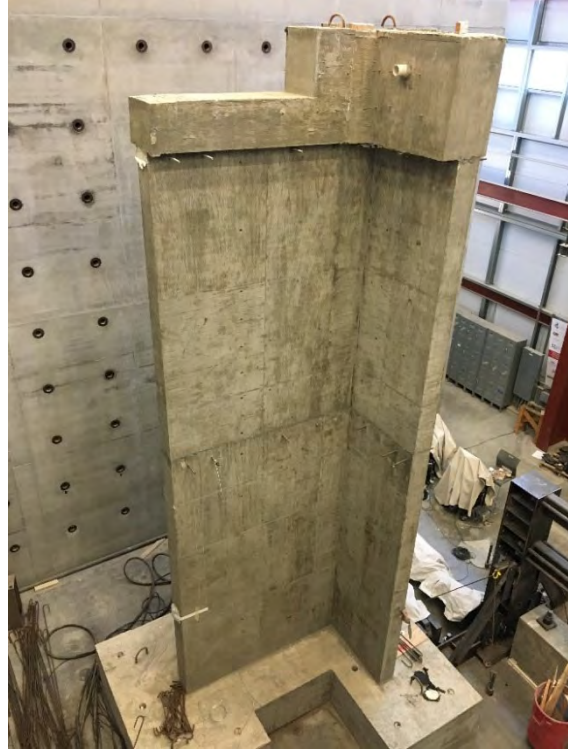


(d) Lift 2 steel cage

Figure 12 - Construction stages



(e) Lift 2



(f) Finished specimen

Figure 12 – Construction stages (cont.)

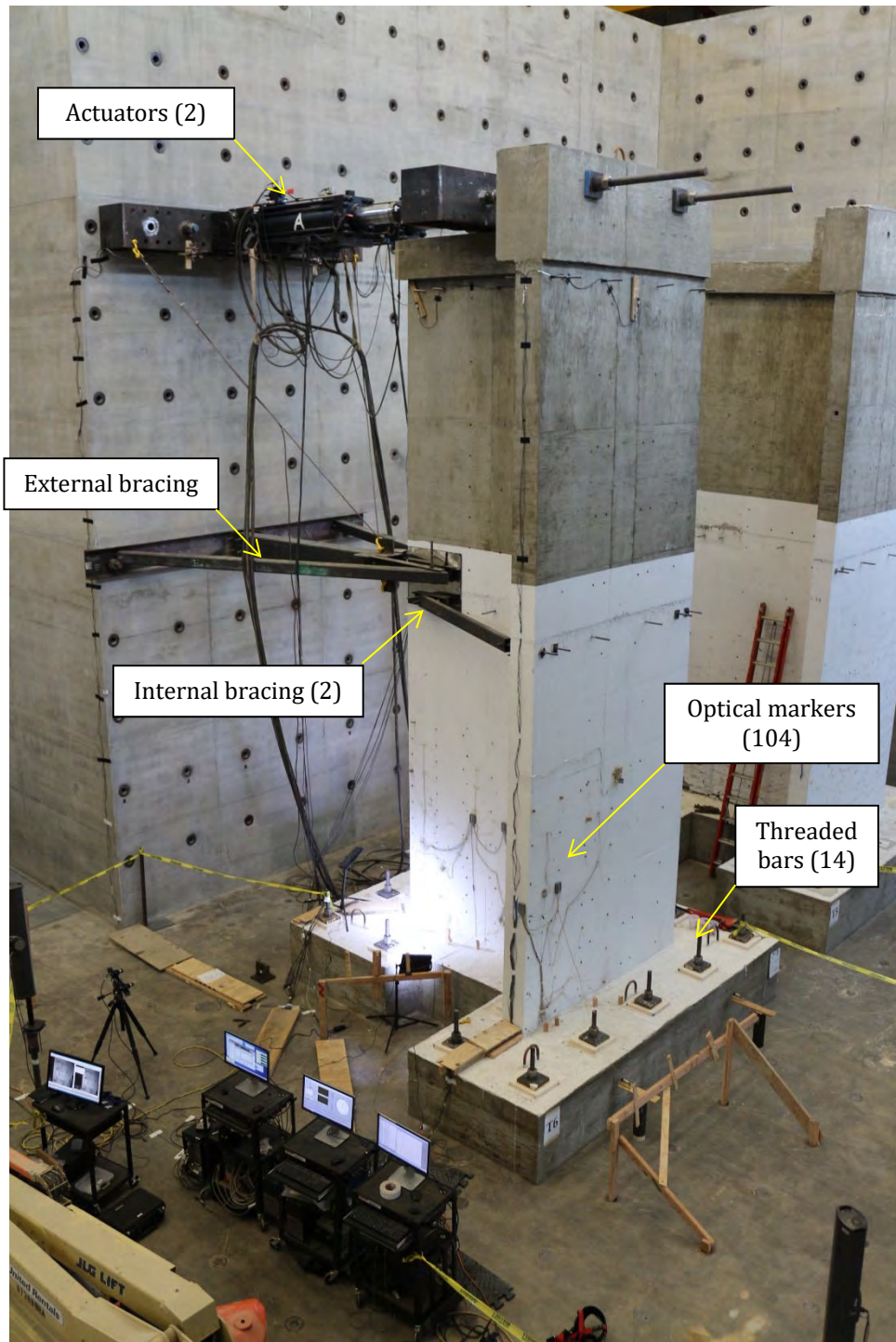


Figure 13 – Test setup

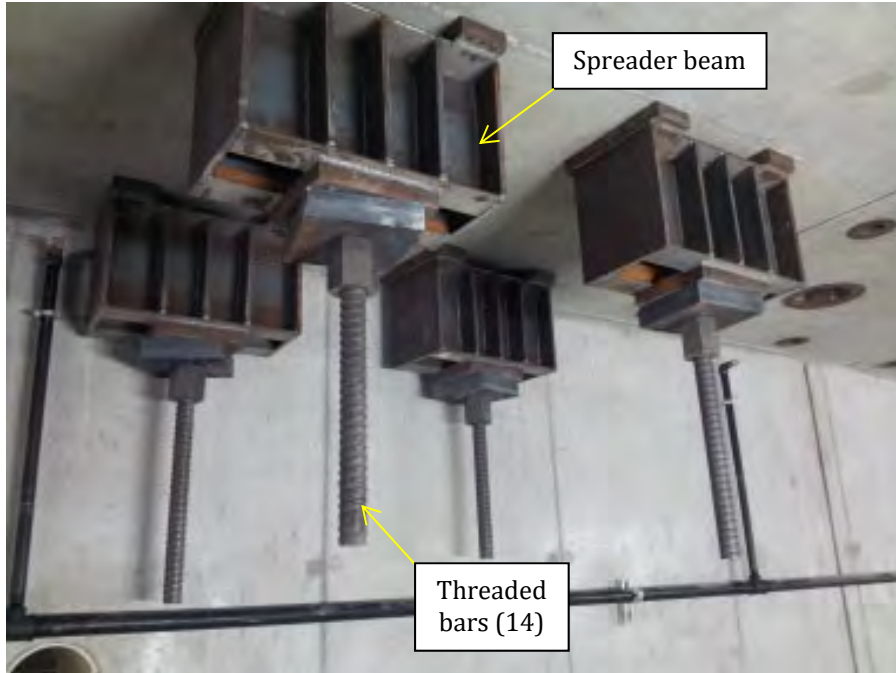


Figure 14 – Steel spreader beams below laboratory strong floor for base block hold-downs^[37]

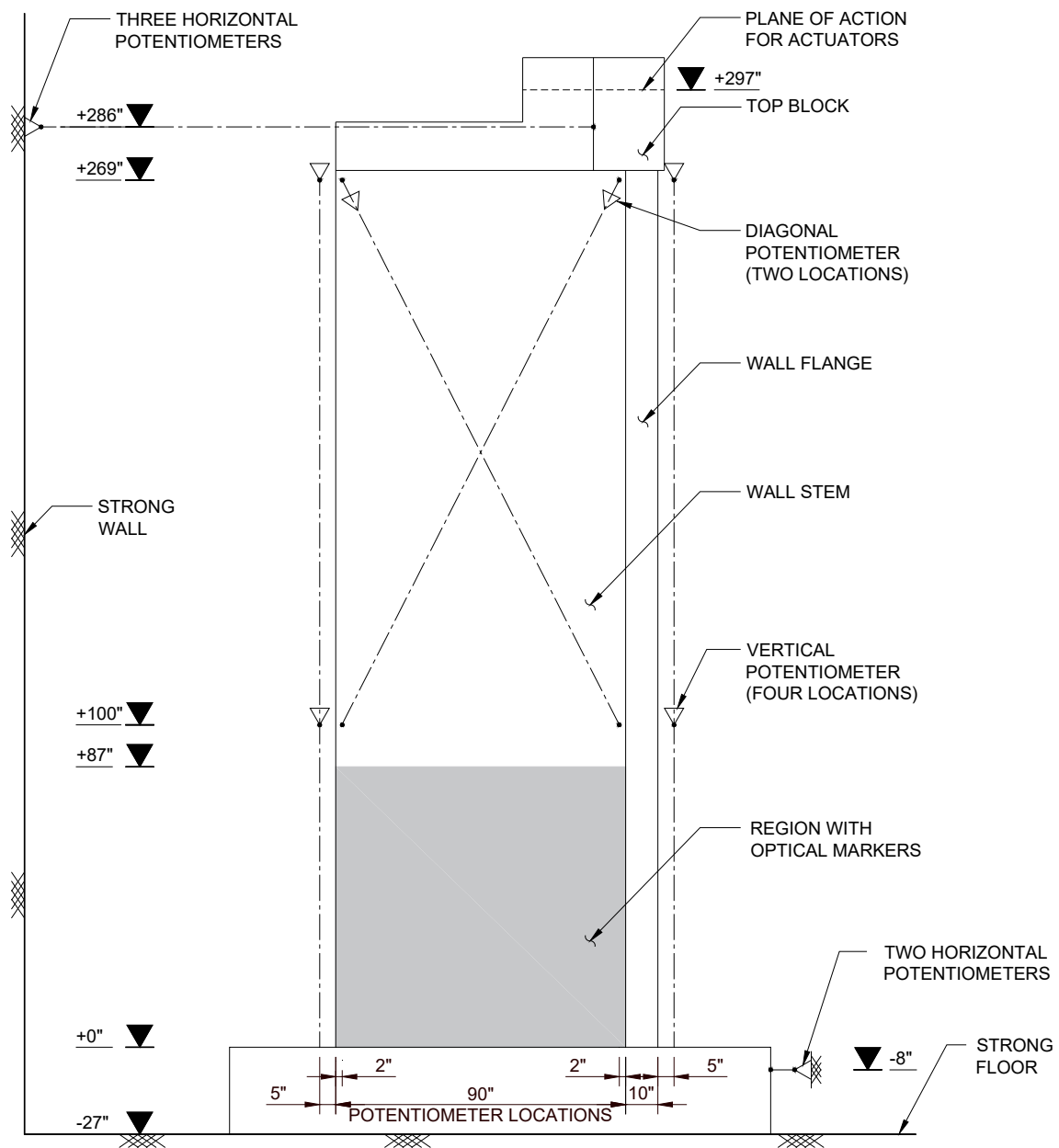


Figure 15 - Wall instrumentation (elevation view of wall stem) (1 in. = 25.4 mm)

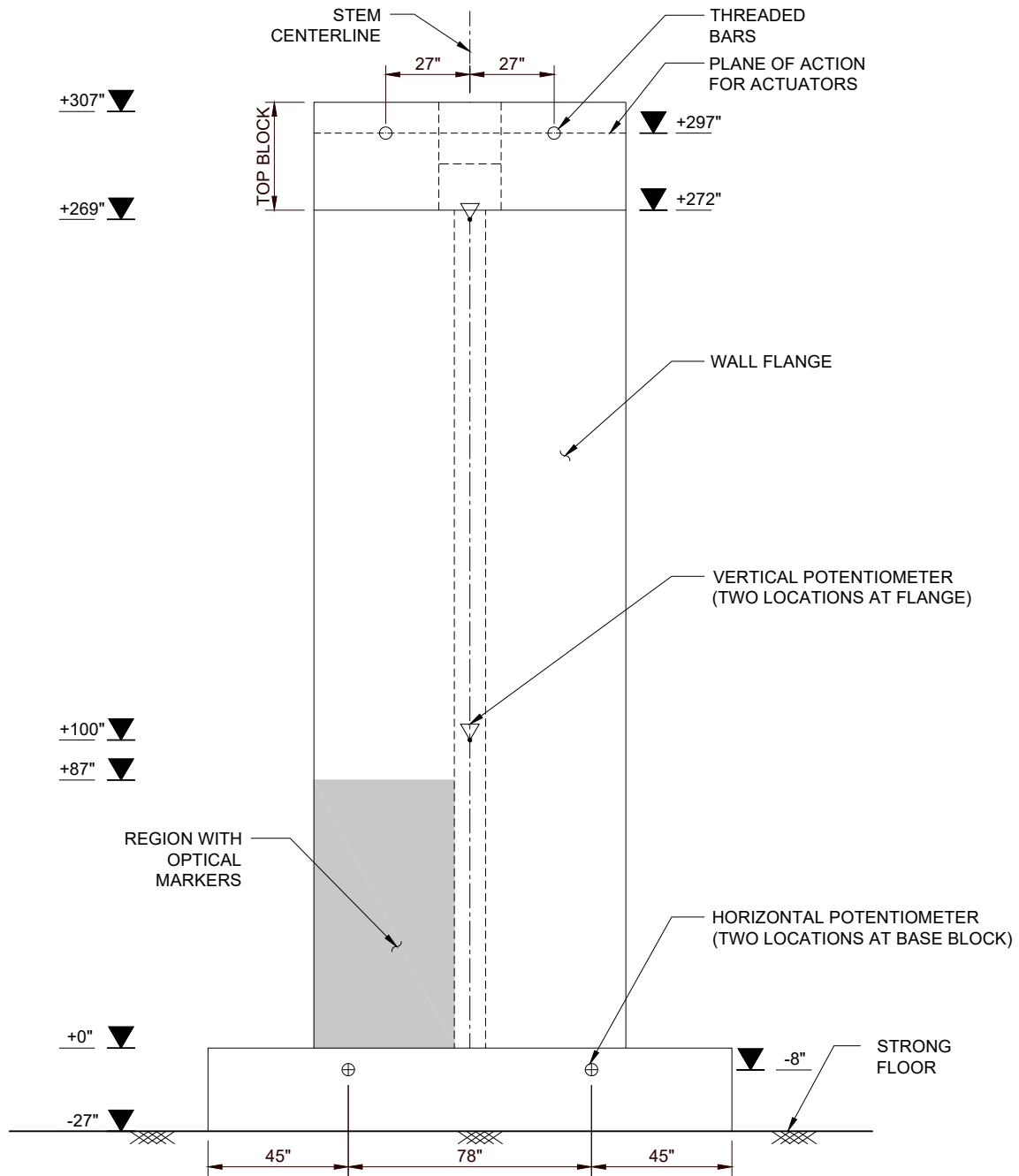


Figure 16 - Wall instrumentation (elevation view of wall flange) (1 in. = 25.4 mm)

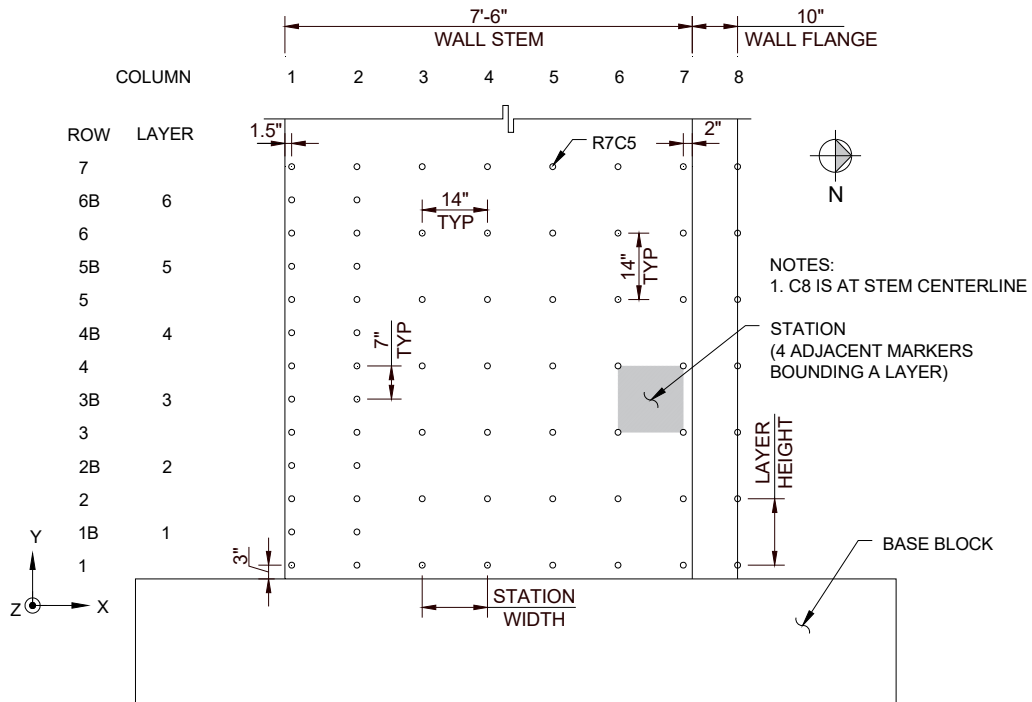


Figure 17 - Locations of optical markers on wall stem (1 in. = 25.4 mm)

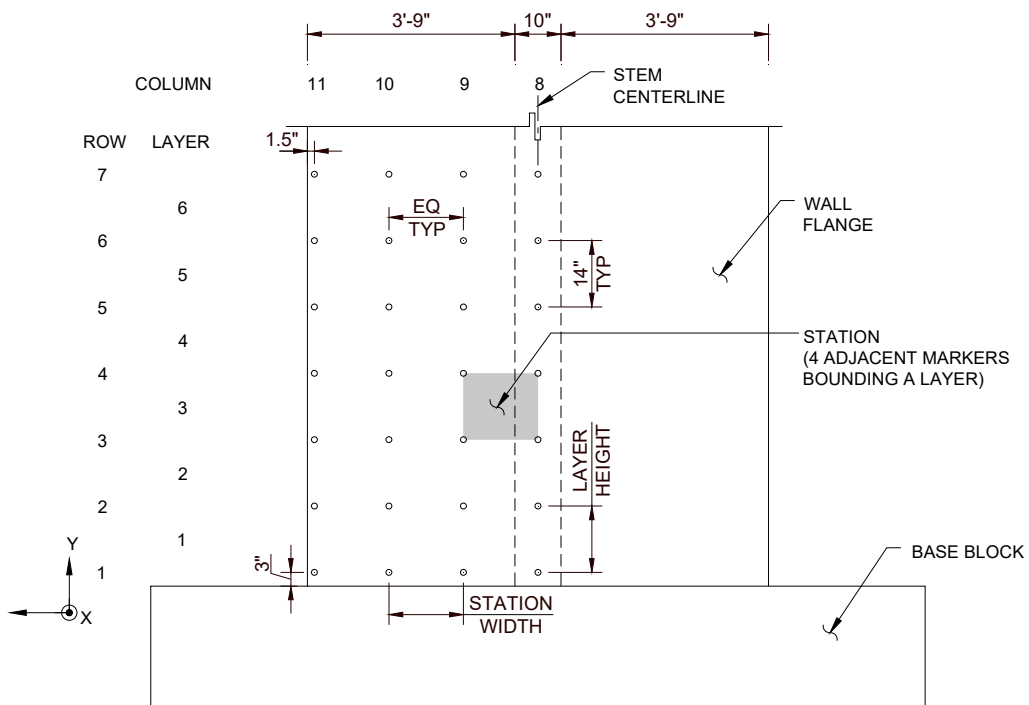


Figure 18 - Locations of optical markers on wall flange (1 in. = 25.4 mm)

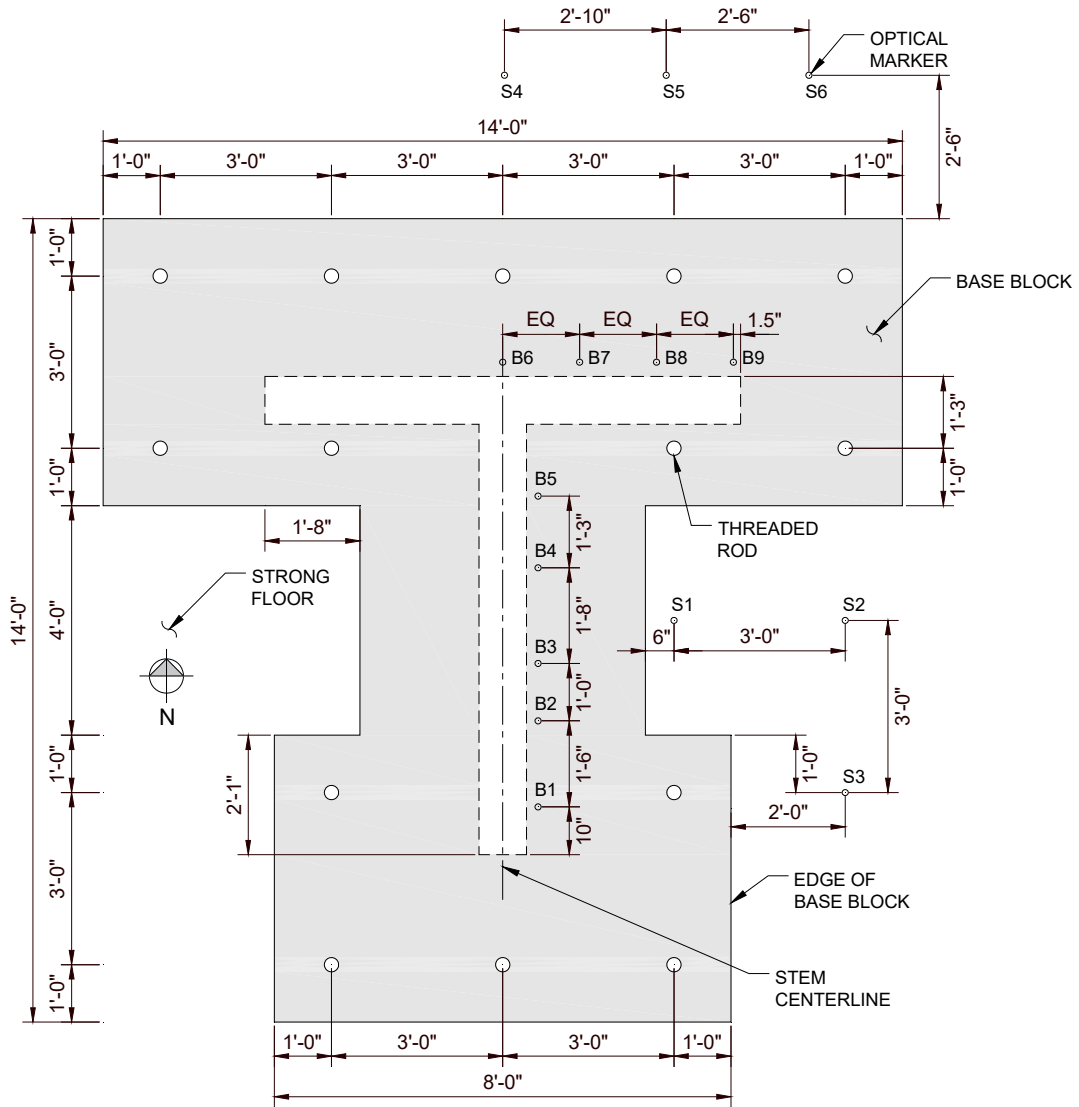


Figure 19 – Plan view of base block indicating locations of optical markers, B1 through B9 and S1 through S6 (1 in. = 25.4 mm)

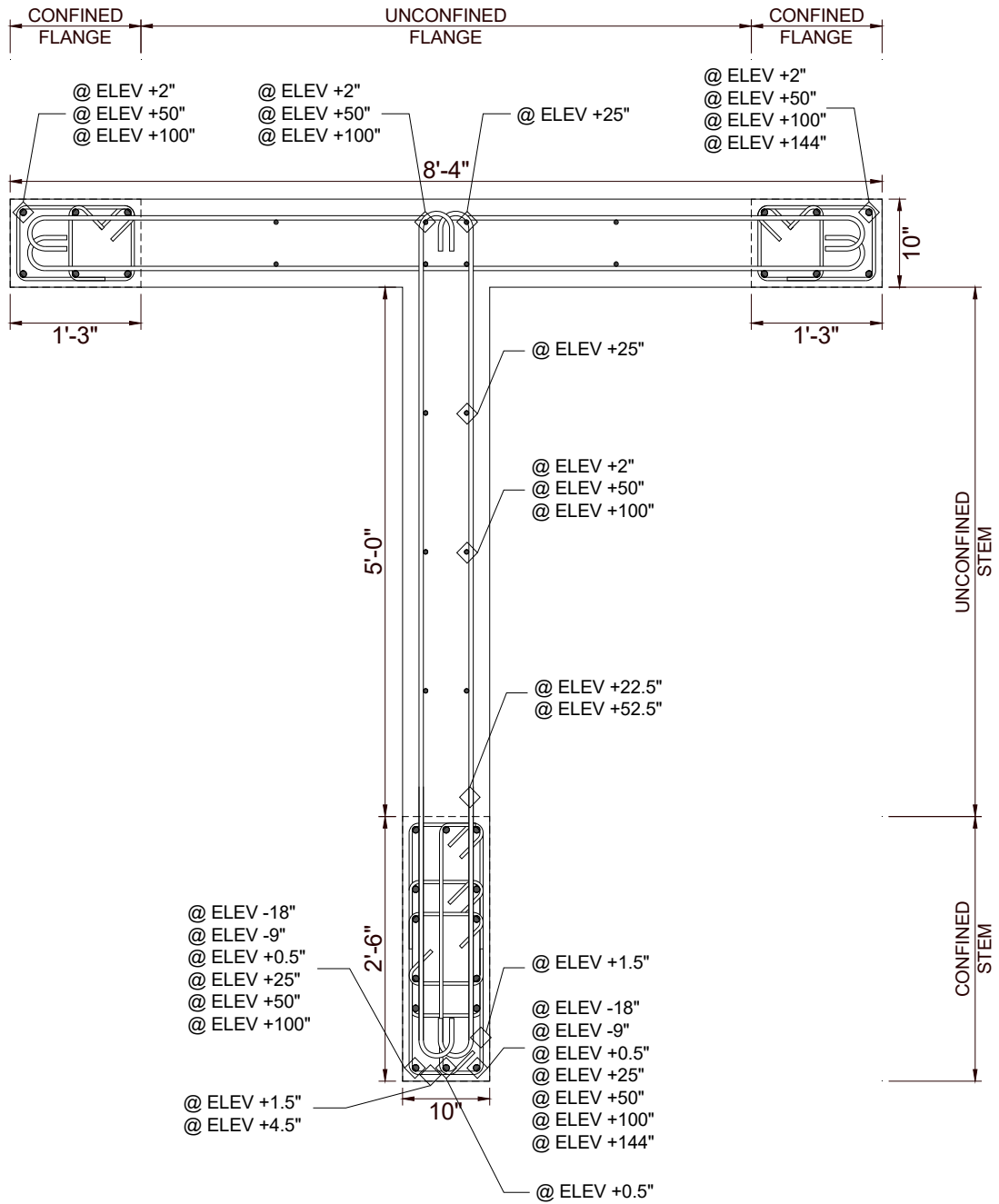


Figure 20 - Strain gauge locations in T5 (1 in. = 25.4 mm)

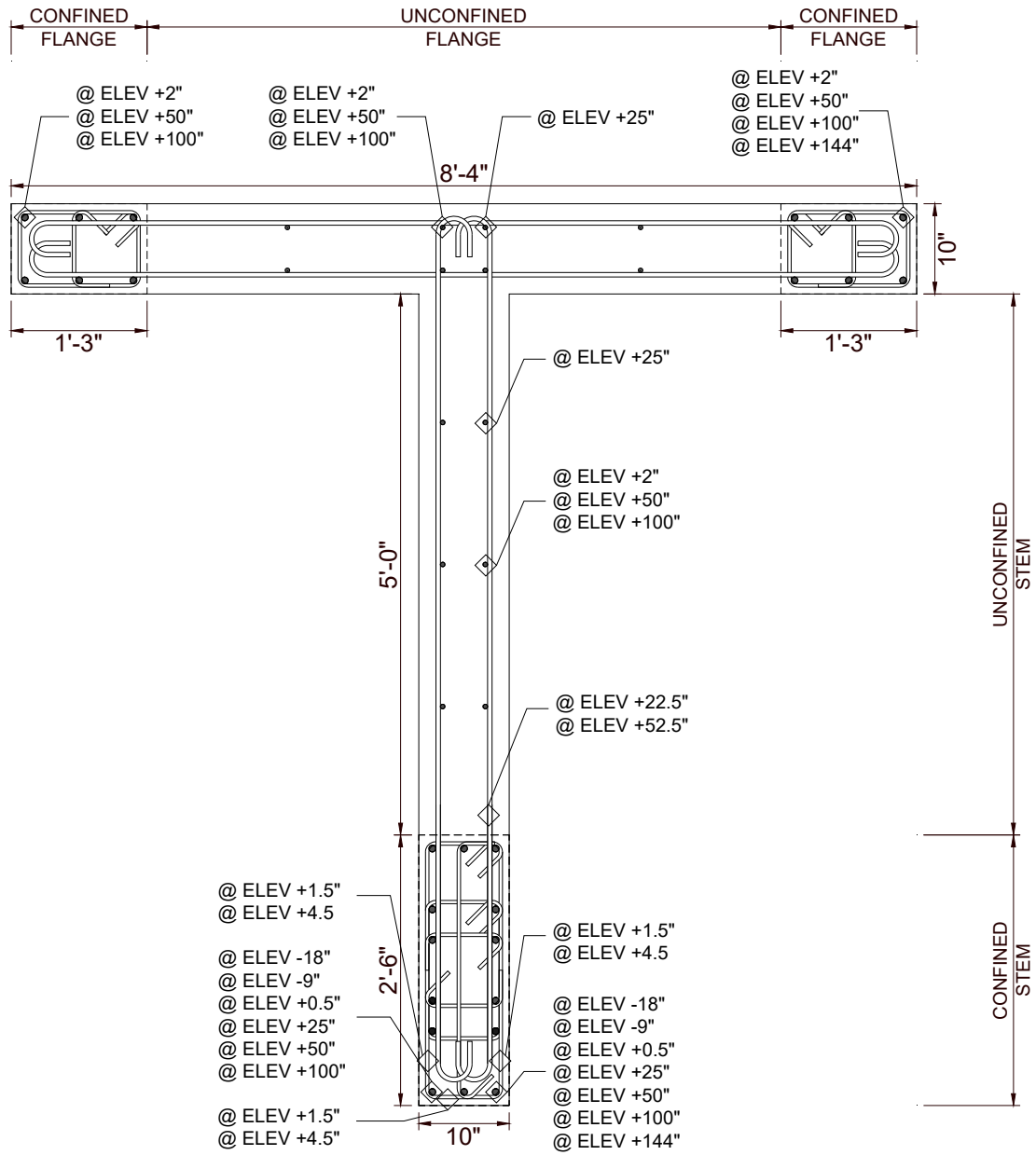


Figure 21 – Strain gauge locations in T6 (1 in. = 25.4 mm)

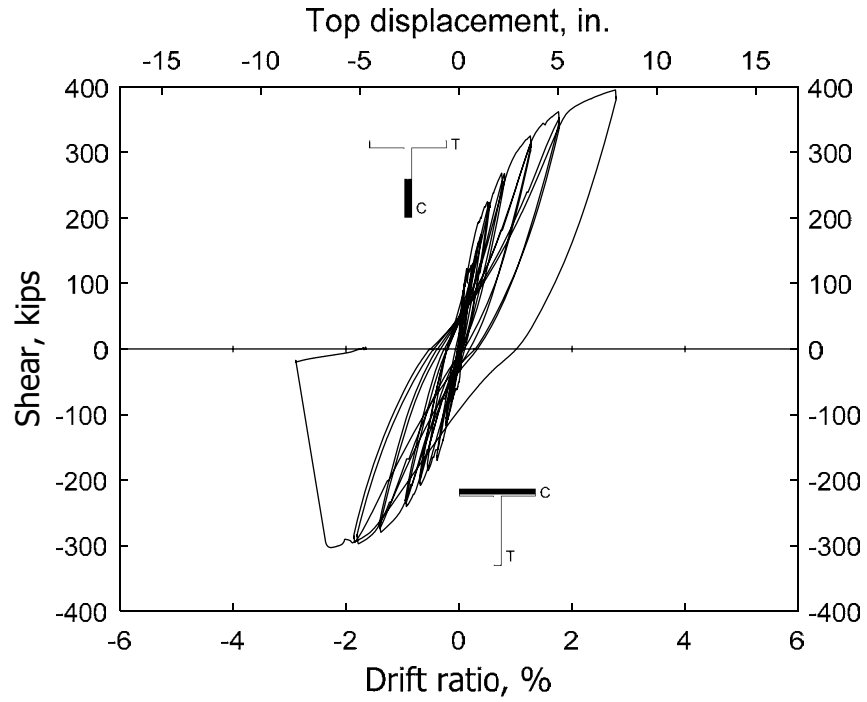


Figure 22 – Shear versus drift ratio for T5 (1 in. = 25.4 mm, 1 kip = 4.45 kN)

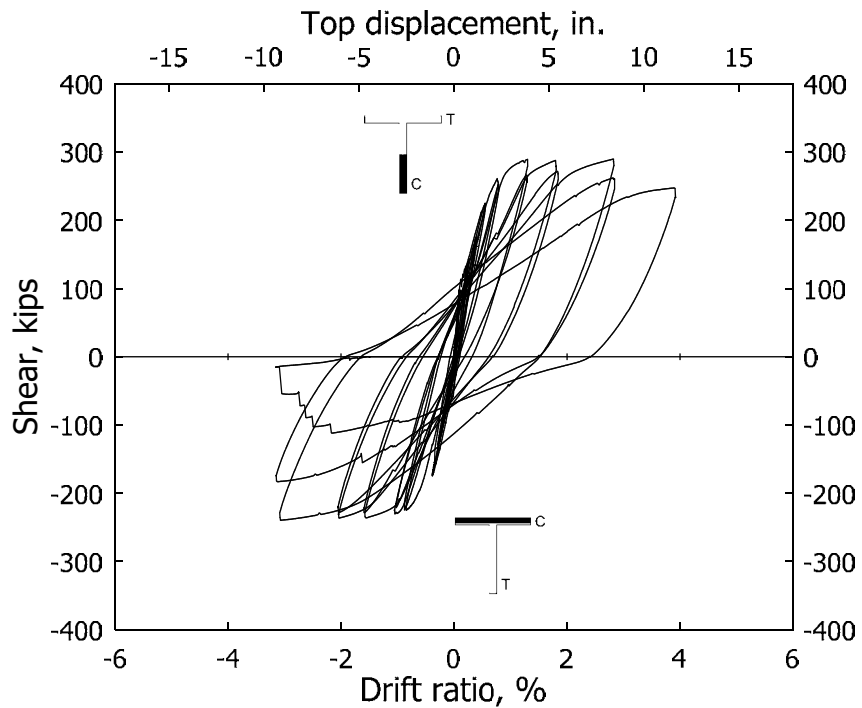


Figure 23 – Shear versus drift ratio for T6 (1 in. = 25.4 mm, 1 kip = 4.45 kN)

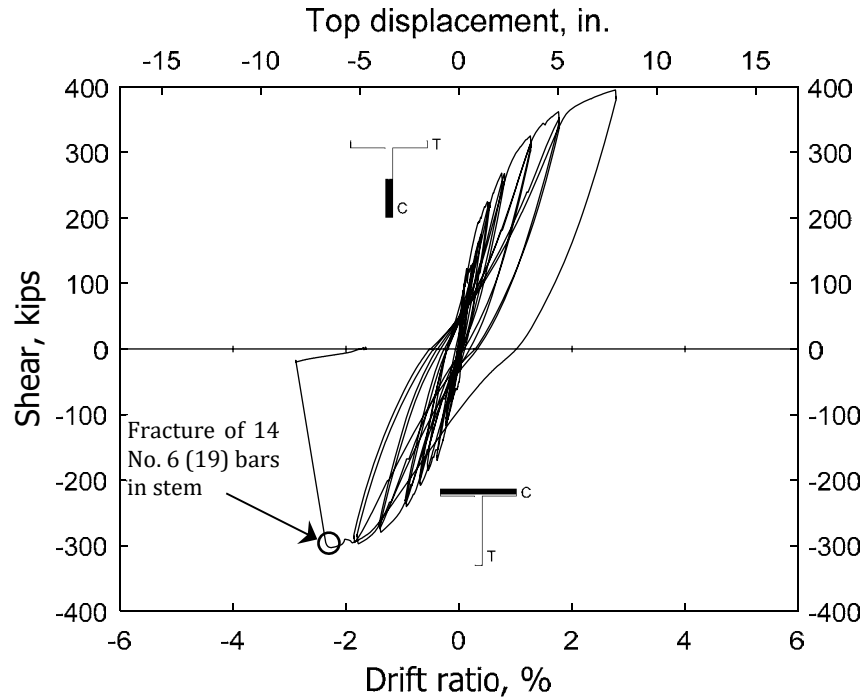


Figure 24 – Shear versus drift ratio for T5 indicating fracture of longitudinal bars (1 in. = 25.4 mm, 1 kip = 4.45 kN)

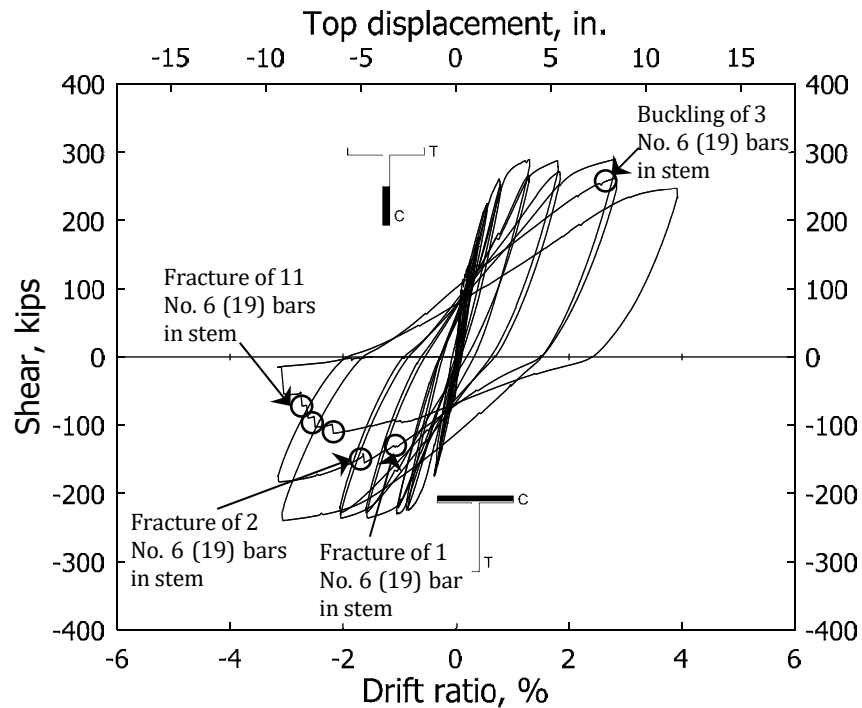


Figure 25 – Shear versus drift ratio for T6 indicating fracture of longitudinal bars (1 in. = 25.4 mm, 1 kip = 4.45 kN)

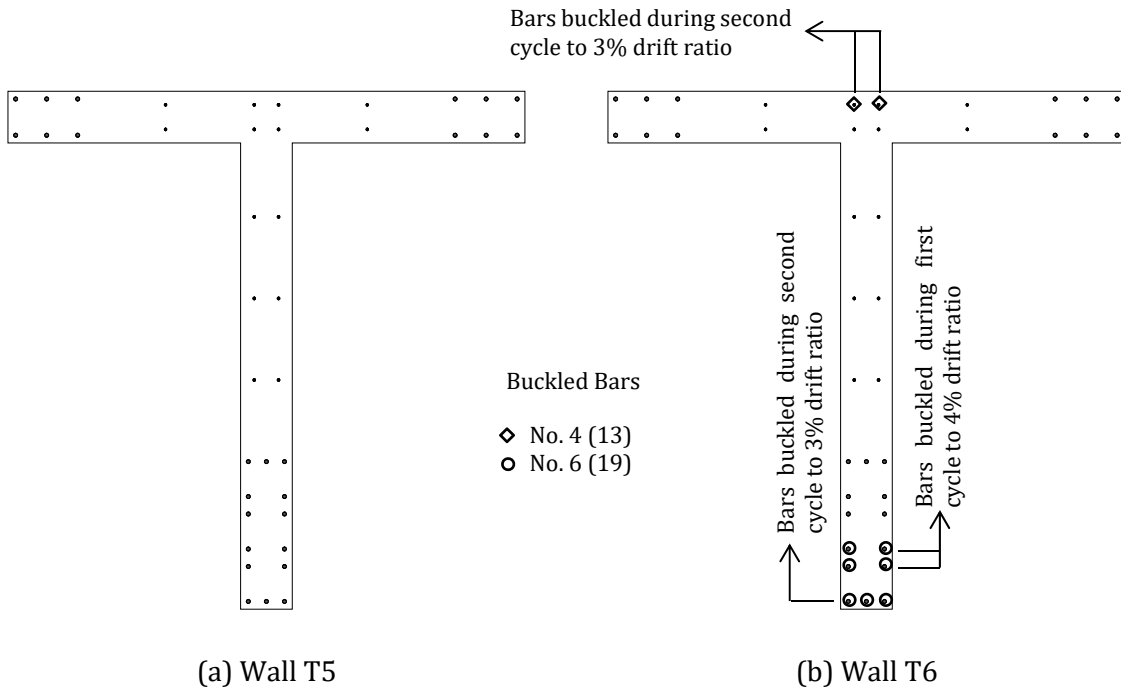


Figure 26 – Map of buckled bars

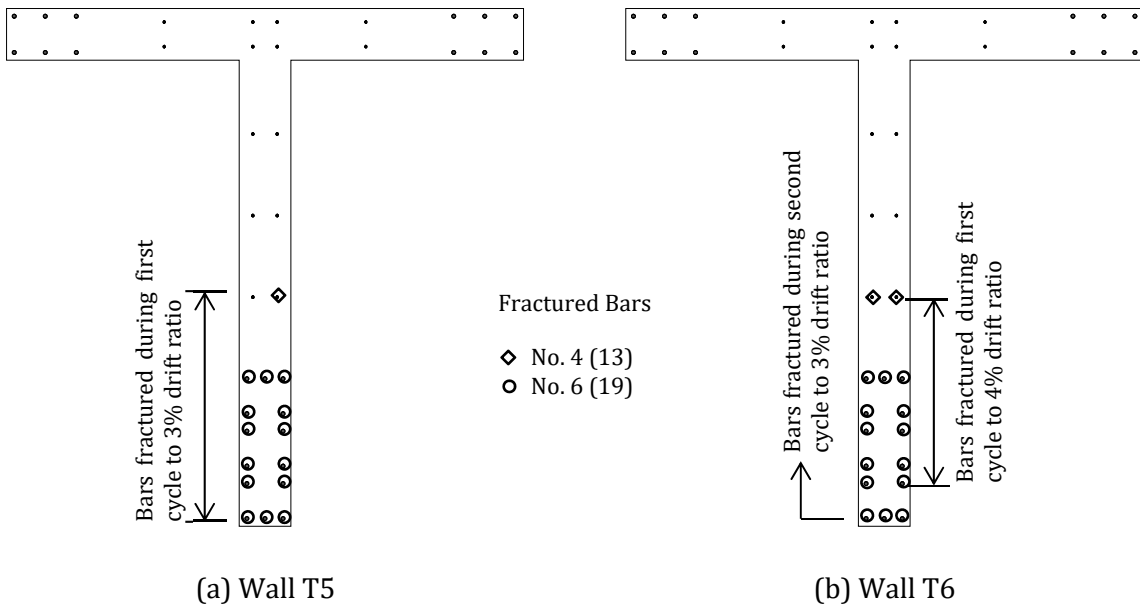


Figure 27 – Map of fractured bars

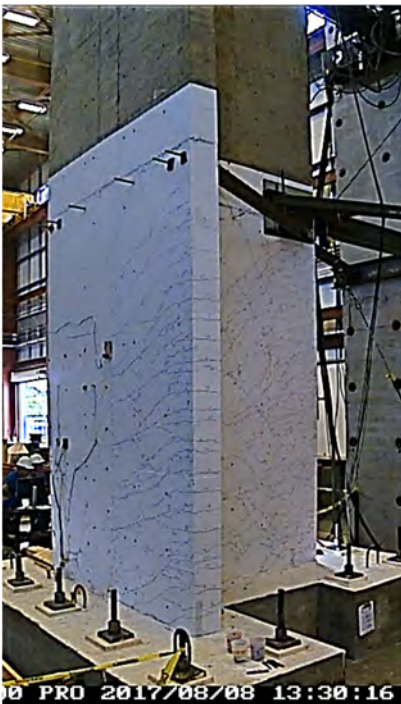


(a) Stem in compression



(b) Stem in tension

Figure 28 – Wall T5 at 1% drift ratio (second cycle)



(a) Stem in compression



(b) Stem in tension

Figure 29 – Wall T6 at 1% drift ratio (second cycle)



(a) Stem in compression

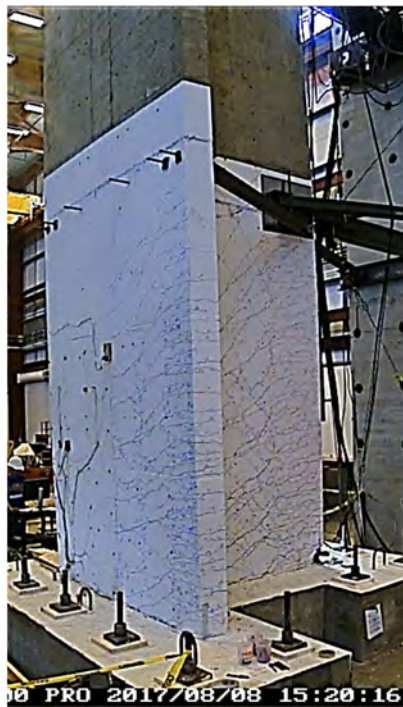


(b) Stem in tension

Figure 30 – Wall T5 at 2% drift ratio (second cycle)



(a) Stem in compression

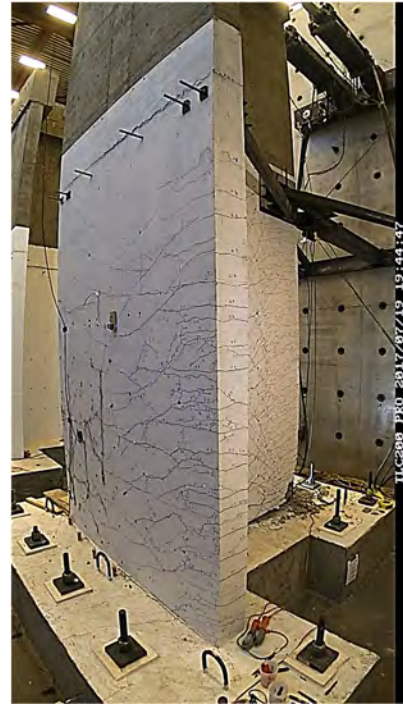


(b) Stem in tension

Figure 31 – Wall T6 at 2% drift ratio (second cycle)



(a) Stem in compression



(b) Stem in tension

Figure 32 – Wall T5 at 3% drift ratio (first cycle)

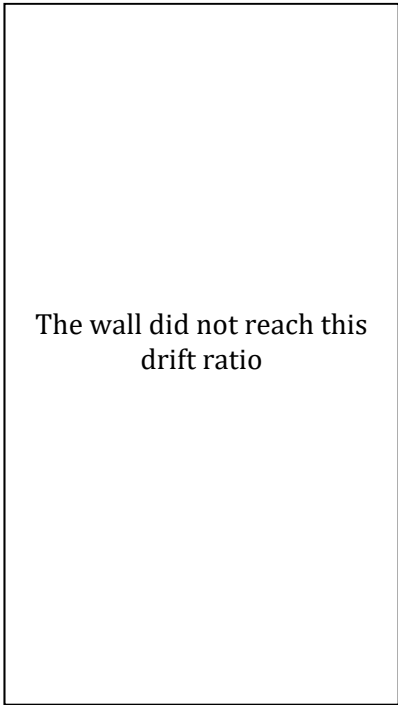


(a) Stem in compression

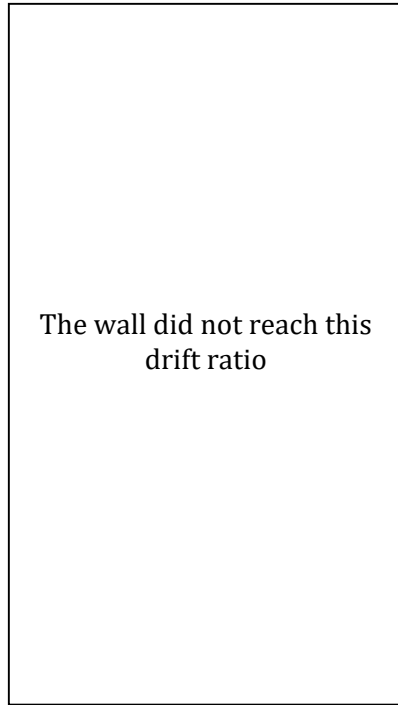


(b) Stem in tension

Figure 33 – Wall T6 at 3% drift ratio (second cycle)

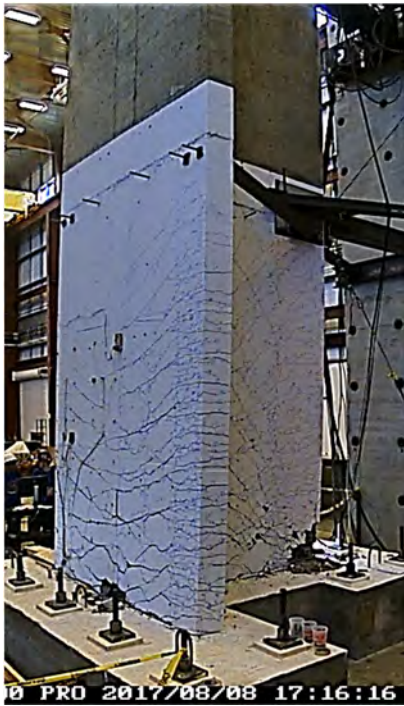


(a) Stem in compression



(b) Stem in tension

Figure 34 – Wall T5 at 4% drift ratio (first cycle)



(a) Stem in compression



(b) Stem in tension

Figure 35 – Wall T6 at 4% drift ratio (first cycle)

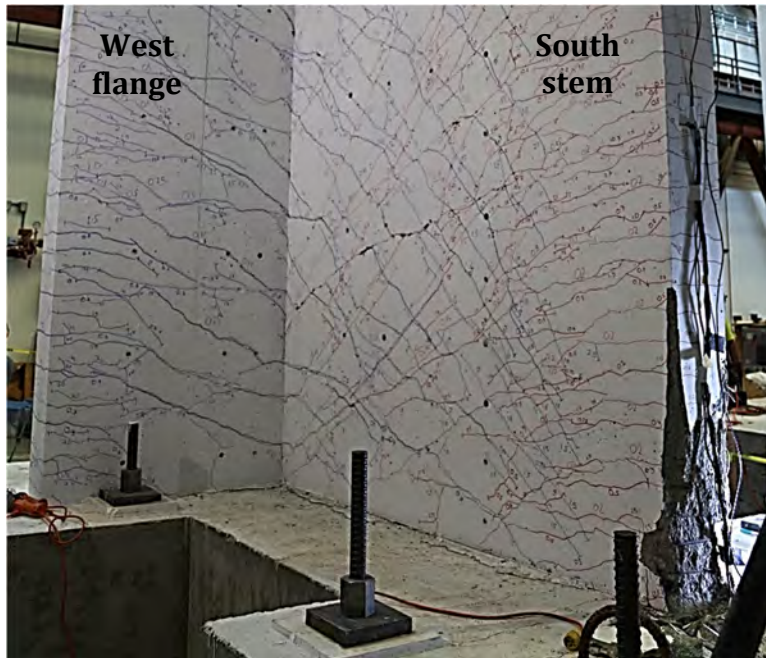


Figure 36 – Wall T5 without buckled bars in confined and unconfined stem during second cycle to 2% drift ratio (stem in compression)

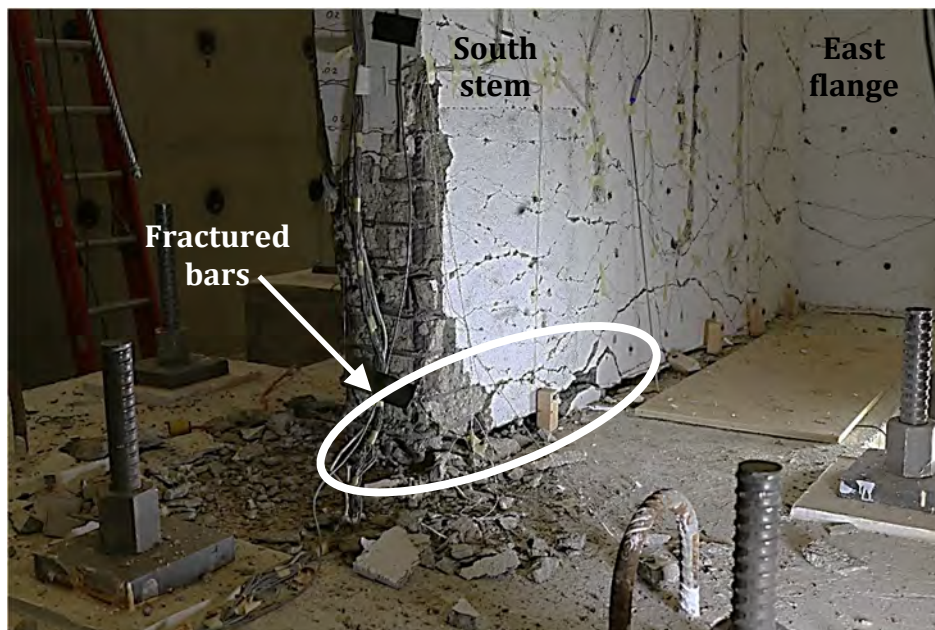


Figure 37 – Wall T5 with fractured bars in confined and unconfined stem during first cycle to 3% drift ratio (stem in tension)

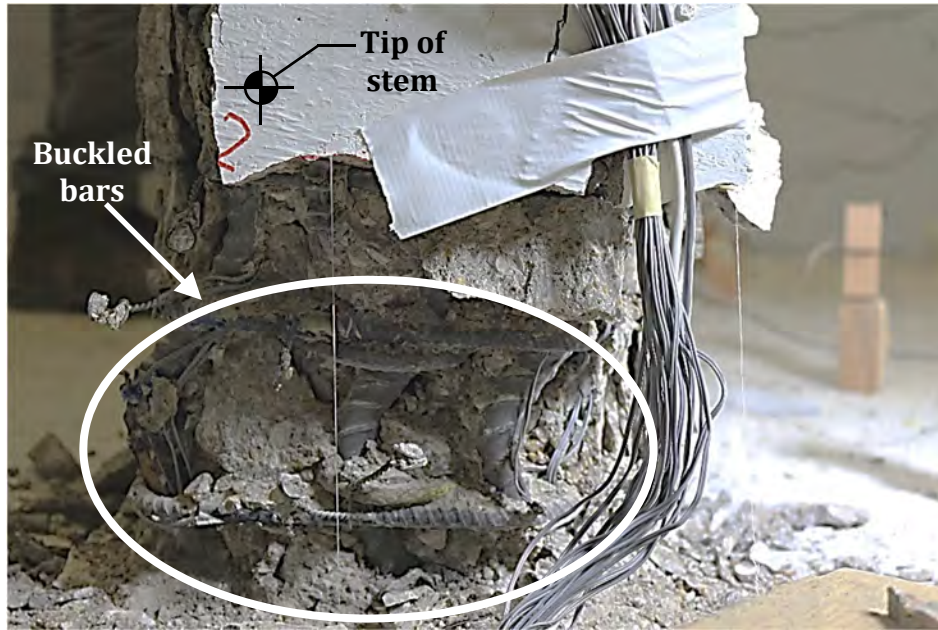


Figure 38 – Wall T6 with buckled bars in confined stem during second cycle to 3% drift ratio (stem in compression)

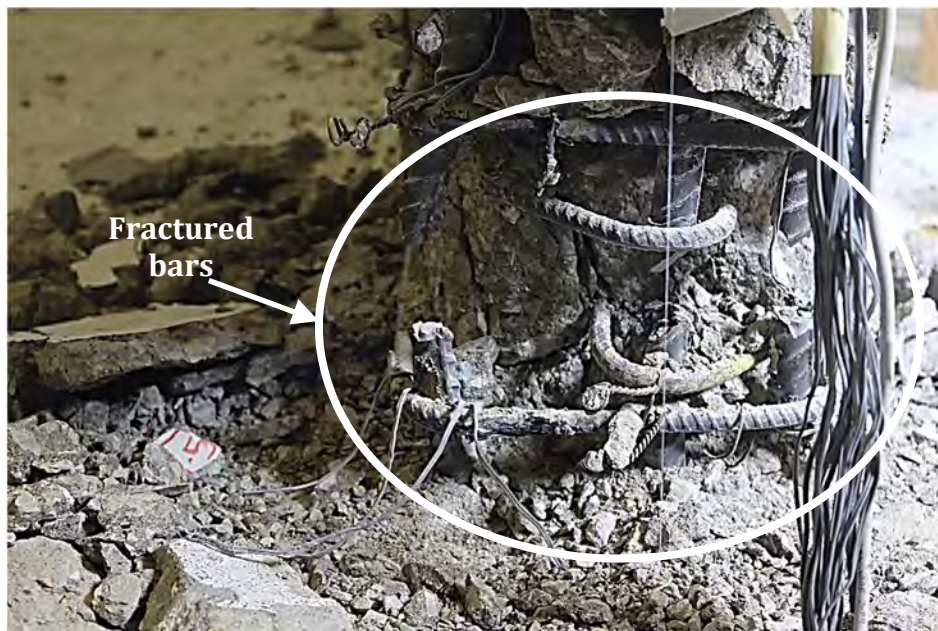


Figure 39 – Wall T6 with fractured bars in confined stem during second cycle to 3% drift ratio (stem in tension)

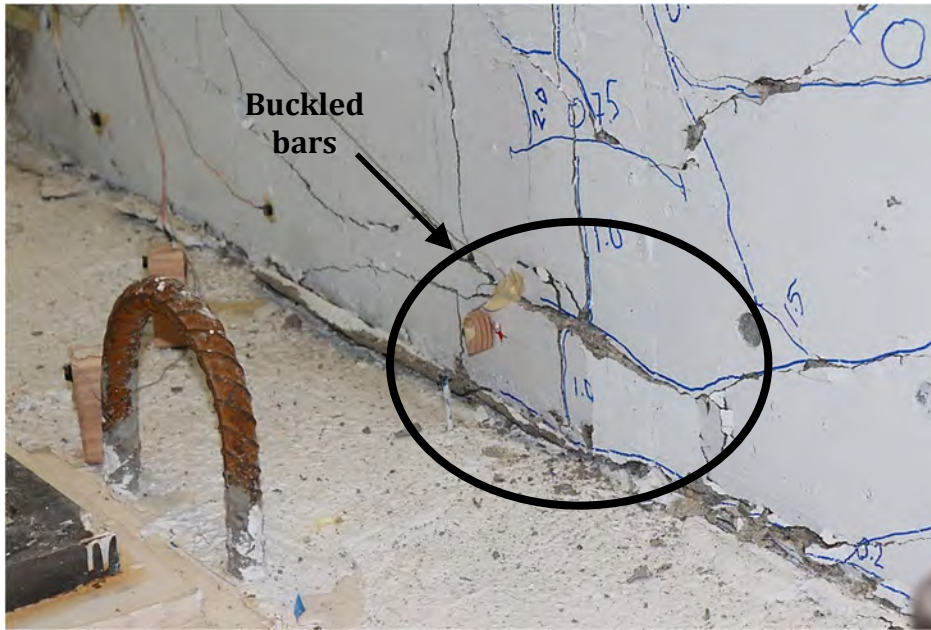


Figure 40 - Wall T6 with buckled bars in unconfined flange during second cycle to 3% drift ratio (stem in tension)

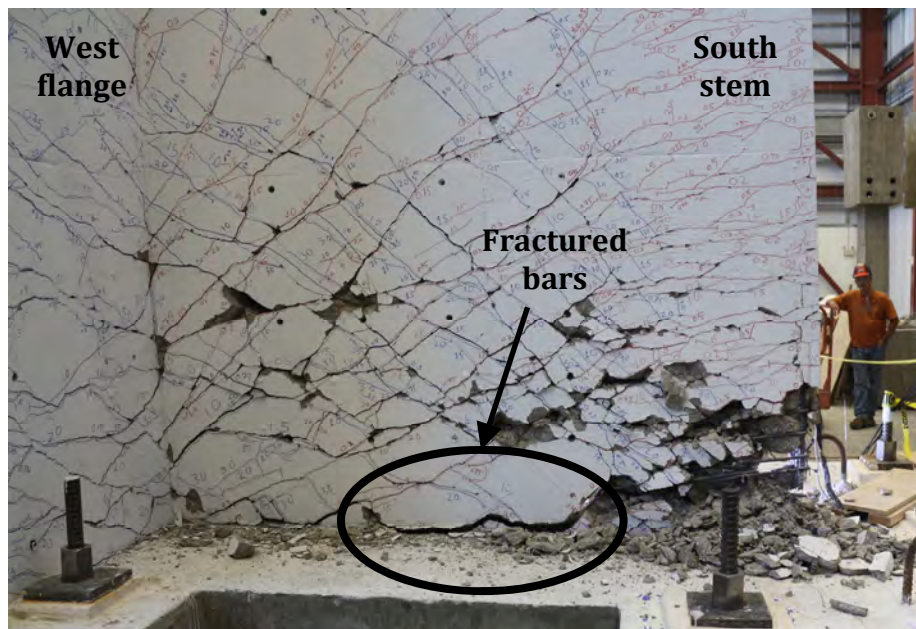
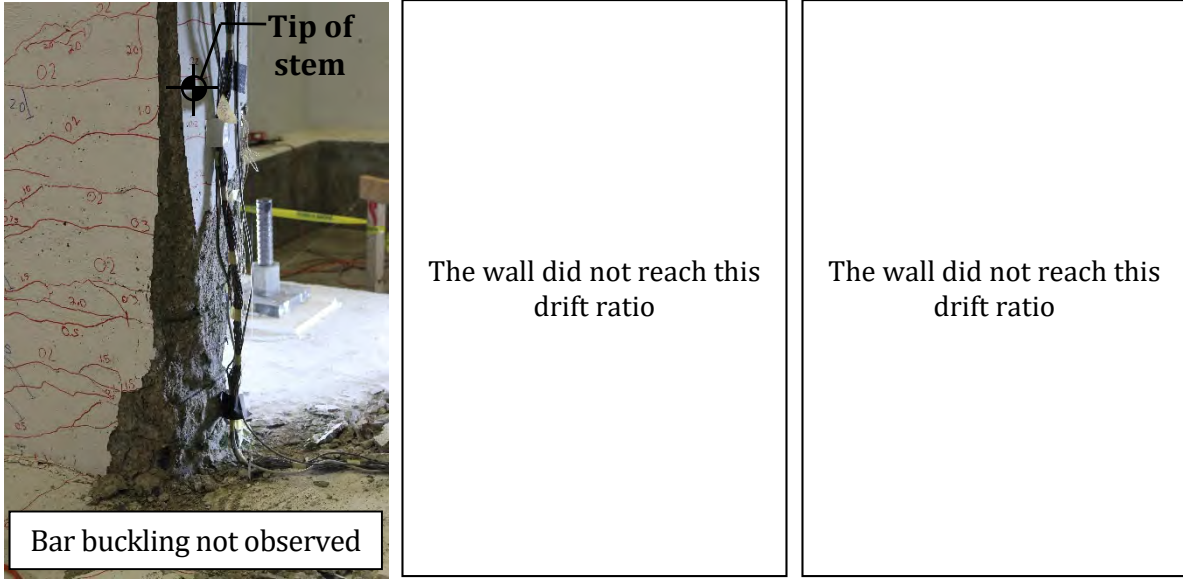
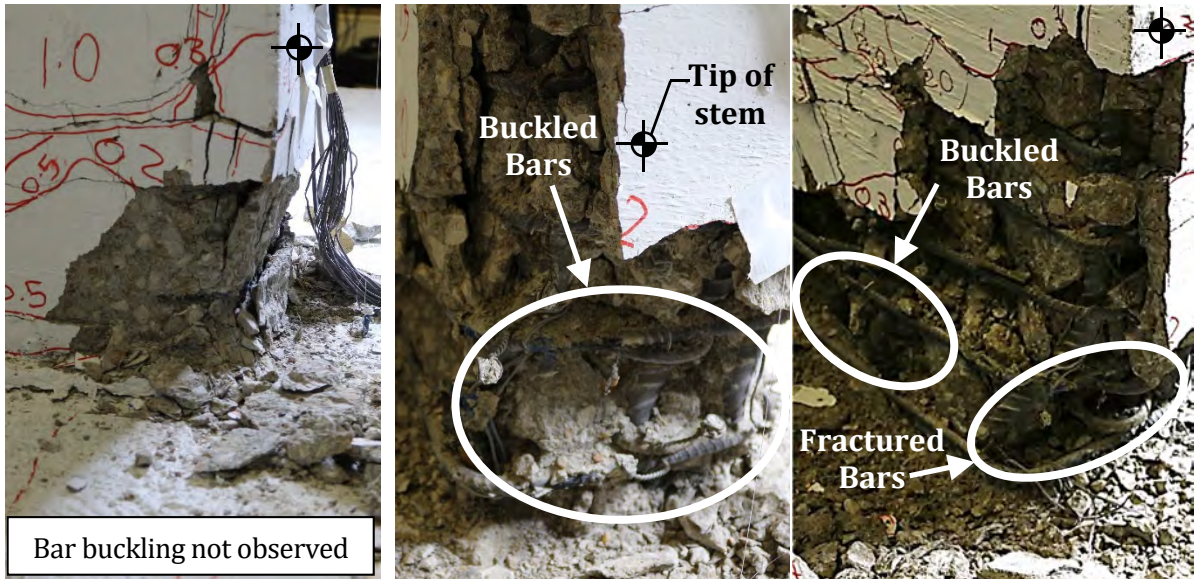


Figure 41 - Wall T6 with fractured bars in unconfined stem during first cycle to 4% drift ratio (stem in tension)



(a) First cycle to 3% drift (b) Second cycle to 3% drift (c) First cycle to 4% drift

Figure 42 – Condition of confined stem in compression leading to bar fracture in T5

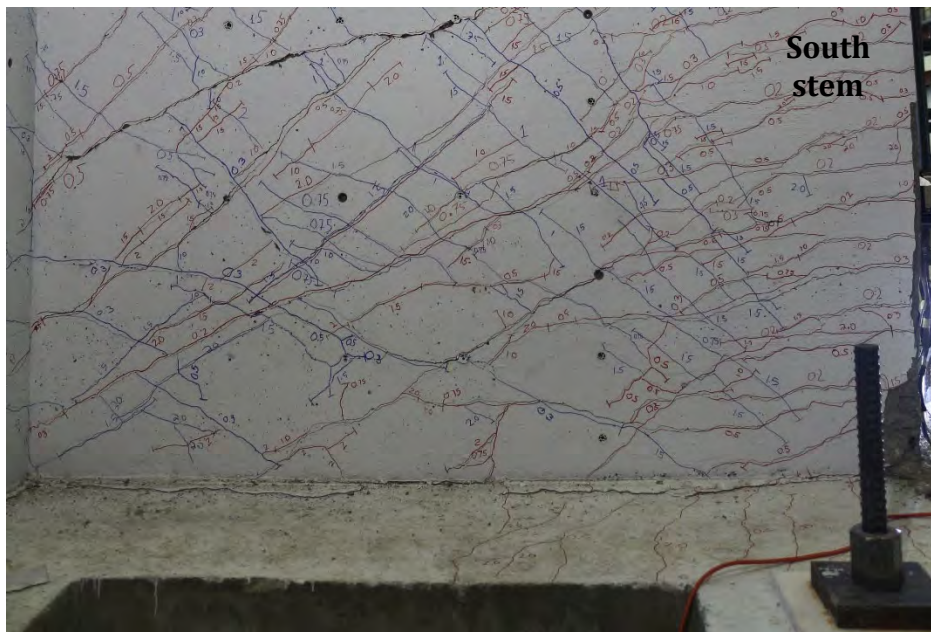


(a) First cycle to 3% drift (b) Second cycle to 3% drift (c) First cycle to 4% drift

Figure 43 – Condition of confined stem in compression leading to bar buckling before bar fracture in T6

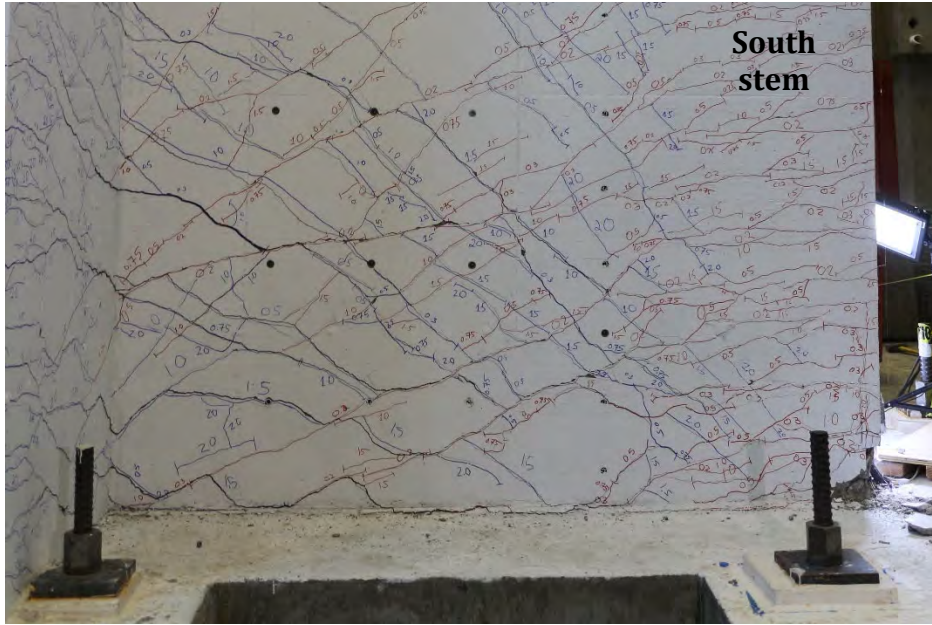


(a) Stem in compression

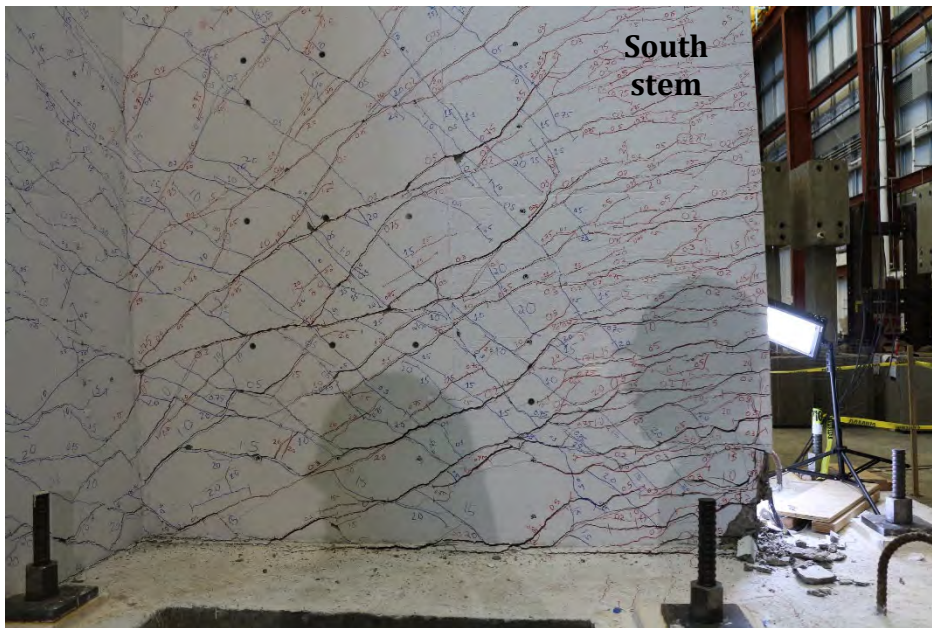


(b) Stem in tension

Figure 44 – Condition of stem in T5 at peak of second cycle to 2% drift ratio

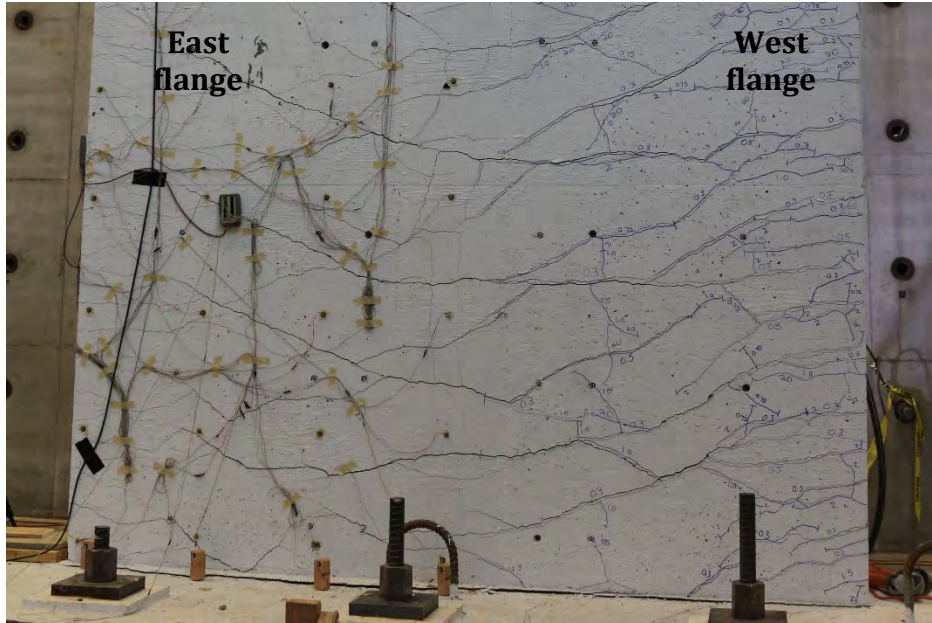


(a) Stem in compression

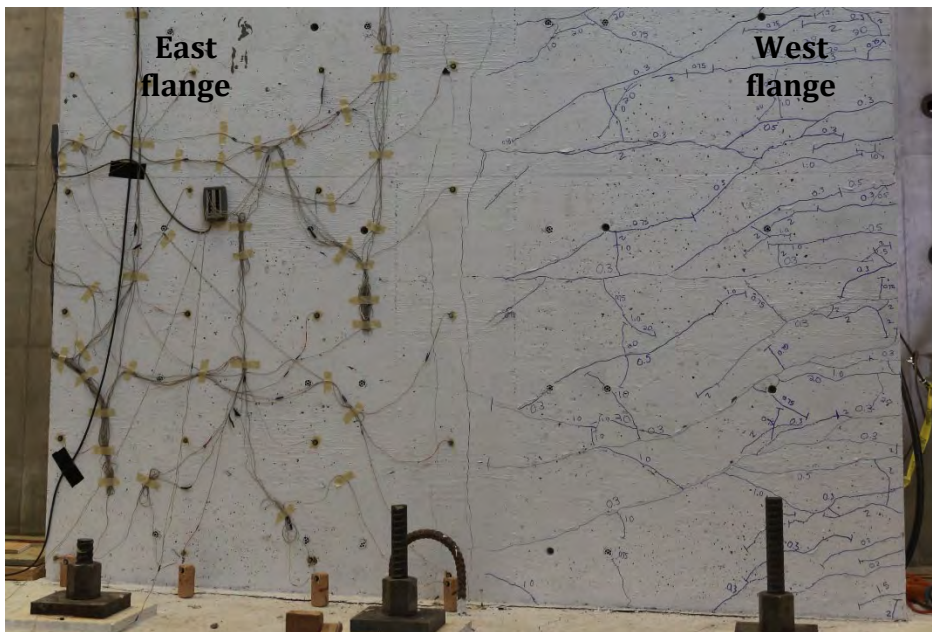


(b) Stem in tension

Figure 45 – Condition of stem in T6 at peak of second cycle to 2% drift ratio

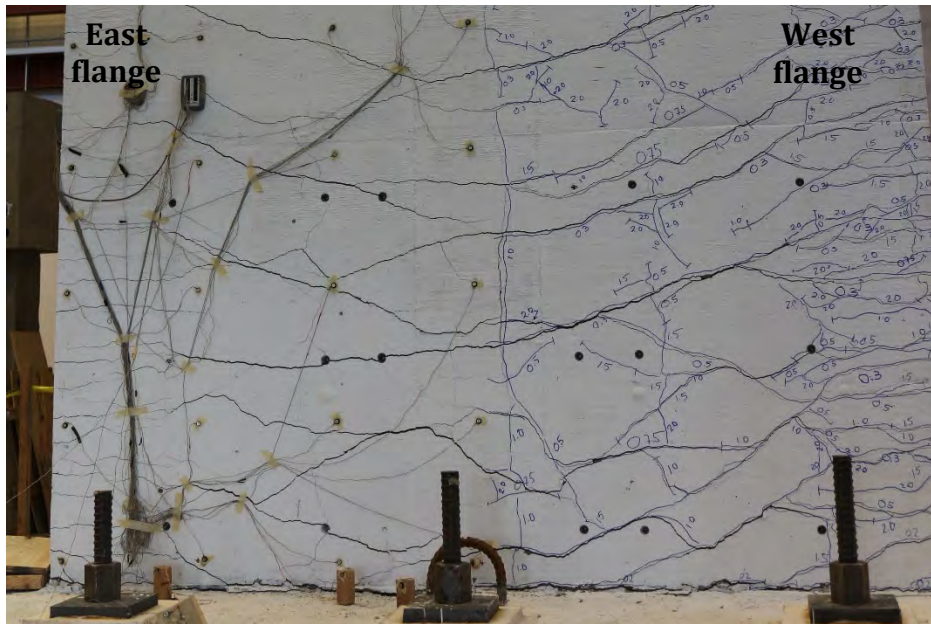


(a) Stem in compression



(b) Stem in tension

Figure 46 – Condition of flange in T5 at peak of second cycle to 2% drift ratio



(a) Stem in compression



(b) Stem in tension

Figure 47 – Condition of flange in T6 at peak of second cycle to 2% drift ratio

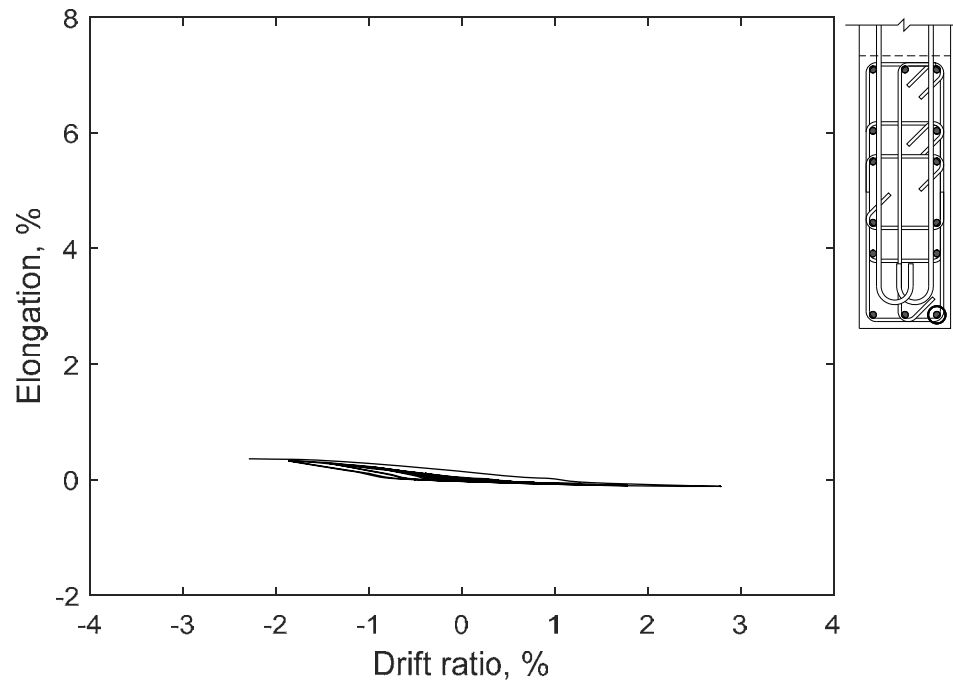


Figure 48 – Measured strain in longitudinal bar at confined stem 18 in. (457 mm) below base of T5

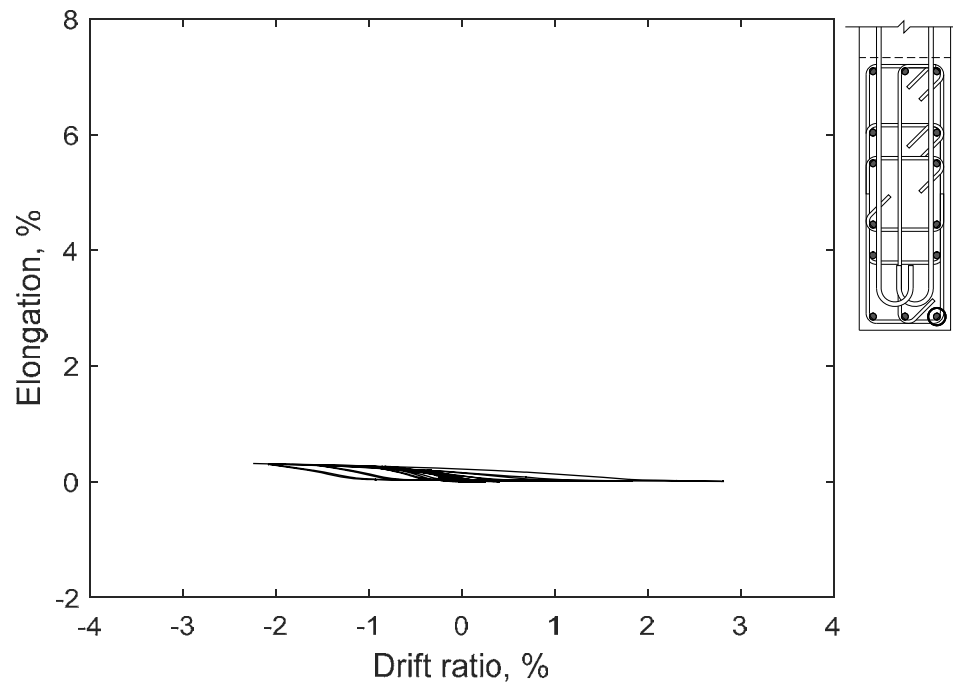


Figure 49 – Measured strain in longitudinal bar at confined stem 18 in. (457 mm) below base of T6

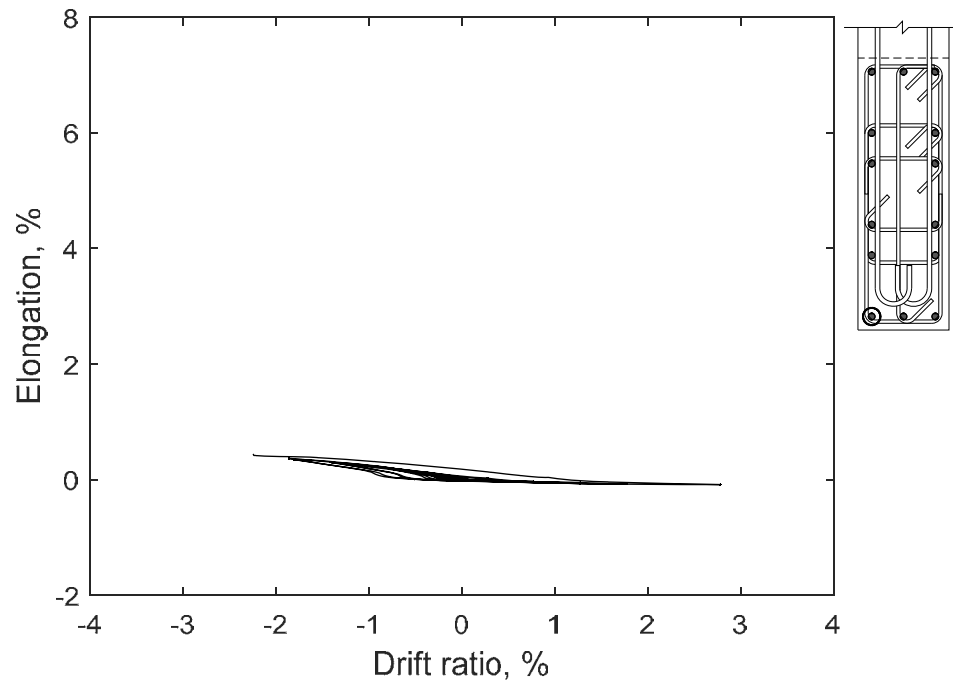


Figure 50 – Measured strain in longitudinal bar at confined stem 18 in. (457 mm) below base of T5

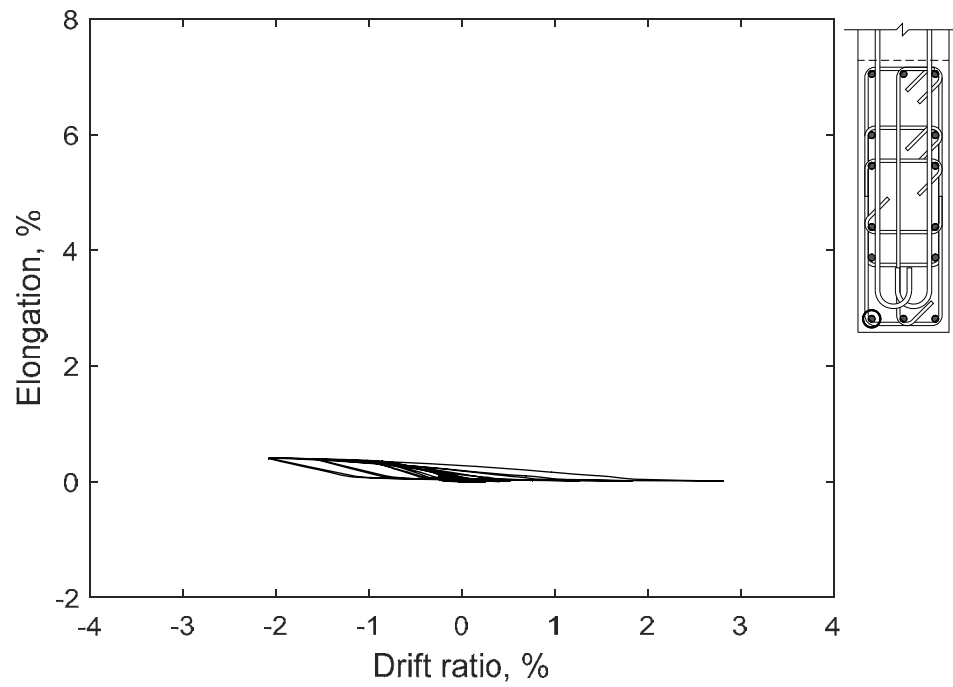


Figure 51 – Measured strain in longitudinal bar at confined stem 18 in. (457 mm) below base of T6

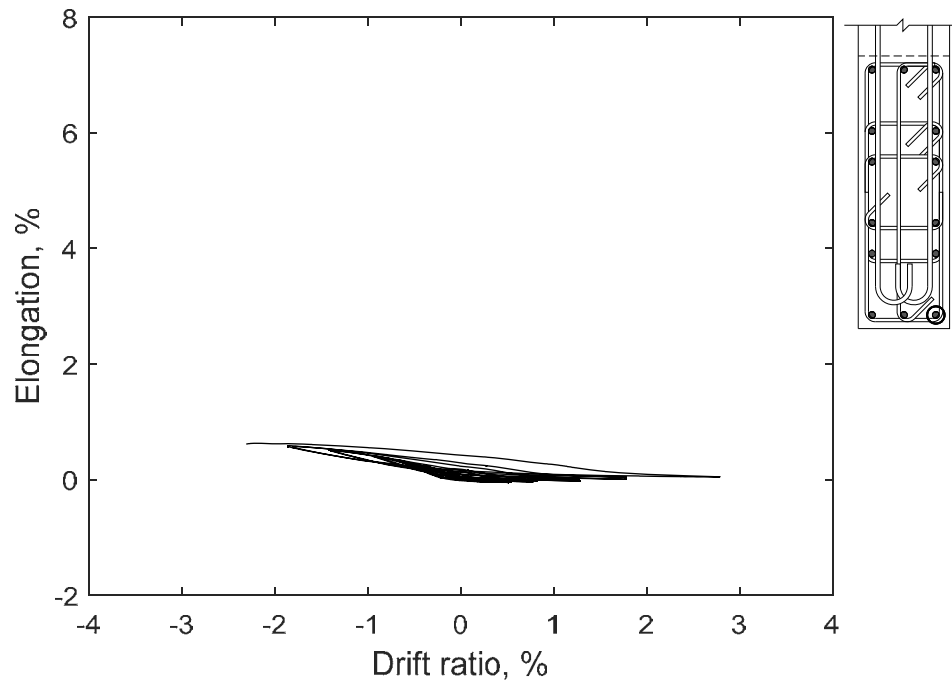


Figure 52 - Measured strain in longitudinal bar at confined stem 9 in. (229 mm) below base of T5

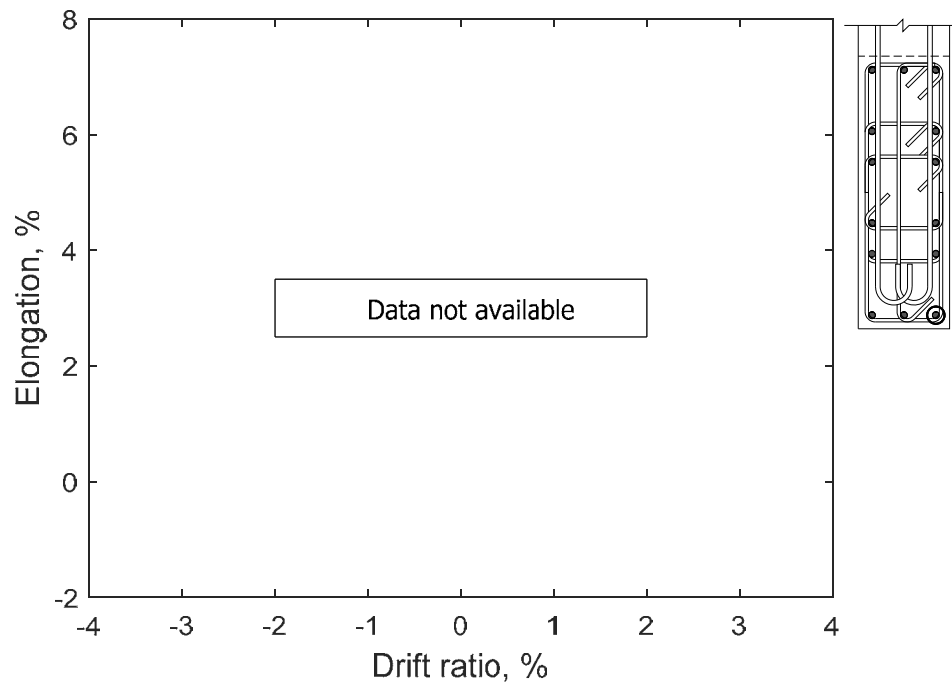


Figure 53 - Measured strain in longitudinal bar at confined stem 9 in. (229 mm) below base of T6

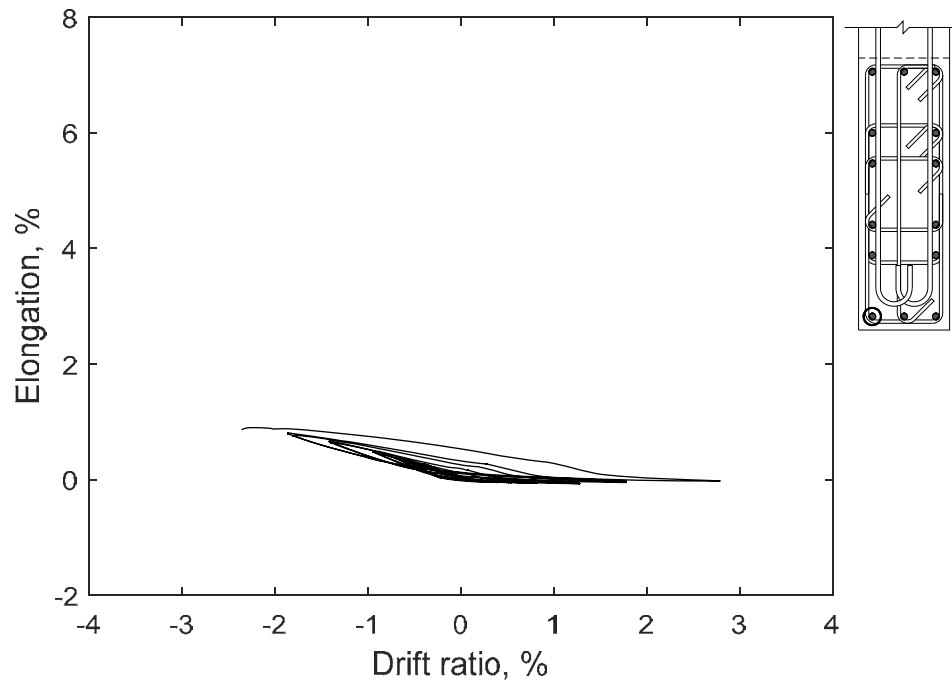


Figure 54 - Measured strain in longitudinal bar at confined stem 9 in. (229 mm) below base of T5

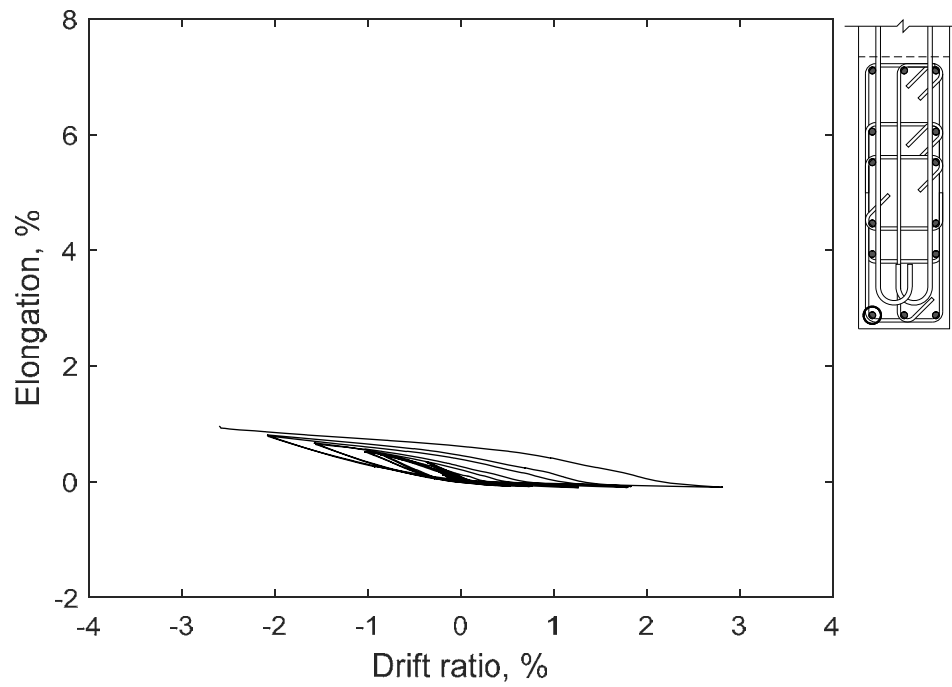


Figure 55 - Measured strain in longitudinal bar at confined stem 9 in. (229 mm) below base of T6

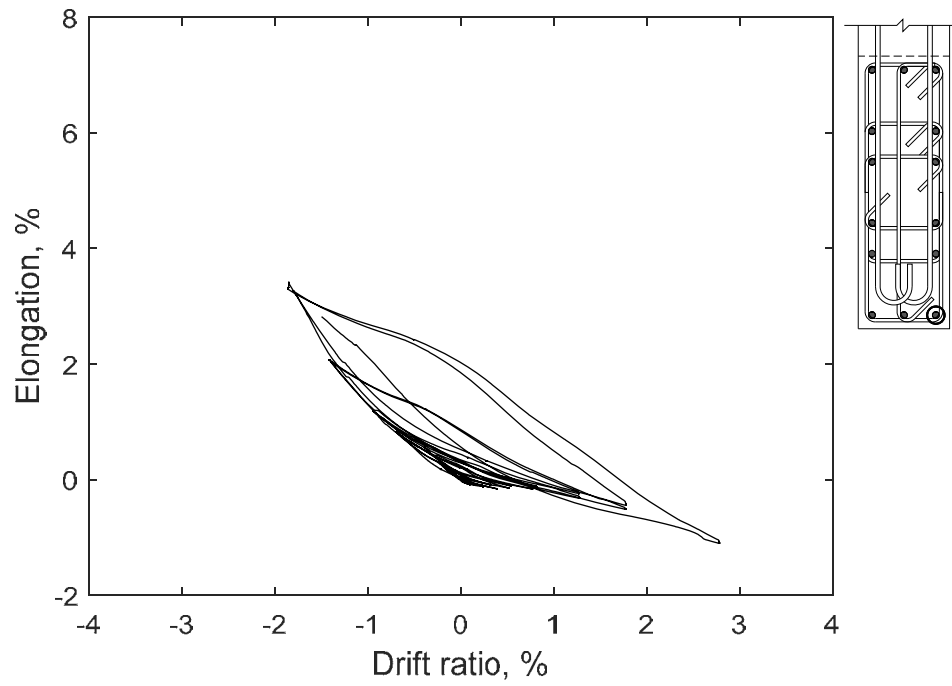


Figure 56 – Measured strain in longitudinal bar at confined stem 0.5 in. (13 mm) above base of T5

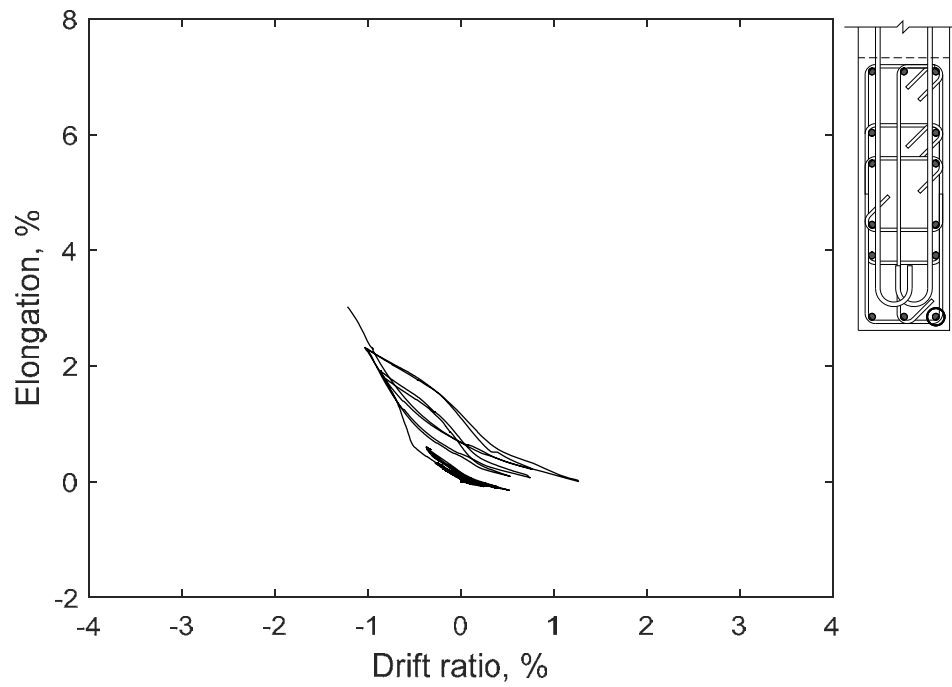


Figure 57 – Measured strain in longitudinal bar at confined stem 0.5 in. (13 mm) above base of T6

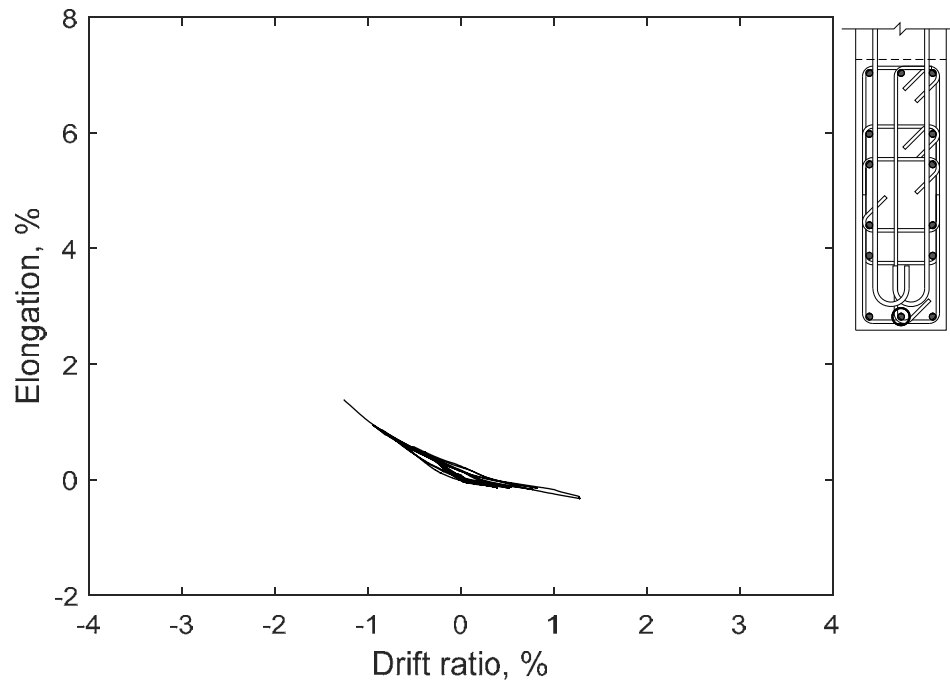


Figure 58 – Measured strain in longitudinal bar at confined stem 0.5 in. (13 mm) above base of T5

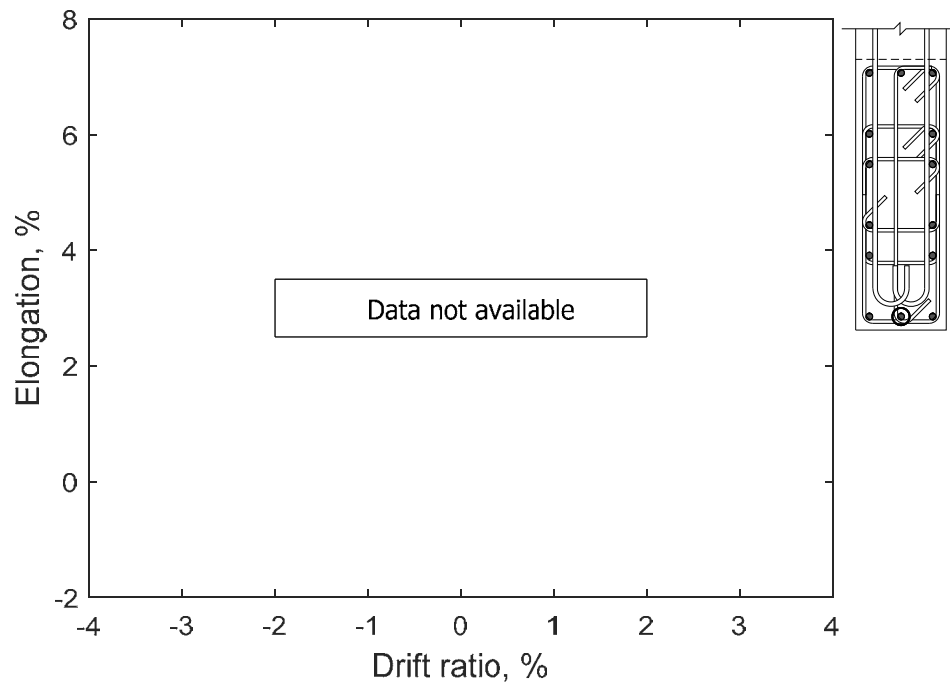


Figure 59 – Measured strain in longitudinal bar at confined stem 0.5 in. (13 mm) above base of T6

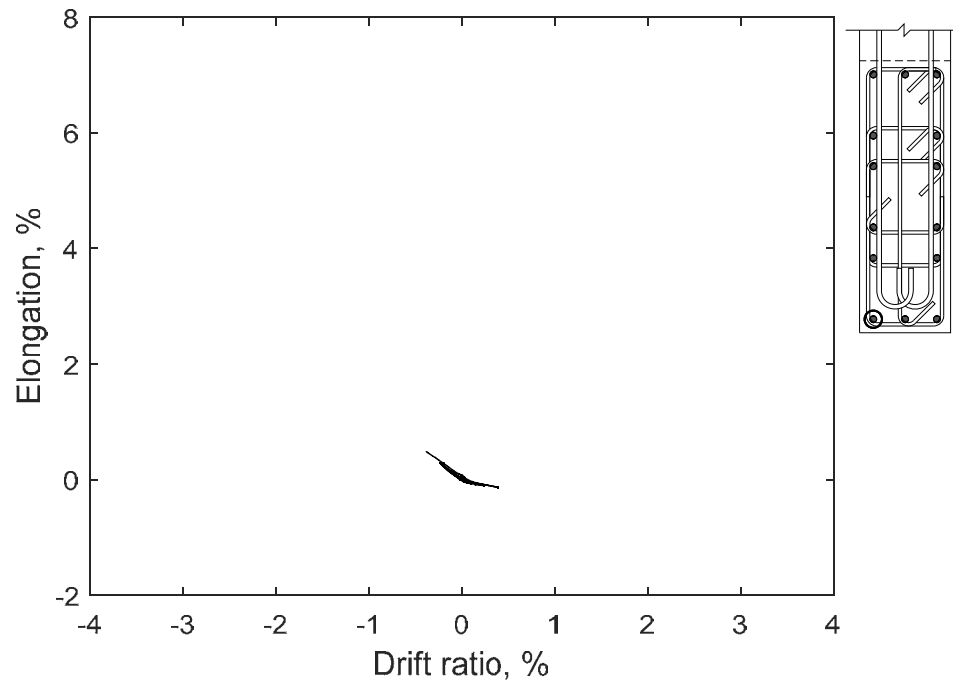


Figure 60 – Measured strain in longitudinal bar at confined stem 0.5 in. (13 mm) above base of T5

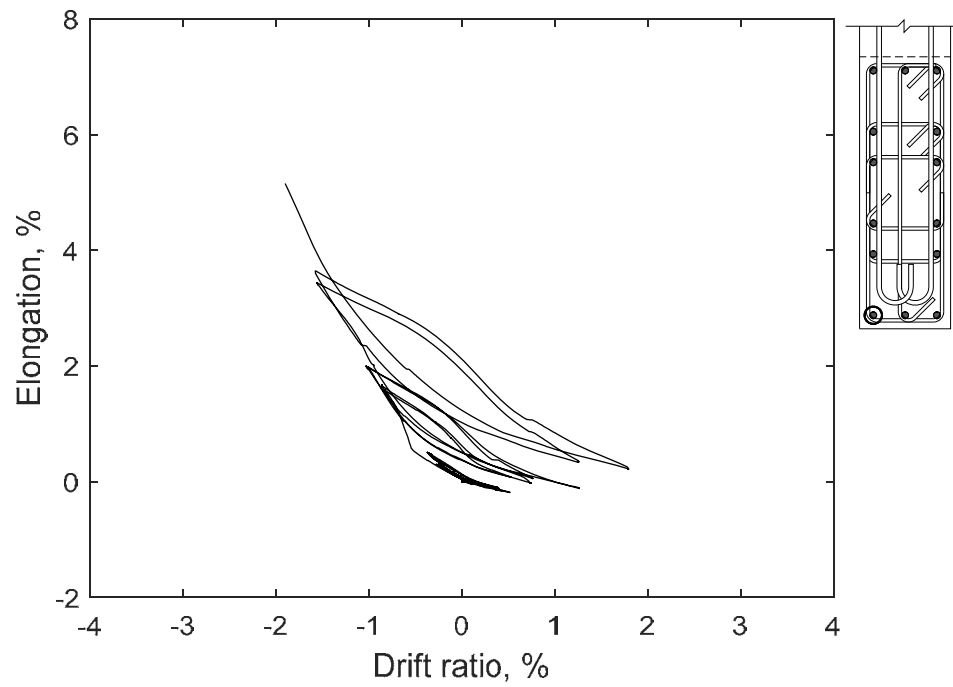


Figure 61 – Measured strain in longitudinal bar at confined stem 0.5 in. (13 mm) above base of T6

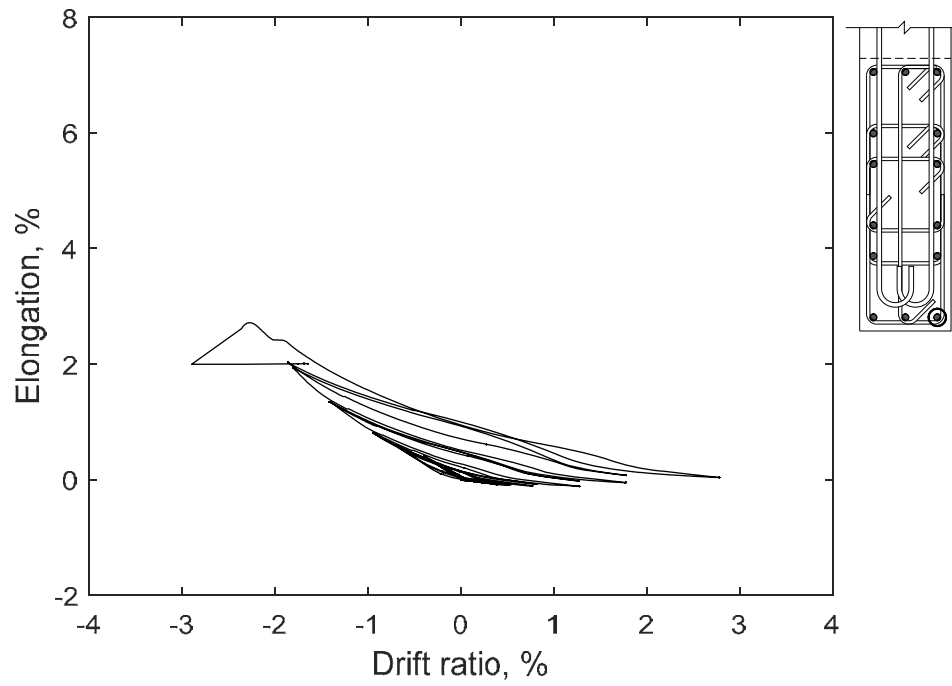


Figure 62 – Measured strain in longitudinal bar at confined stem 25 in. (635 mm) above base of T5

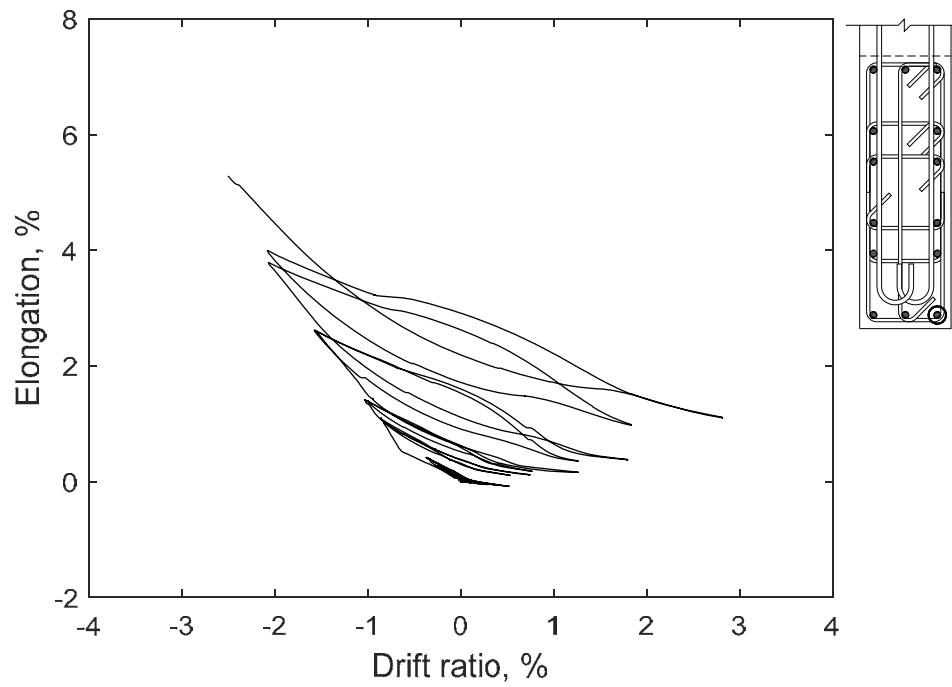


Figure 63 – Measured strain in longitudinal bar at confined stem 25 in. (635 mm) above base of T6

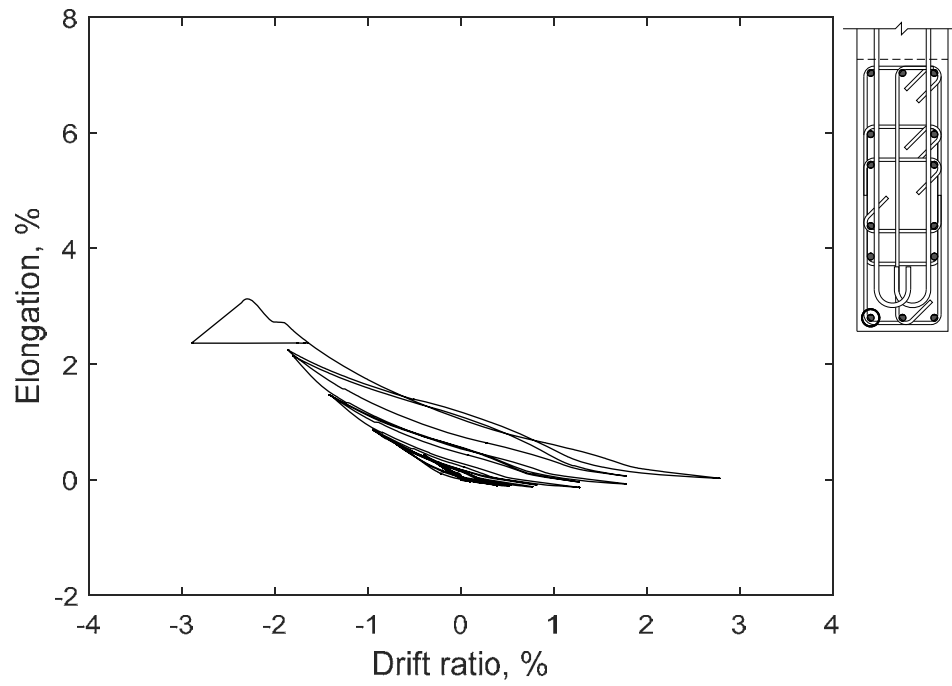


Figure 64 – Measured strain in longitudinal bar at confined stem 25 in. (635 mm) above base of T5

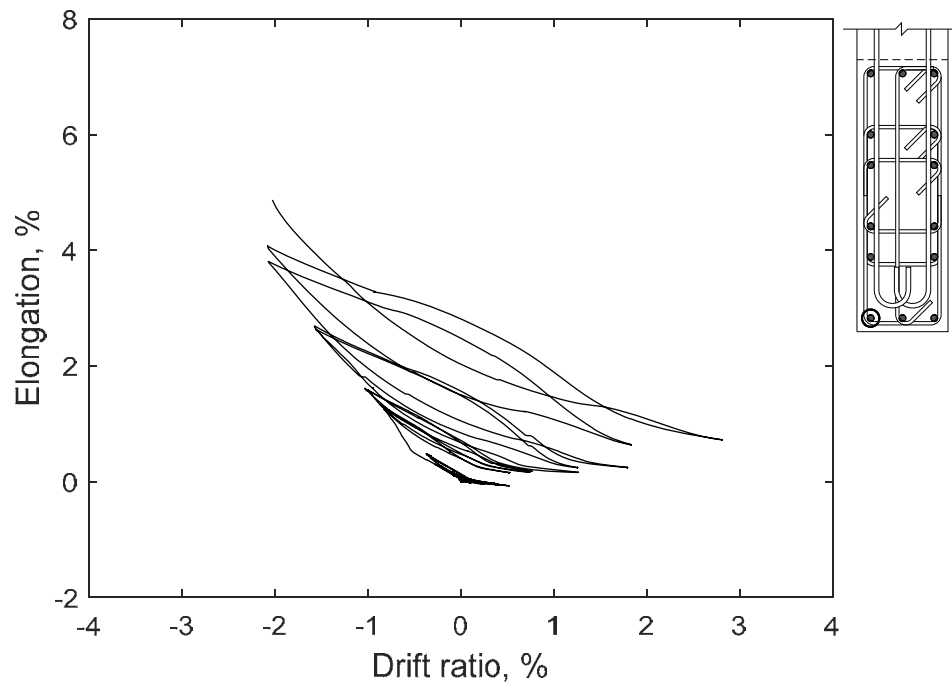


Figure 65 – Measured strain in longitudinal bar at confined stem 25 in. (635 mm) above base of T6

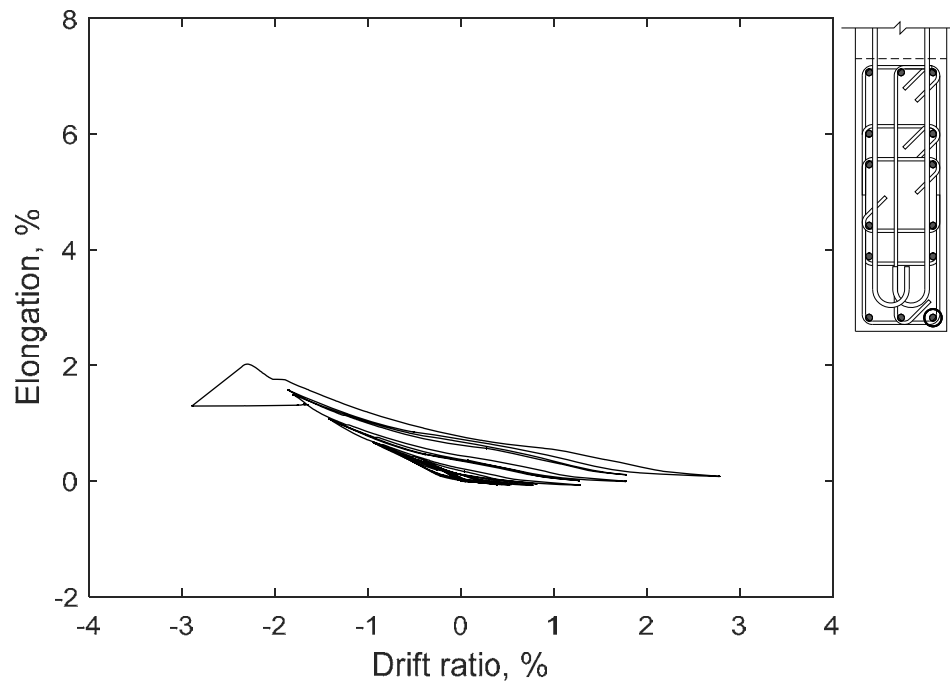


Figure 66 - Measured strain in longitudinal bar at confined stem 50 in. (1270 mm) above base of T5

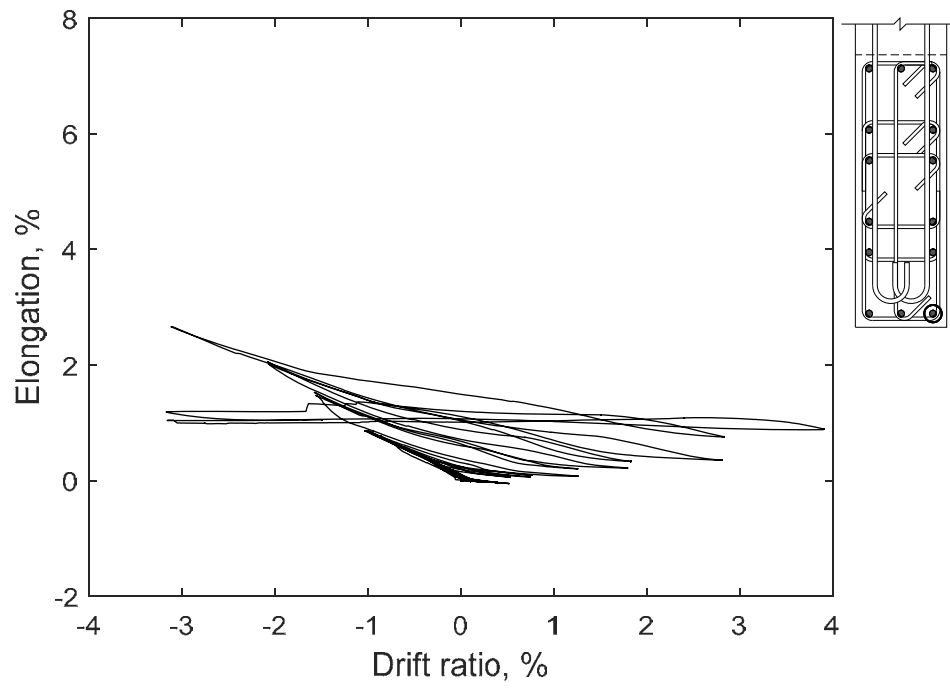


Figure 67 - Measured strain in longitudinal bar at confined stem 50 in. (1270 mm) above base of T6

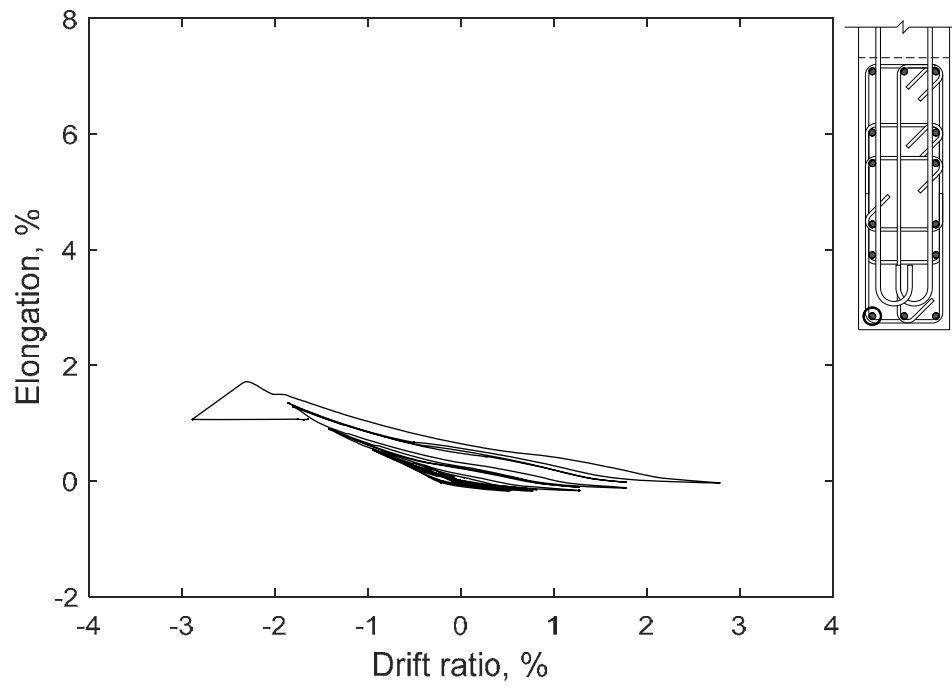


Figure 68 - Measured strain in longitudinal bar at confined stem 50 in. (1270 mm) above base of T5

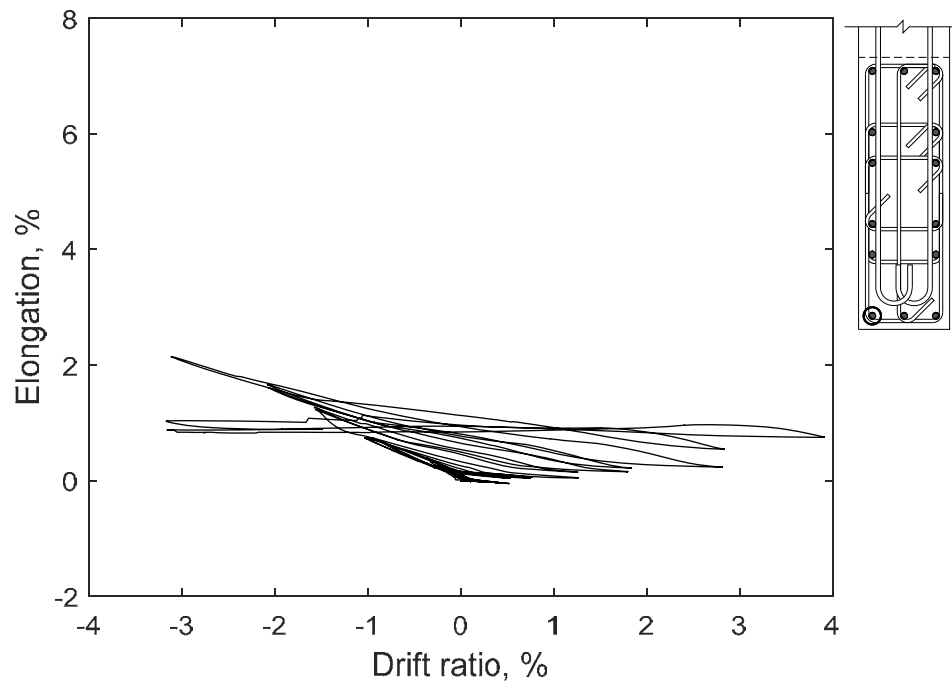


Figure 69 - Measured strain in longitudinal bar at confined stem 50 in. (1270 mm) above base of T6

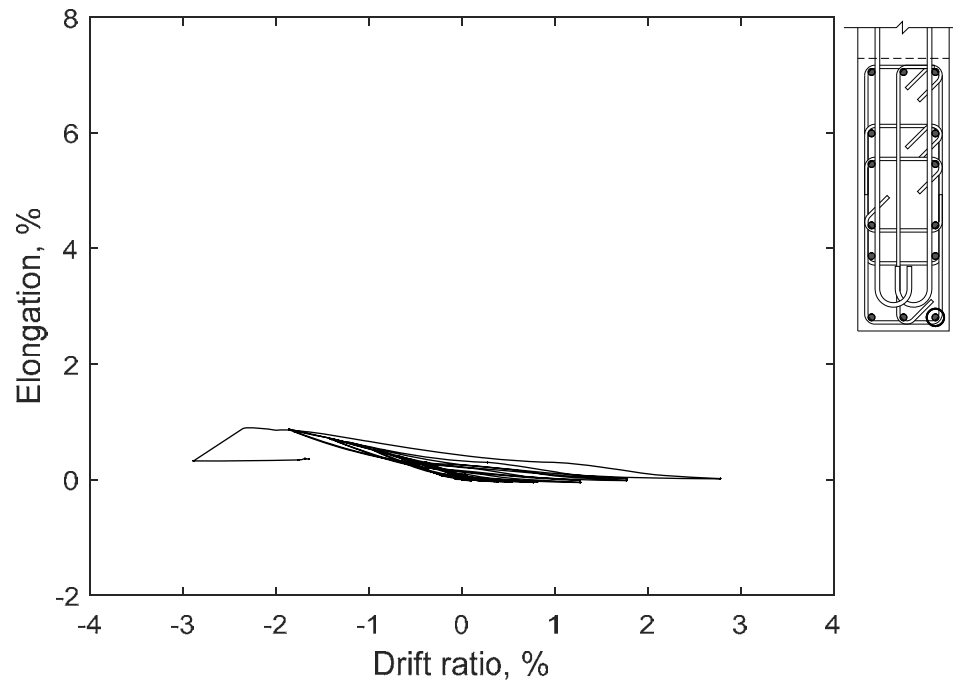


Figure 70 – Measured strain in longitudinal bar at confined stem 100 in. (2540 mm) above base of T5

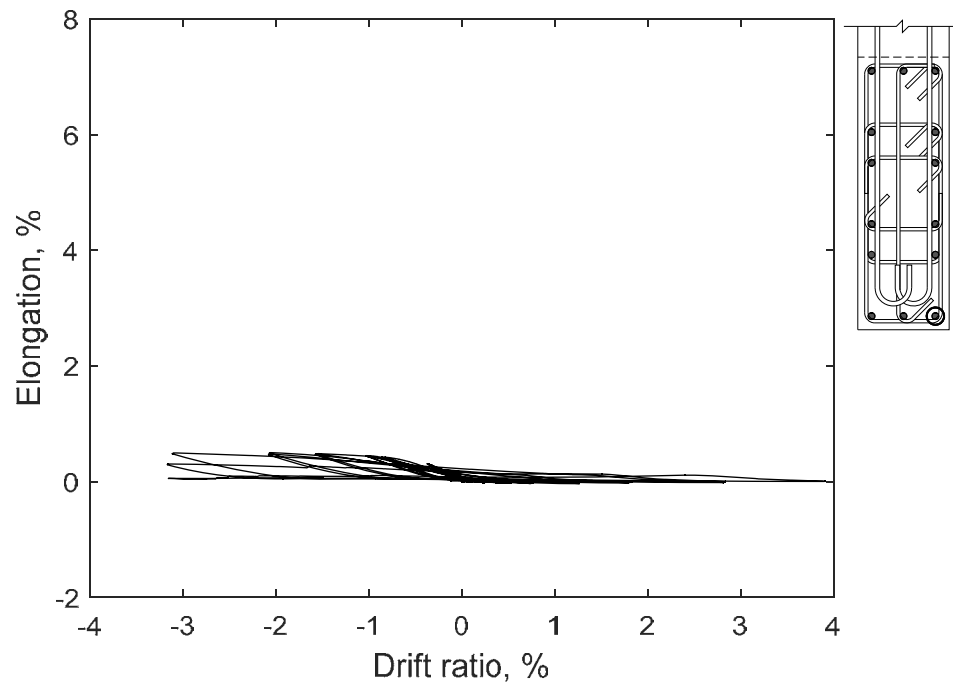


Figure 71 – Measured strain in longitudinal bar at confined stem 100 in. (2540 mm) above base of T6

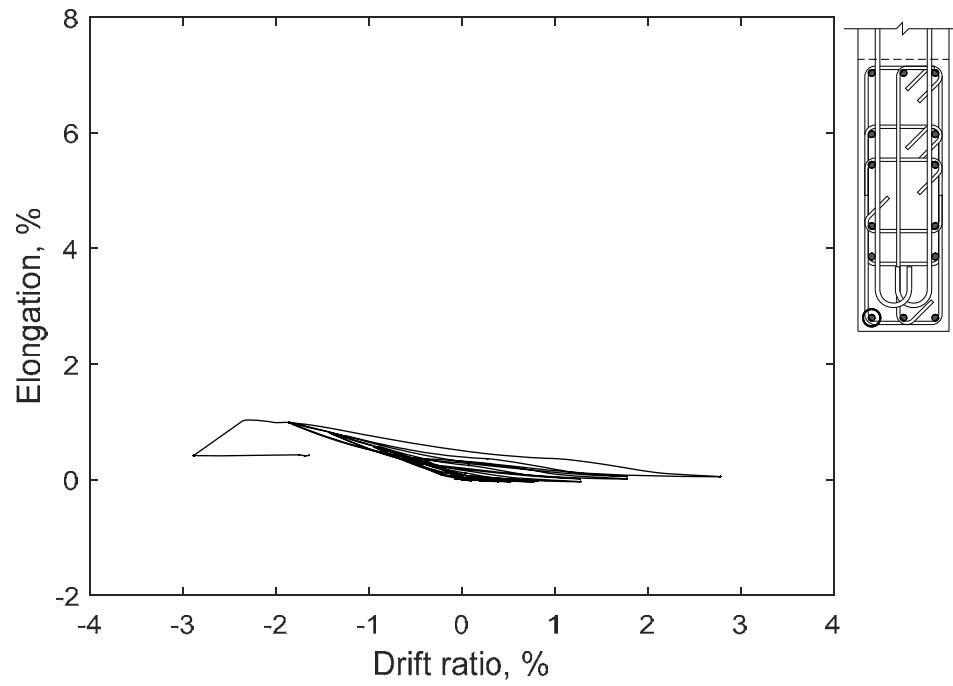


Figure 72 – Measured strain in longitudinal bar at confined stem 100 in. (2540 mm) above base of T5

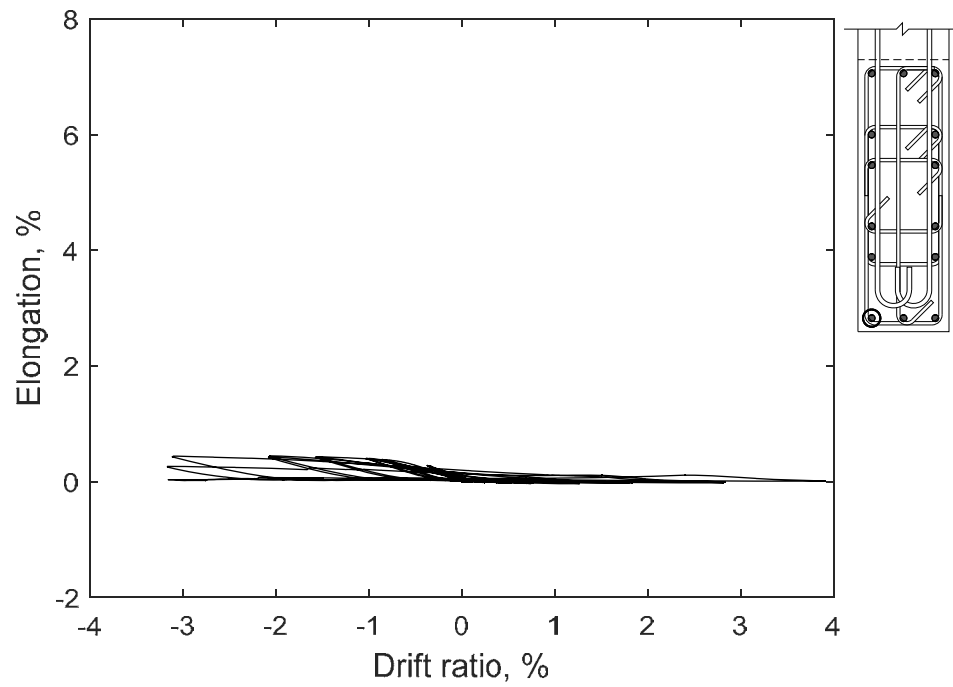


Figure 73 – Measured strain in longitudinal bar at confined stem 100 in. (2540 mm) above base of T6

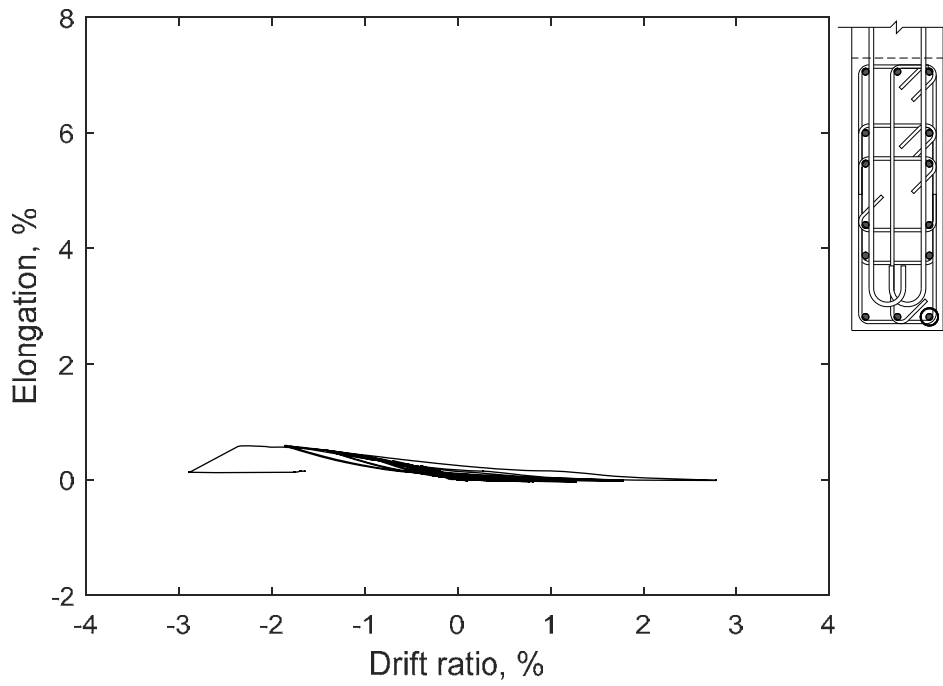


Figure 74 - Measured strain in longitudinal bar at confined stem 144 in. (3660 mm) above base of T5

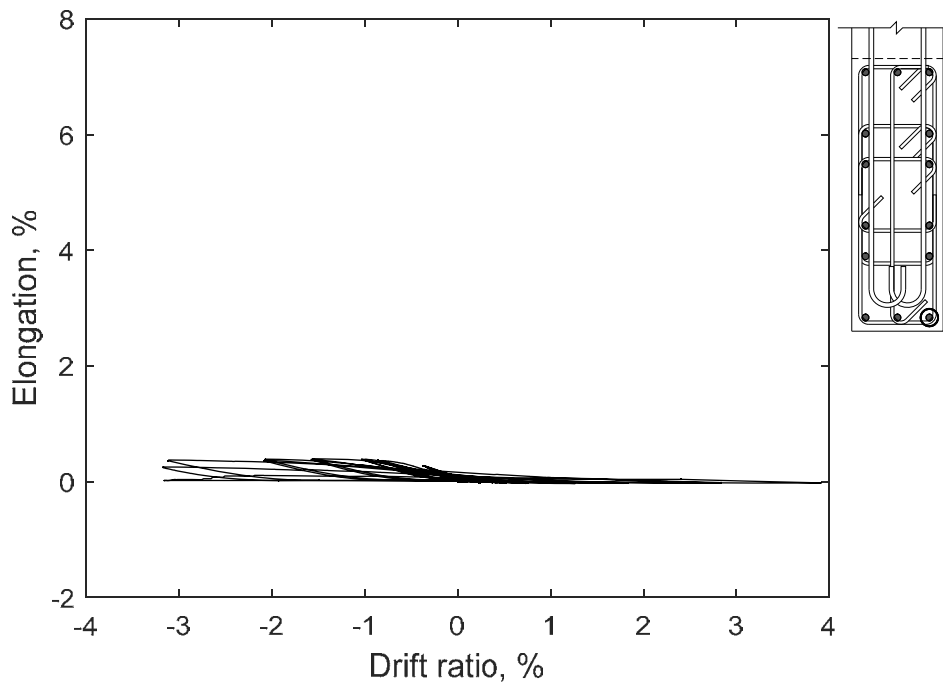


Figure 75 - Measured strain in longitudinal bar at confined stem 144 in. (3660 mm) above base of T6

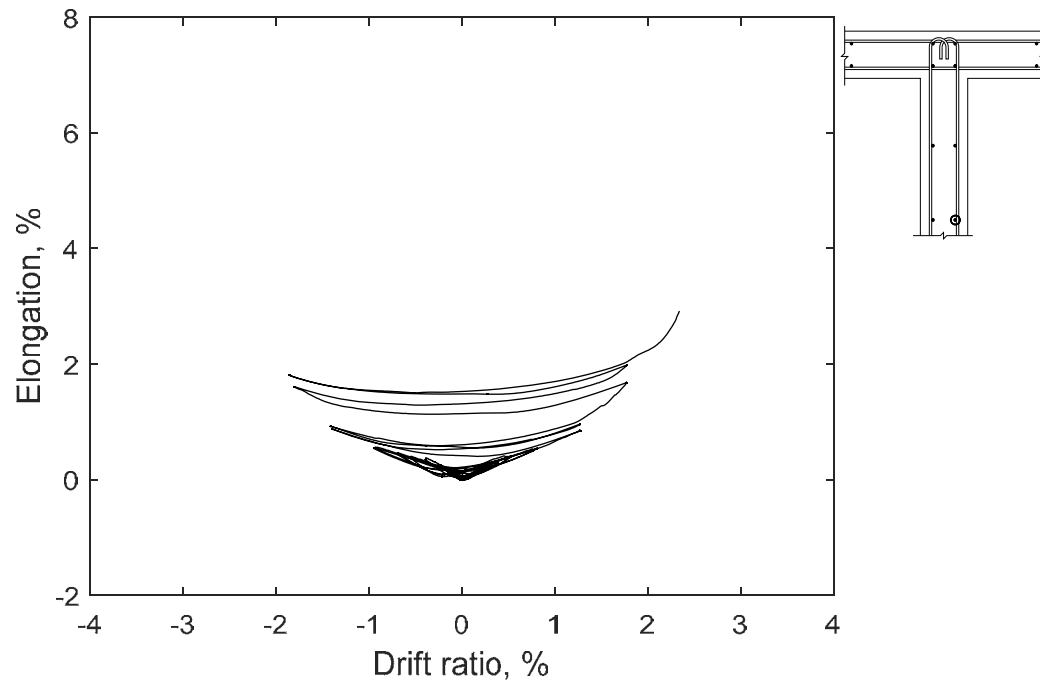


Figure 76 – Measured strain in longitudinal bar at unconfined stem 2 in. (51 mm) above base of T5

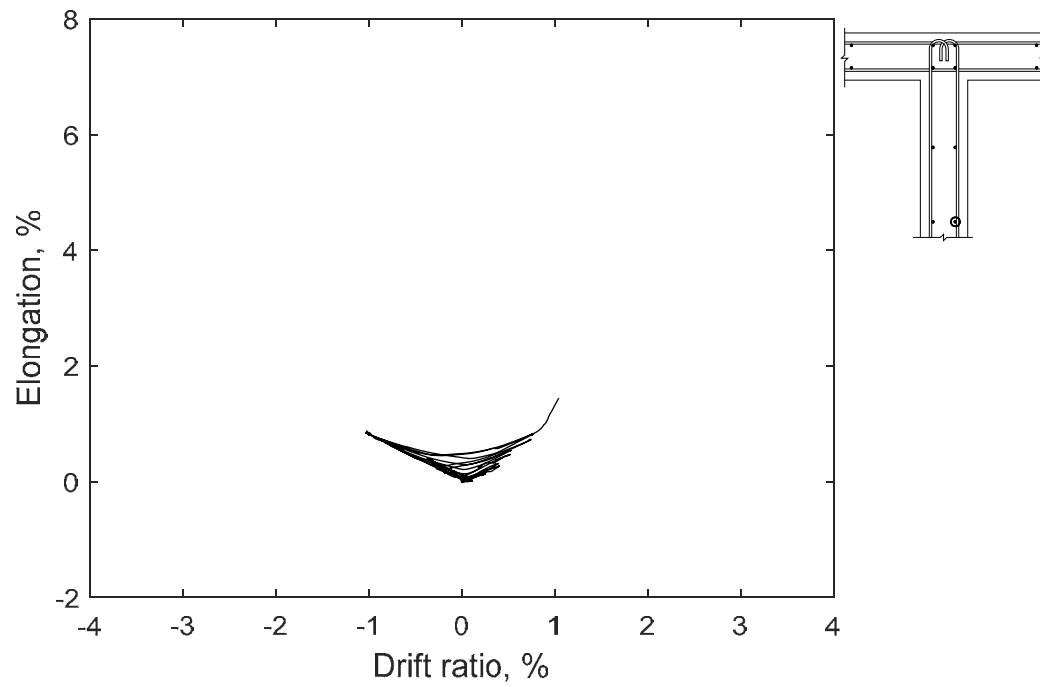


Figure 77 – Measured strain in longitudinal bar at unconfined stem 2 in. (51 mm) above base of T6

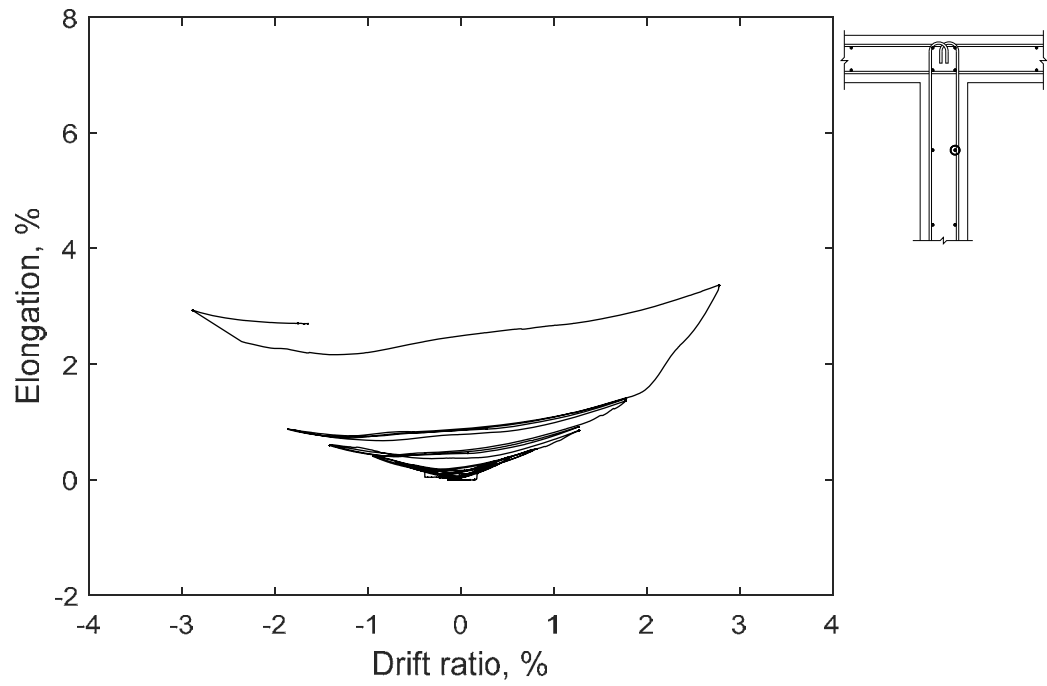


Figure 78 – Measured strain in longitudinal bar at unconfined stem 25 in. (635 mm) above base of T5

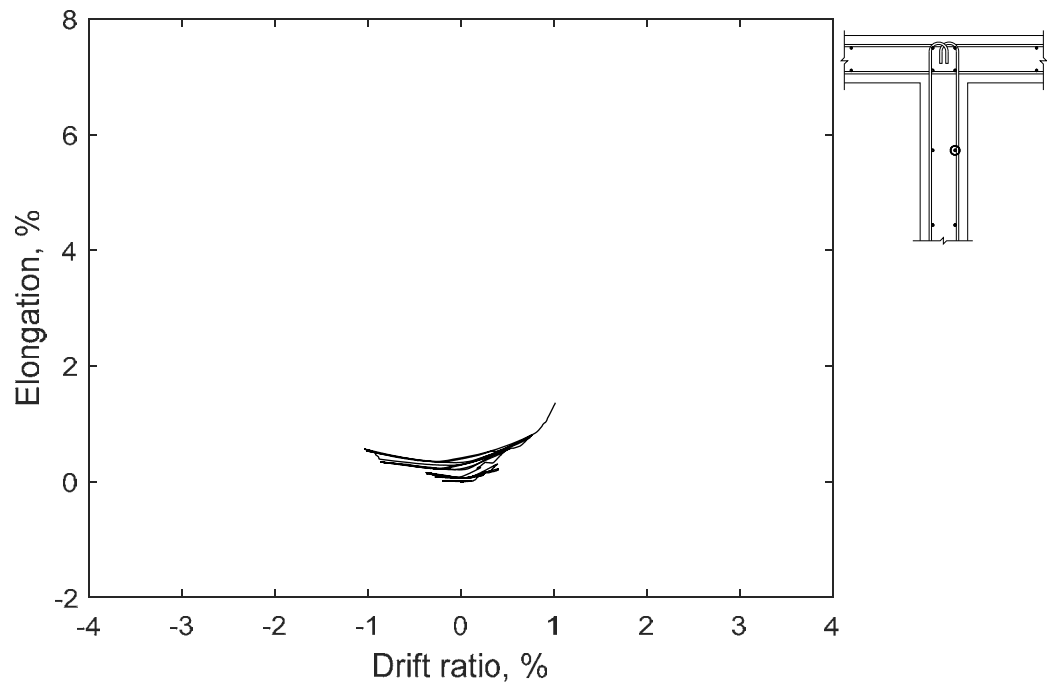


Figure 79 – Measured strain in longitudinal bar at unconfined stem 25 in. (635 mm) above base of T6

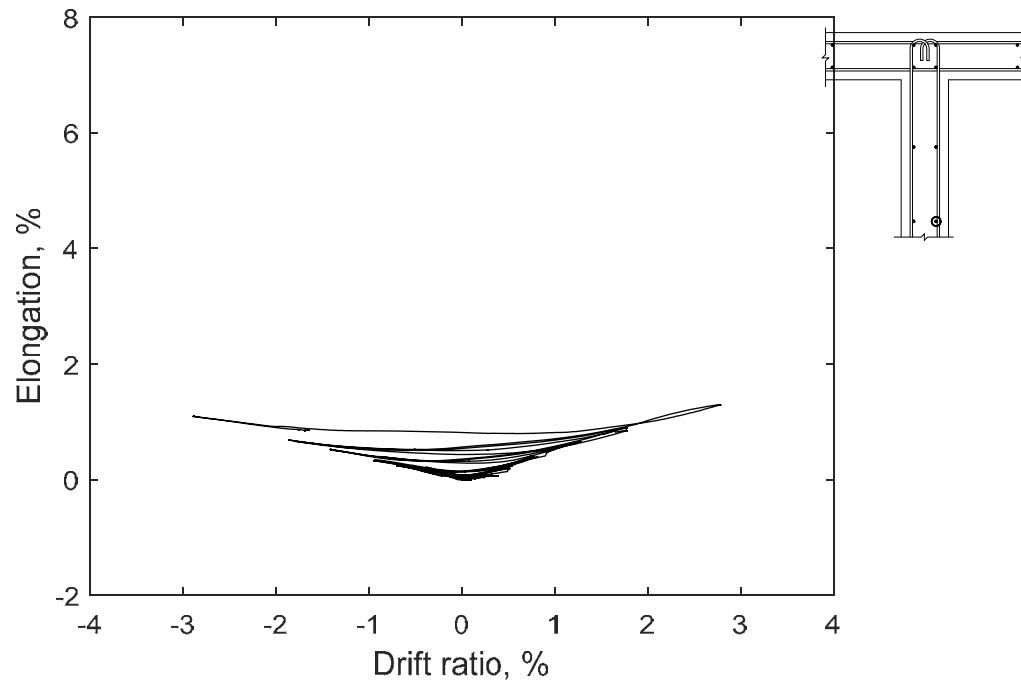


Figure 80 – Measured strain in longitudinal bar at unconfined stem 50 in. (1270 mm) above base of T5

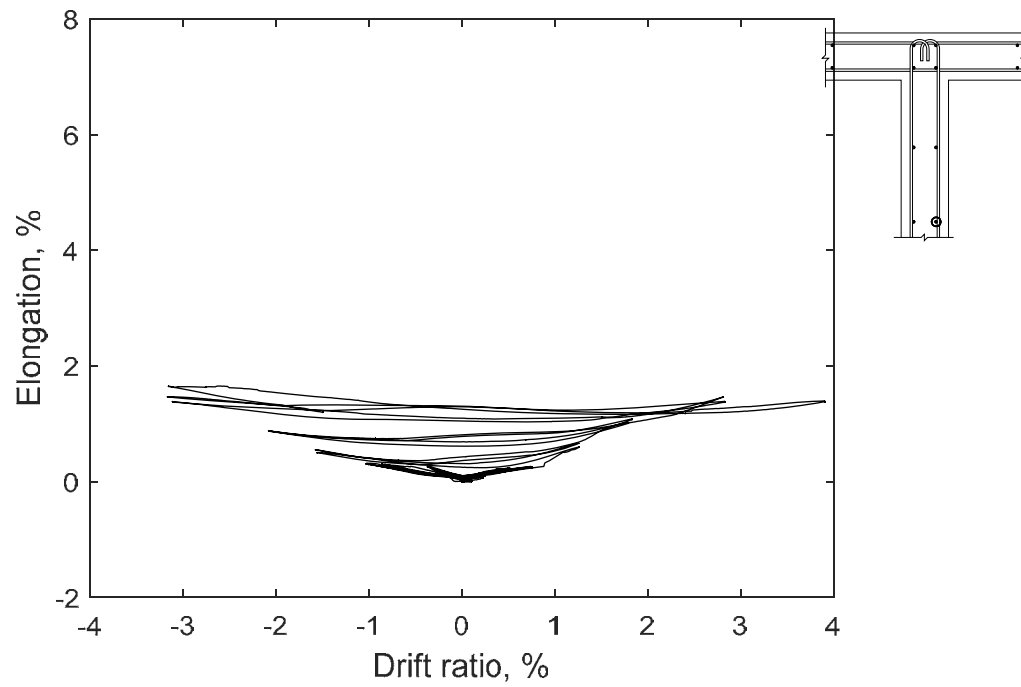


Figure 81 – Measured strain in longitudinal bar at unconfined stem 50 in. (1270 mm) above base of T6

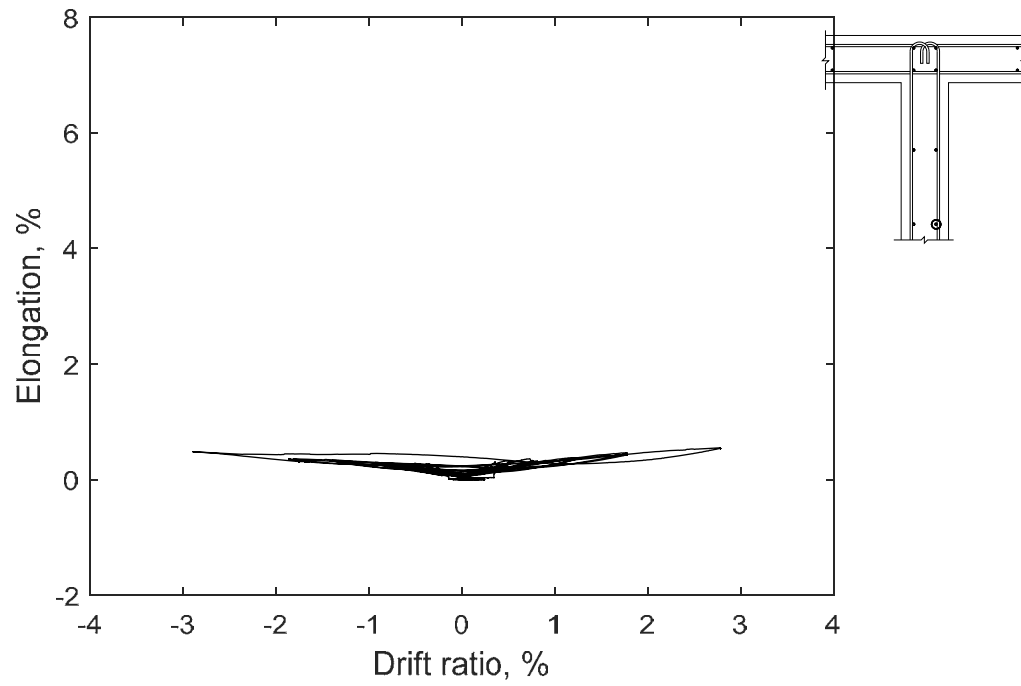


Figure 82 – Measured strain in longitudinal bar at unconfined stem 100 in. (2540 mm) above base of T5

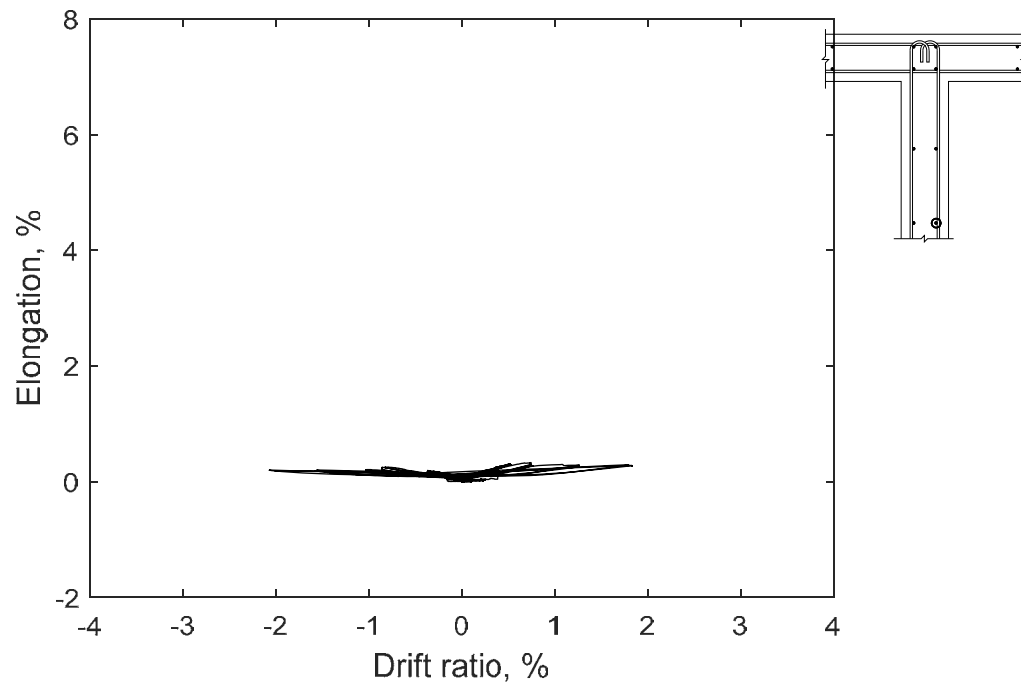


Figure 83 – Measured strain in longitudinal bar at unconfined stem 100 in. (2540 mm) above base of T6

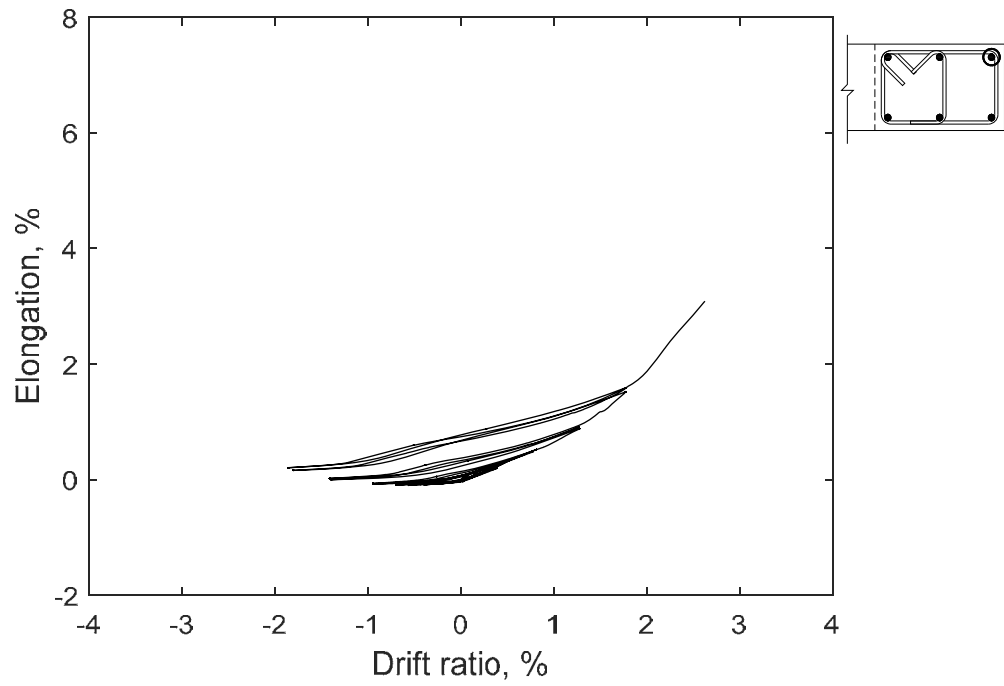


Figure 84 – Measured strain in longitudinal bar at confined flange 2 in. (51 mm) above base of T5

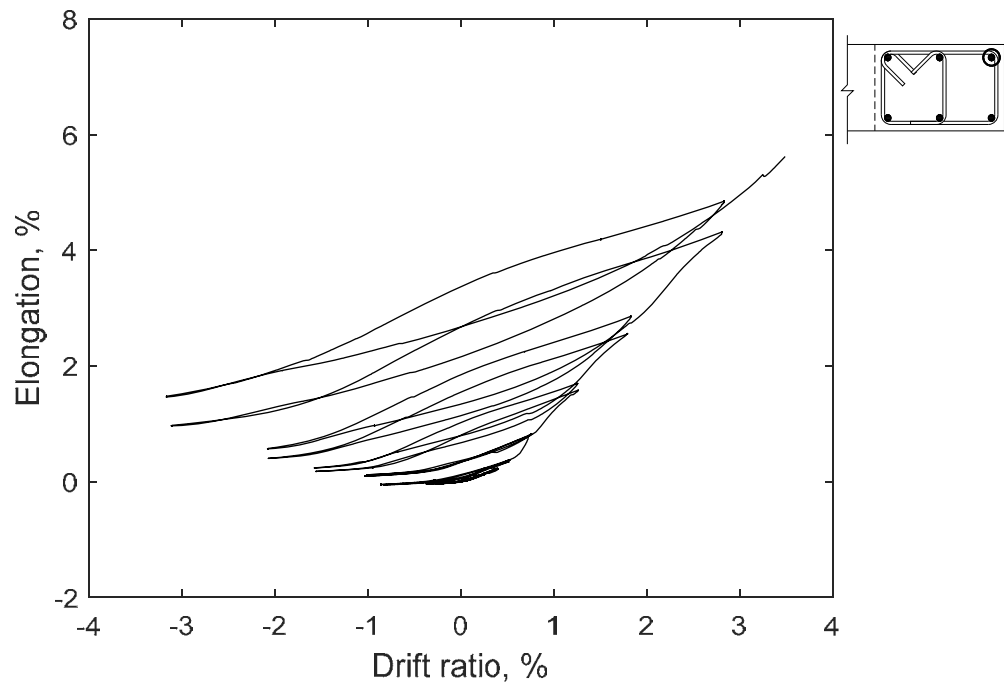


Figure 85 – Measured strain in longitudinal bar at confined flange 2 in. (51 mm) above base of T6

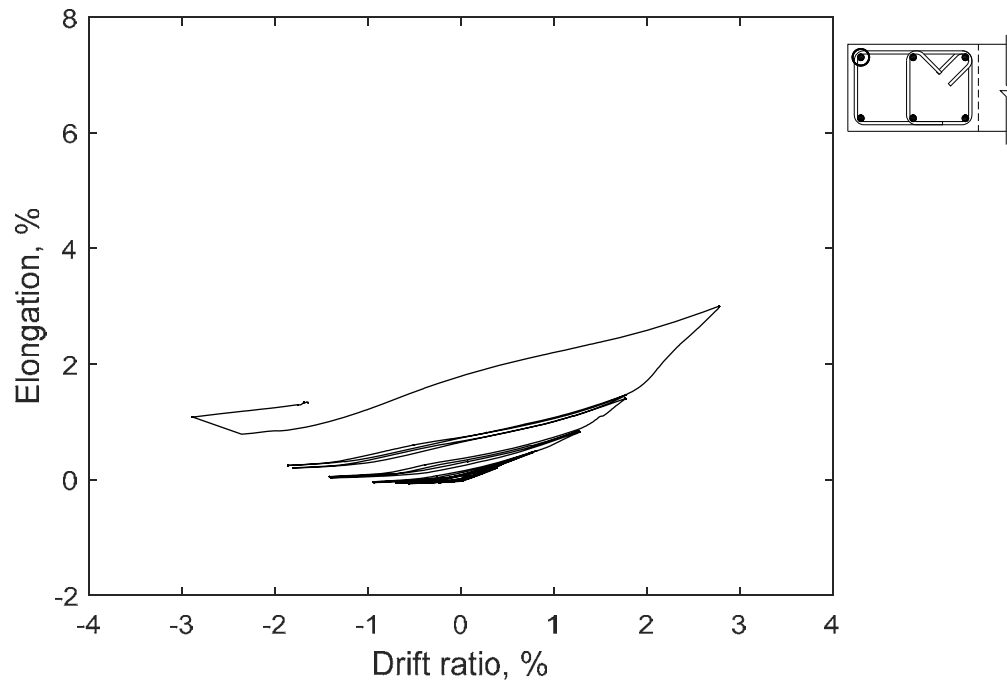


Figure 86 – Measured strain in longitudinal bar at confined flange 2 in. (51 mm) above base of T5

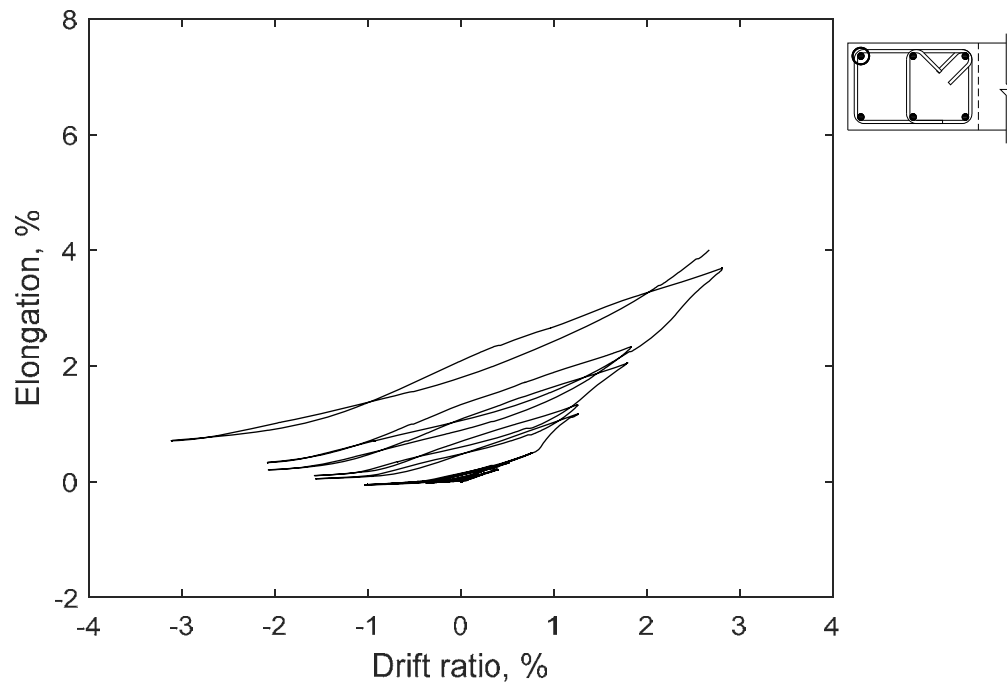


Figure 87 – Measured strain in longitudinal bar at confined flange 2 in. (51 mm) above base of T6

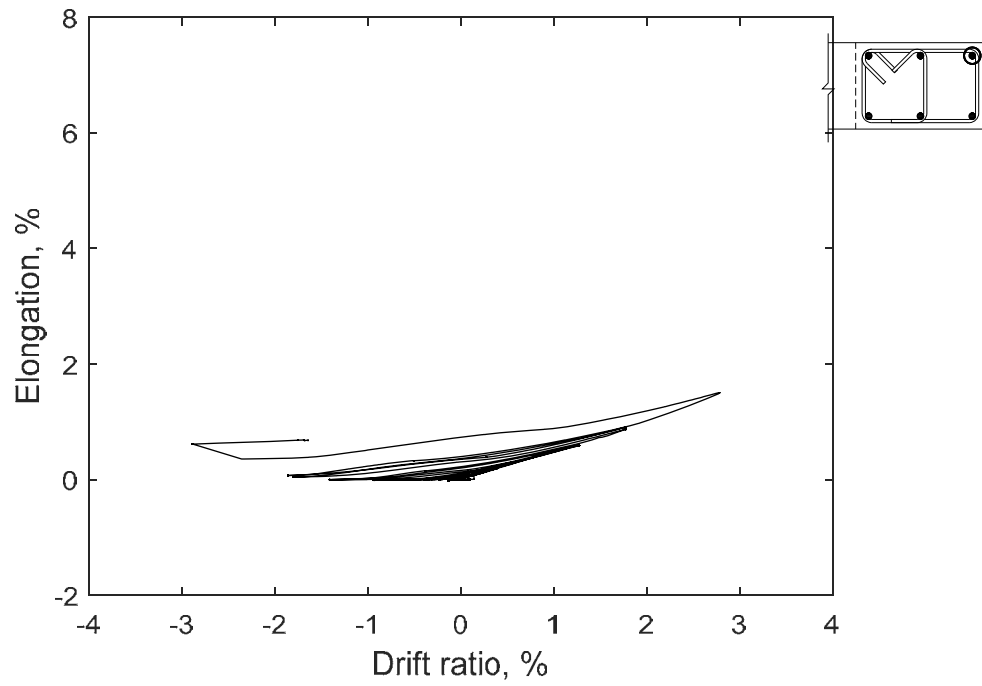


Figure 88 – Measured strain in longitudinal bar at confined flange 50 in. (1270 mm) above base of T5

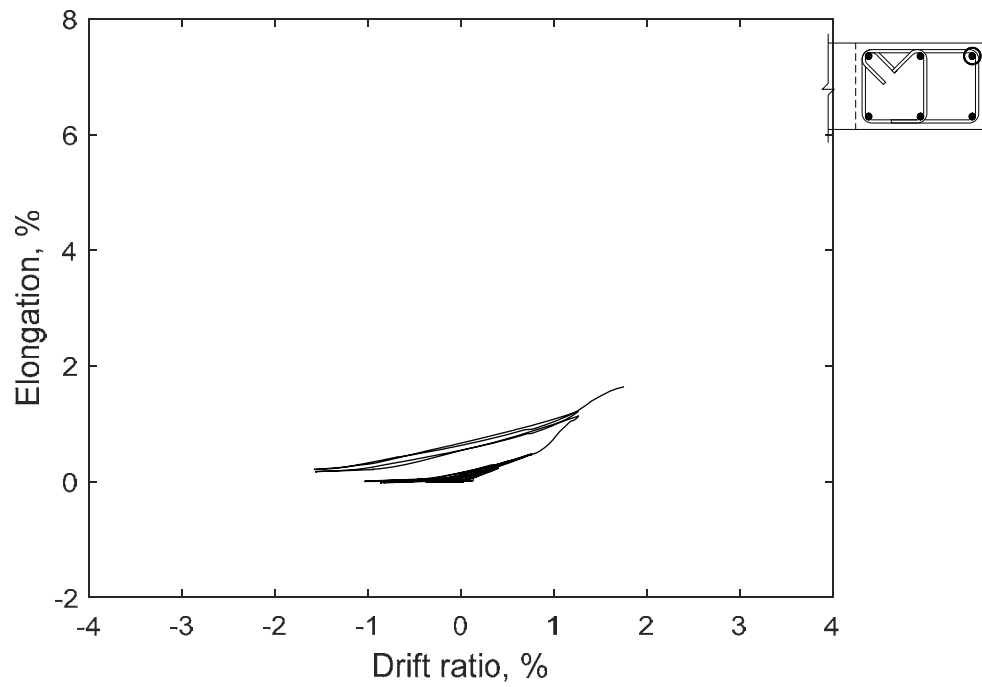


Figure 89 – Measured strain in longitudinal bar at confined flange 50 in. (1270 mm) above base of T6

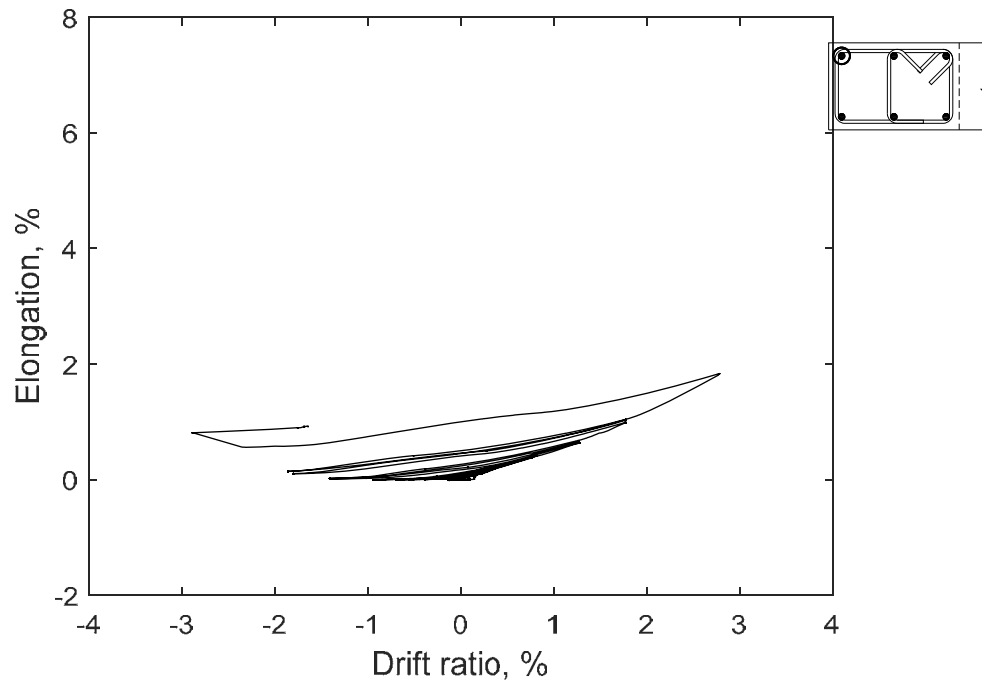


Figure 90 – Measured strain in longitudinal bar at confined flange 50 in. (1270 mm) above base of T5

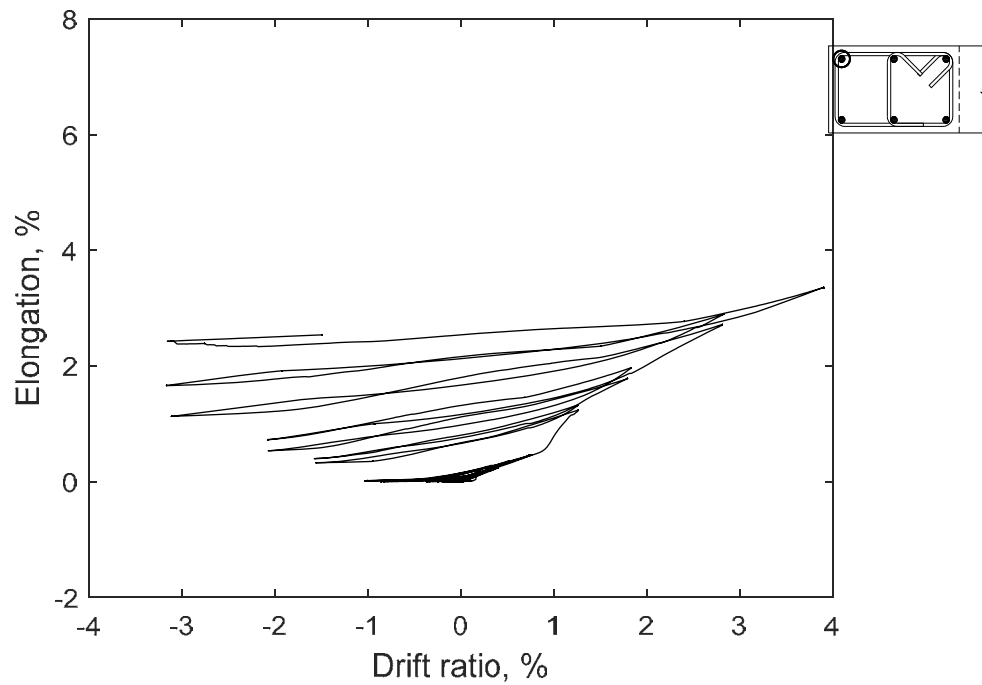


Figure 91 – Measured strain in longitudinal bar at confined flange 50 in. (1270 mm) above base of T6

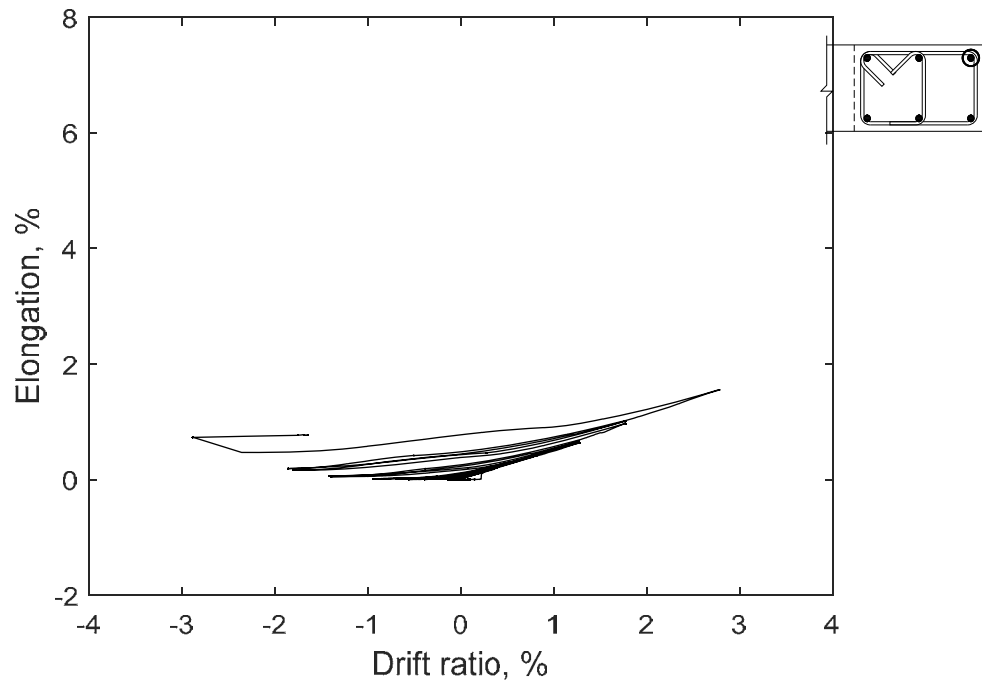


Figure 92 – Measured strain in longitudinal bar at confined flange 100 in. (2540 mm) above base of T5

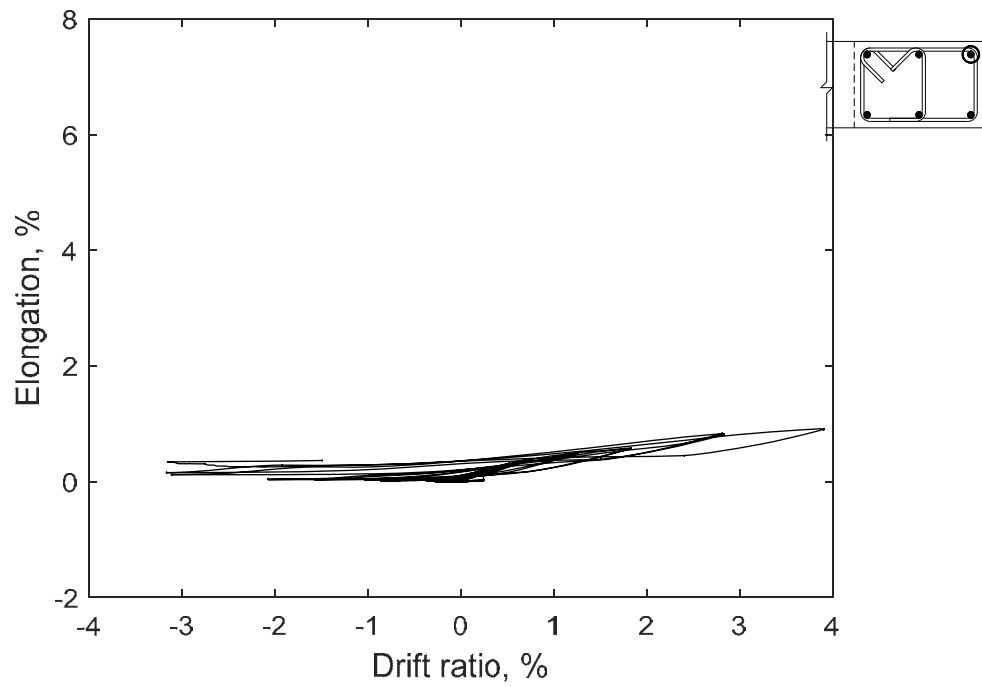


Figure 93 – Measured strain in longitudinal bar at confined flange 100 in. (2540 mm) above base of T6

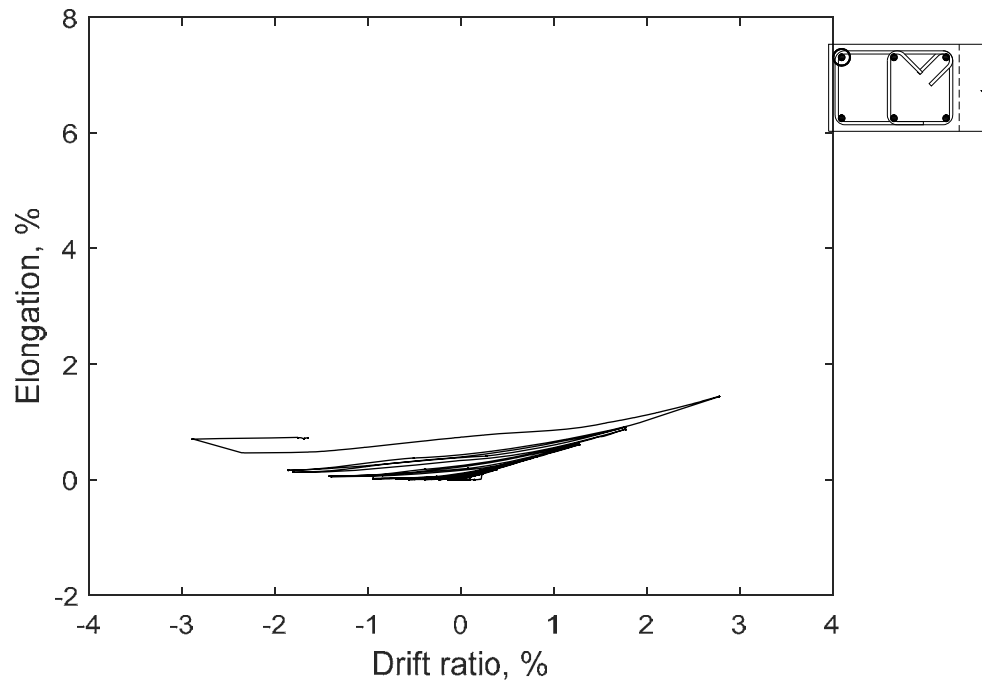


Figure 94 – Measured strain in longitudinal bar at confined flange 100 in. (2540 mm) above base of T5

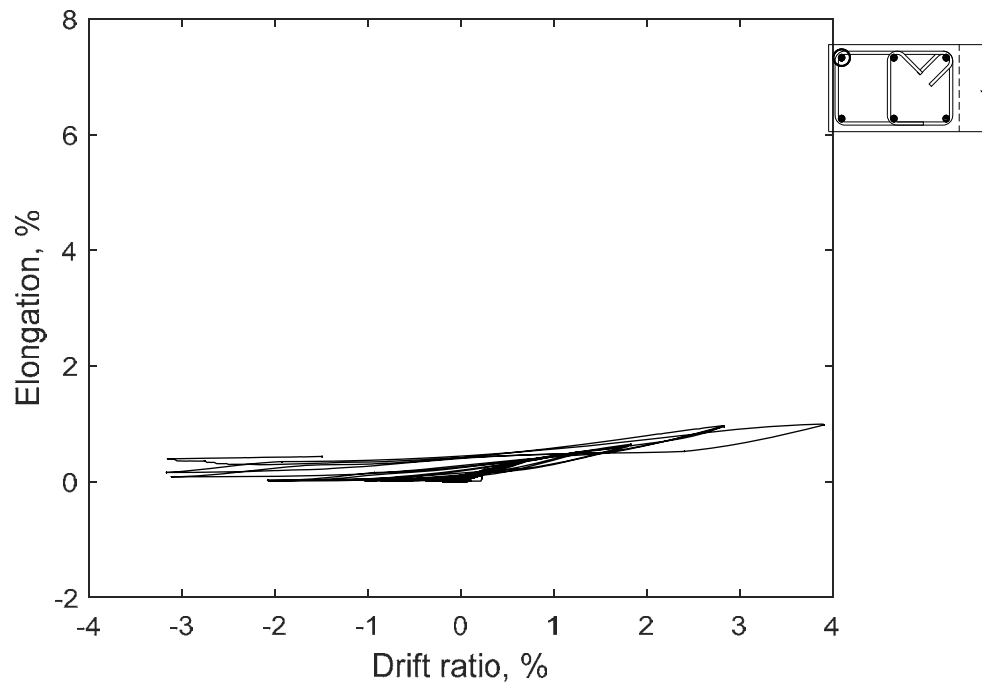


Figure 95 – Measured strain in longitudinal bar at confined flange 100 in. (2540 mm) above base of T6

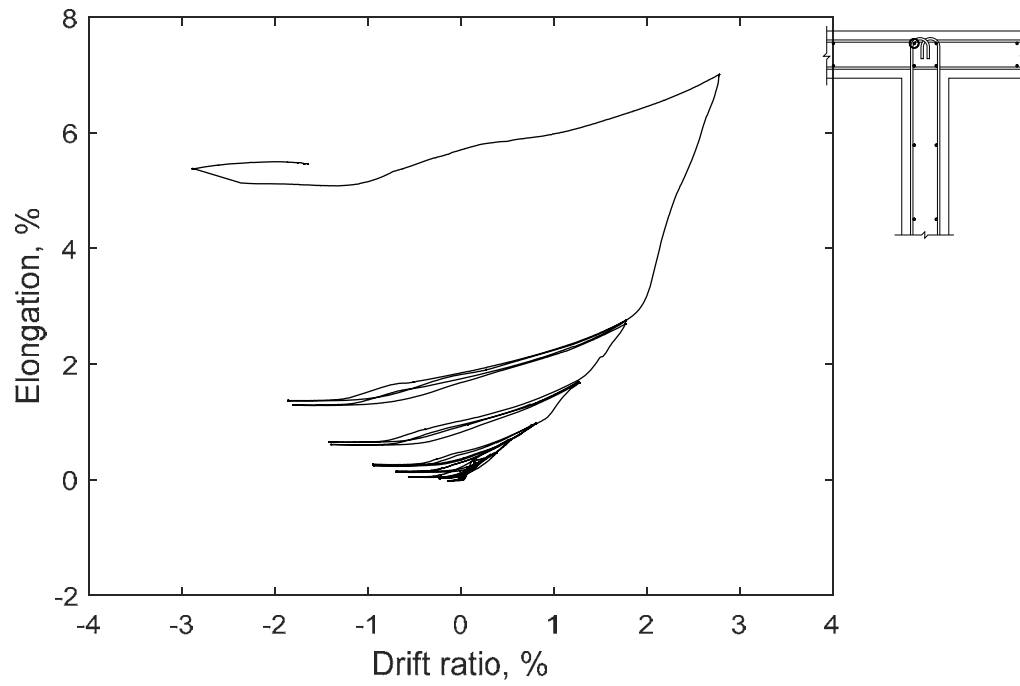


Figure 96 - Measured strain in longitudinal bar at unconfined flange 2 in. (51 mm) above base of T5

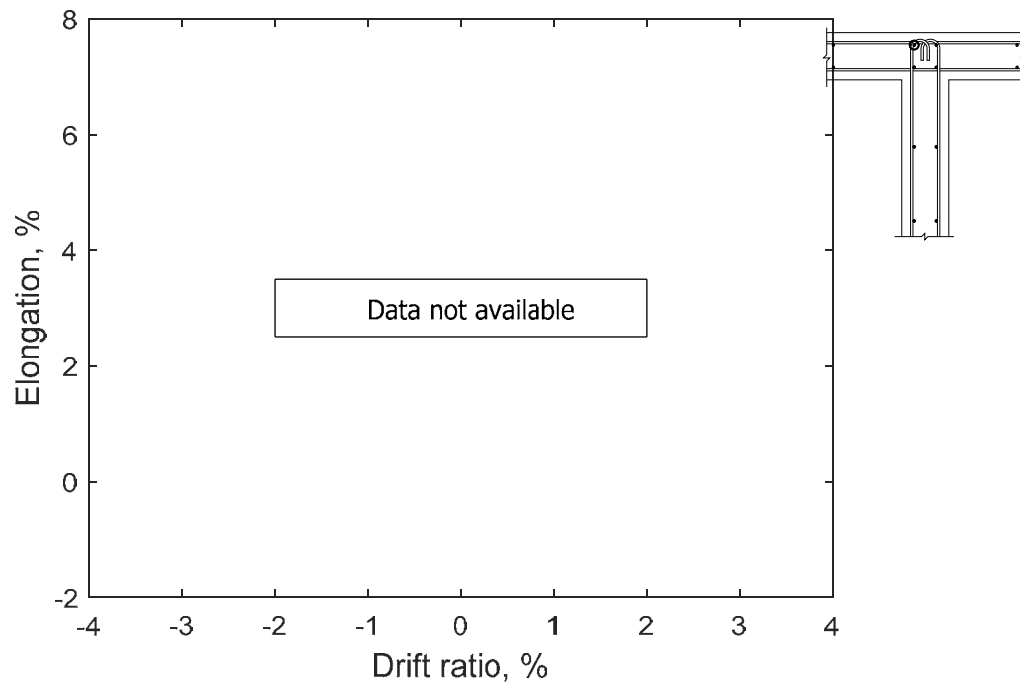


Figure 97 - Measured strain in longitudinal bar at unconfined flange 2 in. (51 mm) above base of T6

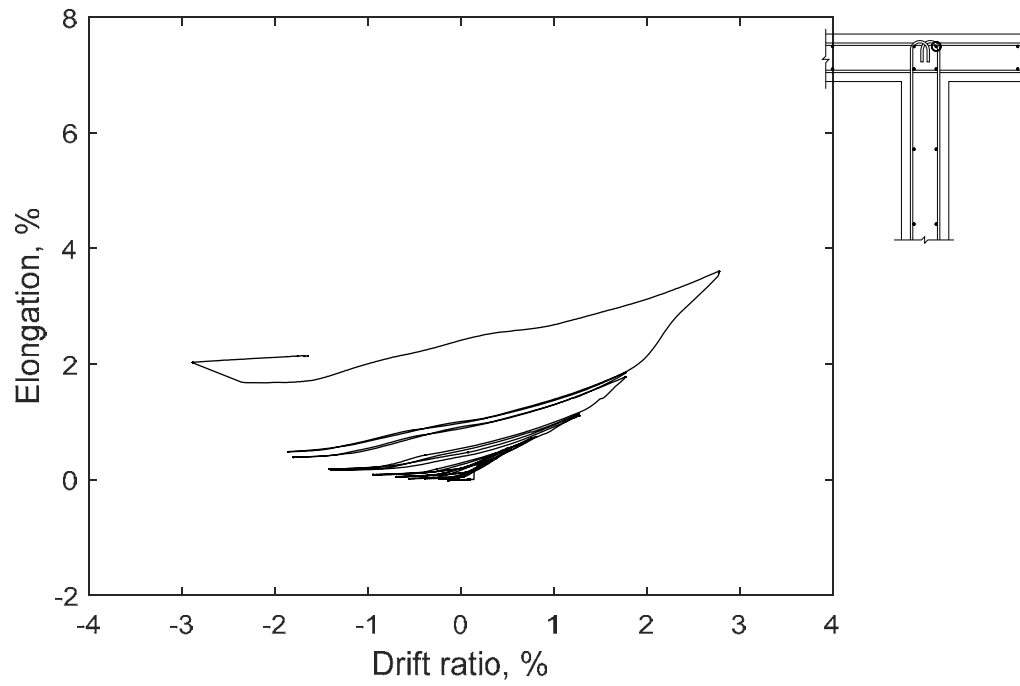


Figure 98 – Measured strain in longitudinal bar at unconfined flange 25 in. (635 mm) above base of T5

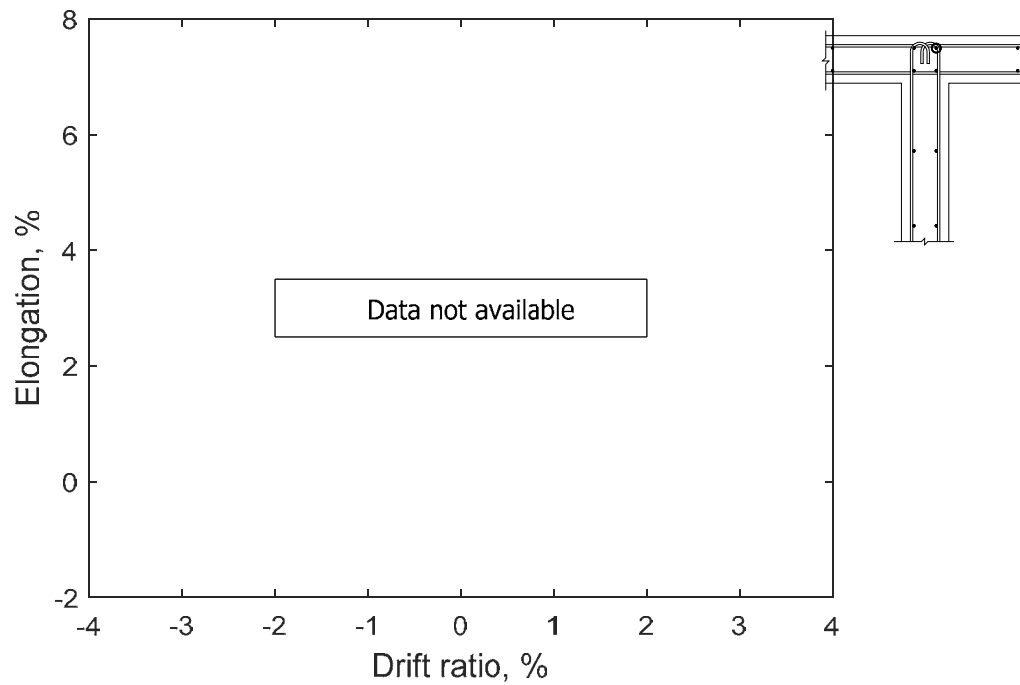


Figure 99 – Measured strain in longitudinal bar at unconfined flange 25 in. (635 mm) above base of T6

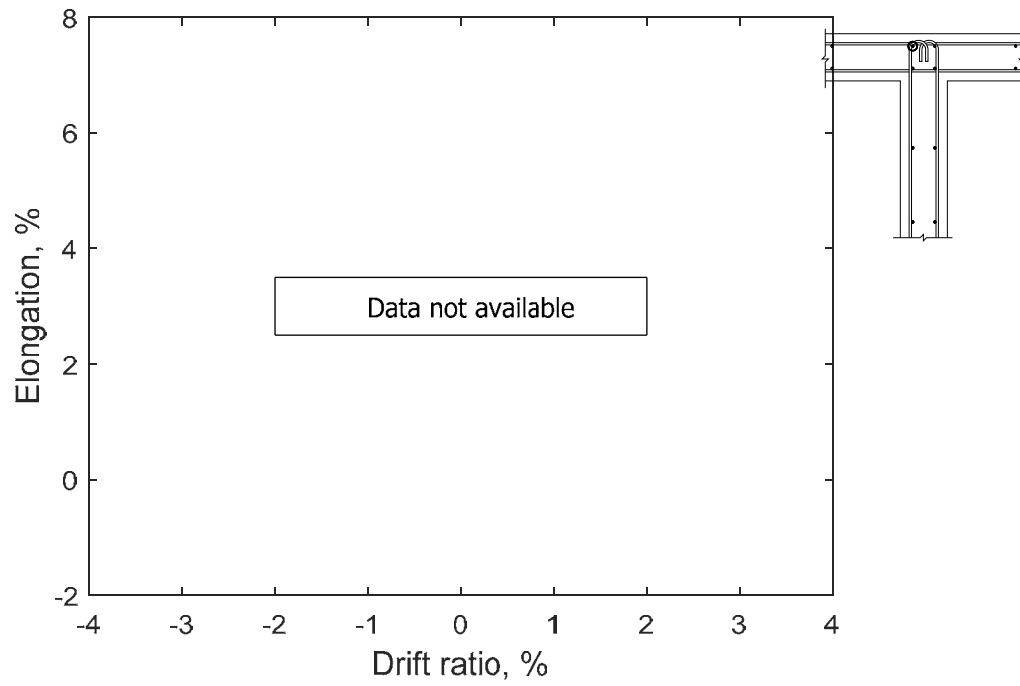


Figure 100 – Measured strain in longitudinal bar at unconfined flange 25 in. (635 mm) above base of T5

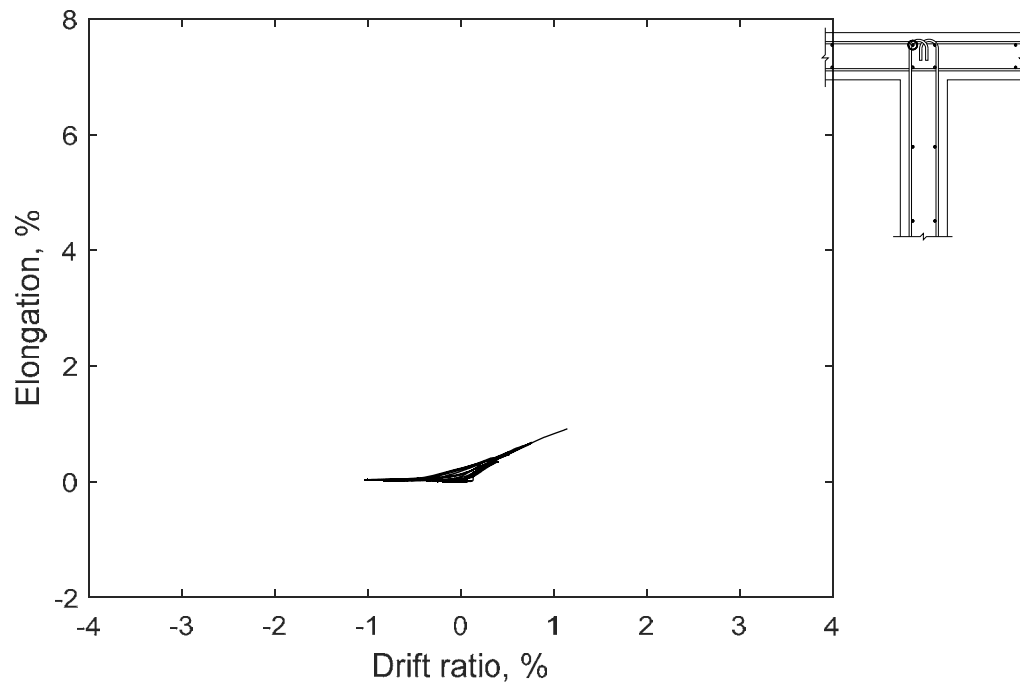


Figure 101 – Measured strain in longitudinal bar at unconfined flange 25 in. (635 mm) above base of T6

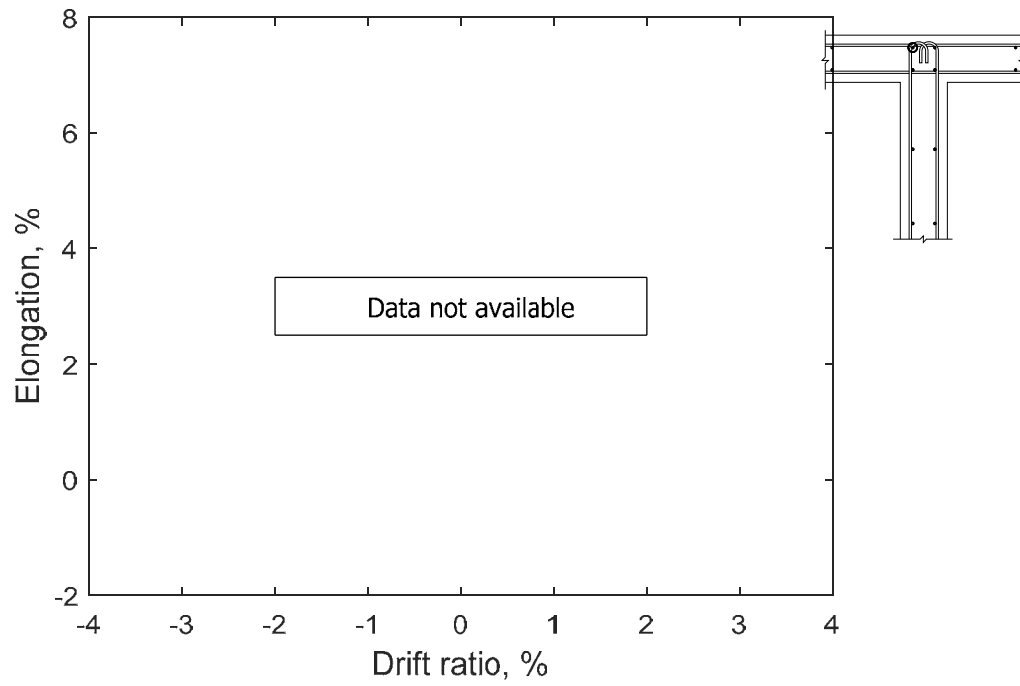


Figure 102 – Measured strain in longitudinal bar at unconfined flange 50 in. (1270 mm) above base of T5

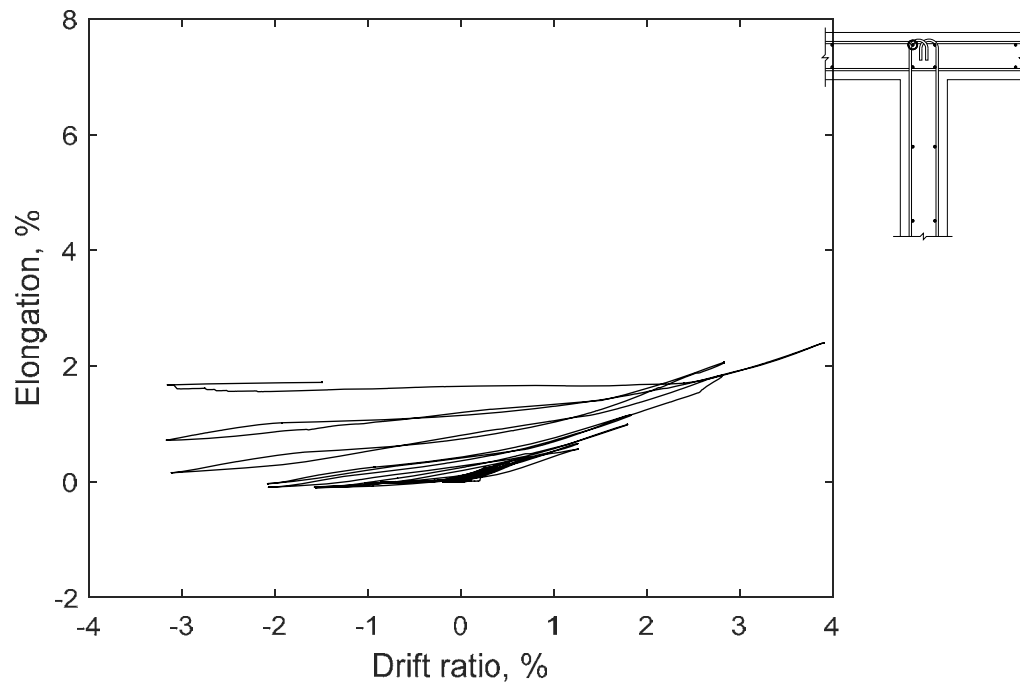


Figure 103 – Measured strain in longitudinal bar at unconfined flange 50 in. (1270 mm) above base of T6

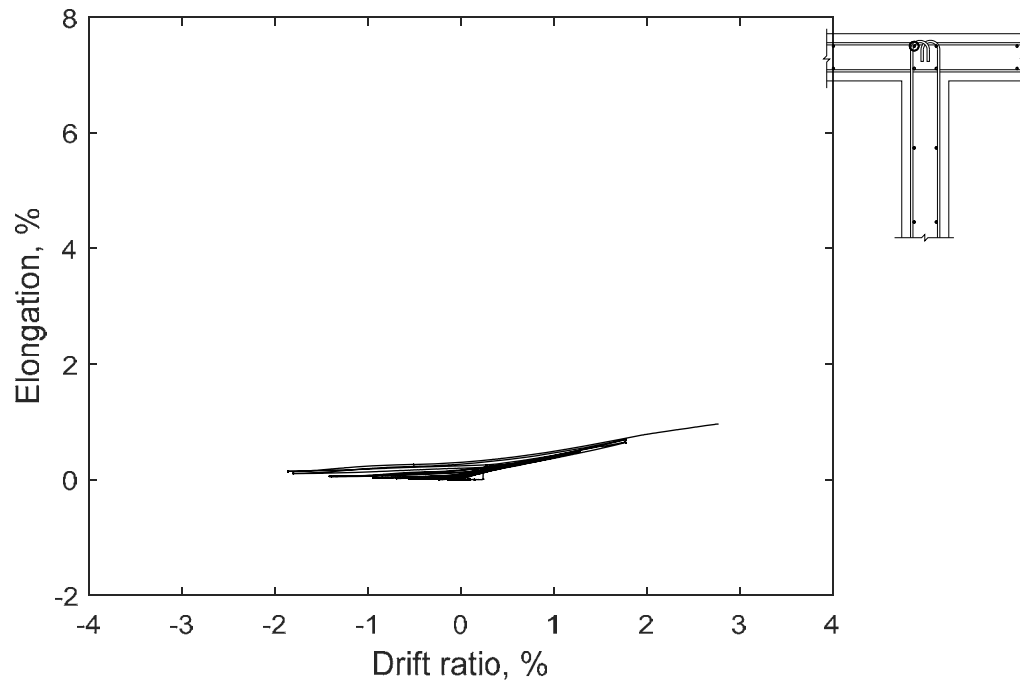


Figure 104 – Measured strain in longitudinal bar at unconfined flange 100 in. (2540 mm) above base of T5

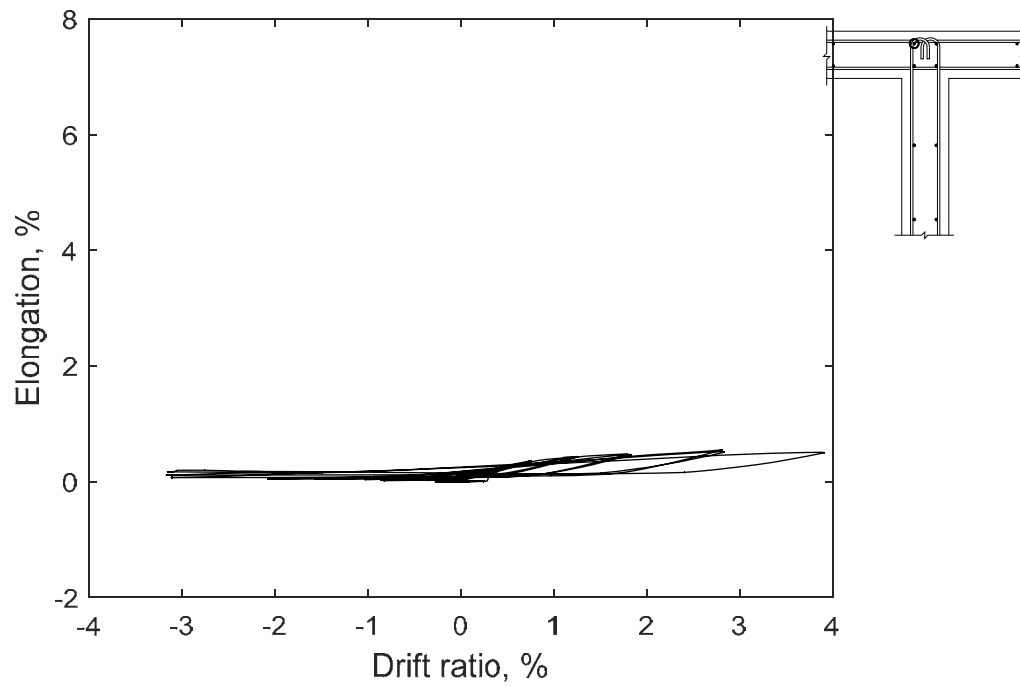


Figure 105 – Measured strain in longitudinal bar at unconfined flange 100 in. (2540 mm) above base of T6

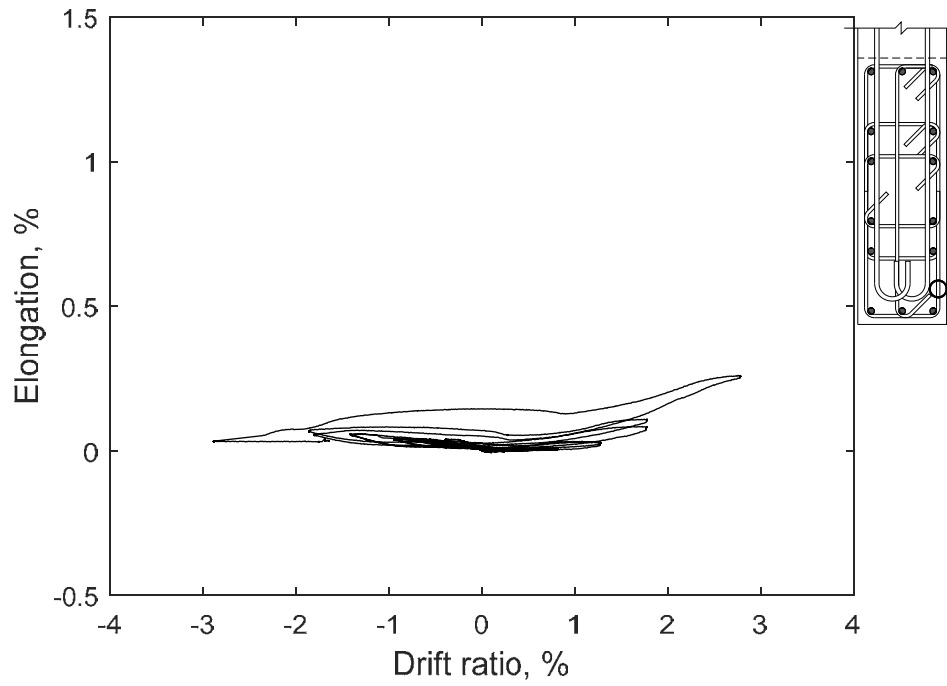


Figure 106 – Measured strain in hoop at confined stem 1.5 in. (38 mm) above base of T5

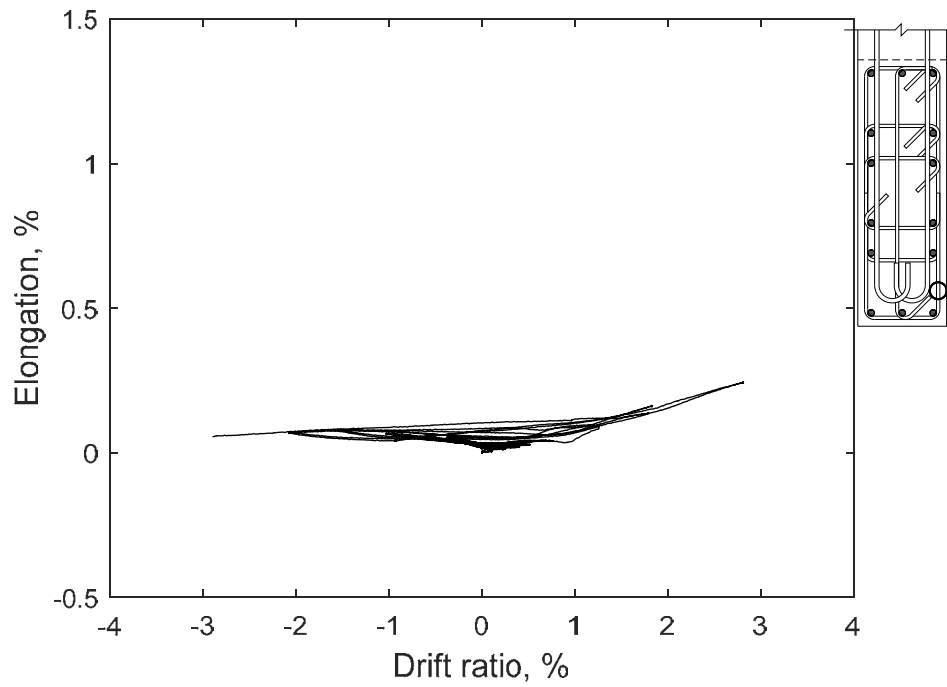


Figure 107 – Measured strain in hoop at confined stem 1.5 in. (38 mm) above base of T6

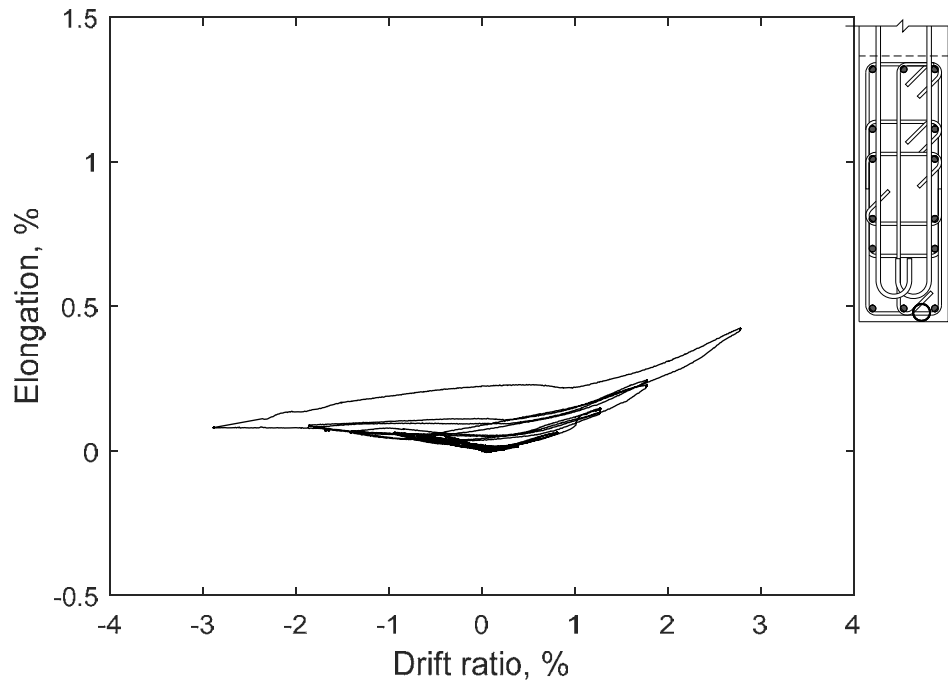


Figure 108 – Measured strain in hoop at confined stem 1.5 in. (38 mm) above base of T5

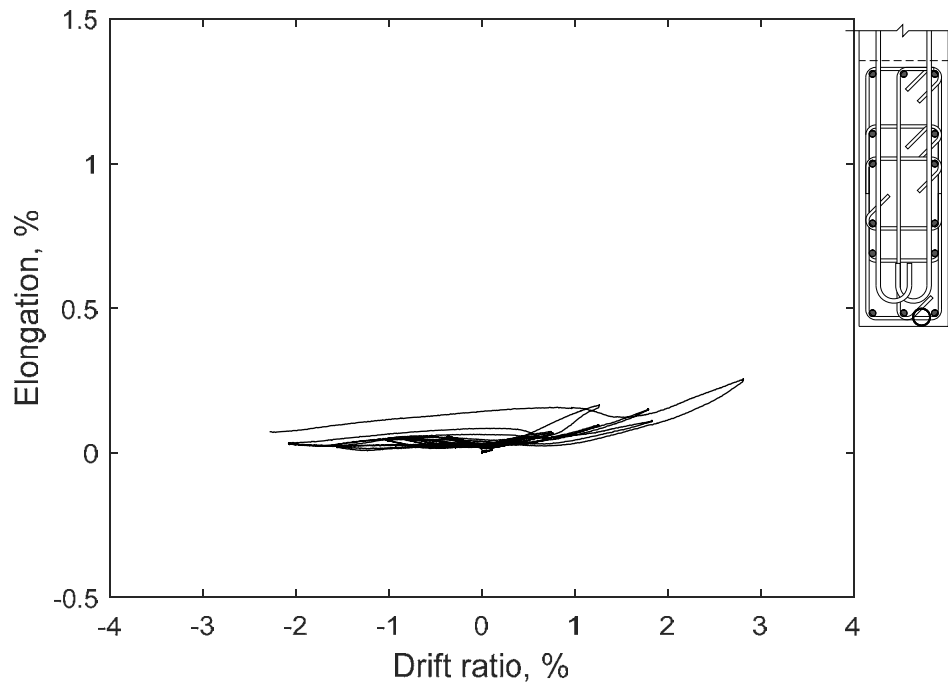


Figure 109 – Measured strain in hoop at confined stem 1.5 in. (38 mm) above base of T6

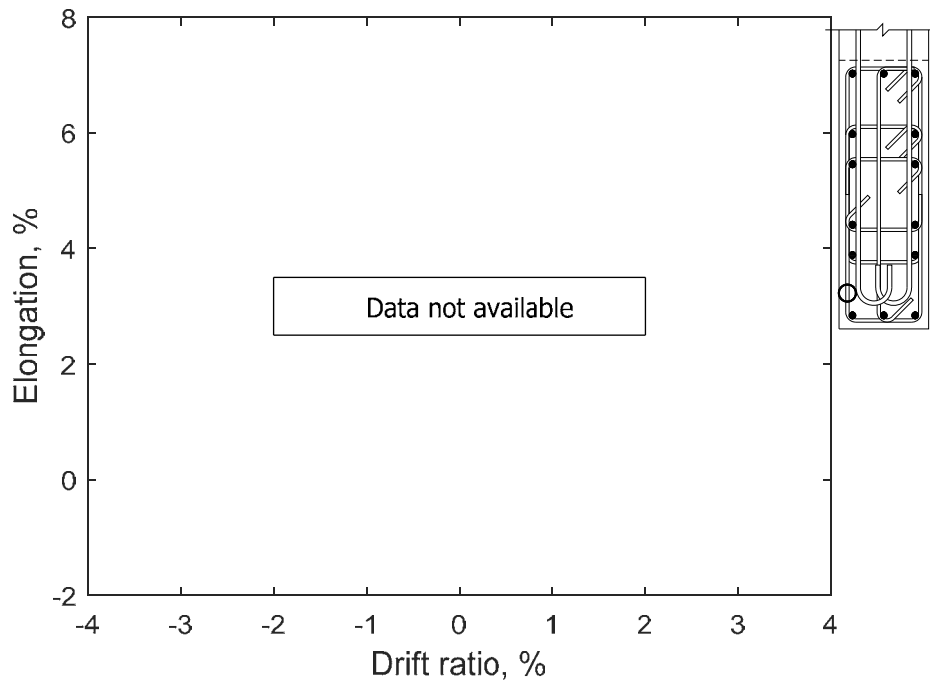


Figure 110 – Measured strain in hoop at confined stem 1.5 in. (38 mm) above base of T5

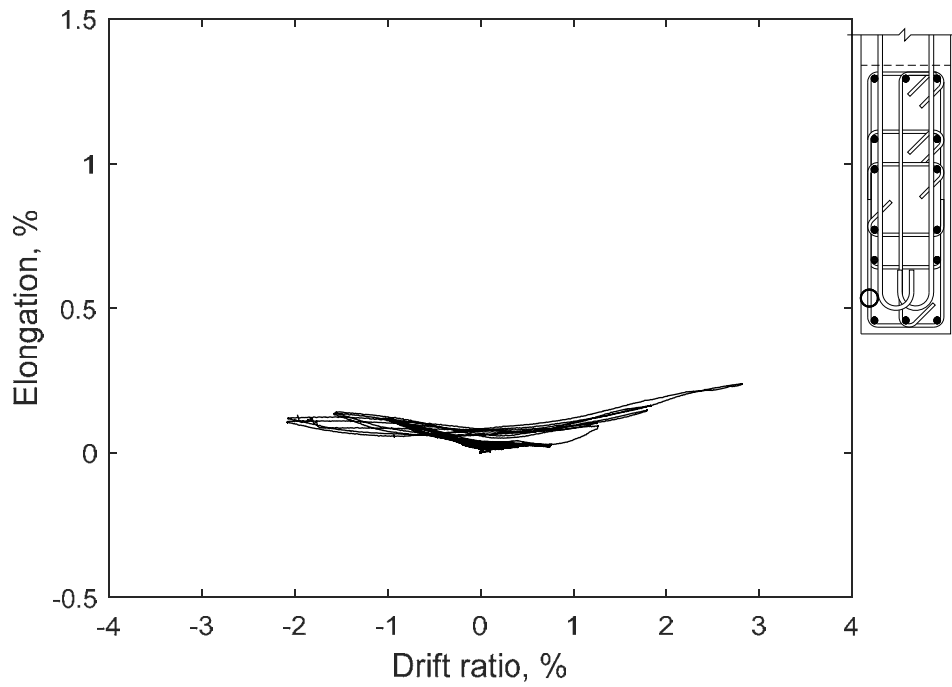


Figure 111 – Measured strain in hoop at confined stem 1.5 in. (38 mm) above base of T6

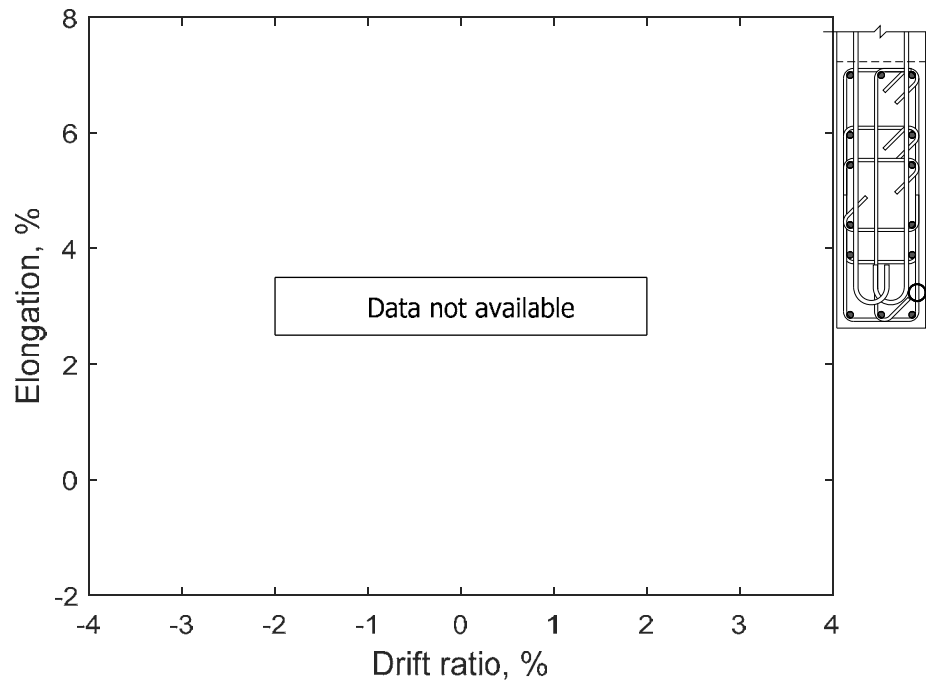


Figure 112 – Measured strain in hoop at confined stem 4.5 in. (114 mm) above base of T5

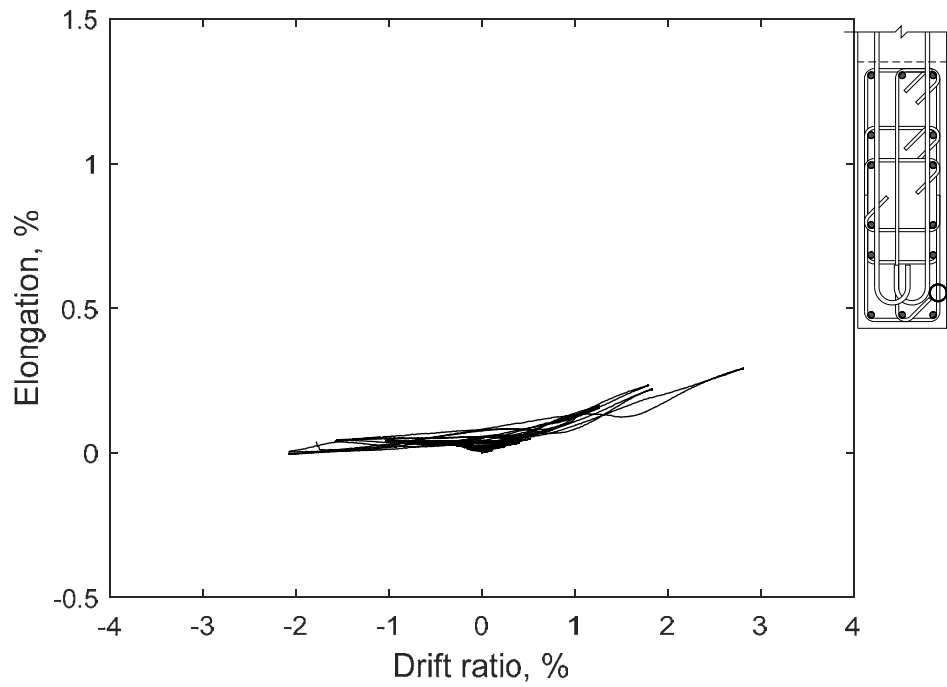


Figure 113 – Measured strain in hoop at confined stem 4.5 in. (114 mm) above base of T6

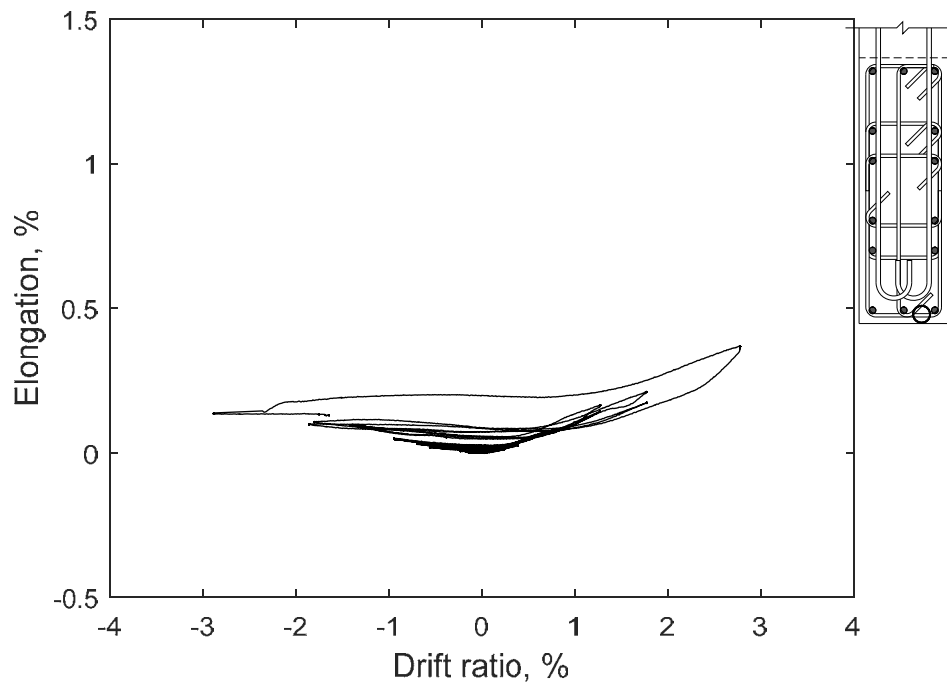


Figure 114 – Measured strain in hoop at confined stem 4.5 in. (114 mm) above base of T5

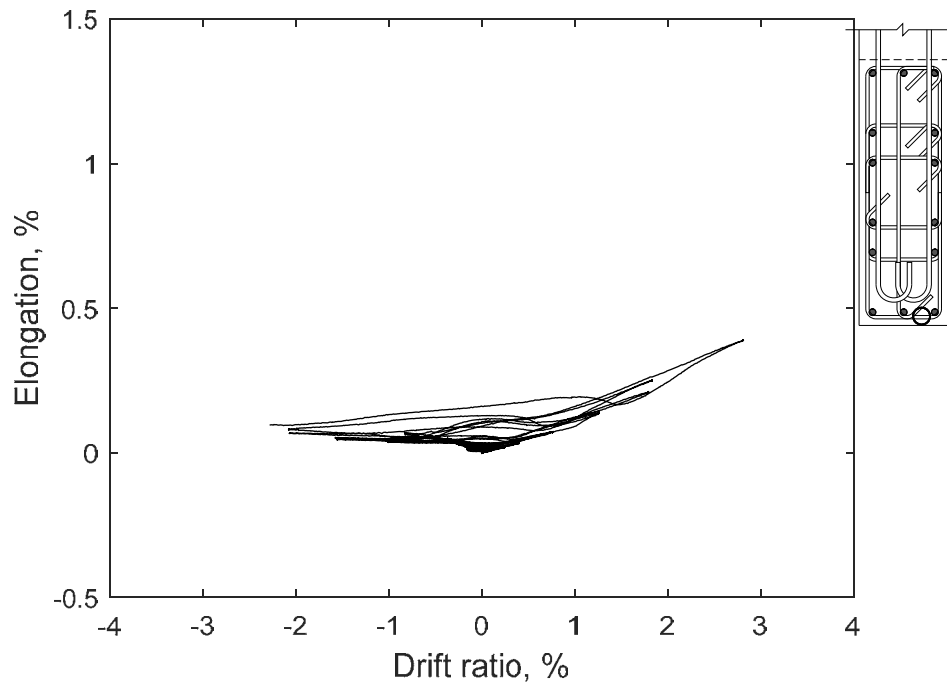


Figure 115 – Measured strain in hoop at confined stem 4.5 in. (114 mm) above base of T6

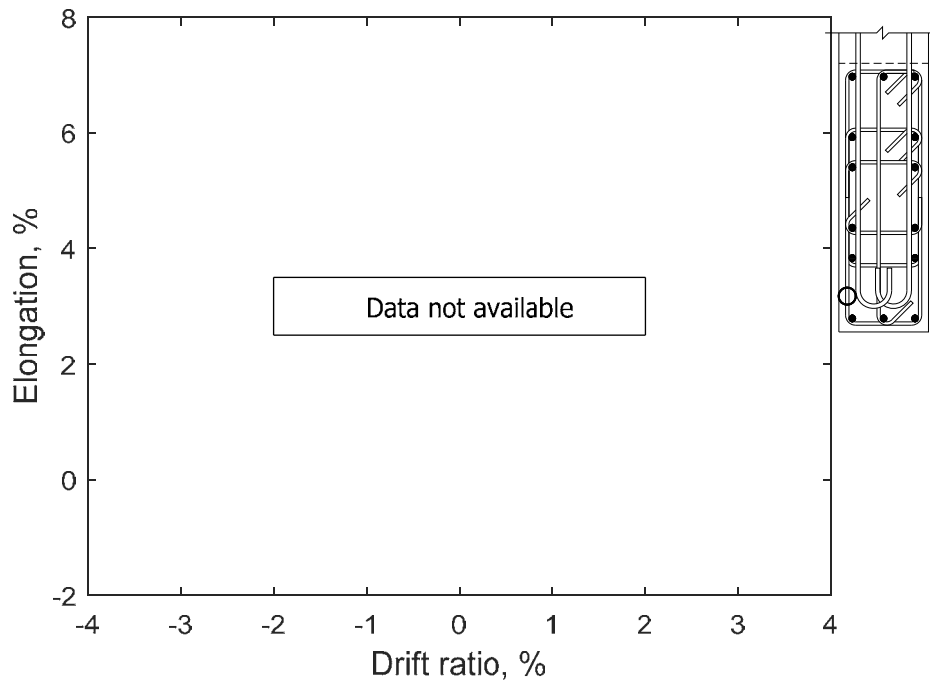


Figure 116 – Measured strain in hoop at confined stem 4.5 in. (114 mm) above base of T5

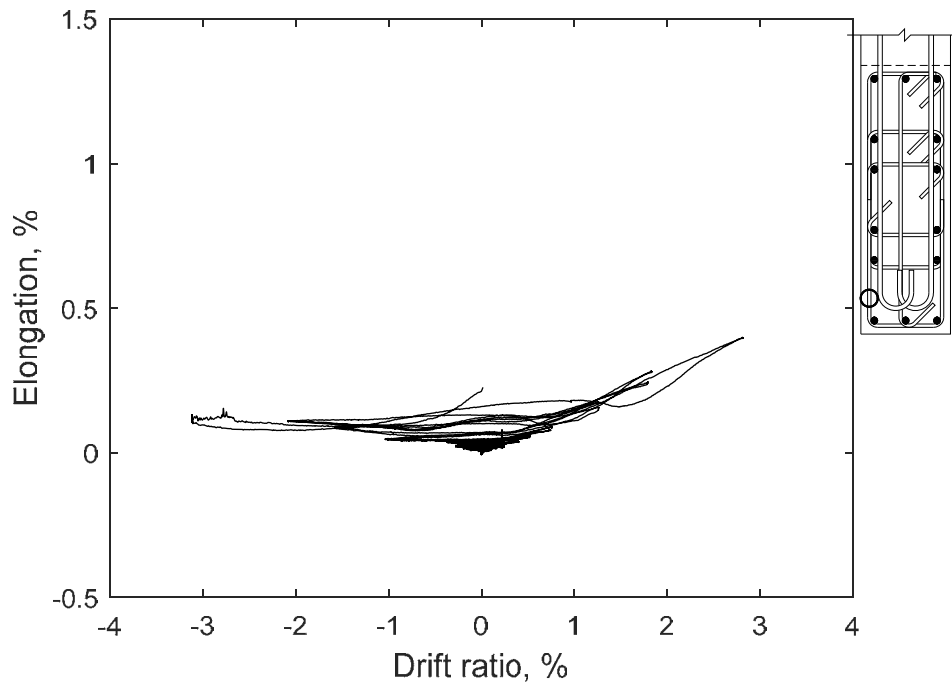


Figure 117 – Measured strain in hoop at confined stem 4.5 in. (114 mm) above base of T6

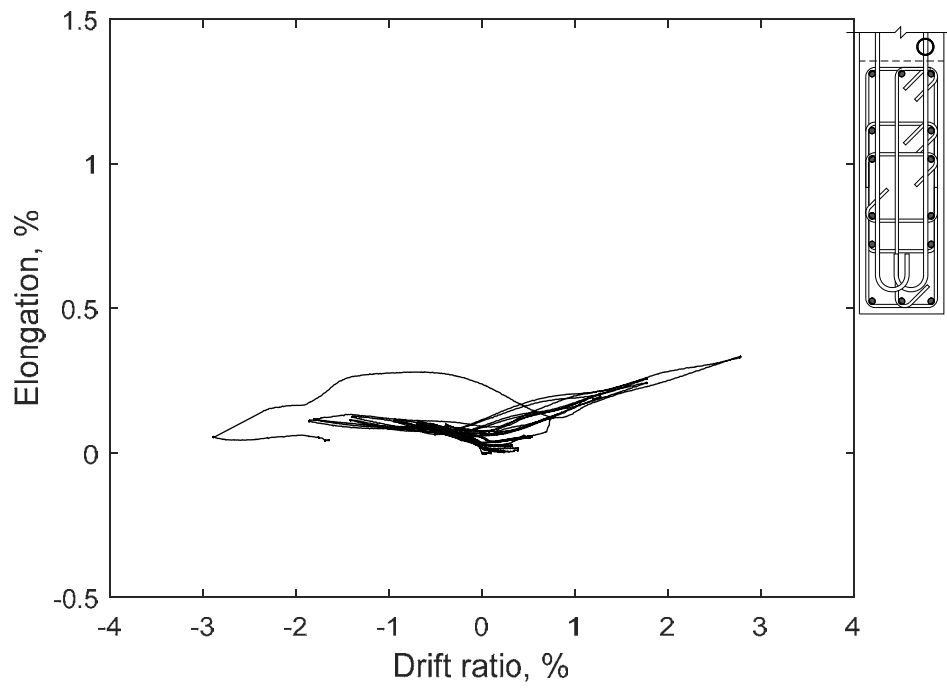


Figure 118 – Measured strain in horizontal bar at unconfined stem 22.5 in. (572 mm) above base of T5

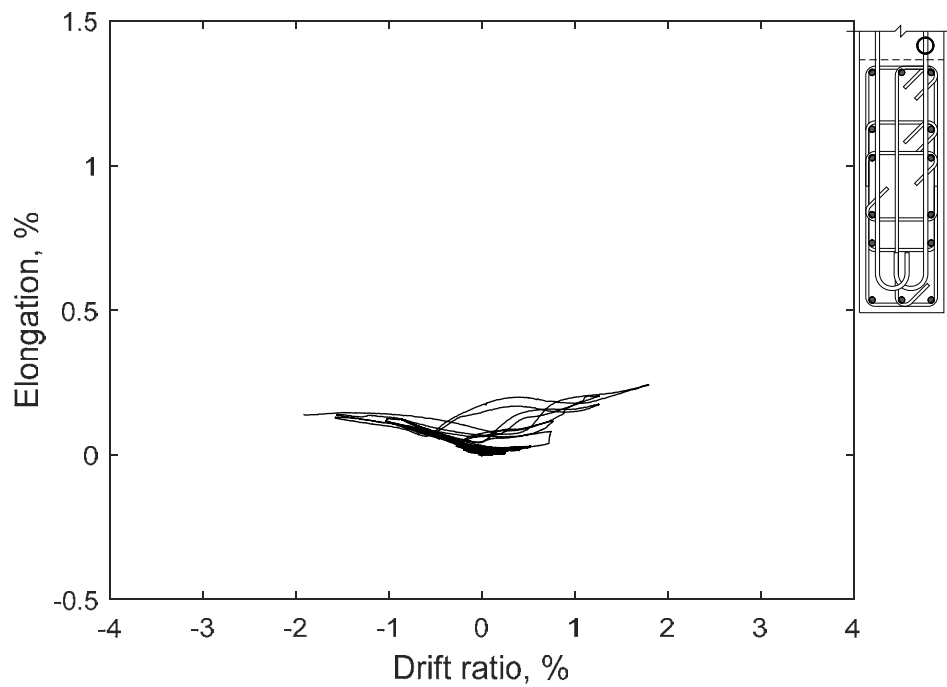


Figure 119 – Measured strain in horizontal bar at unconfined stem 22.5 in. (572 mm) above base of T6

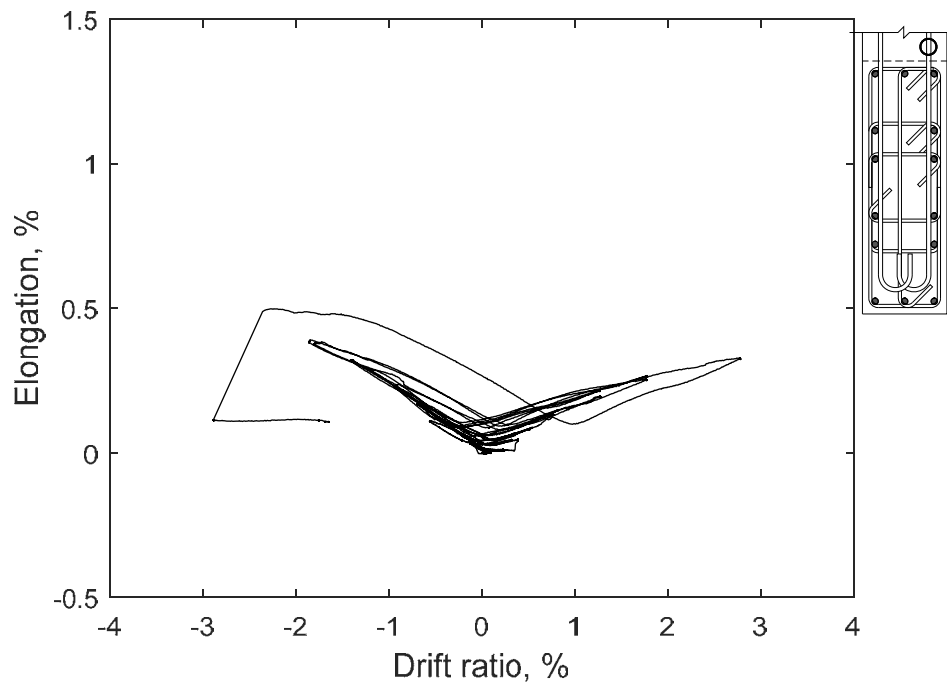


Figure 120 – Measured strain in horizontal bar at unconfined stem 52.5 in. (1330 mm) above base of T5

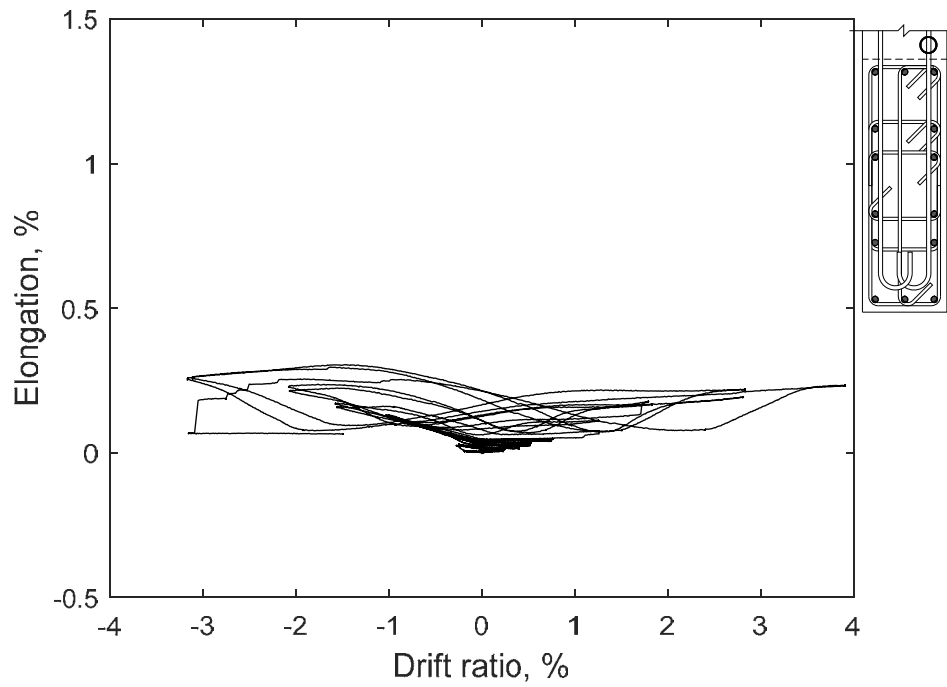
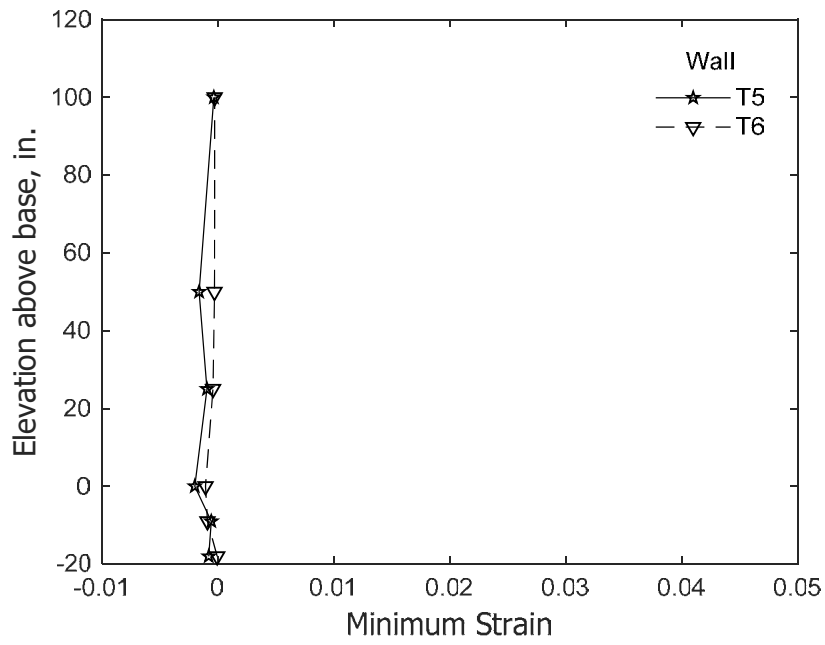
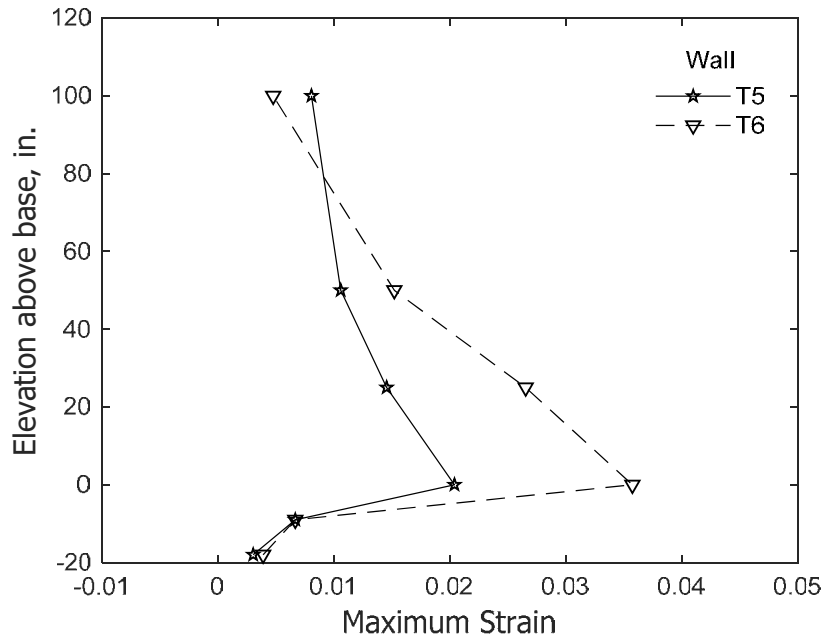


Figure 121 – Measured strain in horizontal bar at unconfined stem 52.5 in. (1330 mm) above base of T6

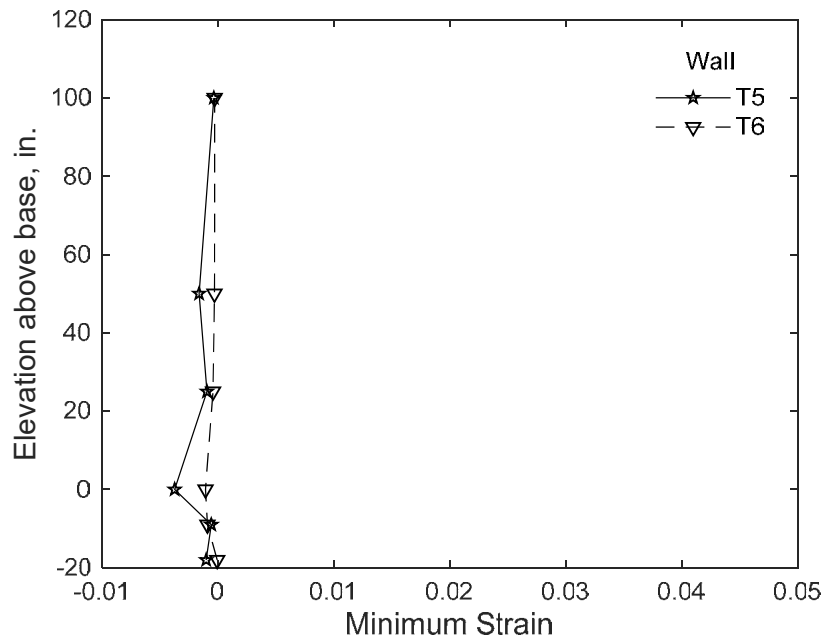


(a) Stem in compression

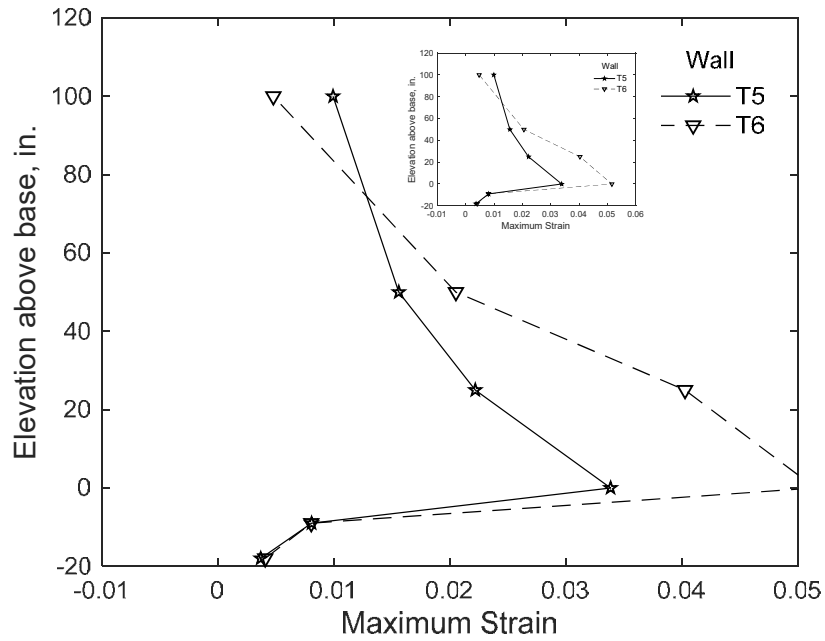


(b) Stem in tension

Figure 122 - Envelopes of measured strain in longitudinal bars at confined stem for 1.5% drift ratio

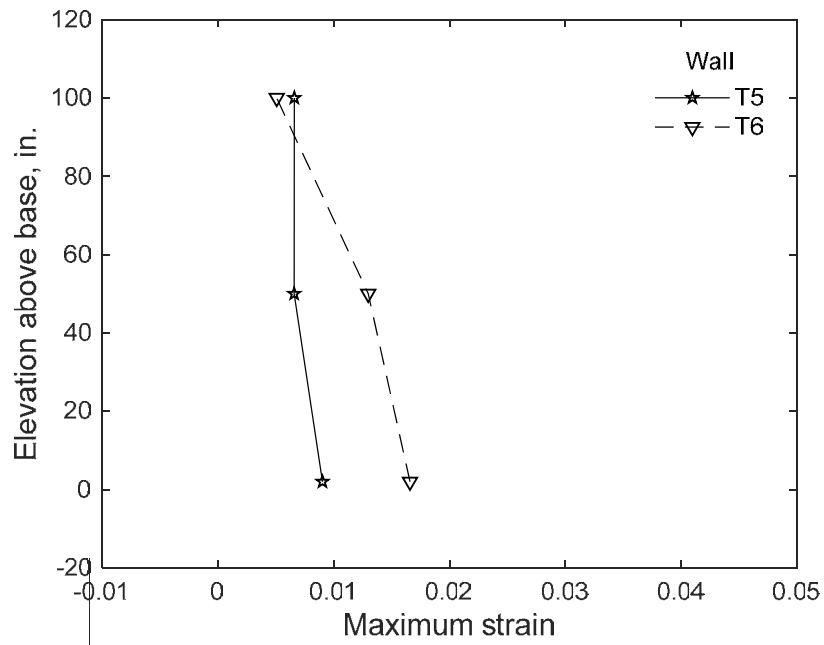


(a) Stem in compression

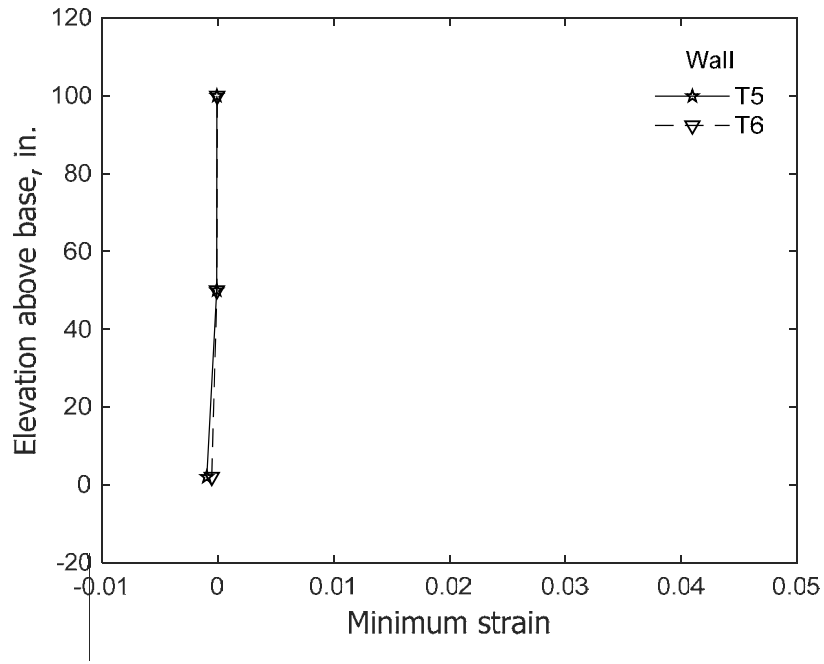


(b) Stem in tension

Figure 123 – Envelopes of measured strain in longitudinal bars at confined stem for 2% drift ratio

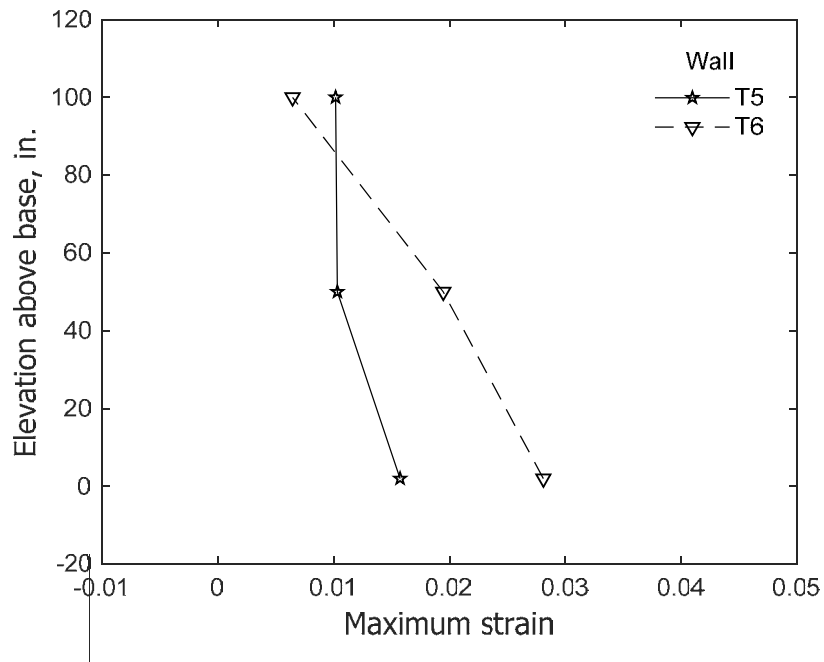


(a) Stem in compression

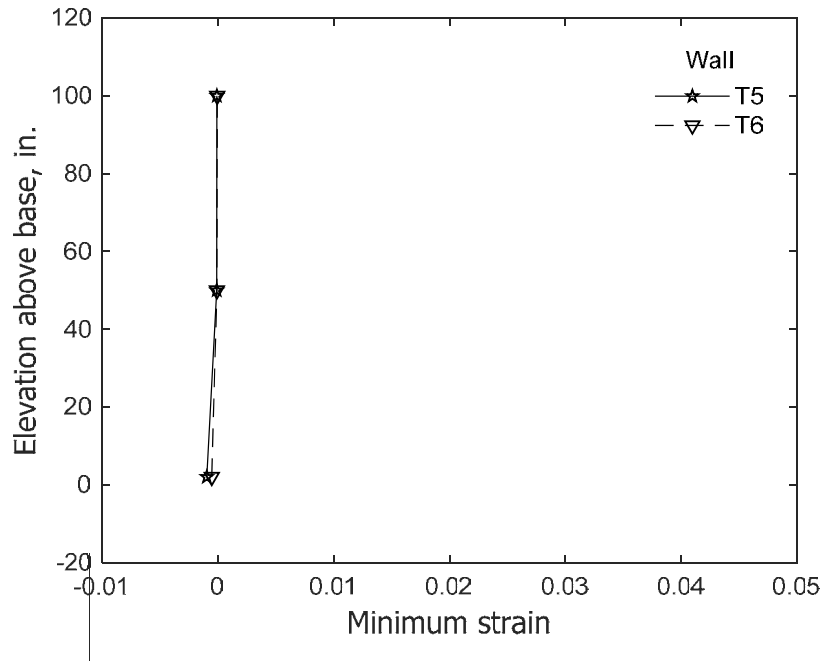


(b) Stem in tension

Figure 124 - Envelopes of measured strain in longitudinal bars at confined flange for 1.5% drift ratio

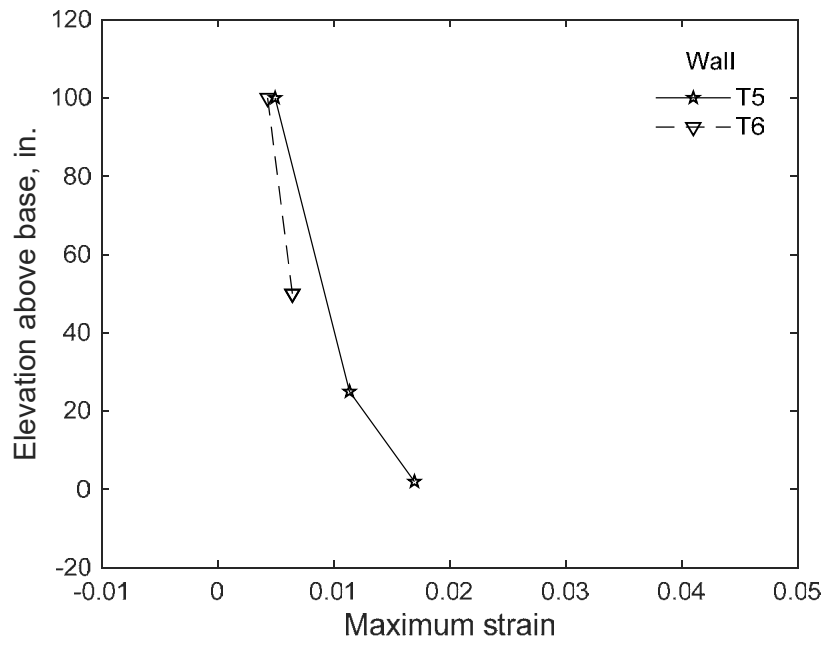


(a) Stem in compression

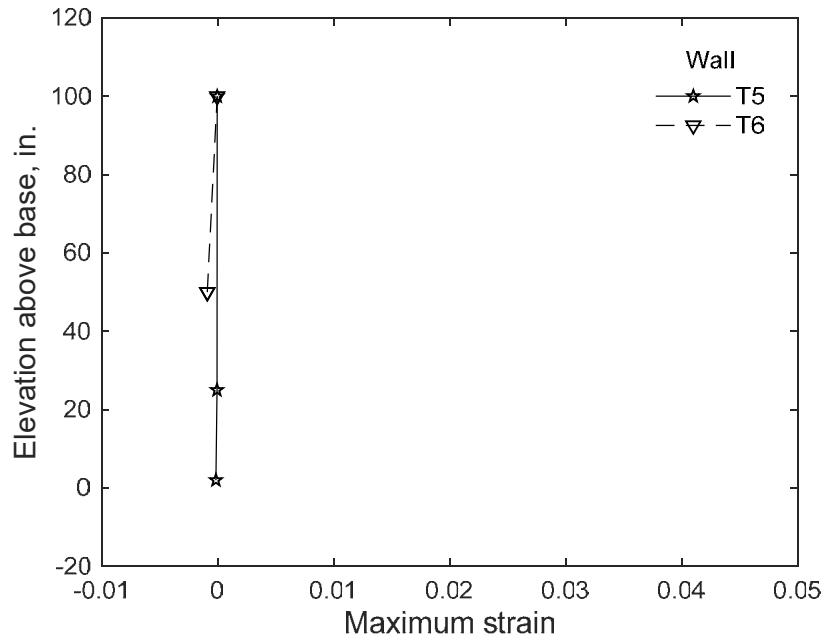


(b) Stem in tension

Figure 125 – Envelopes of measured strain in longitudinal bars at confined flange for 2% drift ratio

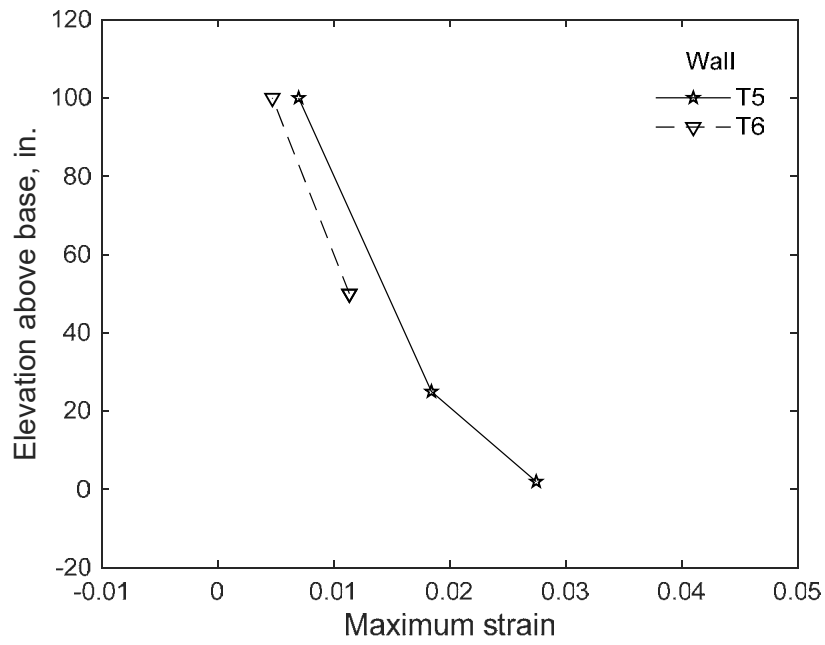


(a) Stem in compression

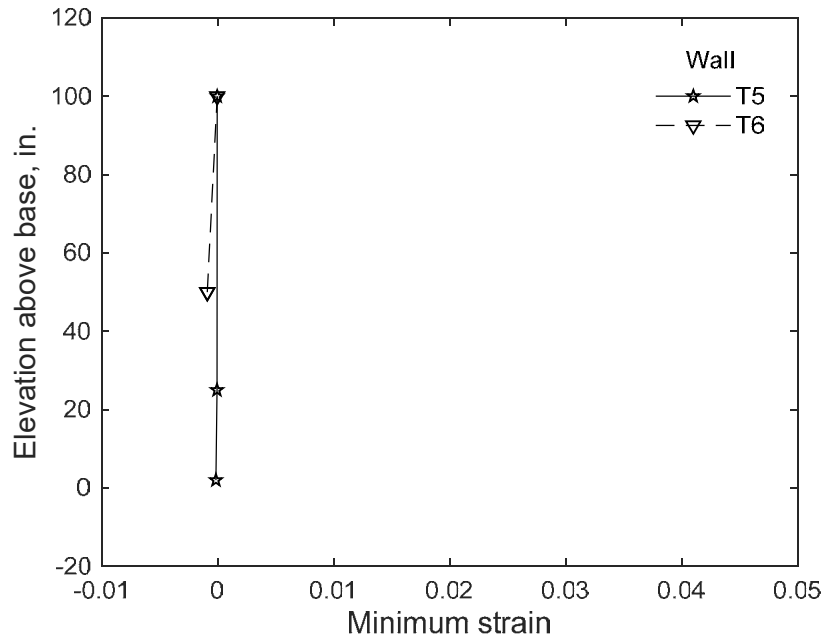


(b) Stem in tension

Figure 126 – Envelopes of measured strain in longitudinal bars at unconfined flange for 1.5% drift ratio

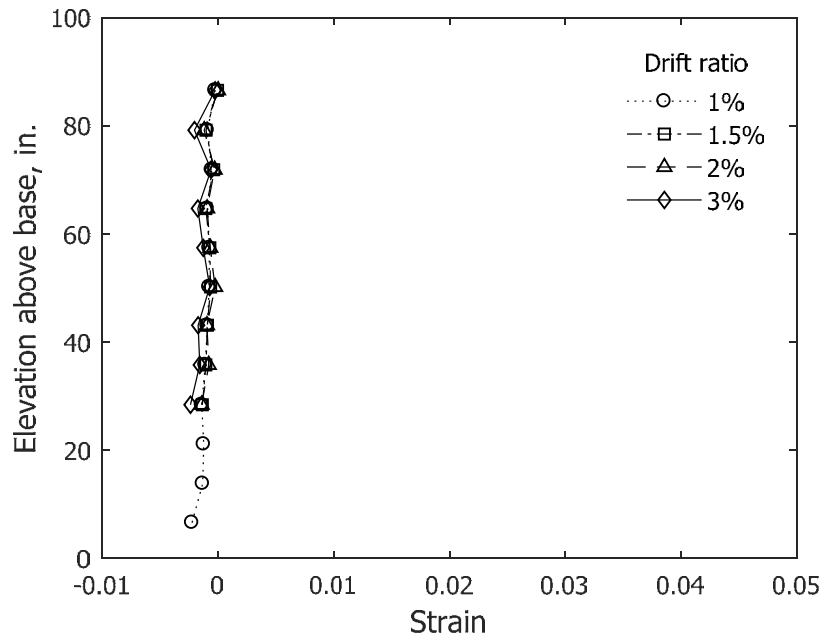


(a) Stem in compression

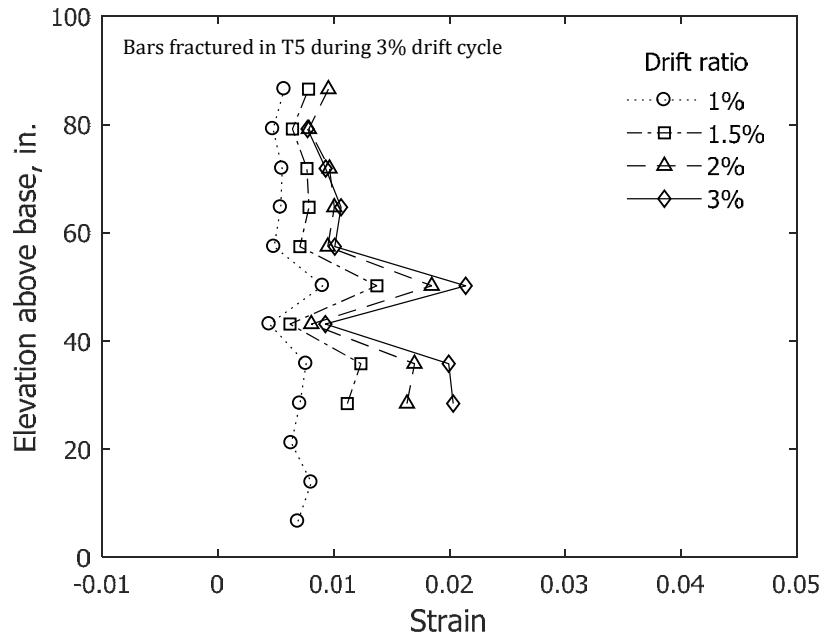


(b) Stem in tension

Figure 127 – Envelopes of measured strain in longitudinal bars at unconfined flange for 2% drift ratio

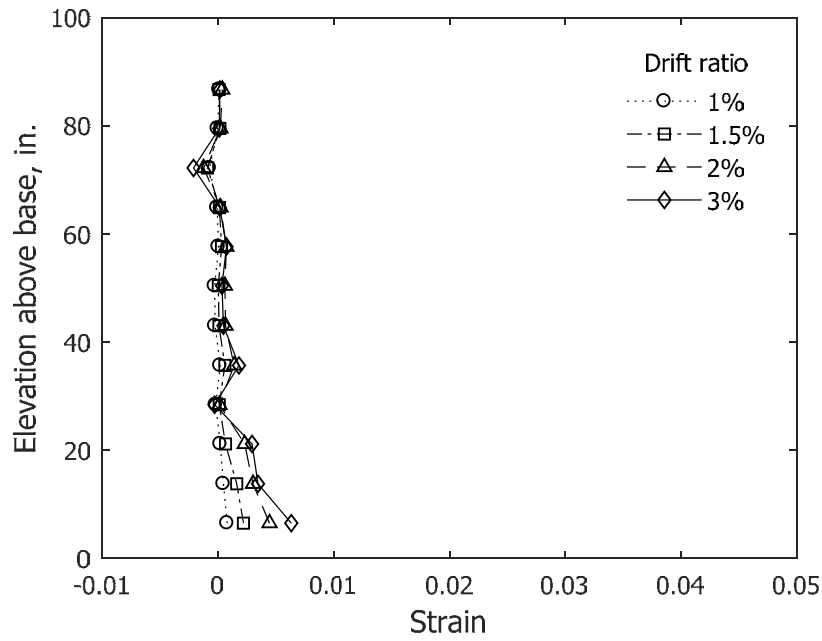


(a) Stem in compression

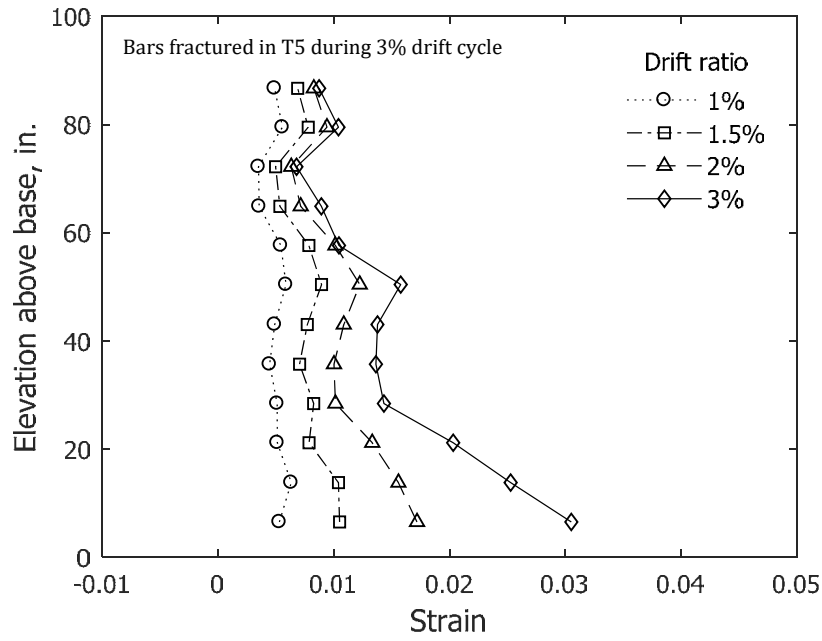


(b) Stem in tension

Figure 128 – Calculated average concrete strain along Column 1 for stem of T5 (1 in. = 25.4 mm)

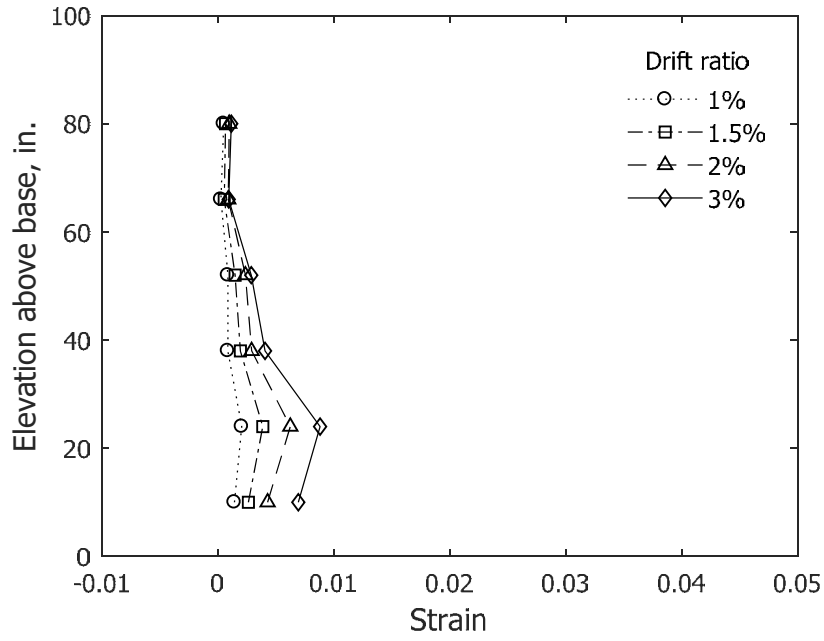


(a) Stem in compression

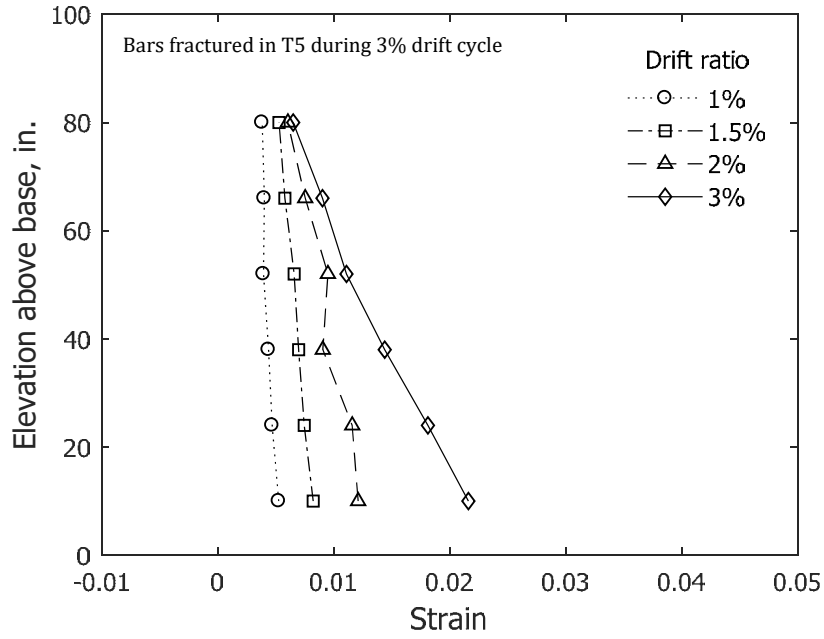


(b) Stem in tension

Figure 129 – Calculated average concrete strain along Column 2 for stem of T5 (1 in. = 25.4 mm)

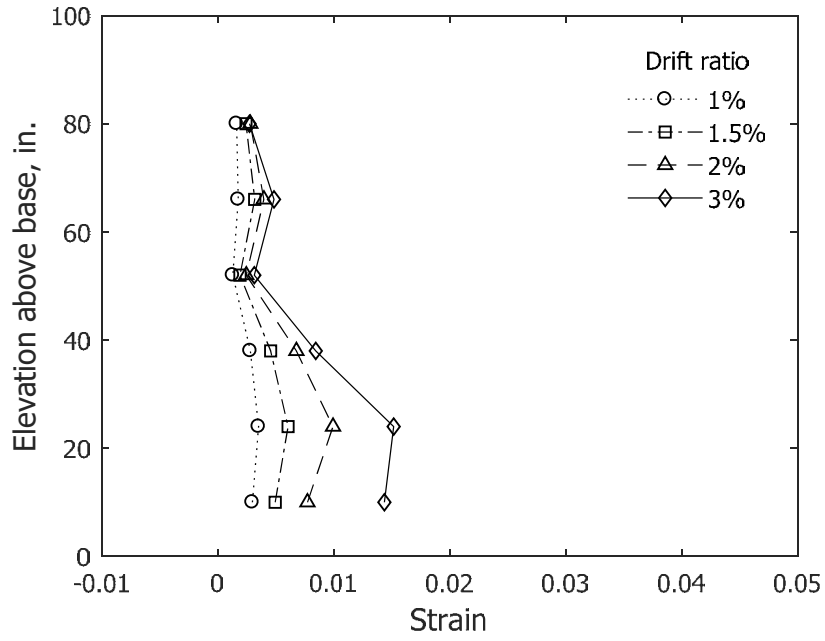


(a) Stem in compression

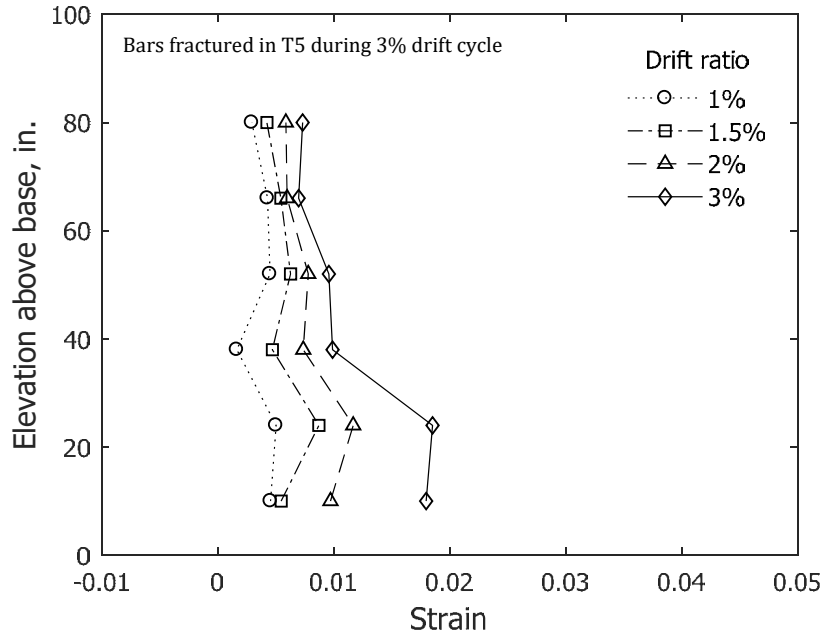


(b) Stem in tension

Figure 130 – Calculated average concrete strain along Column 3 for stem of T5 (1 in. = 25.4 mm)

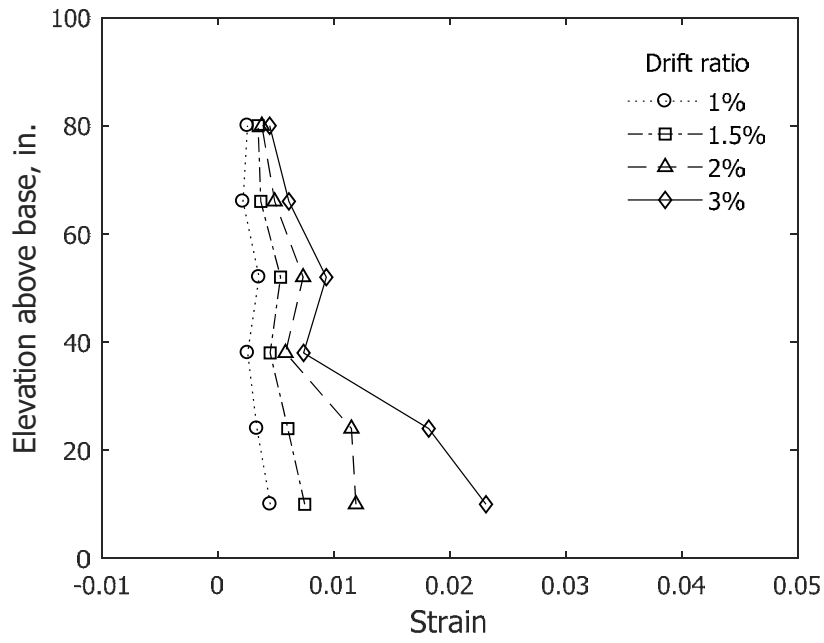


(a) Stem in compression

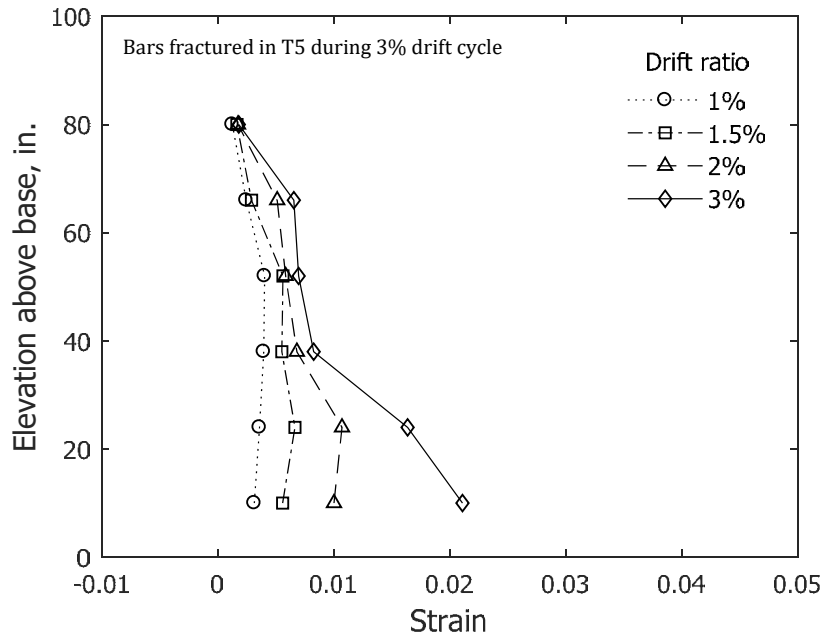


(b) Stem in tension

Figure 131 – Calculated average concrete strain along Column 4 for stem of T5 (1 in. = 25.4 mm)

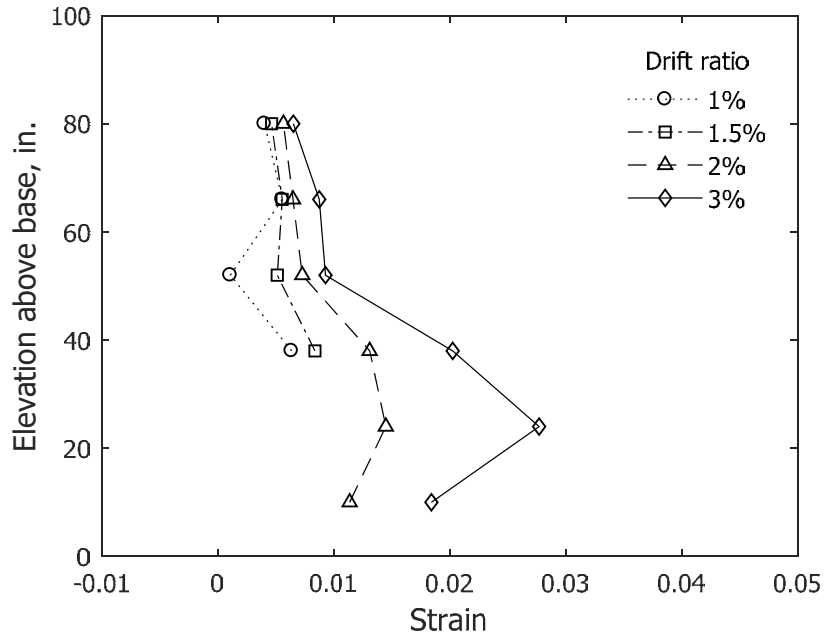


(a) Stem in compression

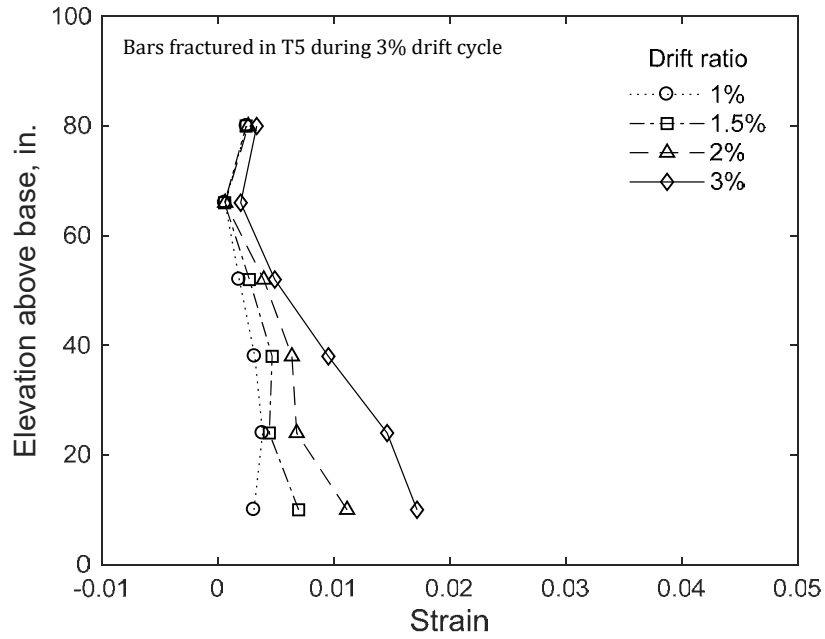


(b) Stem in tension

Figure 132 – Calculated average concrete strain along Column 5 for stem of T5 (1 in. = 25.4 mm)

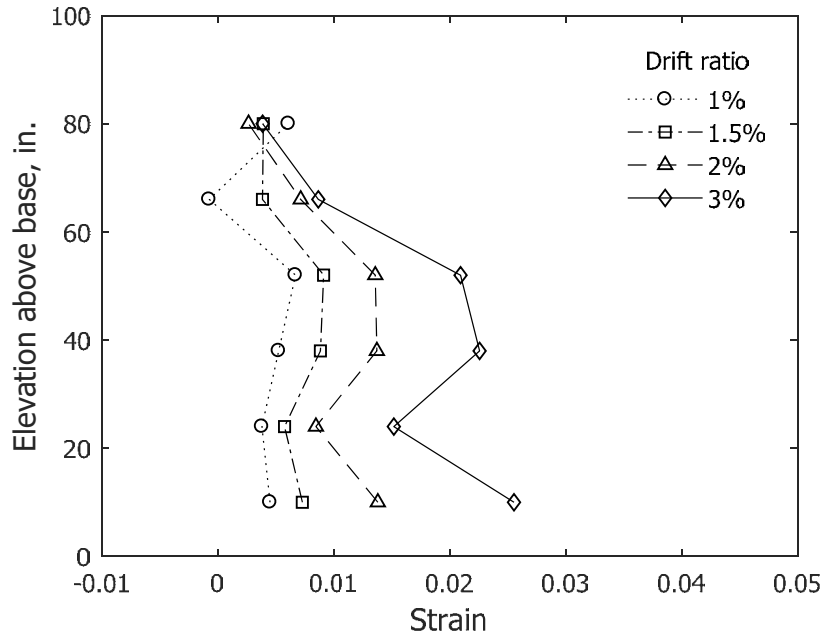


(a) Stem in compression

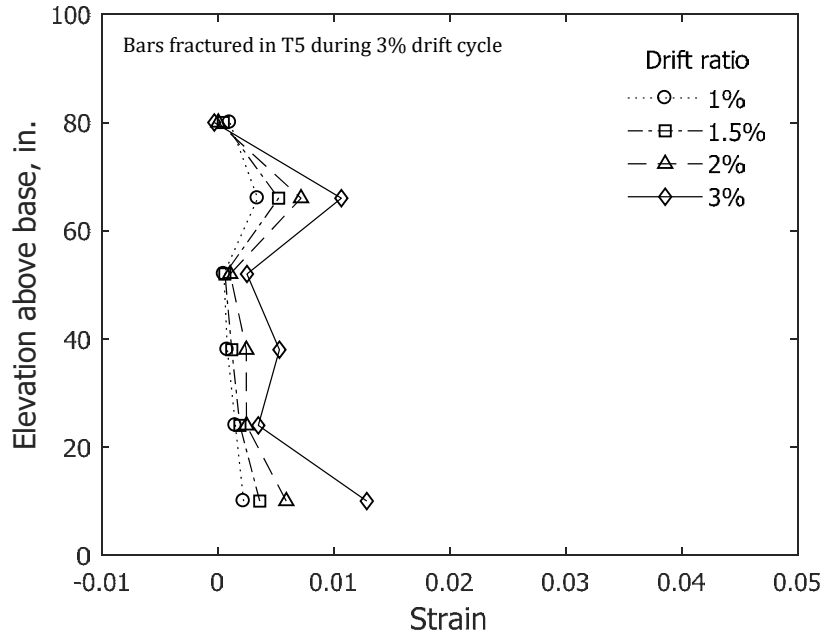


(b) Stem in tension

Figure 133 – Calculated average concrete strain along Column 6 for stem of T5 (1 in. = 25.4 mm)

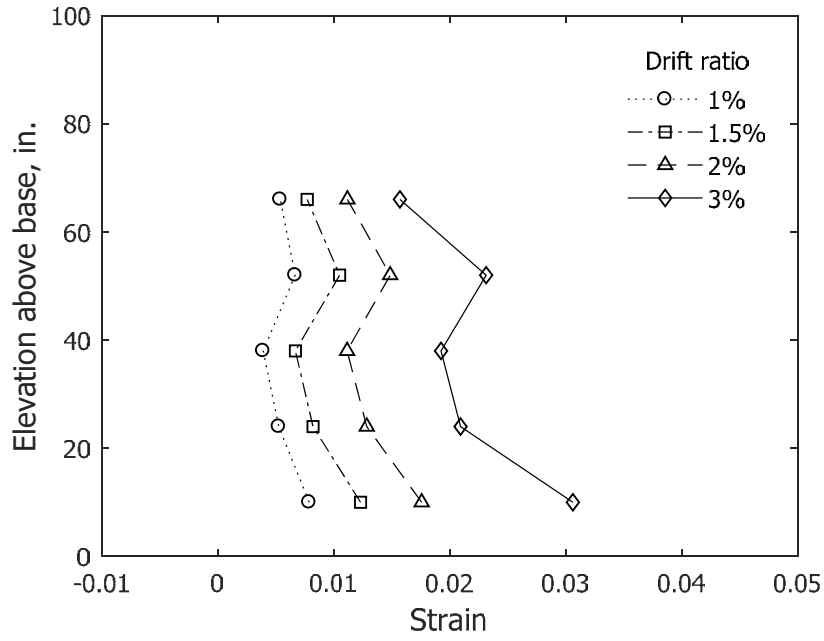


(a) Stem in compression

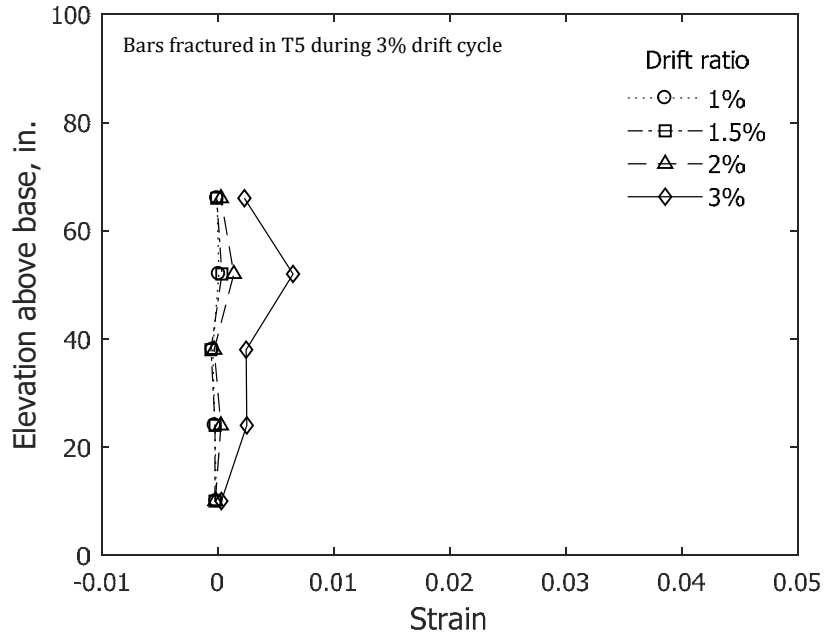


(b) Stem in tension

Figure 134 – Calculated average concrete strain along Column 7 for stem of T5 (1 in. = 25.4 mm)

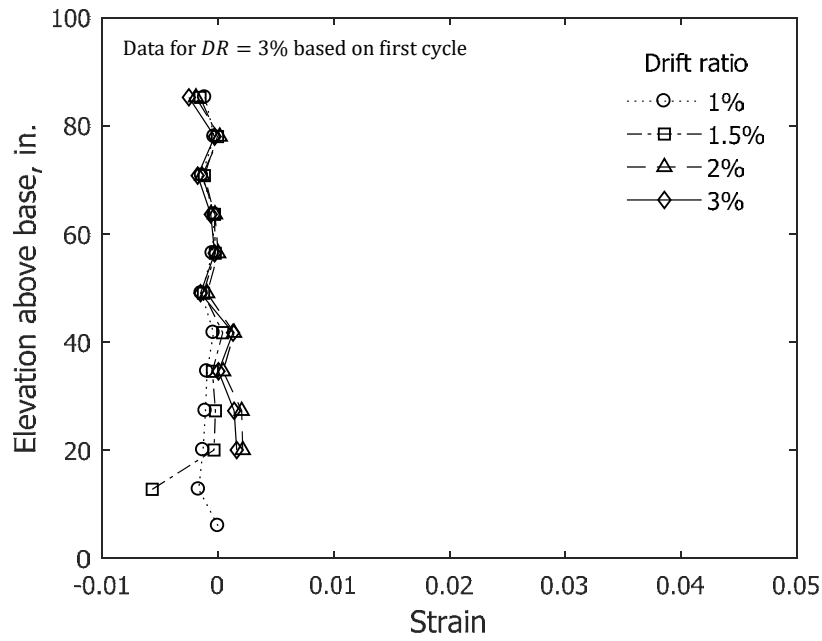


(a) Stem in compression

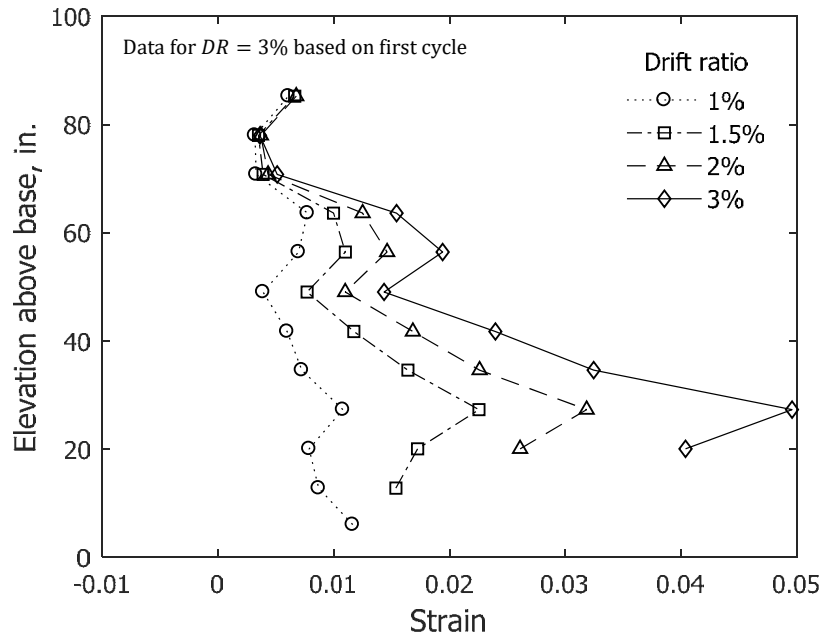


(b) Stem in tension

Figure 135 – Calculated average concrete strain along Column 8 for stem of T5 (1 in. = 25.4 mm)

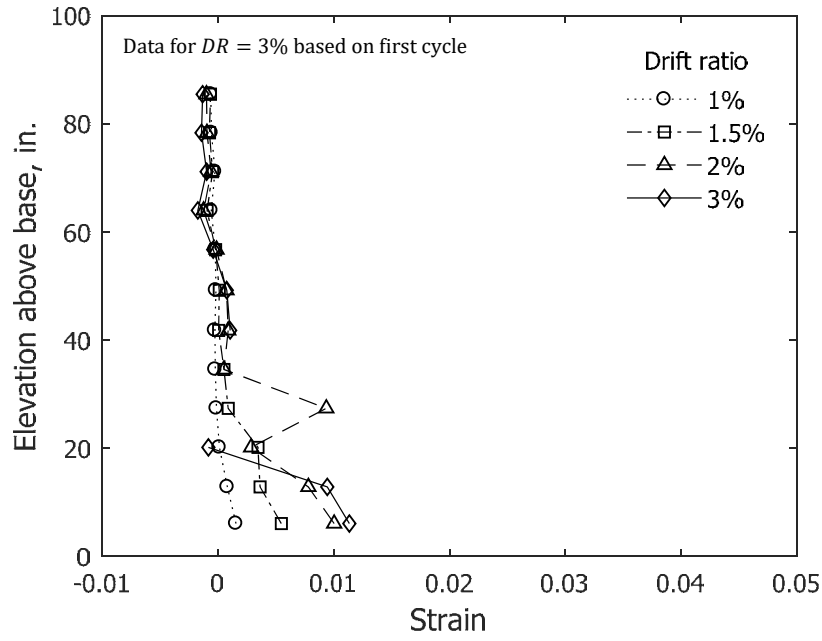


(a) Stem in compression

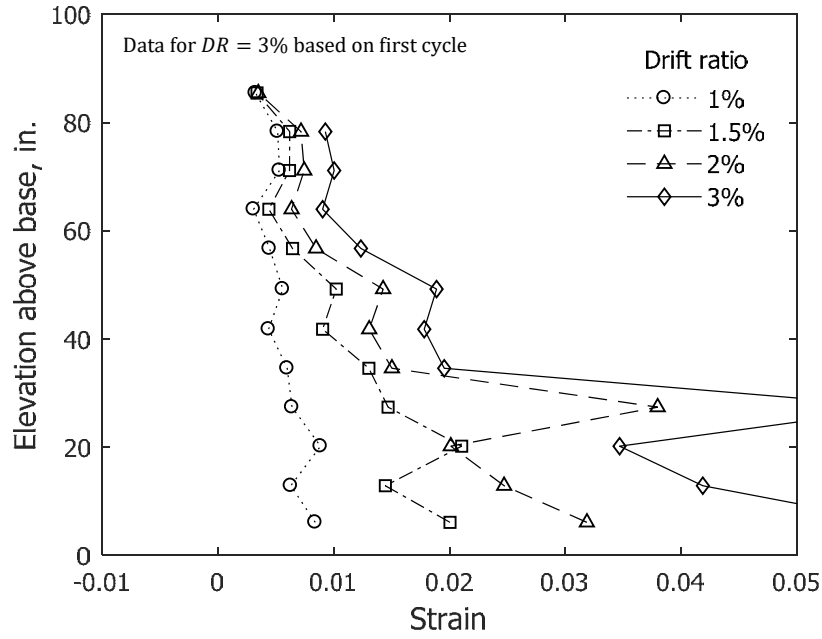


(b) Stem in tension

Figure 136 – Calculated average concrete strain along Column 1 for stem of T6 (1 in. = 25.4 mm)

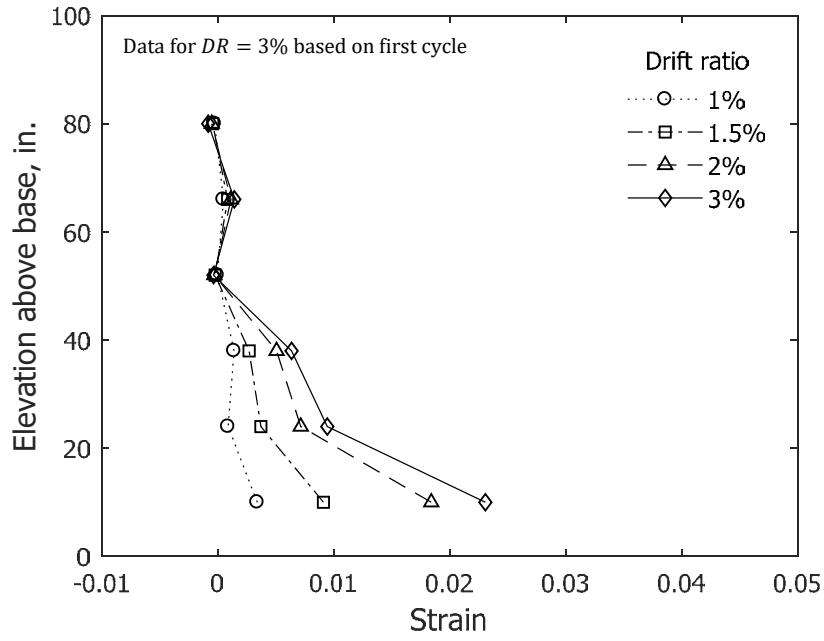


(a) Stem in compression

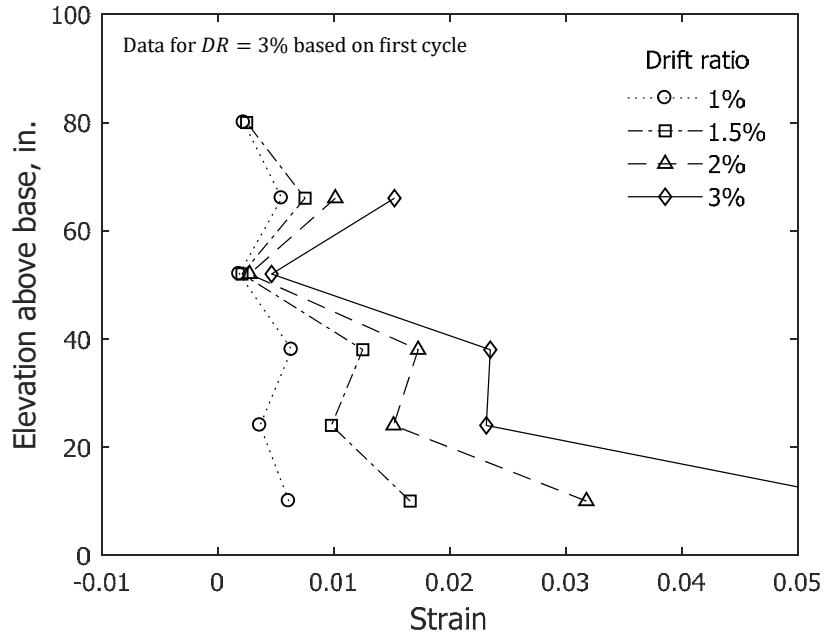


(b) Stem in tension

Figure 137 – Calculated average concrete strain along Column 2 for stem of T6 (1 in. = 25.4 mm)

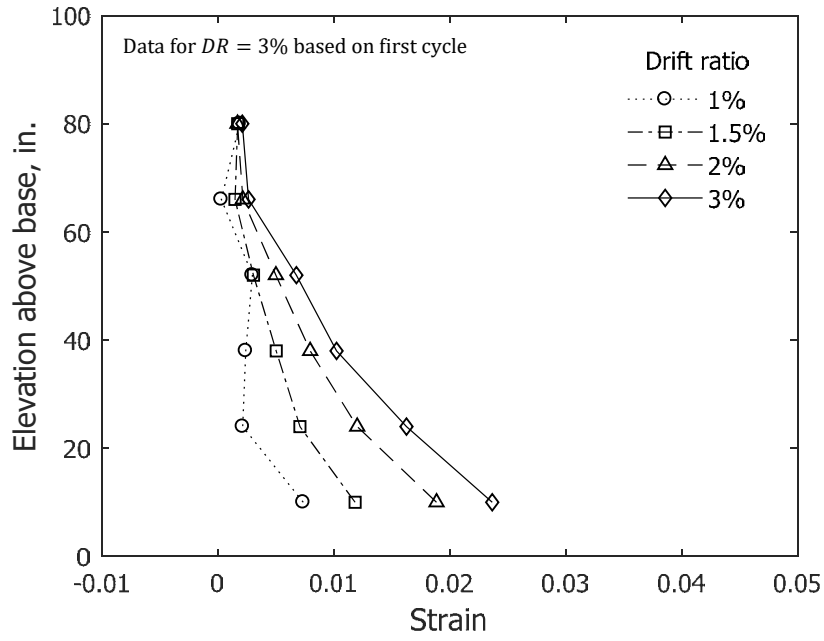


(a) Stem in compression

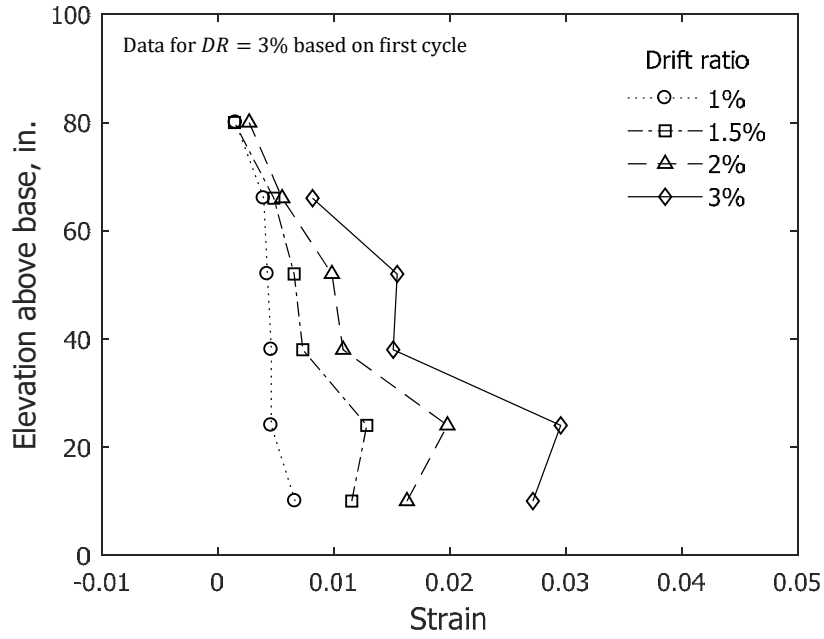


(b) Stem in tension

Figure 138 – Calculated average concrete strain along Column 3 for stem of T6 (1 in. = 25.4 mm)

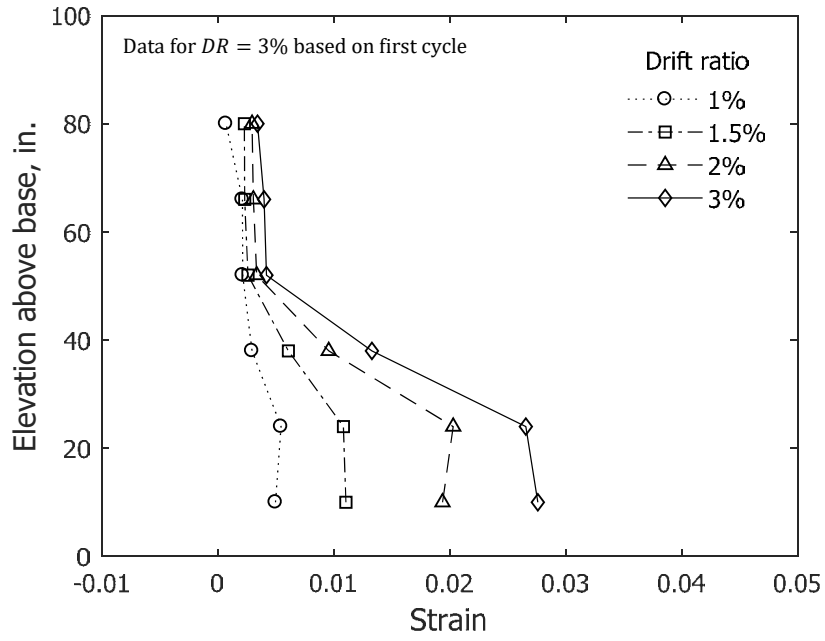


(a) Stem in compression

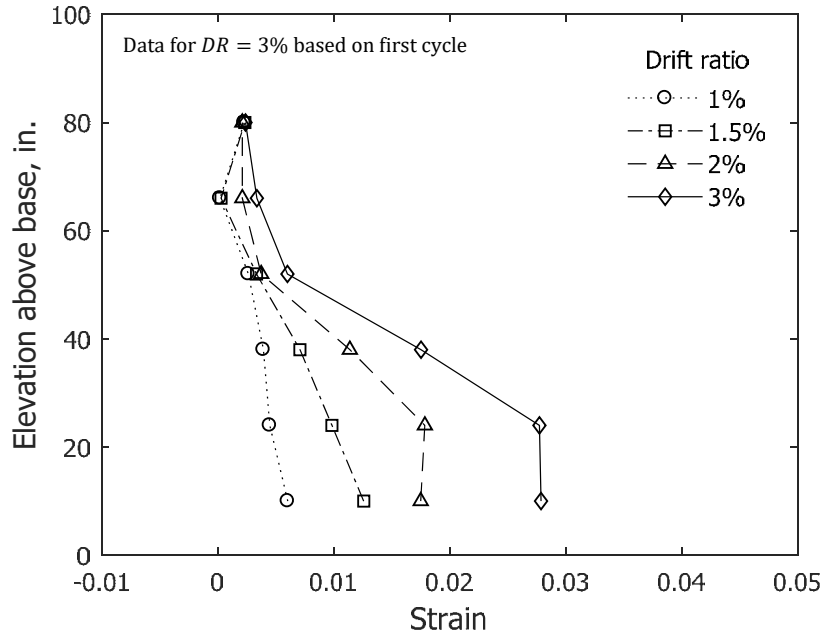


(b) Stem in tension

Figure 139 – Calculated average concrete strain along Column 4 for stem of T6 (1 in. = 25.4 mm)

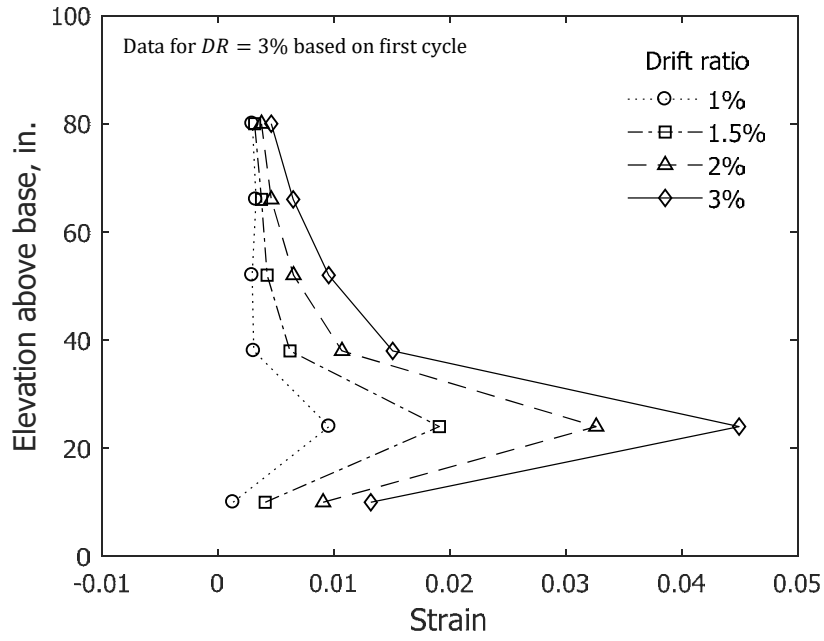


(a) Stem in compression

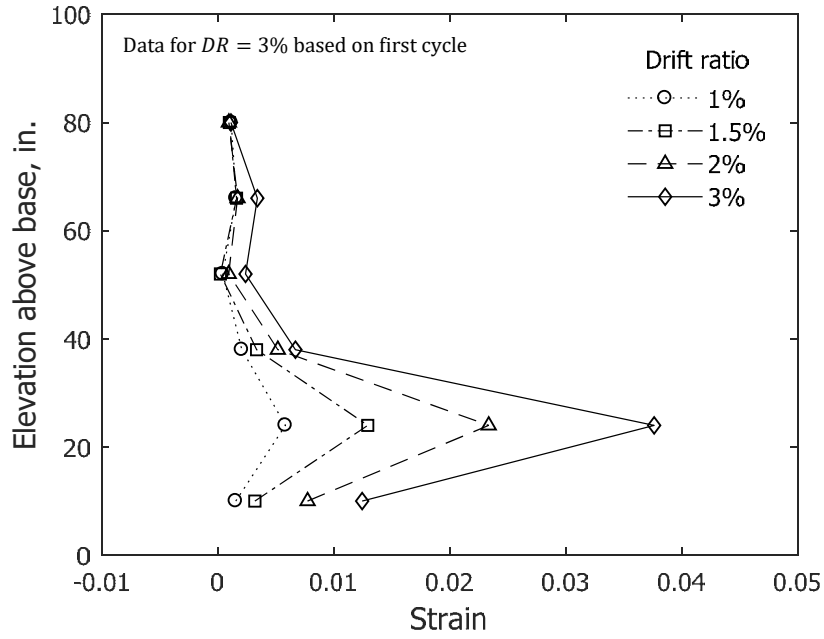


(b) Stem in tension

Figure 140 – Calculated average concrete strain along Column 5 for stem of T6 (1 in. = 25.4 mm)

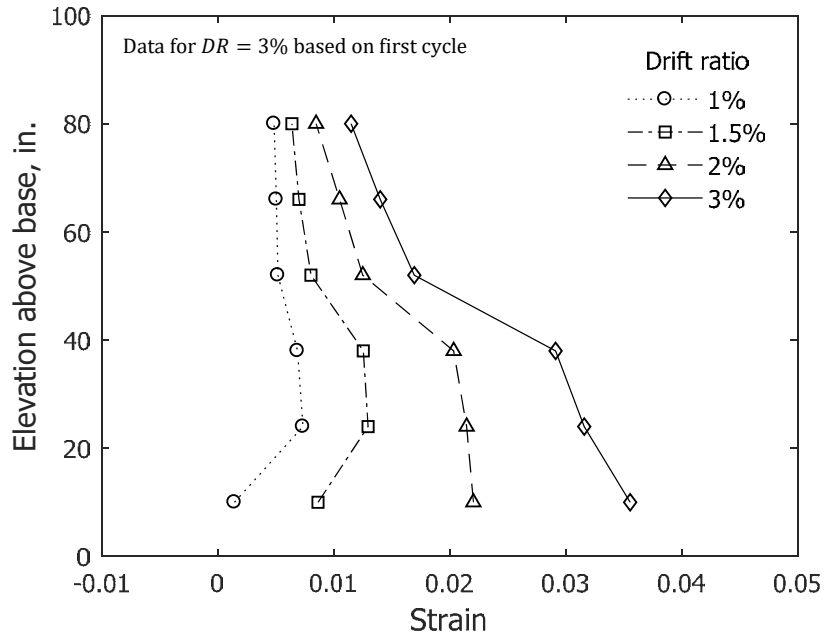


(a) Stem in compression

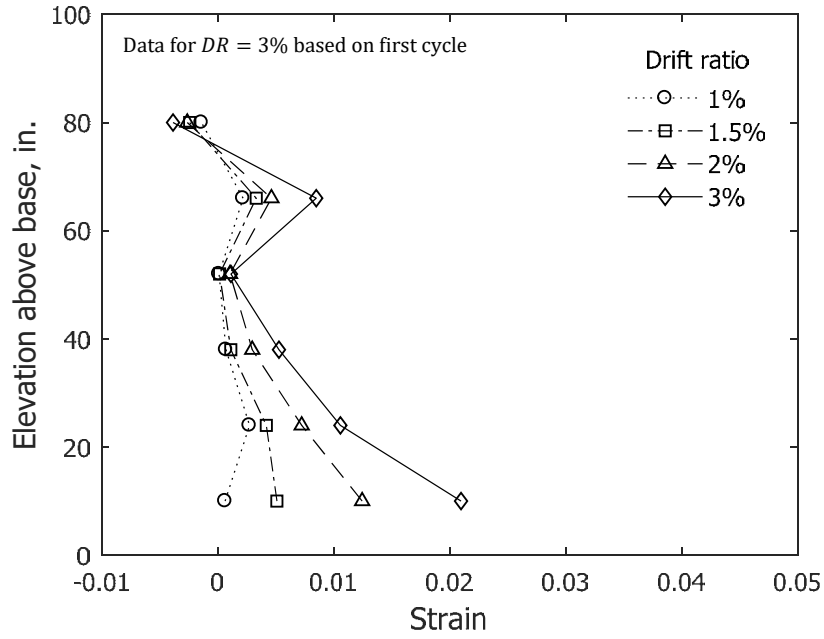


(b) Stem in tension

Figure 141 – Calculated average concrete strain along Column 6 for stem of T6 (1 in. = 25.4 mm)

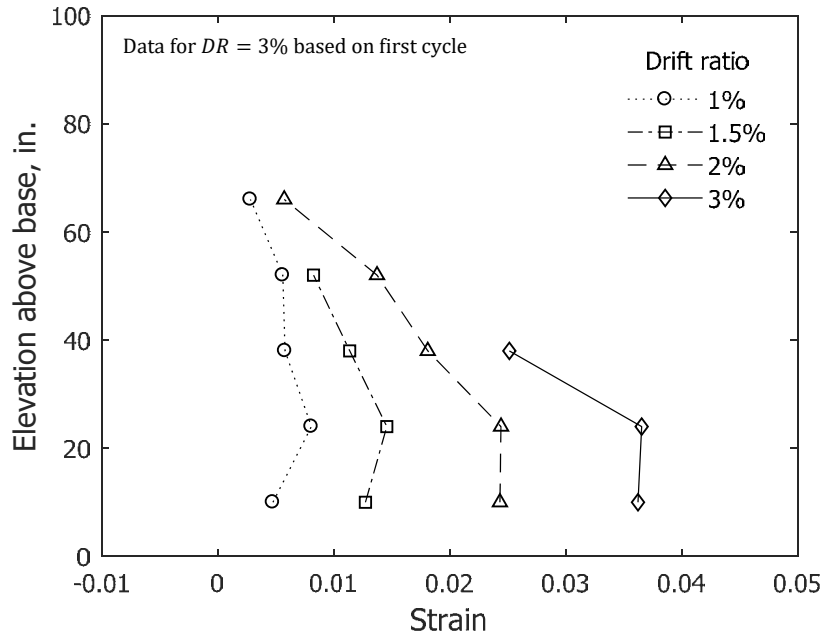


(c) Stem in compression

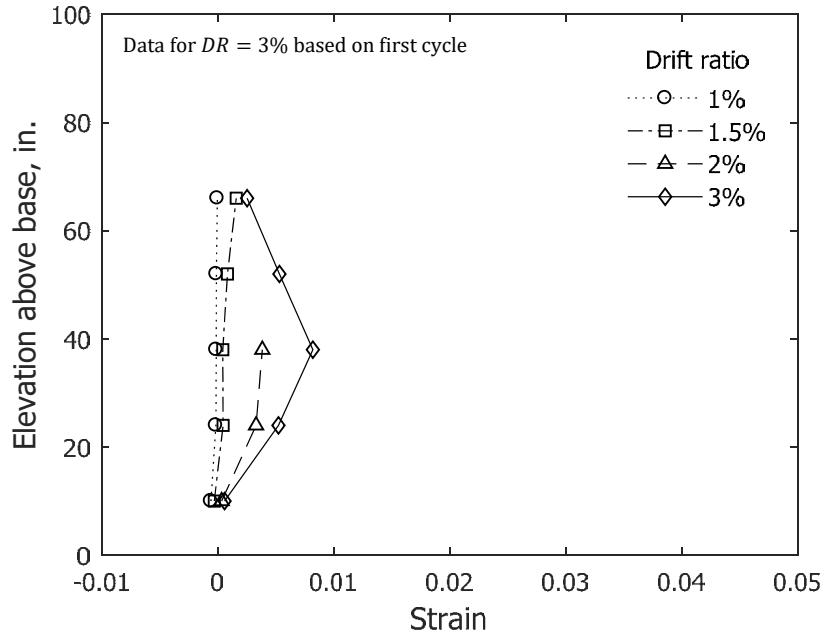


(d) Stem in tension

Figure 142 – Calculated average concrete strain along Column 7 for stem of T6 (1 in. = 25.4 mm)

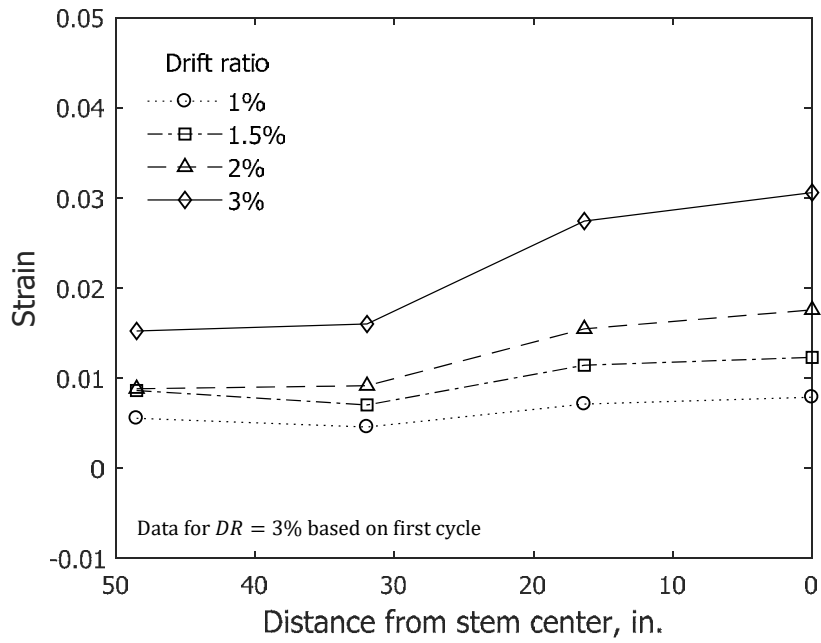


(a) Stem in compression

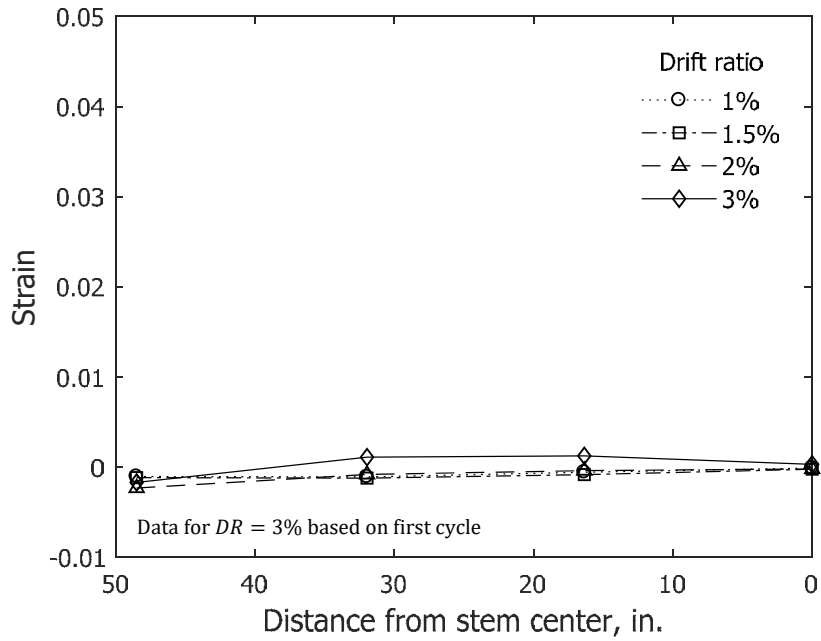


(b) Stem in tension

Figure 143 – Calculated average concrete strain along Column 8 for stem of T6 (1 in. = 25.4 mm)

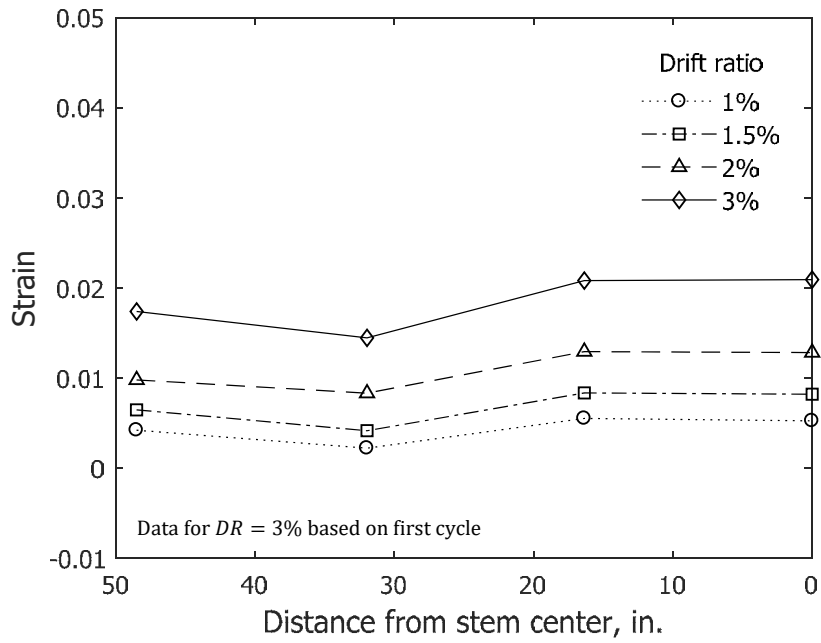


(a) Stem in compression

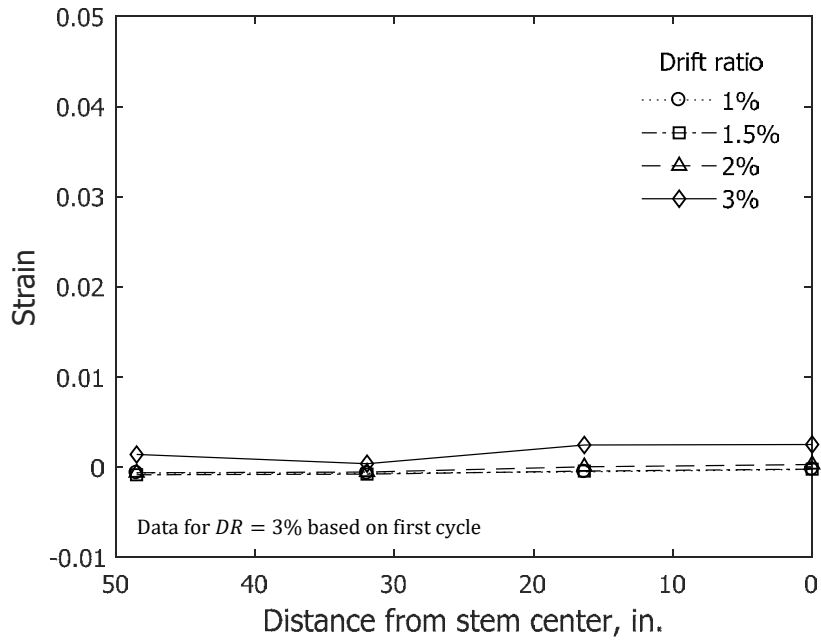


(b) Stem in tension

Figure 144 – Calculated average concrete strain in Layer 1 for flange of T5 (1 in. = 25.4 mm)

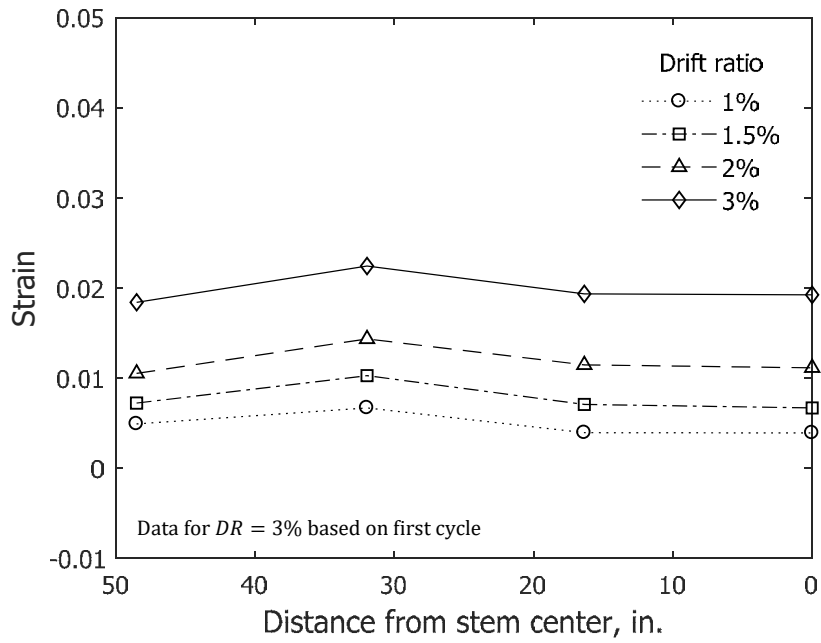


(a) Stem in compression

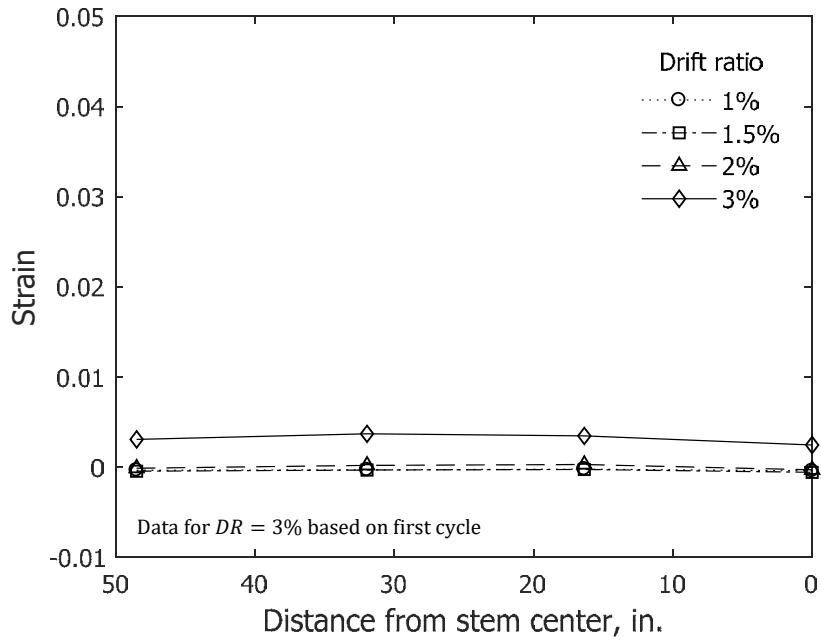


(b) Stem in tension

Figure 145 – Calculated average concrete strain in Layer 2 for flange of T5 (1 in. = 25.4 mm)

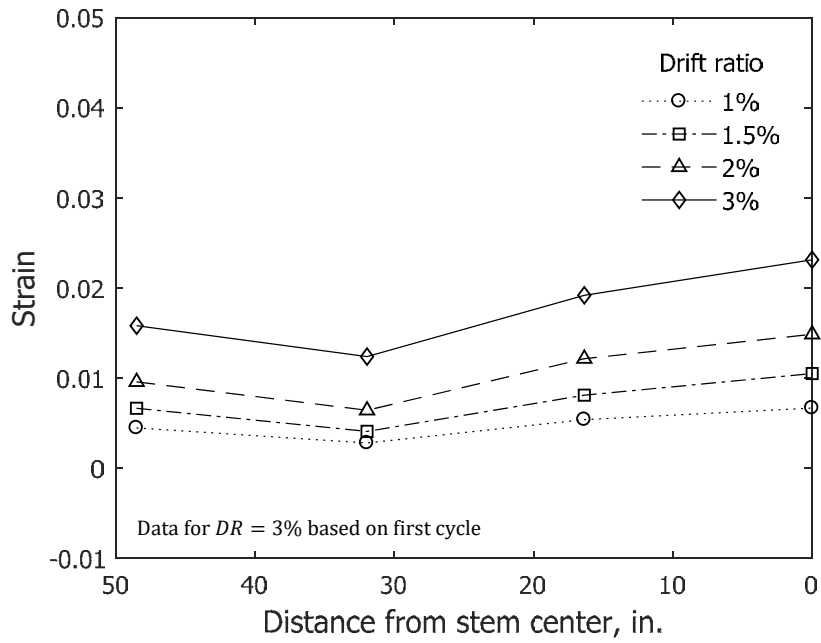


(a) Stem in compression

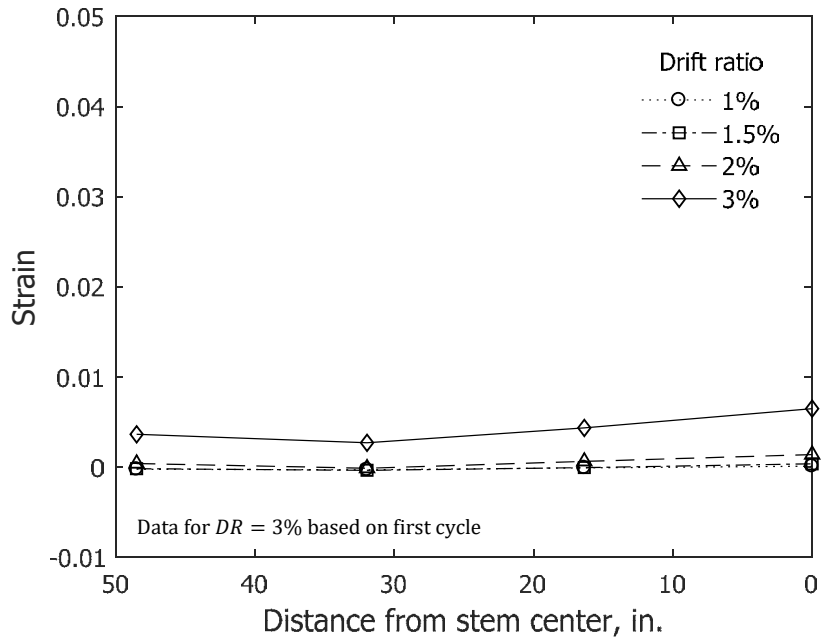


(b) Stem in tension

Figure 146 – Calculated average concrete strain in Layer 3 for flange of T5 (1 in. = 25.4 mm)

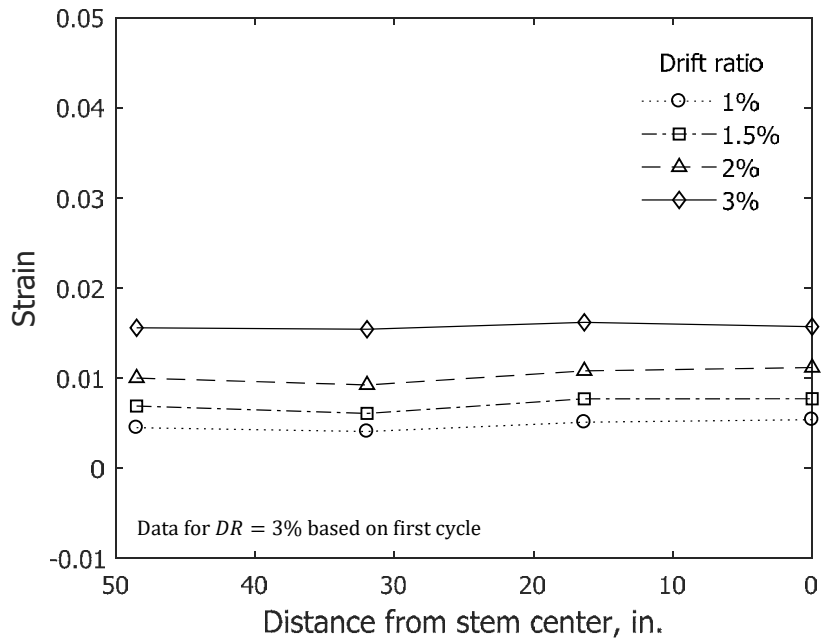


(a) Stem in compression

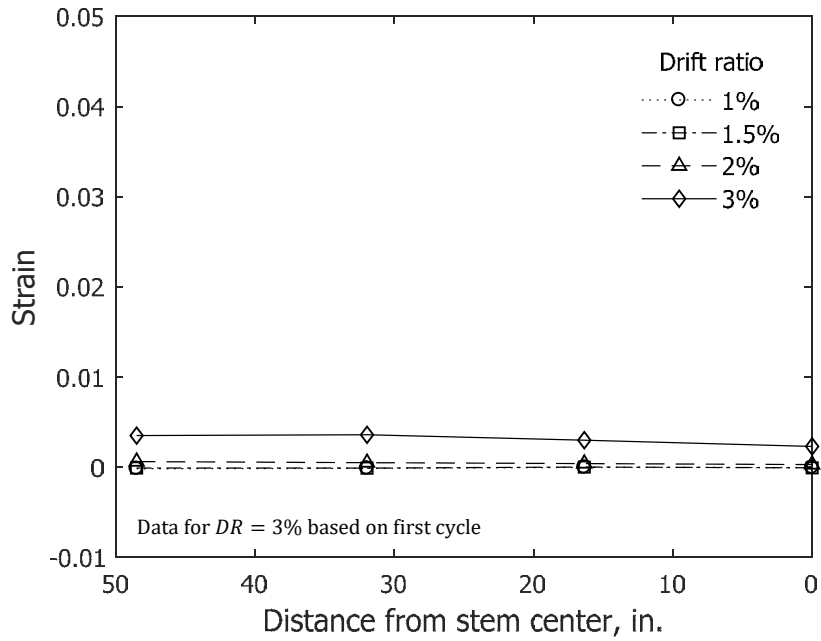


(b) Stem in tension

Figure 147 – Calculated average concrete strain in Layer 4 for flange of T5 (1 in. = 25.4 mm)

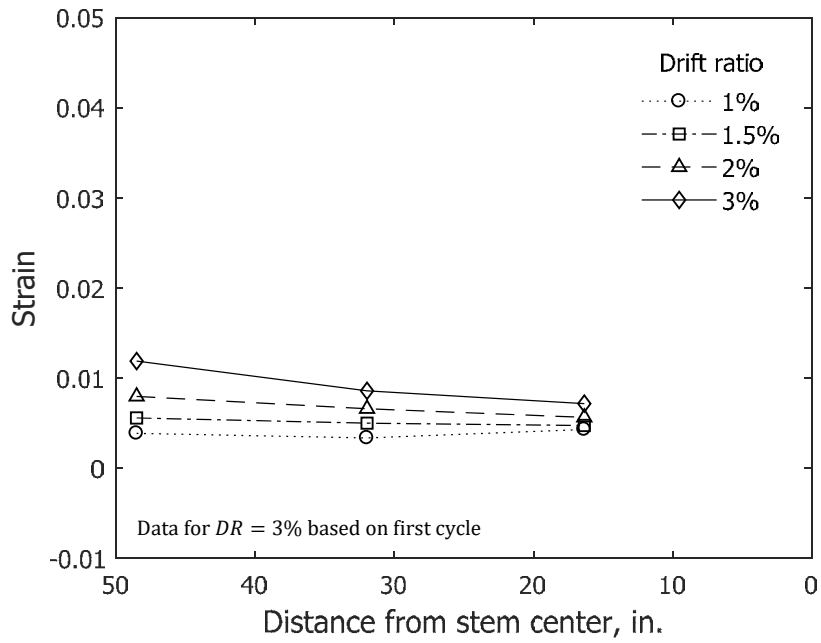


(a) Stem in compression

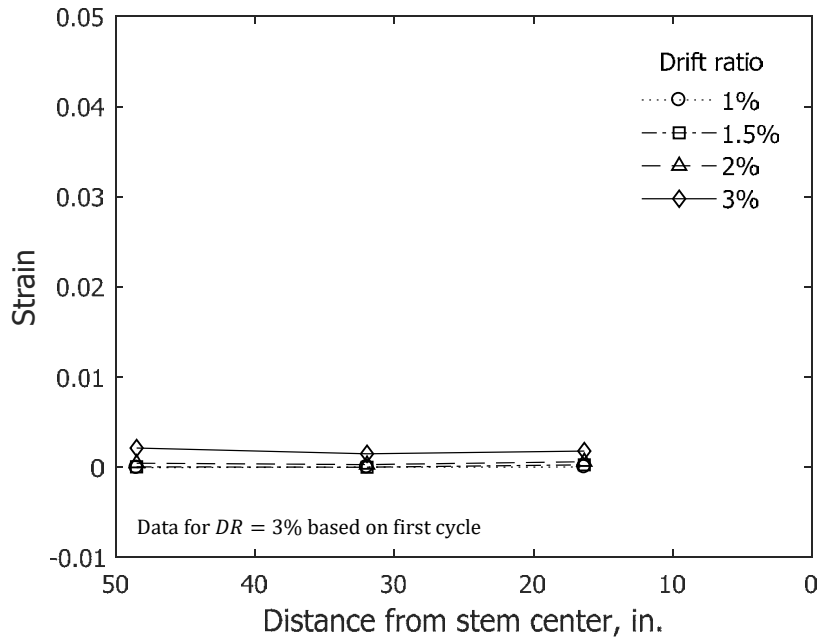


(b) Stem in tension

Figure 148 – Calculated average concrete strain in Layer 5 for flange of T5 (1 in. = 25.4 mm)

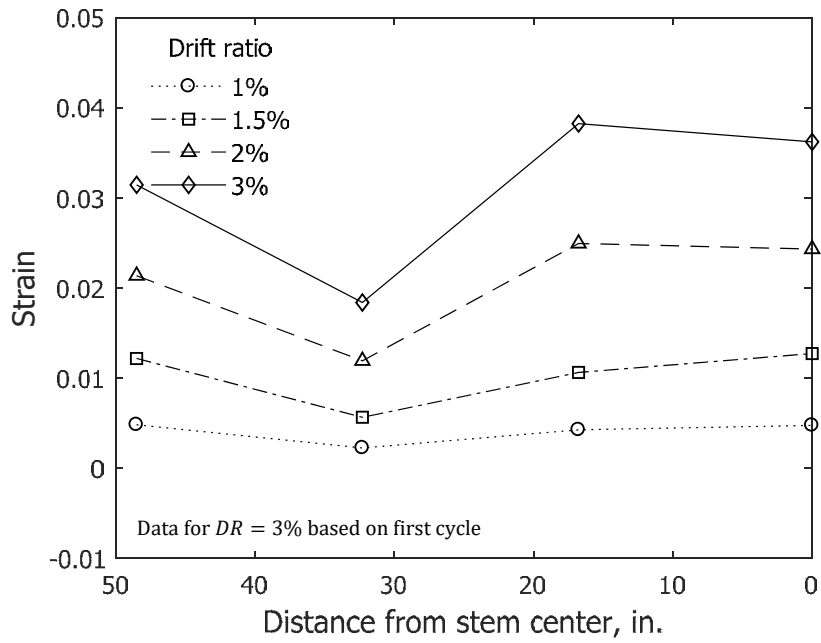


(a) Stem in compression

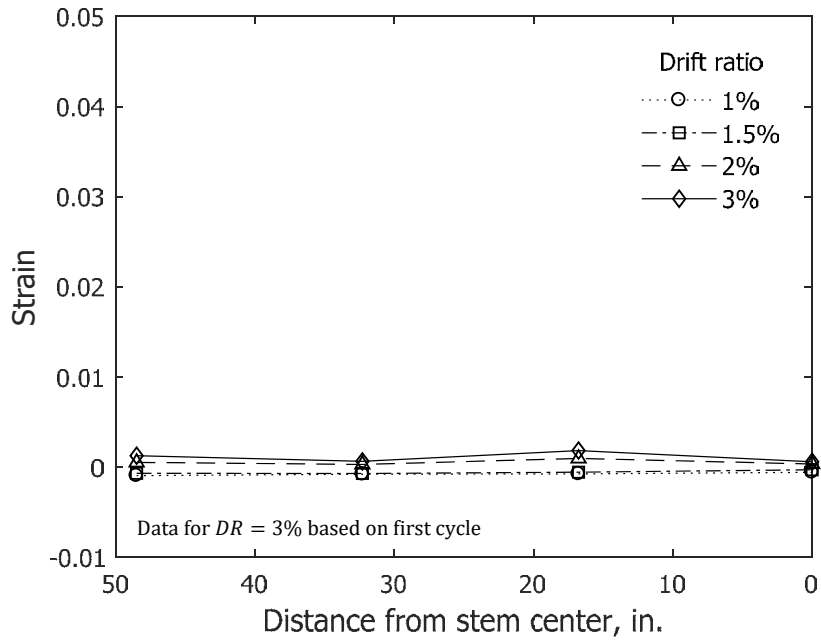


(b) Stem in tension

Figure 149 – Calculated average concrete strain in Layer 6 for flange of T5 (1 in. = 25.4 mm)

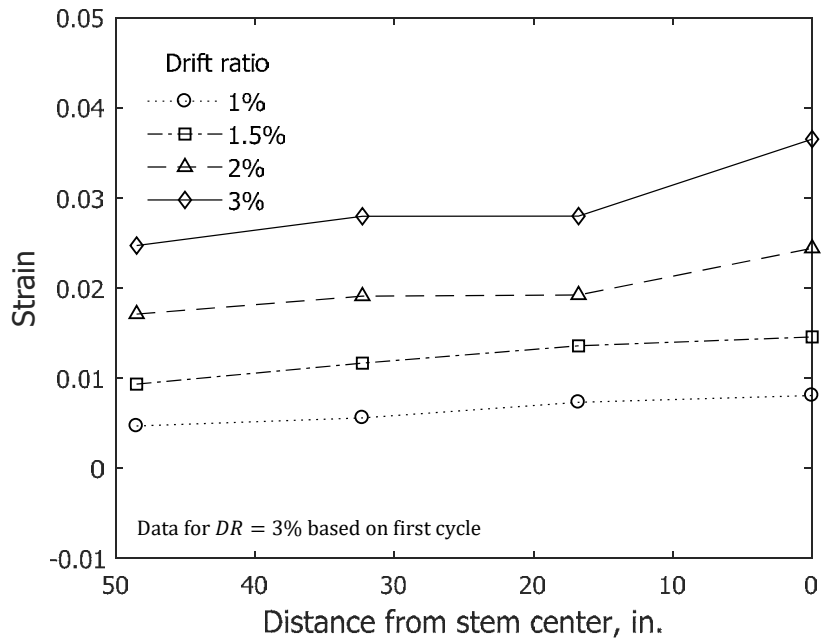


(a) Stem in compression

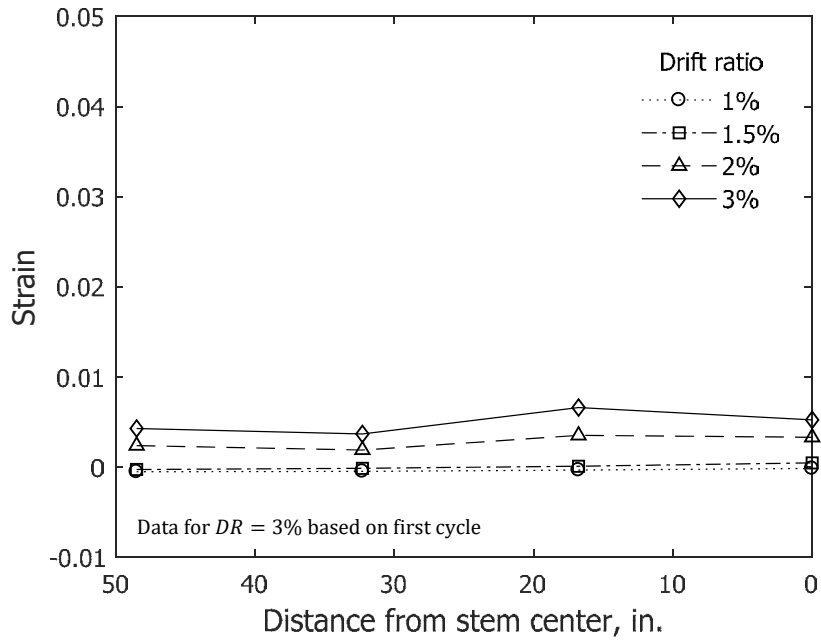


(b) Stem in tension

Figure 150 – Calculated average concrete strain in Layer 1 for flange of T6 (1 in. = 25.4 mm)

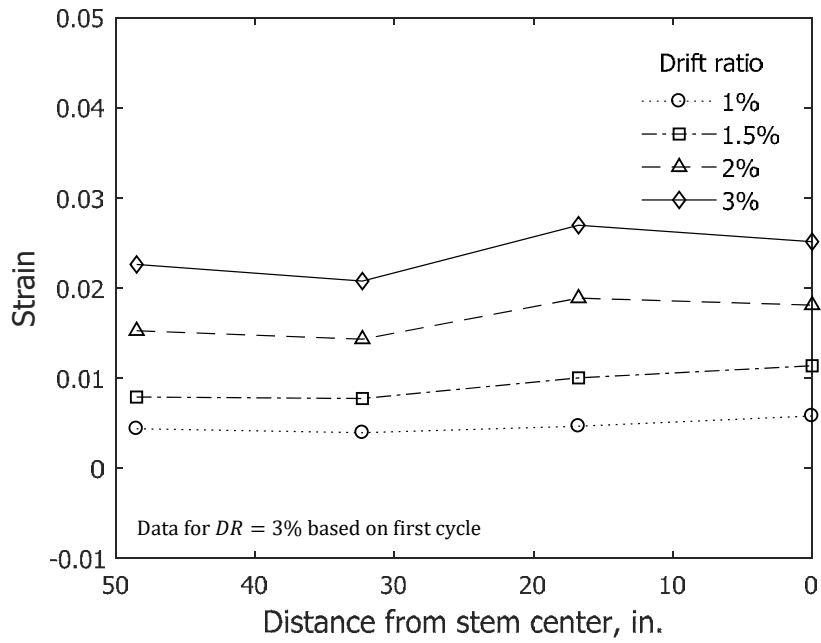


(a) Stem in compression

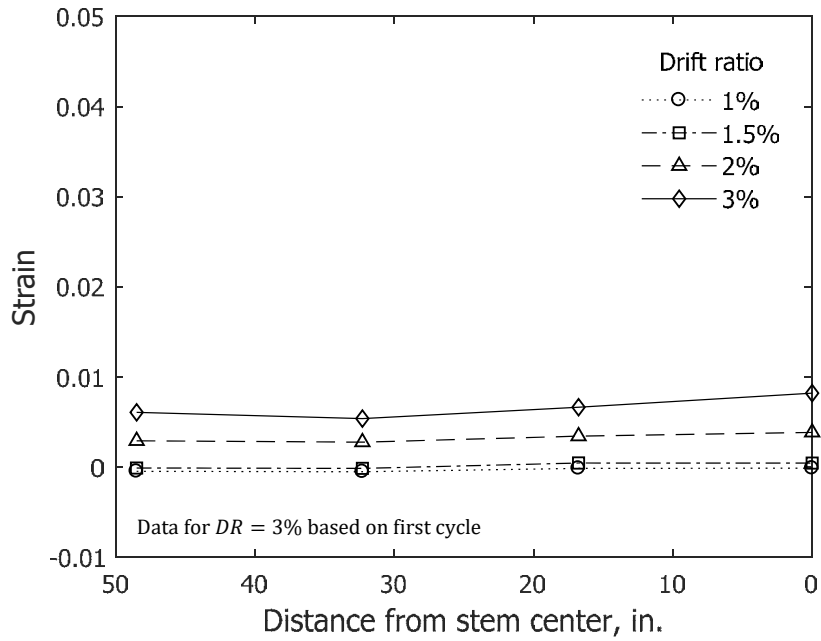


(b) Stem in tension

Figure 151 – Calculated average concrete strain in Layer 2 for flange of T6 (1 in. = 25.4 mm)

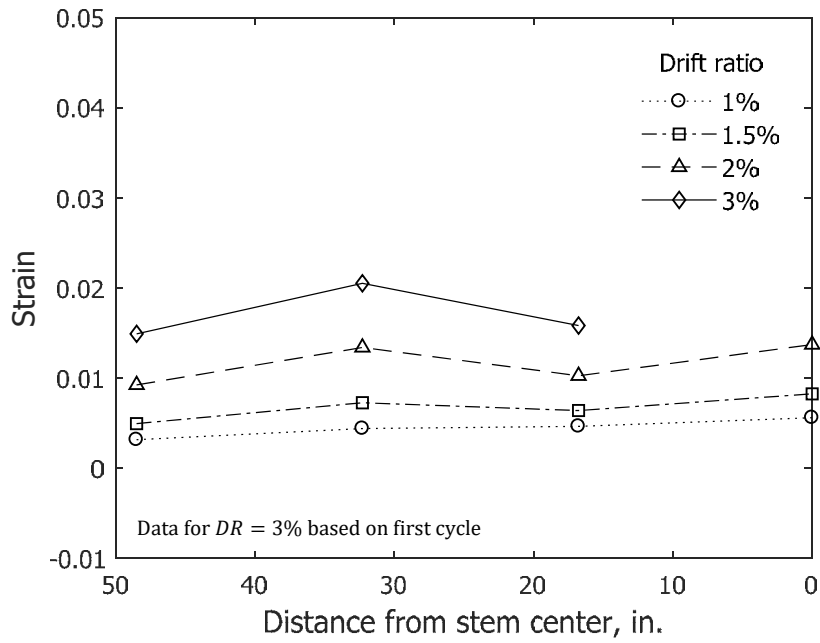


(a) Stem in compression

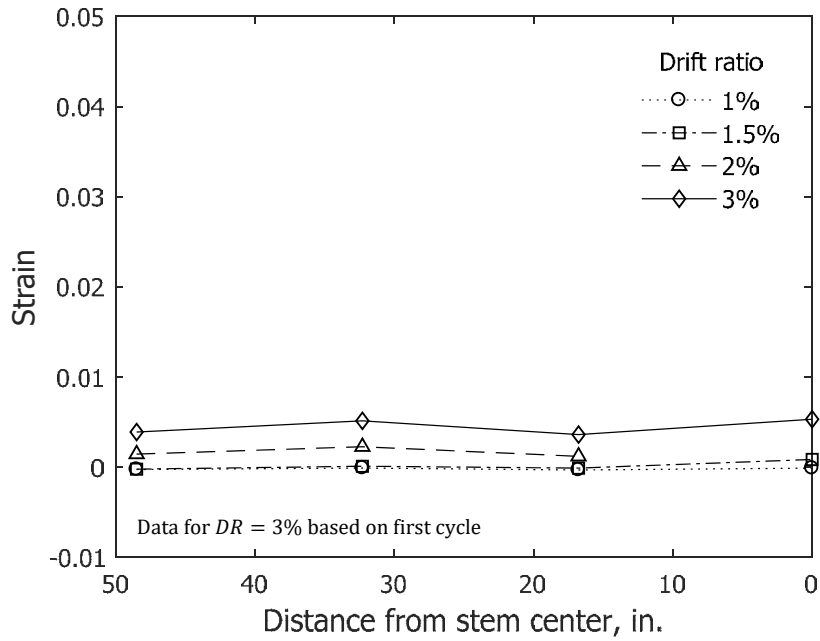


(b) Stem in tension

Figure 152 – Calculated average concrete strain in Layer 3 for flange of T6 (1 in. = 25.4 mm)

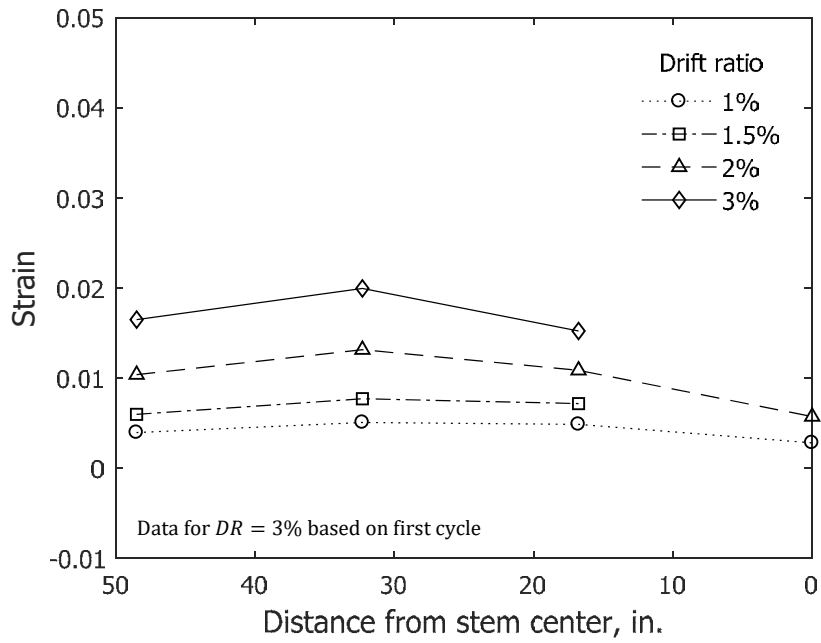


(a) Stem in compression

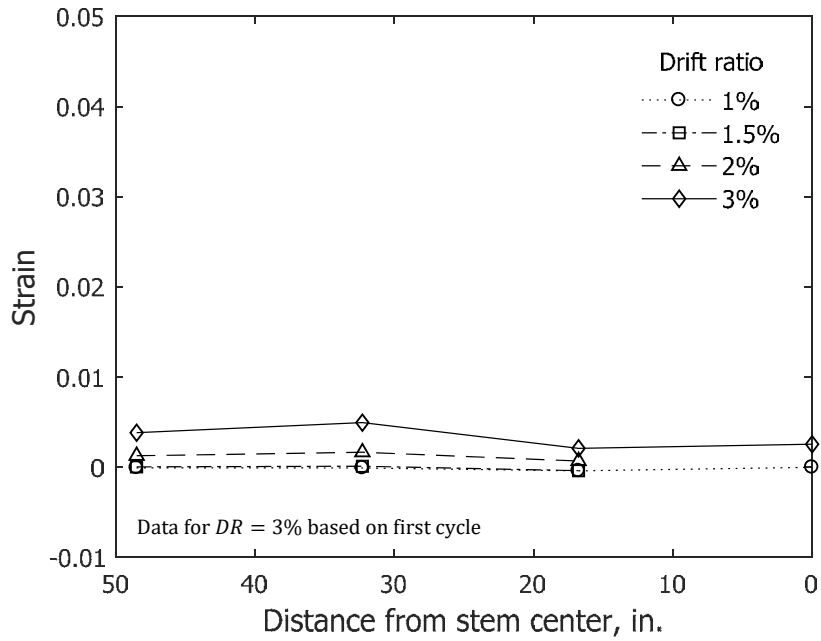


(b) Stem in tension

Figure 153 – Calculated average concrete strain in Layer 4 for flange of T6 (1 in. = 25.4 mm)

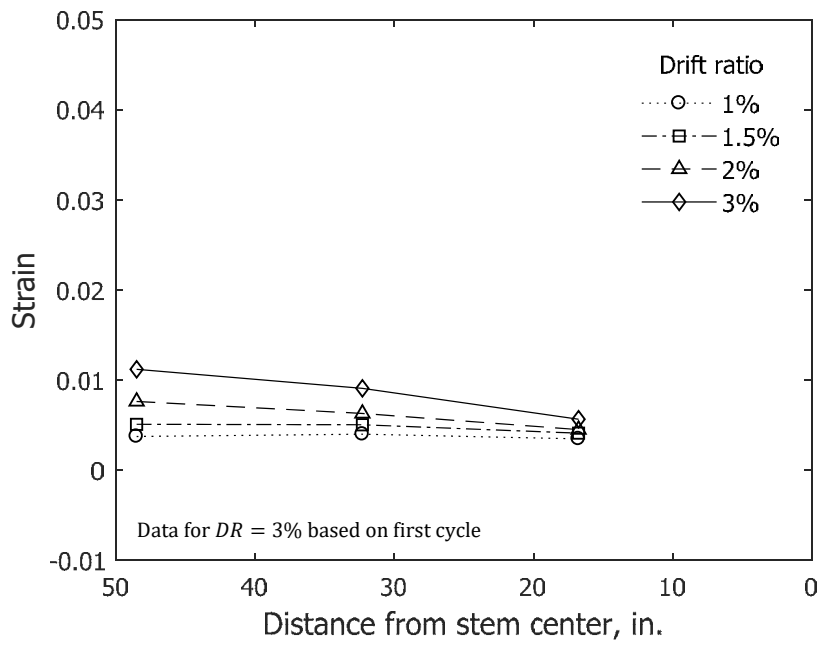


(a) Stem in compression

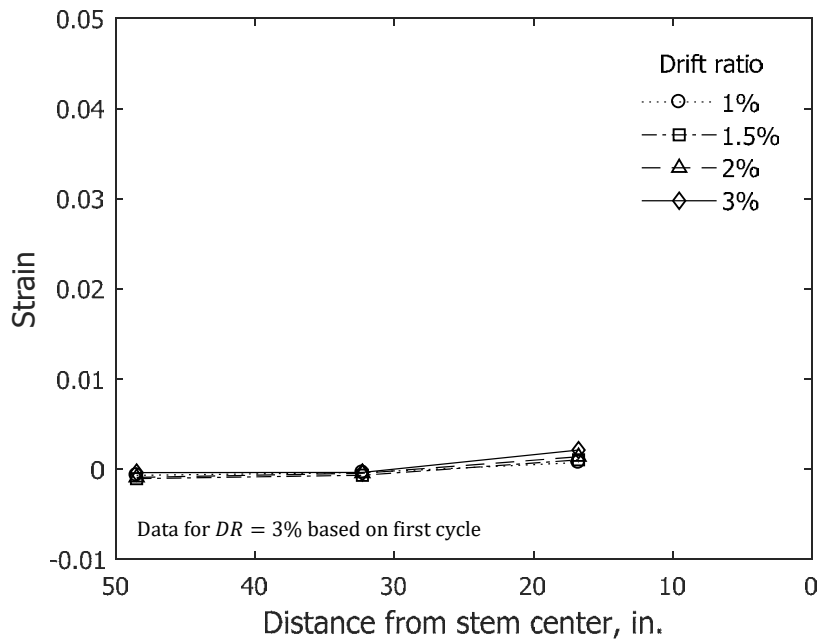


(b) Stem in tension

Figure 154 – Calculated average concrete strain in Layer 5 for flange of T6 (1 in. = 25.4 mm)

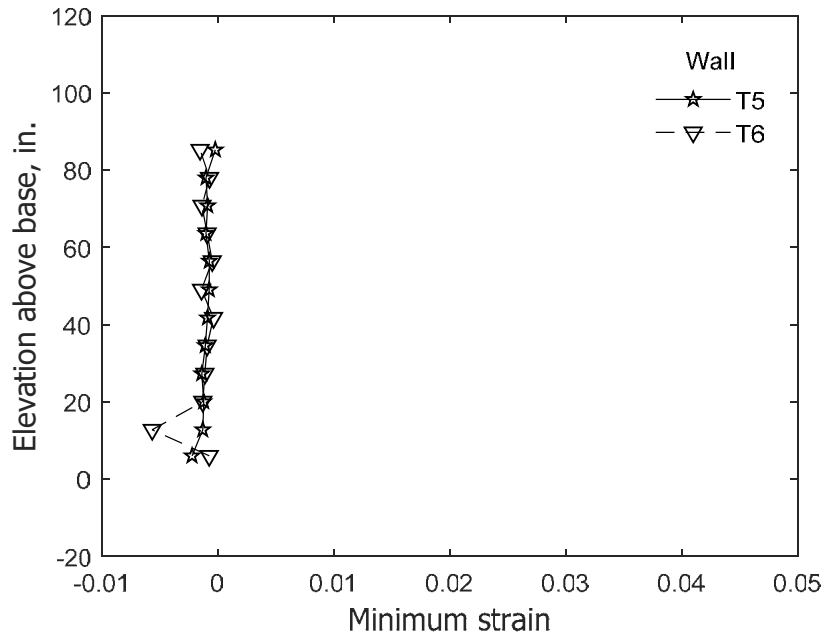


(a) Stem in compression

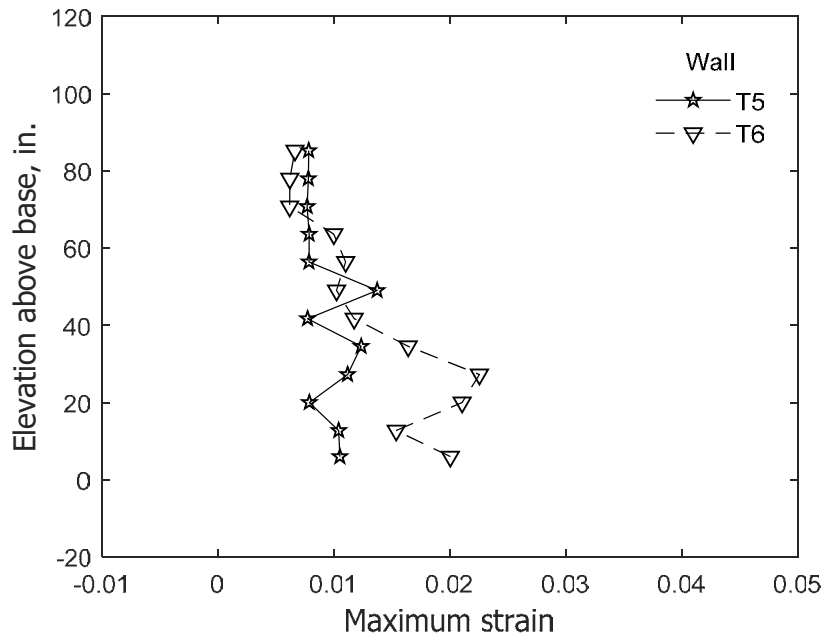


(b) Stem in tension

Figure 155 – Calculated average concrete strain in Layer 6 for flange of T6 (1 in. = 25.4 mm)

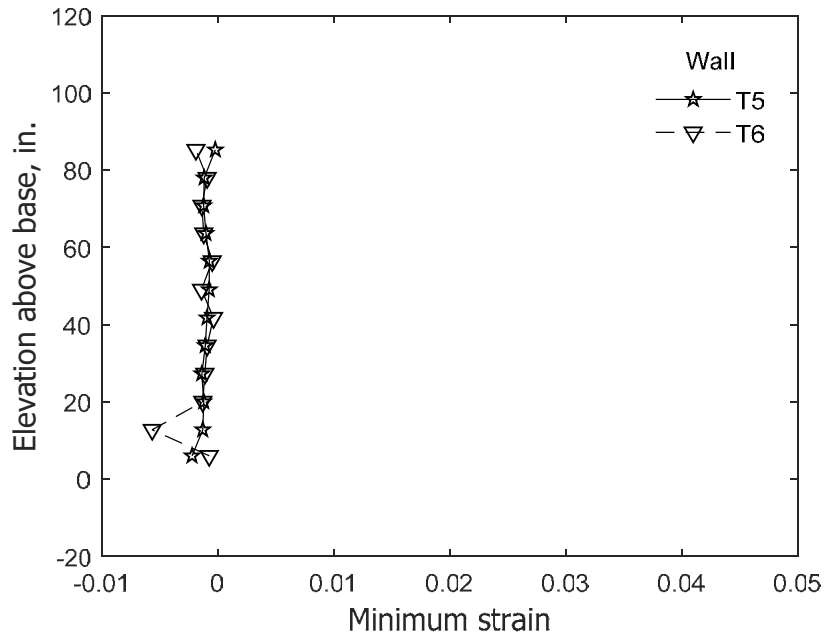


(a) Stem in compression

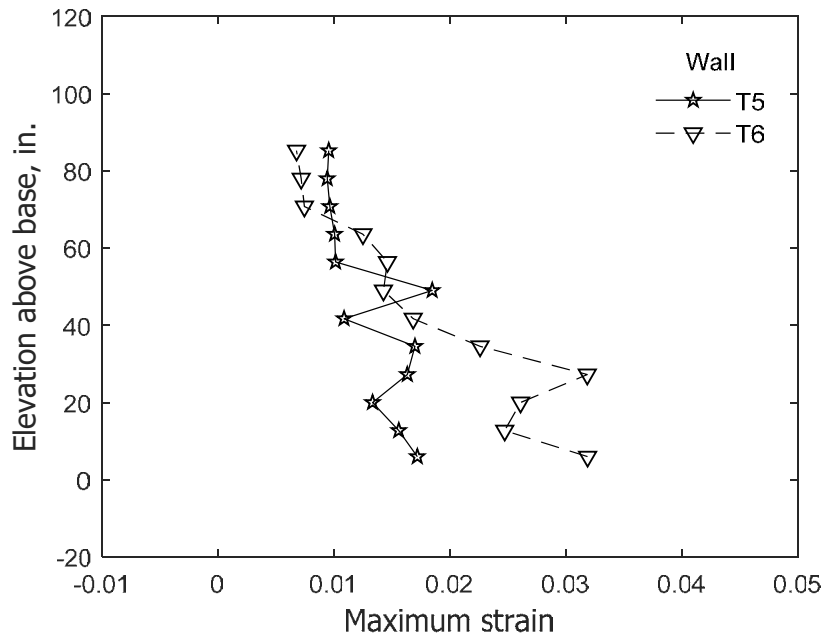


(b) Stem in tension

Figure 156 – Envelopes of concrete strain for confined stem at 1.5% drift ratio (data from optical markers along Columns 1 and 2)

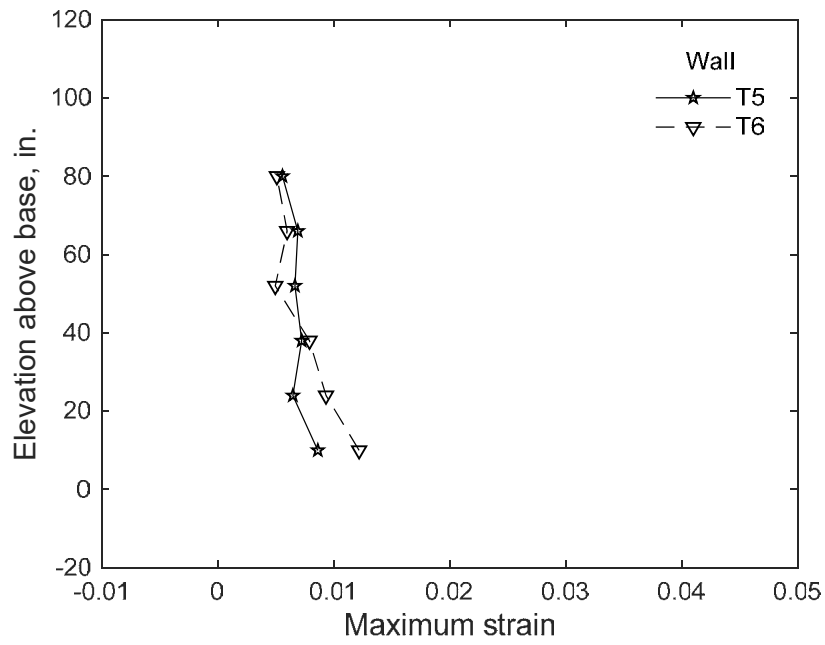


(a) Stem in compression

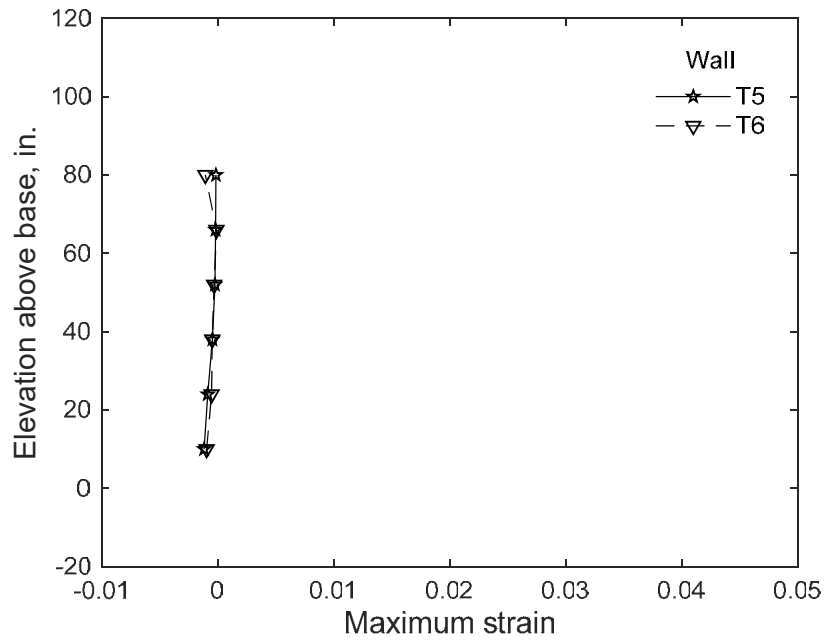


(b) Stem in tension

Figure 157 – Envelopes of concrete strain for confined stem at 2% drift ratio (data from optical markers along Columns 1 and 2)

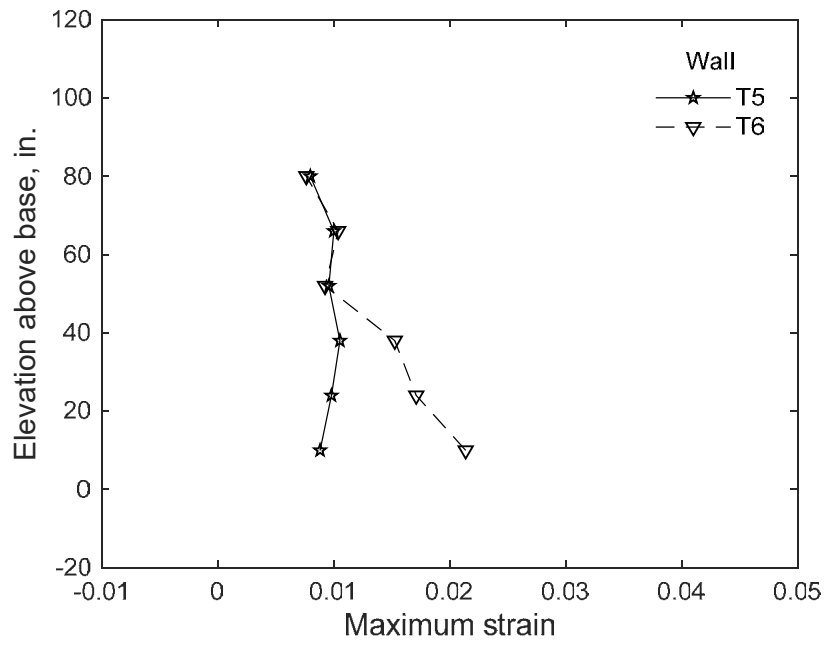


(a) Stem in compression

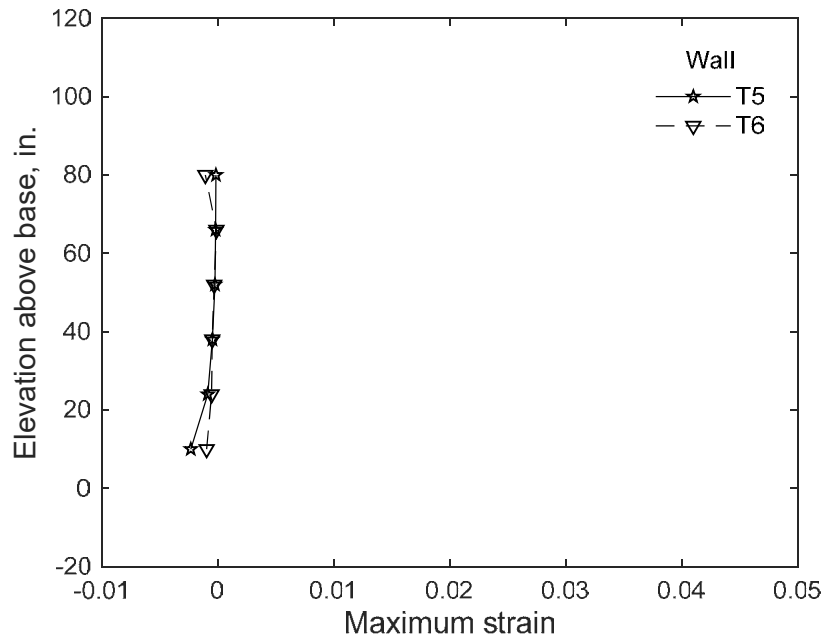


(b) Stem in tension

Figure 158 – Envelopes of concrete strain for confined flange at 1.5% drift ratio (data from optical markers along Column 11)

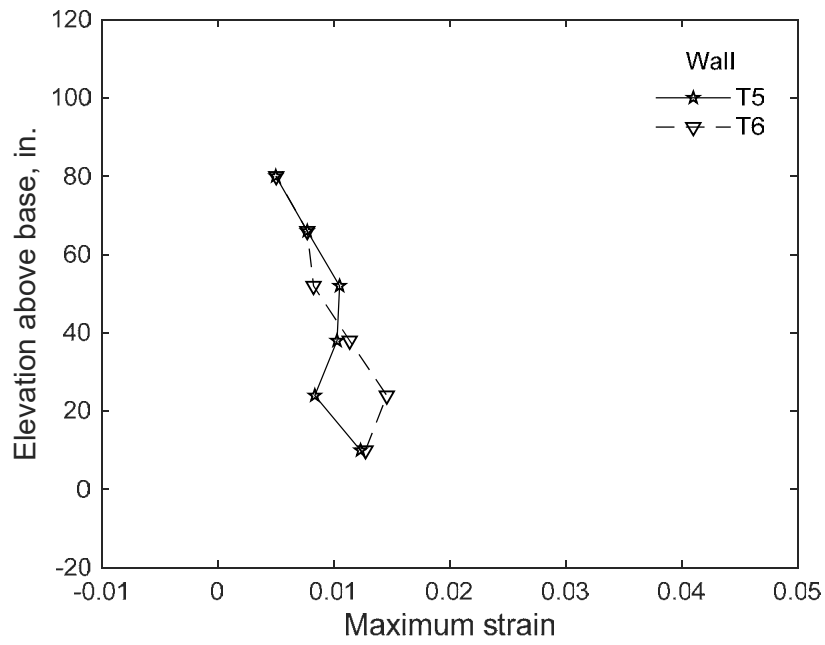


(a) Stem in compression

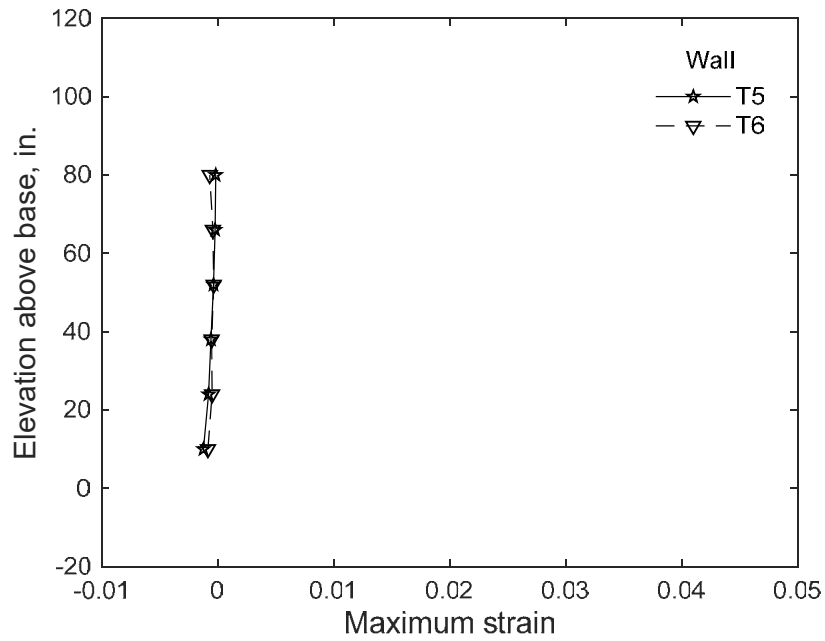


(b) Stem in tension

Figure 159 – Envelopes of concrete strain for confined flange at 2% drift ratio (data from optical markers along Column 11)

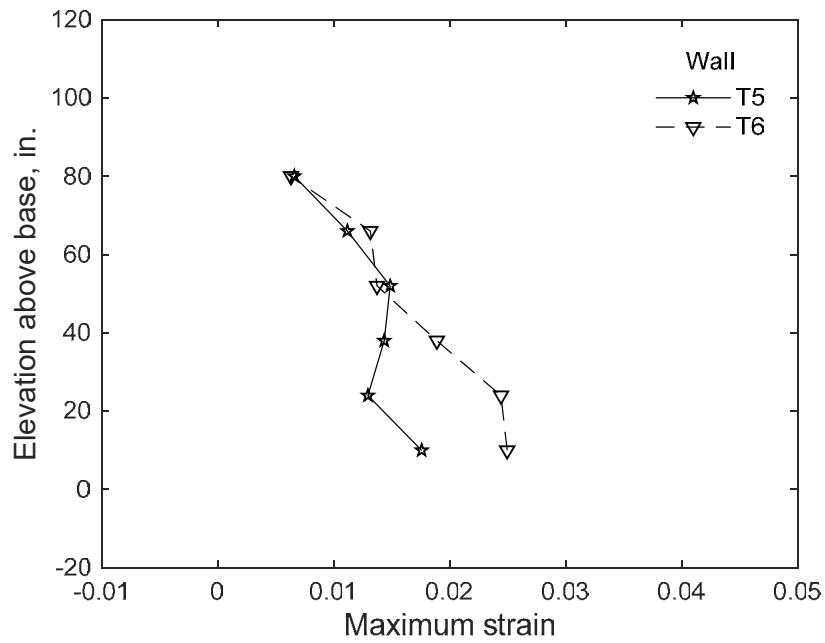


(a) Stem in compression

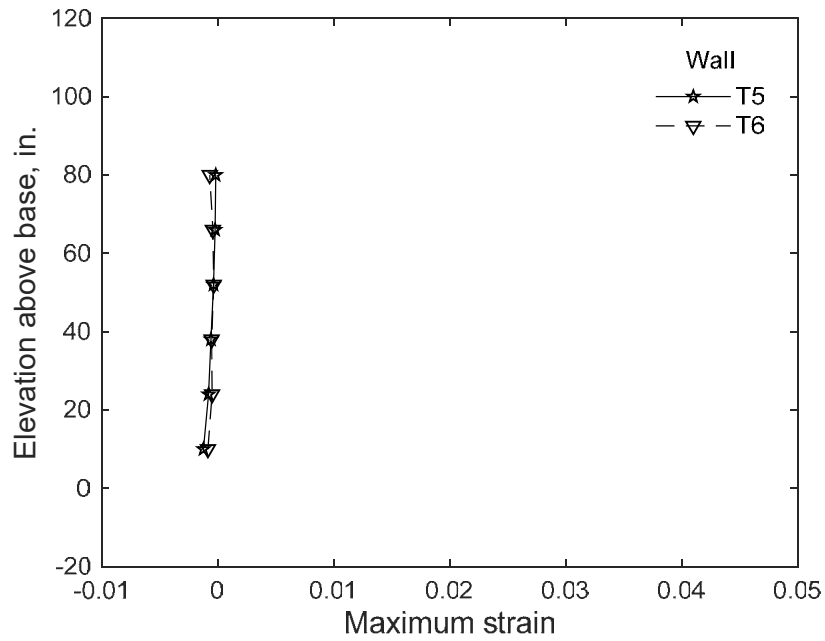


(b) Stem in tension

Figure 160 – Envelopes of concrete strain for unconfined flange at 1.5% drift ratio (data from optical markers along Columns 8, 9, and 10)



(a) Stem in compression



(b) Stem in tension

Figure 161 – Envelopes of concrete strain for unconfined flange at 2% drift ratio (data from optical markers along Columns 8, 9, and 10)

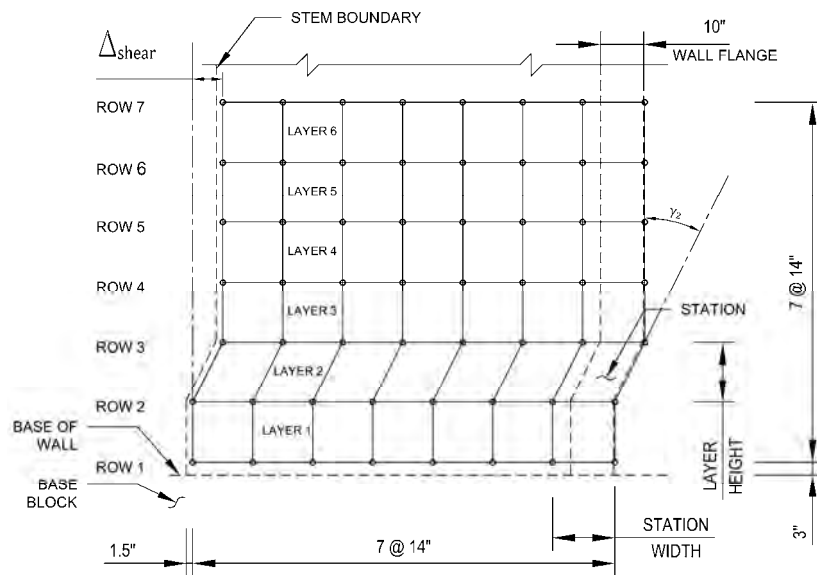


Figure 162 – Shear component of displacement from Layer 2^[37] (1 in. = 25.4 mm)

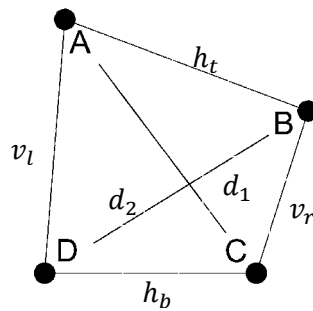


Figure 163 – General deformed shape for a station^[37]

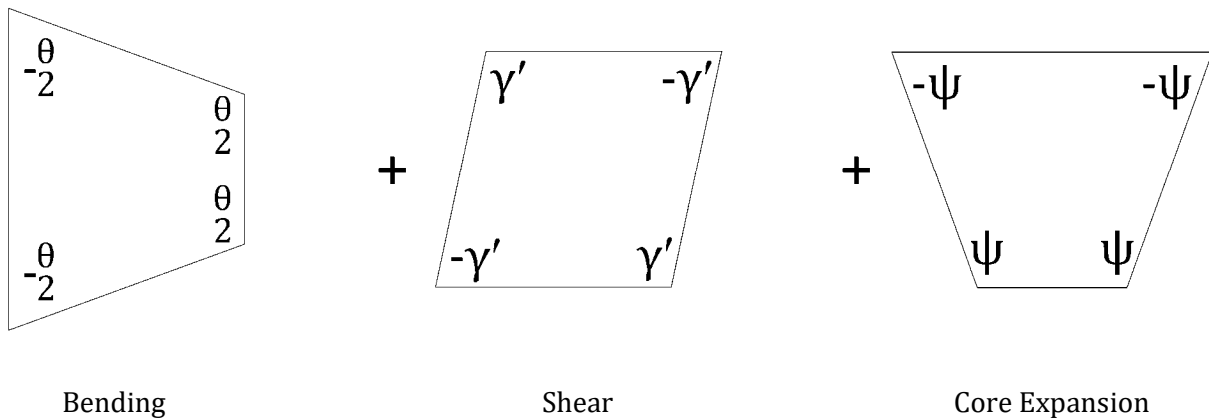
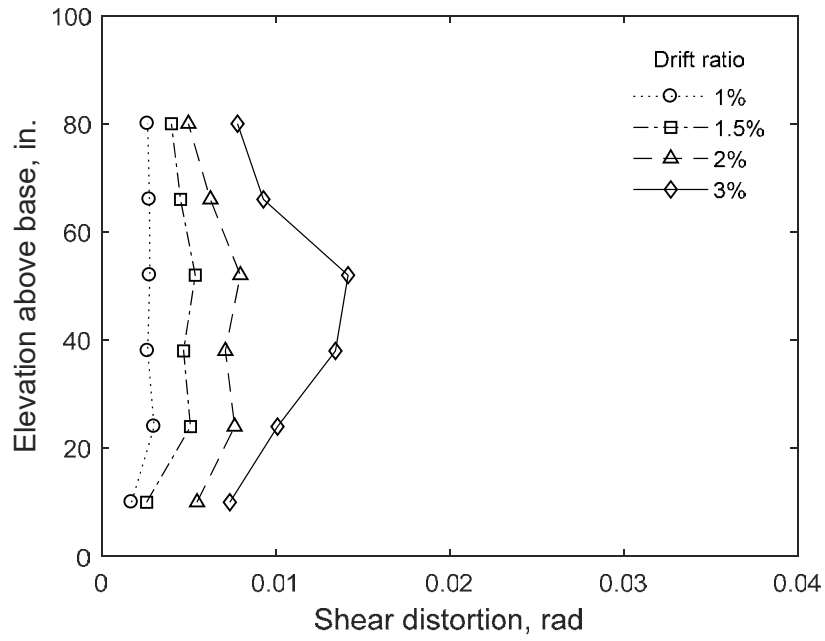
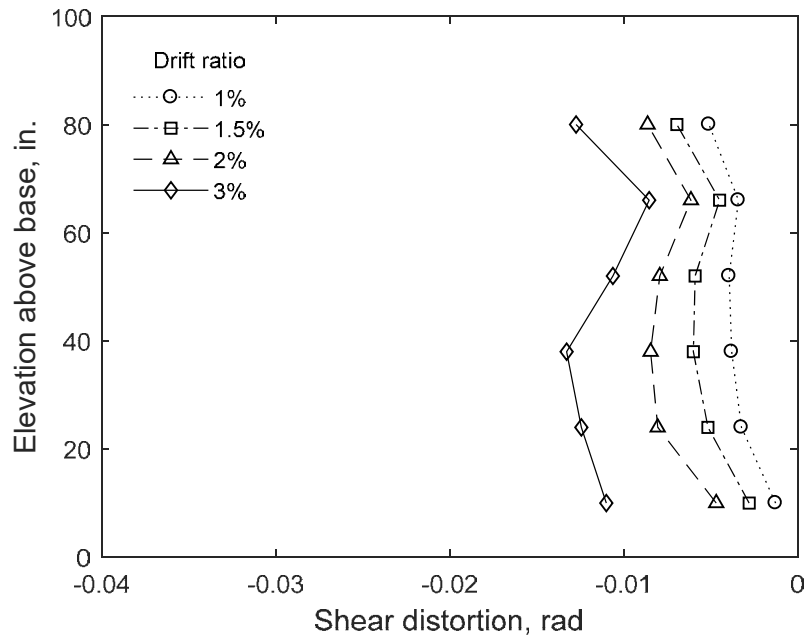


Figure 164 – Components of angular change for a station^[37]

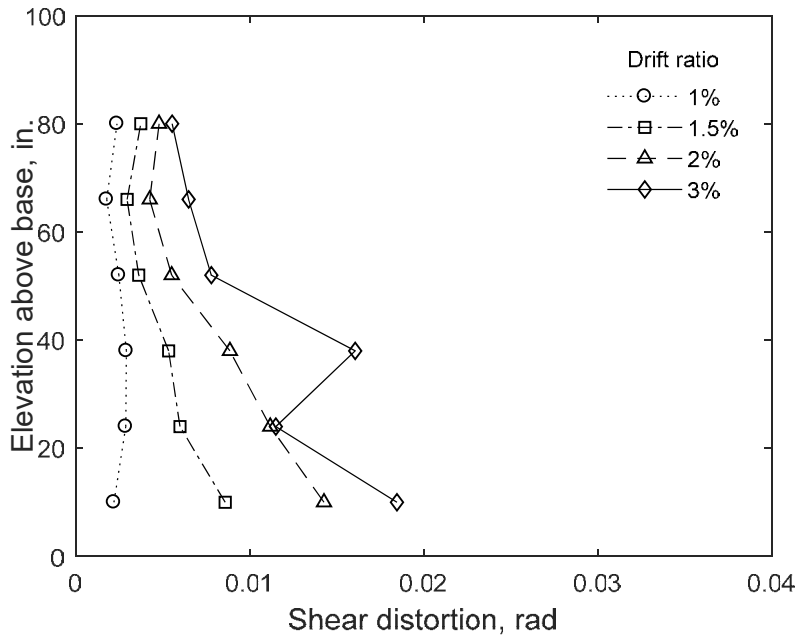


(a) Stem in compression

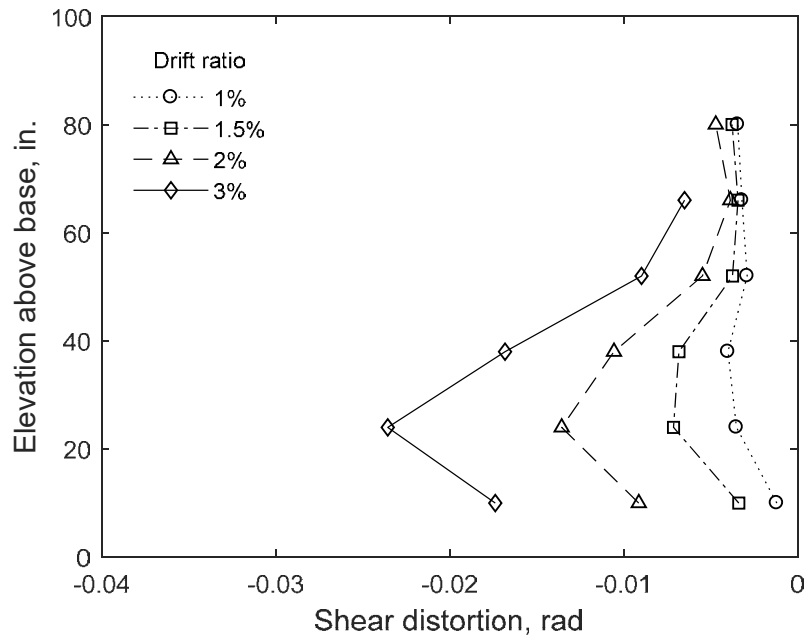


(b) Stem in tension

Figure 165 – Calculated shear distortion for T5, data from optical markers, Columns 1 through 8 (1 in. = 25.4 mm)



(a) Stem in compression



(b) Stem in tension

Figure 166 – Calculated shear distortion for T6, data from optical markers, Columns 1 through 8 (1 in. = 25.4 mm)

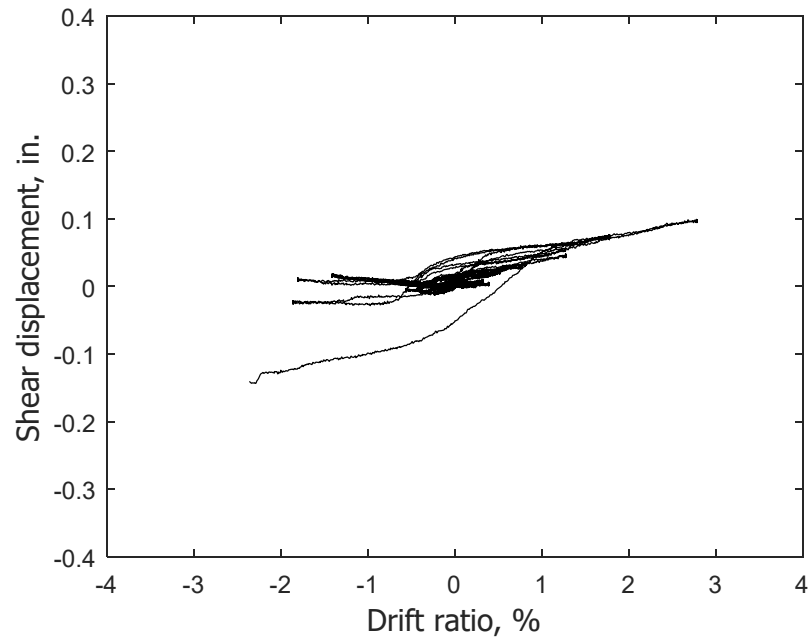


Figure 167 – Base shearing displacement of T5 based on data from optical markers (1 in. = 25.4 mm)

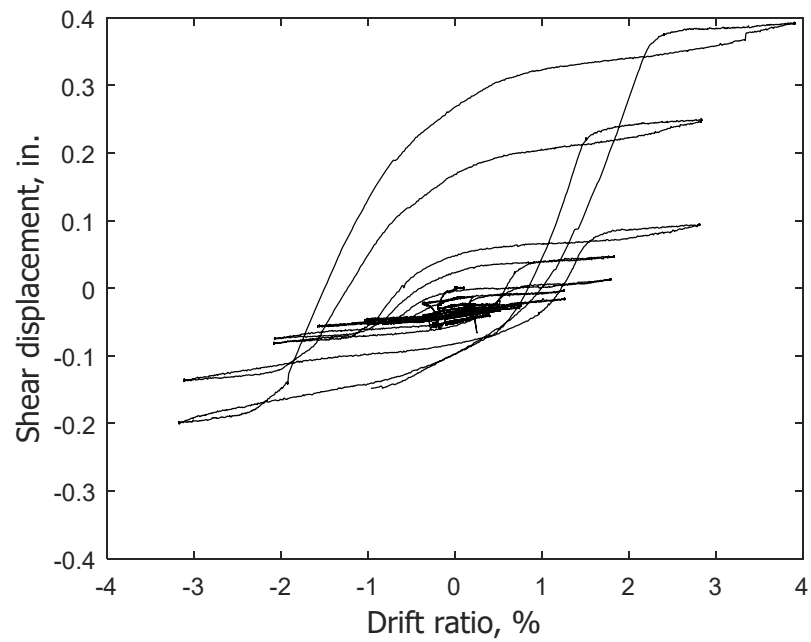
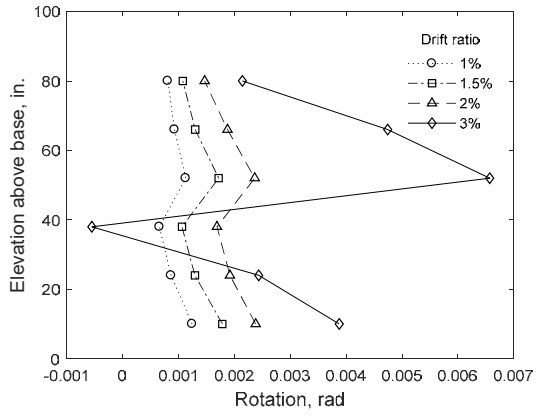
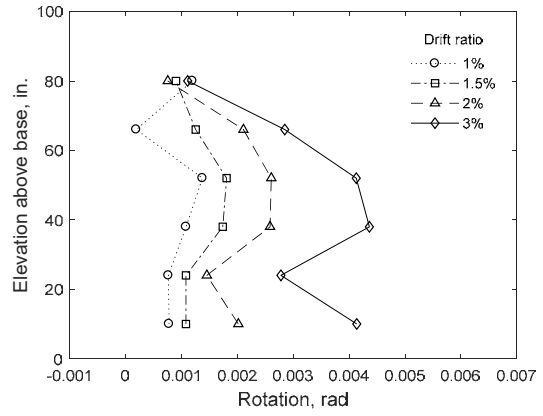


Figure 168 – Base shearing displacement of T6 based on data from optical markers (1 in. = 25.4 mm)

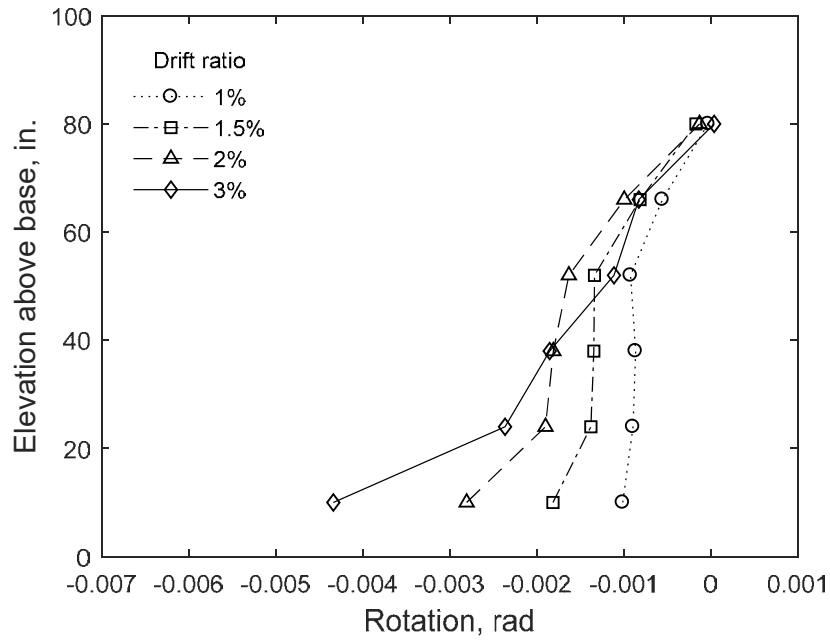


Using Columns 1 and 8



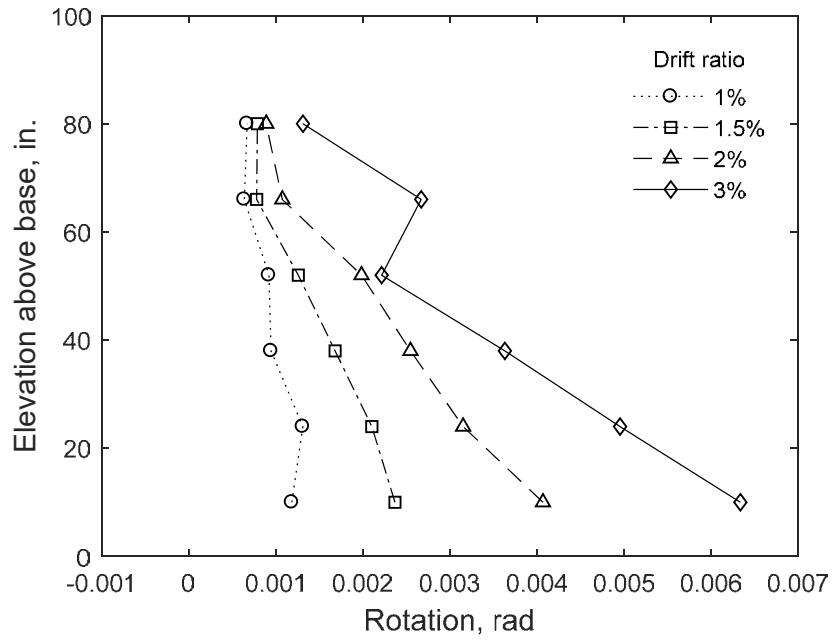
Using Columns 2 and 7

(a) Stem in compression

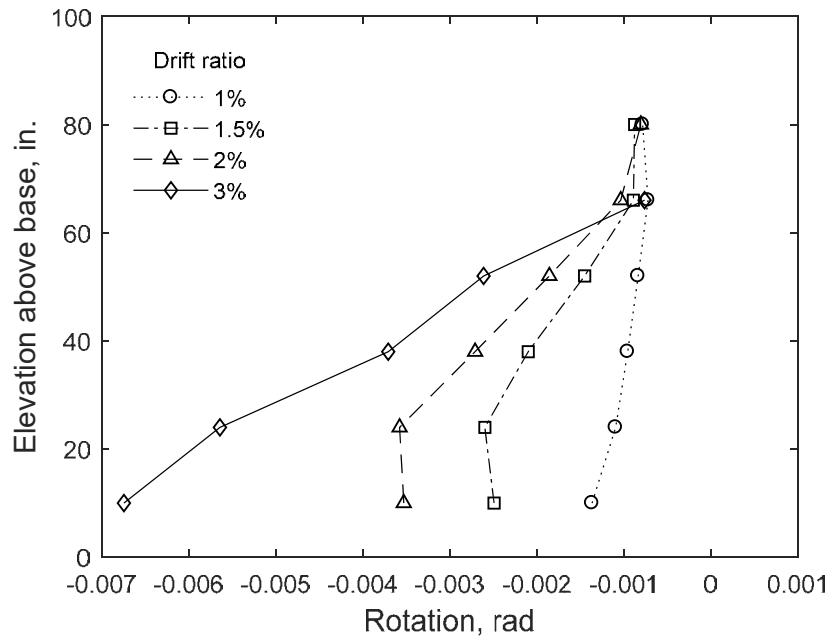


(b) Stem in tension

Figure 169 – Calculated flexural rotation for T5, data from optical markers, Columns 1 through 8 (1 in. = 25.4 mm)

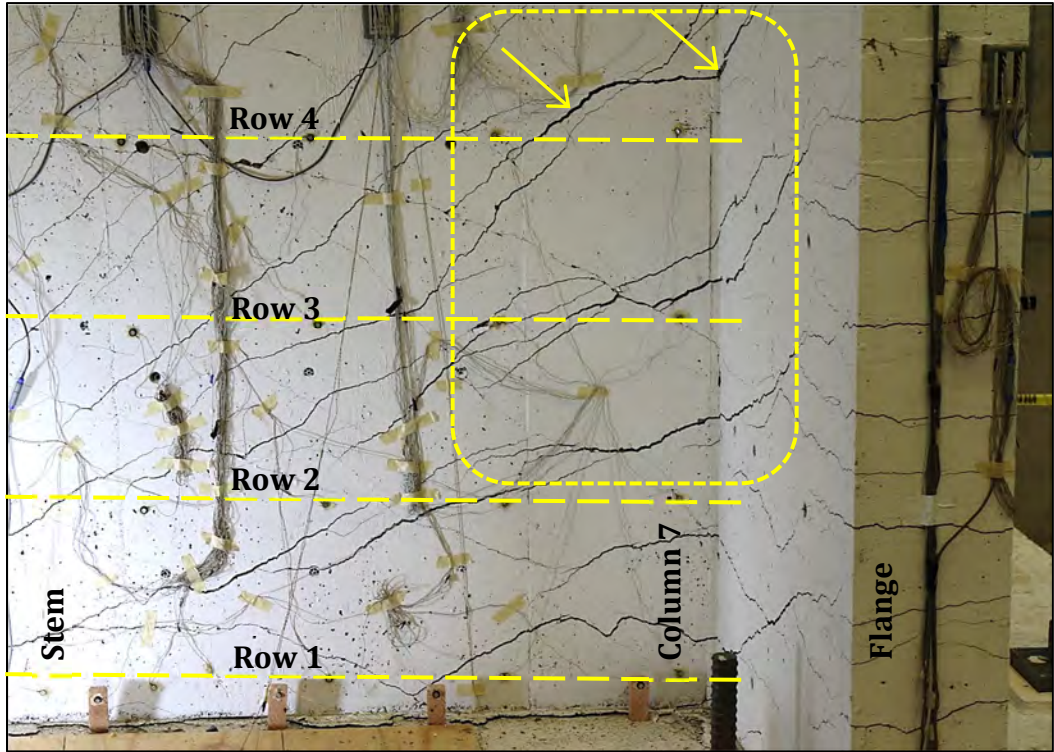


(a) Stem in compression

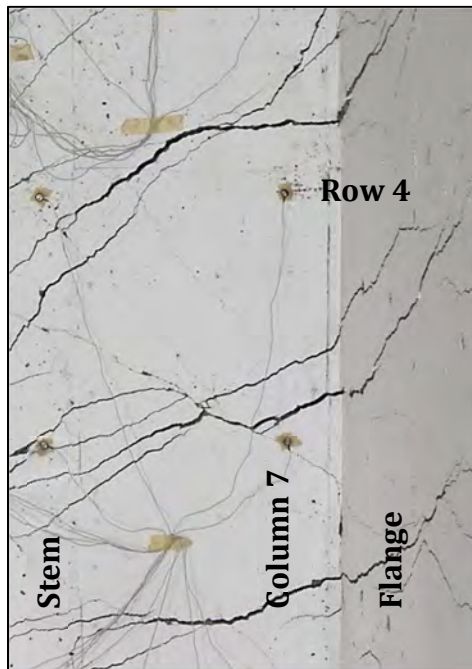


(b) Stem in tension

Figure 170 – Calculated flexural rotation for T6, data from optical markers, Columns 1 through 8 (1 in. = 25.4 mm)



(a) Elevation view



(b) Close-up view of the selected area

Figure 171 - Wall T5 at a drift ratio of 3%

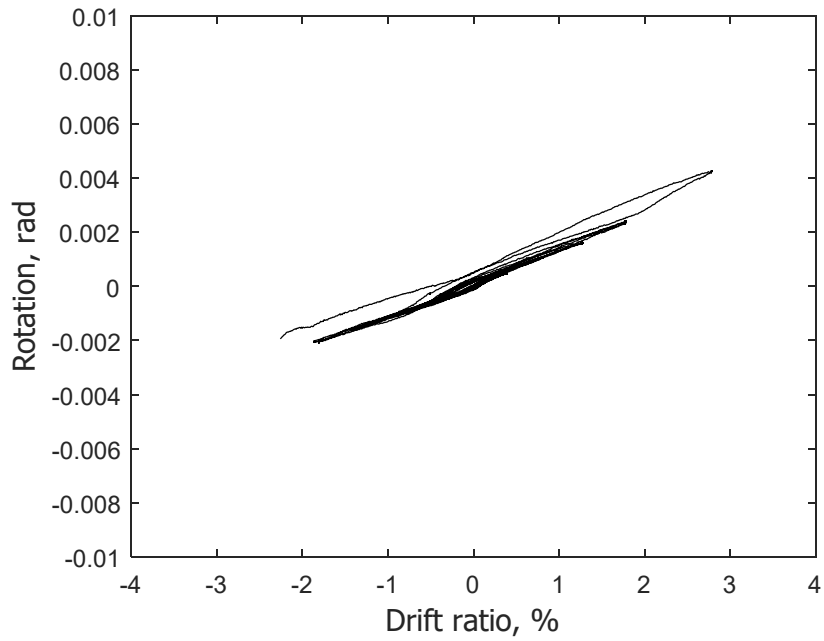


Figure 172 – Rotation due to base opening versus drift ratio for T5 (data from optical markers)

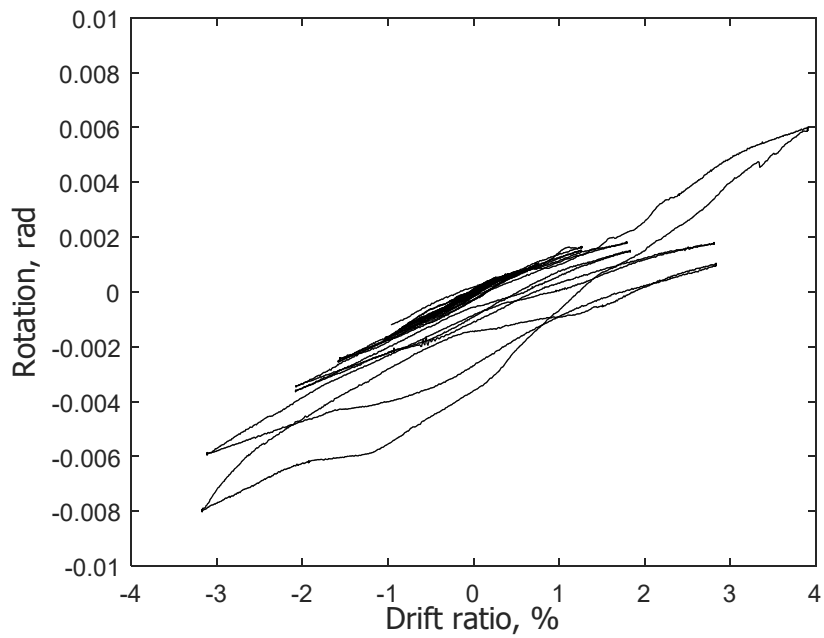
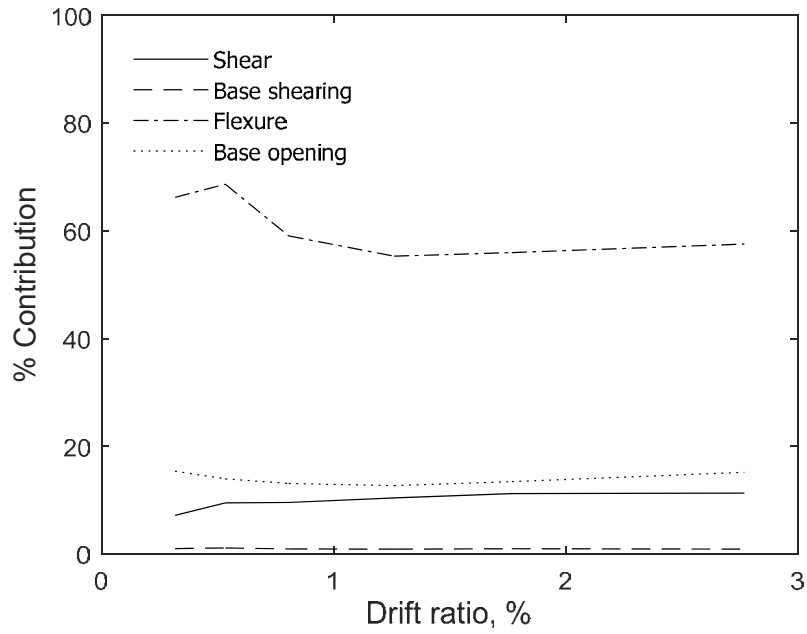
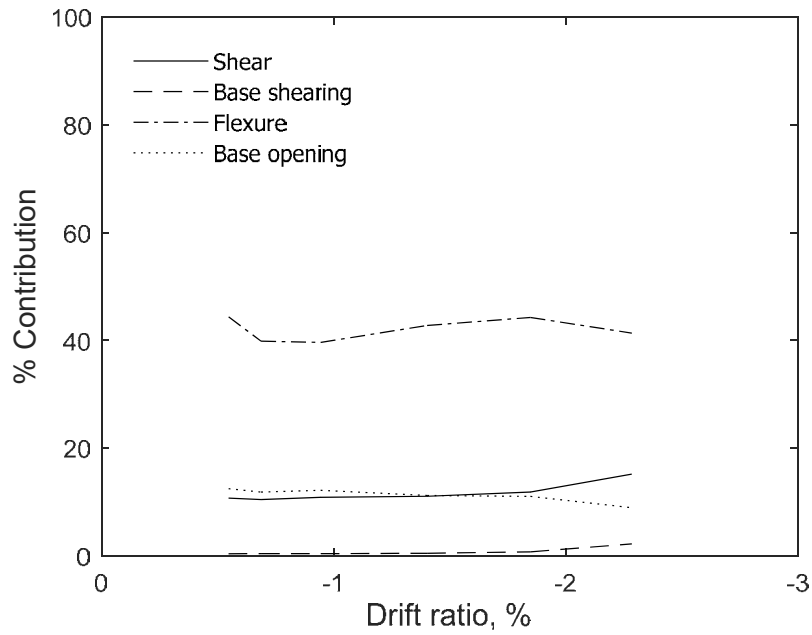


Figure 173 – Rotation due to base opening versus drift ratio for T6 (data from optical markers)

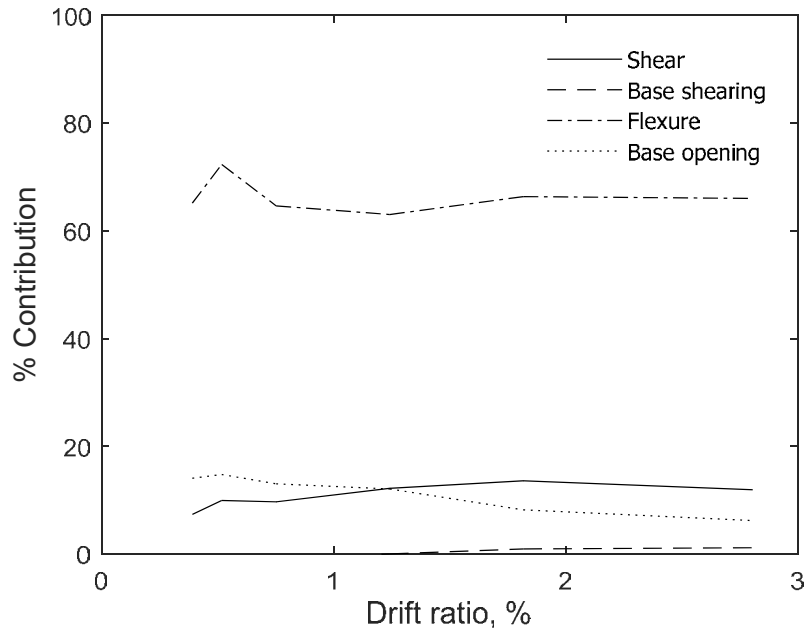


(a) Stem in compression

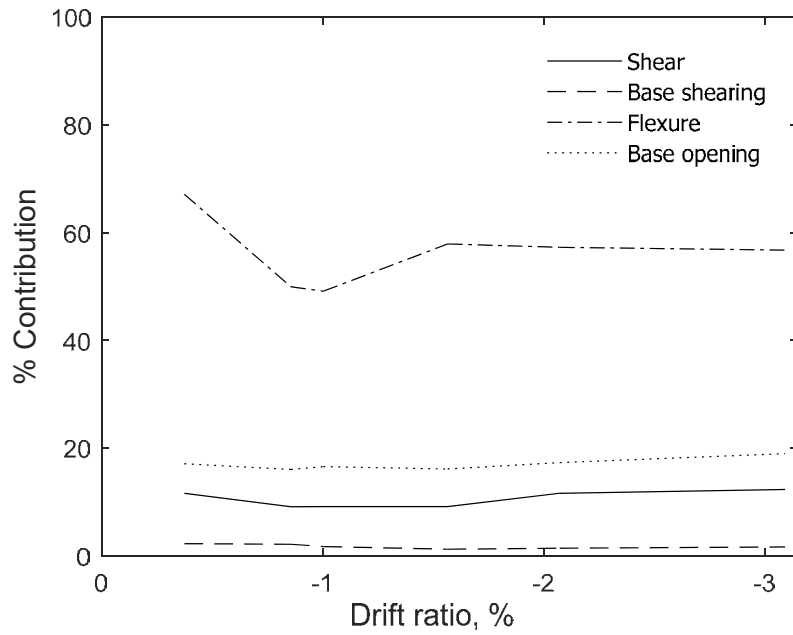


(b) Stem in tension

Figure 174 – Contribution of deformation components from bottom 87 in. (2210 mm) for T5

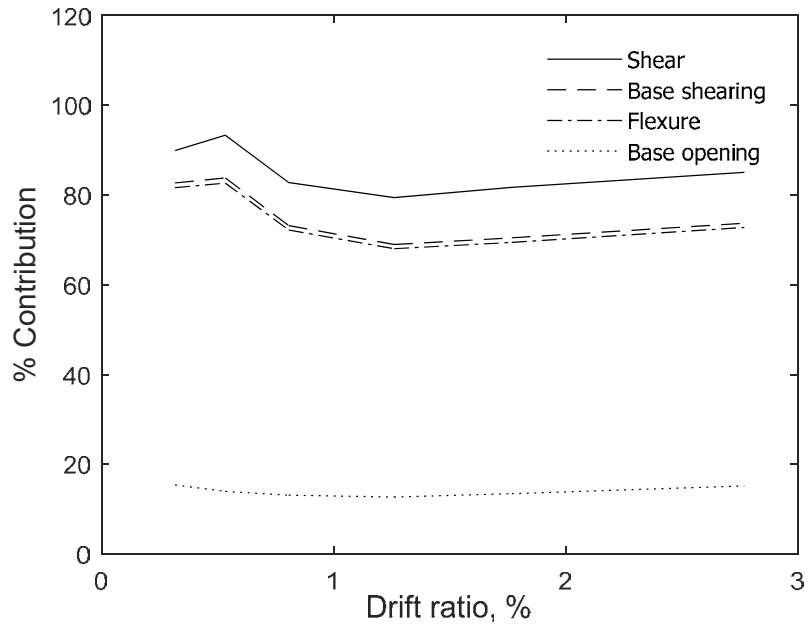


(a) Stem in compression

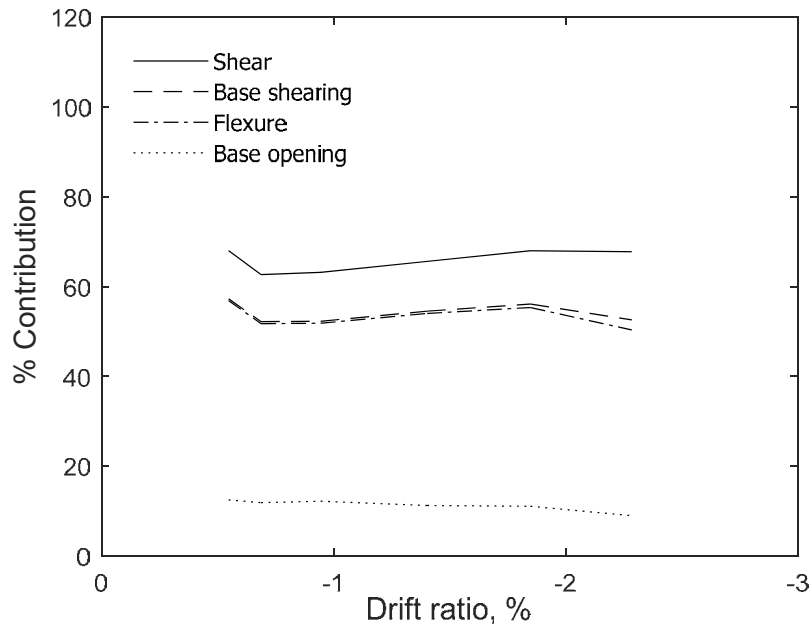


(b) Stem in tension

Figure 175 – Contribution of deformation components from bottom 87 in. (2210 mm) for T6

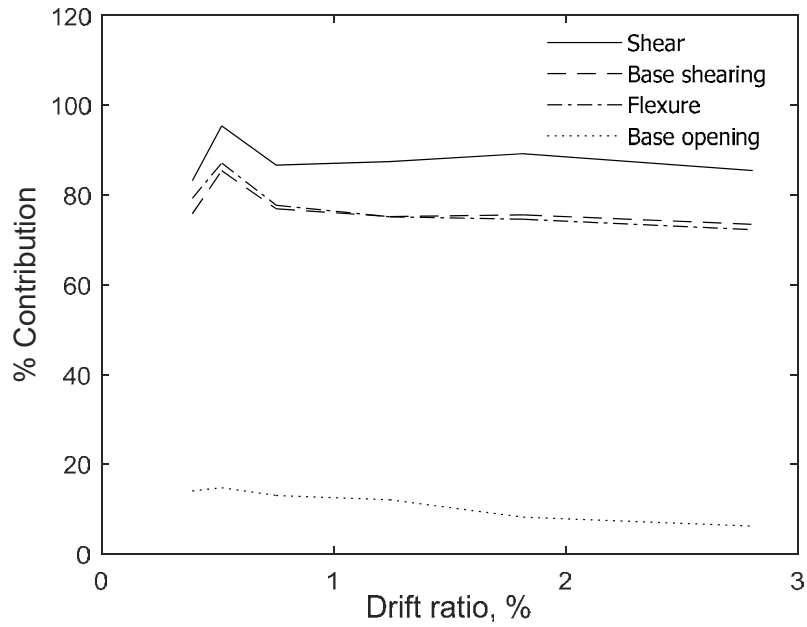


(a) Stem in compression

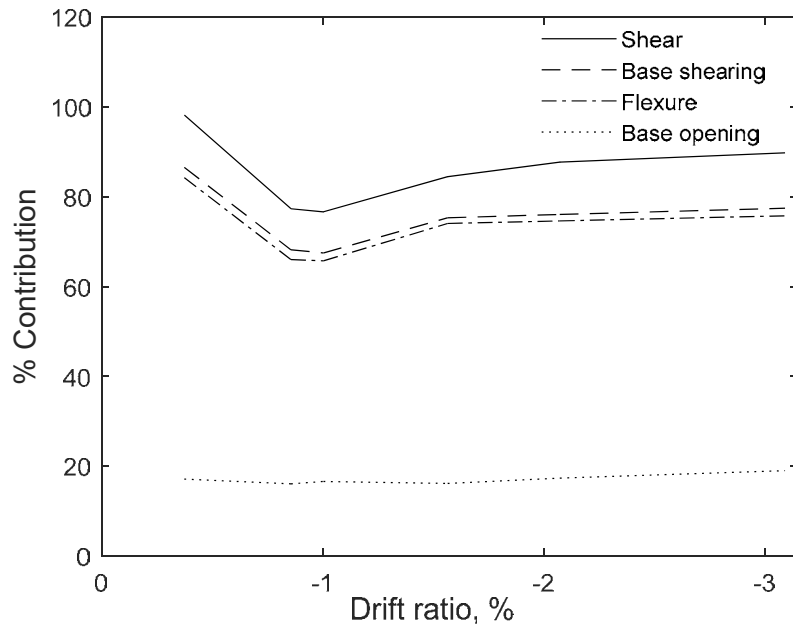


(b) Stem in tension

Figure 176 – Cumulative contribution of deformation components from bottom 87 in. (2210 mm) for T5

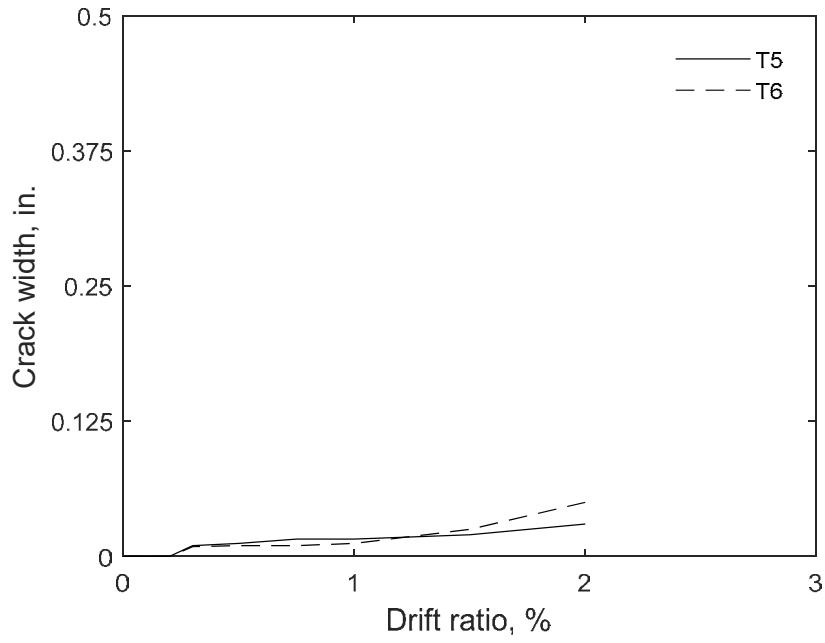


(a) Stem in compression

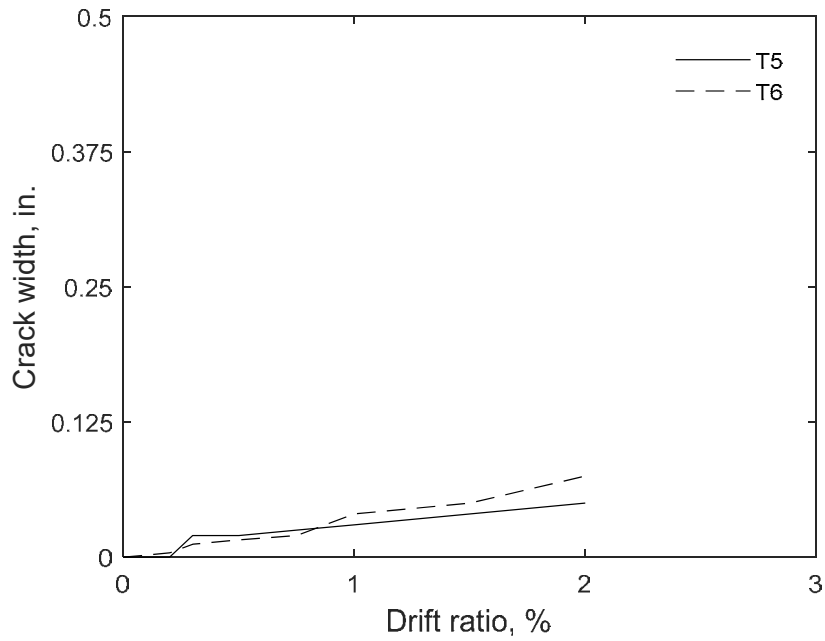


(b) Stem in tension

Figure 177 – Cumulative contribution of deformation components from bottom 87 in. (2210 mm) for T6

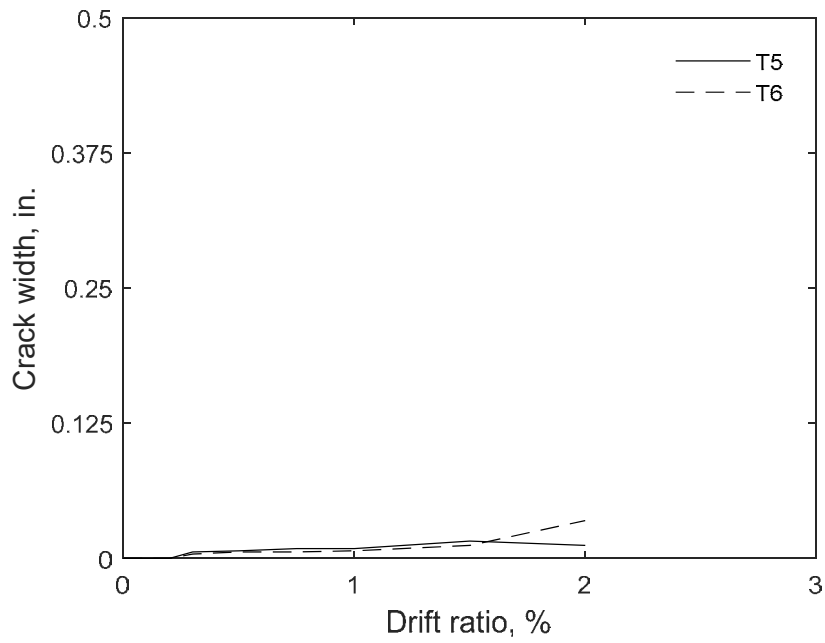


a) Confined flange

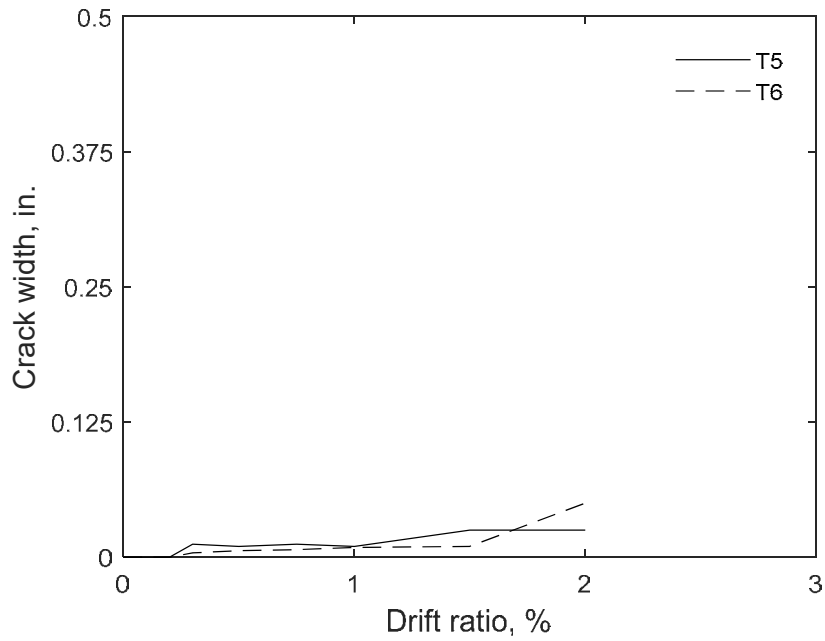


b) Unconfined flange

Figure 178 – Measured crack width at peak drift versus drift ratio, stem in compression (1 in. = 25.4 mm)

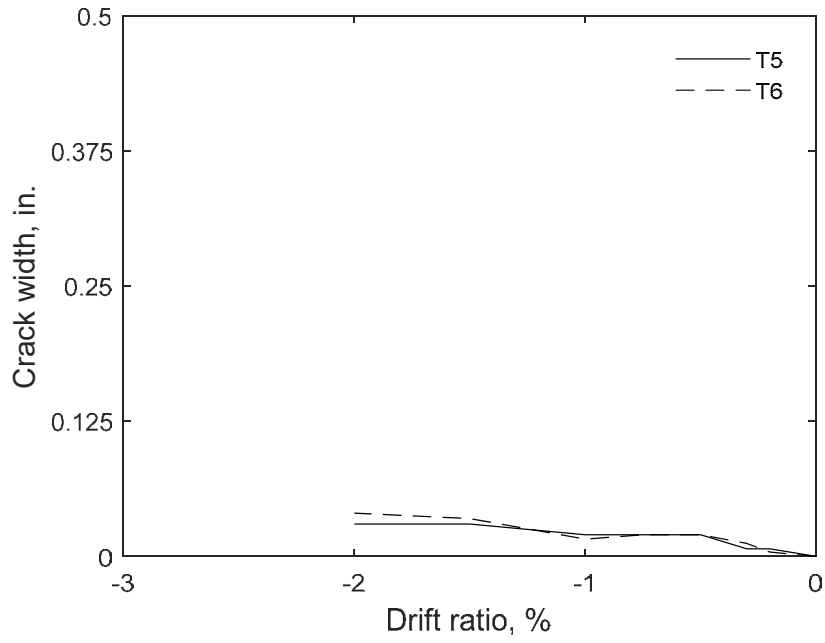


a) Confined flange

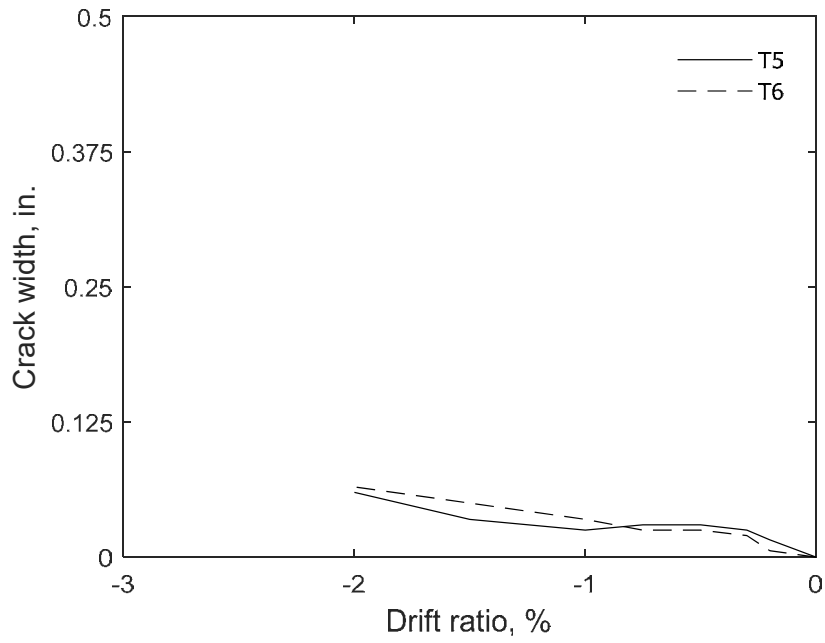


b) Unconfined flange

Figure 179 – Measured crack width at zero shear versus maximum drift ratio attained, stem in compression (1 in. = 25.4 mm)

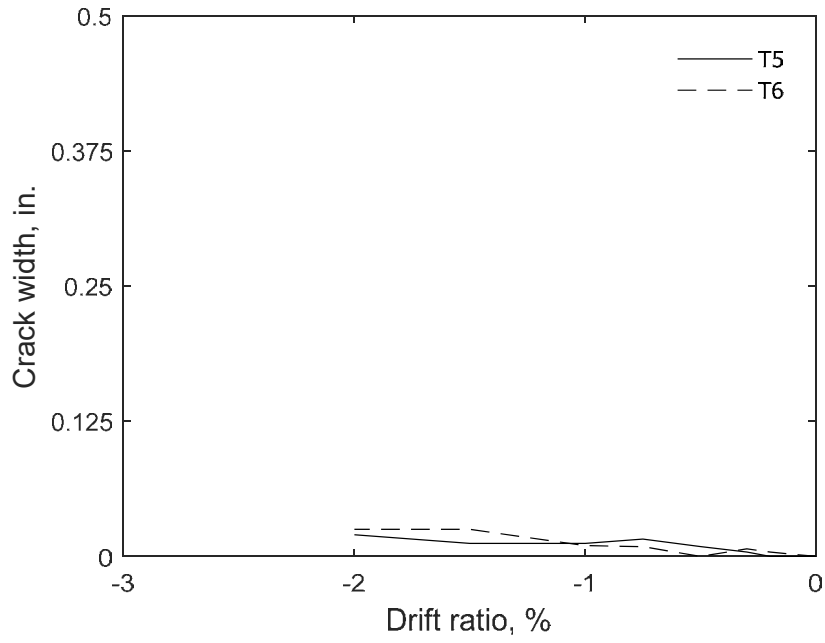


a) Confined stem

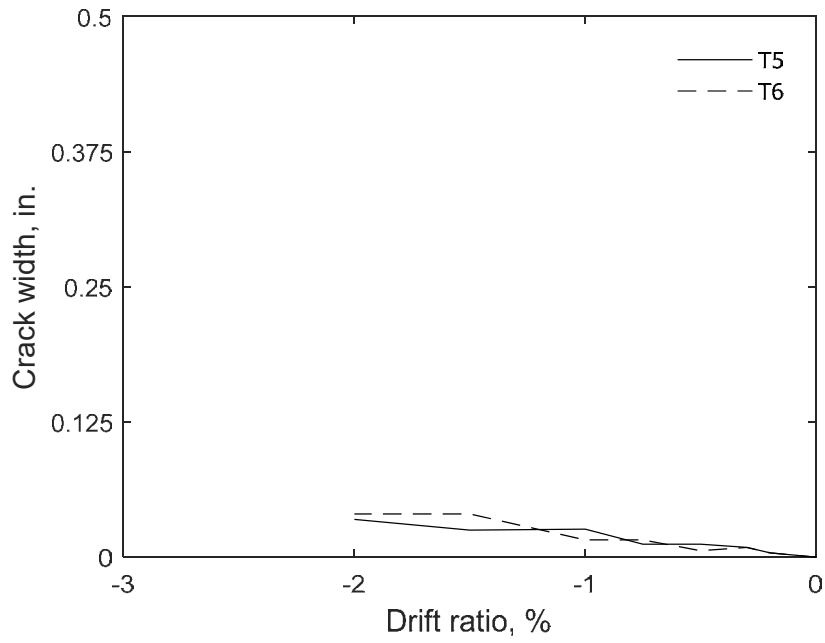


b) Unconfined stem

Figure 180 – Measured crack width at peak drift versus drift ratio, stem in tension (1 in. = 25.4 mm)

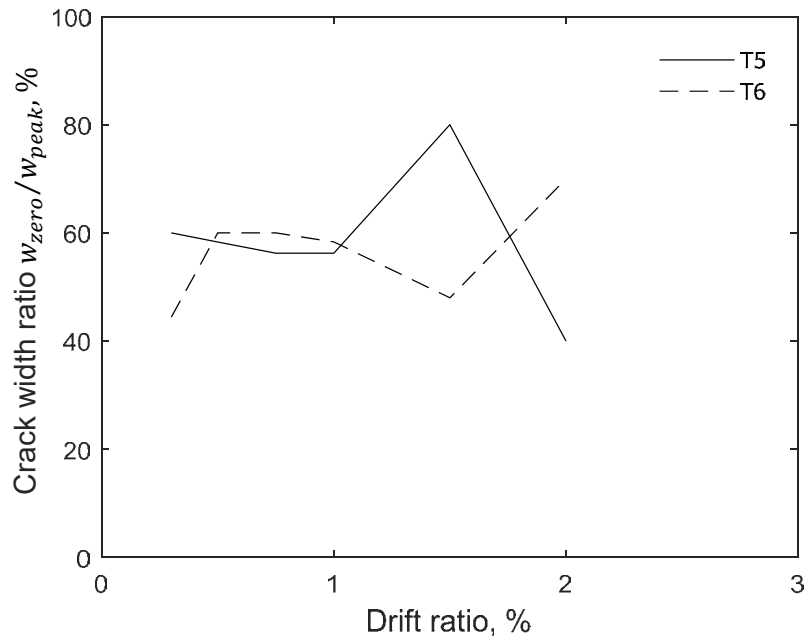


a) Confined stem

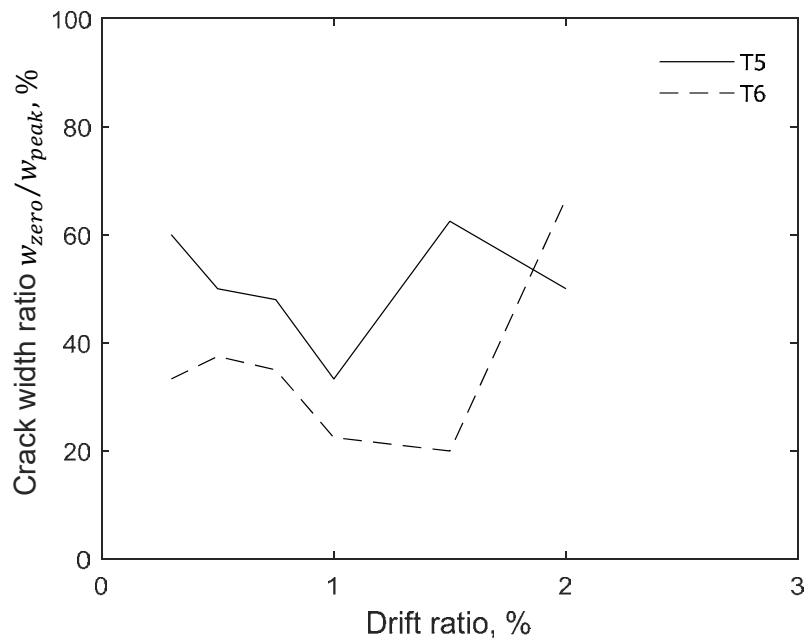


b) Unconfined stem

Figure 181 – Measured crack width at zero shear versus maximum drift ratio attained, stem in tension (1 in. = 25.4 mm)

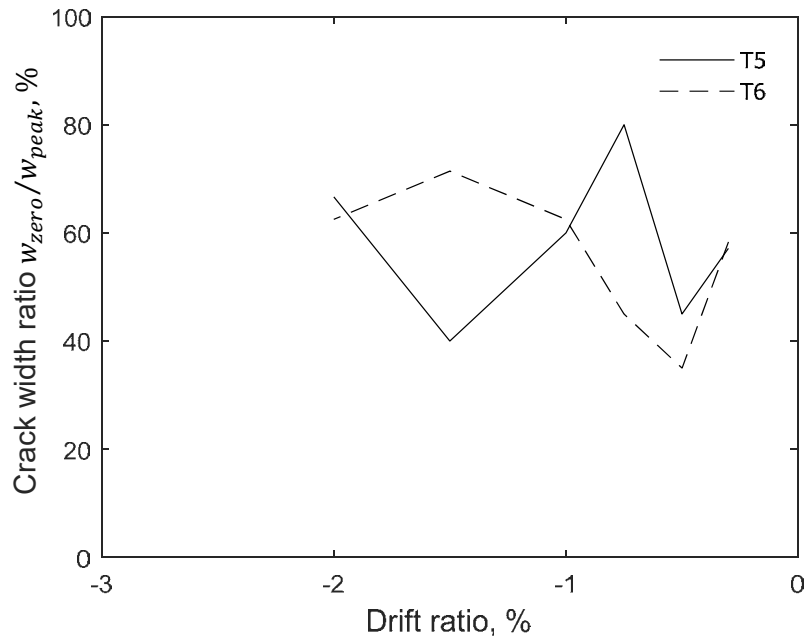


a) Confined flange

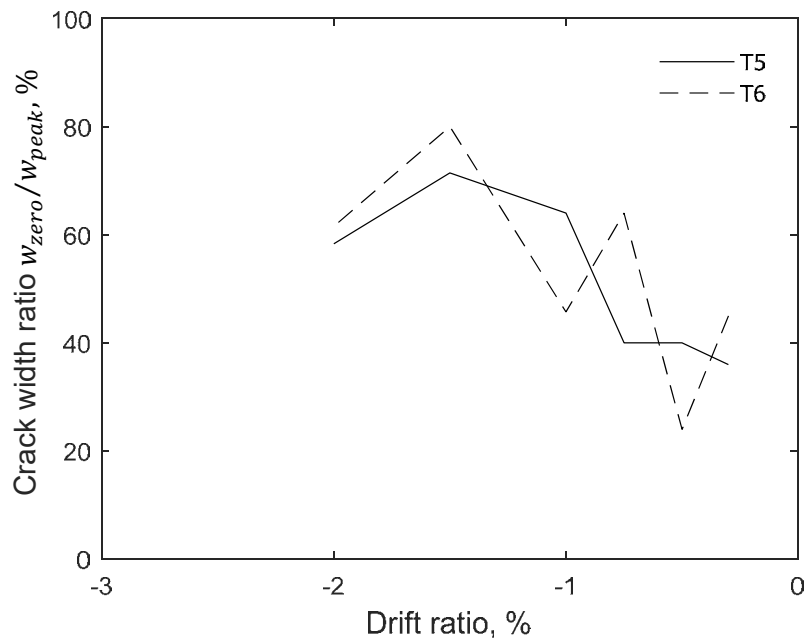


b) Unconfined flange

Figure 182 – Crack width ratio versus drift ratio for positive loading direction, stem in compression (1 in. = 25.4 mm)



a) Confined stem



b) Unconfined stem

Figure 183 – Crack width ratio versus drift ratio for negative loading direction, stem in tension (1 in. = 25.4 mm)

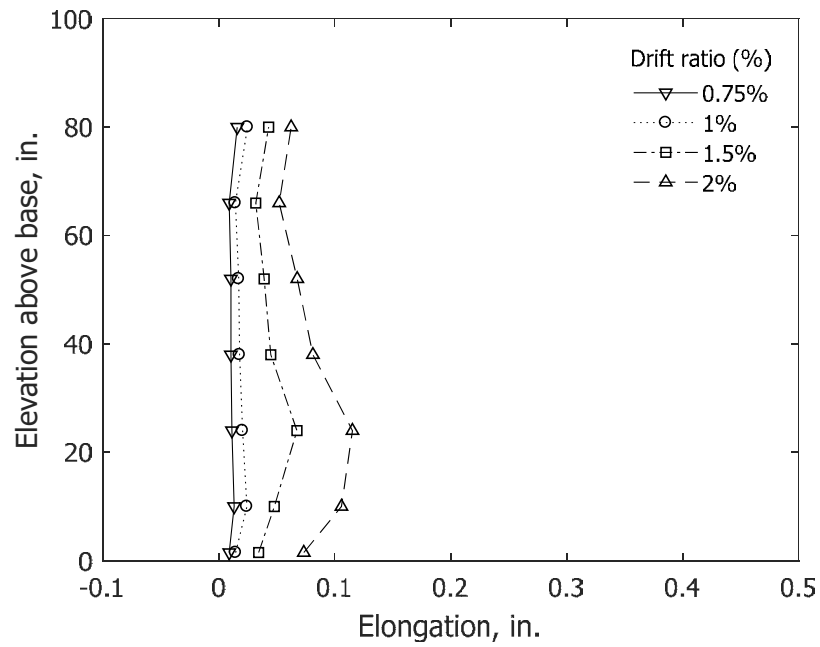


Figure 184 – Calculated elongation at zero shear for T5, data from optical markers, Columns 1 through 8 (1 in. = 25.4 mm)

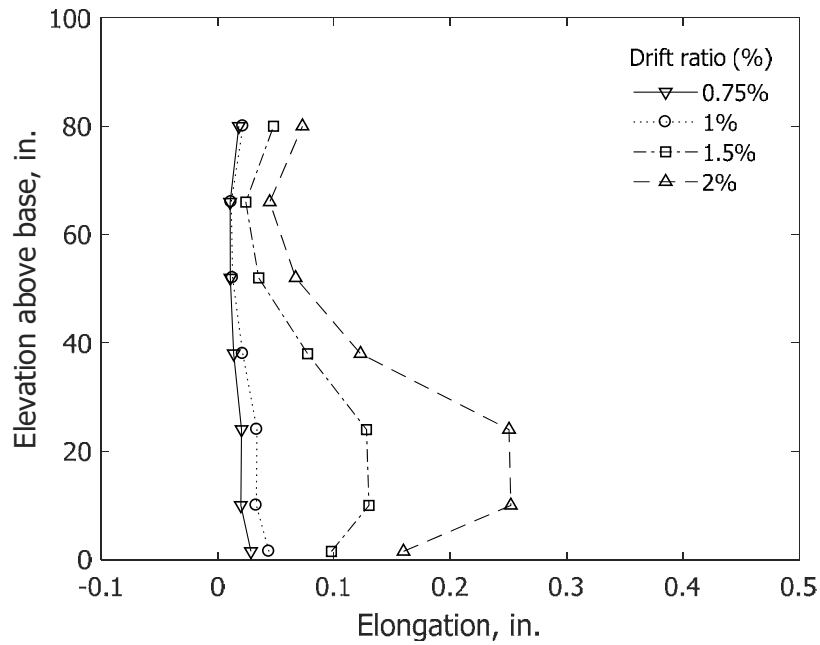


Figure 185 – Calculated elongation at zero shear for T6, data from optical markers, Columns 1 through 8 (1 in. = 25.4 mm)

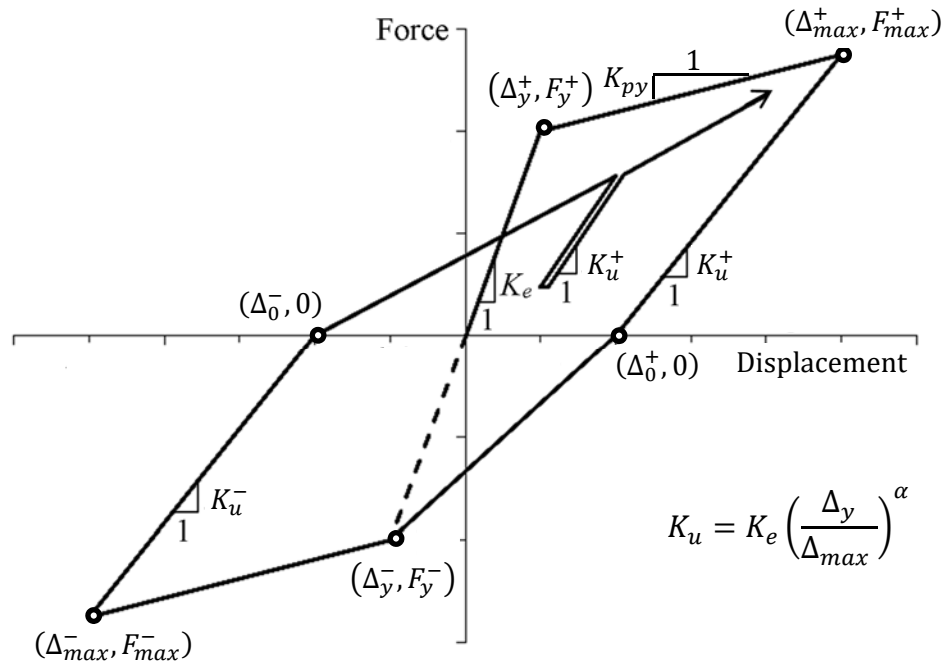


Figure 186 - Idealized force-displacement curve and hysteresis model^[37]

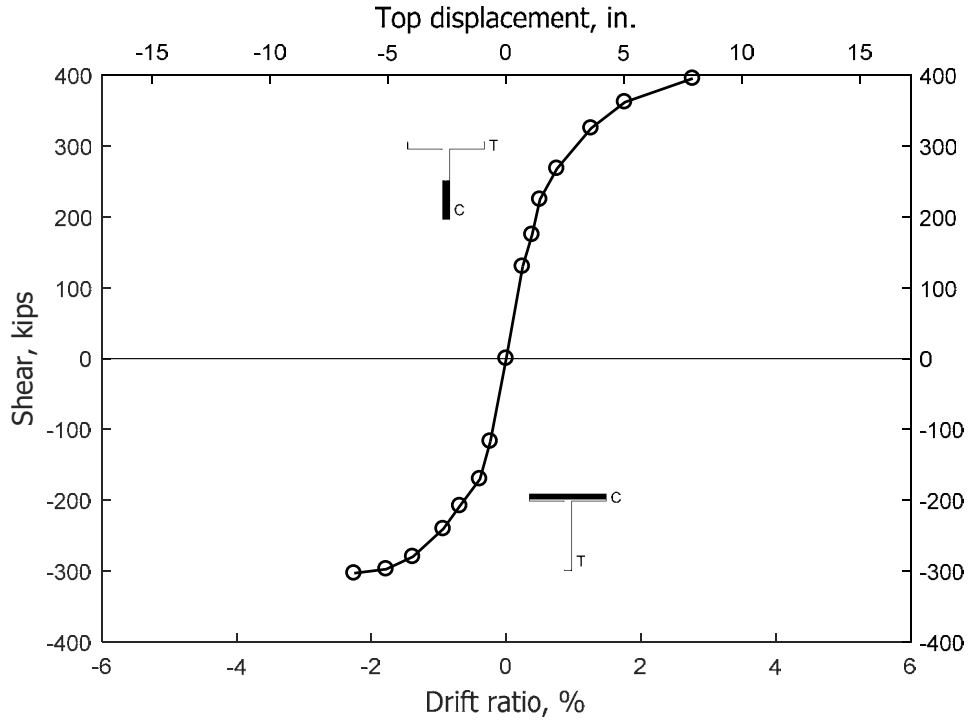


Figure 187 – Envelope of shear versus drift ratio for T5 (1 in. = 25.4 mm, 1 kip = 4.45 kN)

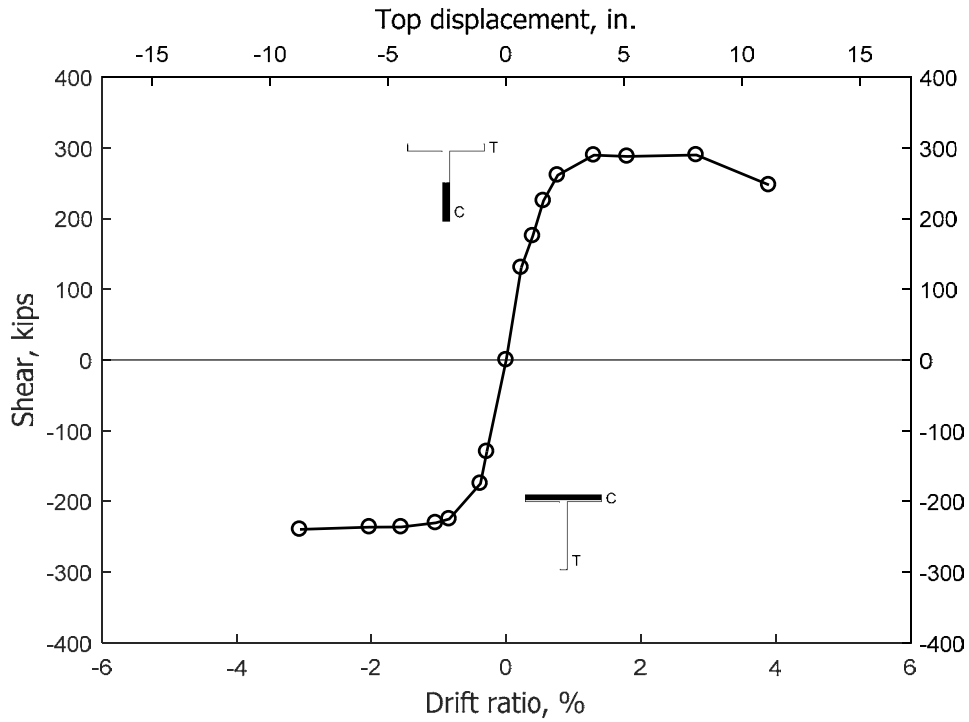


Figure 188 – Envelope of shear versus drift ratio for T6 (1 in. = 25.4 mm, 1 kip = 4.45 kN)

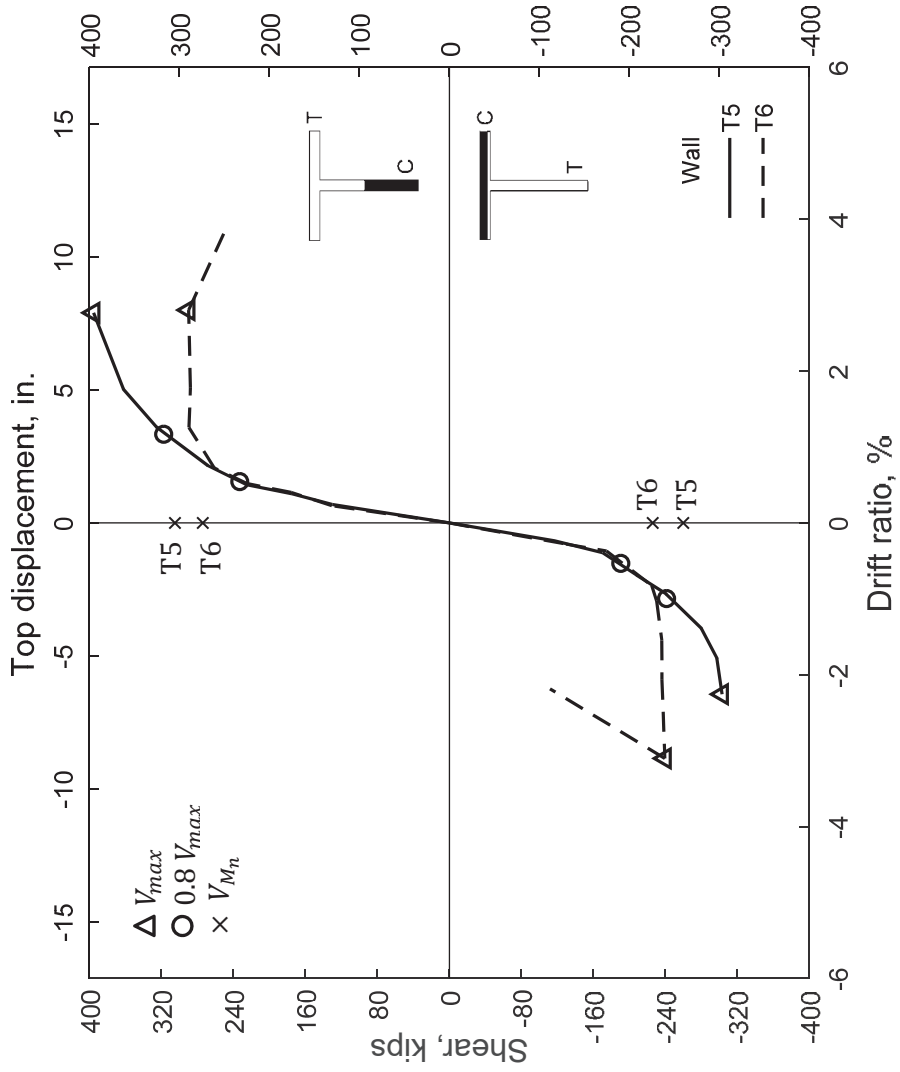


Figure 189 – Envelopes of shear versus drift ratio (1 in. = 25.4 mm, 1 kip = 4.45 kN)

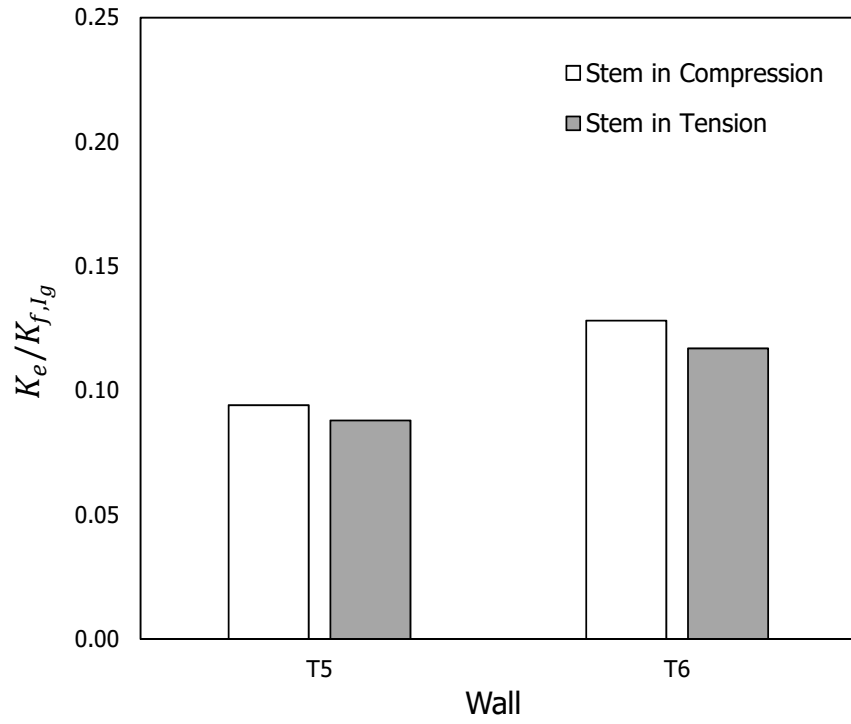


Figure 190 – Effective initial stiffness K_e normalized by flexural stiffness based on gross section

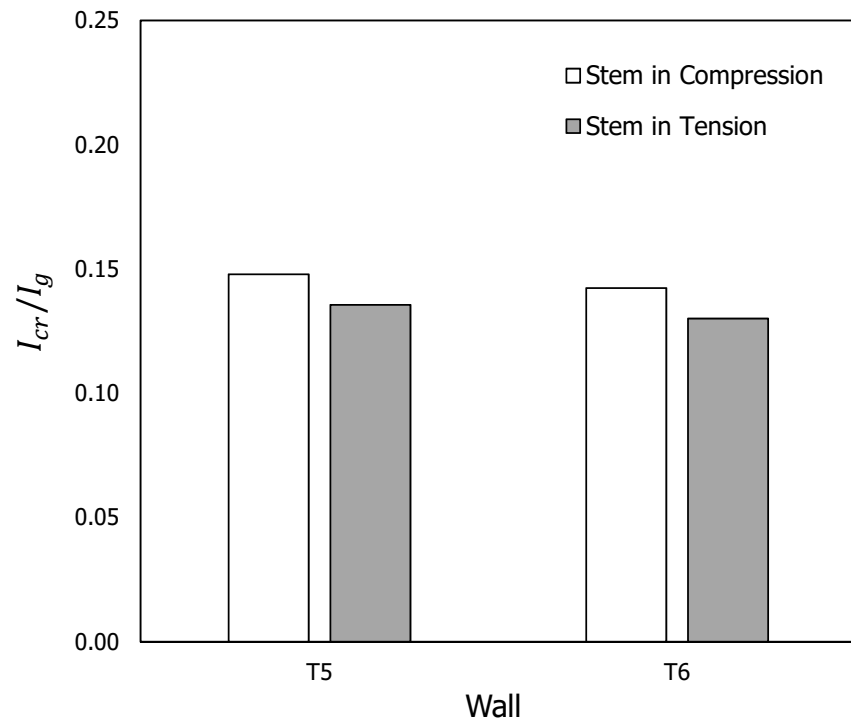


Figure 191 – Cracked moment of inertia normalized by gross moment of inertia

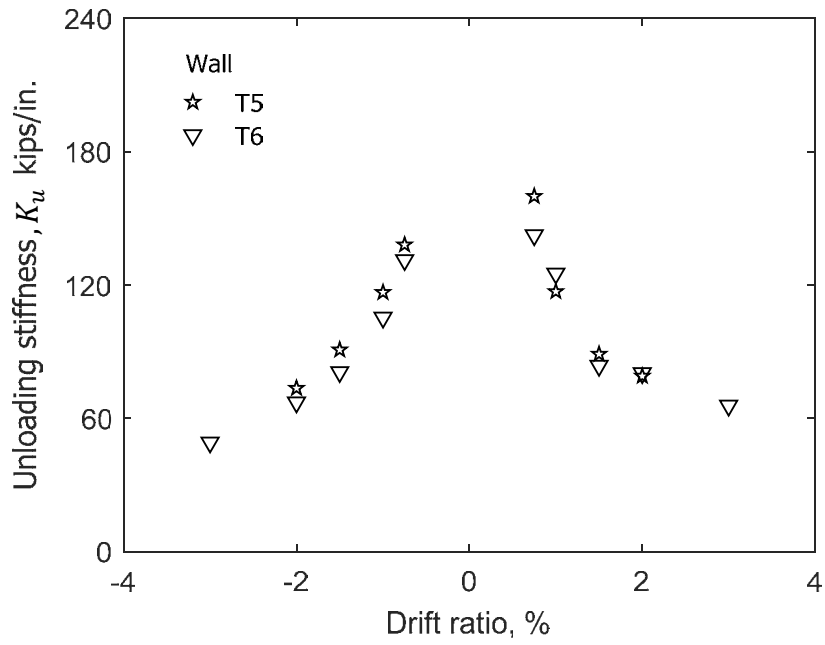


Figure 192 – Unloading stiffness versus drift ratio (1 in. = 25.4 mm, 1 kip = 4.45 kN)

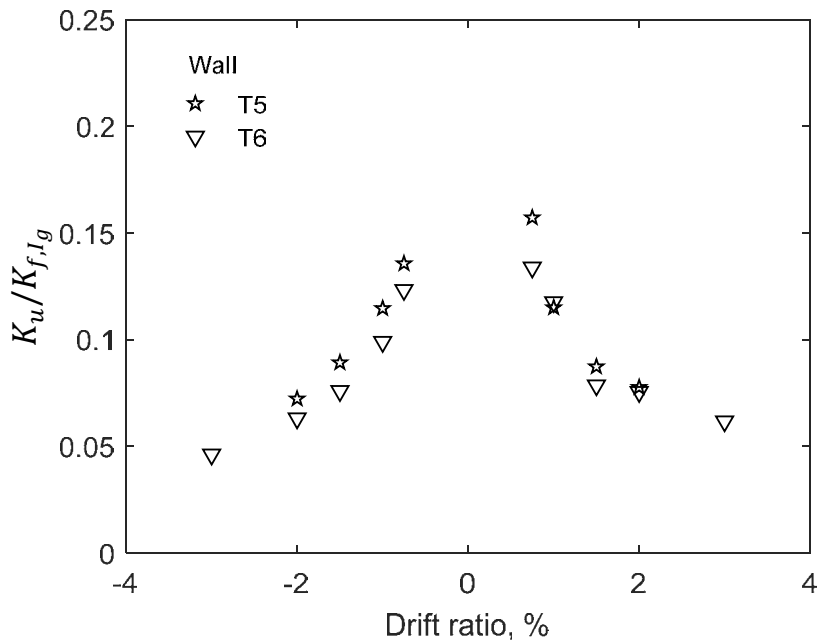
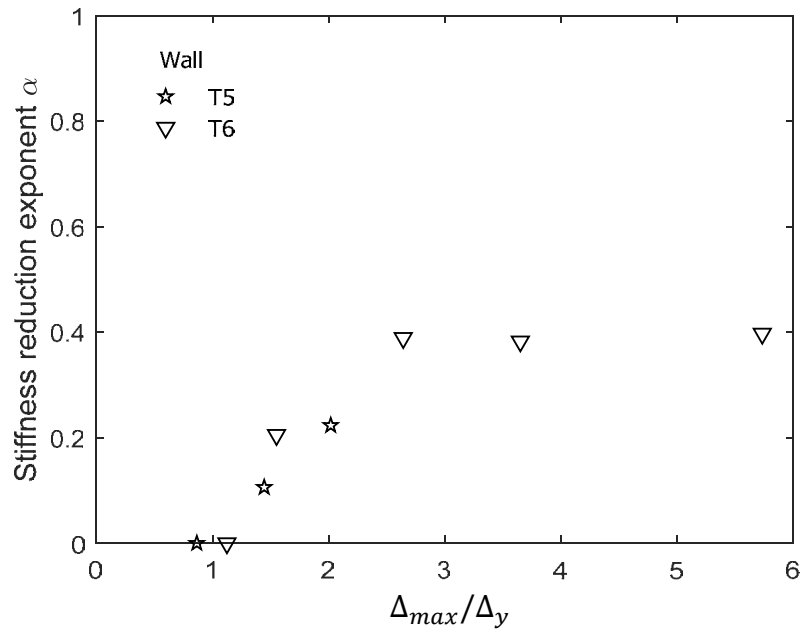
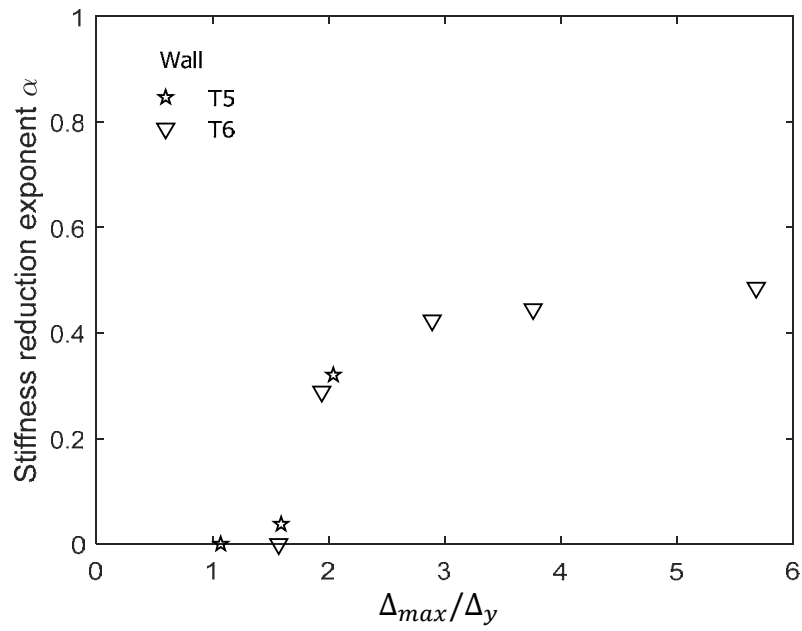


Figure 193 – Normalized unloading stiffness versus drift ratio



(a) Stem in compression



(b) Stem in tension

Figure 194 – Stiffness reducing exponent versus normalized displacement

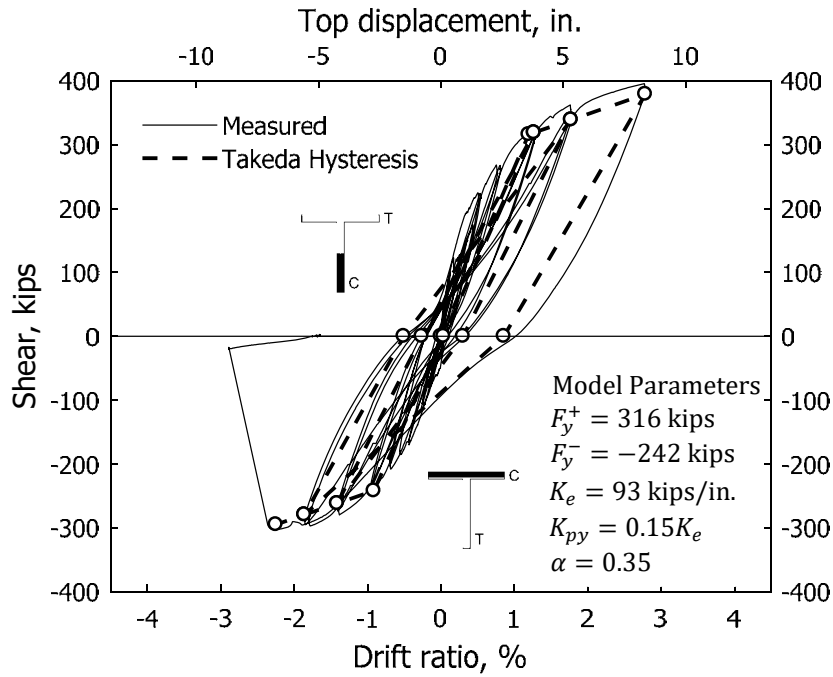


Figure 195 – Comparison of measured response with Takeda hysteresis model for T5 (1 in. = 25.4 mm, 1 kip = 4.45 kN)

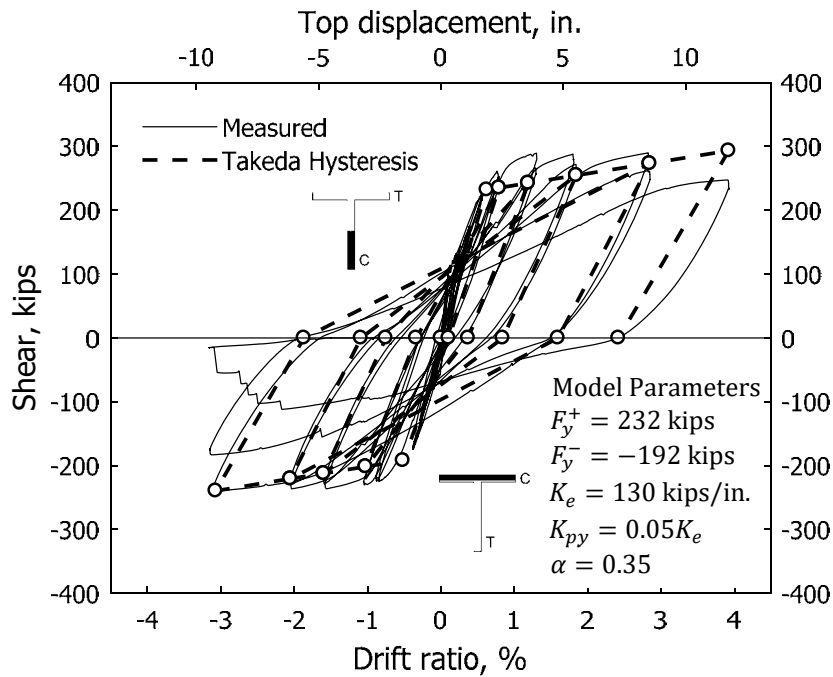


Figure 196 – Comparison of measured response with Takeda hysteresis model for T6 (1 in. = 25.4 mm, 1 kip = 4.45 kN)

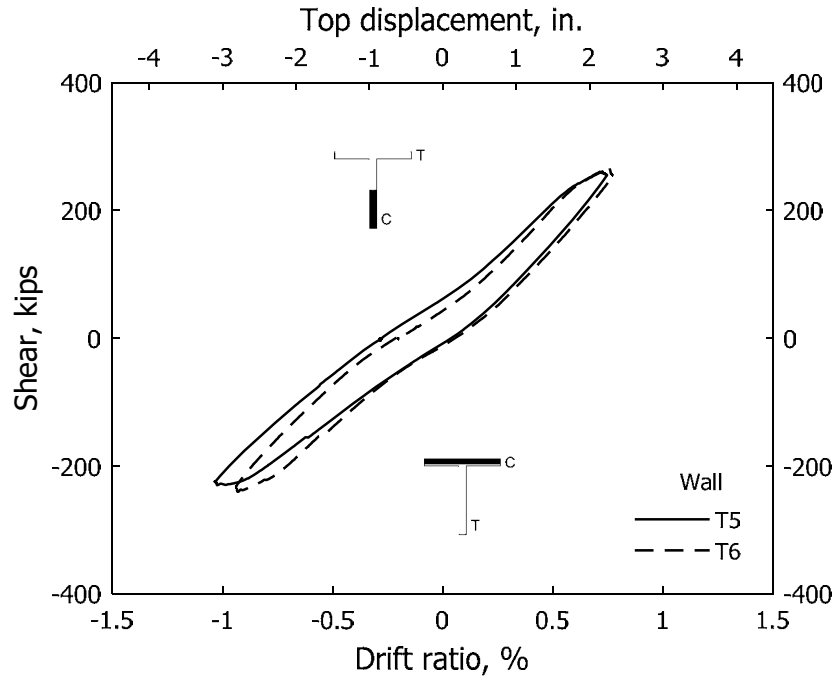


Figure 197 – Shear versus drift ratio during first cycle to 1% drift ratio (1 in. = 25.4 mm, 1 kip = 4.45 kN)

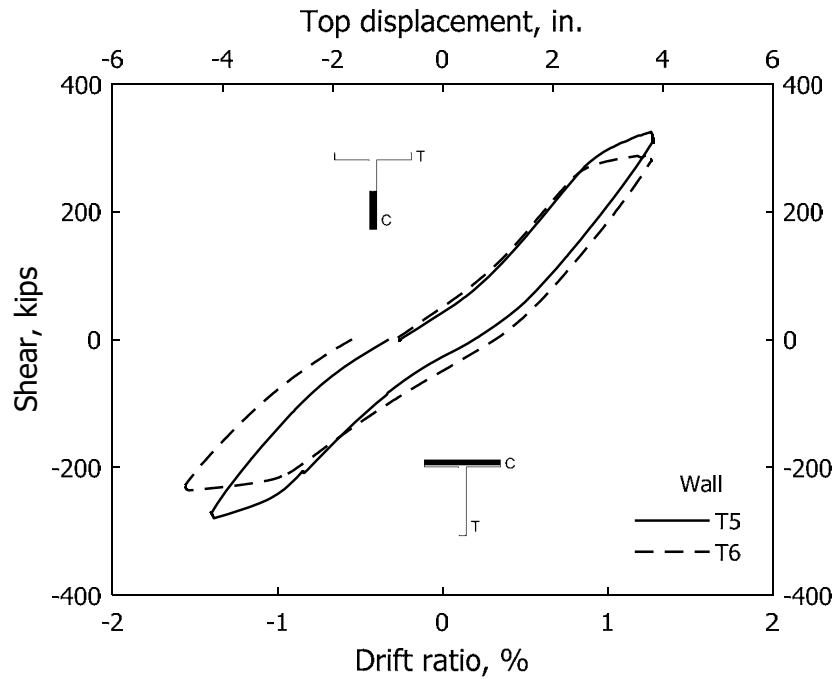


Figure 198 – Shear versus drift ratio during first cycle to 1.5% drift ratio (1 in. = 25.4 mm, 1 kip = 4.45 kN)

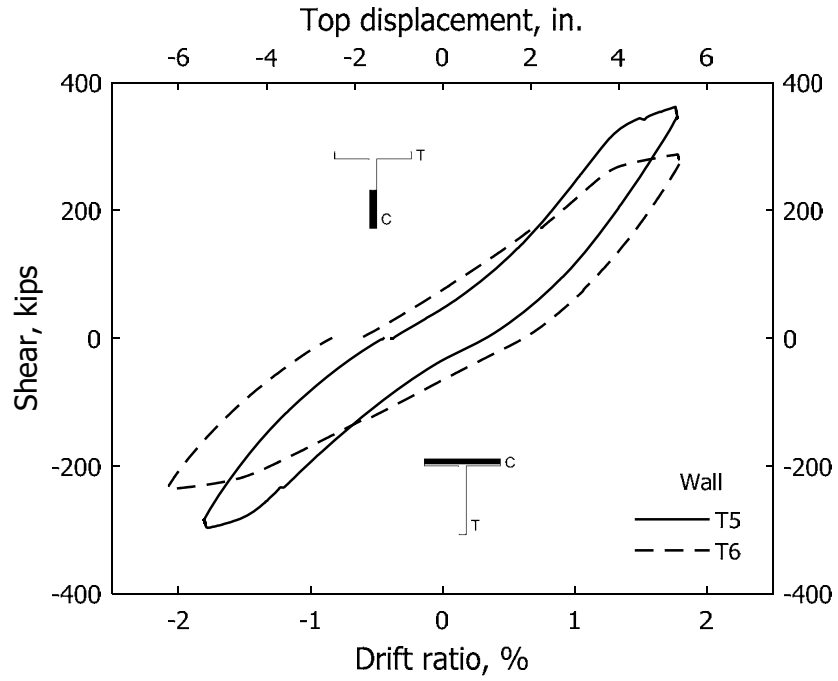


Figure 199 – Shear versus drift ratio during first cycle to 2% drift ratio (1 in. = 25.4 mm, 1 kip = 4.45 kN)

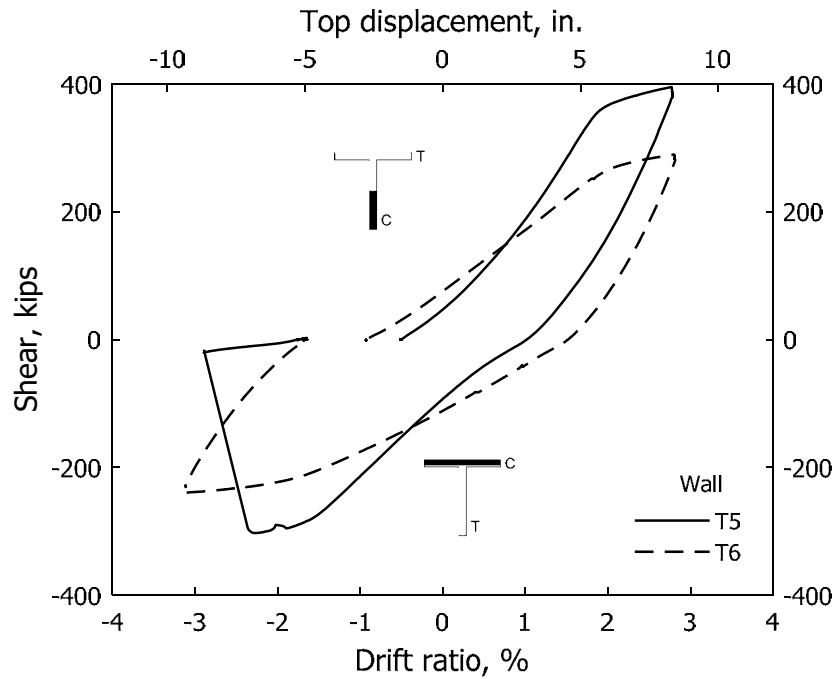
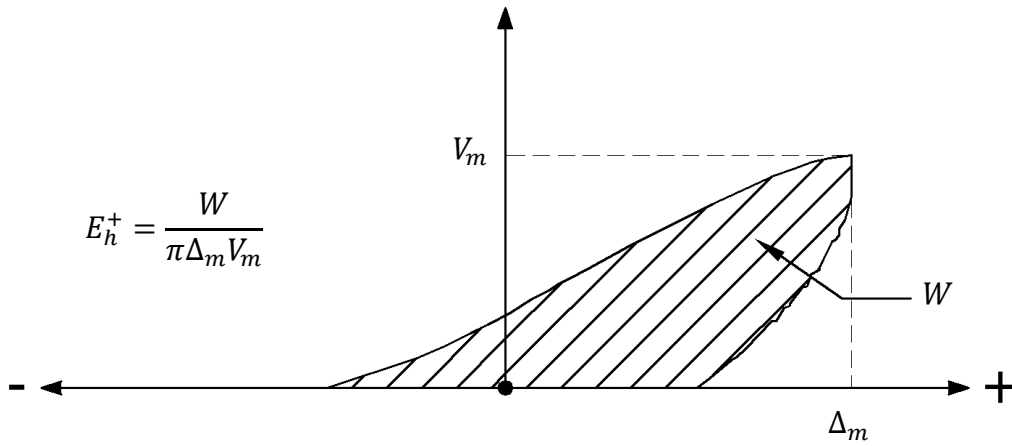
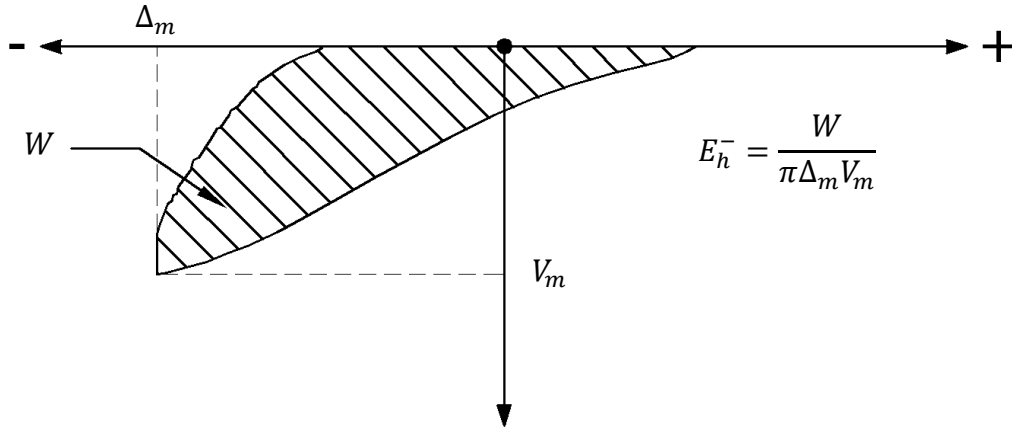


Figure 200 – Shear versus drift ratio during first cycle to 3% drift ratio (1 in. = 25.4 mm, 1 kip = 4.45 kN)

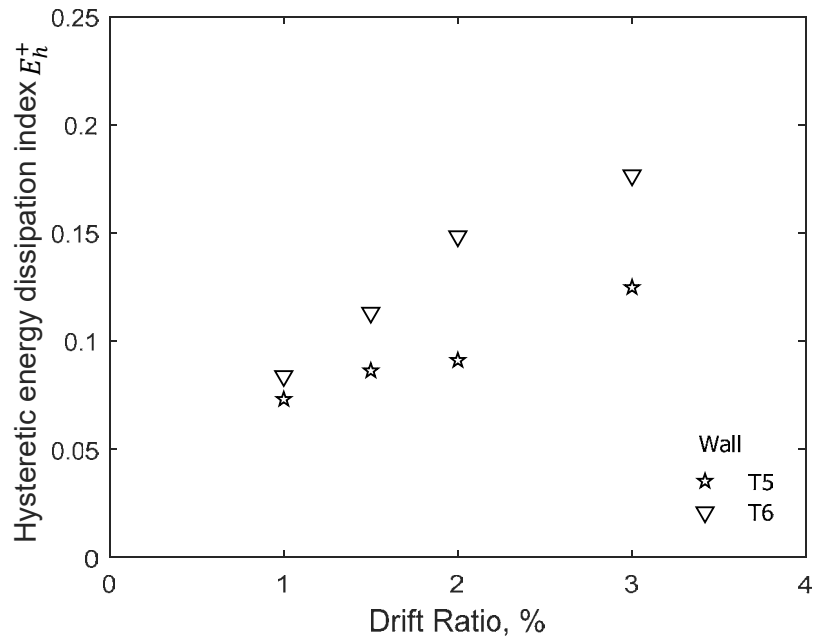


(a) Stem in compression

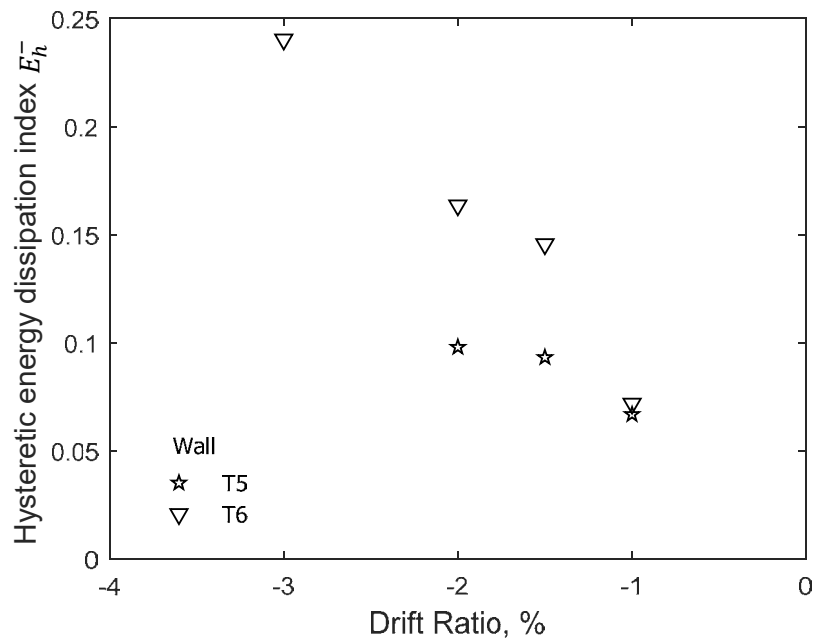


(b) Stem in tension

Figure 201 - Hysteretic energy dissipation index^[37]

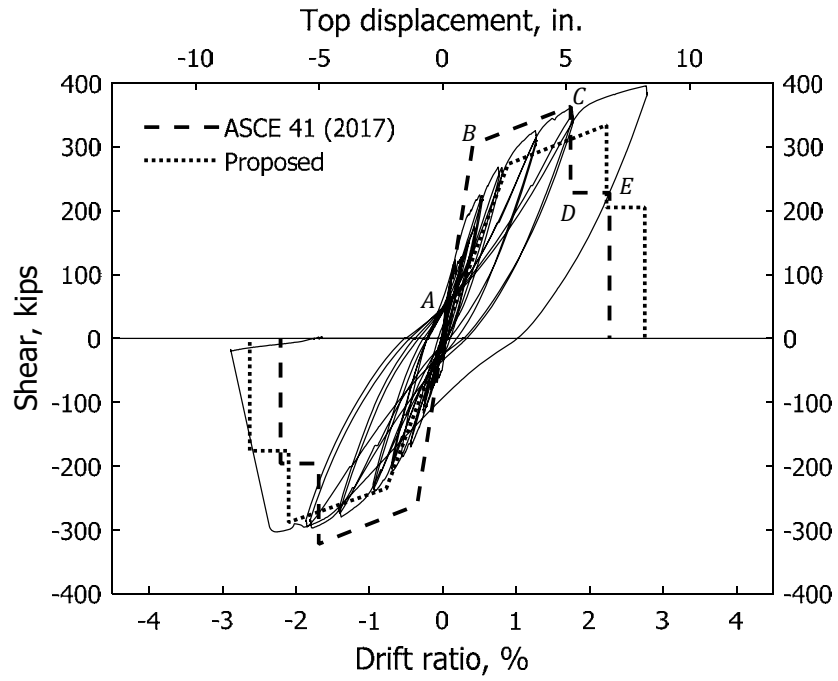


(a) Stem in compression

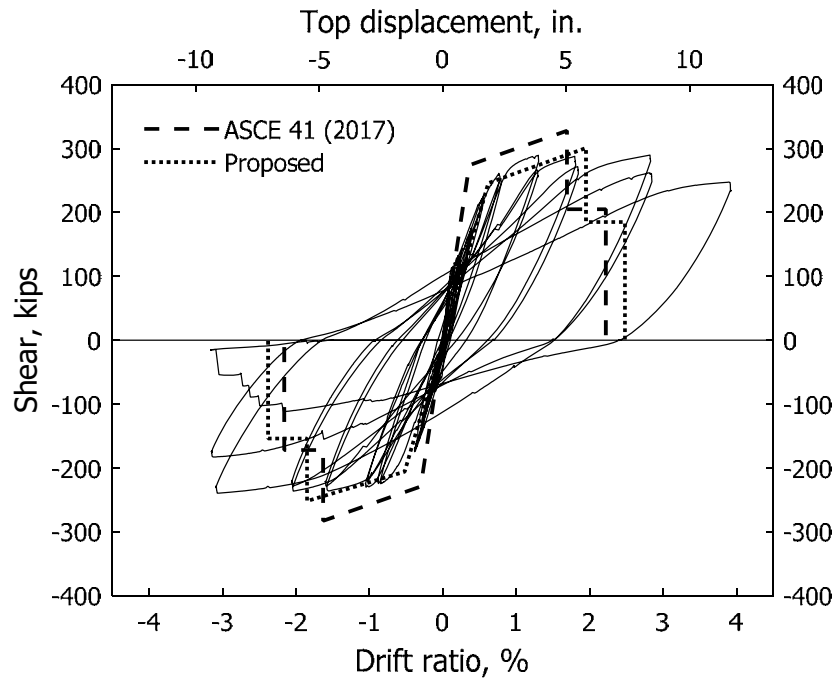


(b) Stem in tension

Figure 202 - Hysteretic energy dissipation index versus drift ratio

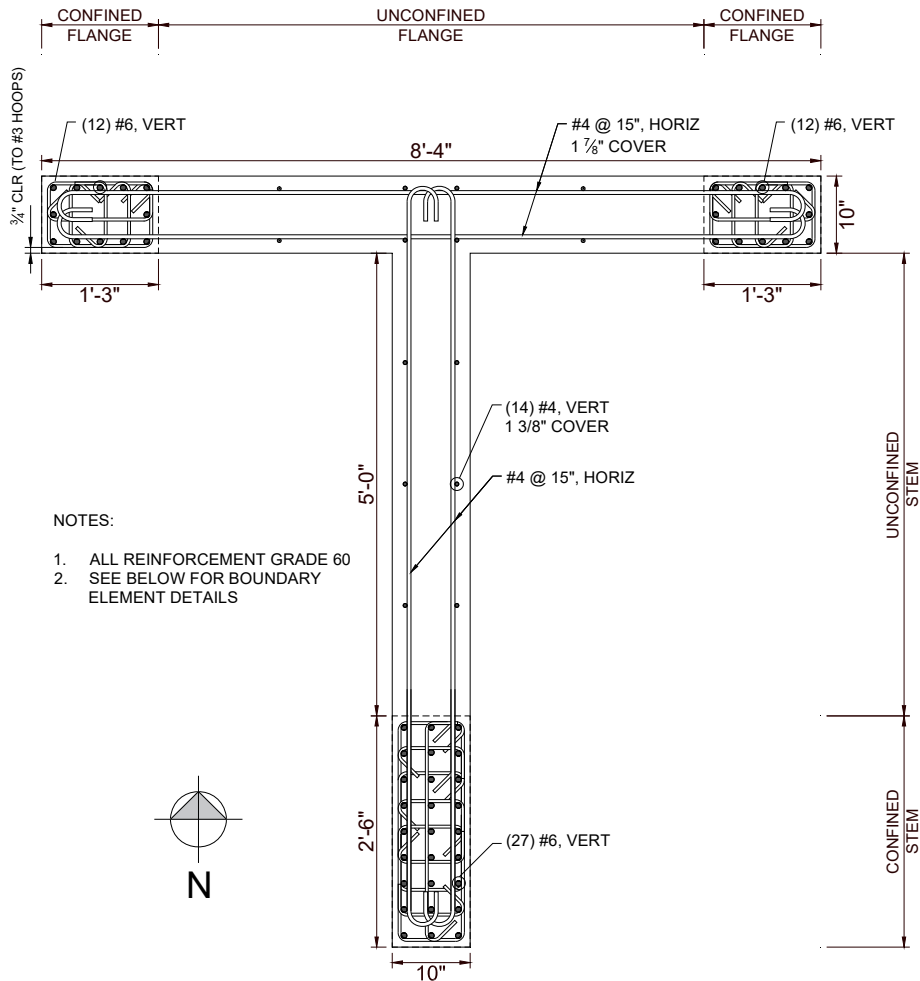


(a) T5

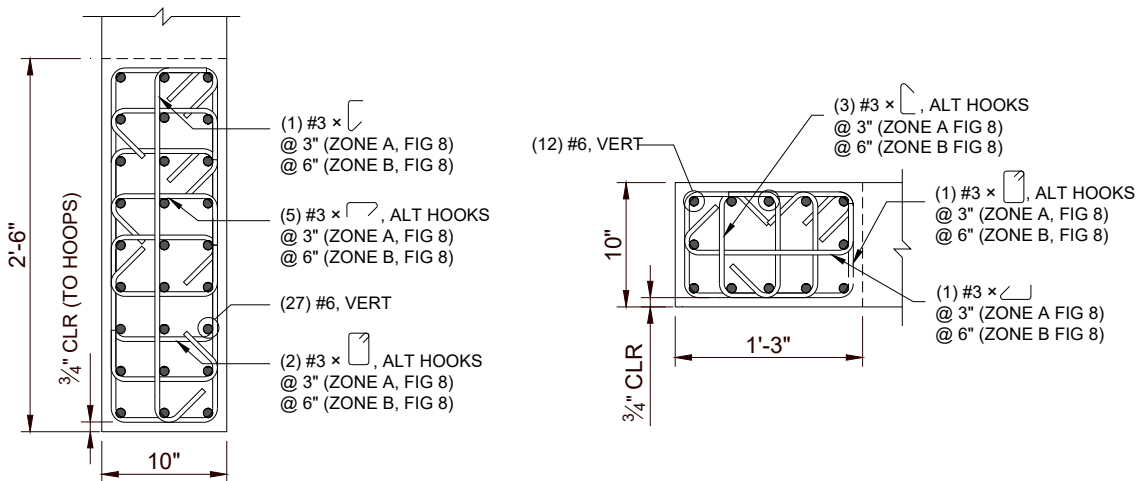


(b) T6

Figure 203 – Measured shear versus drift ratio compared with modeling parameters from Table 15
(1 kip = 4.45 kN)

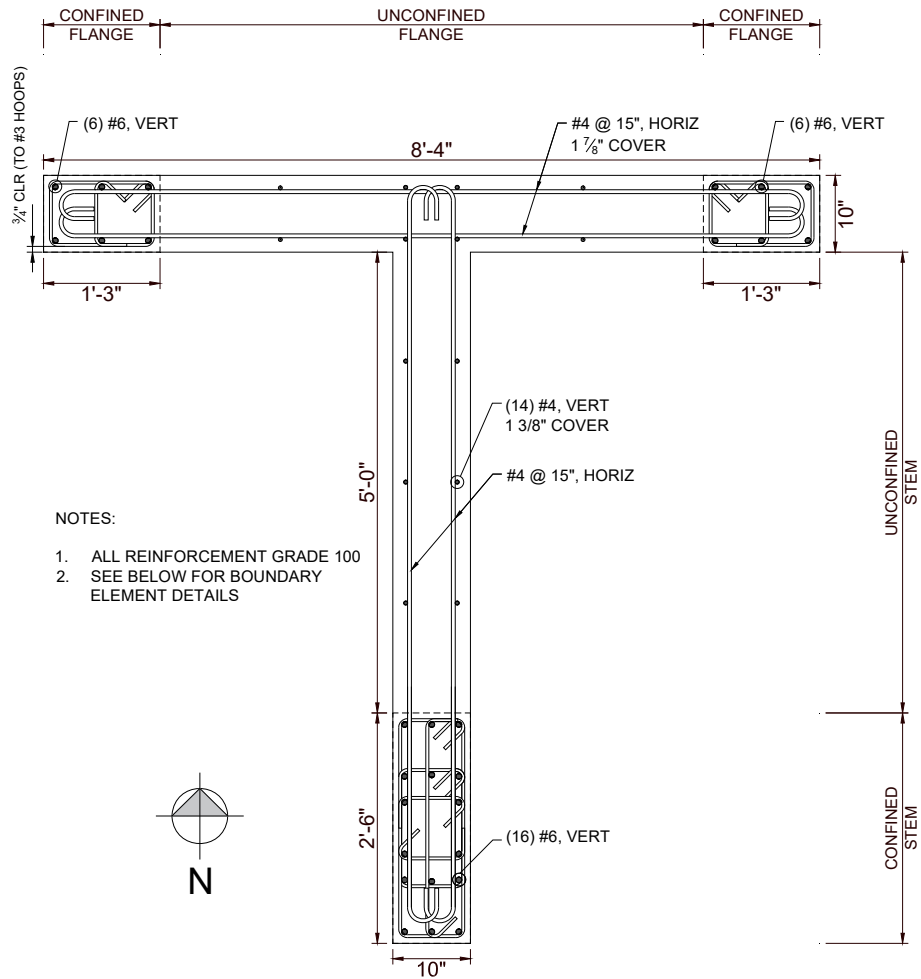


(a) Cross section

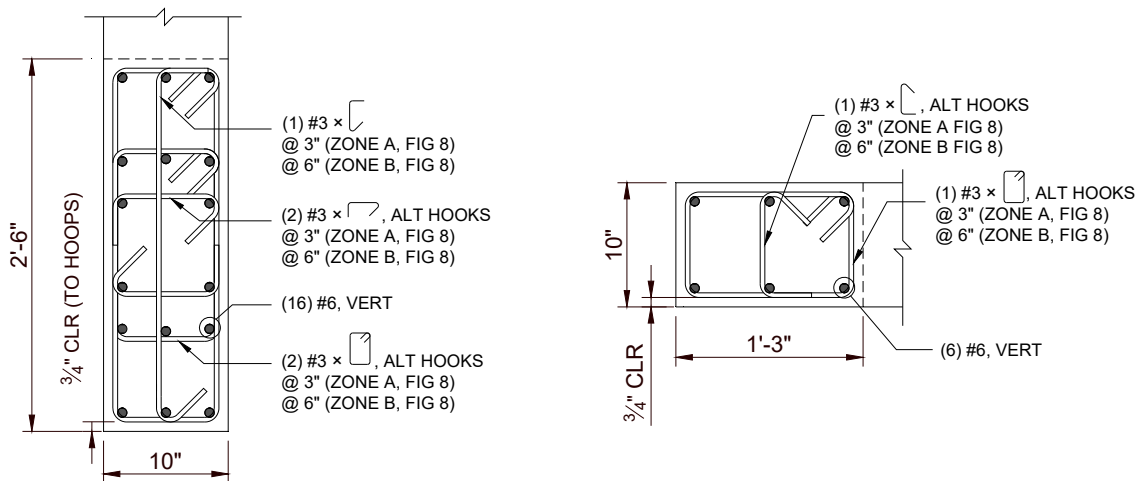


(b) Confined boundary element reinforcement

Figure 204 – Geometry and reinforcement layout for T1

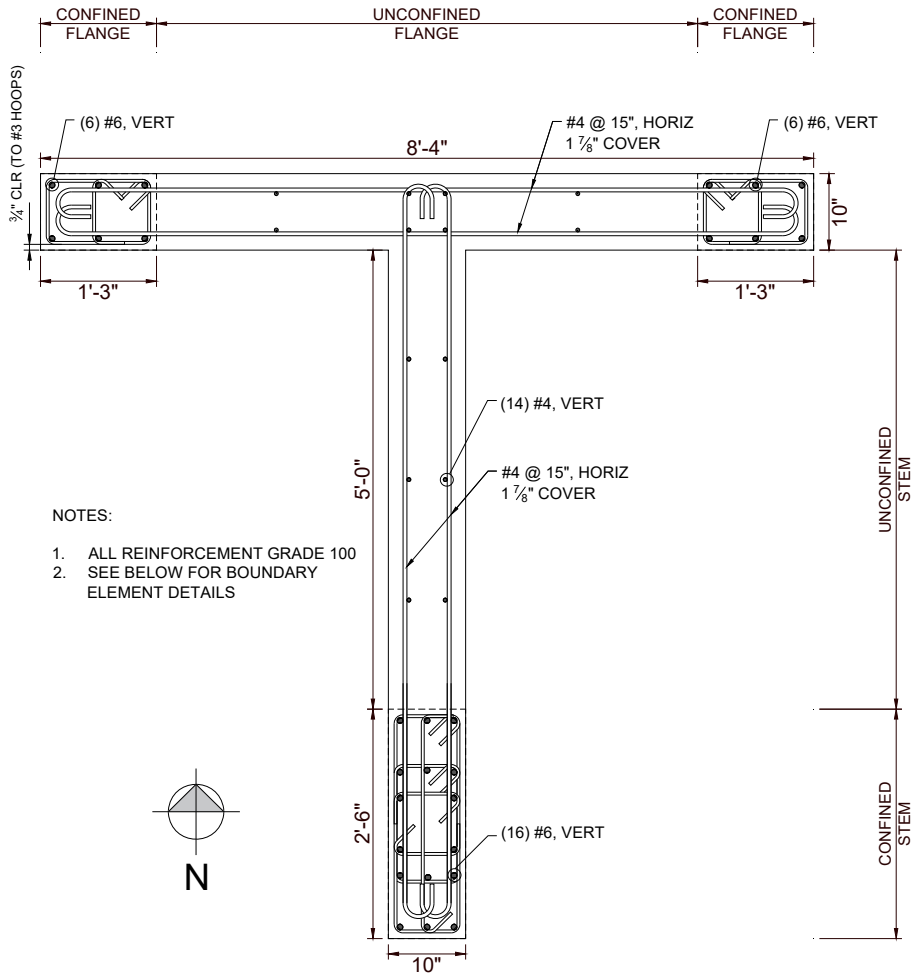


(a) Cross section

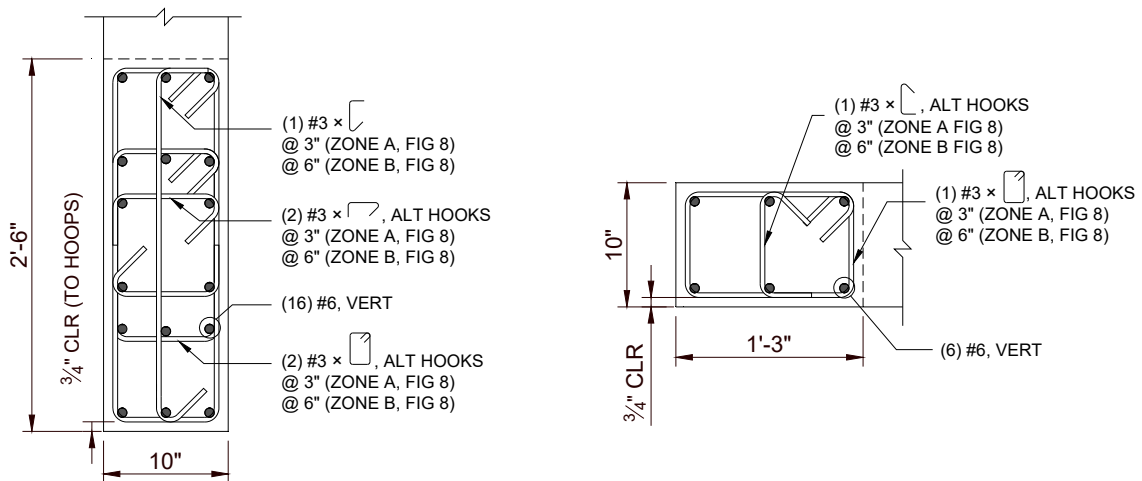


(b) Confined boundary element reinforcement

Figure 205 – Geometry and reinforcement layout for T2 and T3

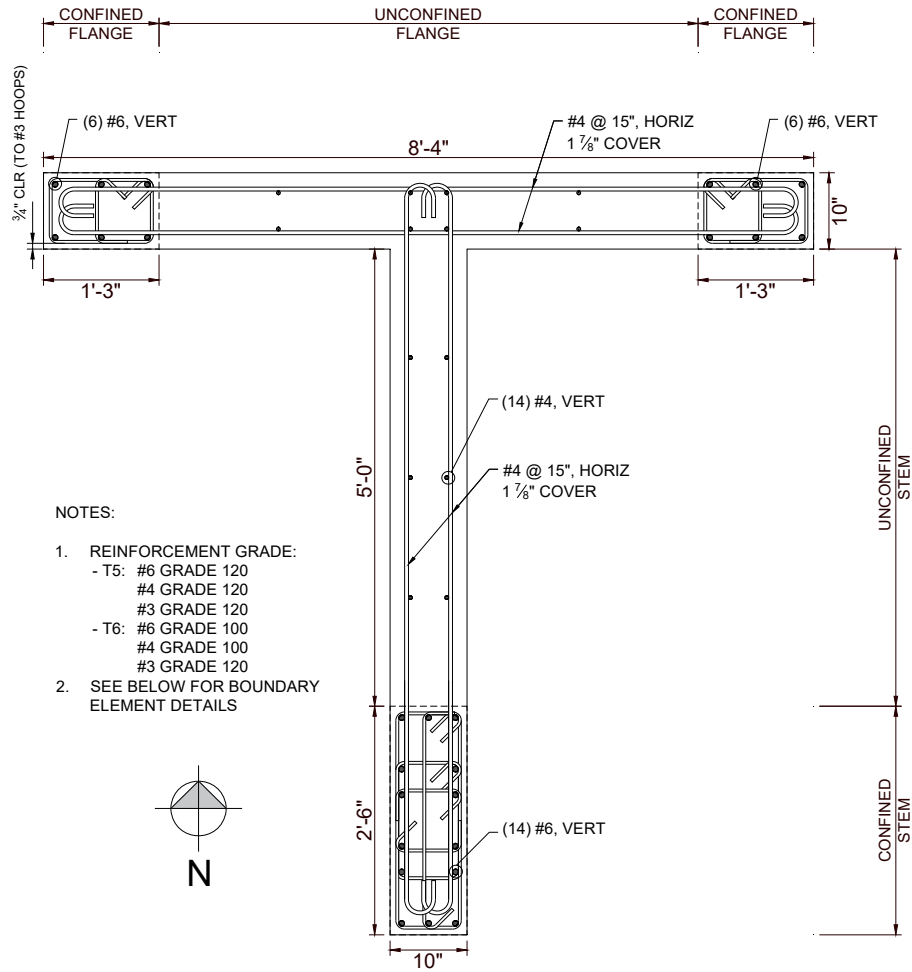


(a) Cross section

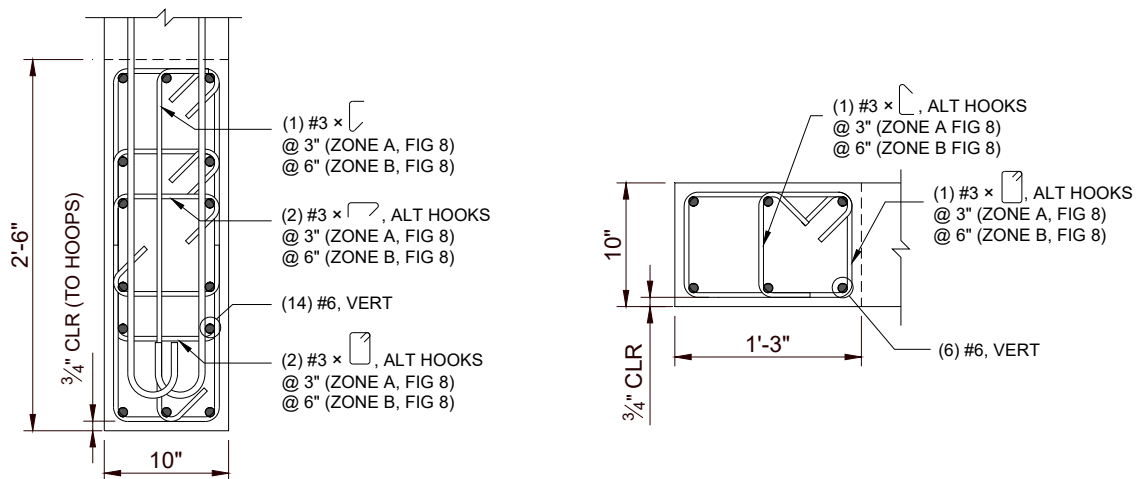


(b) Confined boundary element reinforcement

Figure 206 – Geometry and reinforcement layout for T4



(a) Cross section



(b) Confined boundary element reinforcement

Figure 207 – Geometry and reinforcement layout for T5 and T6

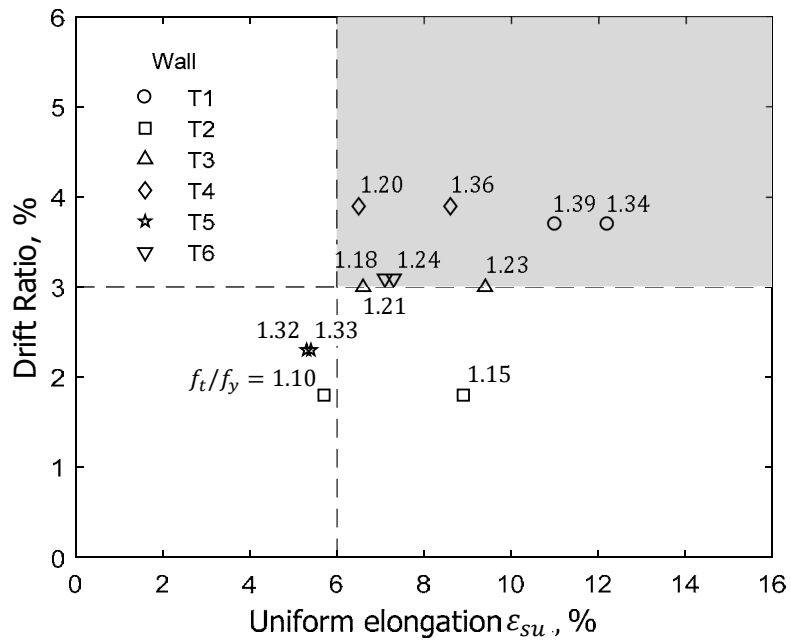


Figure 208 – Drift ratio versus uniform elongation of longitudinal reinforcing bars

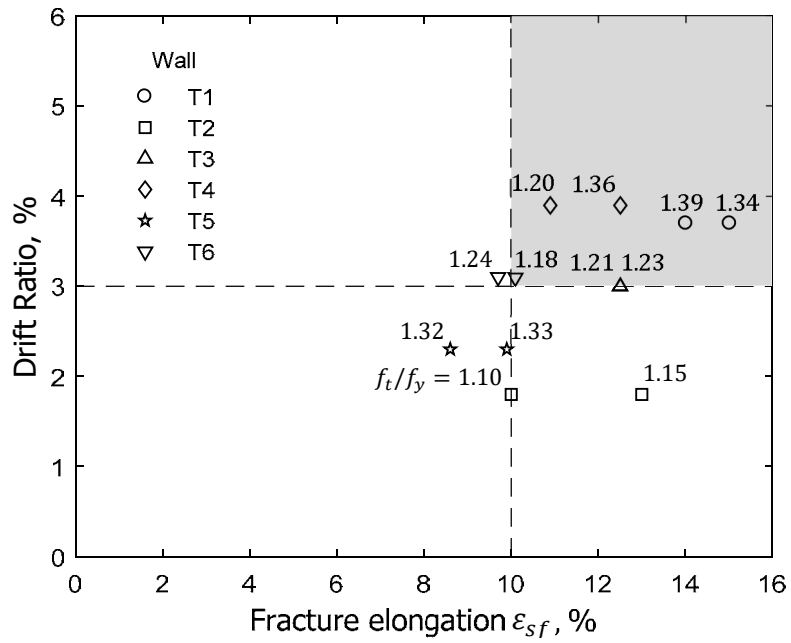


Figure 209 – Drift ratio versus fracture elongation of longitudinal reinforcing bars

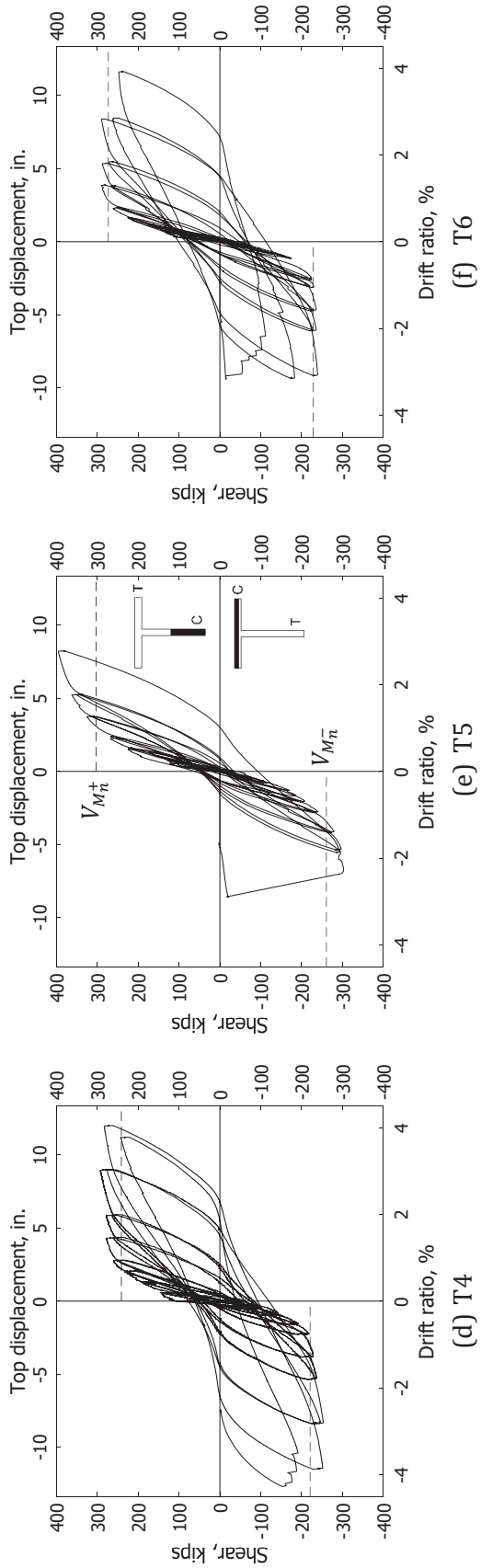
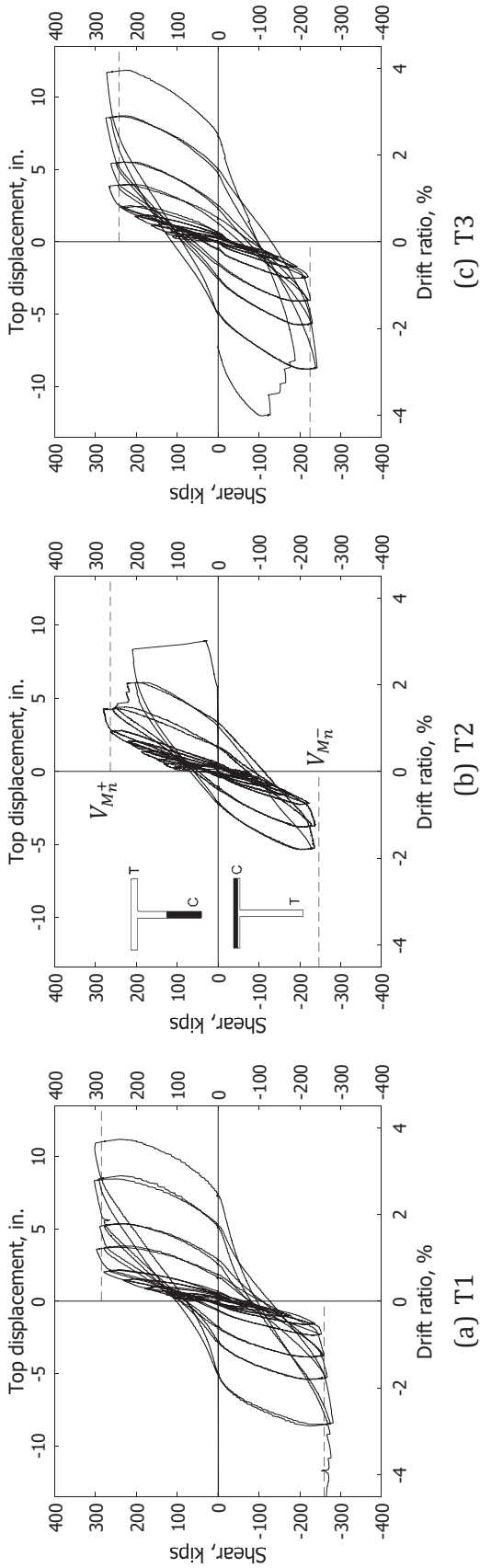
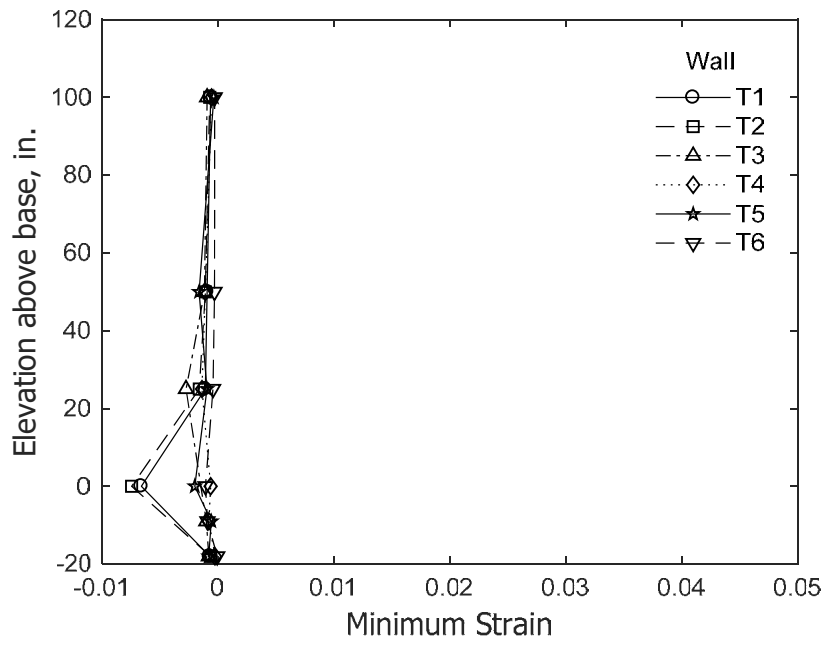
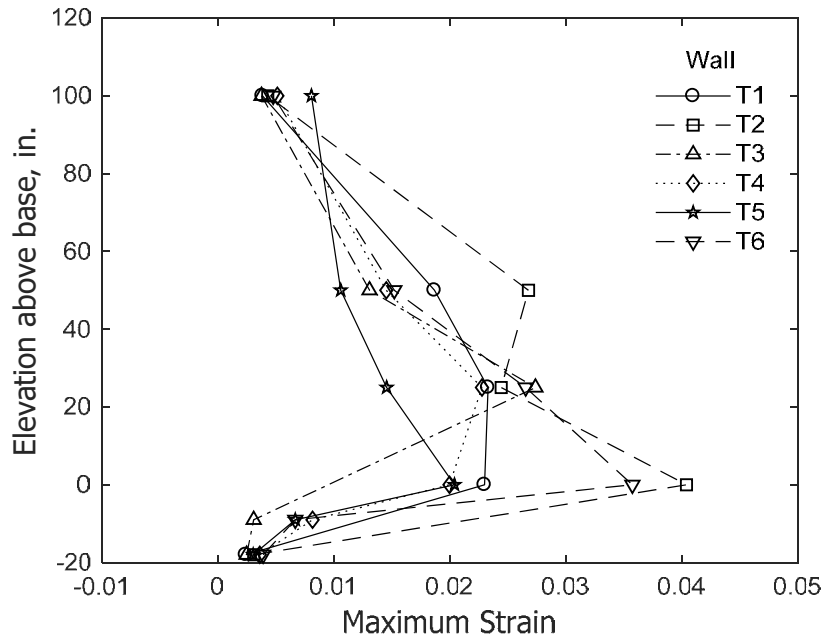


Figure 210 – Shear versus drift ratio (1 in. = 25.4 mm, 1 kip = 4.45 kN)

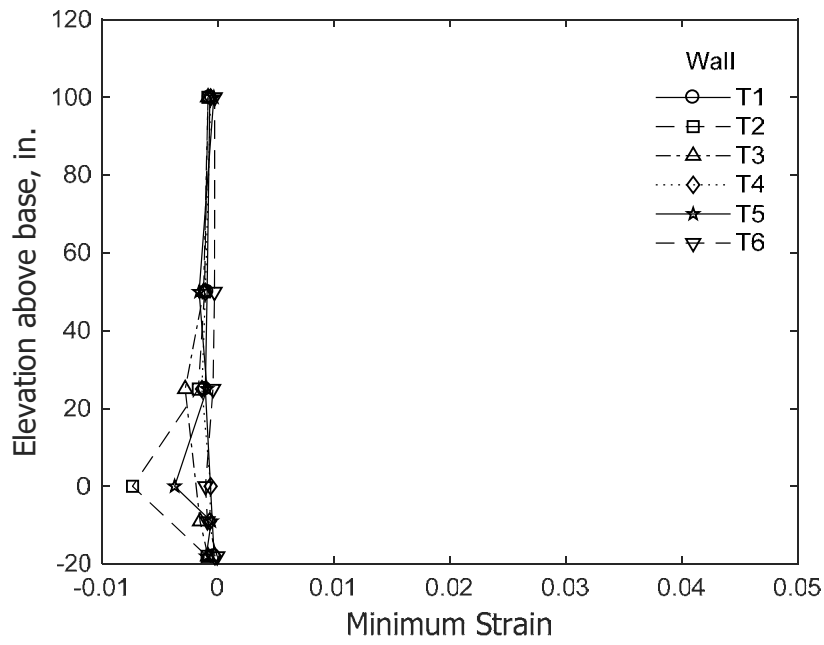


(a) Stem in compression

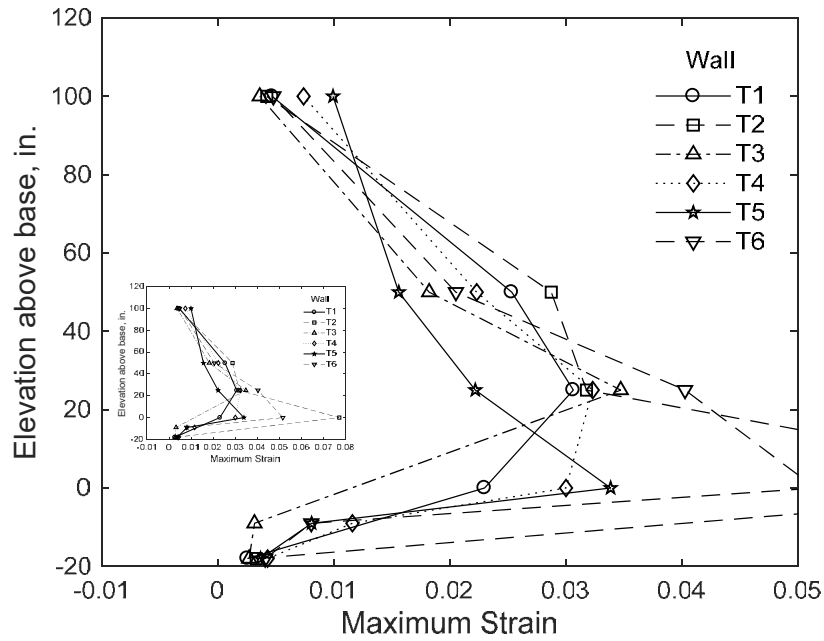


(b) Stem in tension

Figure 211 - Envelopes of measured strain in longitudinal bars at confined stem for 1.5% drift ratio

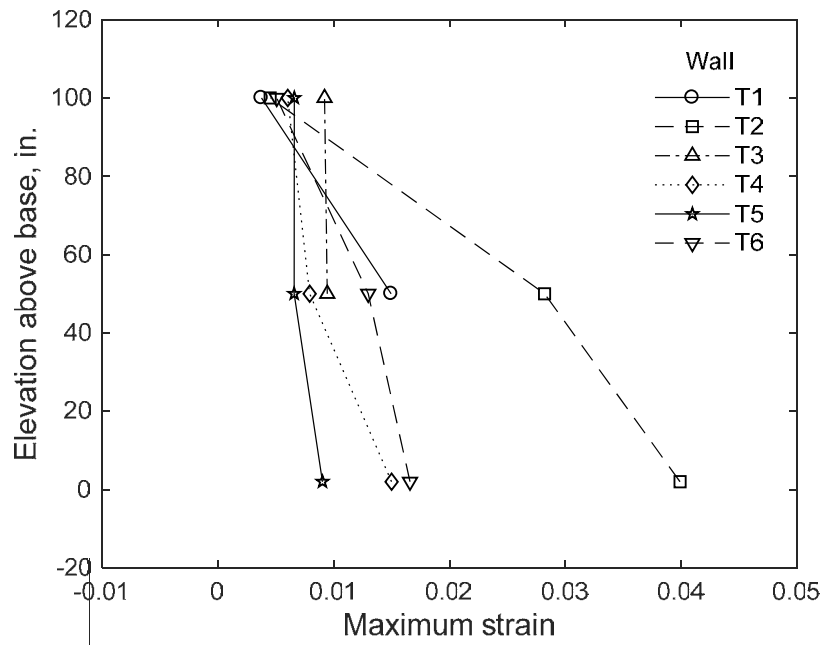


(a) Stem in compression

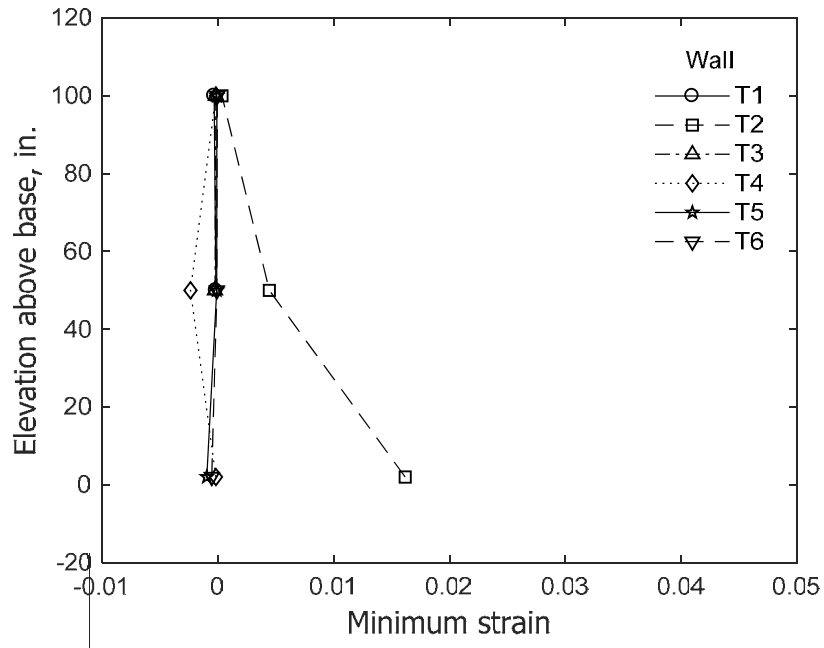


(b) Stem in tension

Figure 212 – Envelopes of measured strain in longitudinal bars at confined stem for 2% drift ratio

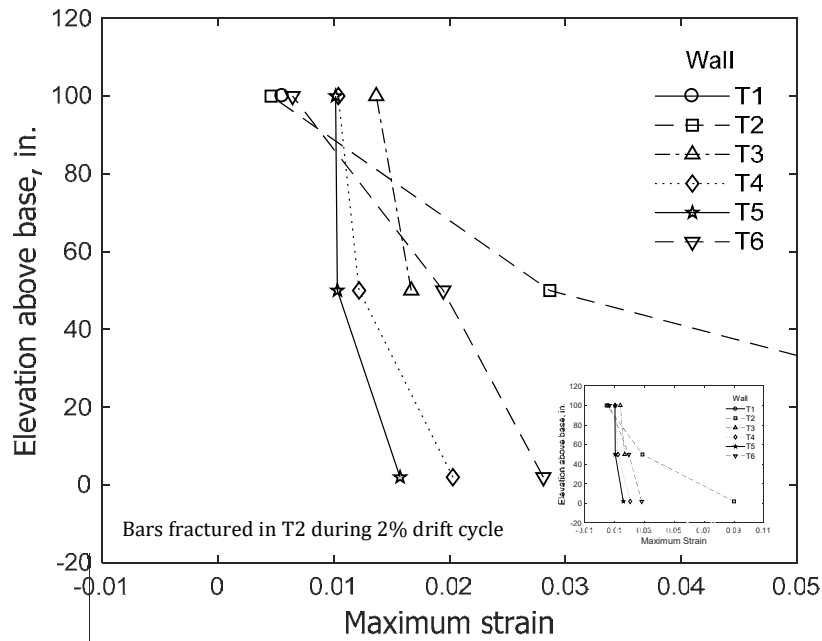


(a) Stem in compression

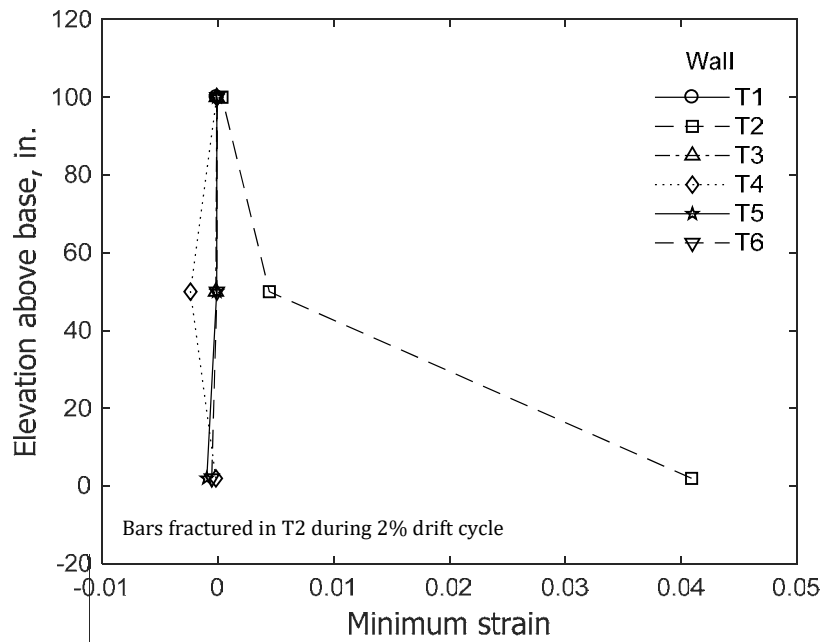


(b) Stem in tension

Figure 213 – Envelopes of measured strain in longitudinal bars at confined flange for 1.5% drift ratio

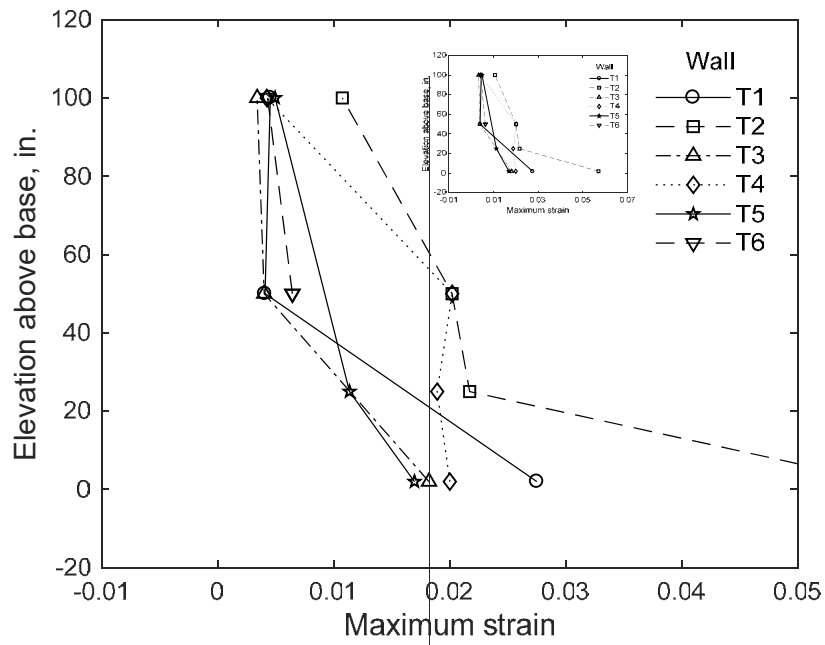


(a) Stem in compression

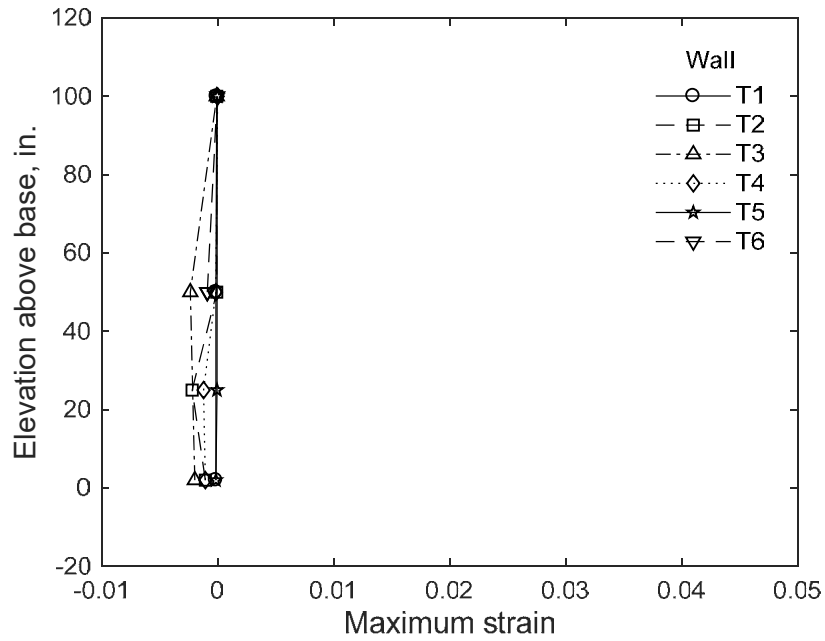


(b) Stem in tension

Figure 214 – Envelopes of measured strain in longitudinal bars at confined flange for 2% drift ratio

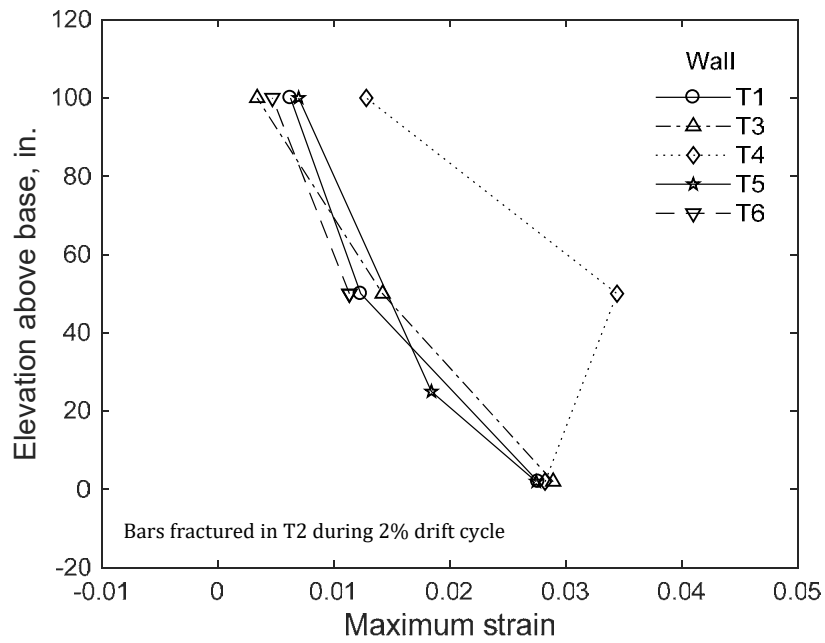


(a) Stem in compression

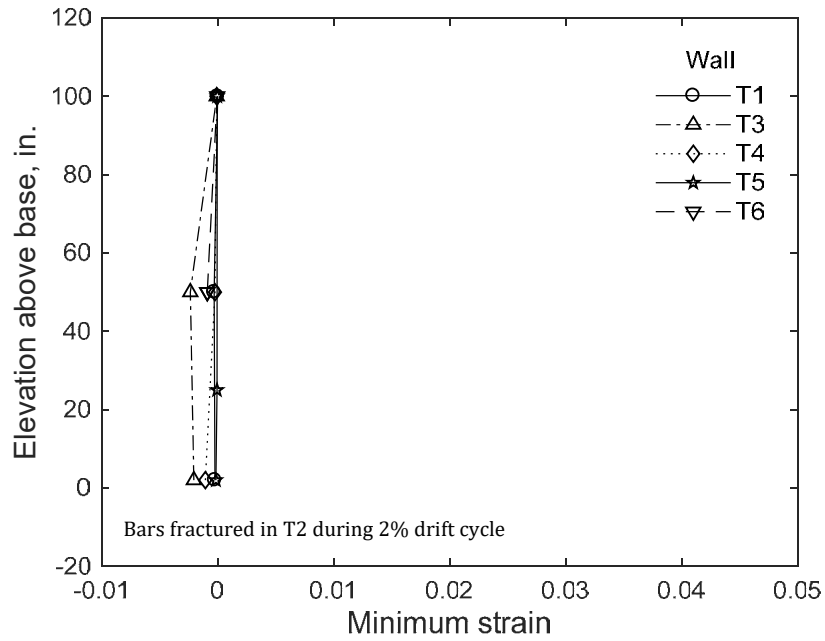


(b) Stem in tension

Figure 215 – Envelopes of measured strain in longitudinal bars at unconfined flange for 1.5% drift ratio

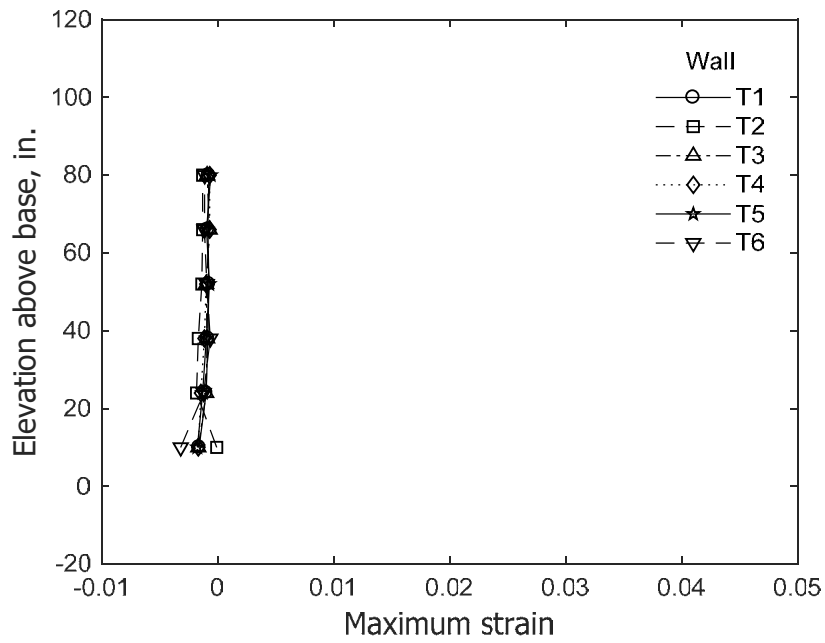


(a) Stem in compression

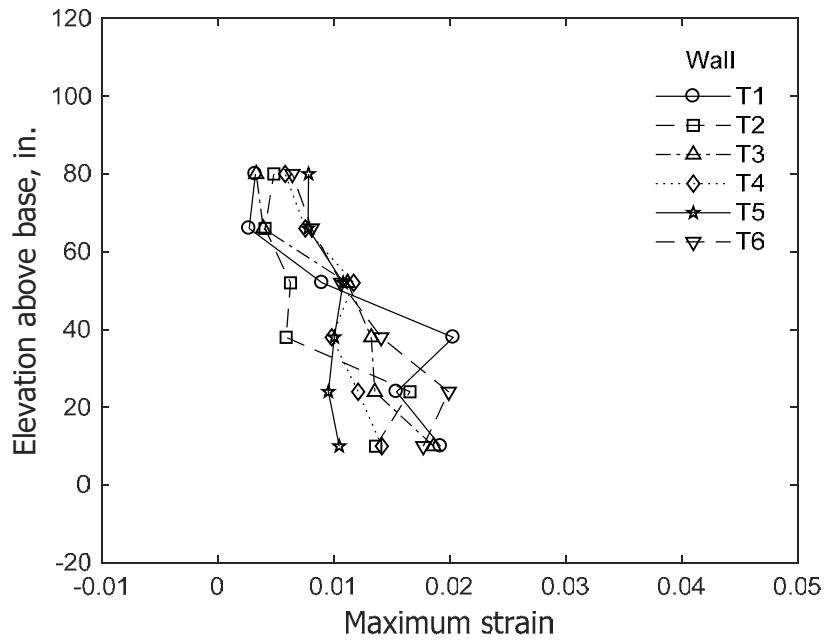


(b) Stem in tension

Figure 216 – Envelopes of measured strain in longitudinal bars at unconfined flange for 2% drift ratio

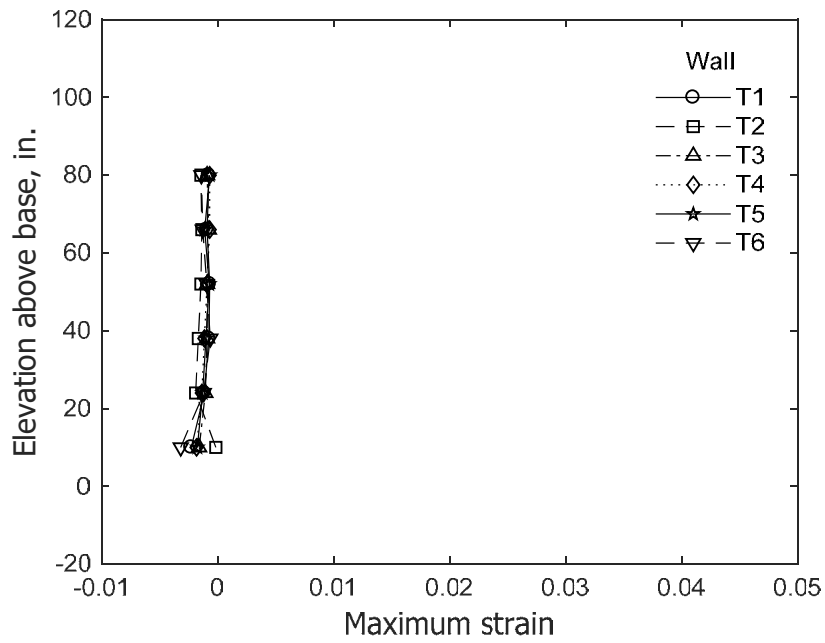


(a) Stem in compression

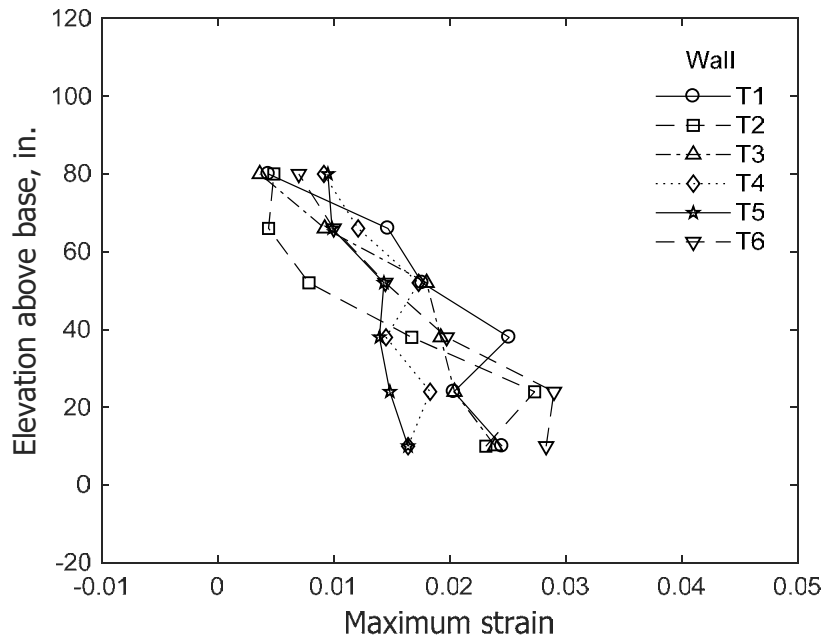


(b) Stem in tension

Figure 217 – Envelopes of concrete strain for confined stem at 1.5% drift ratio (data from optical markers along Columns 1 and 2)

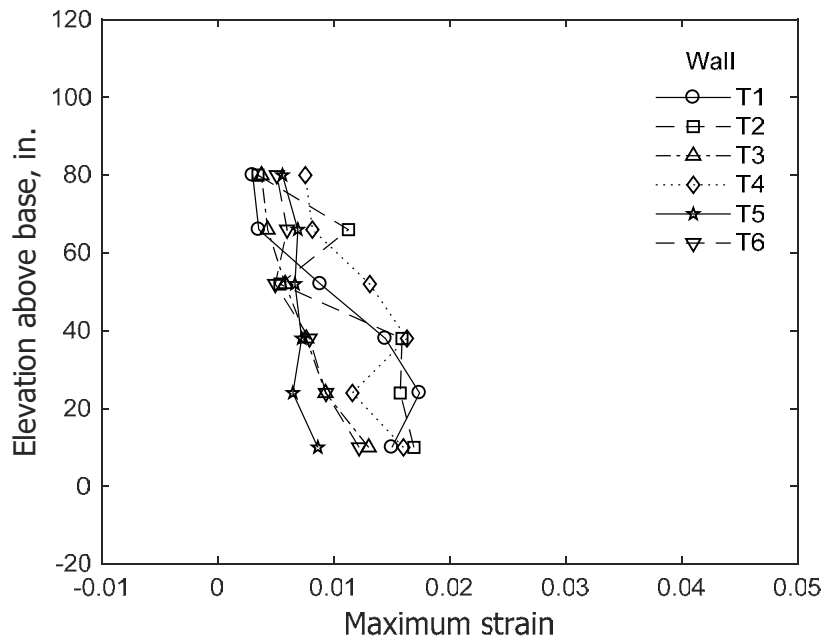


(a) Stem in compression

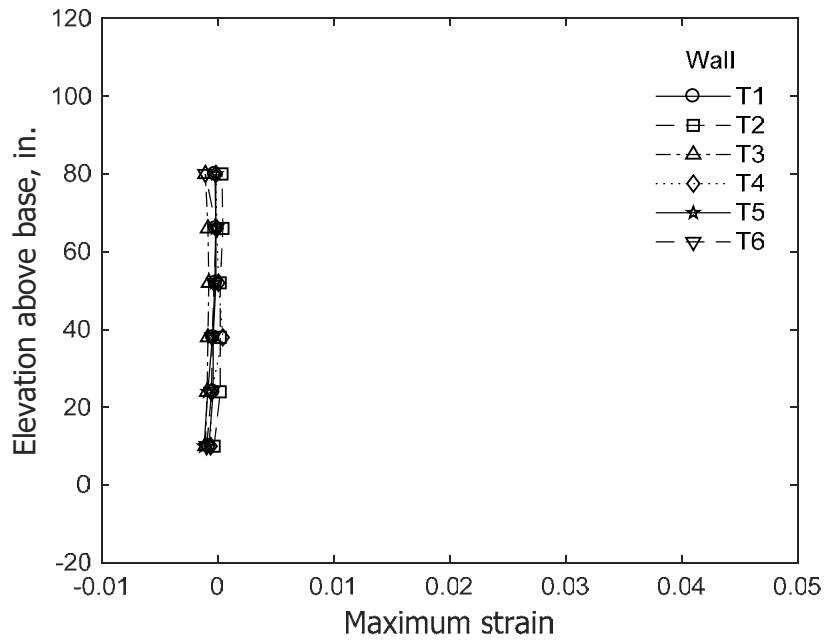


(b) Stem in tension

Figure 218 – Envelopes of concrete strain for confined stem at 2% drift ratio (data from optical markers along Columns 1 and 2)

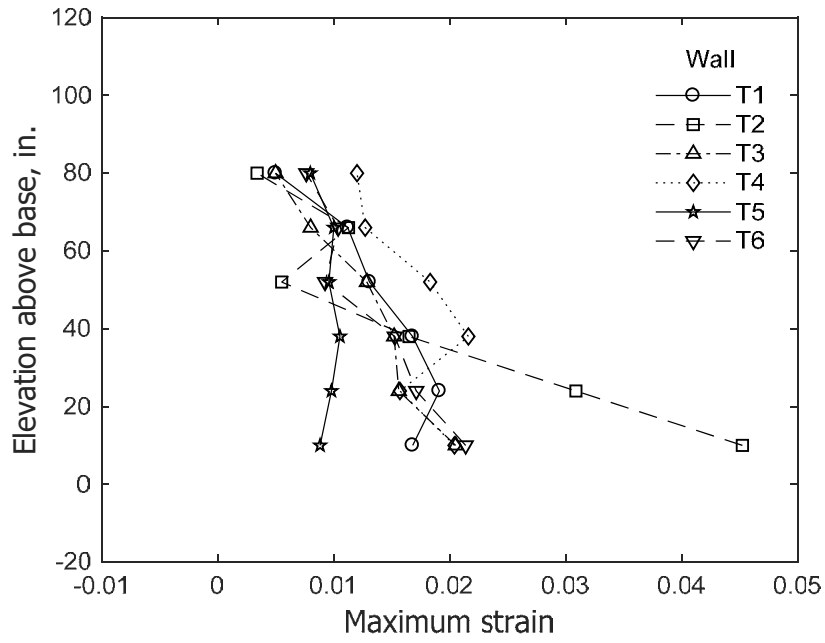


(a) Stem in compression

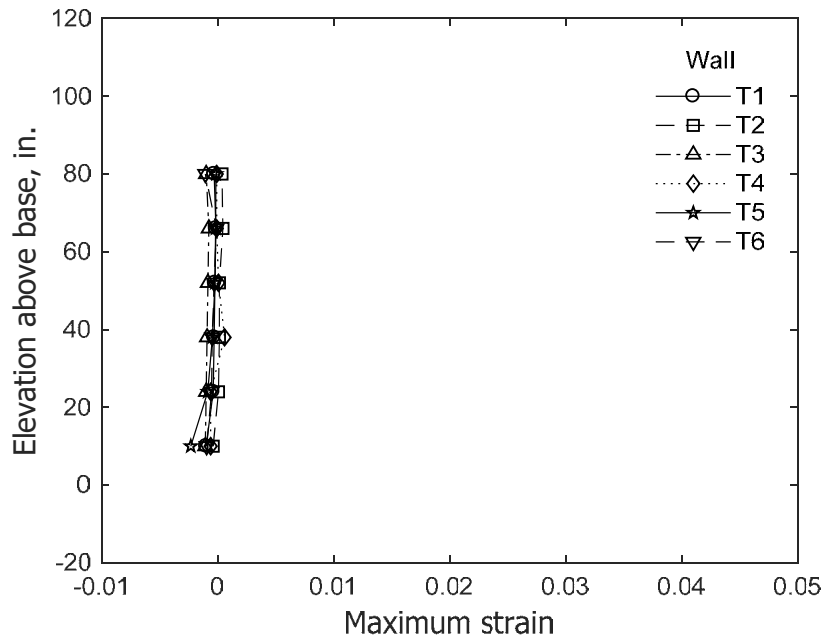


(b) Stem in tension

Figure 219 – Envelopes of concrete strain for confined flange at 1.5% drift ratio (data from optical markers along Column 11)

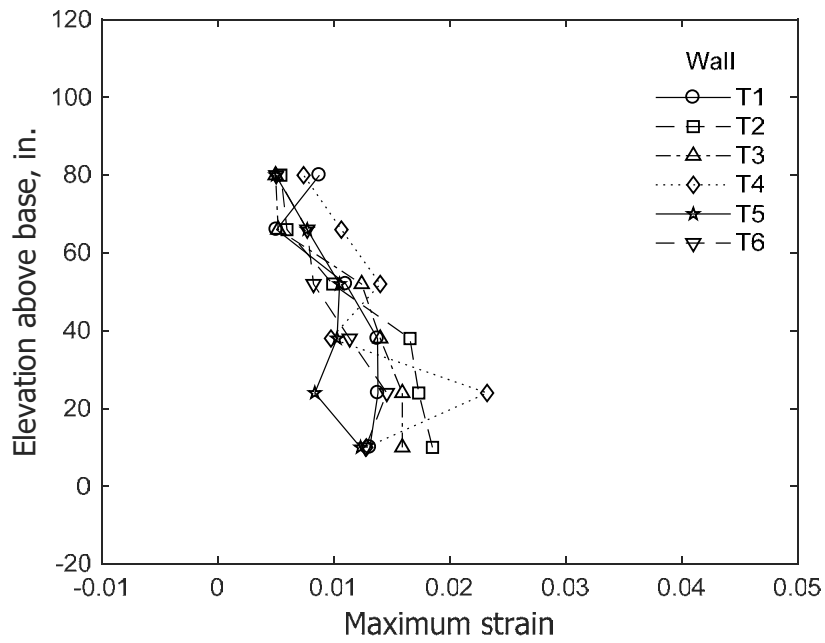


(a) Stem in compression

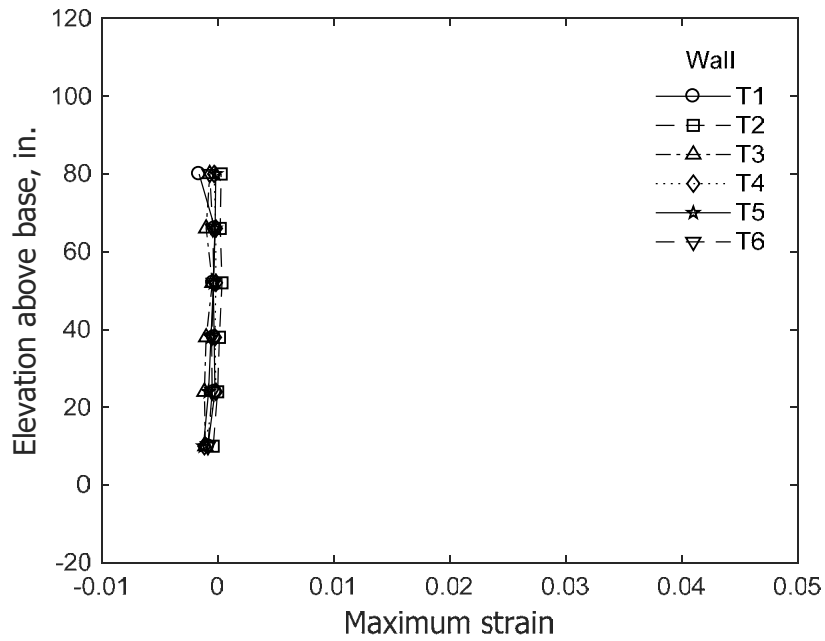


(b) Stem in tension

Figure 220 – Envelopes of concrete strain for confined flange at 2% drift ratio (data from optical markers along Column 11)

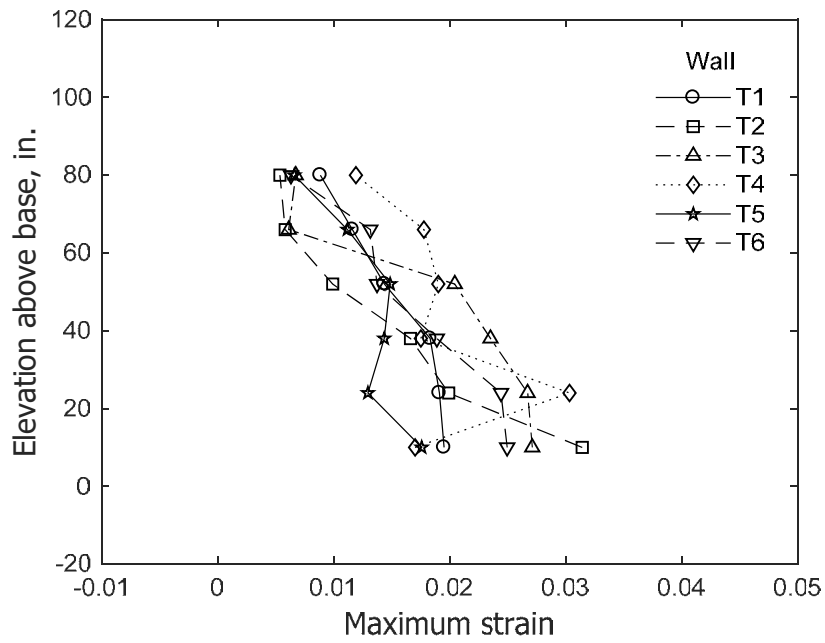


(a) Stem in compression

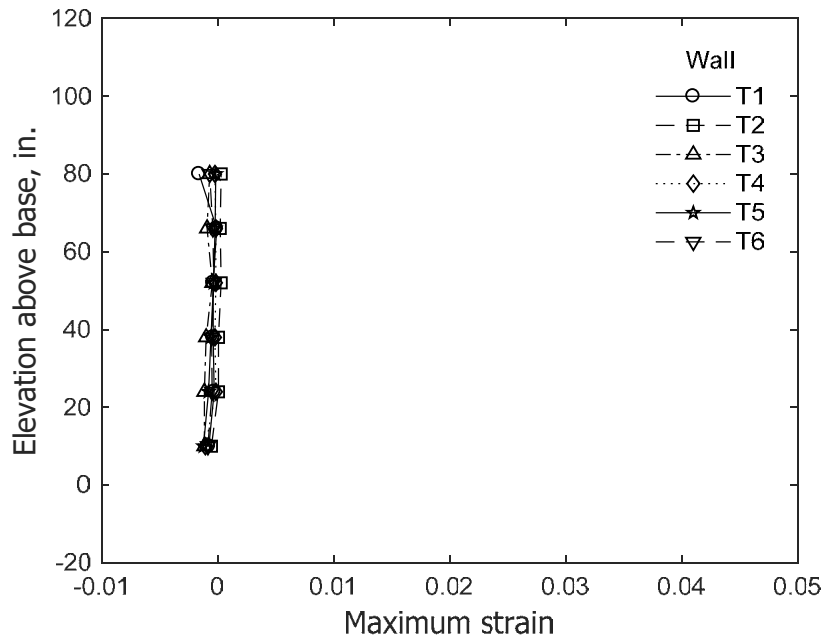


(b) Stem in tension

Figure 221 – Envelopes of concrete strain for unconfined flange at 1.5% drift ratio (data from optical markers along Columns 8, 9, and 10)

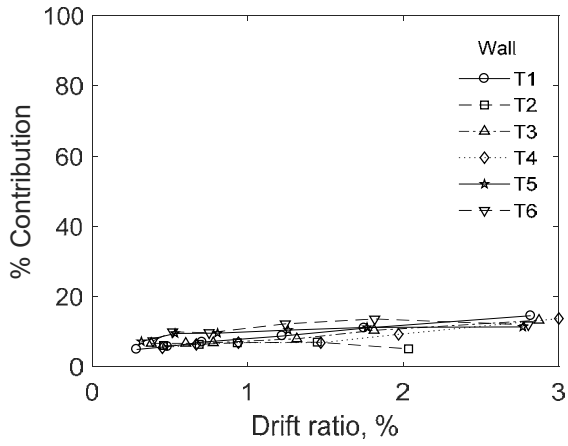


(a) Stem in compression

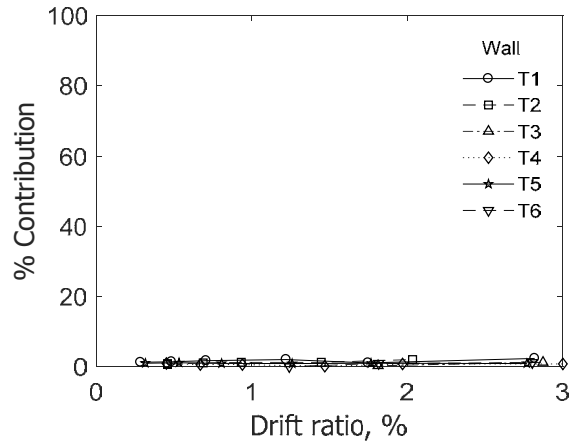


(b) Stem in tension

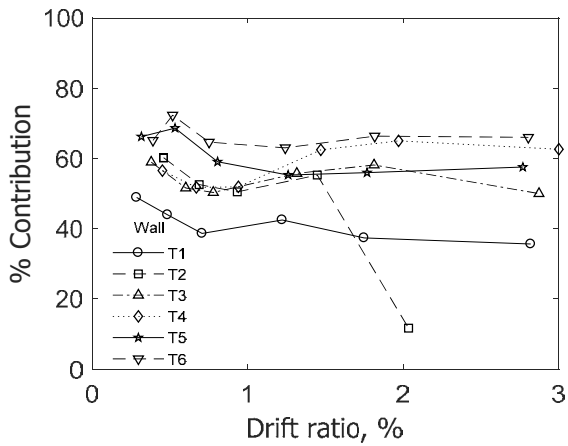
Figure 222 – Envelopes of concrete strain for unconfined flange at 2% drift ratio (data from optical markers along Columns 8, 9, and 10)



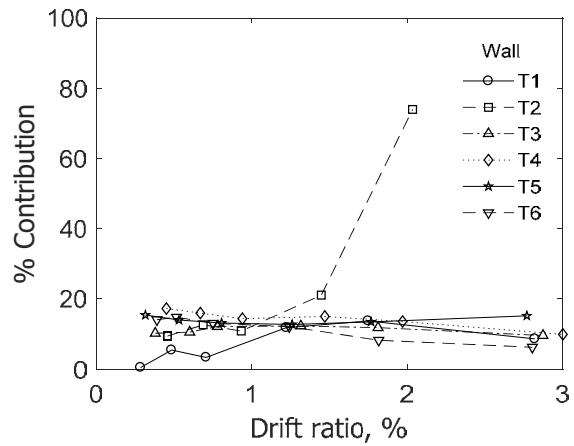
(a) Shear



(b) Base shearing

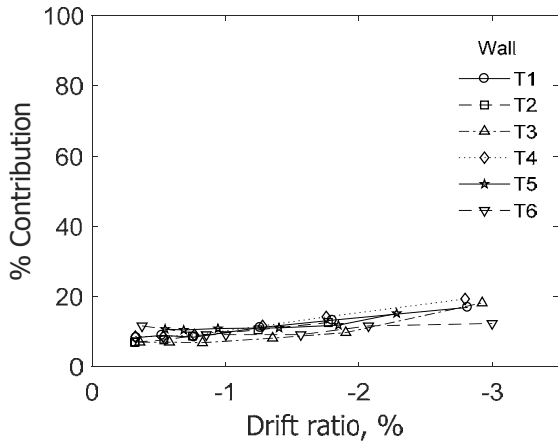


(c) Flexure

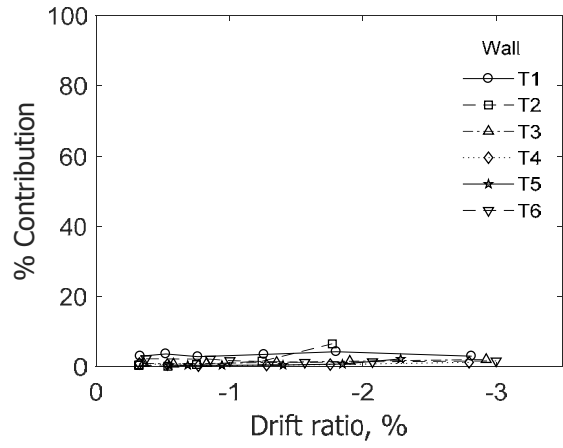


(d) Base opening

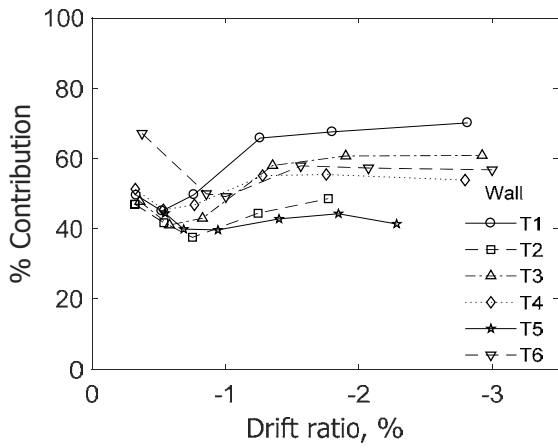
Figure 223 – Contribution of deformation components from bottom 87 in. (2210 mm), stem in compression



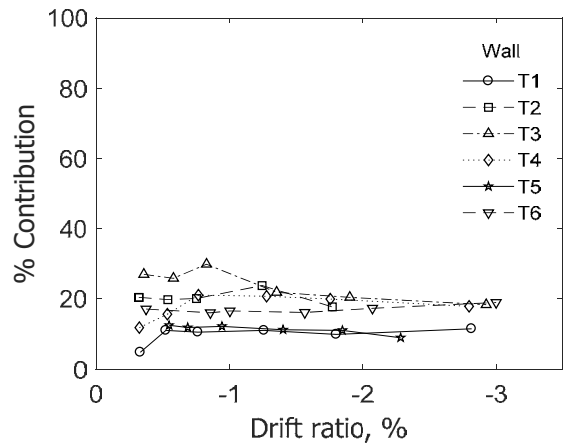
(a) Shear



(b) Base shearing



(c) Flexure



(d) Base opening

Figure 224 – Contribution of deformation components from bottom 87 in. (2210 mm), stem in tension

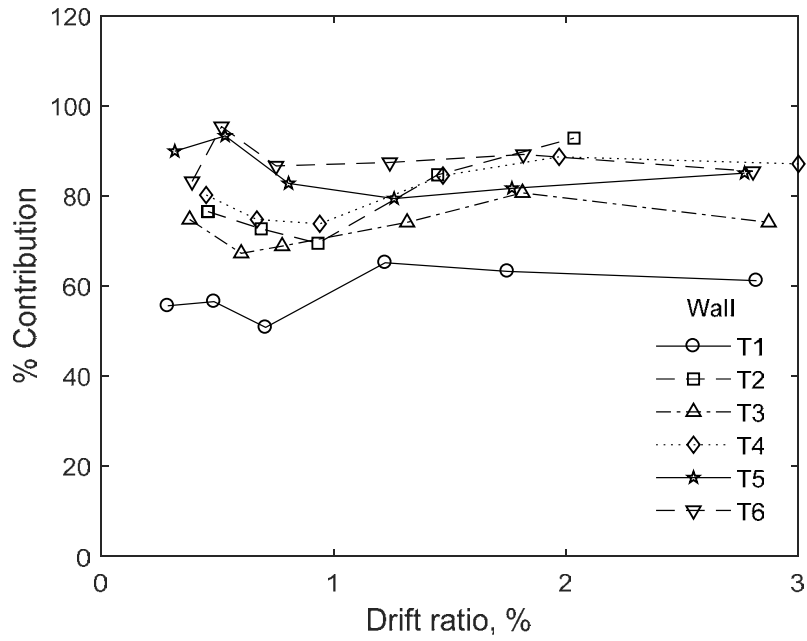


Figure 225 – Cumulative contribution of deformation components from bottom 87 in. (2210 mm), stem in compression

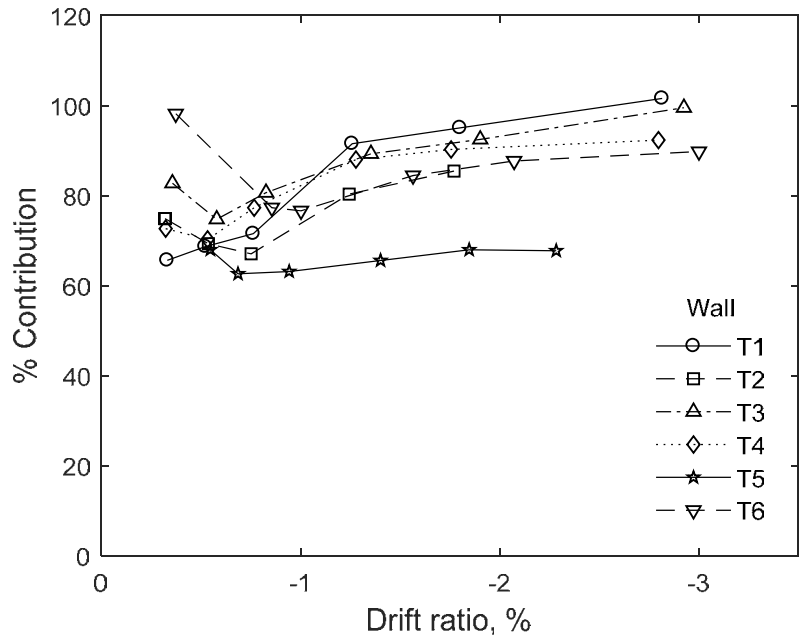


Figure 226 – Cumulative contribution of deformation components from bottom 87 in. (2210 mm), stem in tension

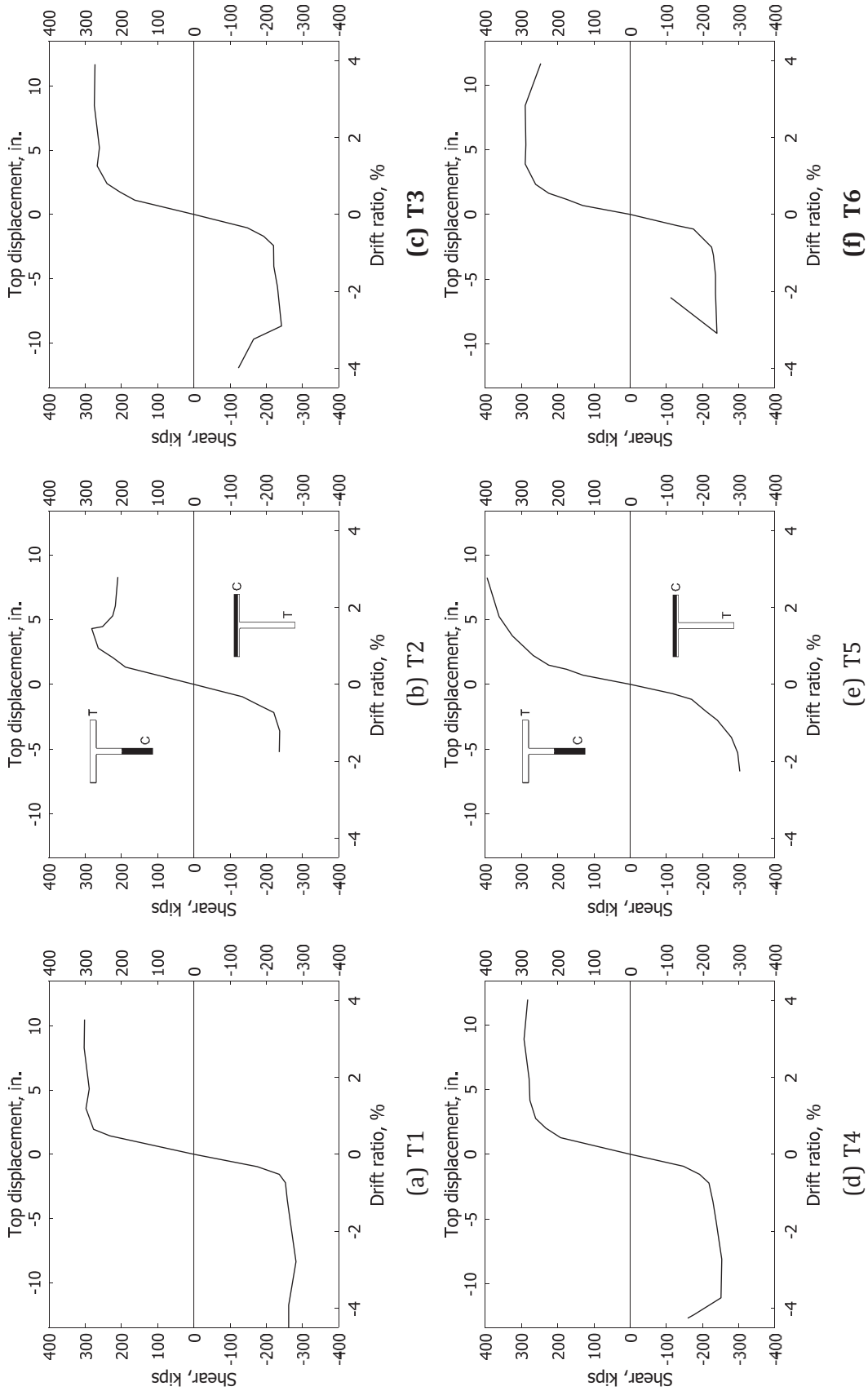


Figure 227 – Envelopes of shear versus drift ratio (1 in. = 25.4 mm, 1 kip = 4.45 kN)

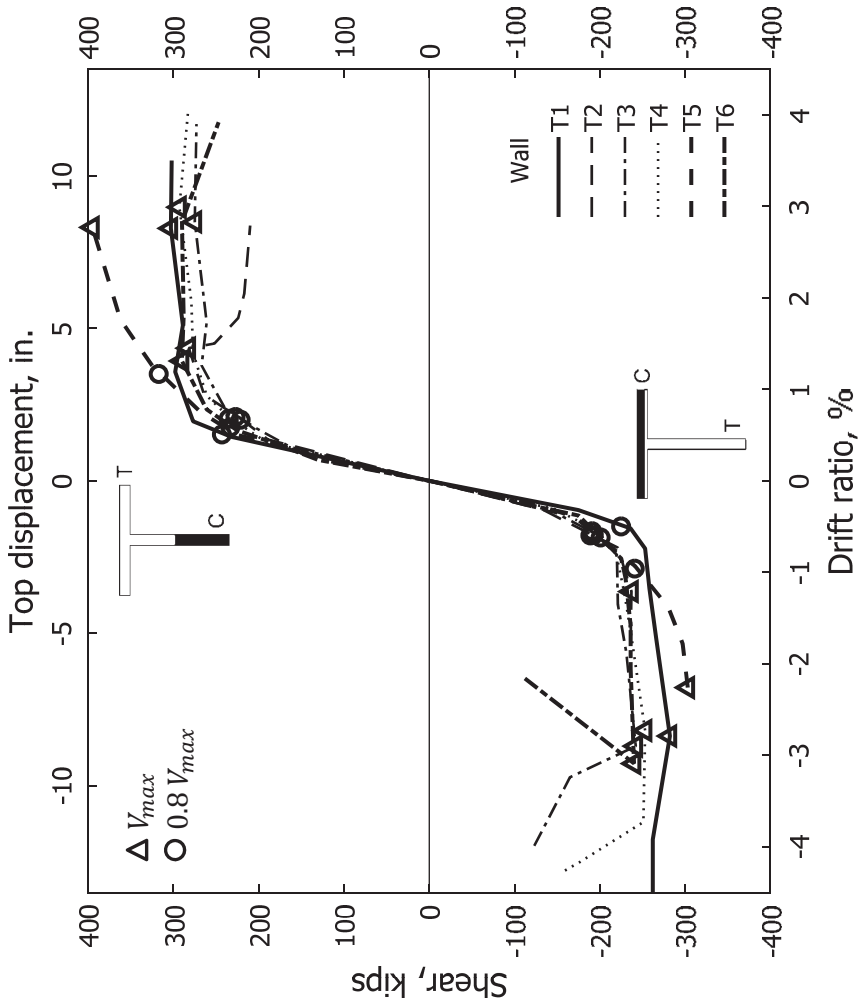


Figure 228 – Envelope comparisons of shear versus drift ratio (1 in. = 25.4 mm, 1 kip = 4.45 kN)

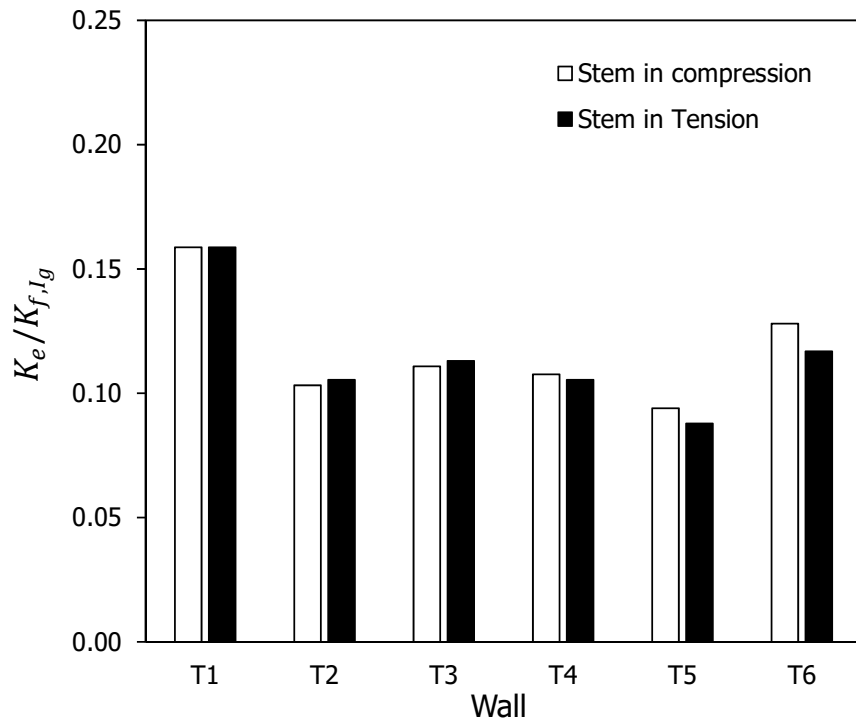


Figure 229 - Normalized effective initial stiffness K_e

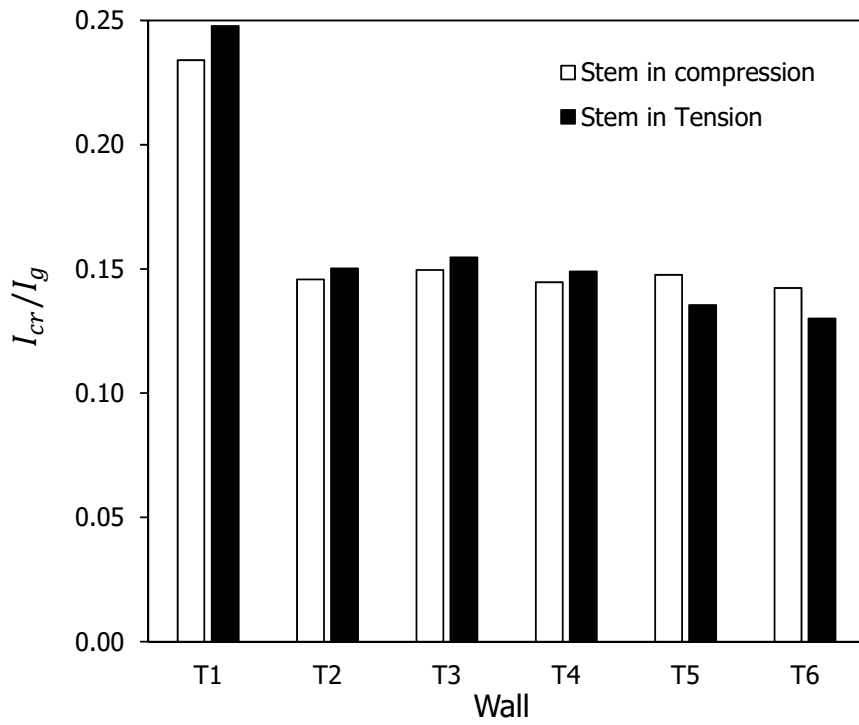


Figure 230 - Normalized cracked moment of inertia

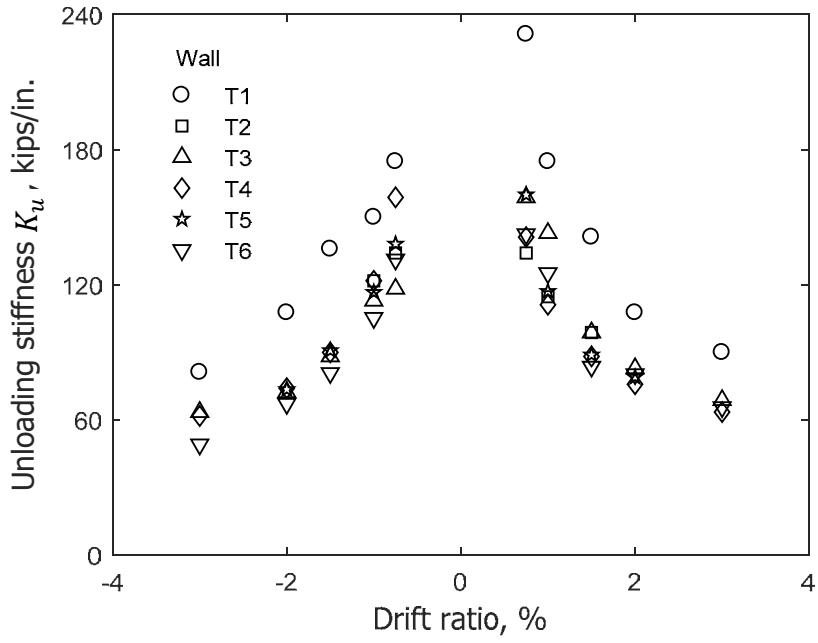


Figure 231 – Unloading stiffness versus drift ratio (1 in. = 25.4 mm, 1 kip = 4.45 kN)

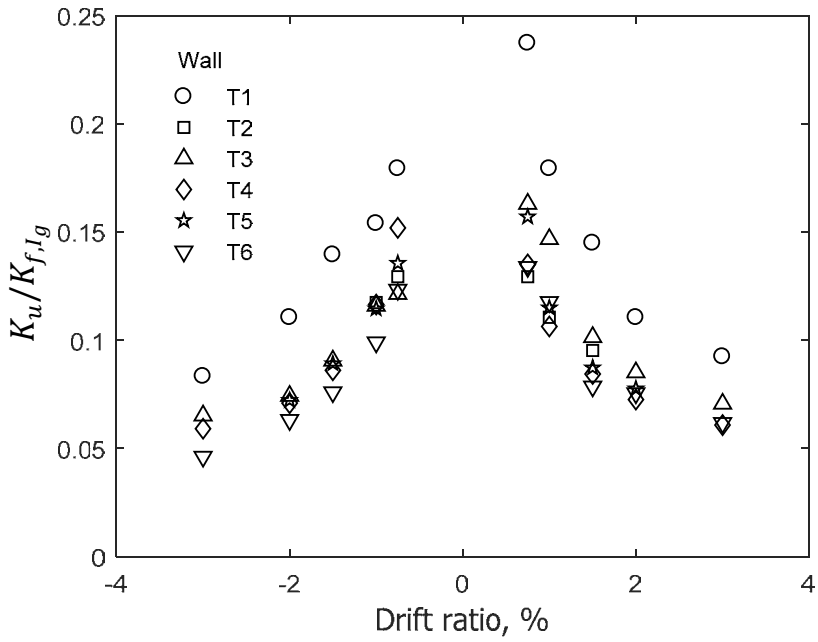
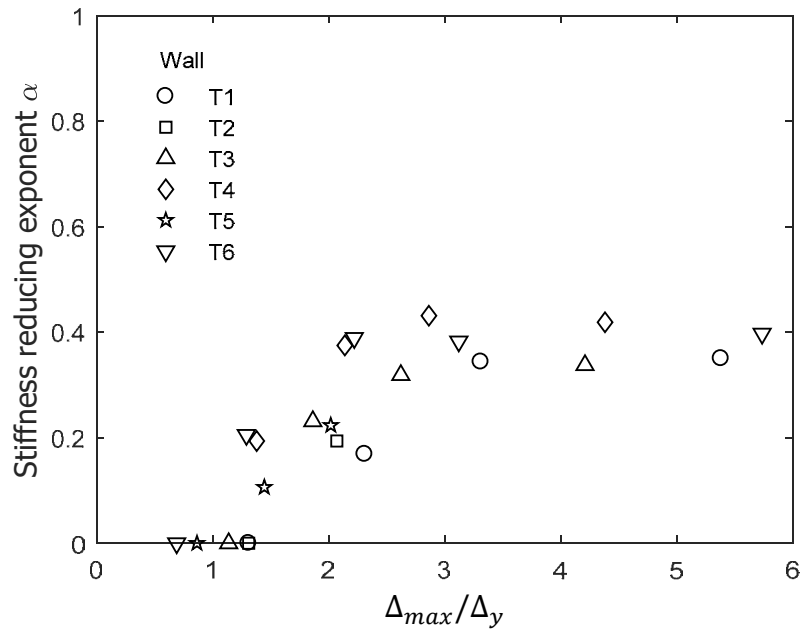
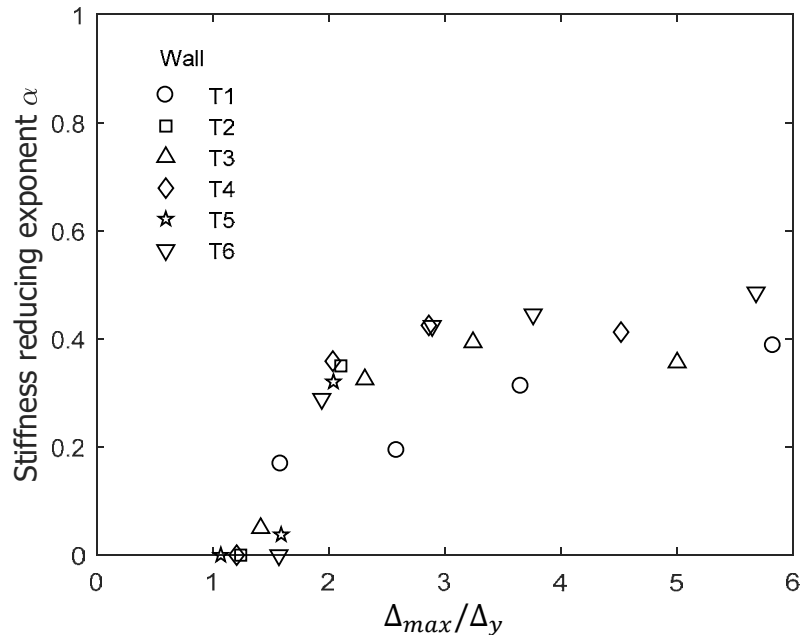


Figure 232 – Normalized unloading stiffness versus drift ratio

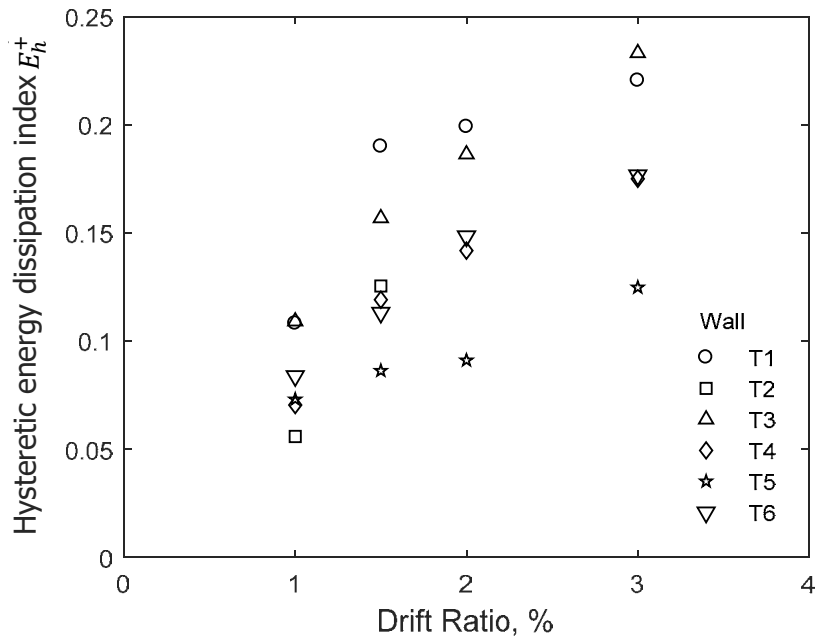


(c) Stem in compression

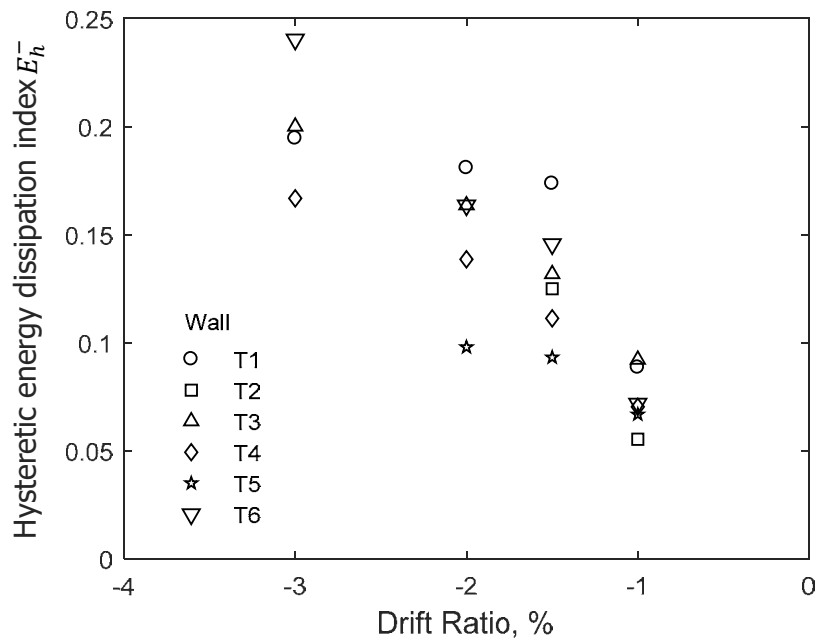


(d) Stem in tension

Figure 233 – Stiffness reducing exponent versus normalized displacement

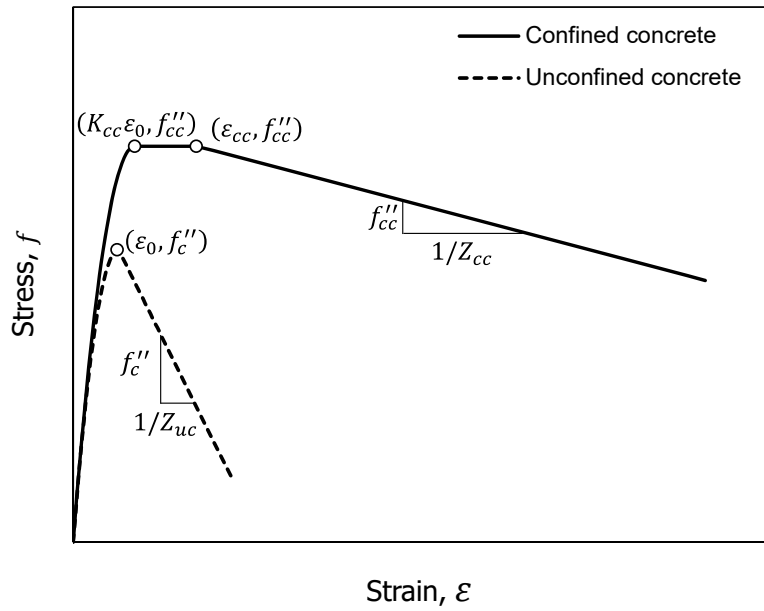


(a) Stem in compression

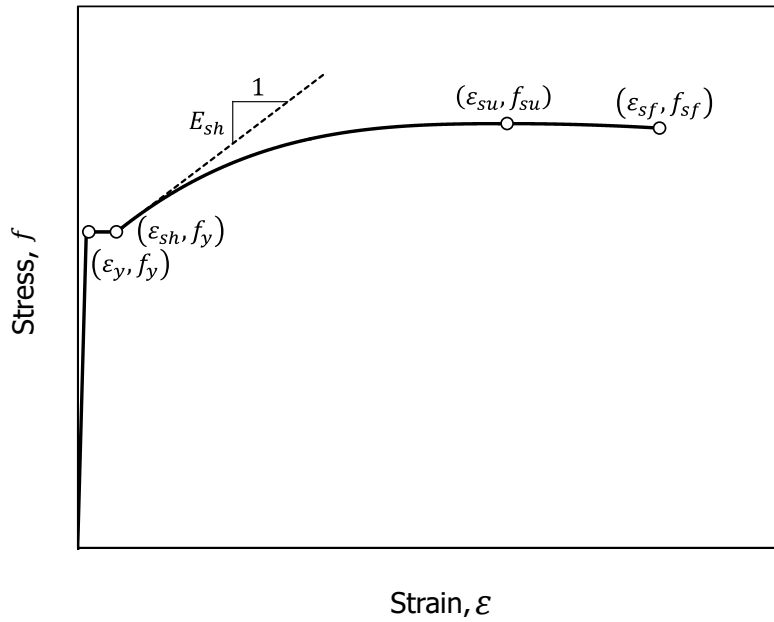


(b) Stem in tension

Figure 234 – Hysteretic energy dissipation index versus drift ratio

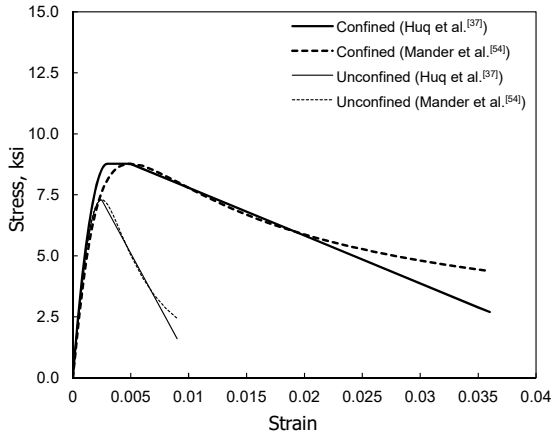


(a) Concrete

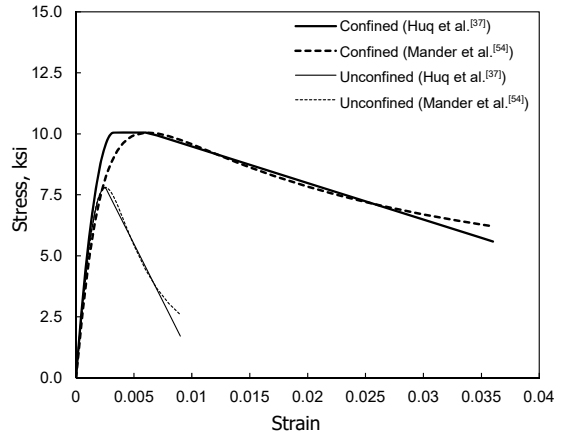


(b) Reinforcing steel

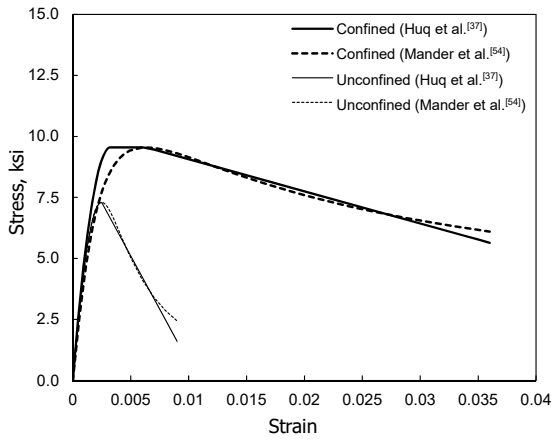
Figure 235 – Idealized stress-strain relationships



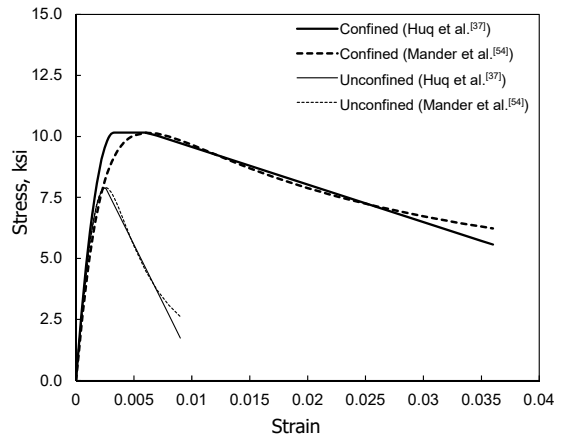
(a) T1



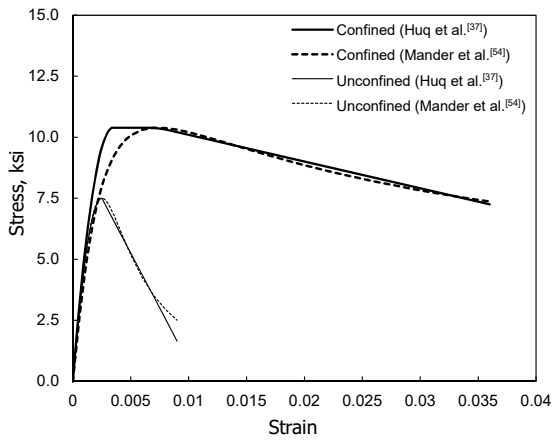
(b) T2



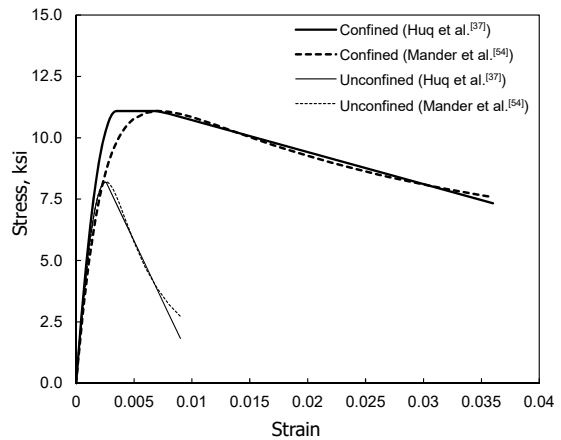
(c) T3



(d) T4

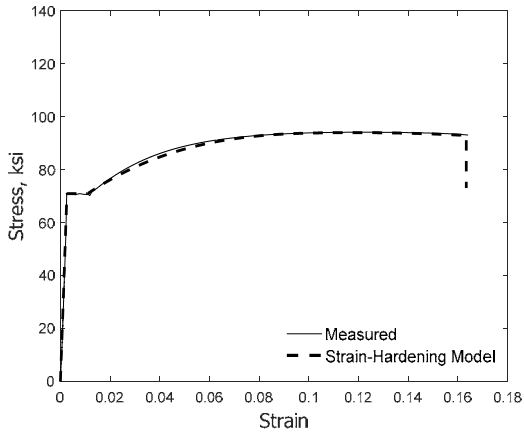


(e) T5

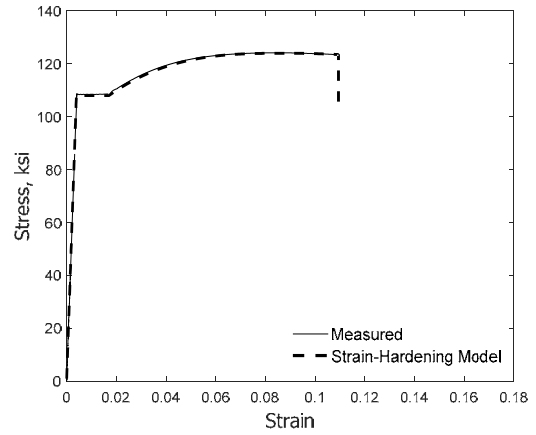


(f) T6

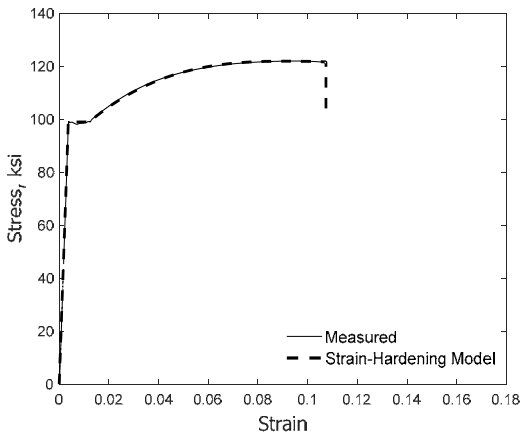
Figure 236 – Stress-strain relationship for confined and unconfined concrete in compression using parameter values from Table 19 compared with model proposed by Mander et al.^[54] (1 in. = 25.4 mm, 1 ft-kips = 1.36 m-kN)



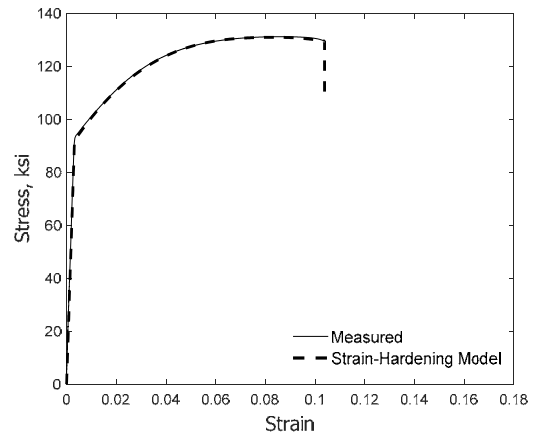
(a) T1^[37]



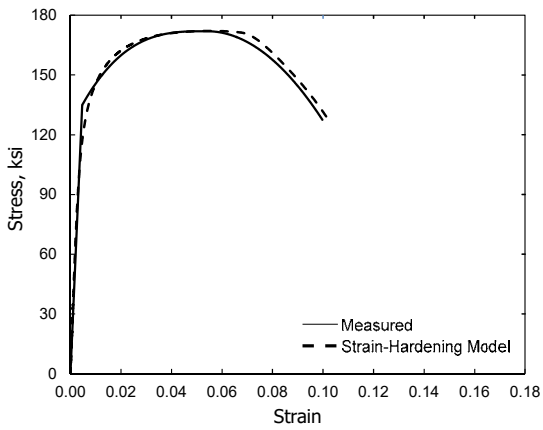
(b) T2^[37]



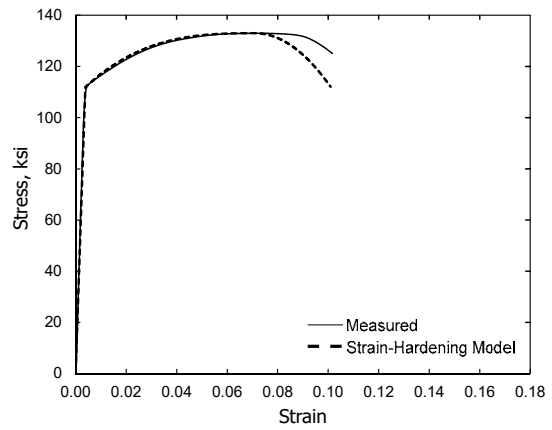
(c) T3^[37]



(d) T4^[37]

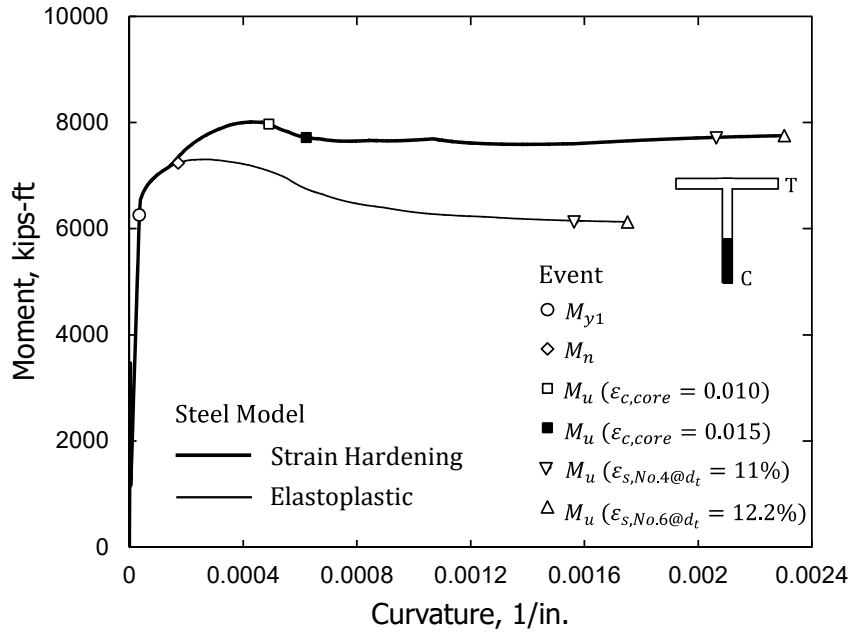


(e) T5

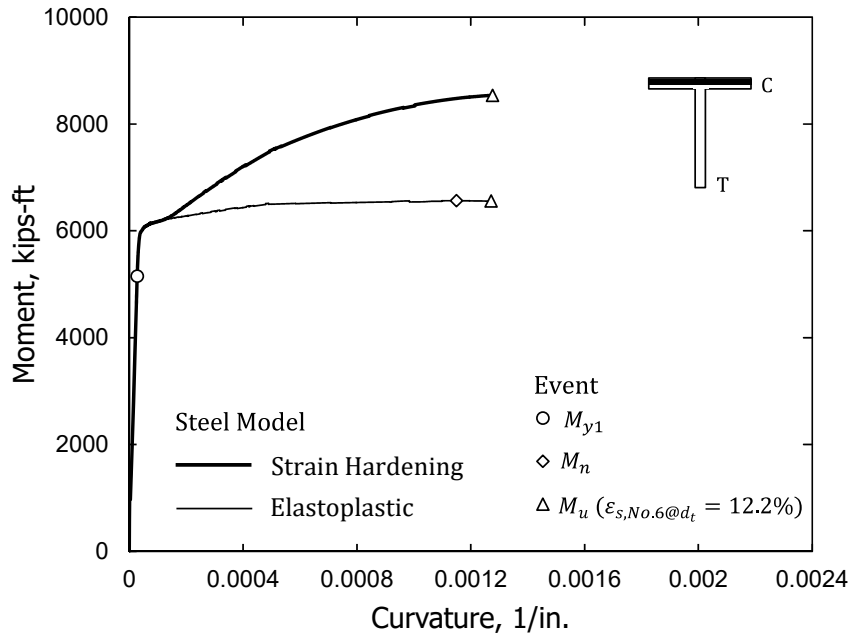


(f) T6

Figure 237 – Comparison between measured and calibrated stress-strain relationships for No. 6 (19) bars (1 in. = 25.4 mm, 1 ft-kips = 1.36 m-kN)

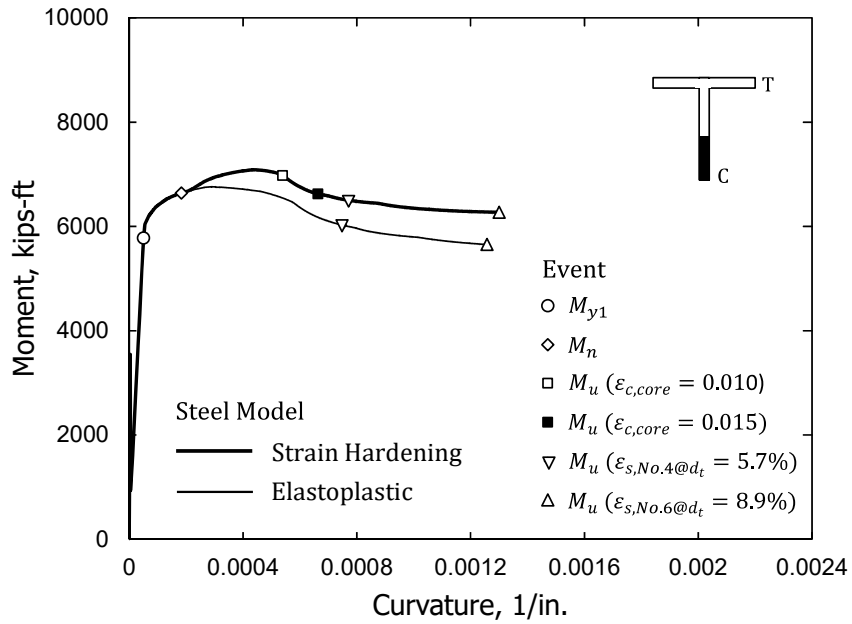


(a) Stem in compression

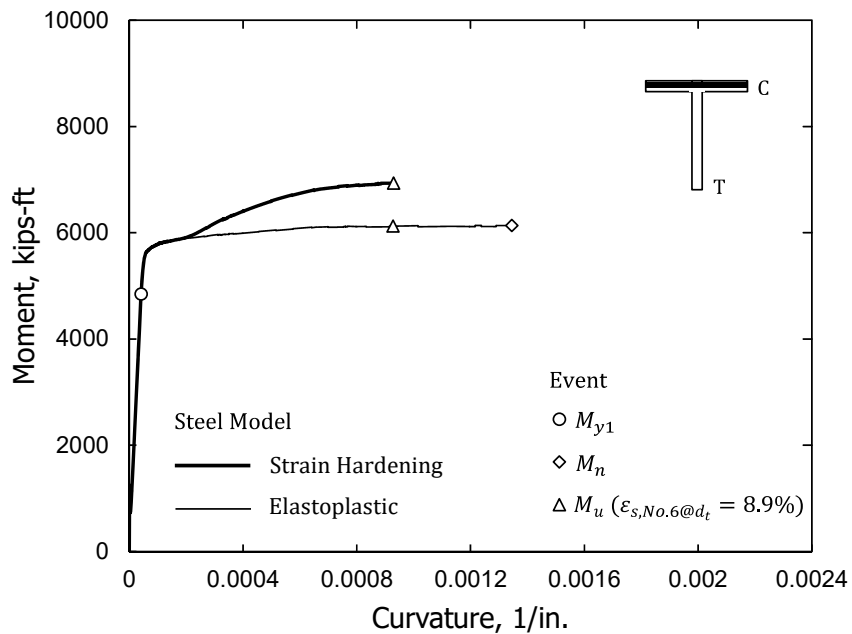


(b) Stem in tension

Figure 238 – Moment-curvature relationships for T1 (1 in. = 25.4 mm, 1 ft-kips = 1.36 m-kN)

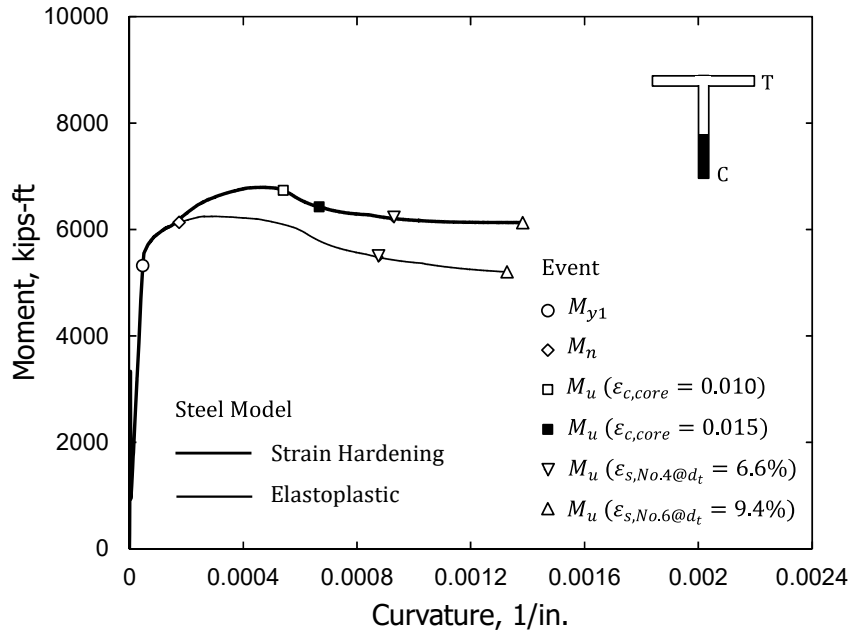


(a) Stem in compression

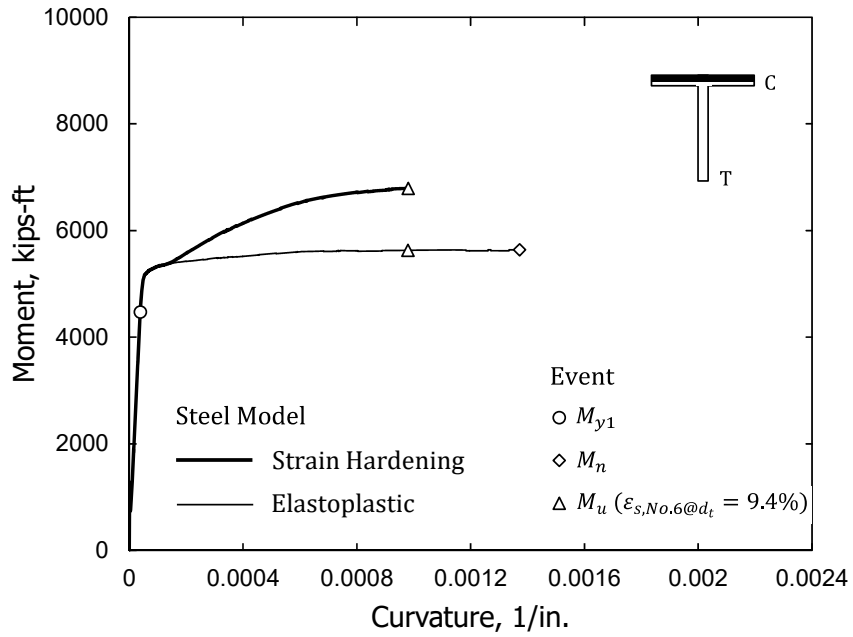


(b) Stem in tension

Figure 239 – Moment-curvature relationships for T2 (1 in. = 25.4 mm, 1 ft-kips = 1.36 m-kN)

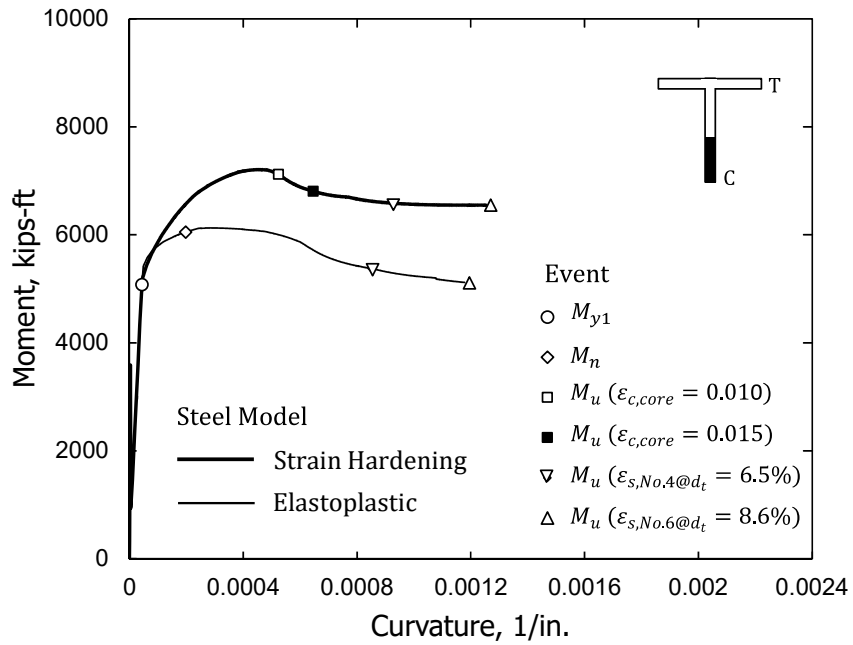


(a) Stem in compression

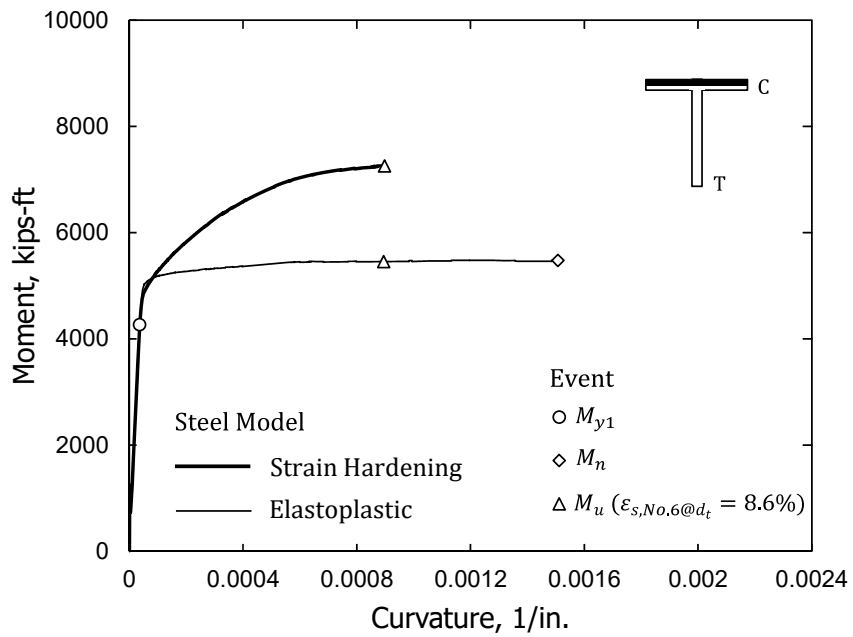


(b) Stem in tension

Figure 240 – Moment-curvature relationships for T3 (1 in. = 25.4 mm, 1 ft-kips = 1.36 m-kN)

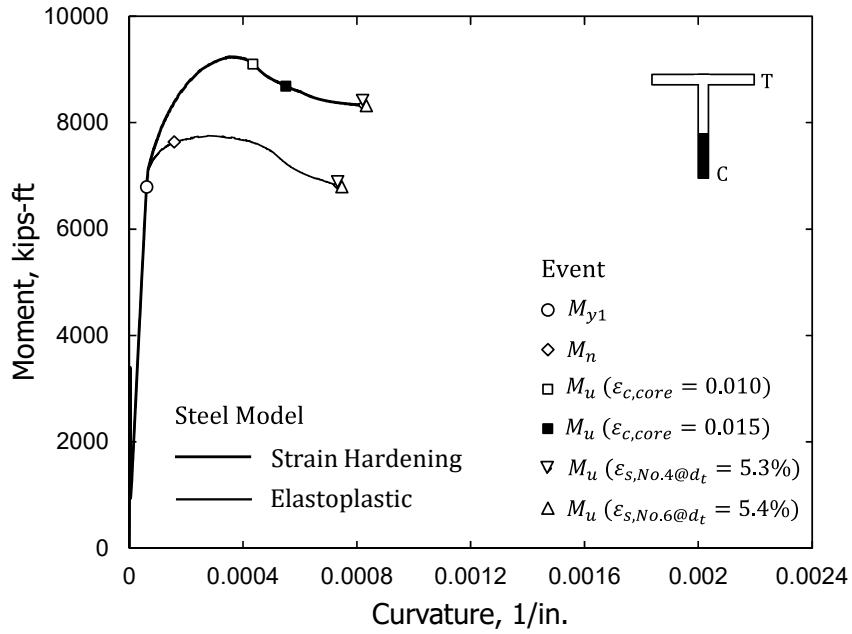


(a) Stem in compression

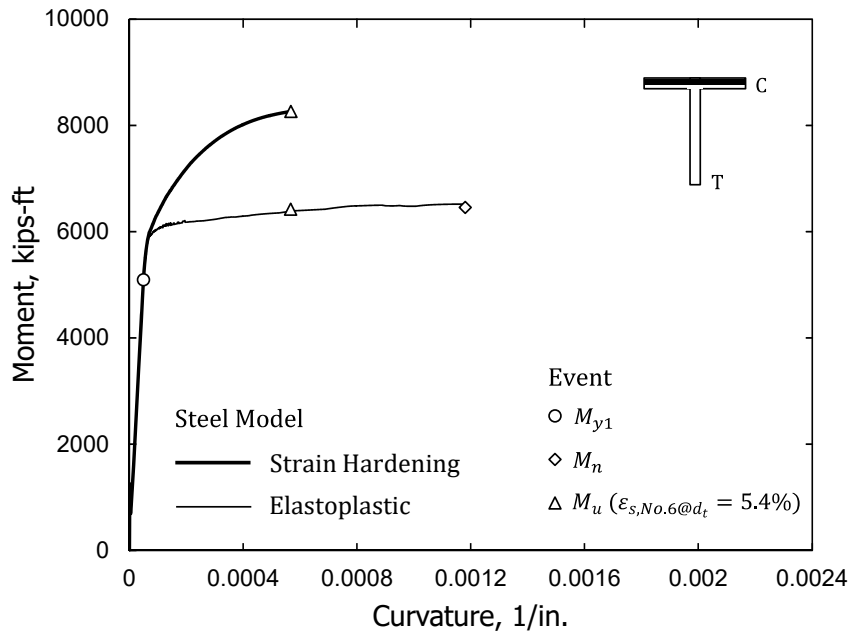


(b) Stem in tension

Figure 241 – Moment-curvature relationships for T4 (1 in. = 25.4 mm, 1 ft-kips = 1.36 m-kN)

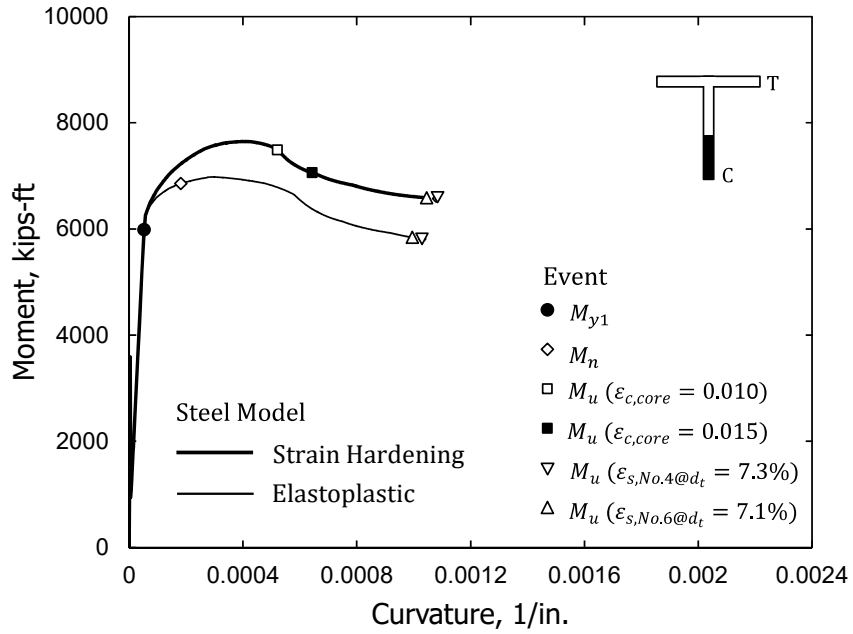


(a) Stem in compression

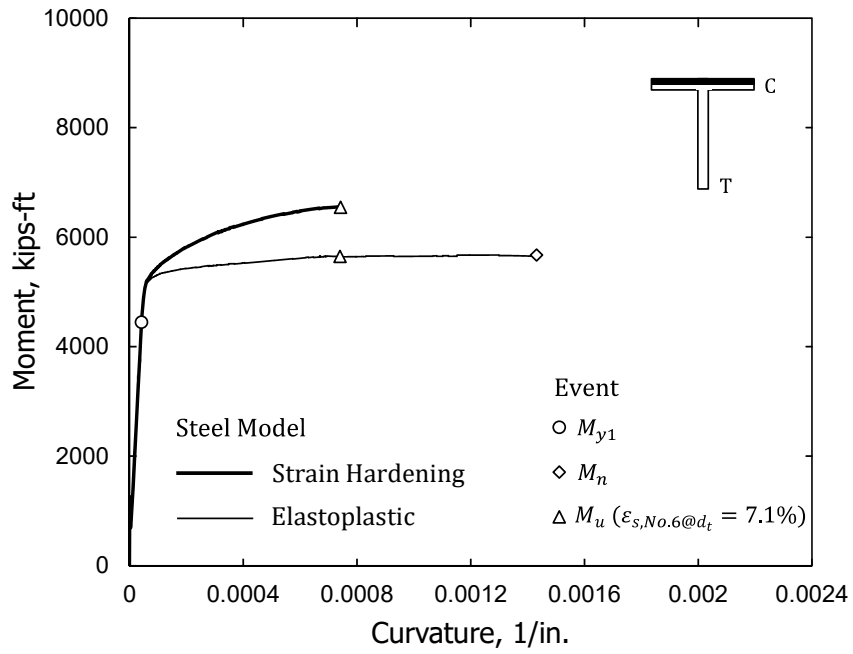


(b) Stem in tension

Figure 242 – Moment-curvature relationships for T5 (1 in. = 25.4 mm, 1 ft-kips = 1.36 m-kN)

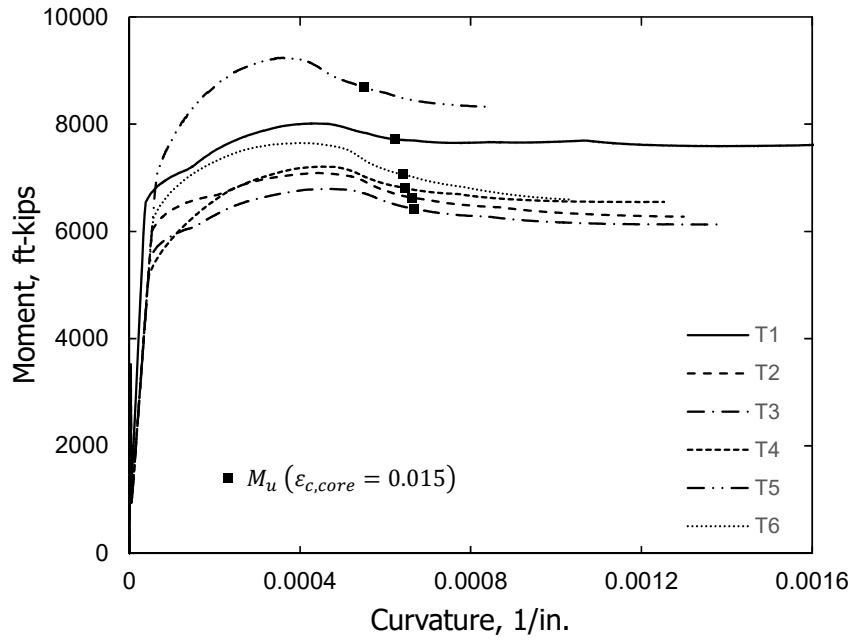


(a) Stem in compression

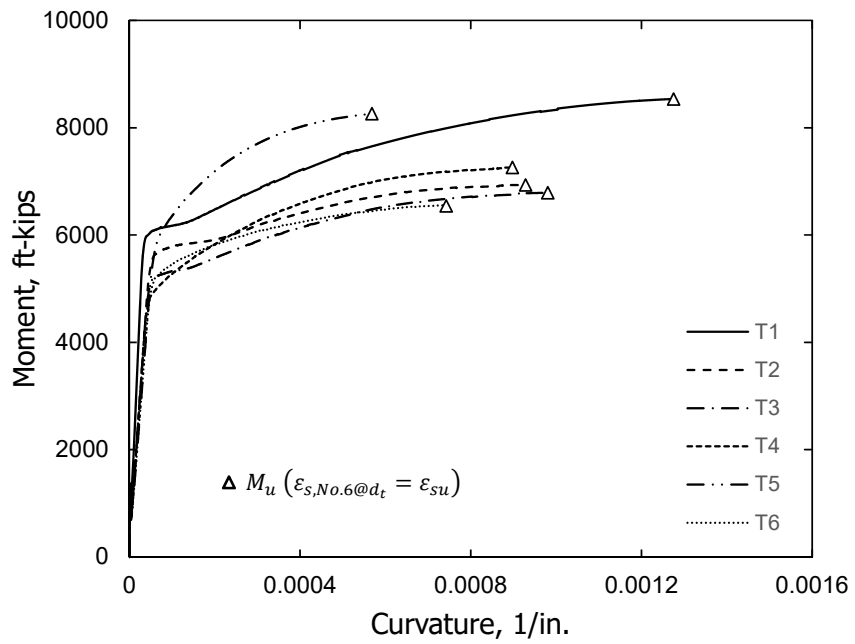


(b) Stem in tension

Figure 243 – Moment-curvature relationships for T6 (1 in. = 25.4 mm, 1 ft-kips = 1.36 m-kN)



(a) Stem in compression



(b) Stem in tension

Figure 244 – Moment-curvature relationships for all walls (1 in. = 25.4 mm, 1 ft-kips = 1.36 m-kN)

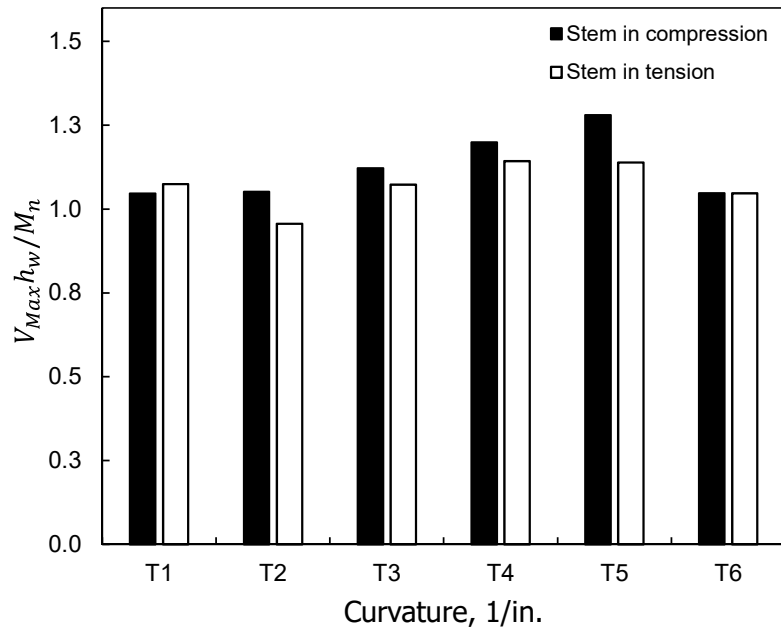


Figure 245 – Normalized maximum measured moment to nominal flexural strength (1 in. = 25.4 mm)

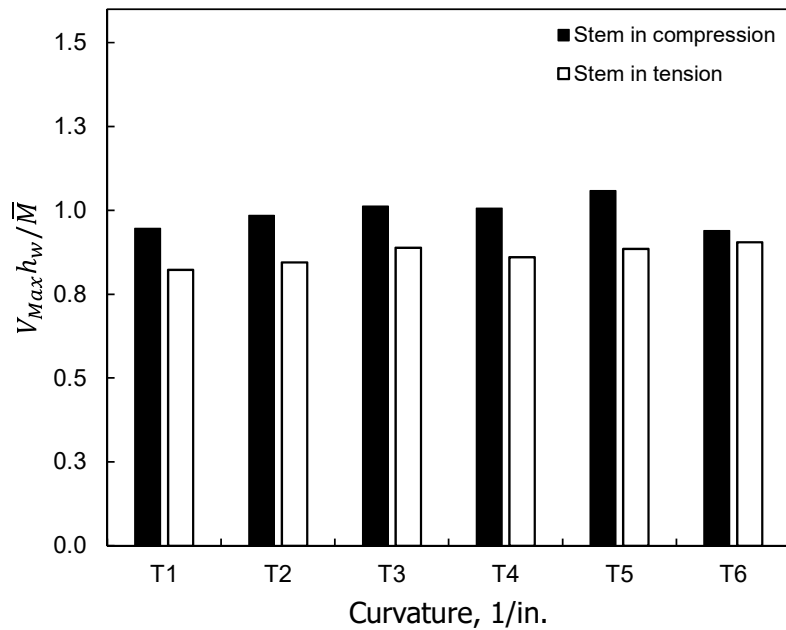
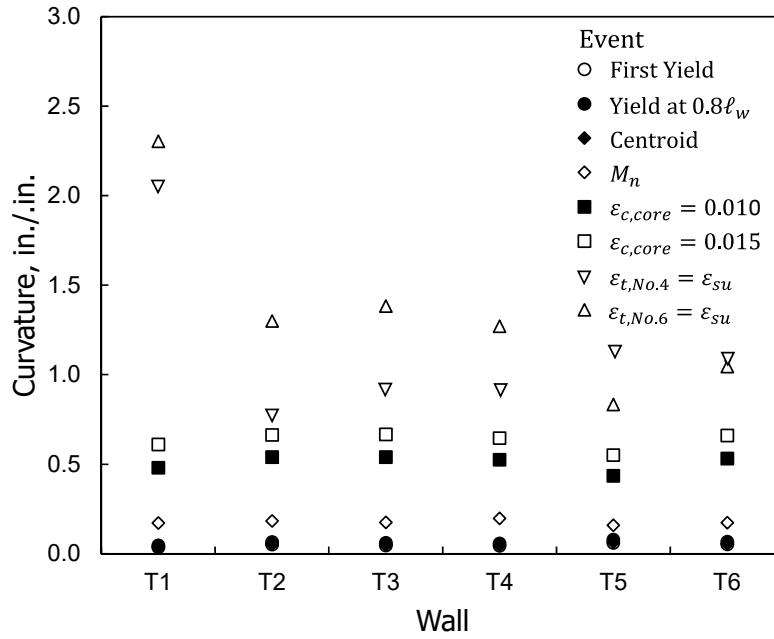
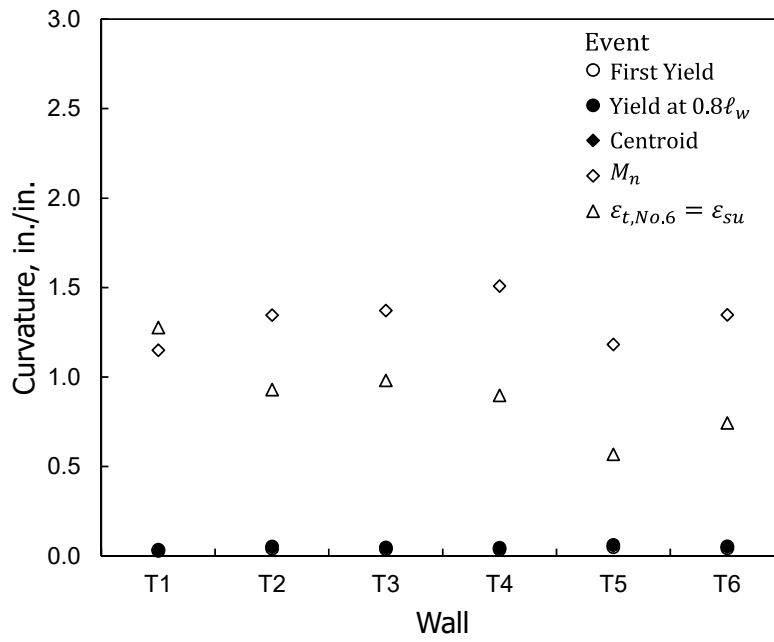


Figure 246 – Normalized maximum measured moment to calculated moment (1 in. = 25.4 mm)



(c) Stem in compression



(d) Stem in tension

Figure 247 – Computed curvature for relevant events (1 in. = 25.4 mm)

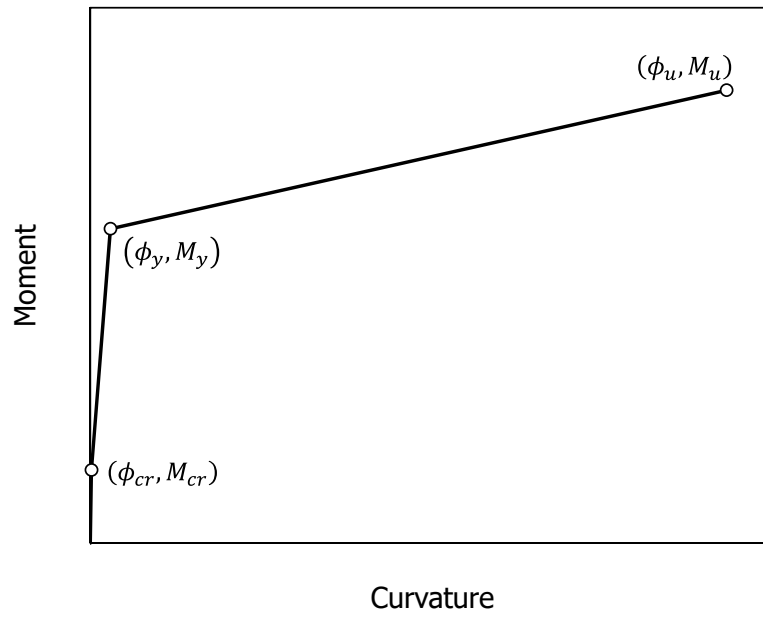
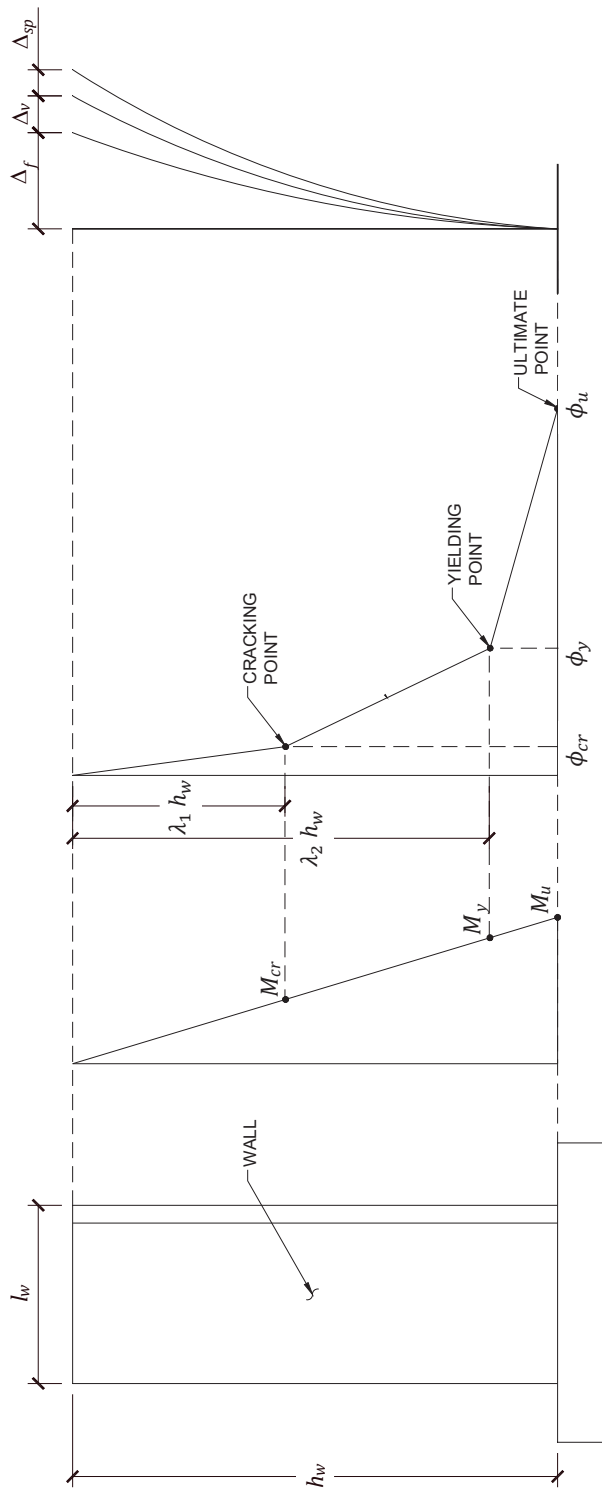
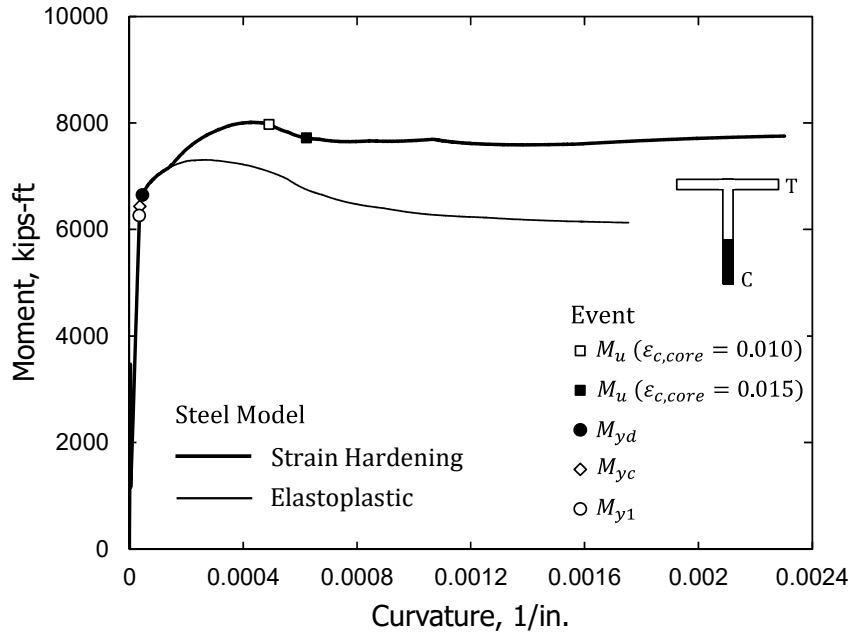


Figure 248 - Idealized Moment-Curvature relationship

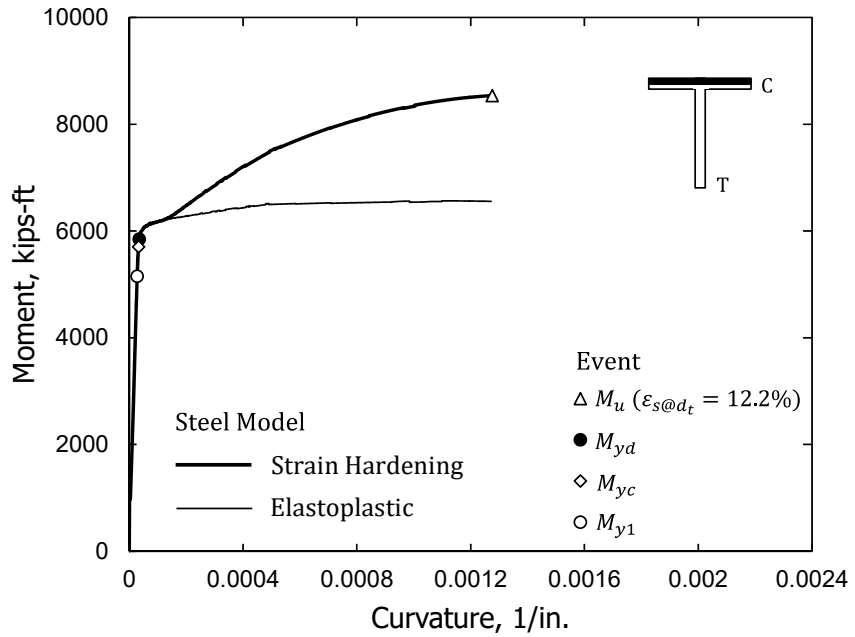


(a) Wall geometry (b) Moment (c) Curvature (d) Deformation components

Figure 249 – Idealized moment and curvature distributions for Model A

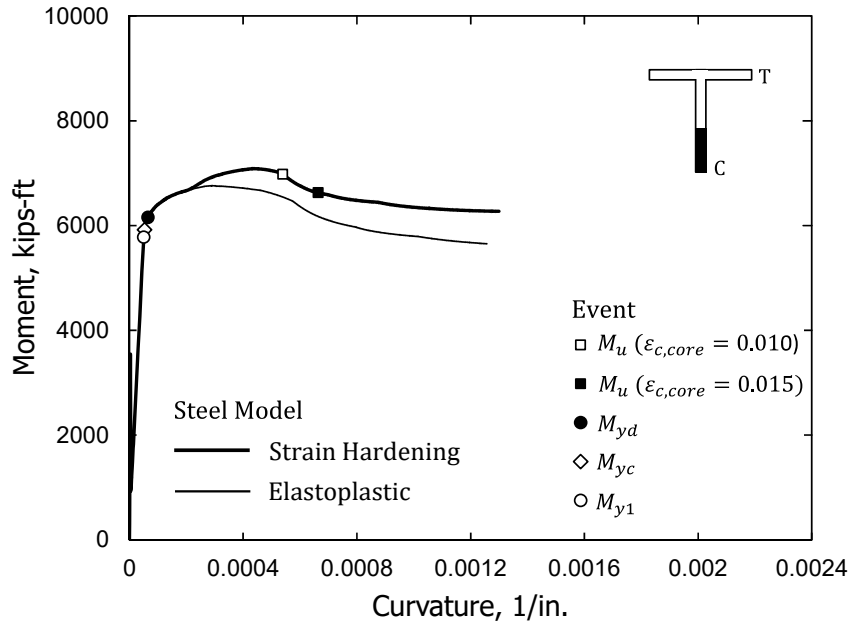


(a) Stem in compression

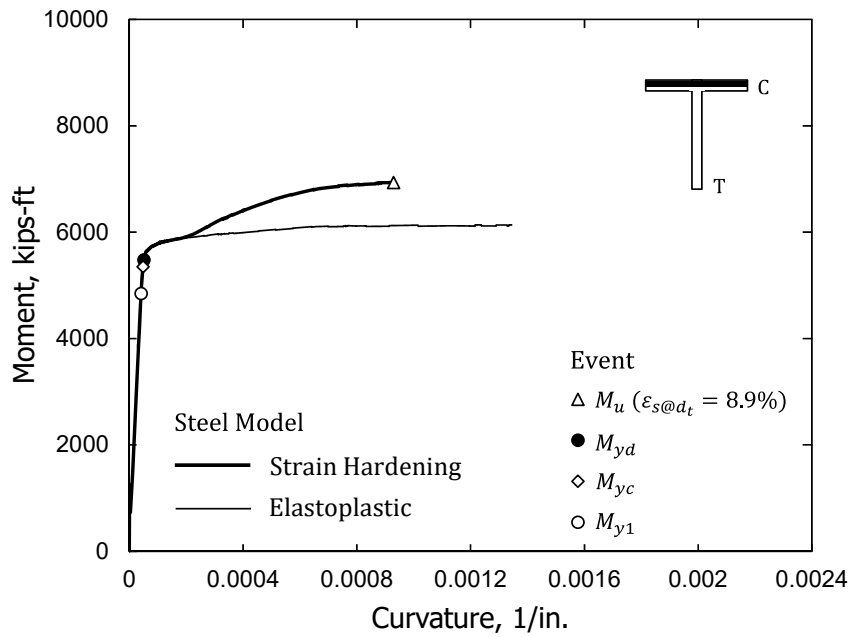


(b) Stem in tension

Figure 250 – Events used to defined the idealized moment-curvature relationship for T1 (1 in. = 25.4 mm, 1 ft-kips = 1.36 m-kN)

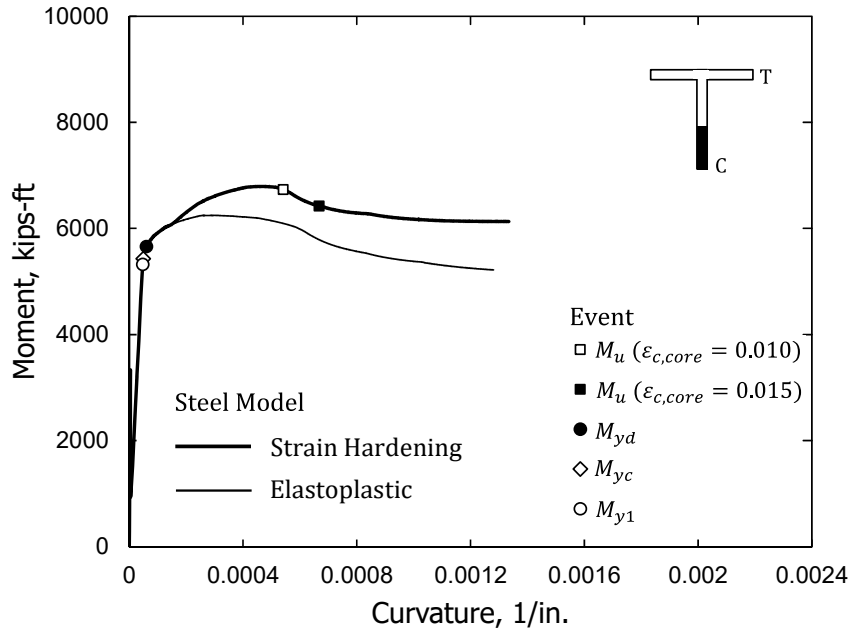


(a) Stem in compression

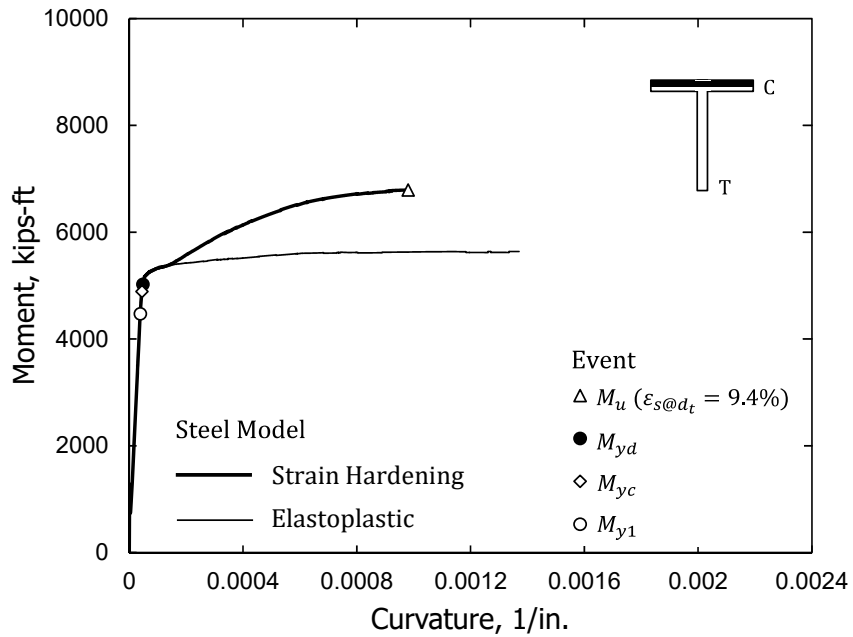


(b) Stem in tension

Figure 251 – Events used to defined the idealized moment-curvature relationship for T2 (1 in. = 25.4 mm, 1 ft-kips = 1.36 m-kN)

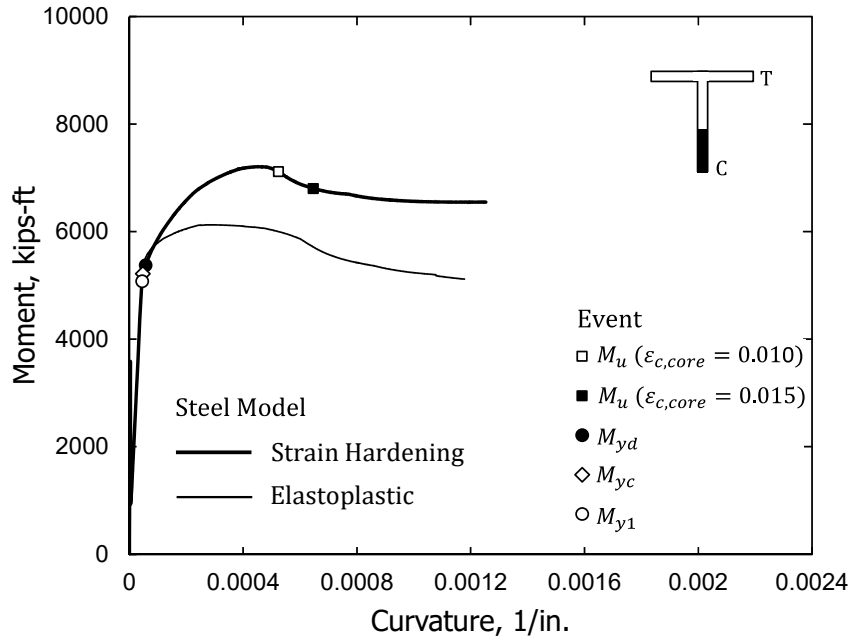


(a) Stem in compression

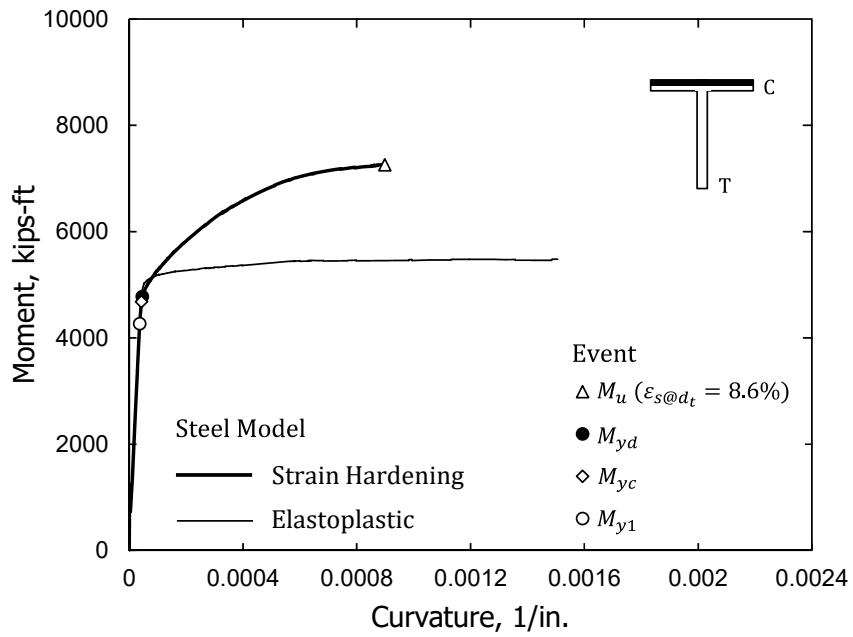


(b) Stem in tension

Figure 252 – Events used to defined the idealized moment-curvature relationship for T3 (1 in. = 25.4 mm, 1 ft-kips = 1.36 m-kN)

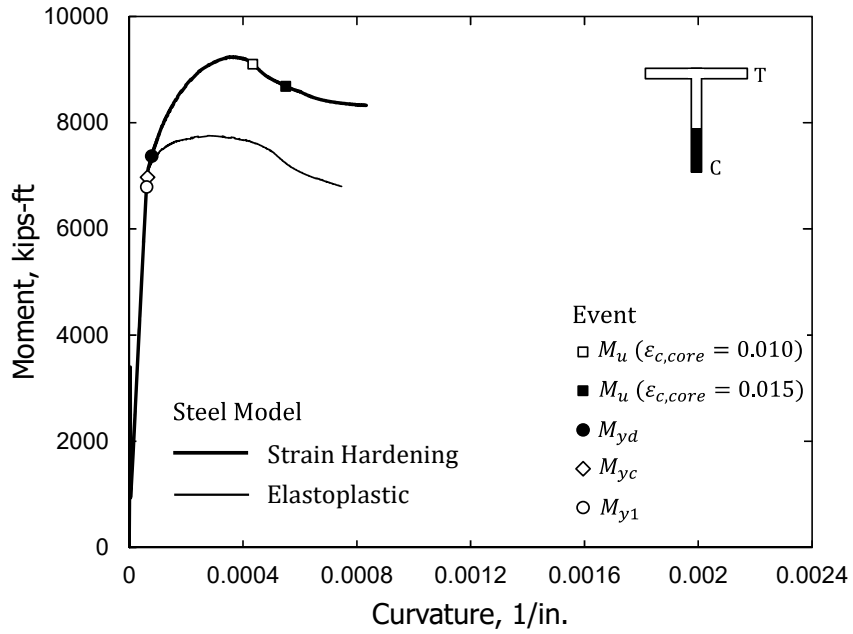


(a) Stem in compression

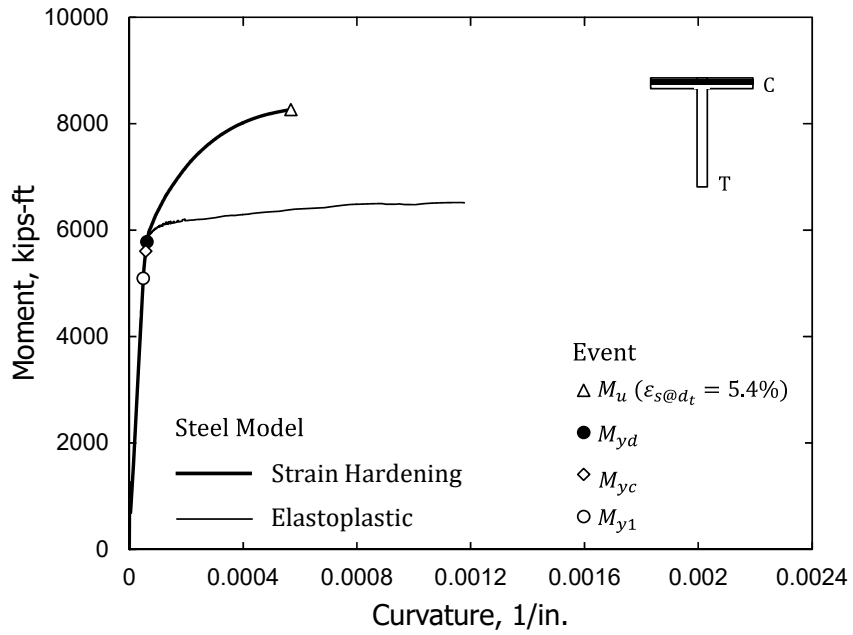


(b) Stem in tension

Figure 253 – Events used to defined the idealized moment-curvature relationship for T4 (1 in. = 25.4 mm, 1 ft-kips = 1.36 m-kN)

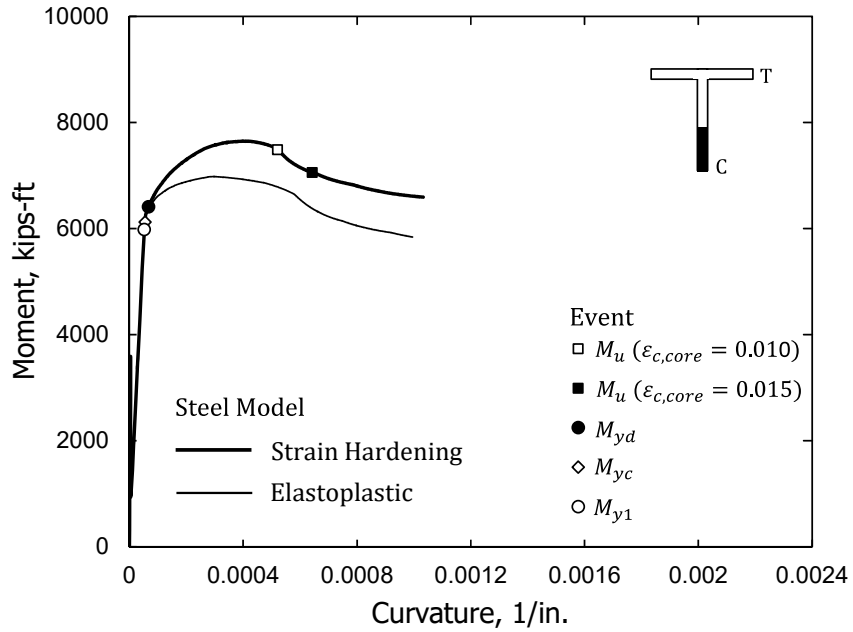


(a) Stem in compression

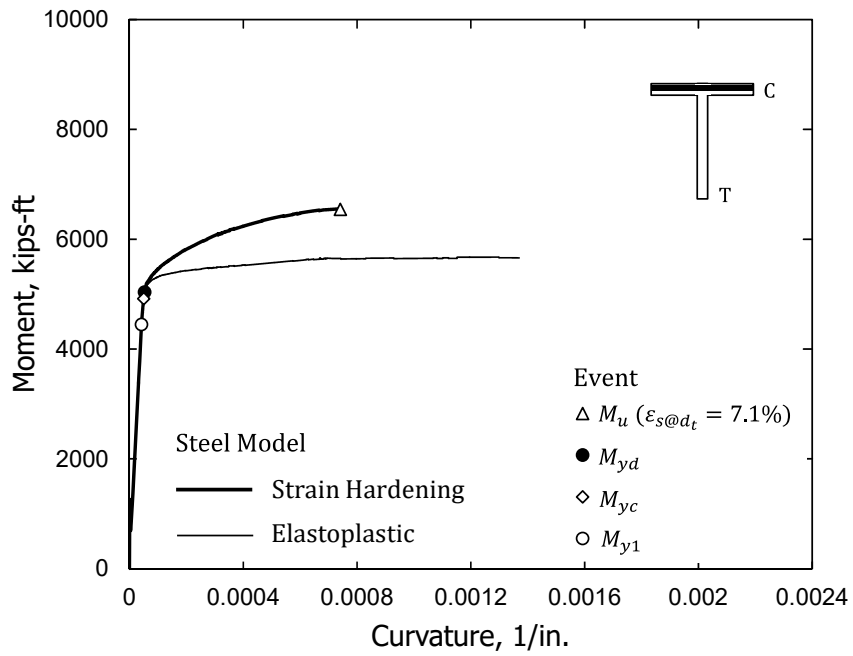


(b) Stem in tension

Figure 254 – Events used to defined the idealized moment-curvature relationship for T5 (1 in. = 25.4 mm, 1 ft-kips = 1.36 m-kN)

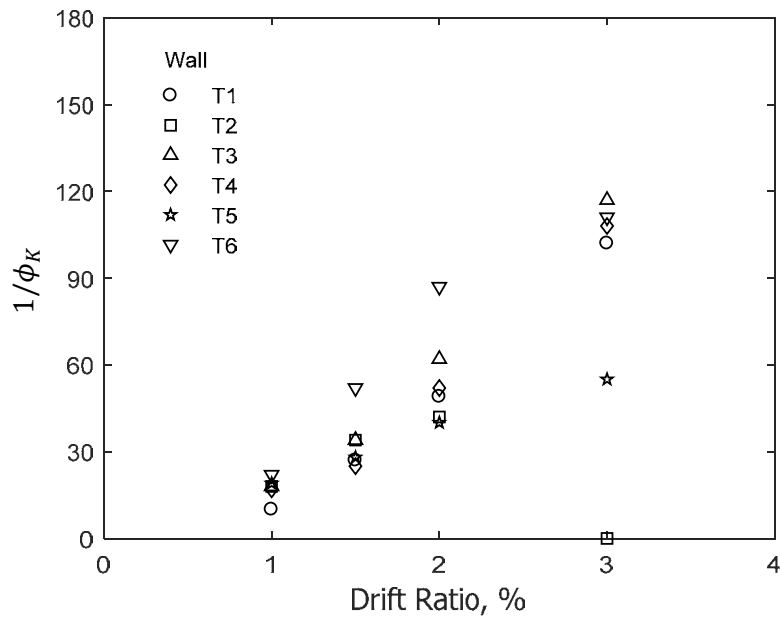


(a) Stem in compression

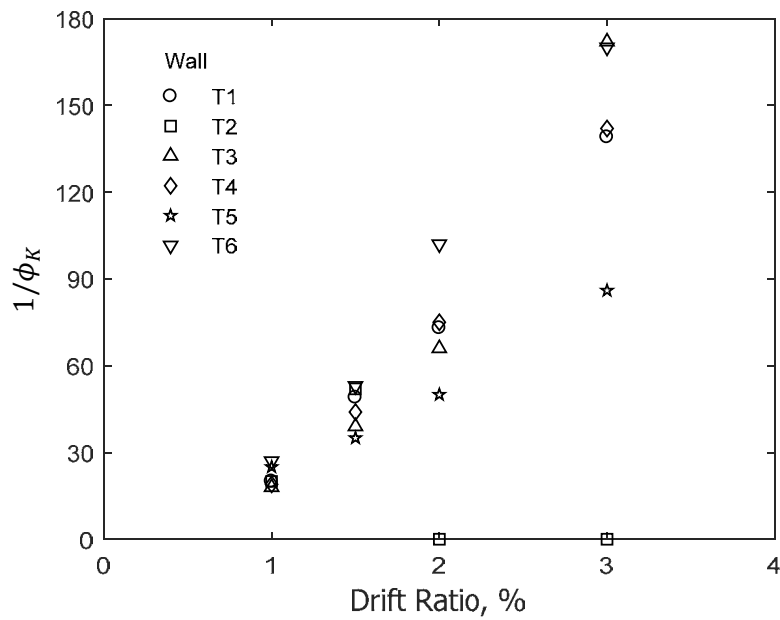


(b) Stem in tension

Figure 255 – Events used to defined the idealized moment-curvature relationship for T6 (1 in. = 25.4 mm, 1 ft-kips = 1.36 m-kN)



(a) Stem in compression



(b) Stem in tension

Figure 256 – Inverse of ϕ_K versus drift ratio for bottom 50 in. (1270 mm)

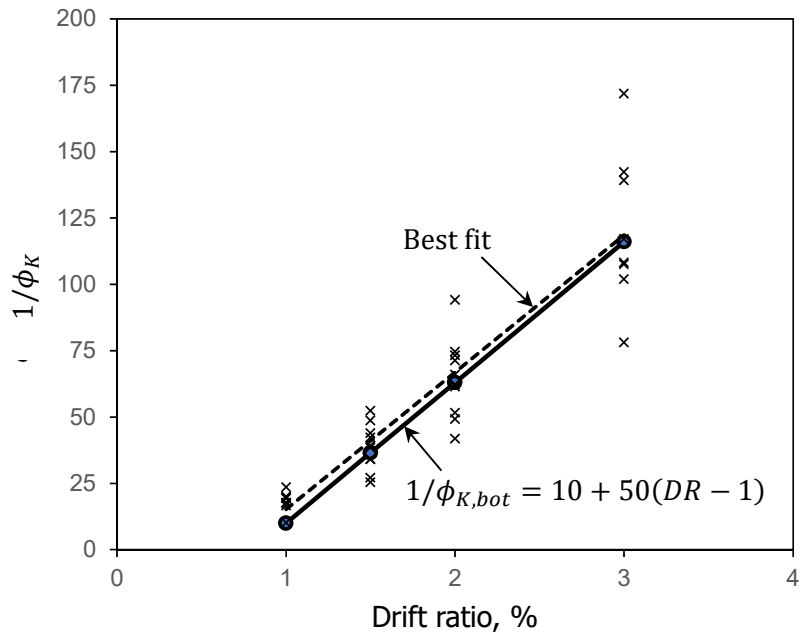


Figure 257 – Inverse of ϕ_K versus drift ratio for bottom 50 in. (1270 mm) of wall (data from Figure 256)

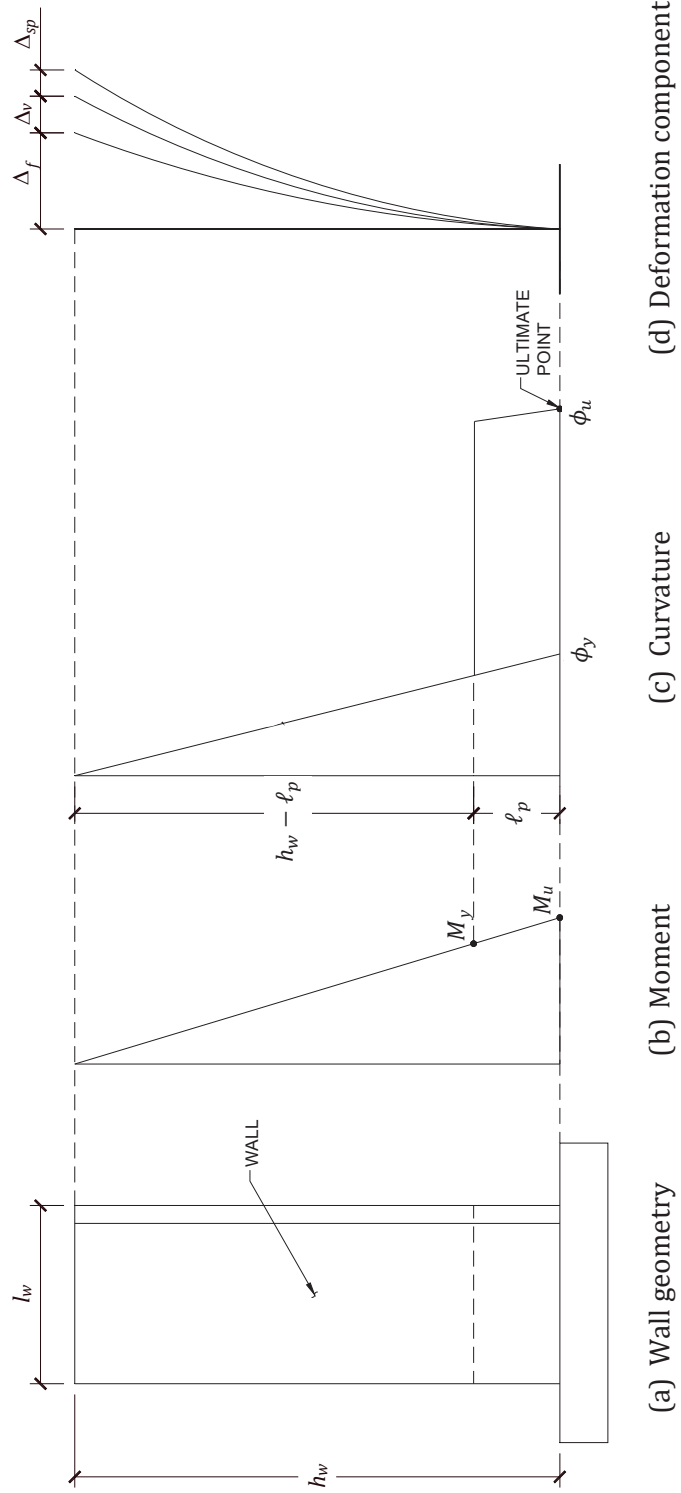
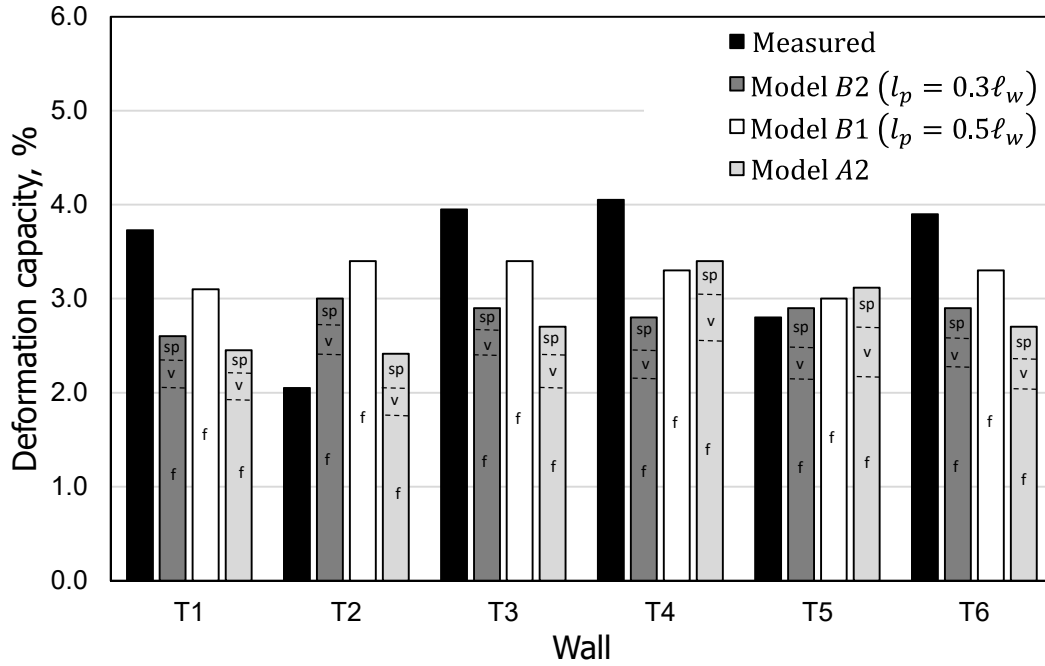
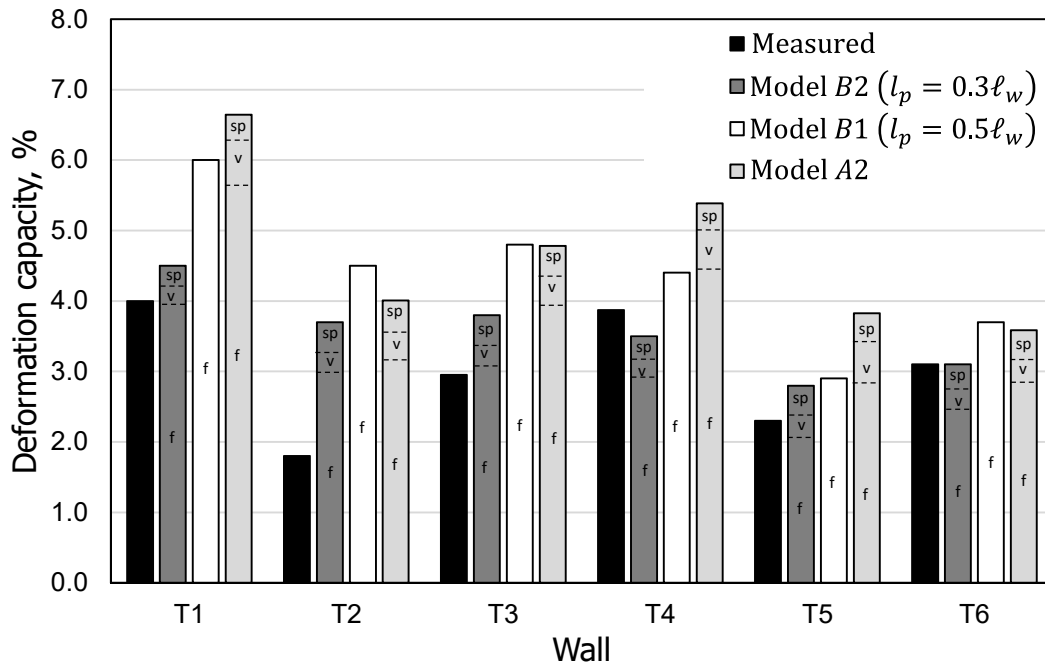


Figure 258 – Idealized moment and curvature distributions for Model B



(a) Stem in compression



(b) Stem in tension

Figure 259 - Comparison of measured and calculated deformation capacity

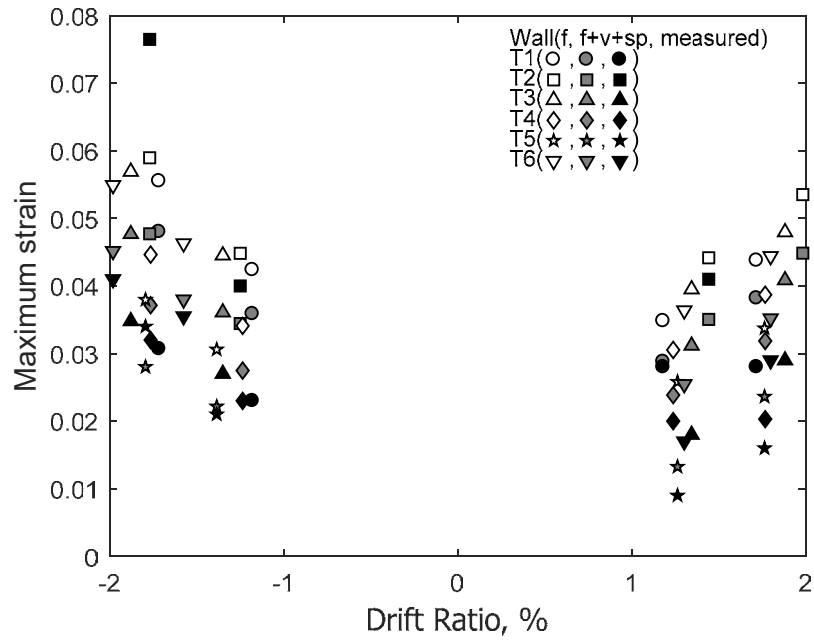


Figure 260 – Measured and calculated maximum tensile strain of the reinforcement using Model A

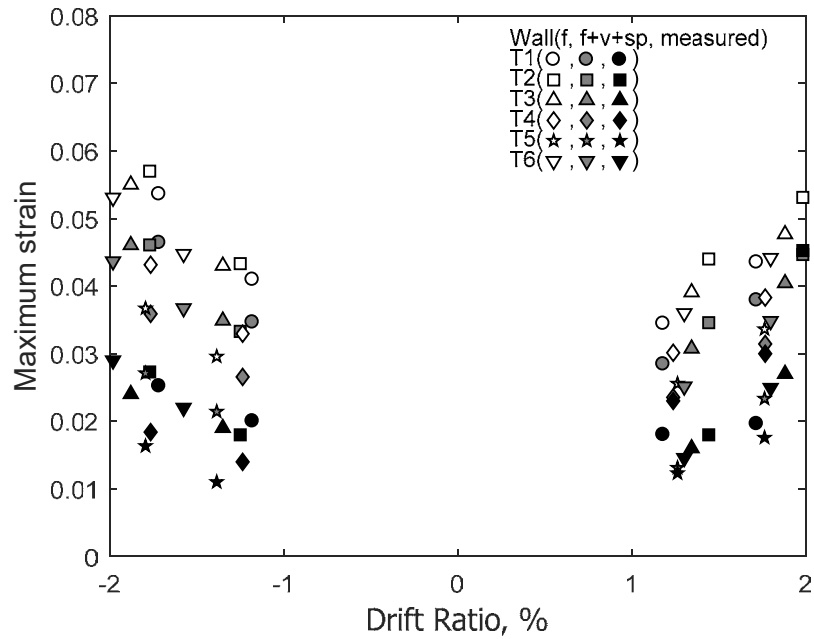


Figure 261 – Measured and calculated maximum tensile strain of concrete surface on a gauge length of 14 in. (356 mm) using Model A

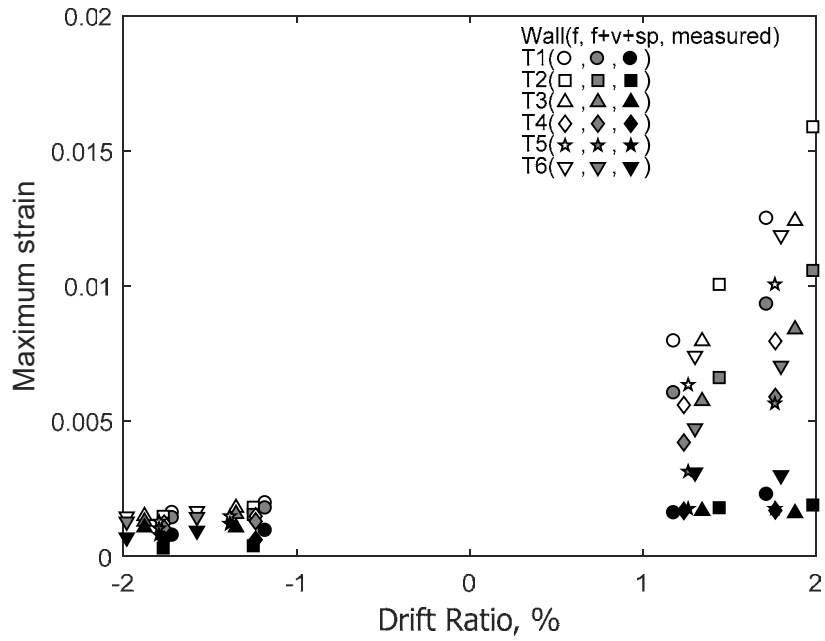


Figure 262 – Measured and calculated maximum compressive strain of concrete surface on a gauge length of 14 in. (356 mm) using Model A

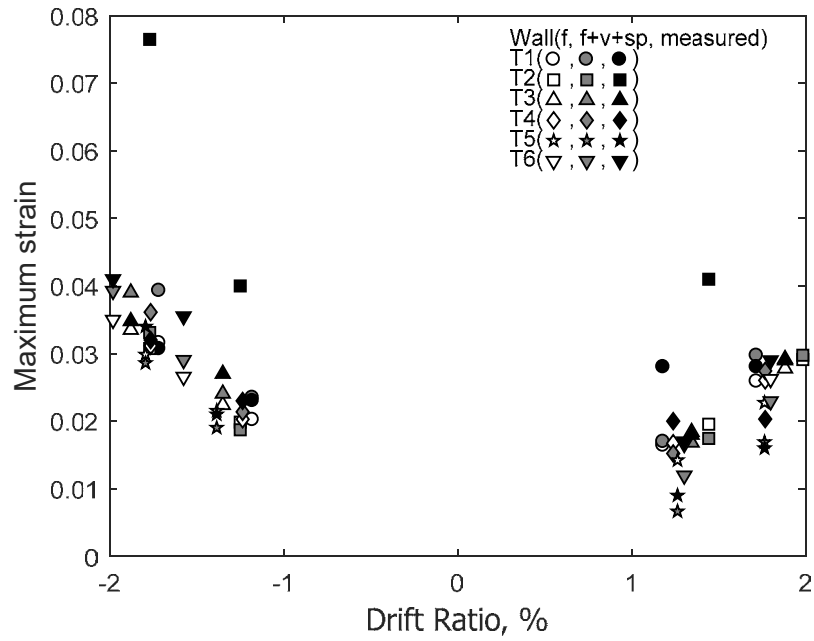


Figure 263 – Measured and calculated maximum tensile strain of the reinforcement using Model B

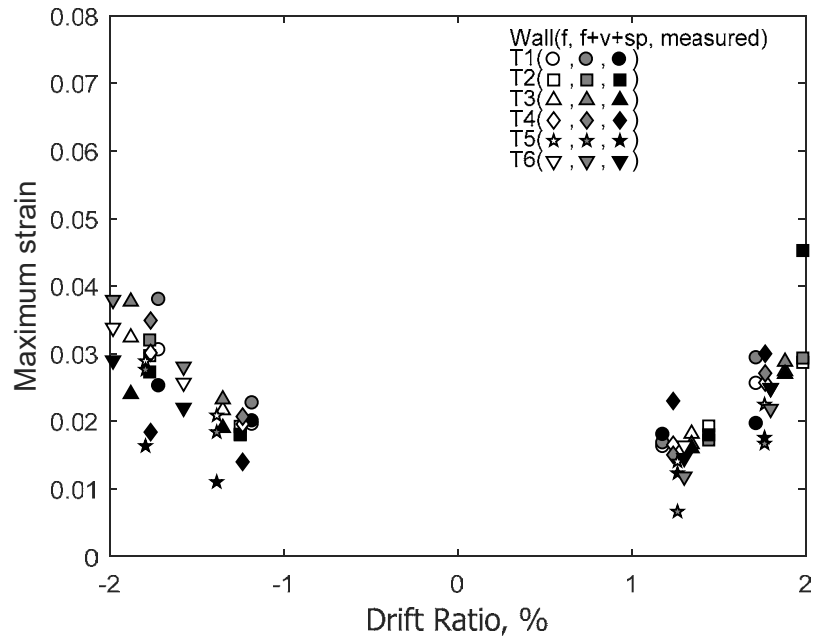


Figure 264 – Measured and calculated maximum tensile strain of concrete surface on a gauge length of 14 in. (356 mm) using Model B

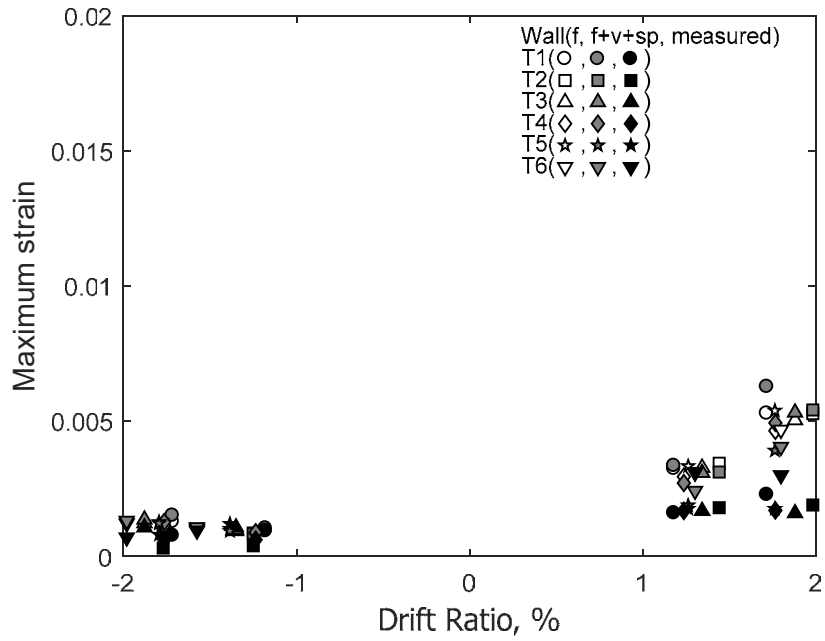


Figure 265 – Measured and calculated maximum compressive strain of concrete surface on a gauge length of 14 in. (356 mm) using Model B

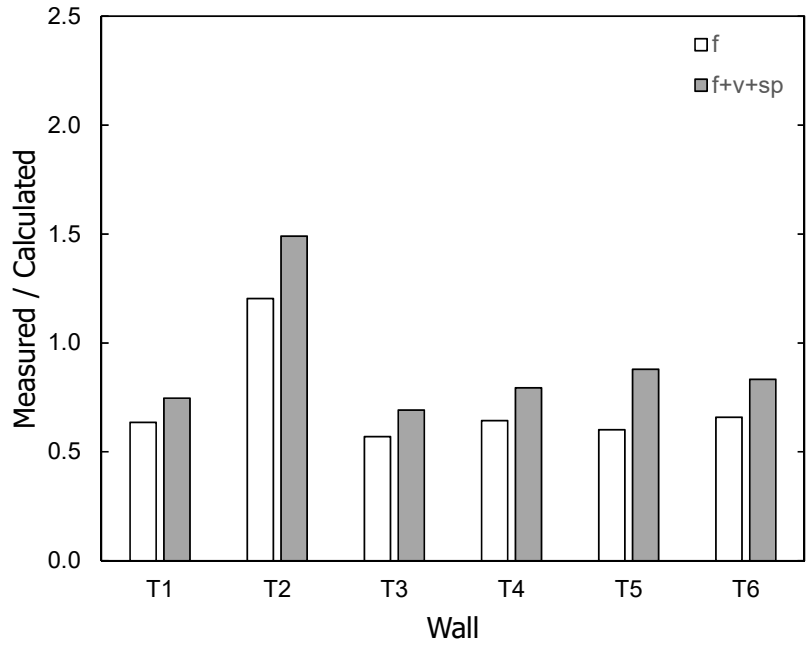


Figure 266 – Average of measured-to-calculated maximum tensile strain of reinforcement using Model A

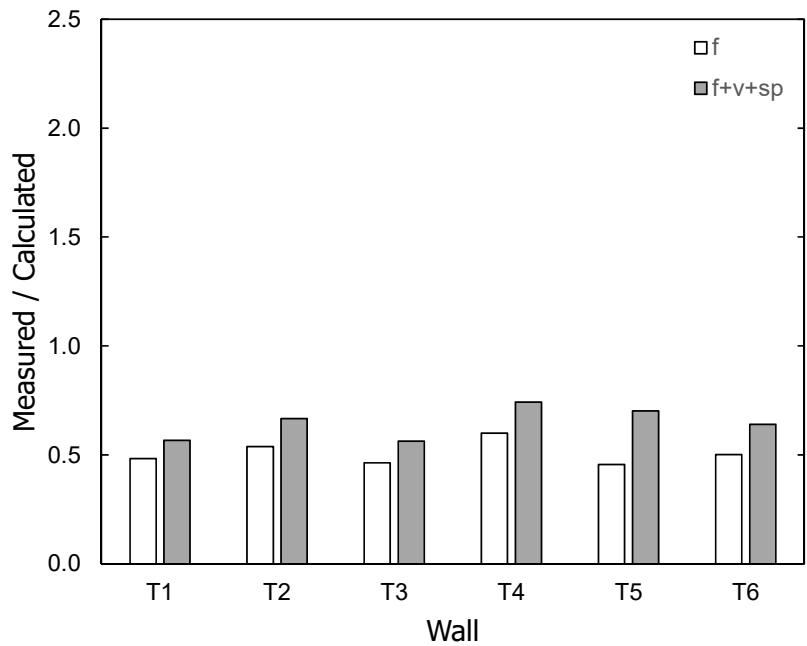


Figure 267 – Average of measured-to-calculated maximum tensile strain of concrete surface using Model A

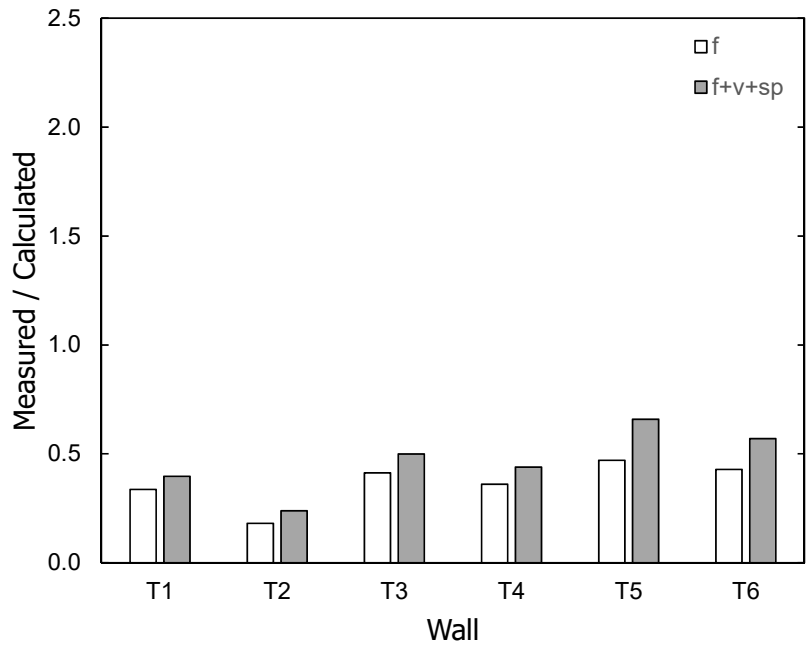


Figure 268 – Average of measured-to-calculated maximum compressive strain of concrete surface using Model A

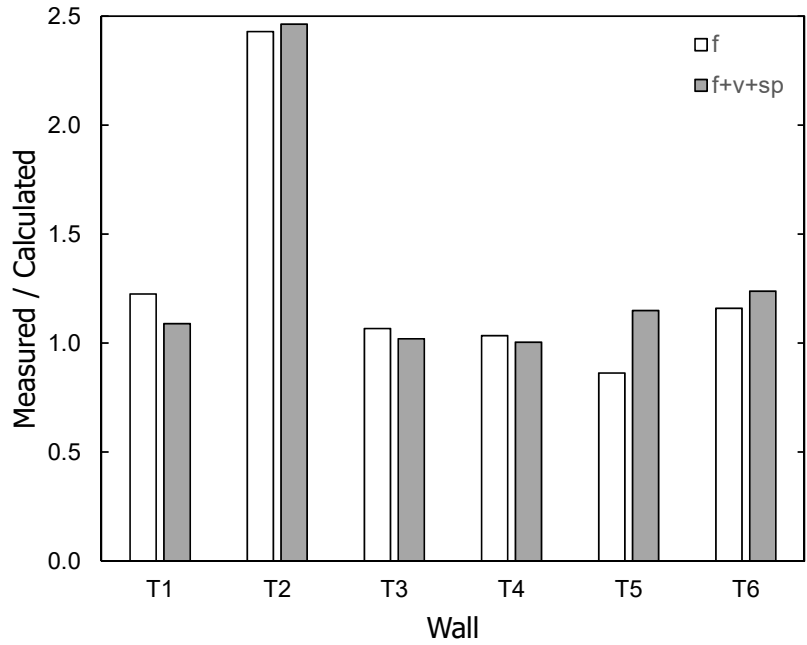


Figure 269 – Average of measured-to-calculated maximum tensile strain of reinforcement using Model B

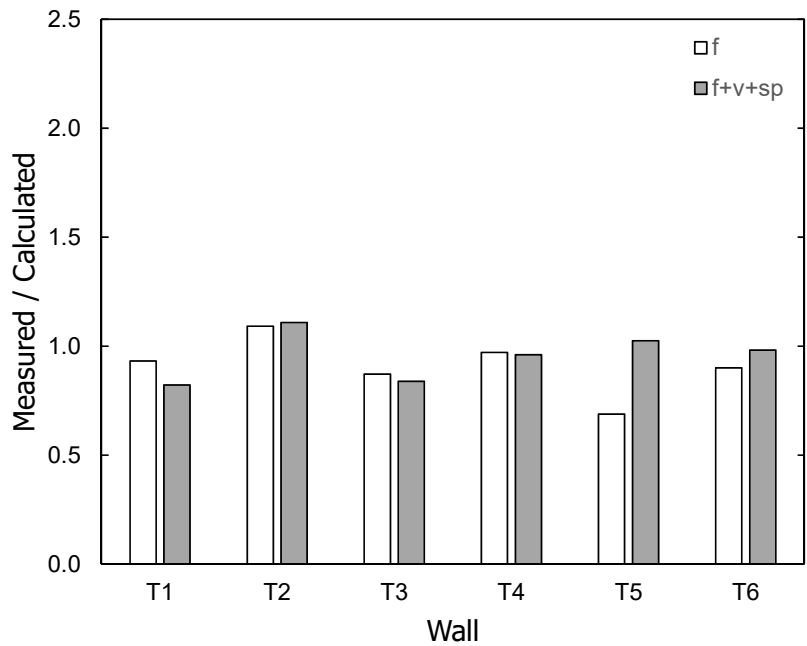


Figure 270 – Average of measured-to-calculated maximum tensile strain of concrete surface using Model B

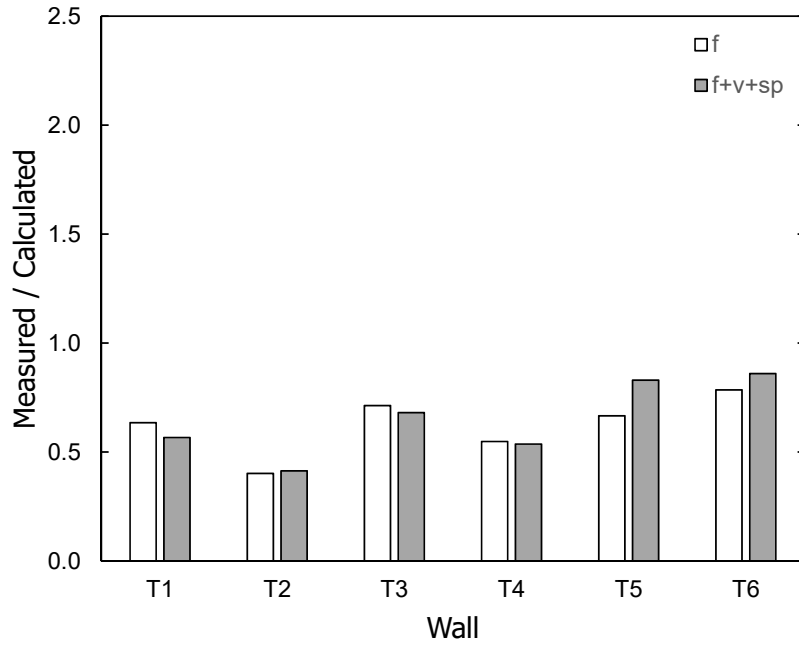


Figure 271 – Average of measured-to-calculated maximum compressive strain of concrete surface using Model B

APPENDIX A: NOTATION

A_{cv}	=	gross area of concrete section resisting shear ($t_w \ell_w$ for a T-shaped wall), in. ² (mm ²)
$A_{cv,eff}$	=	effective area of concrete section resisting shear ($\phi_K t_w \ell_w$ for a T-shaped wall), in. ² (mm ²)
A_g	=	gross area of concrete section, in. ² (mm ²)
A_s	=	area of reinforcement, in. ² (mm ²)
c	=	neutral axis depth measured from extreme compression fiber, in. (mm)
CM	=	cementitious material, includes portland cement and mineral admixtures (fly ash, slag cement, and silica fume)
d_b	=	bar diameter, in. (mm)
d_t	=	distance from extreme compression fiber to extreme layer of longitudinal tension reinforcement, in. (mm)
d_1	=	length of the primary diagonal (from top left to bottom right) of a station, in. (mm) (Figure 163)
d_2	=	length of the secondary diagonal (from bottom left to top right) of a station, in. (mm) (Figure 163)
DR	=	drift (lateral displacement) divided by height (from base of wall to point of drift measurement)
e	=	elongation of flexural reinforcement due to strain penetration, in. (mm)
E_c	=	modulus of elasticity of concrete, ksi (MPa)
E_h	=	hysteretic energy dissipation index, Eq. 21
E_s	=	modulus of elasticity of reinforcement, ksi (MPa)
E_{sh}	=	tangent modulus at the onset of strain-hardening, ksi (MPa)
f'_c	=	specified compressive strength of concrete, ksi (MPa)
f''_c	=	peak compressive stress for unconfined concrete, ksi (MPa)
f''_{cc}	=	peak compressive stress for confined concrete, ksi (MPa)
f_{cm}	=	measured average compressive strength of concrete, ksi (MPa)
f_{cr}	=	critical buckling stress, ksi (MPa)

f_{ct}	=	measured average splitting tensile strength of concrete, psi (MPa)
f_r	=	modulus of rupture of concrete, ksi (MPa)
f_{st}	=	stress corresponding to strain ϵ_{st} at onset of fracture, ksi (MPa)
f_t	=	peak stress or tensile strength of reinforcement, ksi (MPa)
f_y	=	yield strength of reinforcement, ksi (MPa)
f_{yh}	=	yield strength of confinement reinforcement, ksi (MPa)
f_{yp}	=	reinforcement stress defining the proportional limit, ksi (MPa)
F_m	=	force associated with Δ_m , kips (kN)
F_y	=	force associated with yield point, kips (kN)
G_c	=	shear modulus of concrete, taken as $E_c/2.4$, ksi (MPa)
h_b	=	dimension at bottom side of station, in. (mm) (Figure 163)
h_i	=	height of Layer i , in. (mm) (Figure 17 and Figure 18)
h_t	=	dimension at top side of station, in. (mm) (Figure 163)
h_y	=	height from base of wall (top of base block) to top horizontal potentiometers, +286 in. (7260 mm) for specimens T5 and T6, in. (mm) (Figure 15)
$h_{y,i}$	=	distance from centroid of Layer i to top horizontal potentiometers at elevation +286 in. (7260 mm) for specimens T5 and T6, in. (mm) (Figure 15, Figure 17, and Figure 18)
h_w	=	height from base of wall to point of load application, in. (mm)
i	=	counter or index to identify order or position
I_{cr}	=	moment of inertia of cracked transformed section using reinforcement data from Figure 7, in. ⁴ (mm ⁴)
I_{eff}	=	effective moment of inertia, in. ⁴ (mm ⁴)
I_g	=	moment of inertia of gross concrete section about centroidal axis, neglecting reinforcement, in. ⁴ (mm ⁴)
j	=	counter or index to identify order or position
k	=	counter or index to identify order or position
K	=	secant stiffness, kips/in. (kN/m)

K_{cc}	=	ratio of confined to unconfined concrete compressive strength
K_e	=	secant stiffness at $V = V_{0.8} = 0.8 V_{max}$, kips/in. (kN/m)
K_f	=	stiffness associated with flexural deformation, kips/in. (kN/m)
K_{f,I_g}	=	stiffness associated with flexural deformation based on I_g , kips/in. (kN/m)
K_{py}	=	post-yield stiffness, kips/in. (kN/m)
K_{sp}	=	stiffness associated with strain penetration (below base of wall), kips/in. (kN/m)
K_u	=	unloading stiffness, kips/in. (kN/m)
K_v	=	stiffness associated with shear deformation, kips/in. (kN/m)
$K_{wall,calc}$	=	calculated stiffness of wall, kips/in. (kN/m)
$K_{wall,meas}$	=	measured stiffness of wall, kips/in. (kN/m)
ℓ_{Cicj}	=	initial distance along x axis between markers at Columns i and j for a given row (or located at the same elevation), in. (mm) (Figure 17 and Figure 18)
ℓ_d	=	development length or length of embedment required to develop the yield stress of reinforcement, in. (mm)
ℓ_j	=	width of station j , in. (mm) (Figure 17 and Figure 18)
ℓ_p	=	length of plastic hinge, in. (mm)
ℓ_w	=	length of wall section in direction of shear force, in. (mm)
\bar{M}	=	maximum moment from moment-curvature analysis, ft-kips (m-kN)
M_{cr}	=	moment at onset of cracking, ft-kips (m-kN)
M_n	=	nominal flexural strength calculated for a maximum concrete compressive strain of 0.003 and perfectly elastoplastic reinforcement with specified (nominal) yield strength (following ACI 318-14 ^[1]) ft-kips (m-kN)
M_y	=	moment corresponding to curvature ϕ_y , ft-kips (m-kN)
M_{yc}	=	moment corresponding to yield of tension reinforcement at centroid of confined boundary element, ft-kips (m-kN)
M_{yd}	=	moment corresponding to yield of tension reinforcement at distance $0.8\ell_w$ from extreme compression fiber, ft-kips (m-kN)
M_{y1}	=	moment corresponding to first yield of tension reinforcement (reinforcement

		located at d_t), ft-kips (m-kN)
M_u	=	moment corresponding to limiting or ultimate curvature ϕ_u , ft-kips (m-kN)
n_ℓ	=	number of layers bounded by optical markers (Figure 17 and Figure 18)
n_s	=	number of stations bounded by optical markers (Figure 17 and Figure 18)
P	=	axial load at the base of wall, kips (kN)
t_w	=	thickness of wall stem, in. (mm)
u	=	uniform bond stress associated with ℓ_d , psi (MPa)
v_ℓ	=	dimension at left side of a station, in. (mm) (Figure 163)
v_{max}	=	shear stress associated with V_{max} , psi (MPa)
v_r	=	dimension at right side of a station, in. (mm) (Figure 163)
v_s	=	nominal shear stress attributed to the transverse reinforcement, psi (MPa)
V	=	shear force applied at the top of the wall, kips (kN)
V_m	=	shear associated with Δ_m , kips (kN)
V_{max}	=	maximum measured shear force per loading direction, kips (kN)
V_{Mn}	=	shear associated with M_n based on a nominal shear span of 25 ft., kips (kN)
V_n	=	nominal shear strength, kips (kN)
V_u	=	shear force corresponding to ultimate curvature ϕ_u , kips (kN)
V_y	=	shear force corresponding to yield curvature ϕ_y , kips (kN)
w_{peak}	=	crack width measured at peak drift during second excursion to a target drift, in. (mm)
w_{zero}	=	crack width measured at zero applied shear after second excursion to a target drift, in. (mm)
W	=	hysteretic energy dissipated during half cycle of loading, in.-kips (m-kN)
X	=	coordinate of reinforcement layer (Figure 7), in. (mm)
X_{cg}	=	coordinate of centroidal axis of gross section, neglecting reinforcement (Figure 7), in. (mm)
$X_{cg,cr}$	=	distance from extreme compression fiber to neutral axis depth of cracked section transformed to concrete, in. (mm)
Y_{Ricj}	=	displacement of a marker (at Row i Column j) along y axis, in. (mm)

(Figure 17 and Figure 18)

Z_{cc}	=	parameter to define the descending branch of the stress-strain curve for confined concrete
Z_{uc}	=	parameter to define the descending branch of the stress-strain curve for unconfined concrete
α	=	stiffness reducing exponent
α_{sp}	=	strain penetration amplification factor
β_ℓ	=	fraction of ℓ_d
β_u	=	fraction of u
β_y	=	fraction of f_y
γ_i	=	average shear distortion for Layer i , rad
$\gamma'_{i,j}$	=	shear distortion in Layer i at station j , rad
δ_{base}	=	horizontal displacement of the base block, in. (mm)
δ_{top}	=	horizontal displacement measured by top horizontal potentiometers at elevation +286 in. (7260 mm) for specimens T5 and T6, in. (mm)
Δ_{bo}	=	component of drift due to flexural deformation and strain penetration measured between base block optical markers and first row of markers, in. (mm) (Figure 17 and Figure 18)
Δ_{bs}	=	shear component of drift (due to base shearing) measured between base block optical markers and first row of markers, in. (mm) (Figure 17 and Figure 18)
Δ_f	=	drift (lateral displacement) due to flexion, in. (mm)
$\Delta_{f,p}$	=	displacement due to flexure considering only plastic curvature, in. (mm)
$\Delta_{f,y}$	=	displacement due to flexure considering only yield curvature, in. (mm)
Δ_m	=	peak displacement during a loading cycle, in. (mm)
Δ_{max}	=	previously attained maximum displacement in a direction of loading, in. (mm)
Δ_{sp}	=	drift (lateral displacement) due to strain penetration, in. (mm)
Δ_v	=	drift (lateral displacement) due to shear deformation, in. (mm)
Δ_X	=	average horizontal displacement of a row of markers, in. (mm)
Δ_y	=	notional yield displacement, in. (mm)

Δ_0	=	measured drift corresponding to zero shear (unloading from Δ_m), in. (mm)
ε_{cc}	=	maximum strain corresponding to peak stress for confined concrete
$\varepsilon_{c,core}$	=	maximum calculated strain in the confined concrete
ε_{cu}	=	maximum strain capacity assigned to confined concrete
ε_{sf}	=	measured fracture elongation of reinforcement
ε_{sh}	=	post-yield reinforcement strain where strain hardening begins
ε_{st}	=	strain at onset of reinforcement fracture
ε_{su}	=	uniform elongation of reinforcement or strain corresponding to f_t
ε_0	=	strain corresponding to peak stress of unconfined concrete
θ_{base}	=	rotation of the base block about an axis normal to the plane of the wall stem, rad
θ_{bo}	=	base opening rotation due to flexural deformation and strain penetration measured between base block optical markers and first row of markers (Figure 17 and Figure 18), rad
θ_{cr}	=	rotation due to flexural deformation at ϕ_{cr} , rad
θ_f	=	rotation due to flexural deformation, rad
θ_i	=	rotation due to flexural deformation for Layer i , rad
θ_y	=	rotation due to flexural deformation at ϕ_y , rad
θ_u	=	rotation due to flexural deformation at ϕ_u , rad
λ	=	number of bar diameters over which the yield strain of reinforcement is assumed to occur uniformly, $\lambda = \ell_d / (2d_b)$
λ_1	=	coefficient to define the location of the cracking point along the wall height
λ_2	=	coefficient to define the location of the yield point along the wall height
ρ_ℓ	=	ratio of area of distributed longitudinal reinforcement to gross concrete area normal to that reinforcement
ρ_s	=	ratio of volume of confining reinforcement to total volume of confined concrete, measured out-to-out of hoops
ρ_t	=	ratio of area of distributed transverse reinforcement to gross concrete area normal to that reinforcement

- ϕ' = calculated post-yield curvature associated with a target displacement
- ϕ_K = ratio of effective shear stiffness to uncracked stiffness
- ϕ_{cr} = curvature at onset of cracking, 1/in. (1/mm)
- ϕ_y = curvature associated with the tensile reinforcement reaching the yield strain, 1/in. (1/mm)
- ϕ_u = ultimate curvature corresponding to a compressive strain of 0.01 for confined concrete or ε_{su} for reinforcing bars, 1/in. (1/mm)
- ψ = distortion due to expansion (Figure 164), rad

APPENDIX B: POST-YIELD STRAIN PENETRATION

This appendix is based on the model proposed by Huq et al.^[37] The theoretical background presented in Huq et al.^[37] is repeated here for convenience. Experimental data from walls T5 and T6 are included to adjust the model.

Theoretical Background

Reinforcing bars subjected to tension at the base of a reinforced concrete wall can undergo large strain demands that penetrate into the support. Bar strains along the embedded length are associated with bar elongation and reinforcement slip, which manifest as a rotation at the wall base that contributes to the total lateral displacement at the top of the wall.

In this appendix, a model is proposed for estimating the contribution of reinforcement slip (due to strain penetration) to lateral displacement of a reinforced concrete wall responding in the inelastic range.

Assuming a uniform bond stress u acts on a reinforcing bar of diameter d_b along the development length ℓ_d , the total bond force to develop the yield stress f_y is given by

$$\ell_d \pi d_b u = \frac{\pi d_b^2}{4} f_y \quad \text{Eq. B.1}$$

which simplifies to

$$\frac{\ell_d}{d_b} = \frac{f_y}{4u} \quad \text{Eq. B.2}$$

Sezen and Moehle^[80] proposed a model with a stepped bond stress along the embedded length of the reinforcing bar, as shown in Figure B.1. Based on this model, for a bar to develop a post-yield stress of $(1+\beta_y)f_y$ requires an embedment length of $(1+\beta_\ell)\ell_d$. It is assumed that a uniform bond stress u acts over the length ℓ_d where the bar has not yielded and a reduced bond stress $\beta_u u$ acts over the length $\beta_\ell \ell_d$ where the bar has yielded. A relationship between β_ℓ , β_u , and β_y is derived by substituting the above assumptions into Eq. B.2 to obtain

$$\beta_\ell \frac{\ell_d}{d_b} = \frac{\beta_y f_y}{\beta_u 4u} \quad \text{Eq. B.3}$$

where the use of ℓ_d/d_b from Eq. B.2 in Eq. B.3 simplifies into Eq. B.4:

$$\beta_\ell = \frac{\beta_y}{\beta_u} \quad \text{Eq. B.4}$$

The elongation e due to strain penetration of a yielding bar, as shown in Figure B.1 (at the top of the base block), is obtained by integrating the bar strain diagram over the length $\ell_d + \beta_\ell \ell_d$, resulting in

$$e = \frac{\varepsilon_y}{2} \ell_d + \left(\frac{\varepsilon_s + \varepsilon_y}{2} \right) \beta_\ell \ell_d \quad \text{Eq. B.5}$$

Eq. B.5 was derived assuming zero slip at the unloaded end of the bar. To simplify Eq. B.5, ℓ_d is expressed as a function of d_b using

$$\ell_d = 2 \lambda d_b \quad \text{Eq. B.6}$$

where λ represents the number of bar diameters over which the yield strain of reinforcement is assumed to occur uniformly. Substituting Eq. B.6 into Eq. B.5 provides

$$e = \lambda d_b \varepsilon_y \left[1 + \beta_\ell \left(1 + \frac{\varepsilon_s}{\varepsilon_y} \right) \right] \quad \text{Eq. B.7}$$

The rotation at the wall base due to strain penetration is calculated using Eq. B.8 based on the elongation divided by the distance from the bar to the neutral axis depth ($d_t - c$).

$$\theta_{sp} = \frac{e}{d_t - c} = \lambda d_b \frac{\varepsilon_y}{d_t - c} \left[1 + \beta_\ell \left(1 + \frac{\varepsilon_s}{\varepsilon_y} \right) \right] \quad \text{Eq. B.8}$$

from which the displacement at a distance h_w from the support is obtained using

$$\Delta_{sp} = \lambda d_b \phi_y \left[1 + \beta_\ell \left(1 + \frac{\varepsilon_s}{\varepsilon_y} \right) \right] h_w \quad \text{Eq. B.9}$$

where $\varepsilon_y/(d_t - c)$ is taken as an approximate measure of the yield curvature ϕ_y . Eq. B.9 is further simplified using

$$\Delta_{sp} = \alpha_{sp} \lambda d_b \phi_y h_w \quad \text{Eq. B.10}$$

where

$$\alpha_{sp} = \left[1 + \beta_\ell \left(1 + \frac{\varepsilon_s}{\varepsilon_y} \right) \right] \quad \text{Eq. B.11}$$

Eq. B.10 only applies where $\varepsilon_s > \varepsilon_y$ and bar slip at the unloaded end of the bar is negligible. For the condition of $\varepsilon_s = \varepsilon_y$, $\beta_\ell = 0$ (given that ℓ_d is the required embedment length to develop f_y , see Figure B.1) resulting in $\alpha_{sp} = 1$ per Eq. B.11. Therefore, Eq. B.10 can be expressed as a function of the deformation due to strain penetration at yield $\Delta_{sp,y}$, using

$$\Delta_{sp} = \alpha_{sp} \Delta_{sp,y} \quad \text{Eq. B.12}$$

where $\Delta_{sp,y}$ is defined by

$$\Delta_{sp,y} = \lambda d_b \phi_y h_w \quad \text{Eq. B.13}$$

and α_{sp} represents the amplification factor of $\Delta_{sp,y}$ to obtain Δ_{sp} in Eq. B.12. The definition of deformation due to strain penetration at yield in Eq. B.13 is consistent with the definition of deformation due to strain penetration presented in Table 13.

The sensitivity of β_ℓ to parameters β_u and β_y is shown in Figure B.2. Values of $\beta_y = 0.25$ (corresponding to a stress of $1.25f_y$) and β_u between 0.5 and 1.0 provide values of β_ℓ between 0.5 and 0.25, respectively. In this study, $\beta_u = 0.75$ was adopted, which for $\beta_y = 0.25$ provides $\beta_\ell = 0.33$.

It is important to note that to develop $1.25f_y$ based on ACI 408^[2], the development length needs to increase by approximately 1.4 for $f_y = 60$ ksi (414 MPa) and 1.3 for $f_y = 100$ ksi (690 MPa), consistent with $\beta_\rho = 0.33$ for the adopted value of $\beta_u = 0.75$. The development length equations in ACI 408^[2] have been shown to work for high-strength reinforcement subjected to post-yield stresses of up to 155 ksi (1070 MPa)^[49].

For an indication of the range of values to expect for α_{sp} , Table B.1 shows calculated data for T1 and T4 with Grade 60 (420) and Grade 100 (690) reinforcement, respectively, at strains of 0.02, 0.03, 0.04, and 0.05. Values of β_y were assumed to vary from 0.1 to 0.25 for strains between 0.02 and 0.05. A value of $\beta_u = 0.75$ was assumed constant for the values of β_y considered. The data in Table B.1 are plotted in Figure B.3 with a low-bound estimate of α_{sp} given by

$$\alpha_{sp} = 2 DR \quad \text{Eq. B.14}$$

where the drift ratio DR (in percent) is limited to values between 1 and 2. Figure B.3 shows that values of α_{sp} are in the range between 2 and 9 for drift ratios between 1 and 3%.

The measured relationship between the longitudinal strain of reinforcement and the drift ratio for T5 and T6 are combined with the data for T1 and T4^[37] to derive values of α_{sp} as a function of drift ratio in Table B.2. Post-yield strain data from T3 at the base of the wall were not available whereas data from T2 were not considered due to its sub-par performance. The calculated values of α_{sp} in Table B.2 are plotted versus drift ratio in Figure B.4. The plotted data suggest that for walls with Grade 60 (420) and Grade 100 (690) reinforcement, a low-bound estimate for α_{sp} may be defined using Eq. B.14 but for walls with Grade 120 (830) reinforcement a lower value is more appropriate, as defined by

$$\alpha_{sp} = 1.5DR$$

Eq. B.15

The lower value of α_{sp} for T5 is mostly due to lower strains measured in the longitudinal reinforcement of T5 for drift ratios between 1 and 2%. The reinforcement strain demands in T5 were very likely affected by the roundhouse shape (without yield plateau) of the stress-strain curve for the Grade 120 (830) reinforcement.

Table B.1 – Strain penetration amplification factor α_{sp} based on Eq. B.12^{a,b}

ε_s	β_y^c	β_u	β_ℓ	DR^d		α_{sp}^e		α_{sp}/DR^d	
				T1	T4	T1	T4	T1	T4
0.02	0.10	0.75	0.13	1.14	0.89	2.24	1.94	1.96	2.18
0.03	0.15	0.75	0.20	1.71	1.33	3.69	3.01	2.15	2.26
0.04	0.20	0.75	0.27	2.29	1.78	5.69	4.49	2.49	2.53
0.05	0.25	0.75	0.33	2.86	2.22	8.24	6.37	2.88	2.87

^aData from Huq et al.^[37]

^bFor notation and definitions see APPENDIX A: NOTATION.

^cBased on a strain-hardening modulus of $5f_y$ for strains between 0.02 and 0.05.

^dDrift ratio (in percent) defined from $\varepsilon_s \cong 1.75 DR$ for T1 (based on negative loading direction) and $\varepsilon_s \cong 2.25 DR$ for T4 (based on negative loading direction). Negative loading direction corresponds to stem in tension.

^eAmplification factor for strain penetration, $\alpha_{sp} = 1 + \beta_\ell \left(1 + \frac{\varepsilon_s}{\varepsilon_y}\right)$, where $\varepsilon_y = 0.00241$ for T1 and $\varepsilon_y = 0.00331$ for T4.

Table B.2 – Strain penetration amplification factor α_{sp} based on Eq. B.12^a

ε_s	β_y^b	β_u	β_ℓ	DR^c			α_{sp}^d			α_{sp}/DR^c					
				T1	T4	T5	T6	T1	T4	T5	T6	T1	T4	T5	T6
0.02	0.10	0.75	0.13	1.18	0.91	1.18	0.95	2.24	1.94	1.73	1.82	1.90	2.04	1.47	1.92
0.03	0.15	0.75	0.20	1.76	1.36	1.76	1.43	3.69	3.01	2.55	2.75	2.09	2.1	1.44	1.93
0.04	0.20	0.75	0.27	2.35	1.82	2.35	1.90	5.69	4.49	3.66	4.03	2.42	2.36	1.56	2.12
0.05	0.25	0.75	0.33	2.94	2.27	2.94	2.38	8.24	6.37	5.08	5.65	2.80	2.67	1.73	1.92

^aFor notation and definitions see APPENDIX A: NOTATION.

^bBased on a strain-hardening modulus of $5f_y$ for strains between 0.02 and 0.05.

^cDrift ratio (in percent) defined using $\varepsilon_s \cong 1.7 DR$ for T1, $\varepsilon_s \cong 2.1 DR$ for T4 and T6, and $\varepsilon_s \cong 1.7 DR$ for T5. These strains are based on strain gauge data (based on negative loading direction in Figure 113 in reference 43 for T1, Figure 112 in reference 43 for T4, Figure 56 for T5, and Figure 61 for T6). Negative loading direction corresponds to stem in tension.

^dAmplification factor for strain penetration, $\alpha_{sp} = 1 + \beta_\ell \left(1 + \frac{\varepsilon_s}{\varepsilon_y}\right)$, where $\varepsilon_y = 0.00241$ for T1, $\varepsilon_y = 0.00331$ for T4, $\varepsilon_y = 0.00445$ for T5, and $\varepsilon_y = 0.00386$ for T6.

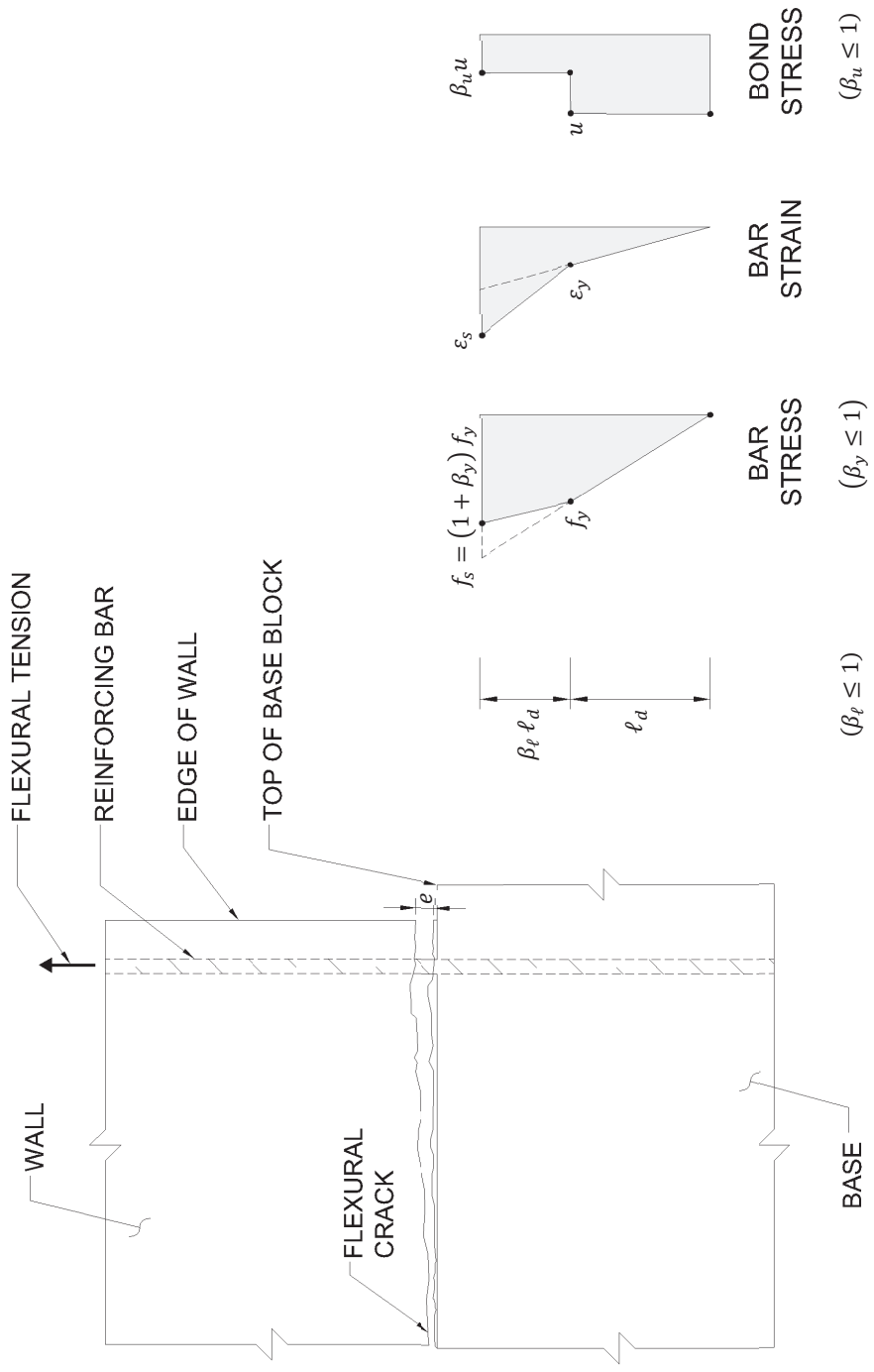


Figure B.1 – Post-yield strain penetration assumptions^[37]

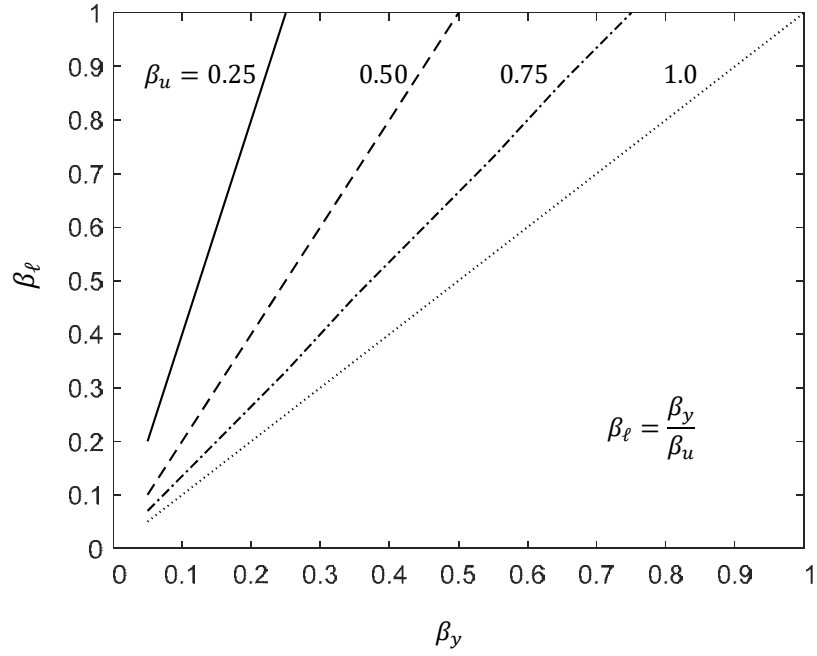


Figure B.2 – Influence of β_u and β_y on β_l ^[37]

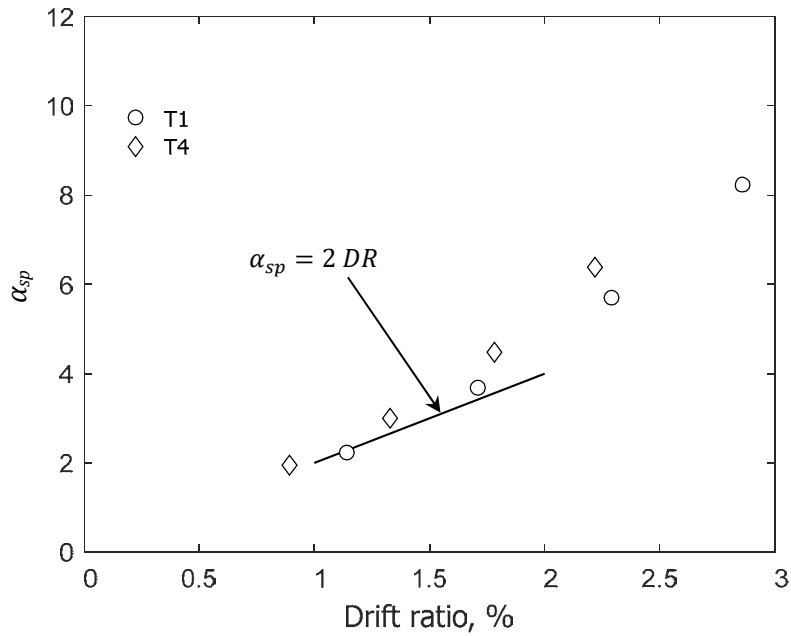


Figure B.3 – Strain penetration amplification factor α_{sp} versus drift ratio, based on Table B.1^[37]

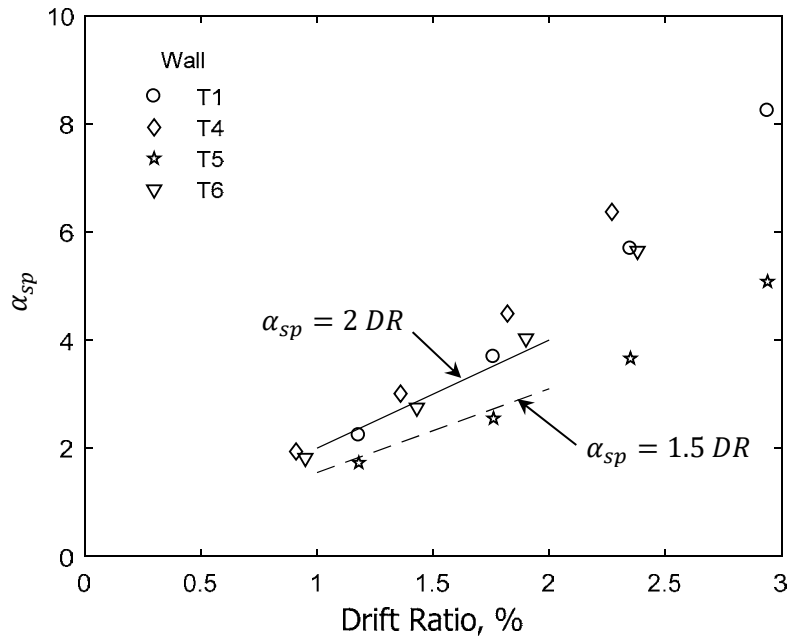


Figure B.4 – Strain penetration factor α_{sp} versus drift ratio, based on Table B.2